

MAY 2022

AJNR

VOLUME 43 • PP 649-789

AJNR

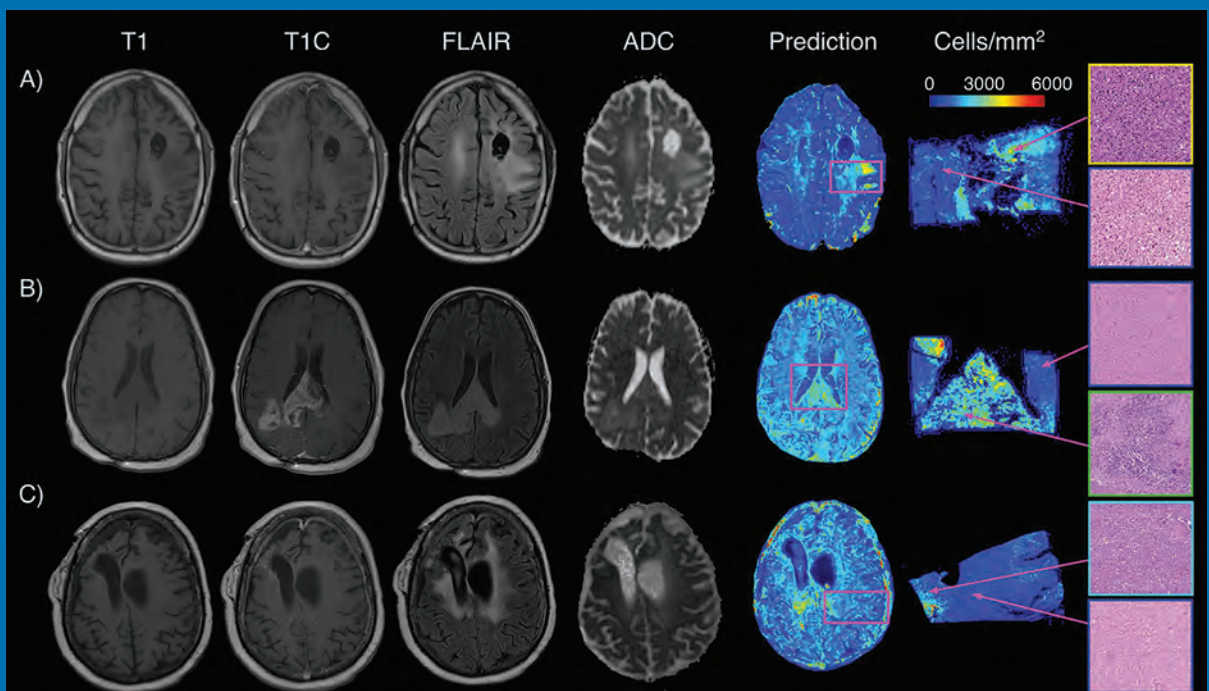
AMERICAN JOURNAL OF NEURORADIOLOGY

MAY 2022
VOLUME 43
NUMBER 5
WWW.AJNR.ORG

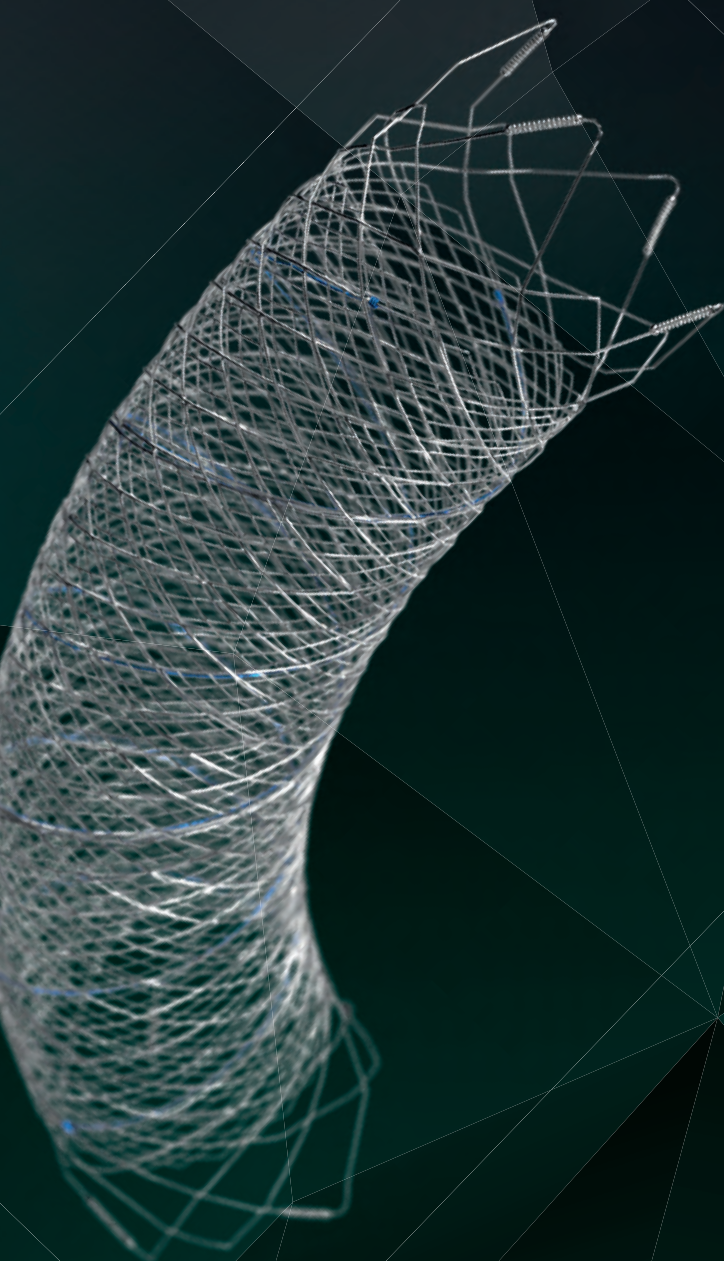
THE JOURNAL OF DIAGNOSTIC AND
INTERVENTIONAL NEURORADIOLOGY

Identification of brain tumor invasion beyond traditional MRI-defined margins
Perfusion alterations in autoimmune encephalitis
Yield of repeat angiography in occult subarachnoid hemorrhage
Stent screw–assisted internal fixation in patients with severe vertebral collapse

Official Journal ASNR • ASFNR • ASHNR • ASPNR • ASSR



Introducing FRED™ X™



THE NEXT ADVANCEMENT IN FLOW DIVERSION TECHNOLOGY

The FRED™ X Flow Diverter features the same precise placement and immediate opening of the FRED™ Device, now with X Technology. X Technology is a covalently bonded, nanoscale surface treatment, designed to:

- » **Reduce material thrombogenicity¹**
- » **Maintain natural vessel healing response^{2,3,4}**
- » **Improve device deliverability and resheathing¹**

The only FDA PMA approved portfolio with a 0.021" delivery system for smaller device sizes, and no distal lead wire.



For more information, contact your local MicroVention sales representative or visit our website. www.microvention.com



* Data is derived from in vivo and ex vitro testing and may not be representative of clinical performance.

¹ Data on file

² Tanaka M et al. Design of biocompatible and biodegradable polymers based on intermediate water concept. *Polymer Journal*. 2015;47:114-121.

³ Tanaka M et al. Blood compatible aspects of poly(2-methoxyethylacrylate) (PMEA) – relationship between protein adsorption and platelet adhesion on PMEA surface. *Biomaterials*. 2000;21:1471-1481.

⁴ Schiel L et al. X Coating™: A new biopassive polymer coating. *Canadian Perfusion Canadienne*. June 2001;11(2):9.

Indications for Use: The FRED X System is indicated for use in the internal carotid artery from the petrous segment to the terminus for the endovascular treatment of adult patients (22 years of age or older) with wide-necked (neck width 4 mm or dome-to-neck ratio < 2) saccular or fusiform intracranial aneurysms arising from a parent vessel with a diameter 2.0 mm and 5.0 mm.

Rx Only: Federal (United States) law restricts this device to sale by or on the order of a physician.

MICROVENTION, FRED and HEADWAY are registered trademarks of MicroVention, Inc. in the United States and other jurisdictions. Stylized X is a trademark of MicroVention, Inc. © 2022 MicroVention, Inc. MM1222 US 02/22

WEB™ 17

Aneurysm Embolization System

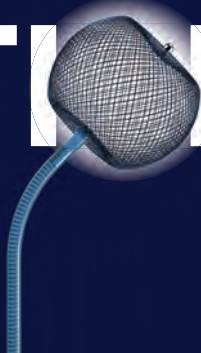
LOWER PROFILE



NEW SIZES



MORE ACCESS OPTIONS



INDICATIONS FOR USE:

The WEB Aneurysm Embolization System is intended for the endovascular embolization of ruptured and unruptured intracranial aneurysms and other neurovascular abnormalities such as arteriovenous fistulae (AVF). The WEB Aneurysm Embolization System is also intended for vascular occlusion of blood vessels within the neurovascular system to permanently obstruct blood flow to an aneurysm or other vascular malformation.

POTENTIAL COMPLICATIONS:

Potential complications include but are not limited to the following: hematoma at the site of entry, aneurysm rupture, emboli, vessel perforation, parent artery occlusion, hemorrhage, ischemia, vasospasm, clot formation, device migration or misplacement, premature or difficult device detachment, non-detachment, incomplete aneurysm filling, revascularization, post-embolization syndrome, and neurological deficits including stroke and death. For complete indications, potential complications, warnings, precautions, and instructions, see instructions for use (IFU provided with the device).

VIA 21, 27, 33 - The VIA Microcatheter is intended for the introduction of interventional devices (such as the WEB device/stents/flow diverters) and infusion of diagnostic agents (such as contrast media) into the neuro, peripheral, and coronary vasculature.

VIA 17, 17 Preshaped - The VIA Microcatheter is intended for the introduction of interventional devices (such as the WEB device/stents/flow diverters) and infusion of diagnostic agents (such as contrast media) into the neuro, peripheral, and coronary vasculature.

The VIA Microcatheter is contraindicated for use with liquid embolic materials, such as n-butyl 2-cyanoacrylate or ethylene vinyl alcohol & DMSO (dimethyl sulfoxide).

The device should only be used by physicians who have undergone training in all aspects of the WEB Aneurysm Embolization System procedure as prescribed by the manufacturer.

RX Only: Federal law restricts this device to sale by or on the order of a physician.

For healthcare professional intended use only.



MicroVention Worldwide
Innovation Center

PH +1.714.247.8000

35 Enterprise
Aliso Viejo, CA 92656 USA
MicroVention UK Limited
MicroVention Europe, S.A.R.L.
MicroVention Deutschland GmbH
Website

PH +44 (0) 191 258 6777
PH +33 (1) 39 21 77 46
PH +49 211 210 798-0
microvention.com



WEB™ and VIA™ are registered trademarks
of Sequent Medical, Inc. in the United States.

©2021 MicroVention, Inc. MM1184 WW 11/2021



TRUST EARNED

What does seeing better with MultiHance® mean?^{1-4*}

MultiHance® demonstrated significantly improved visualization and contrast enhancement of CNS lesions when compared with Gadavist® at 0.1 mmol/kg.^{1†}

- The 0.1 mmol/kg dose of MultiHance demonstrated consistently better lesion visualization for all readers compared to all tested MR contrast agents.¹⁻⁴
- 3 blinded independent readers reported superiority for MultiHance in significantly ($P=.0001$) more patients for all evaluated end points. The opinions of the 3 readers were identical for 61.9%–73.5% of the patients, resulting in values of 0.414–0.629 for inter-reader agreement.

The individuals who appear are for illustrative purposes. All persons depicted are models and not real patients.

Please see Brief Summary of Prescribing Information including Boxed Warning on adjacent page.

*MRI imaging of the CNS in adult and pediatric patients to visualize lesions with abnormal BBB or abnormal vascularity of the brain, spine and associated tissues or to evaluate adults with known or suspected renal or aorto-ilio-femoral occlusive vascular disease.

MultiHance® (gadobenate dimeglumine) injection, 529 mg/mL and MultiHance® Multipack™ (gadobenate dimeglumine) injection, 529 mg/mL

Indications and Usage:

MultiHance® (gadobenate dimeglumine) injection, 529 mg/mL is a gadolinium-based contrast agent indicated for intravenous use in:

- Magnetic resonance imaging (MRI) of the central nervous system (CNS) in adults and pediatric patients (including term neonates) to visualize lesions with abnormal blood-brain barrier or abnormal vascularity of the brain, spine, and associated tissues and
- Magnetic resonance angiography (MRA) to evaluate adults with known or suspected renal or aorto-ilio-femoral occlusive vascular disease

IMPORTANT SAFETY INFORMATION:

WARNING: NEPHROGENIC SYSTEMIC FIBROSIS

Gadolinium-based contrast agents (GBCAs) increase the risk for NSF among patients with impaired elimination of the drugs. Avoid use of GBCAs in these patients unless the diagnostic information is essential and not available with non-contrasted MRI or other modalities. NSF may result in fatal or debilitating systemic fibrosis affecting the skin, muscle and internal organs.

- The risk for NSF appears highest among patients with:
 - chronic, severe kidney disease ($GFR < 30 \text{ mL/min/1.73m}^2$), or
 - acute kidney injury.
- Screen patients for acute kidney injury and other conditions that may reduce renal function. For patients at risk for chronically reduced renal function (e.g. age > 60 years, hypertension or diabetes), estimate the glomerular filtration rate (GFR) through laboratory testing.
- For patients at highest risk for NSF, do not exceed the recommended MultiHance dose and allow a sufficient period of time for elimination of the drug from the body prior to re-administration.

CONTRAINDICATIONS

MultiHance is contraindicated in patients with known allergic or hypersensitivity reactions to gadolinium-based contrast agents.

WARNINGS AND PRECAUTIONS

Nephrogenic Systemic Fibrosis: NSF has occurred in patients with impaired elimination of GBCAs. Higher than recommended dosing or repeated dosing appears to increase risk.

Hypersensitivity Reactions: Anaphylactic and anaphylactoid reactions have been reported, involving cardiovascular, respiratory, and/or cutaneous manifestations. Some patients experienced circulatory collapse and died. In most cases, initial symptoms occurred within minutes of MultiHance administration and resolved with prompt emergency treatment. Consider the risk for hypersensitivity reactions, especially in patients with a history of hypersensitivity reactions or a history of asthma or other allergic disorders.

Gadolinium Retention: Gadolinium is retained for months or years in several organs. The highest concentrations have been identified in the bone, followed by brain, skin, kidney, liver, and spleen. At equivalent doses, retention varies among the linear agents. Retention is lowest and similar among the macrocyclic GBCAs. Consequences of gadolinium retention in the brain have not been established, but they have been established in the skin and other organs in patients with impaired renal function. Minimize repetitive GBCA imaging studies, particularly closely spaced studies when possible.

Acute Renal Failure: In patients with renal insufficiency, acute renal failure requiring dialysis or worsening renal function have occurred with the use of GBCAs. The risk of renal failure may increase with increasing dose of the contrast agent. Screen all patients for renal dysfunction by obtaining a history and/or laboratory tests.

Extravasation and Injection Site Reactions: Extravasation of MultiHance may lead to injection site reactions, characterized by local pain or burning sensation, swelling, blistering, and necrosis. Exercise caution to avoid local extravasation during intravenous administration of MultiHance.

Cardiac Arrhythmias: Cardiac arrhythmias have been observed in patients receiving MultiHance in clinical trials. Assess patients for underlying conditions



MR Suite



LIFE FROM INSIDE

or medications that predispose to arrhythmias. The effects on QTc by MultiHance dose, other drugs, and medical conditions were not systematically studied.

Interference with Visualization of Certain Lesions: Certain lesions seen on non-contrast images may not be seen on contrast images. Exercise caution when interpreting contrast MR images in the absence of companion non-contrast MR images.

ADVERSE REACTIONS

The most commonly reported adverse reactions are nausea (1.3%) and headache (1.2%).

USE IN SPECIFIC POPULATIONS

Pregnancy: GBCAs cross the human placenta and result in fetal exposure and gadolinium retention. Use only if imaging is essential during pregnancy and cannot be delayed.

Lactation: There is no information on the effects of the drug on the breastfed infant or the effects of the drug on milk production. However, limited literature reports that breastfeeding after MultiHance administration to the mother would result in the infant receiving an oral dose of 0.001%-0.04% of the maternal dose.

Pediatric Use: MultiHance is approved for intravenous use for MRI of the CNS to visualize lesions with abnormal blood brain barrier or abnormal vascularity of the brain, spine, and associated tissues in pediatric patients from birth, including term neonates, to less than 17 years of age. Adverse reactions in pediatric patients were similar to those reported in adults. No dose adjustment according to age is necessary in pediatric patients two years of age and older. For pediatric patients, less than 2 years of age, the recommended dosage range is 0.1 to 0.2 mL/kg. The safety of MultiHance has not been established in preterm neonates.

Please see full Prescribing Information and Patient Medication Guide for additional important safety information for/regarding MultiHance (gadobenate dimeglumine) injection, 529 mg/mL at <https://www.braccoimaging.com/us-en/products/magnetic-resonance-imaging/multihance>

You are encouraged to report negative side effects of prescription drugs to the FDA. Visit www.fda.gov/medwatch or call 1-800-FDA-1088.

MultiHance is manufactured for Bracco Diagnostics Inc. by BIPSO GmbH – 78224 Singen (Germany) and by Patheon Italia S.p.A., Ferentino, Italy. MultiHance is a registered trademark of Bracco International B.V. MultiHance Multipack is a trademark of Bracco International B.V. All other trademarks and registered trademarks are the property of their respective owners.

References: 1. Seidl Z, Vymazal J, Mechi M, et al. Does higher gadolinium concentration play a role in the morphologic assessment of brain tumors? Results of a multicenter intraindividual crossover comparison of gadobutrol versus gadobenate dimeglumine (the MERIT Study). *AJNR Am J Neuroradiol.* 2012;33(6):1050-1058. 2. Maravilla KR, Maldjian JA, Schmalfuss IM, et al. Contrast enhancement of central nervous system lesions: multicenter intraindividual crossover comparative study of two MR contrast agents. *Radiology.* 2006;240(2):389-400. 3. Rowley HA, Scialfa G, Gao PY, et al. Contrast-enhanced MR imaging of brain lesions: a large-scale intraindividual crossover comparison of gadobenate dimeglumine versus gadodiamide. *AJNR Am J Neuroradiol.* 2008;29(9):1684-1691. 4. Vaneckova M, Herman M, Smith MP, et al. The benefits of high relaxivity for brain tumor imaging: results of a multicenter intraindividual crossover comparison of gadobenate dimeglumine with gadoterate meglumine (The BENEFIT Study). *AJNR Am J Neuroradiol.* 2015 Sep;36(9):1589-1598.

Bracco Diagnostics Inc.
259 Prospect Plains Road, Building H
Monroe Township, NJ 08831 USA
Phone: 609-514-2200
Toll Free: 1-877-272-2269 (U.S. only)
Fax: 609-514-2446

© 2022 Bracco Diagnostics Inc. All Rights Reserved. US-MH-2100018 02/22



Rx ONLY
Please see full prescribing information.
A brief summary follows.

WARNING: NEPHROGENIC SYSTEMIC FIBROSIS

Gadolinium-based contrast agents (GBCAs) increase the risk for NSF among patients with impaired elimination of the drugs.
Avoid use of GBCAs in these patients unless the diagnostic information is essential and not available with non-contrast MRI or other modalities. NSF may result in fatal or debilitating systemic fibrosis affecting the skin, muscle and internal organs.

- The risk for NSF appears highest among patients with:
 - chronic, severe kidney disease (GFR <30 mL/min/1.73m²), or
 - acute kidney injury.
- Screen patients for acute kidney injury and other conditions that may reduce renal function. For patients at risk for chronically reduced renal function (e.g. age > 60 years, hypertension or diabetes), estimate the glomerular filtration rate (GFR) through laboratory testing.
- For patients at highest risk for NSF, do not exceed the recommended MultiHance dose and allow a sufficient period of time for elimination of the drug from the body prior to re-administration. [see **Warnings and Precautions (5.1)**]

1 INDICATIONS AND USAGE

1.1 MRI of the Central Nervous System (CNS)

MultiHance is indicated for intravenous use in magnetic resonance imaging (MRI) of the central nervous system (CNS) in adults and pediatric patients (including term neonates), to visualize lesions with abnormal blood-brain barrier or abnormal vascularity of the brain, spine, and associated tissues.

1.2 MRA of Renal and Aorto-ilio-femoral Vessels

MultiHance is indicated for use in magnetic resonance angiography (MRA) to evaluate adults with known or suspected renal or aorto-ilio-femoral occlusive vascular disease.

4 CONTRAINDICATIONS MultiHance is contraindicated in patients with known allergic or hypersensitivity reactions to gadolinium-based contrast agents [see **Warnings and Precautions (5.2)**].

5 WARNINGS AND PRECAUTIONS

5.1 Nephrogenic Systemic Fibrosis (NSF) Gadolinium-based contrast agents (GBCAs) increase the risk for nephrogenic systemic fibrosis (NSF) among patients with impaired elimination of the drugs. Avoid use of GBCAs among these patients unless the diagnostic information is essential and not available with non-contrast MRI or other modalities. The GBCA-associated NSF risk appears highest for patients with chronic, severe kidney disease (GFR <30 mL/min/1.73m²) as well as patients with acute kidney injury. The risk appears lower for patients with chronic, moderate kidney disease (GFR 30-59 mL/min/1.73m²) and little, if any, for patients with chronic, mild kidney disease (GFR 60-89 mL/min/1.73m²). NSF may result in fatal or debilitating fibrosis affecting the skin, muscle and internal organs. Report any diagnosis of NSF following MultiHance administration to Bracco Diagnostics (1-800-257-5181) or FDA (1-800-FDA-1088 or www.fda.gov/medwatch).

Screen patients for acute kidney injury and other conditions that may reduce renal function. Features of acute kidney injury consist of rapid (over hours to days) and usually reversible decrease in kidney function, commonly in the setting of surgery, severe infection, injury or drug-induced kidney toxicity. Serum creatinine levels and estimated GFR may not reliably assess renal function in the setting of acute kidney injury. For patients at risk for chronically reduced renal function (e.g. age > 60 years, diabetes mellitus or chronic hypertension), estimate the GFR through laboratory testing.

Among the factors that may increase the risk for NSF are repeated or higher than recommended doses of a GBCA and the degree of renal impairment at the time of exposure. Record the specific GBCA and the dose administered to a patient. For patients at highest risk for NSF, do not exceed the recommended MultiHance dose and allow a sufficient period of time for elimination of the drug prior to re-administration. For patients receiving hemodialysis, physicians may consider prompt initiation of hemodialysis following the administration of a GBCA in order to enhance the contrast agent's elimination. The usefulness of hemodialysis in the prevention of NSF is unknown [see **Dosage and Administration (2)** and **Clinical Pharmacology (12)**].

5.2 Hypersensitivity Reactions Anaphylactic and anaphylactoid reactions have been reported, involving cardiovascular, respiratory, and/or cutaneous manifestations. Some patients experienced oropharyngeal collapse and died. In most cases, initial symptoms occurred within minutes of MultiHance administration and resolved with prompt emergency treatment. Prior to MultiHance administration, ensure the availability of personnel trained and medications to treat hypersensitivity reactions. If such a reaction occurs stop MultiHance and immediately begin appropriate therapy. Additionally, consider the risk for hypersensitivity reactions, especially in patients with a history of hypersensitivity reactions or a history of asthma or other allergic disorders. Observe patients for signs and symptoms of a hypersensitivity reaction during and up to 2 hours after MultiHance administration.

5.3 Gadolinium Retention Gadolinium is retained for months or years in several organs. The highest concentrations (nanomoles per gram of tissue) have been identified in the bone, followed by other organs (e.g. brain, skin, kidney, liver, and spleen). The duration of retention also varies by tissue and is longest in bone. Linear GBCAs cause more retention than macrocyclic GBCAs. At equivalent doses, gadolinium retention varies among the linear agents with Omniscan (gadodiamide) and Optmark (gadotermeol) causing greater retention than other linear agents (Eovist (gadobenate dimeglumine), Magnevist (gadopentetate dimeglumine), MultiHance (gadobenate dimeglumine)). Retention is lowest and similar among the macrocyclic GBCAs (Dotarem (gadotermeol), Gadavist (gadobutrol), ProHance (gadobutrol)).

Consequences of gadolinium retention in the brain have not been established. Pathologic and clinical consequences of GBCA administration and retention in skin and other organs have been established in patients with impaired renal function [see **Warnings and Precautions (5.1)**]. There are rare reports of pathologic skin changes in patients with normal renal function. Adverse events involving multiple organ systems have been reported in patients with normal renal function without an established causal link to gadolinium retention [see **Adverse Reactions (6.2)**]. While clinical consequences of gadolinium retention have not been established in patients with normal renal function, certain patients might be at higher risk. These include patients requiring multiple lifetime doses, pregnant and lactating patients, and patients with inflammatory disorders. Consider the retention characteristics of the agent when choosing a GBCA for these patients. Minimize repetitive GBCA imaging studies, particularly closely spaced studies when possible.

5.4 Acute Renal Failure In patients with renal insufficiency, acute renal failure requiring dialysis or worsening renal function have occurred with the use of gadolinium-based contrast agents. The risk of renal failure may increase with increasing dose of the contrast agent. Screen all patients for renal dysfunction by obtaining a history and/or laboratory tests. Consider follow-up renal function assessments for patients with a history of renal dysfunction.

5.5 Extravasation and Injection Site Reactions Extravasation of MultiHance may lead to injection site reactions, characterized by local pain or burning sensation, swelling, blistering, and necrosis. In animal experiments, local reactions including eschar and necrosis were noted even on Day 8 post percutaneous injection of MultiHance. Exercise caution to avoid local extravasation during intravenous administration of MultiHance. If extravasation occurs, evaluate and treat as necessary if local reactions develop.

5.6 Cardiac Arrhythmias Cardiac arrhythmias have been observed in patients receiving MultiHance in clinical trials [see **Adverse Reactions (6.1)**]. Assess patients for underlying conditions or medications that predispose to arrhythmias.

A double-blind, placebo-controlled, 24-hour post dose continuous monitoring, crossover study in 47 subjects evaluated the effect of 0.2 mmol/kg MultiHance on ECG intervals, including QTc. The average changes in QTc values compared with placebo were minimal (<5 msec). QTc prolongation of 50 to 60 msec were noted in 20 subjects who received MultiHance vs 11 subjects who received placebo. Prolongations ≥ 61 msec were noted in 6 subjects who received MultiHance and in 3 subjects who received placebo. None of these subjects had associated malignant arrhythmias. The effects on QTc by MultiHance dose, other drugs, and medical conditions were not systematically studied.

5.7 Interference with Visualization of Certain Lesions Certain lesions seen on non-contrast images may not be seen on contrast-images. Exercise caution when interpreting contrast MR images in the absence of companion non-contrast MR images.

6 ADVERSE REACTIONS

The following adverse reactions are discussed in greater detail in other sections of the label:

- Nephrogenic systemic fibrosis [see **Warnings and Precautions (5.1)**]

6.1 Hypersensitivity reactions [see **Warnings and Precautions (5.2)]**

6.1.1 Clinical Trials Experience

Because clinical trials are conducted under widely varying conditions, adverse reaction rates observed in the clinical trials of a drug cannot be directly compared to rates in the clinical trials of another drug and may not reflect the rates observed in practice.

Adult In clinical trials with MultiHance, a total of 4967 adult subjects (137 healthy volunteers and 4830 patients) received MultiHance at doses ranging from 0.005 to 0.4 mmol/kg. There were 2838 (57%) men and 2129 (43%) women with a mean age of 56.5 years (range 18 to 95 years). A total of 4043 (89%) subjects were Caucasian, 134 (3%) Black, 275 (6%) Asian, 40 (1%) Hispanic, 70 (1%) in other racial groups, and for 45 (1%) subjects, race was not reported. The most commonly reported adverse reactions in adult subjects who received MultiHance were nausea (1.3%) and headache (1.2%). Most adverse reactions were mild to moderate in intensity. One subject experienced a serious anaphylactoid reaction with laryngeal spasm and dyspnea [see **Warnings and Precautions (5.2)**]. Serious adverse reactions consisted of convulsions, pulmonary edema, acute necrotizing pancreatitis, and anaphylactoid reactions were reported in 0.1% of subjects in clinical trials. Adverse reactions that occurred in at least 0.5% of 4967 adult subjects who received MultiHance are listed below (Table 2), in decreasing order of occurrence within each system.

Number of subjects dosed	517 (10.4%)
Number of subjects with any adverse reaction	517 (10.4%)
Gastrointestinal Disorders	
Nausea	67 (1.3%)
General Disorders and Administration Site Disorders	
Injection Site Reaction	54 (1.1%)
Feeling Hot	49 (1.0%)
Nervous System Disorders	
Dizziness	60 (1.2%)
Dysgeusia	33 (0.7%)
Paresthesia	24 (0.5%)
Dizziness	24 (0.5%)

The following adverse reactions occurred in less than 0.5% of the 4967 adult subjects who received MultiHance. Serious adverse reactions described above are not repeated below.

Blood and Lymphatic System Disorders: Basophilic, Cardiac Disorders: Atrioventricular block first degree; Eye Disorders: Eye pruritus, eye swelling, ocular hyperemia, visual disturbance; Gastrointestinal Disorders: Abdominal pain or discomfort, diarrhea, dry mouth, lip swelling, parosmia oral, tongue edema, vomiting; General Disorders and Administration Site Conditions: Chest pain or discomfort, chills, malaise; Immune System Disorders: Hypersensitivity; Investigations: Non-specific changes in laboratory tests (including hematology, blood chemistry, liver enzymes and urinalysis), blood pressure and electrocardiogram parameters (including PR, QRS and QT intervals and ST-T segment changes); Musculoskeletal and Connective Tissue Disorders: Myalgia; Nervous System Disorders: Paresthesia, tremor; Respiratory, Thoracic and Mediastinal Disorders: Dyspnea, laryngospasm, nasal congestion, sneezing, wheezing; Skin and Subcutaneous Tissue Disorders: Hyperhidrosis, pruritus, rash, swelling face, urticaria.

Pediatric In clinical trials of MultiHance in MRI of the CNS, 217 pediatric subjects received MultiHance at a dose of 0.1 mmol/kg. A total of 112 (52%) subjects were male and the overall mean age was 8.3 years (range 4 days to 17 years). A total of 168 (77%) subjects were Caucasian, 12 (6%) Black, 12 (6%) Asian, 24 (11%), Hispanic, and 1 (<1%) in other racial groups. Adverse reactions were reported for 14 (6.5%) of the subjects. The frequency and the nature of the adverse reactions were similar to those seen in the adult patients. The most commonly reported adverse reactions were vomiting (1.4%), pyrexia (0.9%), and hyperhidrosis (0.9%). No subject died during study participation. A serious adverse reaction of worsening of vomiting was reported for one (0.5%) patient with a brain tumor (glioma) for which a causal relationship to MultiHance could not be excluded.

Pediatric Patients In clinical trials of MultiHance in MRI of the CNS, 307 pediatric subjects received MultiHance at a dose of 0.1 mmol/kg. A total of 160 (52%) subjects were male and the overall mean age was 6.0 years (range, 2 days to 17 years). A total of 211 (69%) subjects were Caucasian, 24 (8%) Black, 15 (5%) Asian, 30 (13%), Hispanic, 2 (<1%) in other racial groups, and for 16 (5%), race was not reported. Adverse reactions were reported for 14 (4.6%) of the subjects and the nature of the adverse reactions were similar to those seen in the adult patients. The most commonly reported adverse reactions were vomiting (1.0%), pyrexia (0.7%), and hyperhidrosis (0.7%). No subject died during study participation.

6.2 Post-marketing Experience

The following adverse reactions have been identified during post approval use of MultiHance. Because these reactions are reported voluntarily from a population of uncertain size, it is not always possible to reliably estimate their frequency or establish a causal relationship to drug exposure.

Immune System Disorders: Anaphylactic, anaphylactoid and hypersensitivity reactions manifested with various degrees of severity up to anaphylaxis; shock, loss of consciousness and death. The reactions generally involved signs or symptoms of respiratory, cardiovascular, and/or mucocutaneous abnormalities.

General Disorders and Administration Site Conditions: Extravasation of MultiHance may lead to injection site reactions, characterized by local pain or burning sensation, swelling, blistering, and necrosis [see **Warnings and Precautions (5.4)**]. Adverse events with variable onset and duration have been reported after GBCA administration [see **Warnings and Precautions (5.3)**]. These include fatigue, asthenia, pain syndromes, and heterogeneous clusters of symptoms in the neurological, cutaneous, and musculoskeletal systems. Skin: Gadolinium associated plaques.

7 DRUG INTERACTIONS

7.1 Transporter-Based Drug-Drug Interactions MultiHance and other drugs may compete for the cellular, multi-specific organic anion transporter (MOAT) also referred to as MRP2 or ABCG2; therefore, MultiHance may prolong the systemic exposure of drugs such as cisplatin, anticholinergics (e.g. dourbanonin, darunavirin), alkalioids (e.g. vincristine), methotrexate, etoposide, tamoxifen, and paliperidone. In particular, consider the potential for prolonged drug exposure in patients with decreased MOAT activity (e.g. Dublin John syndrome).

8 USE IN SPECIFIC POPULATIONS

8.1 Pregnancy Risk Summary GBCAs cross the placenta and result in fetal exposure and gadolinium retention. The human data on the association between GBCAs and adverse fetal outcomes are limited and inconclusive (see Data). In animal reproduction studies, gadobenate dimeglumine has been shown to be teratogenic in rabbits following repeated intravenous administration during organogenesis at doses up to 6 times the recommended human dose. There were no adverse developmental effects observed in rats with intravenous administration of gadobenate dimeglumine during organogenesis at doses up to three times the recommended human dose (see Data). Because of the potential for gadolinium to fetus, use MultiHance only if pregnancy is essential during pregnancy and cannot be delayed. The estimated background risk of major birth defects and miscarriage for the indicated population is unknown. All pregnancies have a background risk of birth defect, loss, or other adverse outcomes. In the U.S. general population, the estimated background risk of major birth defects and miscarriage in clinically recognized pregnancies is 2 to 4% and is 15 to 20%, respectively. **Data: Human Data** Contrast enhancement is visualized in the human placenta and fetal tissues after maternal GBCA administration. Cohort studies and case reports on exposure to GBCAs during pregnancy have not reported a clear association between GBCAs and adverse effects in the exposed neonates. However, a retrospective cohort study, comparing pregnant women who had a GBCA MRI to pregnant women who did not have an MRI, reported a higher occurrence of stillbirths and neonatal deaths in the group receiving GBCA MRI. Limitations of this study include a lack of comparison with non-contrast MRI and lack of information about the maternal indication for MRI. Overall, these data preclude a reliable evaluation of the potential risk of adverse fetal outcomes with the use of GBCAs in pregnancy. **Animal Data** Gadolinium Retention GBCAs administered to pregnant non-human primates (0.1 mmol/kg on gestational days 85 and 135) result in measurable gadolinium concentration in the offspring in bone, brain, skin, liver, kidney, and spleen for at least 7 months. GBCAs administered to pregnant mice (2 mmol/kg daily on gestational days 16 through 19) result in measurable gadolinium concentrations in the pups in bone, brain, kidney, liver, blood, muscle, and spleen at one month postnatal age.

Reproductive Toxicology Gadobenate dimeglumine has been shown to be teratogenic in rabbits when administered intravenously at 2 mmol/kg/day (6 times the recommended human dose based on body surface area) during organogenesis (day 6 to 18) inducing microphthalmia/small eye and/or retinal fold in 3 fetuses from 3 separate litters. In addition, MultiHance intravenously administered at 3 mmol/kg/day (10 times the

recommended human dose based on body surface area) has been shown to increase intrauterine deaths in rabbits. There was no evidence that MultiHance induced teratogenic effects in rats at doses up to 2 mmol/kg/day (3 times the recommended human dose based on body surface area), however, rat dams exhibited no systemic toxicity at this dose. There were no adverse effects on the birth, survival, growth, development and fertility of the F1 generation at doses up to 2 mmol/kg in a rat peri- and post-natal (Segment III) study.

10 OVERDOSAGE

Clinical consequences of overdose with MultiHance have not been reported. Treatment of an overdose should be directed toward support of vital functions and prompt institution of symptomatic therapy. In a Phase I clinical study, doses up to 0.4 mmol/kg were administered to patients. MultiHance has been shown to be dialyzable [see **Clinical Pharmacology (12.3)**].

12 CLINICAL PHARMACOLOGY

12.1 Mechanism of Action Gadobenate dimeglumine is a paramagnetic agent and, as such, develops a magnetic moment when placed in a magnetic field. The large magnetic moment produced by the paramagnetic agent results in a large local magnetic field, which can enhance the relaxation rates of water protons in its vicinity leading to an increase of signal intensity (brightness) of tissue.

In magnetic resonance imaging (MRI), visualization of normal and pathological tissue depends in part on variations in the radiofrequency signal intensity that occur with 1) differences in proton density, 2) differences of the spin-lattice or longitudinal relaxation times (T1), and 3) differences in the spin-spin or transverse relaxation time (T2). When placed in a magnetic field, gadobenate dimeglumine decreases the T1 and T2 relaxation time in target tissues. At recommended doses, the effect is observed with greatest sensitivity in the T1-weighted sequences.

12.2 Pharmacokinetics Unlike other tested paramagnetic contrast agents (See Table 3), MultiHance demonstrates weak and transient interactions with serum proteins that causes slowing in the molecular tumbling dynamics, resulting in strong increases in relaxivity in solutions containing serum protein. The improved relaxation effect can contribute to increased contrast-to-noise ratio and lesion-to-brain ratio, which may improve visualization.

	Human plasma	
	r ₁	r ₂
Gadobenate	9.7 [†]	12.5 [†]
Gadotermeol	4.9 [†]	6.3 [†]
Gadobutrol	5.4 [†]	—

r₁ and r₂ relaxivities indicate the efficiency in shortening T1 and T2 relaxation times, respectively. [†] In heparinized human plasma, at 39°C. ^{††} In citrated human plasma, at 37°C.

— Not available.

Disruption of the blood-brain barrier or abnormal vascularity allows enhancement by MultiHance in lesions such as meningiomas, abscesses, and infarcts. Uptake of MultiHance into hepatocytes has been demonstrated.

12.3 Pharmacokinetics Three single-dose intravenous studies were conducted in 32 healthy male subjects to assess the pharmacokinetics of gadobenate dimeglumine. The doses administered in these studies ranged from 0.005 to 0.4 mmol/kg. Upon injection, the administered salt is completely dissociated from the gadobenate dimeglumine complex. The pharmacokinetics of gadobenate dimeglumine is based on the MRI contrast of gadobenate dimeglumine. Data for plasma concentration and area under the curve demonstrated linear dependence on the administered dose. The pharmacokinetics of gadobenate ion following intravenous administration can be best described using a two-compartment model.

Distribution Gadobenate ion has a rapid distribution half-life (reported as mean ± SD) of 0.084 ± 0.012 to 0.605 ± 0.072 hours. Volume of distribution of the central compartment ranged from 0.074 ± 0.017 to 1.153 ± 0.139 L/kg, and estimates of volume of distribution by area ranged from 0.170 ± 0.016 to 0.282 ± 0.079 L/kg. These latter estimates are approximately equivalent to the average volume of extracellular body water in man. *In vitro* studies showed no appreciable binding of gadobenate ion to human serum proteins.

Elimination Gadobenate ion is eliminated predominantly via the kidneys, with 78% to 96% of an administered dose recovered in the urine. Total plasma clearance and renal clearance estimates of gadobenate ion were similar, ranging from 0.093 ± 0.010 to 133 ± 0.270 L/hr/kg and 0.093 ± 0.010 to 133 ± 0.270 L/hr/kg, respectively. The clearance is similar to that of substances that are subject to glomerular filtration. The mean elimination half-life ranged from 1.17 ± 0.26 to 2.02 ± 0.60 hours. A small percentage of the administered dose (0.6% to 4%) is eliminated via the biliary route and recovered in feces.

Metabolism There was no detectable biotransformation of gadobenate ion. Dissociation of gadobenate ion *in vivo* has been shown to be minimal, with less than 1% of the free chelating agent being recovered alone in feces.

Pharmacokinetics: Special Populations

Renal Impairment A single intravenous dose of 0.2 mmol/kg of MultiHance was administered to 20 subjects with impaired renal function (6 men and 3 women with moderate renal impairment [urine creatinine clearance >30 to <60 mL/min] and 5 men and 6 women with severe renal impairment [urine creatinine clearance >10 to <30 mL/min]). Mean estimates of the elimination half-life were 6.1 ± 3.0 and 9.5 ± 3.1 hours for the moderate and severe renal impairment groups, respectively, as compared with 1.0 to 2.0 hours in healthy volunteers.

Hemodialysis: A single intravenous dose of 0.2 mmol/kg of MultiHance was administered to 11 subjects (5 males and 6 females) with end-stage renal disease requiring hemodialysis to determine the pharmacokinetics and dialyzability of gadobenate. Approximately 72% of the dose was recovered by hemodialysis over a 4-hour period. The mean elimination half-life on dialysis was 1.21 ± 0.29 hours as compared with 42.4 ± 24.4 hours when off dialysis.

Hepatic Impairment: A single intravenous dose of 0.1 mmol/kg of MultiHance was administered to 11 subjects (8 males and 3 females) with impaired liver function (Class B or C modified Child-Pugh Classification). Hepatic impairment had little effect on the pharmacokinetics of MultiHance with the parameters being similar to those calculated for healthy subjects.

Gender, Age, Race: A multiple regression analysis performed using pooled data from several pharmacokinetic studies found no significant effect of sex upon the pharmacokinetics of gadobenate. Clearance appeared to decrease slightly with increasing age. Since variations due to age appeared minimal, dosage adjustment for geriatric population is not recommended. Pharmacokinetic differences due to race have not been systematically studied.

Pediatric: A population pharmacokinetic analysis incorporated data from 25 healthy subjects (14 males and 11 females) and 15 subjects undergoing MR imaging of the central nervous system (7 males and 8 females) between ages of 2 and 16 years. The subjects received a single intravenous dose of 0.1 mmol/kg of MultiHance. The geometric mean C_{max} was 62.3 µg/mL (n=16) in children 2 to 5 years of age, and 64.2 µg/mL (n=24) in children older than 5 years of age. The geometric mean AUC_{0-∞} was 77.9 µg·h/mL in children 2 to 5 years of age (n=16) and 82.6 µg·h/mL in children older than 5 years (n=24). The geometric mean half-life was 1.2 hours in children 2 to 5 years of age and 0.93 hours in children older than 5 years. There was no significant gender-related difference in the pharmacokinetic parameters in the pediatric patients. Over 80% of the dose was recovered in urine after 24 hours. Pharmacokinetic simulations indicate similar AUC and C_{max} values for MultiHance in pediatric subjects less than 2 years when compared to those reported for adults; no age-based dose adjustment is necessary for this pediatric population.

17 PATIENT COUNSELING INFORMATION

17.1 Nephrogenic Systemic Fibrosis Instruct patients to inform their physician if they:

- have a history of kidney and/or liver disease, or • have recently received a GBCA.

GBCAs increase the risk for NSF among patients with impaired elimination of the drugs. To counsel patients at risk for NSF • Describe the clinical manifestations of NSF • Describe procedures to screen for the detection of renal impairment. Instruct the patients to contact their physician if they develop signs or symptoms of NSF following MultiHance administration, such as burning, itching, swelling, scaling, hardening and tightening of the skin; red or dark patches on the skin; stiffness in joints with trouble moving, bending or straightening the arms, hands, legs or feet; pain in the hip bones or ribs; or muscle weakness.

17.2 Common Adverse Reactions

Inform patients that they may experience:

- reactions along the venous injection site, such as mild and transient burning or pain or feeling of warmth or coldness at the injection site • side effects of feeling hot, nausea, and headache.

17.3 General Precautions

Instruct patients scheduled to receive MultiHance to inform their physician if they:

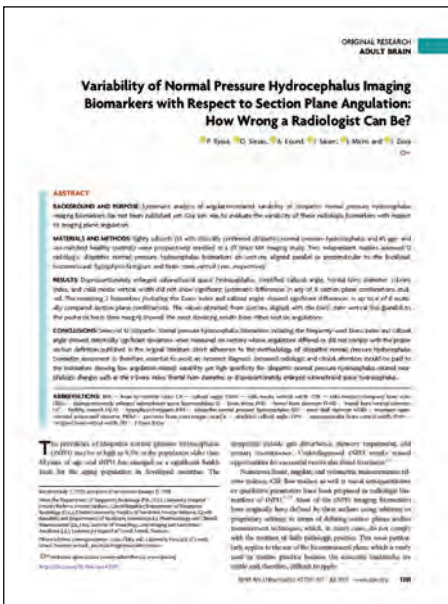
- are pregnant or breast feeding • have a history of renal disease, heart disease, seizure, asthma or allergic respiratory illnesses • are taking any medications • have any allergies to any of the ingredients of MultiHance.

Multicenter double-blind randomized intraindividual crossover study design of 123 patients with known or suspected brain tumors. Each patient received 0.1-mmol/kg doses of MultiHance and Gadavist in 2 identical MR imaging examinations. Contrast agents were administered by IV using manual bolus injection (n=118) or a power injector (n=4). Both agents were administered at 0.1 mmol/kg of body weight, corresponding to 0.2 mL/kg for MultiHance and 0.1 mL/kg for Gadavist. The interval between the 2 MR imaging examinations was ~48 hours to avoid carryover effects but <14 days to minimize the chance of measurable disease progression or lesion evolution. All images were evaluated by 3 blinded, independent experienced radiologists who were unaffiliated with the study centers. Each reader evaluated the patient images separately and independently. Images were evaluated qualitatively for diagnostic information and scored for: 1) lesion border delineation, 2) disease extent, 3) visualization of lesion internal morphology, and 4) lesion contrast enhancement compared with surrounding normal tissue. All assessments used a 3-point scales from 1 (examination 1 superior) through 0 (examinations equal) to 1 (examination 2 superior).

Gadavist® (gadobutrol) is a registered trademark of Bayer Healthcare. Reference: Seidl Z, Vymazal J, Mechl M, et al. Does higher gadolinium concentration play a role in the morphologic assessment of brain tumors? Results of a multicenter intraindividual crossover comparison of gadobutrol versus gadobenate dimeglumine (the MERIT Study). *AJNR Am J Neuroradiol*. 2012 Jun-Jul;33(6):1050-1058.

LUCIEN LEVY BEST RESEARCH ARTICLE AWARD WINNER AND NOMINEES NAMED

This award is named for the late *AJNR* Senior Editor who championed its establishment and recognizes the best original research paper accepted in 2021. The winning paper was published electronically on April 22, 2021. It was selected by a vote of the *Journal's* Editor-in-Chief and Senior Editors.



The Editors of *AJNR* are pleased to announce the annual Lucien Levy Best Research Article Award has been presented to

“Variability of Normal Pressure Hydrocephalus Imaging Biomarkers with Respect to Section Plane Angulation: How Wrong a Radiologist Can Be?”

by P. Ryska, O. Slezak, A. Eklund, J. Salzer, J. Malm, and J. Zizka

Other nominated papers were:

- “Evolution of MRI Findings in Patients with Idiopathic Intracranial Hypertension after Venous Sinus Stenting” by N.F. Belachew, W. Almiri, R. Encinas, A. Hakim, S. Baschung, J. Kaesmacher, T. Dobrocky, C.J. Schankin, M. Abegg, E.I. Piechowiak, A. Raabe, J. Gralla, and P. Mordasini
- “Carotid Plaque Composition Assessed by CT Predicts Subsequent Cardiovascular Events among Subjects with Carotid Stenosis” by E. Choi, E. Byun, S.U. Kwon, N. Kim, C.H. Suh, H. Kwon, Y. Han, T.-W. Kwon, and Y.-P. Cho
- “Development and Practical Implementation of a Deep Learning–Based Pipeline for Automated Pre- and Postoperative Glioma Segmentation” by E. Lotan, B. Zhang, S. Dogra, W.D. Wang, D. Carbone, G. Fatterpekar, E.K. Oermann, and Y.W. Lui
- “Quantifying T2-FLAIR Mismatch Using Geographically Weighted Regression and Predicting Molecular Status in Lower-Grade Gliomas” by S. Mohammed, V. Ravikummar, E. Warner, S.H. Patel, S. Bakas, A. Rao, and R. Jain
- “Assessment of MR Imaging and CT in Differentiating Hereditary and Nonhereditary Paragangliomas” by Y. Ota, S. Naganawa, R. Kurokawa, J.R. Bapuraj, A. Capizzano, J. Kim, T. Moritani, and A. Srinivasan
- “Resting-State Functional MRI for Determining Language Lateralization in Children with Drug-Resistant Epilepsy” by N.L. Phillips, A.S. Shatil, C. Go, A. Robertson, and E. Widjaja
- “Transmantle Pressure Computed from MR Imaging Measurements of Aqueduct Flow and Dimensions” by S.J. Sincomb, W. Coenen, E. Criado-Hidalgo, K. Wei, K. King, M. Borzage, V. Haughton, A.L. Sánchez, and J.C. Lasheras

INNOVATION 4MRI



COME JOIN US
BUILD A COMMUNITY
innovation4MRI.com

BRING THE FUTURE OF MRI INTO FOCUS



Innovation for MRI



MRI Technology



Contrast Agents



Care & Sustainability



COME AND SEE WHAT
IS GOING ON AT:

innovation4MRI.com

CALL FOR AJNR EDITOR-IN-CHIEF CANDIDATES

Over the last 41 years, the editorial team of the *American Journal of Neuroradiology (AJNR)* has played a pivotal role in shaping our specialty of neuroradiology. In June 2023, Jeffrey S. Ross, MD, will complete an 8-year term as the sixth Editor-in-Chief (EIC) of the AJNR. He was preceded by a number of distinguished editors including our first AJNR EIC, Juan M. Taveras, MD (1980-1989), followed by Michael S. Huckman, MD (1990-1997), Robert M. Quencer, MD (1997-2005), Robert I. Grossman, MD (2006-2007), and Mauricio Castillo, MD (2007-2015).

We especially wish to thank Dr. Jeffrey Ross for his extraordinary dedication and exceptional contributions to the AJNR. Under his strong leadership, the AJNR remains the premier clinical neuroimaging journal with high-quality, peer-reviewed articles that serve as a beacon for achieving excellence in patient care, research, and teaching. There are an impressive 6867 subscribers across the globe: 1389 are in print and 5472 are digital.

Dr. Ross has assembled a talented international editorial board during his tenure. The AJNR issues 12 journals each year (± 200 pages per issue)—all with peer-reviewed articles from highly respected researchers in the field. With 1700+ papers, the number of submissions to the journal was record-breaking in 2020. Over 80 COVID-19 papers have received expedited publication to date, and more than 1300 original submissions are projected for 2021. The AJNR website had an incredible 11.7 million visits in 2021. There is also a strong presence on social media and subscribers may now avail themselves of an enhanced website platform. There are 3 monthly podcasts including “Issue Highlights,” “Fellows’ Journal Club,” and “Annotated Bibliography,” which offers continuing medical education. In addition, during Dr. Ross’ tenure, the Impact Factor and h-index for the journal have steadily increased and contribute to the AJNR’s international recognition as the leading journal for all aspects of neuroimaging research, education, and best practice.

A search for a new Editor-in-Chief will begin in early 2022.

The new Editor-in-Chief will be announced in December 2022 and will transition into the position beginning in January 2023. The actual term will begin July 1, 2023. The EIC will provide leadership and strategic vision for the journal as well as report on all editorial matters to the ASNR Board of Directors (BOD). Other responsibilities include maintaining the journal’s standard of excellence building on its reputation nationally and internationally. The EIC will be responsible for conducting, directing, and/or supervising the solicitation, evaluation, revision, and selection of all scientific and other materials to be published in the *American Journal of Neuroradiology*. The incumbent will work efficiently with the journal’s online manuscript processing system to conduct initial screening of manuscripts; make timely decisions about reviewed and revised submissions; provide constructive comments for authors as appropriate; write editorials; and meet with AJNR staff.

In addition, the EIC shall decide upon and approve of the content and design of tables of contents, letters to the editor, book reviews, advertisements, and other pages published in the AJNR as well as oversight of social media related to the journal. The EIC will also work collaboratively with the journal’s editorial board to determine the organizational structure, titles, functions, appointments, and terms of all editorial positions including reviewers, editorial advisory boards, and senior editors. The EIC may appoint senior editors who must be senior members of the ASNR. The number of senior editors shall be budgeted and approved by the ASNR BOD. Senior editors will serve at the pleasure of the EIC who shall establish the terms of service, including supervising and evaluating performance, and will exercise the right to retain or replace any senior editor as the workflow or operational demands require. The appointments of senior editors will be for a term of 1 year initially and may be extended at the discretion of the EIC.

The EIC in performing duties will observe the general *Policies and Procedures* established by the ASNR BOD, and will operate within the budget approved by the Board of Directors. The EIC will be consulted about, and will participate in AJNR operations including advertising, publication channels, expense management, and new or renewed contracts. The EIC will report regularly to the ASNR BOD and will attend Board of Director Meetings and other meetings as requested by the Executive Director. Each year the Editor will develop a budget along with the Managing Editor for approval by the ASNR Financial Management Committee and Board of Directors. This will be done in a manner consistent with the fiscal policies established by the Society.

QUALIFICATIONS OF THE SUCCESSFUL CANDIDATE INCLUDE:

- MD degree; Senior Member of ASNR in North America, neuroradiology subspecialty certification
- Familiarity with AJNR and its mission
- Familiarity with ASNR and its mission

- Presently or recently engaged in a leadership role in neuroradiology with broad neuroradiology knowledge
- Excellent leadership and supervisory skills to motivate and inspire professional staff as well as interpersonal skills—impartiality, diplomacy, high ethical standards and integrity including a clear understanding of the ethical guidelines established for scholarly publishing
- Leadership needed to develop and articulate a vision and the ability to inspire people with that vision
- Demonstrated track record of academic excellence including extensive experience in both publishing in and reviewing for peer-reviewed journals
- Excellent communication and writing skills and experience in critically appraising scientific articles
- Creativity and passion about finding new ways to expand the journal content
- The ability to formulate a budget and assist leadership in oversight of journal business decisions such as selecting major vendors (e.g., printing, composition, redaction, copyediting, and other technical aspects affecting journal operations), as well as expense and revenue related decisions
- Ability to appoint a strong, diverse, and representative team of editors
- High level of organizational skills
- Editorial board or prior editorial experience preferred

The term is for 5 years renewable for an additional 3 years for a total of 8 years and subject to annual review by the ASNR Board of Directors. It is expected the EIC will devote 16-20 hours per week to these duties and a stipend will be provided.

A diverse, experienced, and knowledgeable search committee has been tasked with identifying leading candidates. The search committee consists of Tina Young Poussaint, MD, FACR, Chair, Mauricio Castillo, MD, FACR, Pina Sanelli, MD, MPH, FACR, Carolyn Meltzer, MD, FACR, Erin Simon Schwartz, MD, FACR, Joshua Nickerson, MD, Courtney Tomblinson, MD, and senior editors including Harry Cloft, MD, PhD, Christopher Filippi, MD, Thierry Huisman, MD, Peter D. Chang, MD, Lubdha Shah, MD, Gregory Zaharchuk MD, PhD, C. Douglas Phillips, MD, Yvonne Lui, MD, and Bryan Comstock. The search process will include recruiting and nominating candidates, interviewing candidates, and reviewing vision statements submitted by finalists. The appointment of the new AJNR Editor-in-Chief will be announced in December 2022.

All interested physicians are invited to provide their curriculum vitae and a vision statement to Dr. Tina Young Poussaint, tina.poussaint@childrens.harvard.edu and Karen Halm, khalm@asn.org. To ensure a broad and diverse pool of candidates, the committee welcomes nominations from the ASNR membership. *The deadline for receipt of submissions is August 1, 2022.*

Tina Young Poussaint, MD, FACR
Chair, Editor-in-Chief Search Committee
President, American Society of Neuroradiology

In Planning for Brain Metastases Treatment, Imaging may be the Missing Link in Cost Containment¹

When faced with a patient presenting with metastatic brain cancer, determining whether to use up-front stereotactic radiosurgery (SRS) vs. first treating with whole brain radiotherapy (WBRT) is a significant clinical decision.

WBRT: The whole story on cognitive impairment

While whole brain radiotherapy (WBRT) has been the main treatment option for many years, experts agree that it often results in cognitive deterioration and a negative impact on quality of life. This mental decline has a devastating impact on patients and their families and adds ongoing costs for the healthcare systems managing these symptoms.

Using WBRT instead of SRS in some patients is estimated to decrease the total costs of brain metastasis management, though with increased toxicity.

SRS: Fewer side effects but greater risk of missed tumors

The cost of upfront SRS is the greatest contributor to cost of brain metastasis management.¹ SRS is often more expensive than WBRT. What's more, multiple applications of SRS can increase the cost of treatment greatly.

Stereotactic radiosurgery (SRS) has far fewer side effects, but upfront use of SRS is expensive and can carry the risk of missed tumors, requiring repeat procedures such as salvage SRS.¹

Number of lesions and lesion size are key factors to be considered when determining the treatment plan for these patients. It follows that increased diagnostic information and accuracy could be beneficial in directing the proper therapy and improving overall long-term patient outcomes and containing costs. Getting the diagnosis right the first time is crucial to ensure proper treatment begins quickly, and high cost/high stakes procedures such as SRS need precise surgical planning.

What does optimal visualization mean for outcomes and cost?

For surgical planning with SRS, radiologists need the best visualization achievable to accurately count the number and size of the lesions. These metrics are the key predictors of the need for SRS,¹ WBRT, or a combination of both.

By selecting the ideal contrast agent and equipment protocols, neuroradiologists can identify the proximate numbers of metastases for upfront treatment and reduced salvage treatment occurrences.

The role of radiology

As medical care for oncology patients continues to evolve, it will be increasingly important to assess the cost of various interventions given the often-limited life expectancy of cancer patients, the rising costs of cancer therapy, and the increasing prevalence of cancer in an aging population.

Through seeing all the tumors and tumor borders as clearly as technology allows, radiology can play a part in ensuring that proper treatment can begin quickly,

while containing costs through optimized patient care. Efforts to carefully manage treatment approaches require improvements in protocol design, contrast administration in imaging, and utilizing multimodal imaging approaches.

In this era of precision medicine, radiology departments' contribution to this improved standard of care will have significant short and long-term implications by reducing cost of care, providing a more proximate diagnosis, and ensuring optimal patient outcomes. ■



Getting the diagnosis right the first time is crucial to ensure proper treatment begins quickly.

Reference: 1. Shenker, R. F., McTyre, E. R., Taksler, D et al. Analysis of the drivers of cost of management when patients with brain metastases are treated with upfront radiosurgery. *Clin Neurol Neurosurg.* 2019 Jan;176:10-14.

BALLAST[®]

LONG SHEATH

6F 088



GET THERE >>>

STAY THERE >>>



Image courtesy of
Ameer E. Hassan D.O., FAHA, FSVIN

Visit our products page at www.baltgroup.com to learn more.

For a list of indications, warnings, precautions, and contraindications, refer to IFU-022.

Balt USA

29 Parker, Irvine, CA 92618
tel 949.788.1443 fax 949.788.1444

baltgroup.com

©2022 BALT USA MKTG-290 Rev. A



AJNR

AMERICAN JOURNAL OF NEURORADIOLOGY

MAY 2022
VOLUME 43
NUMBER 5
WWW.AJNR.ORG

Publication Preview at www.ajnr.org features articles released in advance of print. Visit www.ajnrblog.org to comment on AJNR content and chat with colleagues and AJNR's News Digest at <http://ajnrdigest.org> to read the stories behind the latest research in neuroimaging.

649 **PERSPECTIVES** *G. Mamo*

REVIEW ARTICLES

-   650 **Small Vessel Disease, a Marker of Brain Health: What the Radiologist Needs to Know** *A. Mahammedi, et al.* **ADULT BRAIN**
-   661 **Beyond Diffusion Tensor MRI Methods for Improved Characterization of the Brain after Ischemic Stroke: A Review** *E.V.R. DiBella, et al.* **ADULT BRAIN**

PRACTICE PERSPECTIVES

-   670 **Implementation of a Low-Field Portable MRI Scanner in a Resource-Constrained Environment: Our Experience in Malawi** *K. Chetcuti, et al.*

GENERAL CONTENTS

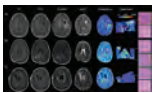
-   675 **Radiomics-Based Machine Learning for Outcome Prediction in a Multicenter Phase II Study of Programmed Death-Ligand 1 Inhibition Immunotherapy for Glioblastoma** *E. George, et al.* **ADULT BRAIN FUNCTIONAL**
-    682 **Radio-Pathomic Maps of Cell Density Identify Brain Tumor Invasion beyond Traditional MRI-Defined Margins** *S.A. Bobholz, et al.* **ADULT BRAIN FUNCTIONAL**
-  689 **DSC Perfusion MRI-Derived Fractional Tumor Burden and Relative CBV Differentiate Tumor Progression and Radiation Necrosis in Brain Metastases Treated with Stereotactic Radiosurgery** *F. Kuo, et al.* **ADULT BRAIN FUNCTIONAL**
-  696 **Interobserver Reliability on Intravoxel Incoherent Motion Imaging in Patients with Acute Ischemic Stroke** *K. Yamashita, et al.* **ADULT BRAIN FUNCTIONAL**
-   701 **Brain Perfusion Alterations on 3D Pseudocontinuous Arterial Spin-Labeling MR Imaging in Patients with Autoimmune Encephalitis: A Case Series and Literature Review** *R. Li, et al.* **ADULT BRAIN FUNCTIONAL**
-   707 **Normative Data for Brainstem Structures, the Midbrain-to-Pons Ratio, and the Magnetic Resonance Parkinsonism Index** *S.T. Ruiz, et al.* **ADULT BRAIN**
-  715 **The Epidermal Growth Factor Domain of the Mutation Does Not Appear to Influence Disease Progression in CADASIL When Brain Volume and Sex Are Taken into Account** *J. Lebenberg, et al.* **ADULT BRAIN**
-  721 **Labeling Noncontrast Head CT Reports for Common Findings Using Natural Language Processing** *M. Iorga, et al.* **ADULT BRAIN**

AJNR (Am J Neuroradiol ISSN 0195-6108) is a journal published monthly, owned and published by the American Society of Neuroradiology (ASNR), 820 Jorie Boulevard, Oak Brook, IL 60523. Annual dues for the ASNR include approximately 21% for a journal subscription. The journal is printed by Intellicor Communications, 330 Eden Road, Lancaster, PA 17601; Periodicals postage paid at Oak Brook, IL and additional mailing offices. Printed in the U.S.A. POSTMASTER: Please send address changes to American Journal of Neuroradiology, P.O. Box 3000, Denville, NJ 07834, U.S.A. Subscription rates: nonmember \$430 (\$505 foreign) print and online, \$320 online only; institutions \$495 (\$565 foreign) print and basic online, \$980 (\$1050 foreign) print and extended online, \$380 online only (basic), \$825 online only (extended); single copies are \$35 each (\$40 foreign). Indexed by PubMed/MEDLINE, BIOSIS Previews, Current Contents (Clinical Medicine and Life Sciences), EMBASE, Google Scholar, HighWire Press, Q-Sensei, RefSeek, Science Citation Index, SCI Expanded, ReadCube, and Semantic Scholar. Copyright © American Society of Neuroradiology.

-   727 **Antithrombotic Treatment after Carotid Stenting in Patients with Concomitant Atrial Fibrillation** *B. Pardo-Galiana, et al.* **INTERVENTIONAL**
-   731 **Angiographically Occult Subarachnoid Hemorrhage: Yield of Repeat Angiography, Influence of Initial CT Bleed Pattern, and Sources of Diagnostic Error in 242 Consecutive Patients** *I. Nguyen, et al.* **INTERVENTIONAL**
-  736 **Recovery from Cranial Nerve Symptoms after Flow Diversion without Coiling for Unruptured Very Large and Giant ICA Aneurysms** *J.K. Lee, et al.* **INTERVENTIONAL**
-   741 **Rabbit Elastase Aneurysm Model Mimics the Recurrence Rate of Human Intracranial Aneurysms following Platinum Coil Embolization** *Y.-H. Ding, et al.* **INTERVENTIONAL**
-   748 **Iodine Maps from Dual-Energy CT to Predict Extrathyroidal Extension and Recurrence in Papillary Thyroid Cancer Based on a Radiomics Approach** *X.-Q. Xu, et al.* **HEAD & NECK**
-   756 **Microstructural Visual Pathway White Matter Alterations in Primary Open-Angle Glaucoma: A Neurite Orientation Dispersion and Density Imaging Study** *S. Haykal, et al.* **HEAD & NECK**
-  764 **An In-Depth Analysis of Brain and Spine Neuroimaging in Children with Abusive Head Trauma: Beyond the Classic Imaging Findings** *G. Orman, et al.* **PEDIATRICS**
-   769 **Dorsal Root Ganglion Volumetry by MR Gangliography** *S. Weiner, et al.* **PERIPHERAL NERVOUS SYSTEM**
-   776 **Minimally Invasive Stent Screw-Assisted Internal Fixation Technique Corrects Kyphosis in Osteoporotic Vertebral Fractures with Severe Collapse: A Pilot “Vertebra Plana” Series** *A. Cianfoni, et al.* **SPINE**
-  784 **MRI Findings after Recent Image-Guided Lumbar Puncture: The Rate of Dural Enhancement and Subdural Collections** *I.T. Mark, et al.* **SPINE**
- 789 **35 YEARS AGO IN AJNR**

BOOK REVIEWS *R.M. Quencer, Section Editor*

Please visit www.ajnrblog.org to read and comment on Book Reviews.



From S.A. Bobholz et al, in this issue: A radio-pathomic model for cellularity trained with tissue samples acquired at postmortem examination is able to identify regions of hypercellular tumor beyond traditional imaging signatures.

 Indicates Editor's Choices selection



Indicates Fellows' Journal Club selection



Indicates open access to non-subscribers at www.ajnr.org



Indicates article with supplemental online data



Indicates article with supplemental online video



Evidence-Based Medicine Level 1



Evidence-Based Medicine Level 2

EDITOR-IN-CHIEF

Jeffrey S. Ross, MD

Professor of Radiology, Department of Radiology,
Mayo Clinic College of Medicine, Phoenix, AZ

SENIOR EDITORS

Harry J. Cloft, MD, PhD

Professor of Radiology and Neurosurgery,
Department of Radiology, Mayo Clinic College of
Medicine, Rochester, MN

Christopher G. Filippi, MD

Professor and Alice Ettinger-Jack R. Dreyfuss
Chair of Radiology,
Tufts University School of Medicine,
Radiologist-in-Chief
Tufts University Medical Center, Boston, MA

Thierry A.G.M. Huisman, MD

Radiologist-in-Chief, Texas Children's Hospital,
Houston, TX

Yvonne W. Lui, MD

Associate Professor of Radiology,
Chief of Neuroradiology,
New York University School of Medicine,
New York, NY

C.D. Phillips, MD, FACR

Professor of Radiology, Weill Cornell Medical
College, Director of Head and Neck Imaging,
New York-Presbyterian Hospital, New York, NY

Lubdha M. Shah, MD, MS

Professor of Radiology and Director of Spine
Imaging, University of Utah Department of
Radiology and Imaging Sciences, Salt Lake City, UT

STATISTICAL SENIOR EDITOR

Bryan A. Comstock, MS

Senior Biostatistician,
Department of Biostatistics,
University of Washington, Seattle, WA

ARTIFICIAL INTELLIGENCE DEPUTY EDITOR

Peter D. Chang, MD

Assistant Professor-in-Residence,
Departments of Radiological Sciences,
Computer Sciences, and Pathology,
Director, Center for Artificial Intelligence in
Diagnostic Medicine (CAIDM),
University of California, Irvine, Irvine, CA

EDITORIAL BOARD

Ashley H. Aiken, Atlanta, GA

Lea M. Alhilali, Phoenix, AZ

Mohammed A. Almekhlafi, Calgary, Alberta,
Canada

Joachim Berkefeld, Frankfurt, Germany

Aashim Bhatia, Pittsburgh, PA

Waleed Brinjikji, Rochester, MN

Judah Burns, New York, NY

Danielle Byrne, Dublin, Ireland

Federico Cagnazzo, Montpellier, France

J. Levi Chazen, New York, NY

James Y. Chen, San Diego, CA

Gloria C. Chiang, New York, NY

Daniel Chow, Irvine, CA

Kars C.J. Compagne, Rotterdam, The Netherlands

Arturo Consoli, Suresnes, France

Seena Dehkharghani, New York, NY

Nilesh K. Desai, Houston, TX

Yonghong Ding, Rochester, MN

Birgit Ertl-Wagner, Toronto, Ontario, Canada

Clifford J. Eskey, Hanover, NH

Massimo Filippi, Milan, Italy

Nils D. Forkert, Calgary, Alberta, Canada

Ana M. Franceschi, New York, NY

Frank Gaillard, Melbourne, Australia

Joseph J. Gemmete, Ann Arbor, Michigan

Wende N. Gibbs, Phoenix, AZ

Philipp Gölitz, Erlangen, Germany

Brent Griffith, Detroit, MI

Joseph M. Hoxworth, Phoenix, Arizona

Raymond Y. Huang, Boston, MA

Gábor Janiga, Magdeburg, Germany

Christof Karmonik, Houston, TX

Timothy J. Kaufmann, Rochester, MN

Hillary R. Kelly, Boston, MA

Toshibumi Kinoshita, Akita, Japan

Alexander W. Korutz, Chicago, IL

Stephen F. Kralik, Houston, TX

Alexander Lerner, Los Angeles, CA

Yinsheng Li, Madison, WI

Franklin A. Marden, Chicago, IL

Markus A. Möhlenbruch, Heidelberg, Germany

Kambiz Nael, Los Angeles, CA

Renato Hoffmann Nunes, Sao Paulo, Brazil

Sasan Partovi, Cleveland, OH

Johannes A.R. Pfaff, Salzburg, Austria

Laurent Pierot, Reims, France

Alireza Radmanesh, New York, NY

Prashant Raghavan, Baltimore, MD

Eytan Raz, New York, NY

Paul M. Ruggieri, Cleveland, OH

Sebastian Schafer, Madison, WI

Maksim Shapiro, New York, NY

Timothy Shepherd, New York, NY

James Shin, New York, NY

Mark S. Shiroishi, Los Angeles, CA

Bruno P. Soares, Burlington, VT

Jason F. Talbott, San Francisco, CA

Ruth Thiex, Everett, Washington

Vincent Thijs, Melbourne, Victoria, Australia

Anderanik Tomasian, Los Angeles, CA

Fabio Triulzi, Milan, Italy

Anja G. van der Kolk, Utrecht, the Netherlands

Arastoo Vossough, Philadelphia, PA

Elysa Widjaja, Toronto, Ontario, Canada

Leonard Yeo, Singapore

Woong Yoon, Gwangju, South Korea

David M. Yousem, Evergreen, CO

Carlos Zamora, Chapel Hill, NC

Chengcheng Zhu, Seattle, WA

EDITORIAL FELLOW

Vivek Yedavalli, Baltimore, MD

SPECIAL CONSULTANTS TO THE EDITOR

AJNR Blog Editor

Neil Lal, Denver, CO

Case of the Month Editor

Nicholas Stence, Aurora, CO

Case of the Week Editors

Matylda Machnowska, Toronto, Ontario, Canada

Anvita Pauranik, Calgary, Alberta, Canada

Vinil Shah, San Francisco, CA

Classic Case Editor

Sandy Cheng-Yu Chen, Taipei, Taiwan

Health Care and Socioeconomics Editor

Pina C. Sanelli, New York, NY

Physics Editor

Greg Zaharchuk, Stanford, CA

Podcast Editor

Courtney Tomblinson, Nashville, TN

Deputy Podcast Editor

Kevin Hiatt, Winston-Salem, NC

Twitter Editor

Jacob Ormsby, Albuquerque, New Mexico

Official Journal:

American Society of Neuroradiology

American Society of Functional Neuroradiology

American Society of Head and Neck Radiology

American Society of Pediatric Neuroradiology

American Society of Spine Radiology

Founding Editor

Juan M. Taveras

Editors Emeriti

Mauricio Castillo, Robert I. Grossman,

Michael S. Huckman, Robert M. Quencer

Managing Editor

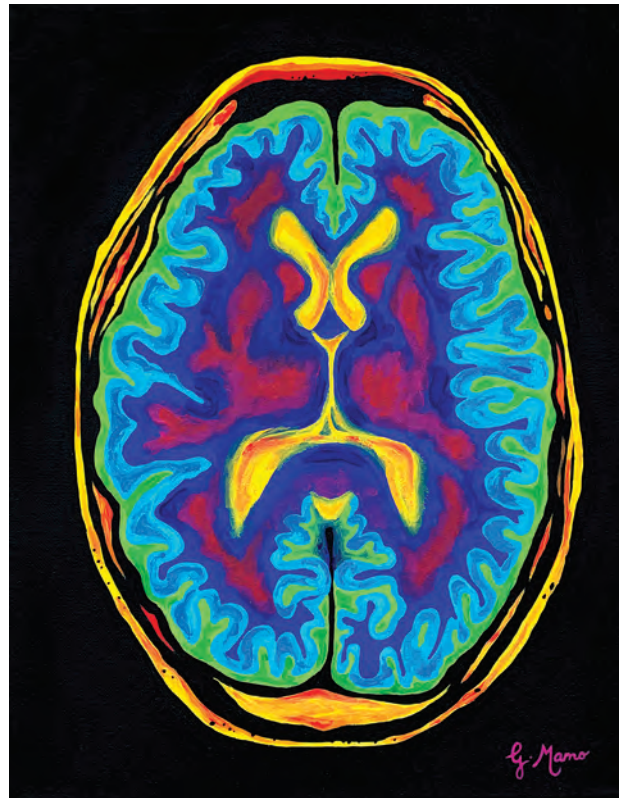
Karen Halm

Assistant Managing Editor

Laura Wilhelm

Executive Director, ASNR

Mary Beth Hepp



Title: Brain MRI. As with any field in medicine, radiologic imaging is constantly evolving and advancing. MRI is one widely used form of imaging, and it is particularly valuable in neuroanatomy. Researchers have developed a way to add color to this form of imaging to aid in the differentiation of various anatomic structures and to enhance the information on the images. Just as the practice of medicine is not always black and white, my goal as both an artist and a medical student is to add vibrance and color to my anatomic images/paintings.

Gabriella Mamo, Philadelphia College of Osteopathic Medicine

Small Vessel Disease, a Marker of Brain Health: What the Radiologist Needs to Know

 A. Mahammedi,  L.L. Wang,  B.J. Williamson,  P. Khatri,  B. Kissela,  R.P. Sawyer,  R. Shatz,  V. Khandwala, and  A. Vagal



ABSTRACT

SUMMARY: Small vessel disease, a disorder of cerebral microvessels, is an expanding epidemic and a common cause of stroke and dementia. Despite being almost ubiquitous in brain imaging, the clinicroadiologic association of small vessel disease is weak, and the underlying pathogenesis is poorly understood. The STAndards for Reporting Vascular changes on nEuroimaging (STRIVE) criteria have standardized the nomenclature. These include white matter hyperintensities of presumed vascular origin, recent small subcortical infarcts, lacunes of presumed vascular origin, prominent perivascular spaces, cerebral microbleeds, superficial siderosis, cortical microinfarcts, and brain atrophy. Recently, the rigid categories among cognitive impairment, vascular dementia, stroke, and small vessel disease have become outdated, with a greater emphasis on brain health. Conventional and advanced small vessel disease imaging markers allow a comprehensive assessment of global brain health. In this review, we discuss the pathophysiology of small vessel disease neuroimaging nomenclature by means of the STRIVE criteria, clinical implications, the role of advanced imaging, and future directions.

ABBREVIATIONS: BOLD = blood oxygen level–dependent; CAA = cerebral amyloid angiopathy (SVD type 2); CMB = cerebral microbleeds; cSS = cortical superficial siderosis; HA = hypertensive arteriosclerosis (SVD type 1); ICH = intracerebral hemorrhage; PVS = prominent perivascular spaces; STRIVE = STAndards for Reporting Vascular changes on nEuroimaging; SVD = small vessel disease; WMH = white matter hyperintensities

Small vessel disease (SVD) is an umbrella term of disease processes affecting the small arteries, arterioles, venules, and capillaries of the brain. The small vessel injuries cause lesions that can be detected on pathologic examination and that are now increasingly being recognized on brain imaging.^{1,2} Although SVD can be asymptomatic, it commonly coexists with neurodegenerative diseases and can exacerbate cognitive impairment, increase the risk of stroke, and worsen outcome after stroke.^{3–6} In fact, SVD is an enormous health burden, causing about 25% of ischemic strokes and most hemorrhagic strokes, is the most common cause of vascular dementia, and contributes to about half of dementias worldwide.^{3,5–8} As the rigid boundaries among vascular dementia, stroke, and SVD fade, the common theme now is brain health.^{9,10} The spectrum of SVD includes white matter hyperintensities (WMH) of presumed vascular origin, recent small subcortical infarcts, lacunes, microbleeds, superficial siderosis,

prominent perivascular spaces, microinfarcts, and brain atrophy.^{11,12} There have been competing systems in the past regarding the neuroimaging standards for classification of SVD. However, due to the substantial variation in how studies have defined SVD on conventional MR imaging,^{13,14} a most recent international effort to establish clinical and research standards to facilitate a more consistent approach in describing SVD neuroimaging was proposed by the STAndards for Reporting Vascular changes on nEuroimaging (STRIVE).¹¹

There are different types and etiopathogenic classifications of SVD, with a proposed classification (Table 1).¹ Type 1, hypertensive arteriosclerosis (HA), and type 2, cerebral amyloid angiopathy (CAA) are, by far, the most common sporadic types of SVD in older adults and the most radiologically well-established entities.¹⁵ Although most SVD is sporadic, likely related to hypertension or other vascular risk factors, a few forms are related to rare genetic diseases (for example, CADASIL; cerebral autosomal recessive arteriopathy with subcortical infarcts and leukoencephalopathy; Fabry disease; Hereditary Endotheliopathy with Retinopathy, Nephropathy, and Stroke syndrome; and COL4AI), of which CADASIL is the most common (Table 1).⁵

In this review, we discuss the underlying mechanisms and pathophysiology of SVD neuroimaging nomenclature using the STRIVE criteria, clinical implications, the role of advanced imaging, and future directions. Because SVD is almost ubiquitous in

Received April 18, 2021; accepted after revision July 5.

From the Departments of Neuroradiology (A.M., L.L.W., B.J.W., V.K., A.V.) and Neurology (P.K., B.K., R.P.S., R.S.), University of Cincinnati Medical Center, Cincinnati, Ohio.

Please address correspondence to Abdelkader Mahammedi, MD, Department of Neuroradiology, University of Cincinnati Medical Center, 234 Goodman St, Cincinnati, OH; e-mail: abdelkm2@gmail.com

 Indicates open access to non-subscribers at www.ajnr.org

 Indicates article with online supplemental data.

<http://dx.doi.org/10.3174/ajnr.A7302>

Table 1: Etiopathogenic classification of cerebral small vessel diseases

Classification
Type 1: HA Fibrinoid necrosis, lipohyalinosis, microatheroma, microaneurysms
Type 2: Sporadic and hereditary CAA
Type 3: Inherited or genetic SVD (distinct from CAA) For example, CADASIL, CARASIL, MELAS, Fabry disease, COL4A1 mutations, and so forth
Type 4: Inflammatory- and immunologically-mediated SVD Examples: Wegener granulomatosis, Churg-Strauss syndrome, microscopic polyangiitis, Henoch-Schönlein purpura, cryoglobulinemic vasculitis, cutaneous leukocytoclastic angiitis, primary angiitis of the CNS, Sjögren syndrome, rheumatoid vasculitis, scleroderma, dermatomyositis, and so forth
Type 5: Venous collagenosis
Type 6: Other SVD Examples: postradiation angiopathy and nonamyloid microvessel degeneration in Alzheimer disease

Note:—MELAS indicates Mitochondrial Encephalopathy, Lactic Acidosis, and Stroke-like episodes; CARASIL, cerebral autosomal recessive arteriopathy with subcortical infarcts and leukoencephalopathy.

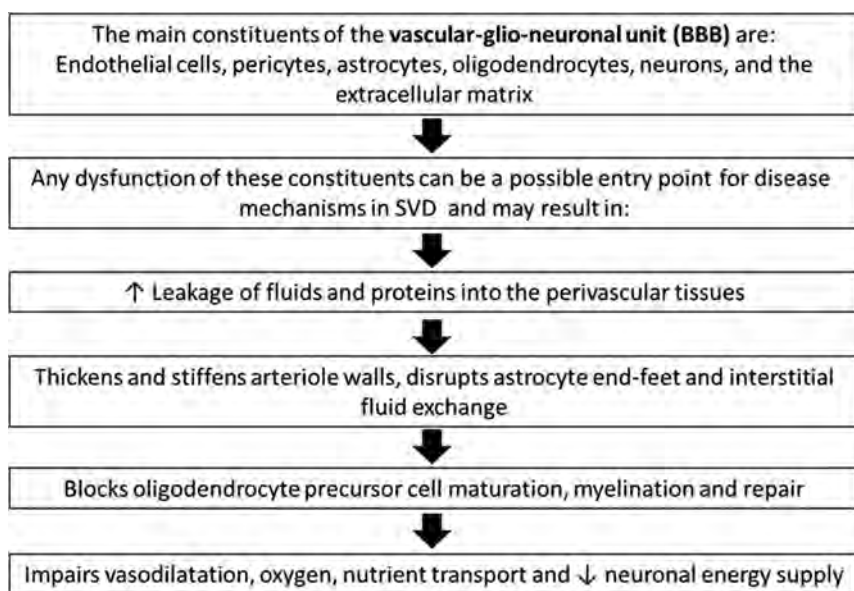


FIG 1. Possible entry points in the pathophysiology of SVD. The order of these events has not been determined.

adult brain imaging, it is important for radiologists to be familiar with the imaging spectrum, nomenclature, and clinical relevance.

Pathophysiology and Epidemiology of SVD

The exact pathogenesis of SVD is incompletely understood, but the most common abnormalities are diffuse arteriolosclerosis, lipohyalinosis, and fibrinoid necrosis of small arterioles.^{2,16-18} Additionally, embolism or atheroma and other vascular risk factors (diabetes mellitus, hypertension, and hypercholesterolemia) are also believed to play a role.² Fisher¹⁶ suggested that symptomatic lacunar infarcts were caused by atherosclerosis or embolism in the larger arterioles, whereas the silent infarcts were likely attributable to lipohyalinosis or fibrinoid necrosis in the smaller arterioles.² Lacunar infarcts were traditionally considered to be mainly caused by lipohyalinosis of small perforating arteries. However, atherosclerosis in the parental artery can produce a similar single lacunar infarct by blocking the orifice of branching arteries.¹⁹ A systematic review of Asian studies reported that parent artery atherosclerosis resulted in 20% of single

lacunar infarcts. There are four possible mechanisms for lacunar ischemic stroke that have been proposed: atheroma of parent arteries (usually MCA) or perforating arterioles, embolism from the heart or carotid arteries, and intrinsic SVD (lipohyalinosis or fibrinoid necrosis).^{19,20}

Although hypertension is a key risk factor, many patients with SVD are not hypertensive.^{2,21-24} Recent studies suggest more complex mechanisms other than arteriolosclerosis that can cause capillary wall dysfunction. The deposition of lipids in arteriolar walls (microatheroma) can damage the endothelium (Fig 1),^{2,5} leading to leakage of plasma proteins and inflammatory cells into the perivascular tissues.^{5,25} The BBB dysfunction involving the neuroglivascular unit can result in vessel stiffening, inflammation, myelin damage, and secondary neurodegeneration.^{2,5,26-28} The

neuroglivascular unit has multiple possible entry points for disease mechanisms (ie, endothelial cells, pericytes, astrocytes, oligodendrocytes, neurons, and the extracellular matrix). At a cellular level, the disruption of normal astrocyte function decreases neuronal energy supply, resulting in BBB leakage.^{2,25,29} Although the exact order of these events is not well-established, these cellular changes of endothelial failure and inflammation are more dynamic and widespread than previously thought.^{2,5} It was also hypothesized that in rodents, prominent perivascular spaces can be associated with a blockage of the drainage of interstitial fluid from increased vessel stiffness and increased arteriolar pulsatility such as with arterial hypertension, which results in fluid stagnation in the perivascular spaces and thus decreased interstitial fluid flushing.^{5,30} This result may impede the clearance of metabolites (including β -amyloid and other proteins) from tissues. Alzheimer disease, cerebral amyloid angiopathy, and several monogenic small vessel diseases are thus being considered as protein elimination failure angiopathies.^{5,30}

Although there is significant variation in the epidemiology of SVD markers, the prevalence of these markers is associated with

Table 2: Visual grading scales for SVD markers and total SVD score

MR Imaging Sequence and Visual Rating	Total SVD Score ^a	
	Type 1: Hypertensive ⁴²	Type 2: CAA ³³
Classic markers		
Lacune	Any lacunes: 1 point	
WMH	Deep WMH (Fazekas 2 or 3) or periventricular WMH (Fazekas 3): 1 point	Deep WMH (Fazekas 2 or 3) or periventricular WMH (Fazekas 3): 1 point
	0 = absent; 1 = caps or pencil-thin; 2 = smooth halo; 3 = irregular extending to deep WM Deep WMH: 0 = absent; 1 = punctate foci; 2 = beginning confluence; 3 = large confluent areas	
PVS	T2WI 4-point visual rating scale: 0: no PVS; 1 (mild): ≤10 PVS; 2 (moderate): 11–20 PVS; 3 (moderate to severe): 21–40 PVS; and 4 (severe): >40 PVS	>20 PVS in the basal ganglia: 1 point
Microbleeds	T2* GRE/SWI; several visual scores are available including MARS and BOMBS	Any microbleed: 1 point
New markers		2–4 Cortical CMB: 1 point; ≥5 cortical CMB: 2 points
cSS	T2* GRE/SWI, categorized as focal or disseminated	Focal cSS: 1 point; disseminated cSS: 2 points
Cortical microinfarct	High-field MR imaging (>3T) 3D TIWI 3D DIR	

Note:—GRE indicates gradient recalled-echo; MARS, Microbleed Anatomical Rating Scale; BOMBS, Brain Observer MicroBleed Scales; CSO, centrum semiovale; cSS, cortical superficial siderosis; BG, basal ganglia; DIR, double inversion recovery.

^a Type 1: Hypertensive; type 2: CAA.

greater age. The association between white matter hyperintensities, lacunes, prominent perivascular spaces (PVS), and cerebral microbleeds (CMB) and aging has been well-documented.³¹ Other demographic factors such as sex and ethnicity/race can also explain the variability in SVD, though the exact mechanism is poorly understood.³¹ It was reported that although Blacks and Asians have a high burden of SVD compared with Whites, Blacks had a lower prevalence of WMH but a higher prevalence of severe WMH.³² Several population-based studies have characterized SVD in the “healthy population” and explored the risk factors for SVD.³²

Neuroimaging of SVD

Nomenclature and Definitions. Radiologists are well-versed with the variations in the radiology reports describing SVD, for example, WMH, cerebral white matter disease, leukoaraiosis, and age-related white matter disease. The STRIVE guidelines and standards were developed to address this variability (Online Supplemental Data).¹¹ The recommendations were initially applied to research studies with the potential goal of widespread clinical use to standardize image interpretation, acquisition, and reporting. The classic MR imaging markers of SVD include recent small subcortical infarctions, lacunes of presumed vascular origin, WMH of presumed vascular origin, PVS, and CMB. Two additional MR imaging markers of SVD that occur with high prevalence in CAA are cortical superficial siderosis (cSS) and cortical microinfarcts (Table 2).³³

Recent Small Subcortical Infarcts. According to the STRIVE criteria, the term “recent small subcortical infarcts” refers to a recent

infarct occurring in the territory of a perforating arteriole with symptoms or imaging features that suggest a timeline of a previous few weeks. However, in most patients, these lesions can appear without apparent clinical symptoms (silent infarcts) (Online Supplemental Data).¹¹ The term “recent” is preferred instead of “acute” because it includes both the hyperacute stage and the first few weeks of the lesion.¹¹ These lesions typically measure ≤20 mm in their maximum diameter in the axial plane, though in the coronal plane, they can appear slightly larger and elongated, reflecting the territory of the occluded perforating arteriole (Fig 2A). They are best identified with hyperintense signal on DWI, hypointense signal on an ADC map, and hyperintense signal on T2-weighted and FLAIR sequences. The most common fate of these lesions on long-term follow-up is cavitation to become a lacune (in 28%–94%, depending on the duration of follow-up), turning into a nonspecific focus of T2/FLAIR hyperintensity, or eventually completely disappearing.^{2,8} Furthermore, STRIVE proposes that lesions in the basal ganglia and internal capsule of >20 mm are a different subtype and, therefore, should be classified as striatocapsular infarcts instead of small subcortical infarcts. Similarly, infarcts of the anterior choroidal artery are etiologically and anatomically distinct.

Lacunes of Presumed Vascular Origin. The STRIVE guidelines define lacunes of presumed vascular origin as round or ovoid, subcortical, fluid-filled cavities (with signal similar to that of CSF in all sequences), measuring between 3 and 15 mm in diameter, consistent with a previous, small subcortical infarct or hemorrhage located in deep gray and white matter and in a territory of perforating arteriole (Fig 2B and Online Supplemental Data). These lesions

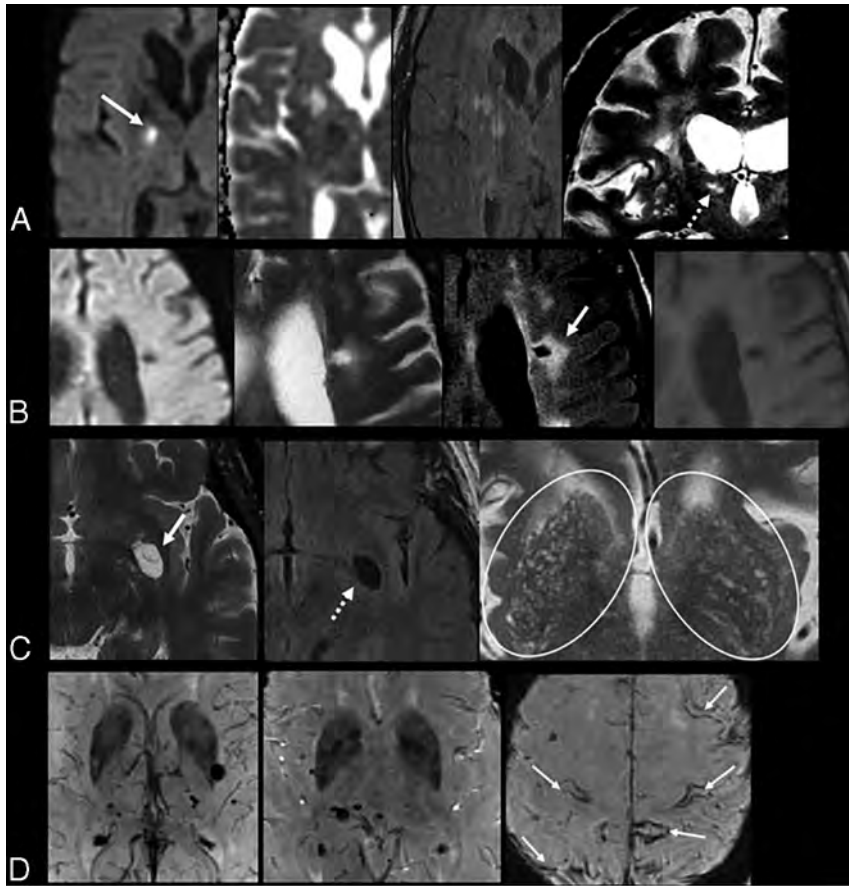


FIG 2. A, Recent subcortical infarct in the right lentiform nucleus in a 59-year-old woman with a history of hypertension. From left to right, axial DWI, ADC map, FLAIR, and coronal T2WI show restricted diffusion (*solid white arrow, A*). On coronal T2WI, the elongated morphology of the acute infarct in the craniocaudal axis (*dashed white arrow, A*) is related to the territory of a perforating artery. B, A lacune of presumed vascular origin in a 67-year-old man with a history of dementia. From left to right, axial DWI, T2WI, FLAIR, and T1WI show a remote lacunar infarct in the left frontal corona radiata, which demonstrates T2 hyperintensity with a peripheral rim of gliosis, best seen on FLAIR image (*solid white arrow, B*). C, Prominent perivascular spaces in a 63-year-old man with a history of dementia. A prominent perivascular space is noted in the left insular region with a centrally traversing vessel (*solid white arrow, C*), without peripheral gliosis on the FLAIR image (*dashed arrow, C*). Additionally, there are >20 dilated perivascular spaces in the bilateral basal ganglia on axial T2WI (*circles, C*). D, Cerebral microbleeds with cSS in an 87-year-old man with a history of CAA who presented with a worsening mental status. Axial SWI demonstrate multiple foci of susceptibility artifacts predominantly involving the basal ganglia and thalami, consistent with microbleeds. Additional areas of scattered cortical subarachnoid hemorrhagic staining (*arrows, D*) indicate cortical superficial siderosis.

typically demonstrate a surrounding gliotic rim of T2 FLAIR hyperintensity (Figs 3 and 4), which can be a useful feature when present. A peripheral gliotic rim can also surround perivascular spaces when they pass through an area of white matter hyperintensity. Although lacunes are commonly seen in older patients without symptoms, they are associated with an increased risk of stroke, dementia, and gait impairment.^{5,11}

WMH of Presumed Vascular Origin. WMH of presumed vascular origin are characterized by hyperintense lesions on T2 FLAIR and decreased attenuation on CT in the periventricular/deep cerebral white matter, subcortical gray matter, basal ganglia, and

brainstem. Although the Fazekas visual rating scale (Fig 3) is the most commonly used method to assess the burden of WMH, there is a lack of a rigorous method to accurately quantify the WMH burden.³⁴ Furthermore, a fronto-occipital gradient was used in few studies to describe the difference in the severity of WMH between the frontal and occipital lobes.^{33,35} It was suggested that patients with obvious occipital-dominant WMH were more likely to develop complications from SVD such as lobar intracranial hemorrhage than healthy controls.³⁵ The severity of WMH is strongly associated with cerebrovascular disease, vascular risk factors, gait disturbance, cognitive symptoms, and poststroke functional outcomes.^{3,11}

Perivascular Spaces, Also Called Virchow-Robin Spaces. Perivascular spaces are extensions of the extracerebral fluid space that are covered by the pia mater, which surrounds cerebral vessels from the brain surface into and through the brain parenchyma. These are commonly microscopic and not visible on conventional neuroimaging, but when they become prominent and numerous, they are considered a marker of SVD. PVS have been shown to be associated with other SVD markers such as WMH and lacunes, but not atrophy.¹¹ PVS have a signal intensity similar to that of CSF in all sequences and appear round or ovoid with a diameter of <3 mm but can appear more elongated when imaged parallel to the course of the penetrating vessel. They are typically located in the inferior basal ganglia, centrum semiovale, and midbrain and do not have a surrounding gliotic rim (in

contrast with lacunes) (Fig 2C and Online Supplemental Data). Although lacunes and PVS can have similar MR imaging features, pathologic studies have demonstrated that lesions that are <3 mm in diameter are more likely to be perivascular spaces than lacunes.¹¹ A traversing vessel can sometimes be seen in the center of a perivascular space when imaged at high resolution, another differentiator of PVS versus lacunes (Fig 2C). The severity of PVS is typically assessed on axial T2-weighted images using a validated 4-point visual rating scale based on the total number of PVS (0 indicating no PVS; 1 [mild], ≤10 PVS; 2 [moderate], 11–20 PVS; 3 [moderate to severe], 21–40 PVS; and 4 [severe], >40 PVS) in the basal ganglia and centrum semiovale (Table

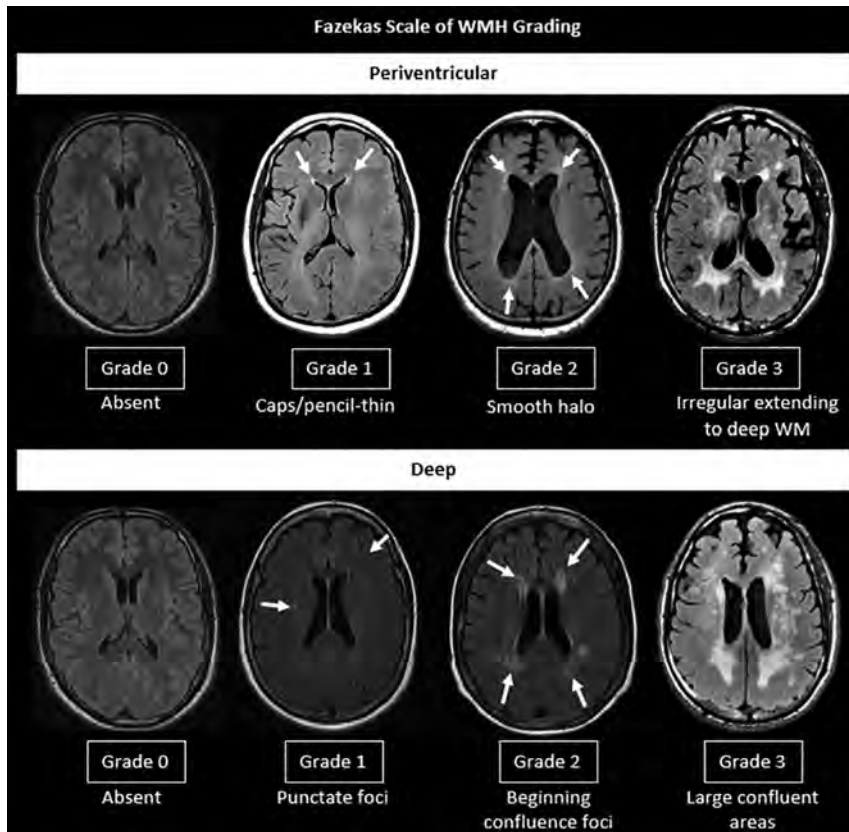


FIG 3. Fazekas scale of WMH grading.

2).³³ The topography of PVS can be a helpful characteristic of the underlying SVD type: PVS are likely associated with arteriolosclerosis when located in the basal ganglia, and they are more likely to be related to CAA when located in the centrum semiovale (Fig 4).¹⁰ However, the clinical significance of PVS remains unclear; a few studies have reported that PVS can be associated with an increased risk of dementia if located in the basal ganglia and white matter.^{5,10,36}

CMB. CMB are small round or ovoid lesions (≤ 10 mm in diameter) of marked hypointensity with associated blooming on T2 gradient-echo (T2*) or other sequences that are sensitive to susceptibility effects, especially SWI (Fig 2D and Online Supplemental Data). CMB correspond to hemosiderin-laden macrophages in perivascular tissue, consistent with vascular leakage of blood cells.⁵ Several visual scores are available, including the Microbleed Anatomical Rating Scale and the Brain Observer MicroBleed Scales, which

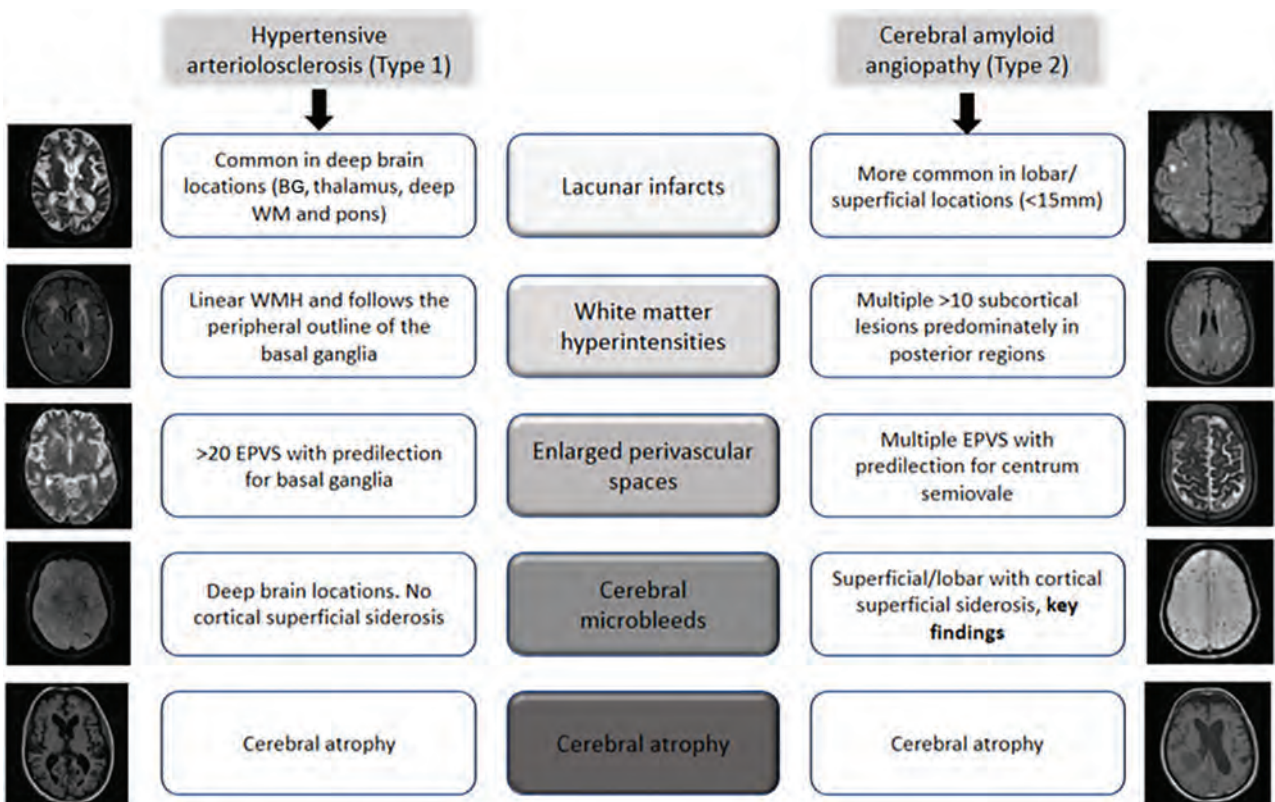


FIG 4. SVD MR imaging markers of the two most common etiopathogenic types of cerebral SVD in older adults, HA and CAA. BG indicates basal ganglia; EPVS: enlarged prominent perivascular spaces.

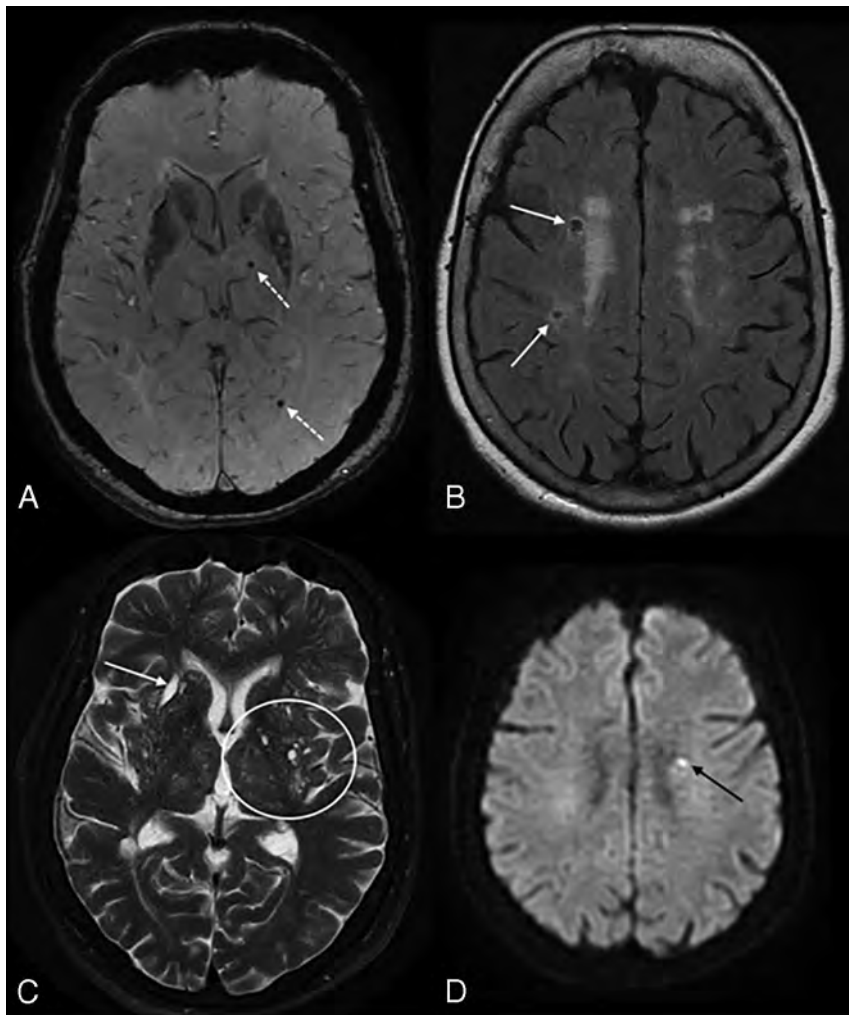


FIG 5. High SVD burden in a 55-year-old man with a history of arterial hypertension. Note multiple microbleeds in the left thalamus and occipital lobe (*dotted arrows*) on SWI (A), remote lacunar infarcts in the right centrum semiovale (*white arrows*, B), and WMH Fazekas 2 on FLAIR (B). More than 20 dilated perivascular spaces are seen on axial T2WI (*circle*, C) and remote lacunar infarct in right lentiform nucleus (*white arrow*, C). The total SVD score is 4. The patient developed an acute lacunar infarct (*black arrow*) on DWI (D) 10 months later.

have reasonable intrarater and interrater reliability for the presence of definite microbleeds.^{37,38} In fact, a few recent publications have proposed a novel automatic method to detect CMB from MR images by exploiting the 3D convolutional neural network.³⁹ CMB are associated with an increased risk of cognitive decline and ischemic and hemorrhagic stroke, though the risk of dementia appears higher in patients with CMB restricted to a superficial/lobar location compared with those with deep involvement.^{5,10} Two other hemorrhagic manifestations of SVD include cSS and spontaneous intracerebral hemorrhage (in contrast to secondary hemorrhage due to other causes such as trauma and vascular malformations).

Total SVD Score

Although the neuroimaging markers have typical characteristics, in practice, it is difficult to distinguish lacunes, PVS, and WMH of presumed vascular origin because they are often closely related. A few studies have suggested combining these MR imaging

markers and using a more comprehensive approach to assess total SVD burden.^{33,40} Total SVD score is a simple and pragmatic way of assessing overall brain health and has been shown to be a prognostic indicator of cognitive decline and recurrent stroke (Fig 5). The total burden of lesions in specific anatomic locations can also be used for lesion-symptom associations and has been shown to be associated with cognitive impairment and gait and mood disorders.^{5,40,41} For instance, a total SVD score in CAA was proposed by Charidimou et al³³ and can potentially provide a more practical framework to better evaluate the effect of CAA-related brain damage on clinical outcomes. A similar total MR imaging SVD burden approach was proposed in HA by Klarenbeek et al.⁴² The imaging rating points of total SVD burden are outlined in Table 2.

Imaging in HA versus CAA

HA (type 1) and CAA (type 2) are the most common sporadic SVD types in older adults (Fig 4 and Table 2) with intrinsically different pathophysiology, clinical significance, and prognosis.¹⁵ HA predominantly affects small perforating end arteries of the deep gray nuclei and deep white matter, whereas CAA results from β -amyloid deposition within the cortical and leptomeningeal arteries. Both types are common causes of ischemic manifestation, intracranial hemorrhage, and cognitive impairment. Although both types can be associated with similar imaging markers, including CMB, WMH, lacunar infarcts, and PVS, the anatomic distribution of these markers can be helpful to differentiate these 2 entities radiologically. Lobar/superficial and cortical distribution is consistently associated with CAA, whereas the involvement of deep brain regions and the basal ganglia is most often associated with HA (Fig 4 and Table 2).^{15,33,36,42-44} Furthermore, deep CMB are typically associated with arteriosclerosis, whereas a strictly superficial/lobar location is characteristic of CAA.¹⁰ CAA is characteristically associated with lobar CMV, cSS, centrum semiovale perivascular spaces, and multiple punctate FLAIR WMH (typically >10) with a predilection for the posterior regions.^{15,33,44} A peri-basal ganglia pattern of WMH is strongly linked to arteriosclerosis (Fig 4).¹⁵

Clinical Implications

Clinical manifestations of SVD and poor brain health can be varied. The presenting clinical symptoms can be abrupt, such as a

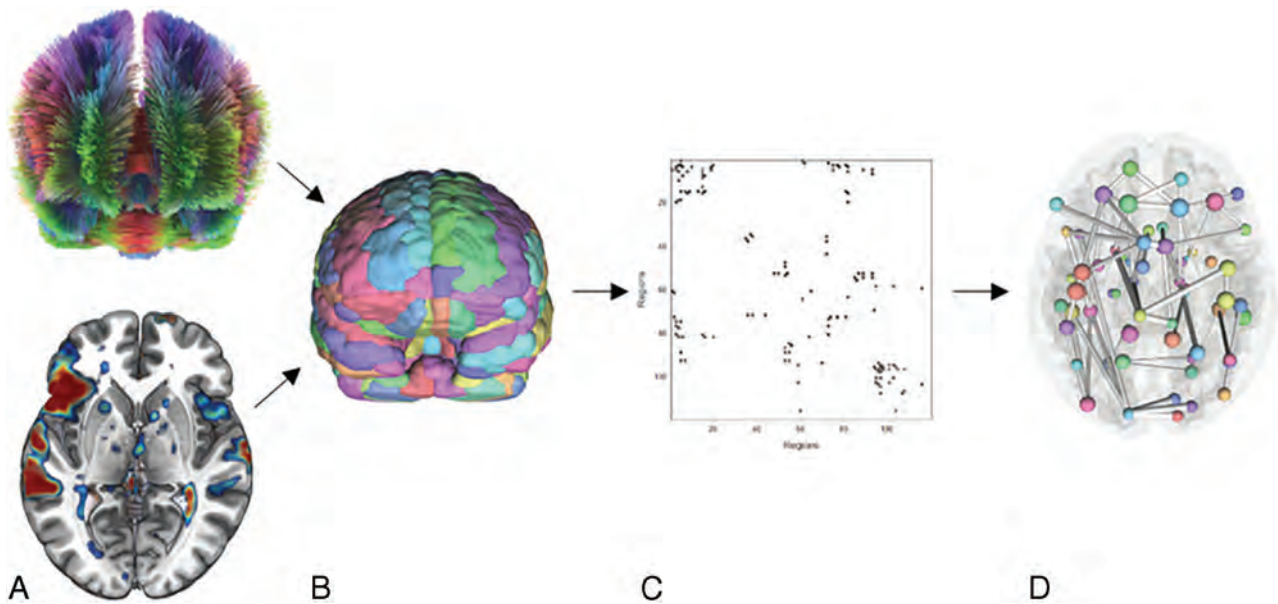


FIG 6. Sample pipeline for studying brain connectivity for assessing global brain health. *A*, Data are processed to generate structural (tractography) or functional (fMRI) connectivity measures. *B*, A parcellation scheme is applied to obtain connectivity between different regions. *C*, The connectivity data are represented as an adjacency matrix. *D*, Network properties are calculated on the adjacency matrix. In the sample image, regions in the network are sized by importance (ie, centrality) and edges are sized by the strength of the connection.

resulting intracerebral hemorrhage (ICH) or, more insidious, manifesting as progressive cognitive decline, mood disorders, extrapyramidal symptoms, and depression. This variability can be due to multiple factors including characteristics of vascular injury (type, location, and extent), the degree of comorbidities, and resilience factors such as brain reserve, which refers to the capacity to cope with brain pathology.⁵ Many clinical symptoms relate to secondary neurodegeneration due to the global effects of SVD such as brain atrophy.^{5,45-50} Several studies have shown that subcortical infarcts and WMH can induce loss of a connected cortex distal to the infarct through degeneration of white matter tracts, which results in secondary cortical thinning, and neurodegeneration.^{45,47,48} The main clinical manifestations of SVD follow.

SVD and Ischemic Stroke. SVD causes approximately 25% of all acute ischemic strokes, mainly in the form of lacunar infarction.¹⁰ Although stroke recurrence is similar to that in other stroke subtypes, the proportion of patients with lacunar infarct who are dependent at 3 years is 42%.¹⁰ Approximately 30% of patients with lacunar stroke will develop cognitive impairment, mostly involving executive functions, attention, and psychomotor speed.¹⁰

SVD and ICH. ICH presumed due to SVD can result in devastating complications with high morbidity and mortality and a significant risk of recurrence.⁵¹ CMB are present in 52% of patients with first-ever ICH and 83% of those with recurrent ICH.⁵¹ The location of recurrent ICH can relate to the distribution and severity of underlying SVD, particularly CMB and superficial siderosis, which could help in identifying patients at high risk of ICH recurrence.⁵¹ Furthermore, it is reported that the presence of ≥ 5 CMB can be associated with recurrent lobar ICH.³³

SVD and Cognitive Decline. SVD coexists with Alzheimer disease and Alzheimer disease–related dementia, can worsen cognitive outcome, and is the most common cause of vascular dementia, contributing to about 50% of dementias.^{5-7,10} Recent data suggest that WMH burden is associated with an increased risk of developing dementia, including the Alzheimer disease type,³ and that arteriosclerosis increases the odds of Alzheimer disease dementia, independent of the effect of Alzheimer disease pathology.¹⁰

SVD and Parkinsonism. SVD at baseline, particularly WMH burden and lacunes, was associated with an increased risk of parkinsonism.⁵² Furthermore, microbleeds and gray matter atrophy were found to increase the risk of vascular parkinsonism.⁴⁷

Advanced Imaging for SVD

While SVD markers are extremely common findings on conventional MR imaging, there are still weak associations of the imaging markers and the heterogeneous clinical expression of SVD.^{8,53} One potential reason is that conventional MR imaging measures tend to be focal, whereas SVD is increasingly thought of as a global, whole-brain phenomenon. Furthermore, the severity and nature of clinical symptoms can be vastly different in patients with radiologically identical SVD lesions.⁴⁷ A network-based and/or global approach to observe subclinical SVD manifestations may explain this discrepancy. Advanced imaging techniques such as high-field MR imaging, DTI, blood oxygen level–dependent (BOLD) MR imaging, and perfusion imaging show considerable promise.²

High-Field MR Imaging. A recent MR imaging–identifiable marker of SVD is cortical microinfarcts. Microinfarcts, especially those in the deep gray matter, are best detected with an MR imaging field strength of ≥ 3 T. High-field (7T) MR imaging shows a greater ability to detect remote microinfarcts.⁵⁴ Most interesting, postmortem

studies have shown that the penumbra of microinfarcts can extend up to 12 times larger than the microinfarct core, which is the only component visible with conventional MR imaging.⁴⁷ Characterizing the penumbra and distribution of microinfarcts may be clinically important because they are known to lead to a reduced capability of adjacent axons to conduct action potentials.⁵⁵

DTI. In addition to measures related to white matter integrity, such as fractional anisotropy, one can also characterize the structural connectivity with tractography, an important marker for global brain health and cognition (Fig 6). In connectivity space, regions are often called “nodes” and the connections between them are called “edges.” The collection of all nodes and edges for a network can be represented as a connectivity matrix, where each row and column represent a node and entries represent connections.⁵⁶ Network properties can be derived from these matrices that describe network integration and which nodes are the most important for successful functioning. Studies using these network measures have shown that patients with SVD have decreased local and global network integration in the prefrontal and interhemispheric tracts, compared with healthy controls.⁵⁷ Additionally, studies have suggested that SVD may lead to loss of energy-dependent long-range white matter connections, which disrupt the structure of the network. This can result in lowered efficiency and connectivity of the most important regions in the brain for normal functioning (sometimes called the “rich-club”), leading to impaired cognition.⁵⁸ The connectivity and whole brain–based studies are gaining popularity and may lead to the discovery of novel biomarkers and explanations for the heterogeneity of symptoms seen in SVD.

BOLD MRI. BOLD MR imaging is a technique that measures cerebral blood flow by detecting relative regional differences in oxygenated and deoxygenated blood supply.⁵⁹ Cerebrovascular reactivity can be derived using this technique in tandem with induced hypercapnia (called a CO₂ challenge). A recent study in patients with SVD showed that lower cerebrovascular reactivity, increased venous pulsatility, and decreased foramen magnum CSF volume were associated with a greater burden of WMH and a more severe basal ganglia rating of PVS.⁶⁰ Other studies have indicated the role of aortic arch stiffening as a potential contributor in SVD through excessive pulsatile energy transmitted to the cerebral vasculature as part of brain-heart coupling.⁶¹

Another use of BOLD MR imaging is fMRI. Like tractography, fMRI can be analyzed in terms of brain connectivity. Using connectivity-based techniques with resting-state fMRI data, researchers have shown that patients with SVD have reduced connectivity in the prefrontal, parietal, and cingulate cortices, with corresponding increases in cerebellar connectivity and impaired deactivation of the default mode network.^{62,63}

Perfusion Imaging. Recently, compromised BBB integrity has gained traction as an early biomarker for SVD and may play an important role in understanding SVD pathogenesis.⁶⁴ There are 2 primary methods for measuring BBB integrity and microvasculature with MR imaging. The first, and most reliable method, is dynamic contrast-enhanced MR imaging with the use of an appropriate pharmacokinetic model.⁶⁵ Using this technique, researchers

have shown a positive correlation of SVD severity (ie, worse SVD = more compromised BBB) and decreased BBB integrity in patients with lacunar stroke and worse clinical outcome.^{66,67} The second method, which does not involve a contrast agent, is arterial spin-labeling.⁶⁸ While arterial spin-labeling has not been used to detect early biomarkers of SVD, it has been used to differentiate subgroups of patients with SVD. For example, a recent study showed that CBF, measured by 3D arterial spin-labeling, was significantly decreased globally and locally in the temporal lobe, frontal lobe, hippocampus, thalamus, and insula in patients with increasing subcortical vascular cognitive impairment.⁶⁹ There is a rich research opportunity to fully characterize the properties of the microvasculature in patients with SVD using arterial spin-labeling.

The multitude of advanced imaging techniques being used now and yet to be developed will undoubtedly lead to a redefinition of how we understand and think about SVD.

Vessel Wall Imaging

MRA and CTA are important to detect abnormalities in the lumen of vessels but cannot characterize the vessel wall.⁷⁰ Vessel wall imaging has recently been developed to address this limitation, enabling better detection of nonstenotic lesions and better characterization of stenotic lesions.^{71,72} Briefly, vessel wall imaging is achieved using a sequence with high spatial resolution with optimal contrast-to-noise, attained by suppressing luminal blood.⁷¹ Several parameters affect the quality of the resulting images, such as field strength, 2D-versus-3D imaging, and a blood-nulling technique, but there has not yet been a thorough analysis of the trade-offs among these permutations.⁷¹ Intracranial atherosclerosis provides a key example of how vessel wall imaging can advance our knowledge of SVD. Intracranial atherosclerosis has been downplayed as a contributor to SVD, likely because traditional vascular sequences (ie, MRA) can only assess luminal stenosis in large arteries.⁷³ Vessel wall imaging has revealed that intracranial atherosclerosis burden, which is dependent on features of both the lumen and the vessel wall, is related to cortical and subcortical infarcts, microinfarcts, and WMH.⁷³ Several other pathologies can be captured by vessel wall imaging and may elucidate the etiology of SVD, such as atherosclerotic plaque, large-vessel vasculitis, and discrimination of reversible cerebral vasoconstriction syndrome.⁷⁰

Artificial Intelligence Advances in SVD

While identifying the presence of at least 1 lacune or cerebral microbleed is straightforward in most situations, visual grading of WMH and PVS poses a unique challenge because the rating scales are inherently subjective, with poor agreement among neuroradiologists.⁷⁴ MR imaging, specifically T2 FLAIR imaging, is the primary way that WMH are assessed due to even higher inter-reader variability using CT scans. An automated algorithm using CT scans was able to perform as well as experts at delineating WM lesions, but it varied widely with >90% around the mean estimate.⁷⁵ Previous studies have shown some success in predicting the evolution of WMH and cognitive outcomes in patients with WMH.^{76,77} However, more research is needed on the quantification of WMH because the studies with this focus have been largely in patients with multiple sclerosis.^{78,79} WMH in patients with additional findings, such as lacunar or cortical infarcts,

present a difficult challenge for current algorithms. Furthermore, fully automated quantification of WMH, either by the Fazekas scale or volumetric measurement using a standard of care medical imaging (rather than research sequences) is difficult. Attempting to grade PVS with automated artificial intelligence tools is even more of a challenge, with only 1 study that showed good performance in the centrum semiovale but poor performance in the basal ganglia.⁸⁰ There are great opportunities for future research to explore these rating scales for greater intersubject agreement, particularly in routine imaging, and come up with efficient and reproducible artificial intelligence brain health solutions.

CONCLUSIONS AND FUTURE DIRECTIONS

Small vessel disease is a rising epidemic associated with detrimental brain health. Neuroimaging plays a fundamental role in identifying SVD. The recognition of endothelial and neurogliovascular unit dysfunction as the main underlying mechanisms of SVD is fundamental to develop the role of advanced neuroimaging techniques. A more comprehensive approach to gauge total SVD burden, rather than individualizing and classifying each of these markers separately, is needed in future studies. This may provide a more complete estimate of the full impact of SVD on the brain to better assess total brain health and the effect of SVD-related brain damage. Finally, as radiologists, it is critical that we use standardized terminology to describe SVD in both clinical and research settings.

Disclosures: Pooja Khatri—RELATED: Grant: National Institutes of Health.* UNRELATED: Consultancy: Lumosa Therapeutics, Diamedica Therapeutics*; Grants/Grants Pending: Cerenovus*; Royalties: UpToDate; Other: Bayer, Basking Biosciences, Comments: Bayer, National Trial Leader; Basking Biosciences, Scientific Advisory Board. Brett Kissela—RELATED: Grant: National Institutes of Health/National Institute of Neurological Disorders and Stroke.* Rhonna Shatz—RELATED: Grant: National Institutes of Health.* Achala Vagal—RELATED: Grant: National Institutes of Health, Cerenovus.* Comments: ROI, National Institutes of Health/National Institute of Neurological Disorders and Stroke,* NS103824; RFI, National Institute of Neurological Disorders and Stroke/National Institute on Aging, NS117643; ROI, National Institutes of Health/National Institute of Neurological Disorders and Stroke, NS100417; National Institutes of Health/National Institute of Neurological Disorders and Stroke, 1U01NS100699; National Institutes of Health/National Institute of Neurological Disorders and Stroke, U01NS110772; Principal Investigator, Imaging Core Lab, ENDOLow Trial, Cerenovus. *Money paid to the institution.

REFERENCES

- Pantoni L. **Cerebral small vessel disease: from pathogenesis and clinical characteristics to therapeutic challenges.** *Lancet Neurol* 2010;9:689–701 CrossRef Medline
- Wardlaw JM, Smith C, Dichgans M. **Mechanisms of sporadic cerebral small vessel disease: insights from neuroimaging.** *Lancet Neurol* 2013;12:483–97 CrossRef Medline
- Debette S, Schilling S, Duperron MG, et al. **Clinical significance of magnetic resonance imaging markers of vascular brain injury: a systematic review and meta-analysis.** *JAMA Neurol* 2019;76:81–94 CrossRef Medline
- Georgakis MK, Duering M, Wardlaw JM, et al. **WMH and long-term outcomes in ischemic stroke: a systematic review and meta-analysis.** *Neurology* 2019;92:e1298–1308 CrossRef Medline
- Wardlaw JM, Smith C, Dichgans M. **Small vessel disease: mechanisms and clinical implications.** *Lancet Neurol* 2019;18:684–96 CrossRef Medline
- Kapasi A, DeCarli C, Schneider JA. **Impact of multiple pathologies on the threshold for clinically overt dementia.** *Acta Neuropathol* 2017;134:171–86 CrossRef Medline
- Bos D, Wolters FJ, Darweesh SKL, et al. **Cerebral small vessel disease and the risk of dementia: a systematic review and meta-analysis of population-based evidence.** *Alzheimers Dement* 2018;14:1482–12 CrossRef Medline
- Shibuya M, da Costa Leite C, Lucato LT. **Neuroimaging in cerebral small vessel disease: update and new concepts.** *Dement Neuropsychol* 2017;11:336–42 CrossRef Medline
- Gorelick PB, Furie KL, Iadecola C, et al. **Defining optimal brain health in adults.** *Stroke* 2017;48:e284–303 CrossRef Medline
- Pasi M, Cordonnier C. **Clinical relevance of cerebral small vessel diseases.** *Stroke* 2020;51:47–53 CrossRef Medline
- Wardlaw JM, Smith EE, Biessels GJ, et al; STandards for Reporting Vascular changes on nEuroimaging (STRIVE v1). **Neuroimaging standards for research into small vessel disease and its contribution to ageing and neurodegeneration.** *Lancet Neurol* 2013;12:822–38 CrossRef Medline
- van Veluw SJ, Shih AY, Smith EE, et al. **Detection, risk factors, and functional consequences of cerebral microinfarcts.** *Lancet Neurol* 2017;16:730–40 CrossRef Medline
- Potter GM, Marlborough FJ, Wardlaw JM. **Wide variation in definition, detection, and description of lacunar lesions on imaging.** *Stroke* 2011;42:359–66 CrossRef Medline
- Zhu YC, Dufouil C, Tzourio C, et al. **Silent brain infarcts.** *Stroke* 2011;42:1140–45 CrossRef Medline
- Charidimou A, Boulouis G, Haley K, et al. **White matter hyperintensity patterns in cerebral amyloid angiopathy and hypertensive arteriopathy.** *Neurology* 2016;86:505–11 CrossRef Medline
- Fisher CM. **Lacunar infarcts: a review.** *Cerebrovascular Diseases* 1991;1:311–20 CrossRef
- Fisher CM. **Lacunar strokes and infarcts.** *Neurology* 1982;32:871–76 CrossRef CrossRef Medline
- Bailey EL, Smith C, Sudlow CL, et al. **Pathology of lacunar ischemic stroke in humans: a systematic review.** *Brain Pathol* 2012;22:583–91 CrossRef Medline
- Kim JS, Yoon Y. **Single subcortical infarction associated with parental arterial disease: important yet neglected sub-type of atherothrombotic stroke.** *Int J Stroke* 2013;8:197–203 CrossRef Medline
- Shi Y, Wardlaw JM. **Update on cerebral small vessel disease: a dynamic whole-brain disease.** *Stroke Vasc Neurol* 2016;1:83–92 CrossRef Medline
- Weber R, Weimar C, Blatchford J, et al; PROfESS Imaging Substudy Group. **Telmisartan on top of antihypertensive treatment does not prevent progression of cerebral white matter lesions in the Prevention Regimen for Effectively Avoiding Second Strokes (PROfESS) MRI substudy.** *Stroke* 2012;43:2336–42 CrossRef Medline
- Jackson CA, Hutchinson A, Dennis MS, et al. **Differing risk factor profiles of ischemic stroke subtypes: evidence for a distinct lacunar arteriopathy?** *Stroke* 2010;41:624–29 CrossRef Medline
- Lammie GA, Brannan F, Slattery J, et al. **Nonhypertensive cerebral small-vessel disease.** *Stroke* 1997;28:2222–29 CrossRef Medline
- Godin O, Tzourio C, Maillard P, et al. **Antihypertensive treatment and change in blood pressure are associated with the progression of white matter lesion volumes.** *Circulation* 2011;123:266–73 CrossRef Medline
- Bosetti F, Galis ZS, Bynoe MS, et al; “Small Blood Vessels: Big Health Problems” Workshop Participants. **Small blood vessels: big health problems? scientific recommendations of the National Institutes of Health Workshop.** *J Am Heart Assoc* 2016;5:e0043898 CrossRef Medline
- Petersen MA, Ryu JK, Akassoglou K. **Fibrinogen in neurological diseases: mechanisms, imaging and therapeutics.** *Nat Rev Neurosci* 2018;19:283–301 CrossRef Medline

27. Wuerfel J, Haertle M, Waiczies H, et al. **Perivascular spaces: MRI marker of inflammatory activity in the brain?** *Brain* 2008;131:2332–40 CrossRef Medline
28. Hawkins BT, Davis TP. **The blood-brain barrier/neurovascular unit in health and disease.** *Pharmacol Rev* 2005;57:173–85 CrossRef Medline
29. Bechmann I, Galea I, Perry VH. **What is the blood-brain barrier (not)?** *Trends Immunol* 2007;28:5–11 CrossRef Medline
30. Iliff JJ, Wang M, Zeppenfeld DM, et al. **Cerebral arterial pulsation drives paravascular CSF–interstitial fluid exchange in the murine brain.** *J Neurosci* 2013;33:18190–99 CrossRef Medline
31. Caunca MR, De Leon-Benedetti A, Latour L, et al. **Neuroimaging of cerebral small vessel disease and age-related cognitive changes.** *Front Aging Neurosci* 2019;11:145 CrossRef Medline
32. Das AS, Regenhardt RW, Vernooij MW, et al. **Asymptomatic cerebral small vessel disease: insights from population-based studies.** *J Stroke* 2019;21:121–38 CrossRef Medline
33. Charidimou A, Martinez-Ramirez S, Reijmer YD, et al. **Total magnetic resonance imaging burden of small vessel disease in cerebral amyloid angiopathy: an imaging-pathologic study of concept validation.** *JAMA Neurol* 2016;73:994–1001 CrossRef Medline
34. Fazekas F, Chawluk J, Alavi A, et al. **MR signal abnormalities at 1.5 T in Alzheimer's dementia and normal aging.** *AJR Am J Roentgenol* 1987;149:351–56 CrossRef Medline
35. Zhu YC, Chabriat H, Godin O, et al. **Distribution of white matter hyperintensity in cerebral hemorrhage and healthy aging.** *J Neurol* 2012;259:530–36 CrossRef Medline
36. Passiak BS, Liu D, Kresge HA, et al. **Perivascular spaces contribute to cognition beyond other small vessel disease markers.** *Neurology* 2019;92:e1309–21 CrossRef Medline
37. Gregoire SM, Chaudhary UJ, Brown MM, et al. **The Microbleed Anatomical Rating Scale (MARS).** *Neurology* 2009;73:1759–66 CrossRef Medline
38. Cordonnier C, Potter GM, Jackson CA, et al. **Improving interrater agreement about brain microbleeds.** *Stroke* 2009;40:94–99 CrossRef Medline
39. Dou Q, Chen H, Yu L, et al. **Automatic detection of cerebral microbleeds from MR images via 3D convolutional neural networks.** *IEEE Trans Med Imaging* 2016;35:1182–95 CrossRef Medline
40. Staals J, Makin SD, Doubal FN, et al. **Stroke subtype, vascular risk factors, and total MRI brain small-vessel disease burden.** *Neurology* 2014;83:1228–34 CrossRef Medline
41. Banerjee G, Jang H, Kim HJ, et al. **Total MRI small vessel disease burden correlates with cognitive performance, cortical atrophy, and network measures in a memory clinic population.** *J Alzheimers Dis* 2018;63:1485–97 CrossRef Medline
42. Klarenbeek P, van Oostenbrugge RJ, Rouhl RPW, et al. **Ambulatory blood pressure in patients with lacunar stroke.** *Stroke* 2013;44:2995–99 CrossRef Medline
43. Pasi M, Boulouis G, Fotiadis P, et al. **Distribution of lacunes in cerebral amyloid angiopathy and hypertensive small vessel disease.** *Neurology* 2017;88:2162–68 CrossRef Medline
44. Shams S, Martola J, Charidimou A, et al. **Topography and determinants of magnetic resonance imaging (MRI)-visible perivascular spaces in a large memory clinic cohort.** *J Am Heart Assoc* 2017;6:e006229 CrossRef Medline
45. Duering M, Righart R, Wollenweber FA, et al. **Acute infarcts cause focal thinning in remote cortex via degeneration of connecting fiber tracts.** *Neurology* 2015;84:1685–92 CrossRef
46. Dickie DA, Karama S, Ritchie SJ, et al. **Progression of white matter disease and cortical thinning are not related in older community-dwelling subjects.** *Stroke* 2016;47:410–16 CrossRef Medline
47. Ter Telgte A, van Leijsen EM, Wiegertjes K, et al. **Cerebral small vessel disease: from a focal to a global perspective.** *Nat Rev Neurol* 2018;14:387–98 CrossRef Medline
48. Peres R, De Guio F, Chabriat H, et al. **Alterations of the cerebral cortex in sporadic small vessel disease: a systematic review of in vivo MRI data.** *J Cereb Blood Flow Metab* 2016;36:681–95 CrossRef Medline
49. Chabriat H, Hervé D, Duering M, et al. **Predictors of clinical worsening in cerebral autosomal dominant arteriopathy with subcortical infarcts and leukoencephalopathy.** *Stroke* 2016;47:4–11 CrossRef Medline
50. Rizvi B, Narkhede A, Last BS, et al. **The effect of white matter hyperintensities on cognition is mediated by cortical atrophy.** *Neurobiol Aging* 2018;64:25–32 CrossRef Medline
51. Charidimou A, Imaizumi T, Moulin S, et al. **Brain hemorrhage recurrence, small vessel disease type, and cerebral microbleeds: a meta-analysis.** *Neurology* 2017;89:820–29 CrossRef Medline
52. van der Holst HM, De Leeuw FE. **Author response.** *Neurology* 2016;86:1268–69 CrossRef Medline
53. Gouw AA, Seewann A, van der Flier WM, et al. **Heterogeneity of small vessel disease: a systematic review of MRI and histopathology correlations.** *J Neurol Neurosurg Psychiatry* 2011;82:126–35 CrossRef Medline
54. van Rooden S, Goos JD, van Opstal AM, et al. **Increased number of microinfarcts in Alzheimer disease at 7-T MR imaging.** *Radiology* 2014;270:205–11 CrossRef
55. Coban H, Tung S, Yoo B, et al. **Molecular disorganization of axons adjacent to human cortical microinfarcts.** *Front Neurol* 2017;8:405 CrossRef Medline
56. Rubinov M, Sporns O. **Complex network measures of brain connectivity: uses and interpretations.** *Neuroimage* 2010;52:1059–69 CrossRef Medline
57. Lawrence AJ, Chung AW, Morris RG, et al. **Structural network efficiency is associated with cognitive impairment in small-vessel disease.** *Neurology* 2014;83:304–11 CrossRef Medline
58. Marebwa BK, Adams RJ, Magwood GS, et al. **Cardiovascular risk factors and brain health: impact on long-range cortical connections and cognitive performance.** *J Am Heart Assoc* 2018;7:e010054 CrossRef Medline
59. Ogawa S, Tank DW, Menon R, et al. **Intrinsic signal changes accompanying sensory stimulation: functional brain mapping with magnetic resonance imaging.** *Proc Natl Acad Sci U S A* 1992;89:5951–55 CrossRef Medline
60. Blair GW, Thrippleton MJ, Shi Y, et al. **Intracranial hemodynamic relationships in patients with cerebral small vessel disease.** *Neurology* 2020;94:e2258–69 CrossRef Medline
61. Aghilinejad A, Amlani F, King KS, et al. **Dynamic effects of aortic arch stiffening on pulsatile energy transmission to cerebral vasculature as a determinant of brain-heart coupling.** *Sci Rep* 2020;10:8784 CrossRef Medline
62. Papma JM, den Heijer T, de Koning I, et al. **The influence of cerebral small vessel disease on default mode network deactivation in mild cognitive impairment.** *Neuroimage Clin* 2012;2:33–42 CrossRef Medline
63. Schaefer A, Quinque EM, Kipping JA, et al. **Early small vessel disease affects frontoparietal and cerebellar hubs in close correlation with clinical symptoms: a resting-state fMRI study.** *J Cereb Blood Flow Metab* 2014;34:1091–95 CrossRef Medline
64. Li Y, Li M, Zuo L, et al. **Compromised blood-brain barrier integrity is associated with total magnetic resonance imaging burden of cerebral small vessel disease.** *Front Neurol* 2018;9:221 CrossRef Medline
65. Heye AK, Thrippleton MJ, Armitage PA, et al. **Tracer kinetic modeling for DCE-MRI quantification of subtle blood-brain barrier permeability.** *Neuroimage* 2016;125:446–55 CrossRef Medline
66. Topkian R, Barrick TR, Howe FA, et al. **Blood-brain barrier permeability is increased in normal-appearing white matter in patients with lacunar stroke and leukoaraiosis.** *J Neurol Neurosurg Psychiatry* 2010;81:192–97 CrossRef Medline
67. Wardlaw JM, Doubal FN, Valdes-Hernandez M, et al. **Blood-brain barrier permeability and long-term clinical and imaging outcomes in cerebral small vessel disease.** *Stroke* 2013;44:525–27 CrossRef Medline
68. Hendrikse J, Petersen ET, Golay X. **Vascular disorders: insights from arterial spin-labeling.** *Neuroimaging Clin N Am* 2012;22:259–69 CrossRef Medline

69. Sun Y, Cao W, Ding W, et al. **Cerebral blood flow alterations as assessed by 3D ASL in cognitive impairment in patients with subcortical vascular cognitive impairment: a marker for disease severity.** *Front Aging Neurosci* 2016;8:211 CrossRef Medline
70. Mandell DM, Mossa-Basha M, Qiao Y, et al; Vessel Wall Imaging Study Group of the American Society of Neuroradiology. **Intracranial vessel wall MRI: Principles and Expert Consensus Recommendations of the American Society of Neuroradiology.** *AJNR Am J Neuroradiol* 2017;38:218–29 CrossRef Medline
71. Lindenholz A, van der Kolk AG, Zwanenburg JJM, et al. **The use and pitfalls of intracranial vessel wall imaging: how we do it.** *Radiology* 2018;286:12–28 CrossRef Medline
72. Farag S, El-Dien HZ, Abdelazeem Y, et al. **Value of vessel wall magnetic resonance imaging in the diagnosis of cerebrovascular diseases.** *Egypt J Neurol Psychiatry Neurosurg* 2020;56:114 CrossRef
73. Zwartbol MH, van der Kolk AG, Kuijf HJ, et al; UCC-SMART Study Group. **Intracranial vessel wall lesions on 7T MRI and MRI features of cerebral small vessel disease: the SMART-MR study.** *J Cereb Blood Flow Metab* 2021;41:1219–28 CrossRef Medline
74. Mårtensson G, Ferreira D, Cavallin L, et al; Alzheimer's Disease Neuroimaging Initiative. **AVRA: Automatic visual ratings of atrophy from MRI images using recurrent convolutional neural networks.** *Neuroimage Clin* 2019;23:101872 CrossRef Medline
75. Chen L, Carlton Jones AL, Mair G, et al; IST-3 Collaborative Group. **Rapid automated quantification of cerebral leukoaraiosis on CT images: a multicenter validation study.** *Radiology* 2018;288:573–81 CrossRef Medline
76. Rachmadi MF, Valdés-Hernández M del C, Makin S, et al. **Automatic spatial estimation of white matter hyperintensities evolution in brain MRI using disease evolution predictor deep neural networks.** April 21, 2020. *bioRxiv*. <https://www.biorxiv.org/content/10.1101/738641v3>. Accessed April 21, 2020
77. Schirmer MD, Dalca AV, Sridharan R, et al. **White matter hyperintensity quantification in large-scale clinical acute ischemic stroke cohorts: the MRI-GENIE study.** *Neuroimage Clin* 2019;23:101884 CrossRef Medline
78. Jiang J, Liu T, Zhu W, et al. **UBO Detector: a cluster-based, fully automated pipeline for extracting white matter hyperintensities.** *Neuroimage* 2018;174:539–49 CrossRef Medline
79. Schmidt P, Pongratz V, Küster P, et al. **Automated segmentation of changes in FLAIR-hyperintense white matter lesions in multiple sclerosis on serial magnetic resonance imaging.** *Neuroimage Clin* 2019;23:101849 CrossRef Medline
80. Dubost F, Yilmaz P, Adams H, et al. **Enlarged perivascular spaces in brain MRI: Automated quantification in four regions.** *Neuroimage* 2019;185:534–44 CrossRef Medline

Beyond Diffusion Tensor MRI Methods for Improved Characterization of the Brain after Ischemic Stroke: A Review

E.V.R. DiBella, A. Sharma, L. Richards, V. Prabhakaran, J.J. Majersik, and S.K. HashemizadehKolowri



ABSTRACT

SUMMARY: Ischemic stroke is a worldwide problem, with 15 million people experiencing a stroke annually. MR imaging is a valuable tool for understanding and assessing brain changes after stroke and predicting recovery. Of particular interest is the use of diffusion MR imaging in the nonacute stage 1–30 days poststroke. Thousands of articles have been published on the use of diffusion MR imaging in stroke, including several recent articles reviewing the use of DTI for stroke. The goal of this work was to survey and put into context the recent use of diffusion MR imaging methods beyond DTI, including diffusional kurtosis, generalized fractional anisotropy, spherical harmonics methods, and neurite orientation and dispersion models, in patients poststroke. Early studies report that these types of beyond-DTI methods outperform DTI metrics either in being more sensitive to poststroke changes or by better predicting outcome motor scores. More and larger studies are needed to confirm the improved prediction of stroke recovery with the beyond-DTI methods.

ABBREVIATIONS: AD = axial diffusivity; AK = axial kurtosis; DKI = diffusional kurtosis imaging; FA = fractional anisotropy; FM = Fugl-Meyer; GFA = generalized fractional anisotropy; MD = mean diffusivity; MK = mean kurtosis; NODDI = neurite orientation dispersion and density imaging; PLIC = posterior limb of the internal capsule; RD = radial diffusivity; SHORE = simple harmonic oscillator-based reconstruction and estimation; v_{ic} = neurite density; WMTI = white matter tract integrity

Stroke or a cerebrovascular accident is a problem worldwide, with 15 million people having a stroke annually, and it is a widespread cause of long-term disability and mortality.¹ MR imaging is a valuable tool for understanding and assessing brain changes after stroke and predicting recovery. Of particular interest is the use of diffusion MR imaging after the hyperacute stage, at 1–30 days poststroke. Thousands of articles have been published on the use of diffusion MR imaging in stroke, including several recent articles reviewing the use of DTI in stroke.^{2–4} The goal of this work was to survey and put into context the recent use of diffusion MR imaging methods beyond DTI, including diffusional kurtosis imaging (DKI),⁵ generalized fractional anisotropy (GFA),⁶ and neurite orientation dispersion and density imaging (NODDI) models,⁷ in patients poststroke. These methods use functional representations that either better match wider

ranges of diffusion data or tie to biophysical models that may better inform stroke studies. Early works report that these types of methods outperform DTI metrics.

Time Course of Ischemic Stroke

Approximately 87% of strokes are ischemic, while 13% are hemorrhagic; this review focuses on ischemic stroke. Because more ischemic strokes occur in the territory of the MCA than in other locations, most ischemic strokes affect the motor system. For example, 80% of individuals with stroke have impaired upper extremity motor function acutely.^{8,9}

The typical time course of ischemic stroke (Online Supplemental Data) begins with an acute phase in which ischemia results from development of either an in situ or embolic thrombus that lodges in a cerebral blood vessel, reducing or stopping blood flow to neural tissue served by that vessel. Soon after reduction of downstream blood flow, cytotoxic edema develops in the ischemic area and the cells in both gray and white matter swell, reducing the extracellular space from ~20% to 4%–10%.¹⁰ Such cell swelling is due to the lack of oxygen that impedes adenosine triphosphate production needed for active transport by Na^+/K^+ ATPase to keep Na ions in balance.¹⁰ Ischemic areas with blood flow of < 10mL/100g become damaged in < 6 minutes,¹⁰ creating an ischemic core.¹¹ Membrane configurations also change and form blebs,^{10,12} also termed

Received September 6, 2021; accepted after revision November 8.

From the Departments of Radiology and Imaging Sciences (E.V.R.D., A.S., S.K.H.), Occupational and Recreational Therapies (L.R.), and Neurology (J.J.M.), University of Utah, Salt Lake City, Utah; and Department of Radiology (V.P.), University of Wisconsin, Madison, Wisconsin.

Please address correspondence to Ed DiBella, PhD, UCAIR/Radiology and Imaging Sciences, 729 Arapeen Dr, Salt Lake City, UT 84108; e-mail: Edward.dibella@hsc.utah.edu

Indicates open access to non-subscribers at www.ajnr.org

Indicates article with online supplemental data.

<http://dx.doi.org/10.3174/ajnr.A7414>

axonal beading.¹³ Acute treatments with tPA or catheter-based clot removal can be very helpful in limiting or avoiding neural damage if the patient presents early poststroke.

During the next weeks and months, the ischemic area turns into a necrotic core and the whole brain changes in a variety of ways. In the peri-ischemic area, Wallerian degeneration¹⁴ of the myelinated tracts is generally detectable at a few days poststroke and continues for months. Wallerian degeneration is the process of demyelination and disintegration of the distal axons that occurs after injury to a neuron. Axonal swelling is also characteristic of the early stage of Wallerian degeneration. Wallerian degeneration may occur both near and far from the ischemic bed. For example, rats with MCA occlusion exhibited Wallerian degeneration in the nonischemic corpus callosum.¹⁴

Lesions in one hemisphere also promote changes in the unlesioned (contralateral) hemisphere, depending on the amount of damage to the ipsilesional motor system. Degeneration of transcallosal fibers, increased branching and pruning of dendrites, and increased contralateral corticospinal tract sprouting have been reported.¹⁵ Jones and Adkins¹⁶ suggest that overcompensation with the nonparetic side promotes remodeling in the contralesional hemisphere and may cause synaptic competition with the lesioned hemisphere and reduce recovery in the paretic limb.

Neuroimaging with MR imaging plays several roles in stroke; the focus of this review is the use of diffusion MR imaging in the nonhyperacute-but-early stage 1–30 days poststroke, sometimes termed the subacute stage.

Diffusion MR imaging is widely used to assess and study stroke. MR imaging diffusion-weighted images reflect how water protons diffuse during short time spans. The water diffusivity depends on the local environment of the water protons. For example, in intact myelinated fibers, water protons diffuse with little restriction along the axon or fiber. In CSF, diffusion is isotropic and protons move relatively freely in all directions. While MR imaging diffusion images are acquired on millimeter scales, the diffusion reflects hindrances and restrictions to water mobility due to microstructures, with scales on the order of microns. Thus, diffusion provides information about the integrity of neural microstructures, but in a complicated way because the brain has a variety of neuronal cell bodies, axons, dendrites, and glial cells in each image voxel. The different compartments and the orientations of the fibers in the cell and the intra- and extracellular spaces influence the diffusion signal.¹⁷

Standard diffusion MR imaging acquires unweighted ($b = 0$) and diffusion-weighted images with diffusion weighting in multiple directions. Parameters such as ADC maps are calculated. The diffusion tensor signal representation uses a low-order cumulant expansion of diffusion¹⁸ and enables obtaining parameters such as fractional anisotropy (FA), mean diffusivity (MD), axial diffusivity (AD), and radial diffusivity (RD). Diffusion imaging and DTI have been reviewed in many places.¹⁹ The Online Supplemental Data show an example of some of these different parameters from DTI.

There has also been a tremendous amount of work, which is doubling every 2.9 years (see Fig 1 in Novikov et al²⁰), on diffusion MR imaging microstructural mapping techniques. These methods use higher-order signal expansions (such as DKI) or

other signal representations²¹ or model-based approximations to the biophysics. The motivation is that these models can be more specific to particular structures in a voxel and thus give more information regarding health or disease. The different signal representations and models are derived in different ways and require different data acquisitions than DTI, in particular with regard to q -space sampling and b -values (Online Supplemental Data). However, many of the parameters can be derived from the same acquisitions, and some of the studies listed in the Online Supplemental Data give parameters from several different representations or models, using the same data set. The Online Supplemental Data also show an example of some of these different parameters from most of the methods that are detailed later in this review.

For stroke, most of the work has focused on the corticospinal tract and white matter.²² Gray matter has been studied in healthy individuals with a NODDI model²³ and with a model designed for gray matter²⁴ (which may require very high b -values). There are limited studies using beyond-DTI microstructural mapping methods to look at gray matter in human subjects with stroke, though DKI⁵ and diffusion spectrum imaging²⁵ have been used.

Diffusion MR Imaging in Stroke

In regions of ischemic stroke, signal in diffusion-weighted images is decreased acutely.²⁶ The reason that diffusion decreases in stroke is not completely understood, though a number of studies give some insight into the process. For example, as described above, ischemic neurons undergo axonal swelling. If axons swell and intra-axon diffusion compared with extra-axonal diffusion is quite different, then having more intra-axonal space, which is more restricted to diffusion, could result in lower diffusion (and higher signal) on the MR images. However, a study using fluoro-deoxyglucose molecules found that the molecule diffuses equally in both intra- and extracellular spaces and diffusion in both spaces decreases ($\sim 40\%$ ADC decrease) in ischemic conditions.²⁷ More recent works have evolved estimates of intra-axonal diffusion and its relation to extracellular diffusion.^{28–30} A likely partial explanation for slower, more restricted diffusion in stroke regions is that axons become “beaded,” more tortuous instead of purely cylindrical structures so that the total cell surface area is preserved during the swelling.³¹ In this case, diffusion may become more restricted, especially in the axonal direction. Simulations have shown that water ADC decreases in beaded structures.^{13,31} Photomicrographs¹² and confocal microscopy have shown such structures.³²

Other factors such as the multiexponential diffusion change with b -value, water exchange, and the axonal g -ratio (outer-to-inner axon diameter ratio),²⁰ also play roles in imaging diffusion after stroke. Water exchange between fast and slow diffusion components has been studied,³³ and the biophysics of white matter in the context of diffusion imaging was reviewed by Nilsson et al.³⁴ More recently, a beyond-DTI method sensitive to exchange was proposed (Online Supplemental Data).³⁵

We move now to consider some of the works that illustrate how MR imaging has been used in the assessment of stroke and for prediction of stroke recovery.

Diffusion MR Imaging for Predicting Recovery from Stroke. Diffusion MR imaging has many potential uses in subacute stroke, including understanding the time course of brain changes, predicting the response to specific therapeutic interventions, and selecting and monitoring therapy. Predicting motor recovery has been a highly studied objective.²

Why Predict Recovery? Stroke research includes both hyperacute evaluation and treatment with thrombolysis or mechanical clot removal and less acute evaluation. “Time is brain,” and as described above, and for suitable patients presenting to the hospital within 24 hours, tPA and thrombectomy procedures often help recovery by reducing the extent of neural damage. Yet, while these procedures reduce damage from stroke, they usually do not eliminate such damage. After hyperacute procedures and for the ~80% of subjects who do not receive such intervention, rehabilitation is commonly needed. How the brain recovers after stroke and the best therapy and therapy timing for each stroke survivor after the hyperacute phase are open questions. Therapy within the first few weeks after stroke is likely to be more effective due to the heightened neuroplasticity potential at that time.

Predicting recovery is, thus, a highly sought-after goal.³⁶⁻³⁸ Accurate prediction is needed to plan discharge, set patient goals, choose therapy (therapies aimed at reducing impairment versus therapies to train compensation strategies and assistive technologies), and offer the patient a prognosis.³⁹ Recovery predictions also allow better testing of newly developed recovery therapies that hope to promote greater recovery than spontaneous recovery or current therapies.

Nonimaging Methods for Stroke Recovery Prediction. A variety of prediction methods have been used, such as those based on changes in the NIHSS,⁴⁰ but prediction methods that do not use imaging typically have poor specificity (36% in Hemmen et al⁴⁰) or only estimate a binary outcome (favorable or not favorable), which is not as useful clinically. Recovery depends, in part, on the size and the location of the ischemic area and on a variety of other factors such as demographics, systemic atherosclerosis, and social support networks.

Strokes causing motor deficits are commonly said to display proportional recovery—that is, in the first 3 months following stroke, 70% of the new impairment is recovered⁴¹⁻⁴⁴ in most individuals, while the other individuals (“atypical responders”) have much less recovery. This finding is based on function at baseline measured with the Fugl-Meyer (FM) upper extremity assessment,⁴⁵ which has a range of 0–66. For example, $\Delta FM = 0.7 \times (66 - FM_{\text{initial}}) + 0.4$ predicted recovery reasonably well in 160 of 211 subjects.⁴³ However, it was recently shown by two separate groups that mathematic coupling and ceiling effects incorrectly biased the previous findings and that random recovery could give results similar to proportional recovery when the previously published analysis methods were used.^{46,47} Thus, we may understand recovery less than we think we do, and there is additional motivation for methods such as MR imaging to bolster our ability to characterize and predict recovery from stroke.

Imaging Methods for Prediction of Stroke Recovery. MR imaging methods such as diffusion, perfusion, fMRI, spectroscopy,

and T1- and T2-weighted images give insight into the location and severity of stroke.^{48,49} Perfusion imaging to delineate ischemic areas is typically used in concert with diffusion imaging at the hyperacute stage of stroke to see if the ischemic area exceeds (defining a larger area at risk) or matches the restricted diffusion area. Match/mismatch criteria can inform the hyperacute use of thrombectomy and tPA.⁵⁰ These methods are applied at the hyperacute stage and are typically less valuable for longer-term recovery prediction. fMRI was shown to relate more weakly to motor deficits than tract integrity based on diffusion imaging.⁵¹ Moreover, task fMRI relies on patient cooperation, effort, and ability to perform motor tasks, which may be compromised on the basis of the severity of stroke, though resting state functional connectivity may be promising.⁵² T1 and T2 methods are often used to size lesions but correlate relatively poorly with motor function compared with also considering lesion location and load on a fiber tract (gauged with diffusion imaging^{53,54}). Lesion load is also a relatively poor predictor of recovery. Adding DTI enables better assessment of stroke and prediction of recovery.

DTI Methods for Predicting Stroke Recovery

DTI uses a signal representation that is limited to representing, for example, a Gaussian distribution of diffusion displacement and a single fiber direction in each voxel, which may not accurately reflect the mixture of glia, myelin, neurons, extracellular space, CSF, and microvasculature that can exist within a voxel. Still, DTI metrics are sensitive to stroke-related changes, and numerous studies have used DTI to better understand and characterize changes after stroke^{48,54} and to gauge the effects of therapies.⁵⁵

While DTI and particularly FA are useful, histology studies have shown that FA is not a specific biomarker because it conflates myelination, fiber dispersion, and intra-/extraneurite contributions. FA is widely used despite its nonspecific nature. For example, a recent review⁴ reported good correlation between a DTI metric such as FA and a motor outcome metric such as FM or NIHSS (which is not as useful a measure of motor capabilities as FM) scores, though a few of the studies did not find significant predictive correlations from the FA metrics at some stages.⁵⁶⁻⁵⁸ Kumar et al² did a meta-analysis on 6 small studies with outcome measures such as NIHSS and reported a pooled $r = 0.82$. They pointed out the need for larger, prospective studies to better determine the utility of FA metrics for predicting outcomes. As highlighted below, these retrospective studies report best-fit linear correlations for the data obtained and would not be expected to perform as well when doing prospective predictions.

Tractography from DTI has also been useful for studying stroke and predicting recovery. For example, tractography methods for defining tract-based ROIs⁴ and connectivity analysis methods^{59,60} have been developed.

Diffusion methods stand to benefit from beyond-DTI methods that can in some ways consider crossing fibers, structural compartments with hindered or restricted diffusion, and non-Gaussian distributions of the diffusive motion of water in the brain. Here, we seek to complement the recent DTI in stroke reviews²⁻⁴ by focusing on works that used beyond-DTI methods for obtaining microstructural parameter maps in stroke. Several

studies have reported better correspondence of these microstructural mapping methods with motor outcomes, and others have reported greater changes between ipsilesional and contralesional regions in the microstructural parameters compared with DTI, implying greater sensitivity to stroke effects.

Beyond-DTI Methods for Stroke

New diffusion methods have been developed that better separate the diffusion signal contributions from fiber dispersion and intra-/extraneurite compartments. More samples in q -space (Online Supplemental Data) provide better angular resolution of fibers,^{61–65} allow estimating the non-Gaussian portions of the signals (kurtosis), and enable estimating models of biophysical compartments along with fiber orientations and dispersions. Such compartment models are well-described in multiple articles, including the supplement in Lakhani et al.⁶⁶ Because the adverse impact of stroke is, in part, from disrupting white matter connectivity, better measures of assessing fiber bundle integrity could give better insight and predictive power over current techniques. This white matter assessment is one way that beyond-DTI methods may provide significant additional information. Currently, the only beyond-DTI methods used with stroke applications to date include the following: DKI, white matter tract integrity (WMTI), GFA, NODDI, simple harmonic oscillator-based reconstruction and estimation (SHORE) parameters, and 1 article using different diffusion times to estimate the rate of kurtosis.

DKI. The standard DTI representation is appropriate in freely diffusing isotropic media such as CSF. For areas with restricted diffusion such as within axons, Jensen et al⁶⁷ proposed extending the DTI signal representation to add a higher-order term:

$$\ln\left(\frac{S(b)}{S(0)}\right) = -bD + \frac{1}{6}b^2D^2K,$$

where K is the kurtosis. To have sufficient data to fit these higher-order terms uniquely, one must have data acquired at multiple nonzero b -values. As with DTI, a kurtosis tensor can be defined to take into account diffusion directions. When DKI is used to fit, the DTI tensor portion has 6 unknowns and the DKI tensor values include 15 unknowns, so at least 21 q -space samples and a $b=0$ image are typically needed. For typical brain microstructure and diffusion acquisition parameters, the non-Gaussian portion of the diffusion signal⁶⁸ will not be prevalent if $b \leq 1000$ mm²/s. Acquisitions vary but may include, for example, 15 directions at $b=1000$ and 15 directions at $b=2000$ (Online Supplemental Data). The additional microenvironment complexity in stroke may make DKI a better approach than DTI.

Most of the beyond-DTI research in stroke has been with DKI, with 10 articles in rat stroke models,^{69–78} a recent review article,⁷⁹ and 10 articles in humans (Online Supplemental Data). The rat model studies found larger changes with mean kurtosis (MK) and axial kurtosis (AK) compared with DTI metrics. Sizing of lesions was also studied with ex vivo MR imaging, and the studies found that DKI metrics such as MK were larger than those in MD and histology.^{72,78} However, with in vivo MR imaging and a different segmentation method, others reported that

the DKI metrics yielded lesion sizes smaller than MD volumes.⁷⁷ In addition, sizing has not been shown to be very predictive of motor recovery.⁸⁰ Possibly more promising from the rat model studies is that the DKI parameters changed more with time (or compared with the contralateral hemisphere) than the DTI parameters due to stroke. This increased sensitivity to stroke was also found in the studies with humans. The Online Supplemental Data summarize the details of each of these DKI human imaging poststroke articles.

The relatively widespread use of DKI compared with other beyond-DTI methods is likely due to modest acquisition requirements, GE Healthcare's early implementation of DKI in their FuncTool software on the scanner, and early reports of potential. For example, Hui et al,⁵ in 2012, reported that MK changed more than FA in stroke regions relative to the nonstroke hemisphere (ipsilesional and contralesional regions) in 44 subjects with stroke, though there was no evaluation of the clinical importance of such changes. Fast kurtosis methods using <20 diffusion-weighted images have also been developed⁸¹ and used in rat studies.^{71,74}

Ideally, FM scores at 6–12 weeks poststroke serve to measure motor outcomes, and such scores were measured in 2 DKI articles. In Spampinato et al,⁸² the MK ipsilesional/contralesional ratio gave the best correlation with FM scores ($r=0.85$). The AK ratio also was predictive ($r=0.78$), while DTI MD ($r=0.69$), and FA ($r=0.4$) ratios had lower associations with FM scores. Li et al⁸³ grouped patients into good responders (>10 -point FM change) or poor responders. Then a relative axial kurtosis AK measure (ipsilesional–contralesional)/contralesional) gave the best discrimination of the 2 groups and was superior to DTI methods. The study in Yu et al⁸⁴ used NIHSS scores rather than FM and found lower correlations, but still the relative AK metric gave the highest correlation ($r=0.3$) with NIHSS scores. DTI methods in Yu et al showed no changes in the cortical spinal tract on the stroke side relative to the contralateral side (and hence no correlation with NIHSS).

The WMTI method was included in 2 of the DKI articles.^{5,82} WMTI assumes intra- and extra-axonal compartments and estimates axonal water fraction, intra-axonal AD, extra-axonal axial and radial diffusivities, and the tortuosity of the extra-axonal space. WMTI assumes all parallel axons and so is only applied in the corpus callosum, or where $FA > 0.3$.^{5,82} WMTI parameters were calculated along with DKI, and the axonal water fraction correlated ($r=0.63$) with FM scores in Spampinato et al.⁸² More recent nonstroke works relaxed the parallel axon requirement using a WMTI-Watson model that includes fiber dispersion, though the method assumes axially symmetric diffusion, so it was only applied in the spinal cord.⁸⁵

Besides DKI, other beyond-DTI methods have been explored for use in patients with stroke. The Online Supplemental Data summarize the 9 articles that have investigated other methods: GFA, SHORE, NODDI, and rate of kurtosis methods have all shown promising results in patients with stroke.

GFA. GFA is obtained from the orientation distribution function, which can be calculated from the 3D ensemble average propagator.²¹ The 3D ensemble average propagator is obtained, for

example, by 3D Fourier transform from Cartesian-sampled q -space data.⁸⁶ Then, similar to how FA is calculated from DTI data as $SD(\lambda) / RMS(\lambda)$, where λ is the eigenvalue of the diffusion tensor and RMS stands for root mean square, $GFA = SD(\varphi) / RMS(\varphi)$, where φ represents the orientation distribution function.²¹ GFA can be considered as an extension of FA in voxels that have crossing/touching fibers, so it may give a better measure of fiber disarray in stroke.

The GFA studies in the Online Supplemental Data came from diffusion spectrum imaging, which acquires a Cartesian grid of q -space samples with a relatively high b_{maximum} (4000–8000 s/mm²). Most of these studies took the unusual approach of studying only the contralesional side. GFA revealed microstructure changes in the contralesional side during poststroke remodeling.^{6,25,87–89} Most of these studies used the same data set of ~10 patients with stroke who had been imaged with a 26-minute diffusion acquisition.^{6,25,89} GFA in the contralesional side was highly predictive of the 6-month NIHSS score ($r^2 = 0.84$ adjusted).⁶ Combining GFA + NIHSS + age had an even higher correlation ($r^2 = 0.96$ adjusted) in this small study.⁶ Other parameters (SHORE) were also calculated from this data set, as described below.

SHORE. The SHORE method calculates propagator anisotropy, along with measures of the ensemble average propagator variance (mean square displacement), return-to-the-origin probability, the return-to-the-axis probability, and the return-to-the-plane probability.⁹⁰ These parameters when evaluated in a subcortical loop of tracts gave high correlations with 6-month NIHSS scores.⁹¹ Galazzo et al²⁵ added comparison with DTI and evaluated findings in gray matter. Both articles used the 10-person diffusion spectrum imaging data set from Granziera et al⁶ and evaluated only the contralesional side.

Compartment Model Methods. Unlike the FA, GFA, and SHORE parameters that arise from signal representations that do not postulate a particular underlying biophysical model, a number of compartment-based models have been developed. These models, of which NODDI is a good example, estimate microstructural multicompartiment (intra-axon, extra-axon, CSF compartments for NODDI) and fiber-dispersion parameters. This approach is thought to be useful for characterizing dispersed or crossing fibers⁹² and for estimating white matter degeneration in the subacute phase of stroke when Wallerian degeneration and glial scarring processes are occurring.⁹³ A few groups have recently reported NODDI models to be useful in stroke imaging in rats⁹⁴ and humans.^{7,95–97} These findings are despite the fact that NODDI fixes diffusivity parameters to 1.7 (and to 3.0 s/mm² in spinal fluid), and these parameters are not uniformly correct in healthy individuals and are less accurate in stroke regions. It is also known that NODDI “neurite density” (also called v_{ic}) does not reflect the density of neurites in tumor and in stroke (where it has been called the “restricted diffusion index”). The only NODDI study including outcome measures (FM scores) was Hodgson et al,⁹⁶ in which the best outcome predictor was found to be the orientation dispersion index (optimism-adjusted $r^2 = 0.83$), though v_{ic} (or the “restricted diffusion index”) also

correlated $r^2 = 0.70$, as did GFA ($r^2 = 0.57$). Other parameters including DTI and stroke size and lesion load did not correlate as well.

The two other NODDI stroke studies included DKI and also studied changes in microstructure across time.^{7,97} The study of Wang et al⁹⁷ was unpaired: The same subject was not imaged at multiple time points. Still, the percentage difference of the orientation dispersion index in the stroke area relative to the contralesional side was larger than other NODDI parameters, MK, FA, or MD. Correlation with time since stroke onset was also highest with the orientation dispersion index. Mastropietro et al⁷ analyzed only the posterior limb of the internal capsule (PLIC) and cerebral peduncle regions and reported significant differences between their ipsilateral and contralateral sides for the orientation dispersion index and other parameters including FA, AD, RD, kurtosis anisotropy, and AK. Other parameters (MD, MK, v_{ic} , isotropic volume fraction) did not show significant differences.

Other biophysical factors, such as different T2s in intra-axonal and extracellular compartments, water exchange, and Gaussian diffusion assumed in compartments, could all be of interest but are not included in the compartment model methods. Using different diffusion times while maintaining the same b -value is also of interest and was recently shown to help predict chronic stroke areas in 5 subjects with stroke.³⁵ That method estimated the exchange rate (rate of kurtosis) using an equation based on a 2-compartment model with exchange. Other models such as NODDI assume no water exchange between the myelin and the intracellular and extracellular compartments, though there is evidence for a mixture of fast and slow exchange.³⁴ Such exchange causes signal changes due to different diffusivities and relaxivities (possibly negligible) in the different compartments.⁹⁸ A multi-shell acquisition with 2 diffusion times was used in Lampinen et al³⁵ to obtain a parameter sensitive to the exchange rate. Results showed faster exchange in the ischemic stroke areas.³⁵

The Online Supplemental Data summarize the methods with outcome measures (FM or NIHSS) graphically, with the graph edges reflecting the number of subjects in each comparison.

Acquisition and Analysis Diversity in Beyond-DTI Methods

The beyond-DTI studies varied considerably in the acquisition. Besides a range of angular q -space sampling and different shells or b -values, there were wide differences in spatial resolution (0.94–3 mm in-plane, 1.5- to 4-mm section thickness), number of slices (range, 9–64), acquisition time (range, 2–27 minutes), and imaging time poststroke (range, 6 hours to 4 weeks). A large high-resolution highly sampled q -space data set similar to that with connectome imaging would be ideal to determine the value of higher resolution and sampling for the use of beyond-DTI methods in stroke.

Different acquisition parameters may lead to different results. This possibility is best known in DTI; for example, Table 1 in Barrio-Arranz et al⁹⁹ describes results from 14 studies of different spatial resolutions, b -values, or diffusion directions and how FA and MD changed. Less has been studied with beyond-DTI methods, but for example, NODDI results are a function of b -values and gradient directions.¹⁰⁰ This finding again is motivation for large rigorous studies in stroke with overcomplete sampling and outcome measures for validation.

Analysis methods tended to be from either ROIs in parts or all of the cortical spinal tract (PLIC, the cerebral peduncle, and the corona radiata) and/or from manually identified ischemic regions. Note that it has been shown in DTI that different fitting methods (linear, nonlinear) give significantly different results.¹⁰¹ Beyond-DTI methods such as a more rapid NODDI fitting method¹⁰² also are known to affect results compared with the original slower NODDI fitting method. A few studies used tract-based analyses and/or voxel-based analyses. Atlas-based regions were often used, though it is not known how well the atlas matches tracts in stroke regions with disrupted fiber tracts. Trade-offs with SNR and with how different beyond-DTI parameters vary with voxel size are yet to be studied in subjects with stroke. Even if ROI analysis methods are used, it could be that imaging with smaller voxels could better inform microstructure and tractography methods.

Note that for predicting stroke recovery and following stroke recovery, we are interested not only in local stroke effects but also global stroke effects. The best focus and most relevant information to understand and predict adaptations are still not known. For example, some have found the PLIC to be the most predictive of future motor function, even if the stroke was not in the PLIC. This finding may be because the PLIC is a hub with incoming sensory neurons and outgoing motor control neurons and the way that stroke, even in other regions, affects the PLIC is telling. Alternatively, this may simply be from the small sample size and limited comparisons with other fiber tracts; other regions or components of regions may provide improved predictive information.

The different acquisitions, nonstandard processing, and few studies with relatively few subjects that include motor stroke outcomes mean that larger studies with FM scores and current acquisition techniques including simultaneous multislice methods¹⁰³ are needed to better understand the impact of beyond-DTI methods. While the scan times vary widely, from 2 to 27 minutes (Online Supplemental Data), this variation is, in part, due to limited coverage, spatial resolution, and q -space sampling choices. Acquisition requirements for optimal performance for the different methods are not yet known in stroke. It is likely that all of the beyond-DTI methods can be made clinically practical (<5 minutes) with advanced acquisition (simultaneous multislice) and deep learning techniques,¹⁰⁴ though those techniques are still evolving and being evaluated. Direct comparisons between the beyond-DTI methods and investigation into combining parameters from different methods should also be performed in the context of stroke.

Other Considerations

As pointed out by Kim et al,³⁸ 90% of neurologic biomarker studies, including most DTI studies as well as most nonimaging methods, did not use an independent set of stroke data to cross-validate their prediction model. Thus, the results are a best case of predicted correlation, retrospectively, with the given data set. The beyond-DTI studies reported in the tables here did not perform cross-validation, though 1 small study used k -fold cross-validation⁹⁶ to have more confidence in the predictive value. The studies also did not identify or discuss minimally clinically important differences,³⁸ which will be essential to further develop and translate these promising new methods to clinical use.

Another open question is how outcome predictions vary as a function of therapy. This question includes acute treatments such as tPA or thrombectomy and therapies such as brain-computer interface methods. The brain-computer interface has shown promising results in small studies of people with chronic stroke; recovery may be enhanced, especially if such therapies are started early after stroke. Indeed, advanced diffusion-based metrics may be able to predict who would benefit the most from the brain-computer interface or other types of therapies; plasticity or reorganization changes may be measurable with beyond-DTI parameters while confounding the interpretation of FA. The ability of diffusion methods to differentiate ipsilateral-versus-contralateral contributions of motor tracts to upper extremity function may also inform stroke rehabilitation approaches.¹⁰⁵

The many exciting new advances in neuroimaging and particularly in beyond-DTI methods are likely to have a highly significant impact in the context of predicting stroke recovery, for improving our understanding of brain changes after stroke, and for providing unique advantages when selecting personalized stroke therapy. However, this review also makes clear that there is a need for rigorous studies to better evaluate and translate these microstructural mapping methods to clinical application.

Disclosure forms provided by the authors are available with the full text and PDF of this article at www.ajnr.org.

REFERENCES

1. Roger VL, Go AS, Lloyd-Jones DM, et al; American Heart Association Statistics Committee and Stroke Statistics Subcommittee. **Heart disease and stroke statistics—2011 update: a report from the American Heart Association.** *Circulation* 2011;123:e18–e209 CrossRef Medline
2. Kumar P, Kathuria P, Nair P, et al. **Prediction of upper limb motor recovery after subacute ischemic stroke using diffusion tensor imaging: a systematic review and meta-analysis.** *J Stroke* 2016;18:50–59 CrossRef Medline
3. Puig J, Blasco G, Schlaug G, et al. **Diffusion tensor imaging as a prognostic biomarker for motor recovery and rehabilitation after stroke.** *Neuroradiology* 2017;59:343–51 CrossRef Medline
4. Moura LM, Luccas R, de Paiva JP, et al. **Diffusion tensor imaging biomarkers to predict motor outcomes in stroke: a narrative review.** *Front Neurol* 2019;10:445 Medline
5. Hui ES, Fieremans E, Jensen JH, et al. **Stroke assessment with diffusional kurtosis imaging.** *Stroke* 2012;43:2968–73 CrossRef Medline
6. Granziera C, Daducci A, Meskaldji DE, et al. **A new early and automated MRI-based predictor of motor improvement after stroke.** *Neurology* 2012;79:39–46 CrossRef Medline
7. Mastropietro A, Rizzo G, Fontana L, et al. **Microstructural characterization of corticospinal tract in subacute and chronic stroke patients with distal lesions by means of advanced diffusion MRI.** *Neuroradiology* 2019;61:1033–45 CrossRef Medline
8. Cramer SC, Nelles G, Benson RR, et al. **Functional MRI study of subjects recovered from hemiparetic stroke.** *Stroke* 1997;28:2518–27 CrossRef Medline
9. Hatem SM, Saussez G, Della Faille M, et al. **Rehabilitation of motor function after stroke: a multiple systematic review focused on techniques to stimulate upper extremity recovery.** *Front Hum Neurosci* 2016;10:442 CrossRef Medline
10. Liang D, Bhatta S, Gerzanich V, et al. **Cytotoxic edema: mechanisms of pathological cell swelling.** *Neurosurg Focus* 2007;22:E2 CrossRef Medline
11. Goyal M, Ospel JM, Menon B, et al. **Challenging the ischemic core concept in acute ischemic stroke imaging.** *Stroke* 2020;51:3147–55 CrossRef Medline

12. Hori N, Carpenter DO. **Functional and morphological changes induced by transient in vivo ischemia.** *Exp Neurol* 1994;129:279–89 CrossRef Medline
13. Baron CA, Kate M, Gioia L, et al. **Reduction of diffusion-weighted imaging contrast of acute ischemic stroke at short diffusion times.** *Stroke* 2015;46:2136–41 CrossRef Medline
14. Zuo M, Guo H, Wan T, et al. **Wallerian degeneration in experimental focal cortical ischemia.** *Brain Res Bull* 2019;149:194–202 CrossRef Medline
15. Jones TA, Schallert T. **Overgrowth and pruning of dendrites in adult rats recovering from neocortical damage.** *Brain Res* 1992;581:156–60 CrossRef Medline
16. Jones TA, Adkins DL. **Motor system reorganization after stroke: stimulating and training toward perfection.** *Physiology (Bethesda)* 2015;30:358–70 CrossRef Medline
17. Alexander DC, Dyrby TB, Nilsson M, et al. **Imaging brain microstructure with diffusion MRI: practicality and applications.** *NMR Biomed* 2019;32:e3841 CrossRef Medline
18. Kiselev VG. **Fundamentals of diffusion MRI physics.** *NMR Biomed* 2017;30 CrossRef Medline
19. Hagmann P, Jonasson L, Maeder P, et al. **Understanding diffusion MR imaging techniques: from scalar diffusion-weighted imaging to diffusion tensor imaging and beyond.** *Radiographics* 2006;26 (Suppl 1):S205–23 Medline
20. Novikov DS, Kiselev VG, Jespersen SN. **On modeling.** *Magn Reson Med* 2018;79:3172–93 CrossRef Medline
21. Tuch DS. **Q-ball imaging.** *Magn Reson Med* 2004;52:1358–72 CrossRef Medline
22. Concha L. **A macroscopic view of microstructure: using diffusion-weighted images to infer damage, repair, and plasticity of white matter.** *Neuroscience* 2014;276:14–28 CrossRef Medline
23. Fukutomi H, Glasser MF, Zhang H, et al. **Neurite imaging reveals microstructural variations in human cerebral cortical gray matter.** *Neuroimage* 2018;182:488–99 CrossRef Medline
24. Palombo M, Ianus A, Guerreri M, et al. **SANDI: A compartment-based model for non-invasive apparent soma and neurite imaging by diffusion MRI.** *Neuroimage* 2020;215:116835 CrossRef Medline
25. Boscolo Galazzo I, Brusini L, Obertino S, et al. **On the viability of diffusion MRI-based microstructural biomarkers in ischemic stroke.** *Front Neurosci* 2018;12:92 CrossRef Medline
26. Schaefer PW, Grant PE, Gonzalez RG. **Diffusion-weighted MR imaging of the brain.** *Radiology* 2000;217:331–45 CrossRef Medline
27. Duong TQ, Ackerman JJ, Ying HS, et al. **Evaluation of extra- and intracellular apparent diffusion in normal and globally ischemic rat brain via 19F NMR.** *Magn Reson Med* 1998;40:1–13 CrossRef Medline
28. Jolescu IO, Veraart J, Fieremans E, et al. **Degeneracy in model parameter estimation for multi-compartmental diffusion in neuronal tissue.** *NMR Biomed* 2016;29:33–47 CrossRef Medline
29. Dhital B, Reisert M, Kellner E, et al. **Intra-axonal diffusivity in brain white matter.** *Neuroimage* 2019;189:543–50 CrossRef Medline
30. Lampinen B, Szczepankiewicz F, Martensson J, et al. **Towards unconstrained compartment modeling in white matter using diffusion-relaxation MRI with tensor-valued diffusion encoding.** *Magn Reson Med* 2020;84:1605–23 CrossRef Medline
31. Budde MD, Frank JA. **Neurite beading is sufficient to decrease the apparent diffusion coefficient after ischemic stroke.** *Proc Natl Acad Sci U S A* 2010;107:14472–77 CrossRef Medline
32. Datar A, Ameeramja J, Bhat A, et al. **The roles of microtubules and membrane tension in axonal beading, retraction, and atrophy.** *Biophys J* 2019;117:880–91 CrossRef Medline
33. Brugières P, Thomas P, Maraval A, et al. **Water diffusion compartmentation at high b values in ischemic human brain.** *AJNR Am J Neuroradiol* 2004;25:692–68 Medline
34. Nilsson M, van Westen D, Stahlberg F, et al. **The role of tissue microstructure and water exchange in biophysical modelling of diffusion in white matter.** *MAGMA* 2013;26:345–70 CrossRef Medline
35. Lampinen B, Latt J, Wasselius J, et al. **Time dependence in diffusion MRI predicts tissue outcome in ischemic stroke patients.** *Magn Reson Med* 2021;86:754–64 CrossRef Medline
36. Kruezelmann A, Kohrmann M, Sobesky J, et al. **Pretreatment diffusion-weighted imaging lesion volume predicts favorable outcome after intravenous thrombolysis with tissue-type plasminogen activator in acute ischemic stroke.** *Stroke* 2011;42:1251–54 CrossRef Medline
37. Campbell BC, Tu HT, Christensen S, et al. **Assessing response to stroke thrombolysis: validation of 24-hour multimodal magnetic resonance imaging.** *Arch Neurol* 2011;69:45–50 CrossRef Medline
38. Kim B, Winstein C. **Can neurological biomarkers of brain impairment be used to predict poststroke motor recovery? A systematic review.** *Neurorehabil Neural Repair* 2017;31:3–24 CrossRef Medline
39. Kwah LK, Herbert RD. **Prediction of walking and arm recovery after stroke: a critical review.** *Brain Sci* 2016;6:53 CrossRef Medline
40. Hemmen TM, Ernstrom K, Raman R. **Two-hour improvement of patients in the National Institute of Neurological Disorders and Stroke trials and prediction of final outcome.** *Stroke* 2011;42:3163–67 CrossRef Medline
41. Prabhakaran S, Zarahn E, Riley C, et al. **Inter-individual variability in the capacity for motor recovery after ischemic stroke.** *Neurorehabil Neural Repair* 2008;22:64–71 CrossRef Medline
42. Krakauer JW, Marshall RS. **The proportional recovery rule for stroke revisited.** *Ann Neurol* 2015;78:845–47 CrossRef Medline
43. Winters C, van Wegen EE, Daffertshofer A, et al. **Generalizability of the proportional recovery model for the upper extremity after an ischemic stroke.** *Neurorehabil Neural Repair* 2015;29:614–22 CrossRef Medline
44. Stinear CM, Byblow WD, Ackerley SJ, et al. **Proportional motor recovery after stroke: implications for trial design.** *Stroke* 2017;48:795–98 CrossRef Medline
45. Fugl-Meyer AR, Jaasko L, Leyman I, et al. **The post-stroke hemiplegic patient, I; a method for evaluation of physical performance.** *Scand J Rehabil Med* 1975;7:13–31 Medline
46. Hawe RL, Scott SH, Dukelow SP. **Taking proportional out of stroke recovery.** *Stroke* 2018 Dec 7. [Epub ahead of print] CrossRef Medline
47. Hope TM, Friston K, Price CJ, et al. **Recovery after stroke: not so proportional after all?** *Brain* 2019;142:15–22 CrossRef Medline
48. Farr TD, Wegener S. **Use of magnetic resonance imaging to predict outcome after stroke: a review of experimental and clinical evidence.** *J Cereb Blood Flow Metab* 2010;30:703–17 CrossRef Medline
49. Sun C, Liu X, Bao C, et al. **Advanced non-invasive MRI of neuroplasticity in ischemic stroke: techniques and applications.** *Life Sci* 2020;261:118365 CrossRef Medline
50. Albers GW, Thijs VN, Wechsler L, et al; DEFUSE Investigators. **Magnetic resonance imaging profiles predict clinical response to early reperfusion: the diffusion and perfusion imaging evaluation for understanding stroke evolution (DEFUSE) study.** *Ann Neurol* 2006;60:508–17 CrossRef Medline
51. Qiu M, Darling WG, Morecraft RJ, et al. **White matter integrity is a stronger predictor of motor function than BOLD response in patients with stroke.** *Neurorehabil Neural Repair* 2011;25:275–84 CrossRef Medline
52. Carter AR, Shulman GL, Corbetta M. **Why use a connectivity-based approach to study stroke and recovery of function?** *NeuroImage* 2012;62:2271–80 CrossRef Medline
53. Zhu LL, Lindenberg R, Alexander MP, et al. **Lesion load of the corticospinal tract predicts motor impairment in chronic stroke.** *Stroke* 2010;41:910–15 CrossRef Medline
54. Kumar MA, Vangala H, Tong DC, et al. **MRI guides diagnostic approach for ischaemic stroke.** *J Neurol Neurosurg Psychiatry* 2011;83:1201–05 CrossRef Medline
55. Song J, Nair VA, Young BM, et al. **DTI measures track and predict motor function outcomes in stroke rehabilitation utilizing BCI technology.** *Front Hum Neurosci* 2015;9:195 CrossRef Medline

56. Puig J, Pedraza S, Blasco G, et al. **Wallerian degeneration in the corticospinal tract evaluated by diffusion tensor imaging correlates with motor deficit 30 days after middle cerebral artery ischemic stroke.** *AJNR Am J Neuroradiol* 2010;31:1324–30 CrossRef Medline
57. Groisser BN, Copen WA, Singhal AB, et al. **Corticospinal tract diffusion abnormalities early after stroke predict motor outcome.** *Neurorehabil Neural Repair* 2014;28:751–60 CrossRef Medline
58. Jang SH, Lee J, Lee MY, et al. **Prediction of motor outcome using remaining corticospinal tract in patients with pontine infarct: diffusion tensor imaging study.** *Somatosens Mot Res* 2016;33:99–103 CrossRef Medline
59. Pannek K, Chalk JB, Finnigan S, et al. **Dynamic corticospinal white matter connectivity changes during stroke recovery: a diffusion tensor probabilistic tractography study.** *J Magn Reson Imaging* 2009;29:529–36 CrossRef Medline
60. Kim KH, Kim YH, Kim MS, et al. **Prediction of motor recovery using diffusion tensor tractography in supratentorial stroke patients with severe motor involvement.** *Ann Rehabil Med* 2015;39:570–76 CrossRef Medline
61. Frank LR. **Anisotropy in high angular resolution diffusion-weighted MRI.** *Magn Reson Med* 2001;45:935–39 CrossRef Medline
62. Tuch DS, Reese TG, Wiegell MR, et al. **High angular resolution diffusion imaging reveals intravoxel white matter fiber heterogeneity.** *Magn Reson Med* 2002;48:577–82 CrossRef Medline
63. Wedeen VJ, Wang RP, Schmahmann JD, et al. **Spectrum magnetic resonance imaging (DSI) tractography of crossing fibers.** *Neuroimage* 2008;41:1267–77 CrossRef Medline
64. Van AT, Granziera C, Bammer R. **An introduction to model-independent diffusion magnetic resonance imaging.** *Top Magn Reson Imaging* 2010;21:339–54 CrossRef Medline
65. Jones DK, Knosche TR, Turner R. **White matter integrity, fiber count, and other fallacies: The do's and don'ts of diffusion MRI.** *Neuroimage* 2013;73:239–54 CrossRef Medline
66. Lakhani DA, Schilling KG, Xu J, et al. **Advanced multicompartiment diffusion MRI models and their application in multiple sclerosis.** *AJNR Am J Neuroradiol* 2020;41:751–57 CrossRef Medline
67. Jensen JH, Helpern JA, Ramani A, et al. **Diffusional kurtosis imaging: the quantification of non-Gaussian water diffusion by means of magnetic resonance imaging.** *Magn Reson Med* 2005;53:1432–40 CrossRef Medline
68. Lu H, Jensen JH, Ramani A, et al. **Three-dimensional characterization of non-Gaussian water diffusion in humans using diffusion kurtosis imaging.** *NMR Biomed* 2006;19:236–47 CrossRef Medline
69. Cheung JS, Wang E, Lo EH, et al. **Stratification of heterogeneous diffusion MRI ischemic lesion with kurtosis imaging: evaluation of mean diffusion and kurtosis MRI mismatch in an animal model of transient focal ischemia.** *Stroke* 2012;43:2252–54 CrossRef Medline
70. Hui ES, Du F, Huang S, et al. **Spatiotemporal dynamics of diffusional kurtosis, mean diffusivity and perfusion changes in experimental stroke.** *Brain Res* 2012;1451:100–09 CrossRef Medline
71. Sun PZ, Wang Y, Mandeville E, et al. **Validation of fast diffusion kurtosis MRI for imaging acute ischemia in a rodent model of stroke.** *NMR Biomed* 2014;27:1413–18 CrossRef Medline
72. Umesh Rudrapatna S, Wieloch T, Beirup K, et al. **Can diffusion kurtosis imaging improve the sensitivity and specificity of detecting microstructural alterations in brain tissue chronically after experimental stroke? Comparisons with diffusion tensor imaging and histology.** *Neuroimage* 2014;97:363–73 CrossRef Medline
73. Weber RA, Hui ES, Jensen JH, et al. **Diffusional kurtosis and diffusion tensor imaging reveal different time-sensitive stroke-induced microstructural changes.** *Stroke* 2015;46:545–50 CrossRef Medline
74. Wu Y, Kim J, Chan ST, et al. **Comparison of image sensitivity between conventional tensor-based and fast diffusion kurtosis imaging protocols in a rodent model of acute ischemic stroke.** *NMR Biomed* 2016;29:625–30 CrossRef Medline
75. Zhang S, Yao Y, Shi J, et al. **The temporal evolution of diffusional kurtosis imaging in an experimental middle cerebral artery occlusion (MCAO) model.** *Magn Reson Imaging* 2016;34:889–95 CrossRef Medline
76. Wang E, Wu Y, Cheung JS, et al. **pH imaging reveals worsened tissue acidification in diffusion kurtosis lesion than the kurtosis/diffusion lesion mismatch in an animal model of acute stroke.** *J Cereb Blood Flow Metab* 2017;37:3325–33 CrossRef Medline
77. Lu D, Jiang Y, Ji Y, et al. **JOURNAL CLUB: evaluation of diffusion kurtosis imaging of stroke lesion with hemodynamic and metabolic MRI in a rodent model of acute stroke.** *AJR Am J Roentgenol* 2018;210:720–27 CrossRef Medline
78. Bay V, Kjolby BF, Iversen NK, et al. **Stroke infarct volume estimation in fixed tissue: Comparison of diffusion kurtosis imaging to diffusion weighted imaging and histology in a rodent MCAO model.** *PLoS One* 2018;13:e0196161 CrossRef Medline
79. Cheung J, Doerr M, Hu R, et al. **Refined ischemic penumbra imaging with tissue pH and diffusion kurtosis magnetic resonance imaging.** *Transl Stroke Res* 2021;12:742–53 CrossRef Medline
80. Puig J, Pedraza S, Blasco G, et al. **Acute damage to the posterior limb of the internal capsule on diffusion tensor tractography as an early imaging predictor of motor outcome after stroke.** *AJNR Am J Neuroradiol* 2011;32:857–63 CrossRef Medline
81. Hansen B, Jespersen SN. **Recent developments in fast kurtosis imaging.** *Frontiers in Physics* 2017;5 CrossRef
82. Spampinato MV, Chan C, Jensen JH, et al. **Diffusional kurtosis imaging and motor outcome in acute ischemic stroke.** *AJNR Am J Neuroradiol* 2017;38:1328–34 CrossRef Medline
83. Li C, Lan C, Zhang X, et al. **Evaluation of diffusional kurtosis imaging in sub-acute ischemic stroke: comparison with rehabilitation treatment effect.** *Cell Transplant* 2019;28:1053–61 CrossRef Medline
84. Yu X, Jiaerken Y, Wang S, et al. **Changes in the corticospinal tract beyond the ischemic lesion following acute hemispheric stroke: a diffusion kurtosis imaging study.** *J Magn Reson Imaging* 2020;52:512–19 CrossRef Medline
85. Chung S, Fieremans E, Wang X, et al. **White matter tract integrity: an indicator of axonal pathology after mild traumatic brain injury.** *J Neurotrauma* 2018;35:1015–20 CrossRef Medline
86. Wedeen VJ, Hagmann P, Tseng WY, et al. **Mapping complex tissue architecture with diffusion spectrum magnetic resonance imaging.** *Magn Reson Med* 2005;54:1377–86 CrossRef Medline
87. Jiang Q, Zhang ZG, Chopp M. **MRI evaluation of white matter recovery after brain injury.** *Stroke* 2010;41:S112–13 CrossRef Medline
88. Tang PF, Ko YH, Luo ZA, et al. **Tract-specific and region of interest analysis of corticospinal tract integrity in subcortical ischemic stroke: reliability and correlation with motor function of affected lower extremity.** *AJNR Am J Neuroradiol* 2010;31:1023–30 CrossRef Medline
89. Granziera C, Daducci A, Gigandet X, et al. **Diffusion spectrum imaging after stroke shows structural changes in the contra-lateral motor network correlating with functional recovery.** In: *Proceedings of the International Society for Magnetic Resonance in Medicine Conference*, Montreal, Quebec, Canada. May 7–13, 2011
90. Ozarslan E, Koay CG, Shepherd TM, et al. **Mean apparent propagator (MAP) MRI: a novel diffusion imaging method for mapping tissue microstructure.** *Neuroimage* 2013;78:16–32 CrossRef Medline
91. Brusini L, Obertino S, Galazzo IB, et al. **Ensemble average propagator-based detection of microstructural alterations after stroke.** *Int J Comput Assist Radiology Surg* 2016;11:1585–97 CrossRef Medline
92. Zhang H, Schneider T, Wheeler-Kingshott CA, et al. **NODDI: practical in vivo neurite orientation dispersion and density imaging of the human brain.** *Neuroimage* 2012;61:1000–16 CrossRef Medline
93. Anderova M, Vorisek I, Pivonkova H, et al. **Cell death/proliferation and alterations in glial morphology contribute to changes in diffusivity in the rat hippocampus after hypoxia-ischemia.** *J Cereb Blood Flow Metab* 2011;31:894–907 CrossRef Medline

94. Bagdasarian FA, Yuan X, Athey J, et al. **NODDI highlights recovery mechanisms in white and gray matter in ischemic stroke following human stem cell treatment.** *Magn Reson Med* 2021;86:3211–23 CrossRef Medline
95. Adluru G, Gur Y, Anderson J, et al. **Assessment of white matter microstructure in stroke patients using NODDI.** *Annu Int Conf IEEE Eng Med Biol Soc* 2014;2014:742–45 CrossRef Medline
96. Hodgson K, Adluru G, Richards LG, et al. **Predicting motor outcomes in stroke patients using diffusion spectrum MRI microstructural measures.** *Front Neurol* 2019;10:72 CrossRef Medline
97. Wang Z, Zhang S, Liu C, et al. **A study of neurite orientation dispersion and density imaging in ischemic stroke.** *Magn Reson Imaging* 2019;57:28–33 CrossRef Medline
98. Latt J, Nilsson M, van Westen D, et al. **Diffusion-weighted MRI measurements on stroke patients reveal water-exchange mechanisms in sub-acute ischaemic lesions.** *NMR Biomed* 2009;22:619–28 CrossRef Medline
99. Barrio-Arranz G, de Luis GR, Tristan-Vega A, et al. **Impact of MR acquisition parameters on DTI scalar indexes: a tractography based approach.** *PLoS One* 2015;10:e0137905 CrossRef Medline
100. Parvathaneni P, Nath V, Blaber JA, et al. **Empirical reproducibility, sensitivity, and optimization of acquisition protocol, for neurite orientation dispersion and density imaging using AMICO.** *Magn Reson Imaging* 2018;50:96–109 CrossRef Medline
101. Bergamino M, Keeling EG, Walsh RR, et al. **Systematic assessment of the impact of DTI methodology on fractional anisotropy measures in Alzheimer’s disease.** *Tomography* 2021;7:20–38 CrossRef Medline
102. Daducci A, Canales-Rodriguez EJ, Zhang H, et al. **Accelerated Microstructure Imaging via Convex Optimization (AMICO) from diffusion MRI data.** *Neuroimage* 2015;105:32–44 CrossRef Medline
103. HashemizadehKolowri K, Chen RR, Adluru G, et al. **Simultaneous multi-slice image reconstruction using regularized image domain split slice-GRAPPA for diffusion MRI.** *Med Image Anal* 2021;70:102000 CrossRef Medline
104. Ye C, Li Y, Zeng X. **An improved deep network for tissue microstructure estimation with uncertainty quantification.** *Med Image Anal* 2020;61:101650 CrossRef Medline
105. Bundy DT, Souders L, Baranyai K, et al. **Contralesional brain-computer interface control of a powered exoskeleton for motor recovery in chronic stroke survivors.** *Stroke* 2017;48:1908–15 CrossRef Medline

Implementation of a Low-Field Portable MRI Scanner in a Resource-Constrained Environment: Our Experience in Malawi

K. Chetcuti, C. Chilingulo, M.S. Goyal, L. Vidal, N.F. O'Brien, D.G. Postels, K.B. Seydel, and T.E. Taylor



ABSTRACT

SUMMARY: Low-field, portable MR imaging may expedite patient management in the setting of critical illness. We successfully implemented low-field MR imaging at the Queen Elizabeth Central Hospital in Malawi; a low-resource setting. We present our experience of low-field, portable MR imaging start-up and use in Malawi; the first of its kind in Sub-Saharan Africa, together with complementary troubleshooting mechanisms that may be used especially in similar resource-constrained contexts.

Low-field, portable MR imaging scanners may aid in the care of critically ill patients, especially those in whom transport to fixed magnets is challenging. These include unconscious comatose patients undergoing evaluation in emergency departments or bed-bound in-patients who have developed sudden-onset neurologic deficits. Portability of this family of MR imaging scanners enables this imaging technique to be used as a point-of-care tool, potentially leading to a faster diagnosis and expedited treatment, which may be life-saving. Other favorable characteristics that separate this type of low-field scanner from a high-field scanner include reduced overall scanner purchase price and running costs (reduced energy consumption), reduced costs relating to infrastructure requirements to house and operate it compared with a high-field scanner, reduced or often nullified electromagnetic interference, and increased patient comfort (reduced noise during scan acquisition and reduced patient-perceived claustrophobia). Conversely, low-field portable scanners have lower resolution and contrast of acquired images, constraints with regard to coil types limiting the body parts accessible to imaging, and limited

sequence acquisitions (as in for example the current inability to acquire postcontrast T1-weighted images).^{1,2}

Although most experience with this imaging technique has taken place in high-income countries, medical care facilities in low-resource settings may also benefit from this technology. In many low- and middle-income countries, there is a high burden of both communicable and noncommunicable diseases with a predilection for the neuroaxis. MR imaging diagnostics may be pivotal in establishing diagnoses and optimizing patient management. In environments where conventional CT and MR imaging are often unavailable, access to a low-field, portable MR imaging scanner may transform a wide variety of patients' diagnostic journeys, treatment plans, and outcomes.

We recently implemented a low-field (0.0625T), portable MR imaging scanner at the Queen Elizabeth Central Hospital in Blantyre, Malawi. In the past year, our facility has acquired 260 brain scans using this technology. Indications for imaging are divided into the routine clinical care arm (for which infections, pediatric developmental delay, and, to a smaller extent, posttrauma prognostication are the most common indications) (Fig 1), and the clinical research arm (Fig 2).

Here, we describe the challenges that our group encountered during this process of low-field MR imaging scanner implementation in a resource-constrained environment and the solutions we implemented to overcome these problems. Our experiences may be applicable to implementation of such technology in other low-resource environments (Table).

Challenge I: Logistics of Delivery and Receipt of Equipment

Currently, the only available portable low-field MR imaging scanner is Hyperfine Swoop (Hyperfine Research). The first challenge in implementing this technology for our group in Malawi was transporting the scanner to southeastern Africa. Safe and efficient

Received January 19, 2022; accepted after revision March 3.

From the Department of Paediatrics and Child Health (K.C.) and Blantyre Malaria Project (C.C., N.F.O., D.G.P., K.B.S., T.E.T.), Kamuzu University of Health Sciences, Blantyre, Malawi; Department of Radiology (C.C.), Queen Elizabeth Central Hospital, Blantyre, Malawi; Mallinckrodt Institute of Radiology (M.S.G.), Washington University School of Medicine, St. Louis, Missouri; Division of Neuroradiology (L.V.), Department of Radiology, Children's Hospital of Philadelphia, Philadelphia, Pennsylvania; Division of Critical Care Medicine (N.F.O.), Department of Pediatrics, Nationwide Children's Hospital, Ohio State University, Columbus, Ohio; Department of Neurology (D.G.P.), George Washington University/Children's National Medical Center, Washington, DC; and Department of Osteopathic Medical Specialties (K.B.S., T.E.T.), College of Osteopathic Medicine, Michigan State University, East Lansing, Michigan. This work was supported by the National Institutes of Health, grant No: 5U01AI126610.

Please address correspondence to Karen Chetcuti, MD, Department of Paediatrics and Child Health, Kamuzu University of Health Sciences, Private bag 360, Chichiri, Blantyre 3, Malawi; e-mail: kchetcuti@kuhes.ac.mw

Indicates open access to non-subscribers at www.ajnr.org

<http://dx.doi.org/10.3174/ajnr.A7494>

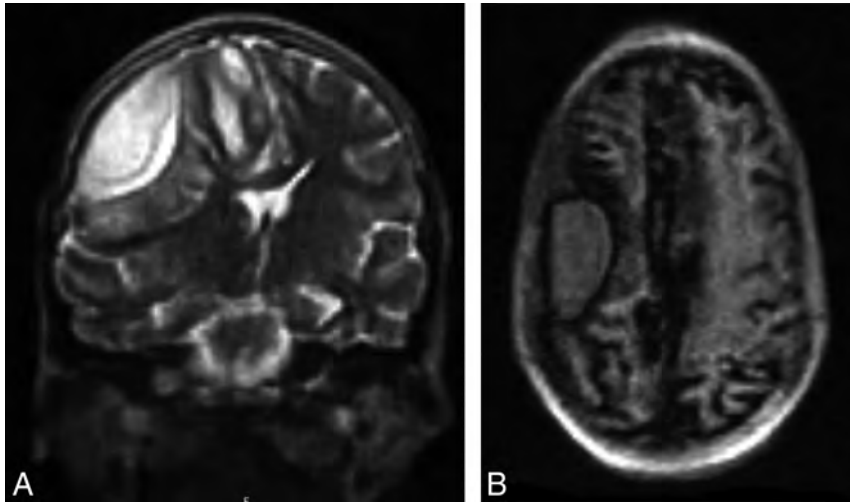


FIG 1. Hyperfine Swoop MR images of a 12-year-old child who was admitted to the pediatric ward at our institution with focal neurology, reduced consciousness, and septicemia when CT imaging was not available at our institution. The child's MR imaging demonstrated a right-sided subdural empyema, which was confirmed at surgery. MR imaging findings were of a well-defined, septated T2-weighted hyperintense subdural fluid collection associated with mass effect (A), with a corresponding T1-weighted hyperintense subdural fluid collection (B).

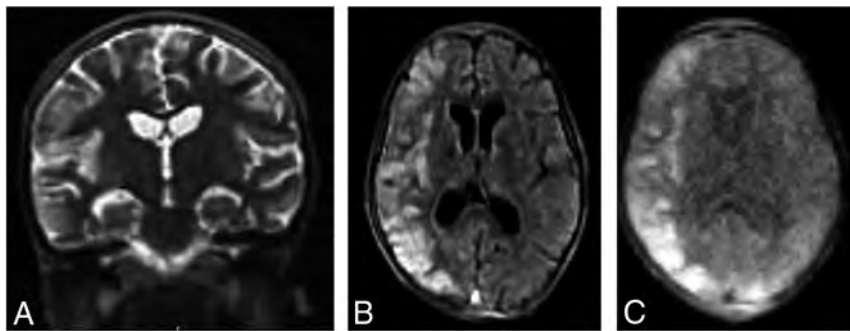


FIG 2. Hyperfine Swoop MR images of a 6-year-old child who was admitted to our institution under the research study arm with a decreased level of consciousness and malaria parasitemia. The child's MR imaging demonstrates typical findings associated with malarial encephalopathy of diffuse right-sided parietotemporal T2-weighted hyperintensity in the gray and subcortical white matter with an associated localized mass effect in the form of sulcal effacement on the coronal T2-weighted sequence (A), with corresponding restriction of diffusion on the DWI $b=900$ image and ADC images (B and C).

equipment transportation from the manufacturer to the receiving hospital is often a daunting and multistep process. There are few shippers with experience in the transportation of large, heavy, delicate imaging equipment. When the equipment reaches its final destination, it is often received only by those working in the hospital and not by manufacturer's representatives (Fig 3). Because uncrating and setup is a complex process, it is important that at least 1 person with prior training on the container-unpacking process be present during equipment receipt. The process of uncrating and setup requires supplementary tools at the receiving site and knowledge of the indicators on the external shell of the container to ensure proper care of the equipment during transportation. At the time of receipt, the container must be examined for gauges indicating possible equipment malalignment or temperature breaches during transit. Once the Hyperfine Swoop is unpacked, it can be set up so that the scanner is ready for use immediately. In our facility, the time interval between opening the crate and scanning our first patient was 4 hours.

Solutions. Once a suitable shipper is identified, flexibility and back-up plans (in case the route of travel is interrupted) are needed. Accuracy and clear communication with shipping agents relating to the dimensions of the holding crate are vital to avoid unnecessary in-transit equipment-delivery delays.

Challenges encountered and proposed solutions for low-field MR imaging implementation in a resource-limited setting

Challenge	Proposed Solution/Troubleshooting Option
Equipment delivery and receipt logistics	Needs assessment of the most reliable and safe equipment transportation route Use of a reputable carrier with tracking facilities Insurance coverage Uncrating and setup training before equipment receipt Acquisition of tools needed for uncrating and setup before equipment receipt On receipt, close inspection of external container gauges for warnings
Equipment roadmap	Needs assessment of the expected routes of equipment portability within the health care facility Construction of low-incline, smooth ramps to mitigate steep and irregular terrain
Equipment storage	Needs assessment of storage and operating conditions inclusive of temperature and humidity
Equipment operation	Training of end user operators
Equipment utilities	Needs assessment of hospital infrastructure including electricity supply and Internet speed Acquisition of a manufacturer-recommended compatible electrical surge protector
Non-resource-constrained specific items	Patient and equipment safety Patient privacy and confidentiality



FIG 3. The Hyperfine Swoop, still crated, at the time of receipt at our institution.

In our case, a member of our team traveled to the manufacturer's headquarters in Connecticut to receive training on how to uncrate and inspect the equipment on receipt at its final destination.

Challenge II: Building a Roadmap for Equipment Movement

The Hyperfine Swoop MR imaging scanner weighs 630 kg and is moved by a motor at its base. Movement of the equipment up or down inclines of $>5^\circ$ is not recommended by the manufacturer because the motor may not be powerful enough to safely navigate these inclines or declines. Therefore, the terrain over which the MR imaging scanner is to be transported must be closely examined before equipment receipt. Off-loading from long-distance transport, often by forklift, may not be able to deliver the machine close to its final location. Challenges in low-resource hospital settings include steep or rough terrain inclinations, narrow passageways (the Hyperfine Swoop is 158 cm wide), or unroofed building routes.

Solutions. We suggest a thorough predelivery review of the roadmap on which the scanner will be maneuvered to allow mitigation of terrain challenges before equipment receipt. In our case, terrain challenges required a re-evaluation of the setting in which the scanner would be housed. Additional troubleshooting mechanisms include the construction of strong, shallow-incline, smooth ramps at crucial locations.

Challenge III: Equipment Storage

As with all imaging equipment, low-field, portable MR imaging scanners must be stored and operated within a range of temperature and humidity conditions. These variables are especially important in low-resource peri-equatorial locations where a stable and uniform health care facility environment may not be present.

Solutions. Our group suggests a thorough needs assessment focusing on optimal environment preparation through the installation of air conditioning and dehumidifier units at sites where equipment is intended to be stored before equipment receipt. The manufacturer recommends that the Hyperfine Swoop be operated and stored at temperatures of 15–30 °C with an operating humidity of 15%–85%, noncondensing.

Challenge IV: Operating the Equipment

The lower magnetic field strength of portable MR imaging systems results in fewer restrictions on the site of equipment storage or operation. Metal objects are allowed in the scanning room in proximity to the scanner. This adds to the cost-effectiveness of this type of imaging because acquiring MR imaging-compatible equipment (eg, patient monitors and transportation trolleys) is unnecessary. No previous radiography technology training is required to operate a portable, low-field MR imaging scanner; the equipment was designed for use by clinicians at the point of care—a quality that makes it very attractive for use in resource-constrained settings where trained radiographers are uncommon. Nonetheless, operators require training from the manufacturer. Optimally, they should be identified and trained before scanner receipt.

Solutions. While the Queen Elizabeth Central Hospital is fortunate to have an MR imaging-trained radiographer on staff, other nonradiography team members have successfully operated the equipment. A manufacturer-led remote training session on equipment operation and a user-friendly iPad (Apple) control panel interface led to successful scan acquisition by non-radiography-trained operators. Excellent support from the manufacturer, including trouble shooting and periodic software upgrades, is crucial to the smooth operation of the equipment.

Challenge V: Adapting to Different Patient Populations

The Hyperfine Swoop is FDA-approved for use in children. However, currently available portable, low-field MR imaging scanners only accommodate adult-sized head coils. Head positioning of young children within the coil is challenging. If a child's head is not placed far in enough into the coil, it produces an artifact in the occipital region of the images, impacting the completeness of interpretation.

Solutions. The percentage of the patient's head that is located within the scanner is indicated on the Hyperfine app when imaging begins. Our group recommends that after acquiring the first localizer sequence, special attention be paid to a flashing red alert icon in the top right of the iPad controller screen. If this icon is clicked and the error message indicates that the

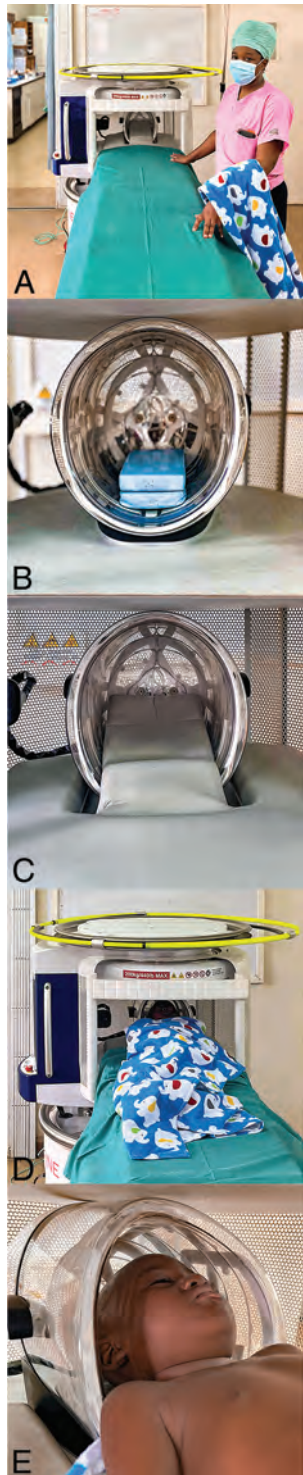


FIG 4. The Hyperfine Swoop at our institution is set up in an appropriately optimized temperature- and humidity-controlled dedicated scanning room (A) with a patient scanning couch of an appropriate height adjacent to it. B and C, The blue padding block was sourced by our group and is applied within the head coil of the scanner with the gray manufacturer-provided padding applied over it, extending onto the patient's scanning couch. The role of the blue padding block is to elevate the patient's head a little further, thereby optimizing the patient's head position further in the scanner head coil for more optimal head coverage during scanning. A patient model within the scanner (D) demonstrating the swaddling technique and a detailed view of the patient's head position within the head coil (E).

“percentage of section detected” is $<75\%$, the patient needs to be repositioned with the head placed further into the coil. Our preferred technique to overcome this challenge is to swaddle and cross the child's arms over the thorax in a cloth, allowing the patient to be placed further within the coil. Padding under the patient's upper back also aids in moving the head further into the coil (Fig 4). We suggest noting this alert immediately after obtaining localizer sequences to correct the patient's position and avoid artifacts on subsequently acquired images.

Challenge VI: Equipment Utility Challenges

Images obtained by the scanner are stored in the Internet cloud. Both a stable electrical supply and adequate Internet speed and stability are required for the scan acquisition and uploading of images for interpretation. Achieving appropriate Internet bandwidth speed and stability can be challenging in resource-constrained environments. A slow or unstable Internet connection results in loss of communication between the iPad console and the scanner, necessitating a complete restart of the scan. Slow uploading of images to the cloud results in delays in both image interpretation and patient management. In Malawi, an Internet bandwidth speed of ≥ 2.1 MB per second allows smooth image acquisition and uploading.

Solutions. Before the receipt and setup of the equipment in Malawi, our group acquired a permanently connected voltage-compatible, manufacturer-recommended electrical surge protector. The scanner is otherwise operated through a standard AC wall power outlet.

In the relatively infrequent instances in which image upload to the cloud platform was delayed due to temporary Internet unavailability, our group resorted to 1 of 2 troubleshooting mechanisms. If a radiologist was on site during acquisition, the images may be directly visualized on the iPad controller. If a radiologist was not physically present, screenshots of the iPad controller could be emailed to remotely placed radiologists for preliminary interpretation. Once Internet connectivity was restored, radiologists provided full interpretation using conventional methods using the full PACS functionality. These 2 troubleshooting mechanisms enabled a short turnaround time to provide a preliminary report, ensuring little-to-no adverse clinical care impact related to delayed MR imaging interpretation.

Challenge VII: Site Nonspecific Challenges

Other implementation challenges are not context- or equipment-specific. These include gentle patient maneuvering into the scanner to avoid patient or equipment harm and ensuring equipment cleanliness. As with high-field scanners, patient noncooperation leading to motion artifacts may reduce the ability to acquire high-quality images. We use “feed and wrap” techniques for neonates, swaddling and imaging during periods of natural sleep whenever possible, in a sleep-conducive MR imaging scanner environment. Sensitivity to patient privacy and confidentiality is a further priority.

Solutions. We have a predefined equipment-cleaning program followed by designated, preselected personnel. We ensure patient privacy and confidentiality through restriction of image access on the cloud platform to preselected authorized personnel.

Our successful implementation of this technology at the Queen Elizabeth Central Hospital, the largest public health care facility in Malawi, has facilitated patient care. Successful implementation required a large amount of logistical planning, flexibility, and improvisation. Close and timely postdelivery support by the manufacturer is crucial to our ongoing success. With careful planning, imaging modalities such as this low-field, portable MR imaging scanner now in place in

our hospital can be implemented in other resource-constrained environments.

[Disclosure forms](#) provided by the authors are available with the full text and PDF of this article at www.ajnr.org.

REFERENCES

1. Lee CS, Davis SM, McGroder C, et al. **Analysis of low-field MRI scanners for evaluation of shoulder pathology based on arthroscopy.** *Orthop J Sports Med* 2014;2:2325967114540407 CrossRef Medline
2. Deoni SC, Bruchhage MM, Beauchemin J, et al. **Accessible pediatric neuroimaging using a low field strength MRI scanner.** *Neuroimage* 2021;238:118273 CrossRef Medline

Radiomics-Based Machine Learning for Outcome Prediction in a Multicenter Phase II Study of Programmed Death-Ligand 1 Inhibition Immunotherapy for Glioblastoma

E. George, E. Flagg, K. Chang, H.X. Bai, H.J. Aerts, M. Vallières, D.A. Reardon, and R.Y. Huang



ABSTRACT

BACKGROUND AND PURPOSE: Imaging assessment of an immunotherapy response in glioblastoma is challenging due to overlap in the appearance of treatment-related changes with tumor progression. Our purpose was to determine whether MR imaging radiomics-based machine learning can predict progression-free survival and overall survival in patients with glioblastoma on programmed death-ligand 1 inhibition immunotherapy.

MATERIALS AND METHODS: Post hoc analysis was performed of a multicenter trial on the efficacy of durvalumab in glioblastoma ($n = 113$). Radiomics tumor features on pretreatment and first on-treatment time point MR imaging were extracted. The random survival forest algorithm was applied to clinical and radiomics features from pretreatment and first on-treatment MR imaging from a subset of trial sites ($n = 60-74$) to train a model to predict long overall survival and progression-free survival and was tested externally on data from the remaining sites ($n = 29-43$). Model performance was assessed using the concordance index and dynamic area under the curve from different time points.

RESULTS: The mean age was 55.2 (SD, 11.5) years, and 69% of patients were male. Pretreatment MR imaging features had a poor predictive value for overall survival and progression-free survival (concordance index = 0.472–0.524). First on-treatment MR imaging features had high predictive value for overall survival (concordance index = 0.692–0.750) and progression-free survival (concordance index = 0.680–0.715).

CONCLUSIONS: A radiomics-based machine learning model from first on-treatment MR imaging predicts survival in patients with glioblastoma on programmed death-ligand 1 inhibition immunotherapy.

ABBREVIATIONS: AUC = area under the curve; C-index = concordance index; ET = enhancing tumor; IQR = interquartile range; OS = overall survival; PFS = progression-free survival; PD-1 = programmed cell death protein 1; PD-L1 = programmed death-ligand 1; WT = whole tumor

Glioblastoma is the most common primary malignant brain tumor among adults.¹ The current standard of care is maximal surgical resection followed by radiation and temozolomide chemotherapy. However, eventual progression of the tumor is typical with limited further treatment options and a dismal median overall survival (OS) of 15 months and 5-year survival of

<10%.² Despite advances in the understanding of molecular changes in glioblastoma, effective targeted therapies are lacking, and bevacizumab, a monoclonal antibody against the vascular

The clinical study was funded by Medimmune, the Cancer Research Institute, and the Ludwig Institute for Cancer Research. Dr Huang received support from the American Roentgen Ray Society/American Society of Neuroradiology Scholar grant. Dr George received support from the American Society of Neuroradiology Scholar Award. Dr Bai received support from the Radiological Society of North America Scholar grant. Research reported in this publication was supported by a training grant from the National Institute of Biomedical Imaging and Bioengineering of the National Institutes of Health under award No. 5T32EB1680 and by the National Cancer Institute of the National Institutes of Health under award No. F30CA239407 to Dr Chang and by the National Cancer Institute of the National Institutes of Health under Award No. R03CA249554 to Dr Bai. Dr Vallières acknowledges funding from the Canada CIFAR AI Chairs Program.

Please address correspondence to Raymond Y. Huang, MD, PhD, Department of Radiology, Brigham and Women's Hospital, 75 Francis St, Boston, MA 02115; e-mail: ryhuang@bwh.harvard.edu; @LizzRad

Indicates open access to non-subscribers at www.ajnr.org

Indicates article with online supplemental data.

<http://dx.doi.org/10.3174/ajnr.A7488>

Received October 20, 2021; accepted after revision February 17, 2022.

From the Department of Radiology and Biomedical Imaging (E.G.), University of California San Francisco, San Francisco, California; Department of Radiology (E.F., R.Y.H.), Brigham and Women's Hospital, Boston, Massachusetts; Massachusetts Institute of Technology (K.C.), Cambridge, Massachusetts; Department of Diagnostic Imaging (H.X.B.), Rhode Island Hospital and Warren Alpert Medical School of Brown University, Providence, Rhode Island; Artificial Intelligence in Medicine Program (H.J.A.), Brigham and Women's Hospital, Harvard Medical School, Boston, Massachusetts; Departments of Radiation Oncology and Radiology (H.J.A.), Brigham and Women's Hospital, Dana-Farber Cancer Institute, Harvard Medical School, Boston, Massachusetts; Department of Computer Science (M.V.), Université de Sherbrooke, Sherbrooke, Quebec, Canada; and Center for Neuro Oncology (D.A.R.), Dana-Farber Cancer Institute, Boston, Massachusetts.

E. George and E. Flagg contributed equally to the study.

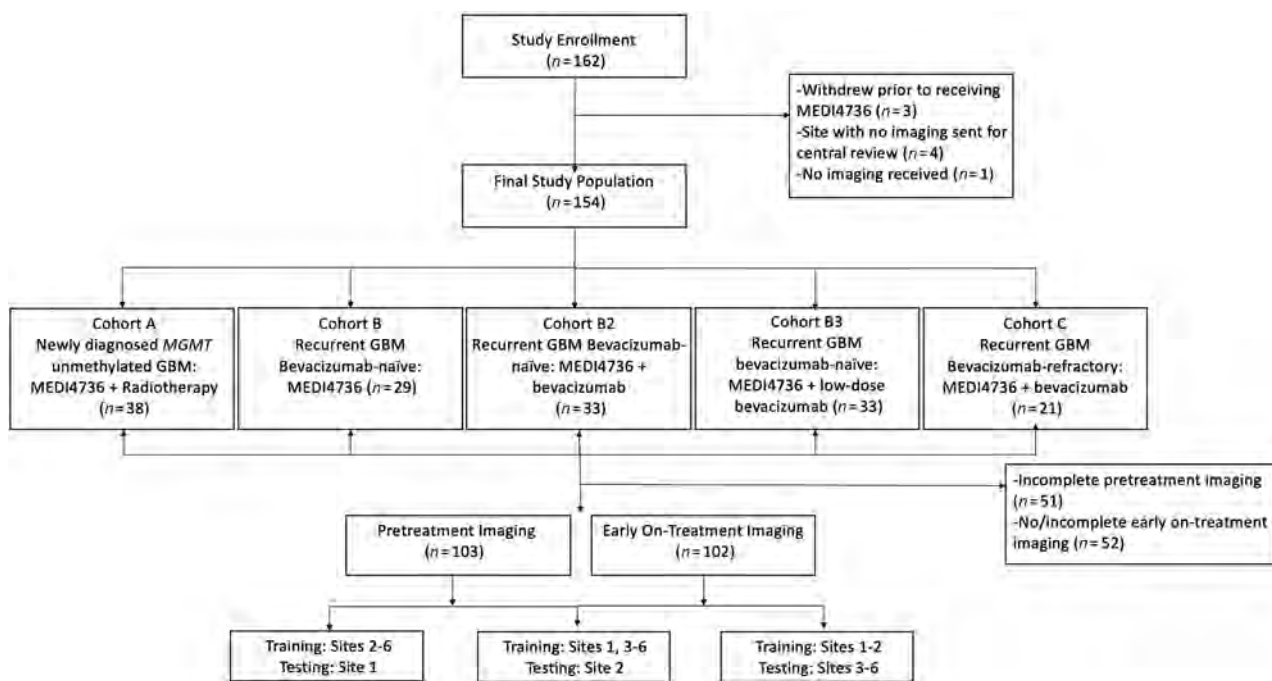


FIG 1. Flow chart of the study population.

endothelial growth factor, is the only approved addition to recurrent glioblastoma management.³

Preclinical studies of programmed cell death protein 1 (PD-1) pathway inhibition showed promising results in glioma.^{4,5} However, in clinical trials, PD-1 inhibition via nivolumab concurrently with chemoradiotherapy or radiation therapy did not improve progression-free survival (PFS) or OS in newly diagnosed glioblastoma^{6,7} or improve OS compared with bevacizumab in recurrent glioblastoma.⁸ Although the overall response rate to nivolumab was low (8%) in patients with recurrent glioblastoma, the response was more durable relative to bevacizumab.⁸ Durvalumab (MEDI4736) is a monoclonal antibody against human programmed death-ligand 1 (PD-L1) that has shown clinical efficacy with an acceptable safety profile⁹ and is being studied in multiple cancer subtypes, including glioblastoma.

Imaging assessments in glioma are challenging due to the overlap in the appearance of treatment-related changes with tumor progression, particularly in the setting of multimodality treatment.^{10,11} Considering the possible low response rate to immunotherapy¹² and the poor median OS in glioblastoma, imaging-based metrics to predict response and improved survival early are desirable to make appropriate treatment decisions. Radiomics methods enable quantification of multisequence imaging data from spatially heterogeneous tissues, and machine learning techniques allow integration of these multiple quantitative metrics.

Here, we performed a post hoc analysis of a multicenter Phase II study (NCT02336165) of patients with glioblastoma undergoing durvalumab therapy with MR imaging radiomics and machine learning techniques. The aim of this study was to determine whether MR imaging radiomics-based machine learning can predict PFS and OS in patients with glioblastoma on PD-L1 inhibition immunotherapy.

MATERIALS AND METHODS

This was a post hoc analysis of data from a Phase II clinical trial to evaluate the clinical efficacy and safety of durvalumab (MEDI4736) in glioblastoma (NCT02336165) conducted at 8 sites (7 in the United States, 1 in Australia) and enrolling 162 patients between March 2015 and January 2017 into 5 noncomparative patient cohorts (Fig 1 and Online Supplemental Data). The Online Supplemental Data summarize the trial inclusion/exclusion criteria. The institutional review board (Dana-Farber Cancer Institute) approved this trial, and all patients provided written informed consent. Of the 162 patients enrolled, 3 did not receive MEDI4736 due to clinical decline ($n=1$), seizure ($n=1$), or withdrawal of consent ($n=1$) before drug administration (Fig 1).

Imaging

MR imaging was performed approximately every 2 months during treatment, once during on-study follow-up, and at least every 6 months during poststudy follow-up. Brain MR imaging was performed on 1.5T or 3T scanners before and after the administration of gadolinium-based contrast media. Brain MR imaging protocol included sagittal and/or axial T1-weighted images, axial T2, axial T2-FLAIR, postcontrast axial or coronal fast spin-echo or 3D T1-weighted gradient-echo images, and susceptibility weighted imaging (Online Supplemental Data).

Imaging data were not available for central review for the Australian site ($n=4$) and for 1 US patient ($n=1$); hence, these were excluded. For this study, imaging performed pretreatment and at the first on-treatment time point was analyzed. First on-treatment MR imaging refers to the first MR imaging obtained after starting treatment and was performed approximately 8 weeks after initiation of treatment. Only patients with complete T1 precontrast, T2, T2-FLAIR, and T1 postcontrast imaging were included in the study for each time point (Fig 1).

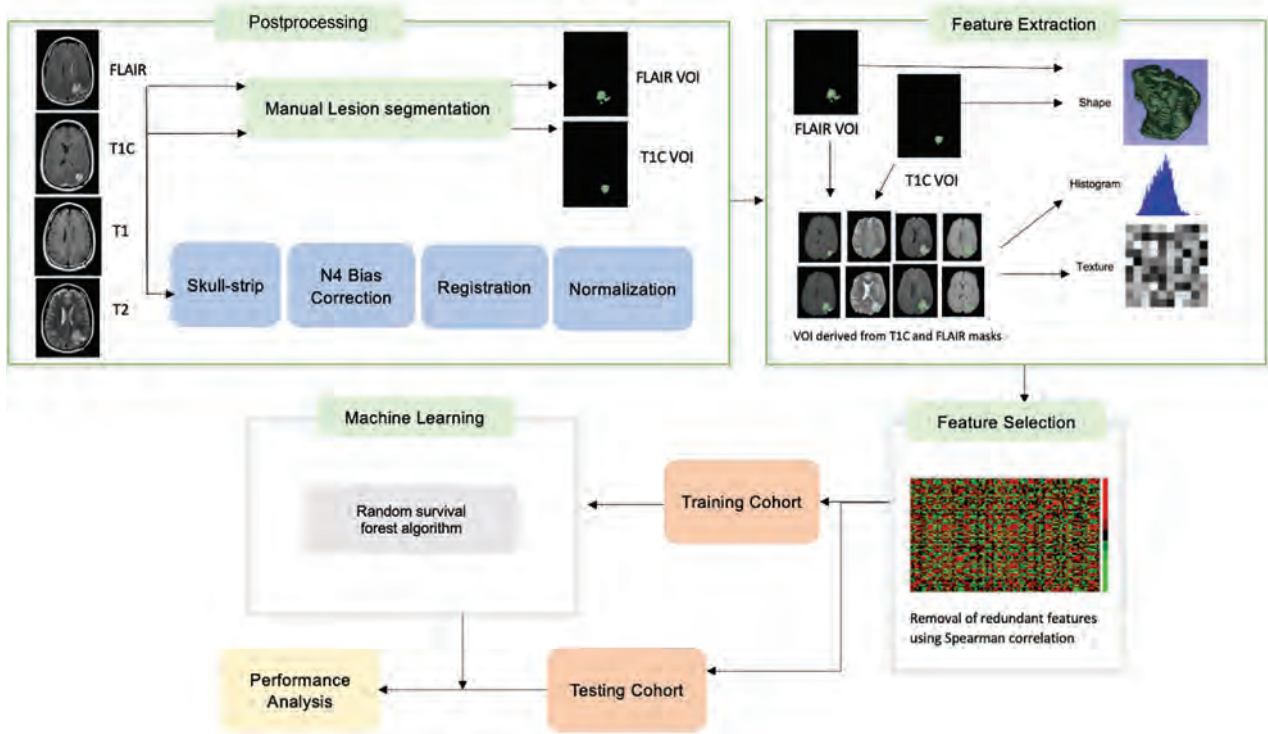


FIG 2. Radiomics and machine learning workflow. TIC indicates T1 post contrast imaging.

Progression was defined on the basis of the modified Response Assessment in Neuro-Oncology criteria^{13,14} if the patient met any one of the following criteria:

1. A 25% increase in the sum of the products of perpendicular diameters of enhancing lesions (over best response or baseline if no decrease) on stable or increasing doses of corticosteroids
2. Any new lesion
3. Clear clinical deterioration not attributable to other causes apart from the tumor
4. Failure to return for evaluation due to death or deteriorating condition.

Patients with suspected progression were permitted to continue therapy at least until confirmation of progression on follow-up imaging in 8 weeks.

Image Postprocessing

Image postprocessing methods are reported per the Image Biomarker Standardization Initiative guidelines (Online Supplemental Data).¹⁵ The T2-FLAIR images were used to segment the whole tumor (WT) VOI, which includes enhancing tumor, infiltrating tumor, and vasogenic edema while postcontrast T1 images were used to determine the enhancing tumor (ET) VOI on the pretreatment and first on-treatment time point MR imaging. For segmentation, we used a semiautomated level tracing tool on 3D Slicer, Version 4.4 (<http://www.slicer.org>). All included imaging sequences (T2, T2-FLAIR, T1, T1 postcontrast) were skull-stripped,¹⁶ and image intensities were corrected for low-frequency intensity nonuniformity via N4 bias field correction. Image intensities were then normalized using the median

and interquartile range (IQR) of image intensities¹⁷ of the normal brain VOI (defined as the region outside the WT VOI, Fig 2) using Matlab (R2015a; MathWorks). All imaging sequences were resampled to 1 mm and spatially registered to the T1 postcontrast images using rigid followed by affine transformation with the Matlab Imaging Processing Toolbox.

Radiomics Feature Extraction and Feature Selection

The radiomics feature extraction was performed using Matlab and included features from the open-source radiomics package by Vallières et al^{18,19} (Online Supplemental Data). In this package, 3 feature categories were included to characterize the tumor shape (10 features), intensity histogram (18 features each for 4 sequences [T1, T2, T2-FLAIR, T1 postcontrast]), and texture (40 features each for the aforementioned 4 sequences).^{18,20} A total of 242 features were included for each VOI (WT and ET) for a total of 484 imaging features for each time point in addition to 5 clinical features of age, race, sex, study site, and treatment regimen. The treatment regimen was included as a feature to account for the heterogeneity in population (newly diagnosed versus recurrent glioblastoma and durvalumab monotherapy versus combination therapy).

Feature selection was performed using feature variability and redundancy. Feature variability, a measure of stability, was assessed as the percentage difference between the feature value before and after shifting the tumor VOI 3 voxels in all directions. The variability for each feature was obtained for each case and then averaged over all cases to obtain the average feature variability for each feature. Features with a variability of >150% were removed. Next, redundant features, defined as features with a

Spearman correlation of >0.8 , $P < .05$ with another feature, were removed.

Radiomics Model Training

The random survival forest algorithm²¹ was applied using the scikit-survival 0.17.1 Python module.²² Censored survival data (see Statistical Analysis section) including event (death or progression) and time to event were input into the algorithm along with the selected feature set. Tuning of hyperparameters was performed using a grid search, and the optimized parameters are included in the Online Supplemental Data.

Radiomics Model Performance

To assess the generalizability of radiomics models across multiple centers, we designed 3 separate experiments using data from different sites for model training and model testing, while keeping the ratio of the number of patients in training and testing groups to about 2–3:1 (Fig 1 and Online Supplemental Data). After each model was trained using the “training” group, the model performance was evaluated in an intentionally withheld external “testing” group.

1. Training with sites 2–6 ($n = 70$ – 72) and testing with site 1 ($n = 31$ – 32)
2. Training with sites 1 and 3–6 ($n = 73$ – 74) and testing with site 2 ($n = 29$)
3. Training with sites 1 and 2 ($n = 60$ – 61) and testing with sites 3–6 ($n = 41$ – 43).

These experiments were conducted separately for pretreatment and first on-treatment MR imaging–derived features (combined with clinical variables, Online Supplemental Data). Model performance was assessed using both the concordance index (C-index) and dynamic area under the curve (AUC) for different time points.²³

Top-Performing Features

For each experiment, the top 20 features were reported along with their corresponding weights in the trained model (Online Supplemental Data). The top features were calculated using “out of bag” samples, which are sets of outcomes in the training set that are randomly excluded from model training. This step avoids overlap with the training data when analyzing the strength of a given feature.

Statistical Analysis

Overall survival was defined as the time from therapy initiation to death, and progression-free survival was defined as the time from therapy initiation to progression of disease. If the patient was alive at the last follow-up, the OS was censored at the time of last clinical follow-up; in patients with stable or improved disease at last follow-up, PFS was censored at the last imaging follow-up. These results are based on the data lock date of November 20, 2019, for OS and September 6, 2019, for PFS. The accuracy of the model was assessed using the C-index and dynamic AUC for different time points. Statistical analyses used Python, Version 3.7.6.

Table 1: Patient characteristics

Characteristics	n = 113
Age (mean) (yr)	55.2 (SD, 11.5)
Male (No.) (%)	78 (69%)
Race	
White	99 (87.6%)
African American	1 (0.9%)
Asian	1 (0.9%)
Other	3 (2.7%)
Unknown	9 (8.0%)
Treatment regimen	
Cohort A	30 (26.5%)
Cohort B	26 (23.0%)
Cohort B2	23 (20.4%)
Cohort B3	19 (16.8%)
Cohort C	15 (13.3%)
Median PFS (IQR) (days)	106 (56–150.5)
Median OS (IQR) (days)	207.5 (150.5–393.5)

RESULTS

Patient Characteristics

A total of 113 patients with complete imaging of the 154 enrolled in this trial were included in this analysis, including 103 patients who had complete pretreatment imaging and 102 who had complete first on-treatment imaging (Fig 1). The demographics and treatment regimen of the included patients are presented in Table 1. Of the 113 patients included in the study, 103 had progression (median PFS = 106 days; IQR = 56–150.5 days) and the remaining 10 were censored at the last imaging follow-up available. Ninety of the 113 patients died during follow-up (median OS = 207.5 days; IQR = 150.5–393.5 days), and the remaining 23 were censored at the last clinical follow-up.

The median time from pretreatment imaging to the start of treatment was 7 days (IQR = 6–14 days) and from the start of treatment to first on-treatment imaging was 55.5 days (IQR = 54–56 days).

Radiomics Model Performance

After we removed high-variability features and redundant features from the original 489 features, the pretreatment models each included 162–267 features and the first on-treatment models included 168–200 features. The radiomics models trained using pretreatment imaging features showed poor performance in predicting OS and PFS (C-index = 0.472–0.521 for OS and C-index = 0.472–0.524 for PFS in the testing cohort). Conversely, the radiomics models trained using first on-treatment imaging features showed a high C-index for the prediction of OS in the out of bag training cohort (C-index = 0.690–0.721) and testing cohort (C-index = 0.692–0.750, Table 2). Dynamic AUC plots for the first on-treatment models predicting OS (Online Supplemental Data) showed a peak AUC between 300 and 600 days postenrollment.

The first on-treatment imaging features–based radiomics model also showed a high C-index for the prediction of PFS in the out of bag training (C-index = 0.641–0.660) cohort and in the testing cohort (C-index = 0.680–0.715, Table 2). Dynamic AUC plots for the first on-treatment models predicting PFS showed variable AUC peak times, ranging from approximately 125 to 400 days.

Table 2: Radiomics model performance for prediction of OS and PFS

Outcome/ MR Imaging Time Point	Training Site	Testing Site	OOB Training, Mean C-Index (95% CI)	Testing AUC, Mean C-Index (95% CI)	
OS	Pretreatment	Sites 2–6 (n = 72)	Site 1 (n = 31)	0.471 (0.467–0.474)	0.521 (0.515–0.527)
		Site 1, 3–6 (n = 74)	Site 2 (n = 29)	0.523 (0.517–0.530)	0.472 (0.468–0.476)
		Site 1–2 (n = 60)	Site 3–6 (n = 43)	0.529 (0.526–0.532)	0.485 (0.483–0.488)
	First on-treatment	Sites 2–6 (n = 70)	Site 1 (n = 32)	0.690 (0.688–0.692)	0.750 (0.747–0.753)
		Site 1, 3–6 (n = 73)	Site 2 (n = 29)	0.710 (0.708–0.713)	0.748 (0.744–0.752)
		Site 1–2 (n = 61)	Site 3–6 (n = 41)	0.721 (0.719–0.723)	0.692 (0.691–0.694)
PFS	Pretreatment	Sites 2–6 (n = 72)	Site 1 (n = 31)	0.469 (0.467–0.472)	0.524 (0.518–0.530)
		Site 1, 3–6 (n = 74)	Site 2 (n = 29)	0.521 (0.515–0.526)	0.472 (0.469–0.476)
		Site 1–2 (n = 60)	Site 3–6 (n = 43)	0.528 (0.524–0.531)	0.486 (0.484–0.488)
	First on-treatment	Sites 2–6 (n = 70)	Site 1 (n = 32)	0.660 (0.658–0.663)	0.691 (0.688–0.693)
		Site 1, 3–6 (n = 73)	Site 2 (n = 29)	0.641 (0.640–0.643)	0.715 (0.712–0.717)
		Site 1–2 (n = 61)	Site 3–6 (n = 41)	0.648 (0.645–0.650)	0.680 (0.677–0.683)

Note:—OOB indicate out of bag.

Top-Performing Features

Because the models trained using first on-treatment MR imaging features had the best performance, they were used for determination of top-performing features. In each experiment with first on-treatment MR imaging features, the 20 top-performing features were predominantly texture features with a few shape features included (Online Supplemental Data). The treatment regimen was feature 12 of 20 in one of the models (Online Supplemental Data), but it was not a top-performing feature in any of the other first on-treatment models. Demographics and study site were not included in the top features for any of the first on-treatment models.

DISCUSSION

There is a need for identification of specific imaging features for response assessment and reliable imaging-based prognostic markers in glioblastoma. Our multicenter study demonstrates that a radiomics model combining first on-treatment MR imaging features and clinical variables can accurately predict OS and PFS on durvalumab PD-L1 inhibition immunotherapy. The results were consistent across treatment sites with heterogeneous imaging protocols as confirmed by site-specific analysis with independent testing.

An increasing number of clinical trials are evaluating immunotherapy approaches for malignant glioma, but there are limited data assessing machine learning–based or other quantitative methods for imaging-based prognosis in patients with gliomas on immunotherapy. Radiomics prediction of survival on PD-L1 inhibition immunotherapy has previously been studied in other malignancies, including bladder cancer²⁴ and non-small-cell lung cancer.²⁵ In glioma, previous work has used radiomics features and machine learning to predict PD-L1 expression and subsequently found that the predicted high PD-L1 subgroup correlated with better prognosis.²⁶ There is also an extensive body of literature that has assessed the role of machine learning in various other aspects of glioma imaging,²⁷ including determination of glioma grade,²⁸ genomic status,²⁹ segmentation,³⁰ and prediction of survival.³¹ Radiomics-based supervised machine learning algorithms have shown that shape and texture features extracted from

conventional and advanced MR images can predict survival in gliomas of varying grades.^{32,33} In recurrent glioblastoma treated with bevacizumab, pretreatment texture and volumetric features were predictive of progression and survival.^{34,35} However, in recurrent high-grade gliomas treated with bevacizumab and radiation, posttherapy scan texture features were predictive of overall survival.³⁶ Despite the differences in study populations, these models are similar to our results in which 75%–85% of top-performing first on-treatment features were texture features (Online Supplemental Data). A combination of deep and supervised learning using clinical features, tumor location, size, and features extracted from postcontrast T1 images, fMRI, and DTI have also been successful in predicting survival accurately in newly diagnosed glioblastoma.³⁷

Our study identified texture features from all conventional imaging sequences for both enhancing and WT volume contributory to predicting survival from first on-treatment MR imaging. Our goal using first on-treatment MR imaging was to assess immunotherapy-related imaging changes as opposed to progression-related changes because progression timelines and types vary across the dataset. The predictive value of first on-treatment imaging features may reflect biologic differences in responders versus nonresponders to immunotherapy, including molecular alterations and changes in immune expression and infiltration.³⁸ The heterogeneity of the study population and integration of varied imaging protocols are strengths of the study. Similar out-of-bag and testing C-index values in each of the site-specific first-on-treatment analyses demonstrate that the first on-treatment imaging feature-based prediction model is generalizable (Table 2).

Although overall survival in the durvalumab study was low, with a median survival of 208 days, 20% of the study population was alive at the time of last follow-up. The response rate to immunotherapy in solid and hematologic malignancies is also reported to be 20%–30%.³⁹ Although the efficacy of checkpoint inhibitors in glioblastoma is unclear, preliminary results suggest a durable response in a small subset of patients.⁴⁰ Early imaging-based biomarkers that predict response to immunotherapy⁴¹ can inform clinical decision-making.

Our study has several limitations. The relatively small sample size is a limitation, and the results need verification in larger

prospective trials and assessment for generalizability to other immune checkpoint inhibitors. The sample size also did not allow us to analyze advanced MR imaging variables such as DWI/ADC or perfusion and various molecular alterations or study the radiomics features in individual treatment regimens or progression patterns separately. Instead, the treatment regimen was included as a variable in the random forest survival analysis, where it was among the top-performing features in only one of the first on-treatment models. In a larger checkpoint inhibitor trial, we hope to conduct similar experiments to further investigate the impact of treatment variation on model performance, expand on this work to train models based on distinct progression mechanisms, and validate results across other checkpoint inhibitors. Last, while the variation in image-acquisition parameters in this study supports the potential generalizability of the model, it also limits the reproducibility of the imaging dataset used for model training.

CONCLUSIONS

We created and validated a robust machine learning model for prediction of OS and PFS in patients with glioblastoma on PD-L1 inhibition immunotherapy using first on-treatment MR imaging features across multiple institutions with varying imaging protocols. Future studies are necessary to further assess the generalizability of the model and to combine additional clinical and advanced imaging features for more robust prediction of survival and progression.

ACKNOWLEDGMENTS

The authors acknowledge the Ludwig Institute for Cancer Research, Cancer Research Institute, AstraZeneca, and Cure Brain Cancer Foundation for supporting the conduction of the trial, the site investigators and their teams, and the patients and their families for participating in the study.

Disclosure forms provided by the authors are available with the full text and PDF of this article at www.ajnr.org.

REFERENCES

- Ostrom QT, Cioffi G, Gittleman H, et al. **CBTRUS Statistical Report: Primary Brain and Other Central Nervous System Tumors Diagnosed in the United States in 2012-2016.** *Neuro Oncol* 2019;21:v1-100 CrossRef Medline
- Stupp R, Hegi ME, Mason WP, et al; European Organisation for Research and Treatment of Cancer Brain Tumour and Radiation Oncology Groups; National Cancer Institute of Canada Clinical Trials Group. **Effects of radiotherapy with concomitant and adjuvant temozolomide versus radiotherapy alone on survival in glioblastoma in a randomised phase III study: 5-year analysis of the EORTC-NCIC trial.** *Lancet Oncol* 2009;10:459-66 CrossRef Medline
- Lombardi G, Pambuku A, Bellu L, et al. **Effectiveness of antiangiogenic drugs in glioblastoma patients: a systematic review and meta-analysis of randomized clinical trials.** *Crit Rev Oncol Hematol* 2017;111:94-102 CrossRef Medline
- Wainwright DA, Chang AL, Dey M, et al. **Durable therapeutic efficacy utilizing combinatorial blockade against IDO, CTLA-4, and PD-L1 in mice with brain tumors.** *Clin Cancer Res* 2014;20:5290-301 CrossRef Medline

- Zeng J, See AP, Phallen J, et al. **Anti-PD-1 blockade and stereotactic radiation produce long-term survival in mice with intracranial gliomas.** *Int J Radiat Oncol Biol Phys* 2013;86:343-49 CrossRef Medline
- Bristol-Myers Squibb Announces Phase 3 CheckMate-498 Study Did Not Meet Primary Endpoint of Overall Survival with Opdivo (nivolumab) Plus Radiation in Patients with Newly Diagnosed MGMT-Unmethylated Glioblastoma Multiforme.** <https://news.bms.com/press-release/corporatefinancial-news/bristol-myers-squibb-announces-phase-3-checkmate-498-study-did>. May 9, 2019. Accessed March 30, 2020
- Bristol-Myers Squibb Provides Update on Phase 3 Opdivo (nivolumab) CheckMate-548 Trial in Patients with Newly Diagnosed MGMT-Methylated Glioblastoma Multiforme.** <https://news.bms.com/press-release/corporatefinancial-news/bristol-myers-squibb-provides-update-phase-3-opdivo-nivolumab->. September 5, 2019. Accessed March 30, 2020.
- Reardon DA, Brandes AA, Omuro A, et al. **Effect of nivolumab vs bevacizumab in patients with recurrent glioblastoma: the CheckMate 143 Phase 3 randomized clinical trial.** *JAMA Oncol* 2020;6:1003-10 CrossRef Medline
- Reardon DA, Kaley TJ, Dietrich J, et al. **Phase 2 study to evaluate safety and efficacy of MEDI4736 (durvalumab [DUR]) in glioblastoma (GBM) patients: an update.** *J Clin Oncol* 2017;35:2042 CrossRef
- Huang RY, Wen PY. **Response assessment in neuro-oncology criteria and clinical endpoints.** *Magn Reson Imaging Clin N Am* 2016;24:705-18 CrossRef Medline
- Okada H, Weller M, Huang R, et al. **Immunotherapy response assessment in neuro-oncology: a report of the RANO working group.** *Lancet Oncol* 2015;16:e534-42 CrossRef Medline
- Reardon DA, Omuro A, Brandes AA, et al. **OS10.3 randomized Phase 3 study evaluating the efficacy and safety of nivolumab vs bevacizumab in patients with recurrent glioblastoma: CheckMate 143.** *Neuro Oncol* 2017;19:iii21 CrossRef
- Phase 2 Study of Durvalumab (MEDI4736) in Patients With Glioblastoma.** <https://clinicaltrials.gov/ct2/show/NCT02336165>. Accessed February 1, 2022
- Reardon DA, Kaley TJ, Dietrich J, et al. **Phase II study to evaluate safety and efficacy of MEDI4736 (durvalumab) + radiotherapy in patients with newly diagnosed unmethylated MGMT glioblastoma (new unmeth GBM).** *J Clin Oncol* 2019;37(15 Suppl):2032 CrossRef
- Zwanenburg A, Leger S, Vallieres M, et al. **Image biomarker standardisation initiative.** <https://arxiv.org/abs/1612.07003>. December 2, 2016. Accessed February 1, 2022
- Documentation/Nightly/Modules/SwissSkullStripper.** <https://www.slicer.org/wiki/Documentation/Nightly/Modules/SwissSkullStripper>. Accessed February 1, 2022
- Chang K, Zhang B, Guo X, et al. **Multimodal imaging patterns predict survival in recurrent glioblastoma patients treated with bevacizumab.** *Neuro Oncol* 2016;18:1680-87 CrossRef Medline
- Vallières M, Freeman CR, Skamene SR, et al. **A radiomics model from joint FDG-PET and MRI texture features for the prediction of lung metastases in soft-tissue sarcomas of the extremities.** *Phys Med Biol* 2015;60:5471-96 CrossRef Medline
- Vallieres M, Kay-Rivest E, Perrin LJ, et al. **Radiomics strategies for risk assessment of tumour failure in head-and-neck cancer.** *Sci Rep* 2017;7:10117 CrossRef Medline
- A repository to develop code for IBSI compliant radiomics applications.** <https://github.com/mvallieres/radiomics-develop>. Accessed April 26, 2020
- Ishwaran H, Kogalur UB, Blackstone EH, et al. **Random survival forests.** *Annals of Applied Statistics* 2008;2:841-60
- scikit-survival.** <https://scikit-survival.readthedocs.io/en/stable/>. Accessed February 1, 2022
- Hung H, Chiang C. **Estimation methods for time-dependent AUC models with survival data.** *The Canadian Journal of Statistics* 2009;38:8-26
- Rundo F, Spampinato C, Banna GL, et al. **Advanced deep learning embedded motion radiomics pipeline for predicting anti-PD-1/**

- PD-L1 immunotherapy response in the treatment of bladder cancer: preliminary results.** *Electronics* 2019;8:1134 CrossRef
25. Jazieh K, Khorrami M, Saad AM, et al. **Novel imaging biomarkers predict progression-free survival in stage 3 NSCLC treated with chemoradiation and durvalumab.** *J Clin Oncol* 2021;39(15 Suppl):3054–54 CrossRef
 26. Sforazzini F, Salome P, Kudak A, et al. **PD-L1-R: A MR based surrogate for PD-L1 expression in glioblastoma multiforme.** *J Clin Oncol* 2021;39:2041 CrossRef
 27. Lotan E, Jain R, Razavian N, et al. **State of the art: machine learning applications in glioma imaging.** *AJR Am J Roentgenol* 2019;212:26–37 CrossRef Medline
 28. Sengupta A, Ramaniharan AK, Gupta RK, et al. **Glioma grading using a machine-learning framework based on optimized features obtained from T1 perfusion MRI and volumes of tumor components.** *J Magn Reson Imaging* 2019;50:1295–1306 CrossRef Medline
 29. Zhang B, Chang K, Ramkissoon S, et al. **Multimodal MRI features predict isocitrate dehydrogenase genotype in high-grade gliomas.** *Neuro Oncol* 2017;19:109–17 CrossRef Medline
 30. Chang K, Beers AL, Bai HX, et al. **Automatic assessment of glioma burden: a deep learning algorithm for fully automated volumetric and bidimensional measurement.** *Neuro Oncol* 2019;21:1412–22 CrossRef Medline
 31. Macyszyn L, Akbari H, Pisapia JM, et al. **Imaging patterns predict patient survival and molecular subtype in glioblastoma via machine learning techniques.** *Neuro Oncol* 2016;18:417–25 CrossRef Medline
 32. Sanghani P, Ang BT, King NK, et al. **Overall survival prediction in glioblastoma multiforme patients from volumetric, shape and texture features using machine learning.** *Surg Oncol* 2018;27:709–14 CrossRef Medline
 33. Kickingereder P, Burth S, Wick A, et al. **Radiomic profiling of glioblastoma: identifying an imaging predictor of patient survival with improved performance over established clinical and radiologic risk models.** *Radiology* 2016;280:880–89 CrossRef Medline
 34. Grossmann P, Narayan V, Chang K, et al. **Quantitative imaging biomarkers for risk stratification of patients with recurrent glioblastoma treated with bevacizumab.** *Neuro Oncol* 2017;19:1688–97 CrossRef Medline
 35. Kickingereder P, Gotz M, Muschelli J, et al. **Large-scale radiomic profiling of recurrent glioblastoma identifies an imaging predictor for stratifying anti-angiogenic treatment response.** *Clin Cancer Res* 2016;22:5765–71 CrossRef Medline
 36. Wang C, Sun W, Kirkpatrick J, et al. **Assessment of concurrent stereotactic radiosurgery and bevacizumab treatment of recurrent malignant gliomas using multi-modality MRI imaging and radiomics analysis.** *J Radiosurg SBRT* 2018;5:171–81 Medline
 37. Nie D, Lu J, Zhang H, et al. **Multi-channel 3D deep feature learning for survival time prediction of brain tumor patients using multimodal neuroimages.** *Sci Rep* 2019;9:1103 CrossRef Medline
 38. Zhao J, Chen AX, Gartrell RD, et al. **Immune and genomic correlates of response to anti-PD-1 immunotherapy in glioblastoma.** *Nat Med* 2019;25:462–69 CrossRef Medline
 39. Lipson EJ, Forde PM, Hammers HJ, et al. **Antagonists of PD-1 and PD-L1 in cancer treatment.** *Semin Oncol* 2015;42:587–600 CrossRef Medline
 40. De Felice F, Pranno N, Marampon F, et al. **Immune check-point in glioblastoma multiforme.** *Crit Rev Oncol Hematol* 2019;138:60–69 CrossRef Medline
 41. Burugu S, Dancsok AR, Nielsen TO. **Emerging targets in cancer immunotherapy.** *Semin Cancer Biol* 2018;52:39–52 CrossRef Medline

Radio-Pathomic Maps of Cell Density Identify Brain Tumor Invasion beyond Traditional MRI-Defined Margins

 S.A. Bobholz,  A.K. Lowman,  M. Brehler,  F. Kyereme,  S.R. Duenweg,  J. Sherman,  S.D. McGarry,  E.J. Cochran,  J. Connelly,  W.M. Mueller,  M. Agarwal,  A. Banerjee, and  P.S. LaViolette



ABSTRACT

BACKGROUND AND PURPOSE: Currently, contrast-enhancing margins on T1WI are used to guide treatment of gliomas, yet tumor invasion beyond the contrast-enhancing region is a known confounding factor. Therefore, this study used postmortem tissue samples aligned with clinically acquired MRIs to quantify the relationship between intensity values and cellularity as well as to develop a radio-pathomic model to predict cellularity using MR imaging data.

MATERIALS AND METHODS: This single-institution study used 93 samples collected at postmortem examination from 44 patients with brain cancer. Tissue samples were processed, stained with H&E, and digitized for nuclei segmentation and cell density calculation. Pre- and postgadolinium contrast T1WI, T2 FLAIR, and ADC images were collected from each patient's final acquisition before death. In-house software was used to align tissue samples to the FLAIR image via manually defined control points. Mixed-effects models were used to assess the relationship between single-image intensity and cellularity for each image. An ensemble learner was trained to predict cellularity using 5×5 voxel tiles from each image, with a two-thirds to one-third train-test split for validation.

RESULTS: Single-image analyses found subtle associations between image intensity and cellularity, with a less pronounced relationship in patients with glioblastoma. The radio-pathomic model accurately predicted cellularity in the test set (root mean squared error = 1015 cells/mm²) and identified regions of hypercellularity beyond the contrast-enhancing region.

CONCLUSIONS: A radio-pathomic model for cellularity trained with tissue samples acquired at postmortem examination is able to identify regions of hypercellular tumor beyond traditional imaging signatures.

ABBREVIATIONS: CD31 = cluster of differentiation 31; CPM = cellularity prediction map; GBM = glioblastoma; IHC = immunohistochemically; MIB-1 = Mindbomb Homolog 1 index; NGG = non-GBM glioma; RMSE = root mean squared error; TIC = gadolinium-enhanced T1WI

High-grade primary brain tumors such as glioblastomas (GBMs) are associated with particularly dismal prognoses, with a mean survival rate of around 12–18 months postdiagnosis.¹ Precise localization of tumor margins, currently performed using

multiparametric MR imaging, is essential to maximizing the efficacy of surgical and radiation treatments for these tumors as well as monitoring tumor progression. T1WI acquired following injection with a gadolinium contrast agent (T1C) is used to identify regions where active tumor has disrupted the blood-brain barrier. Contrast enhancement is used to define the extent of the primary tumor region.² Hyperintense regions on FLAIR images are thought to indicate a combination of tumor-related edema^{3–5} and infiltrative non-enhancing tumor.⁶ Multi-b-value DWI is also typically included in glioma imaging protocols and is used to calculate quantitative ADC maps. These maps identify areas of restricted diffusion that may indicate either hypercellular tumor^{7–10} or coagulative necrosis.¹¹

Tumor heterogeneity has been a recent focus in imaging studies of GBM. With noninvasive imaging, regional heterogeneity is readily measurable, but capturing heterogeneity with pathology samples is challenging. It can be achieved with en bloc resection^{12,13} or repeat sampling with image-guided biopsies. Each of these techniques requires properly aligning samples to their location on the imaging, which can be difficult due to the loss of

Received October 8, 2021; accepted after revision February 7, 2022.

From the Departments of Biophysics (S.A.B., S.R.D., J.S., S.D.M.), Radiology (A.L., M.B., M.A., P.S.L.), Pathology (E.J.C.), Neurology (J.C.), Neurosurgery (W.M.M.), Biostatistics (A.B.), and Biomedical Engineering (P.S.L.), Medical College of Wisconsin, Milwaukee, Wisconsin.

This work was supported by the American Brain Tumor Association, Grant DG160004; the Froedtert Foundation; the Strain for the Brain 5K Run, Milwaukee, Wisconsin; and National Institutes of Health/National Cancer Institute grants, R01CA218144, R01CA218144-02S1, R21CA231892, and R01CA249882.

Paper previously presented, in part, at: Annual Meeting of the Society for Neuro-Oncology, June 8, 2020; Austin, Texas; and Annual Meeting of the International Society for Magnetic Resonance in Medicine, May 2021; Virtual.

Please address correspondence to Peter S. LaViolette, PhD, Departments of Radiology and Biomedical Engineering, Medical College of Wisconsin, 8701 Watertown Plank Rd, Milwaukee, WI; e-mail: plaviole@mcw.edu

 Indicates open access to non-subscribers at www.ajnr.org

 Indicates article with online supplemental data.

<http://dx.doi.org/10.3174/ajnr.A7477>

Table 1: Clinical and demographic summary for study sample^a

	Overall	GBM	NGG	Other
No. of subjects	44	32	10	2
Age (yr)	60.2 (13.7)	62.4 (11.6)	50.3 (15.3)	75.5 (13.4)
Overall survival (mo)	40.4 (61.5)	35.3 (64.9)	64.3 (46.1)	2.0 (0)
Radiation treatment (y/n)	39/5	29/3	10/0	0/2
Chemotherapy (y/n)	40/4	30/2	10/0	0/2
Tumor-treating fields (y/n)	28/16	16/16	0/10	0/2
Other treatment (y/n)	7/37	5/27	2/8	0/2
Time between last MR imaging and death (days)	63.0 (62.1)	49.6 (42.3)	111.8 (93.1)	33.0 (13.4)

Note:—Y/n indicates yes/no.

^aQuantitative values are presented as mean (SD).

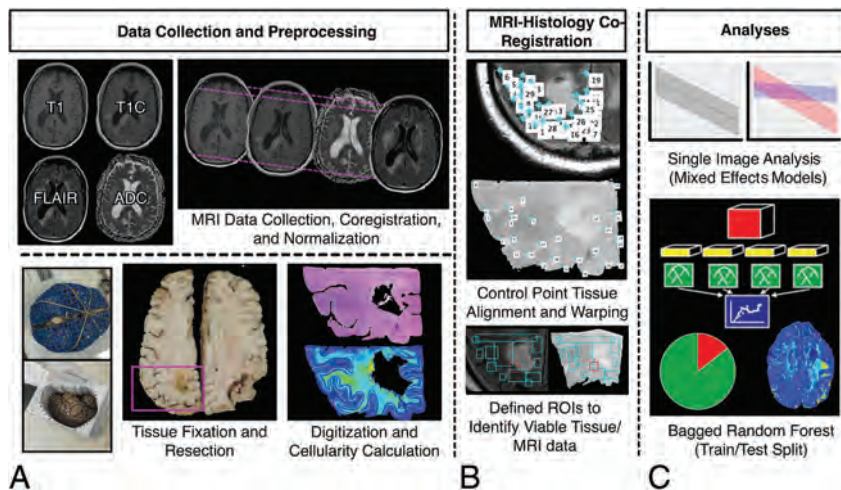


FIG 1. Overview of the data-collection process. A, MR imaging data are collected from the patient's final imaging session before death and coregistered, and T1, T1C, and FLAIR images are intensity-normalized. Tissue fixation and sampling involve the use of 3D printed brain cages and slicing jigs to preserve structural integrity relative to the MR imaging. Following staining, tissue samples are digitized for cellularity calculation using an automated nuclei segmentation algorithm. B, In-house software is used to align each tissue sample to the FLAIR image using manually defined control points and ROIs. C, Single-image cellularity associations are computed using mixed-effects models, and a bagging regression ensemble is trained to predict cellularity using 5×5 voxel tiles from each image using a two-thirds to one-third train-test split.

orientation information during sectioning. Other issues such as brain shift during craniotomy and the inability to sample regions outside the suspected tumor region further complicate these strategies. Despite these challenges, pathologic measurement of tumor heterogeneity is crucial to improving the localization of multiple tumor pathologies as well as validating imaging signatures beyond the currently accepted tumor boundary.

Studies at postmortem examination have shown that viable tumor can exist as far as 10 cm beyond contrast enhancement, where heterogeneous pathologic features may confound traditional MR imaging interpretations.^{9,11,14} Due to the sampling limitations of biopsy samples, pathologic validation of the MR imaging signatures is warranted beyond the contrast-enhancing region and in the post-treatment state. This study used large tissue samples collected across the brain at postmortem examination to validate current imaging signatures as well as develop predictive tools to assess prospective tumor beyond the contrast-enhancing region. Specifically, this study tested the hypotheses that multiparametric MR imaging

intensity values are associated with tumor cellularity at postmortem examination and that a radio-pathomic model trained on postmortem data can accurately identify regions of hypercellular tumor beyond traditional imaging signatures.

MATERIALS AND METHODS

Patient Population

This single-institution study was approved by the institutional review board of the Medical College of Wisconsin, and written, informed consent was obtained from each participant. A total of 44 consecutive patients with pathologically confirmed brain tumors were enrolled in this study. Subjects collected before 2021 have been retrospectively reclassified in concordance with the 2021 World Health Organization Classification standards for brain tumors.¹⁵ Patients underwent, on average, 1.55 operations, with 19 patients undergoing >1 operation and 3 patients undergoing no operation. Subjects included in this study partially overlap with small subsets used for prior articles.^{9,16,17} Clinical histories and demographic information are shown in Table 1. A diagrammatic representation of the tissue and the imaging data-collection process is shown in Fig 1.

MR Image Acquisition and Preprocessing

T1, T1C, and FLAIR and DWI-derived ADC images collected from the patient's last clinical imaging session before death were included for analysis (See the Online Supplemental Data for sample acquisition parameters). All images were rigidly aligned with each subject's FLAIR image using the FMRIB Linear Image Registration Tool (FLIRT; <http://www.fmrib.ox.ac.uk/fsl/fslwiki/FLIRT>).¹⁸⁻²⁰ All nonquantitative images (T1, T1C, FLAIR) were intensity-normalized by dividing the voxel intensity by its whole-brain SD.^{21,22} Gray and white matter probability maps were computed using SPM12 (<https://www.fil.ion.ucl.ac.uk/spm/software/spm12/>).

Pathologic Feature Extraction

A total of 93 tissue samples were collected across all patients using previously described methods (See the Online Supplemental Data for further details).^{9,11,16} After digitization, images were processed using Matlab 2020b (MathWorks) to extract pathologic features for quantitative analyses. First, a color deconvolution algorithm was used to project color data in terms of relative stain intensities, resulting in an image with color channels representing hematoxylin,

eosin, and residual color information.^{23,24} Images were then down-sampled by a factor of 10 to smooth color data for improved nuclei segmentation as well as to decrease processing time. Cell nuclei were highlighted by applying filters on each color channel to selectively identify positive hematoxylin staining, and individual nuclei were identified using Matlab's *regionprops* function. Cell count was computed across 50×50 superpixels and converted to cells per square millimeter. Segmentations for extracellular fluid and cytoplasm were computed and converted to proportions of the superpixel occupied by the component of interest. All segmentations were visually inspected for quality assurance, and sample segmentations are provided in the Online Supplemental Data.

MRI-Histology Coregistration

Previously published in-house software (written in Matlab) was used to precisely align histology images to each patient's clinical imaging (See the Online Supplemental Data for further details).^{9,11,16,25,26} Voxel intensity values from T1, T1C, FLAIR, and ADC images as well as cellularity values for each studied voxel were then collected across the aligned tissue sample area and used for subsequent analyses. Across all 93 samples, a total of 578,668 voxels were included. All MR imaging and histology data were then sampled to the most common cross-sectional MR imaging dimensions (matrix size = 512×512 , voxel size = 0.4397×0.4397 mm).

Statistical Analyses

Single-Image Analyses. Linear mixed-effects models were used to quantify associations between MR imaging values and cellularity. Image intensity was included as a main effect, with time between the last MR imaging and patient death (in days) and gray/white matter probability included as covariates. Patient number was included in the model to account for patient-specific confounds. Regression coefficients and R^2 values (conditional and marginal) were reported to quantify the relationship between MR imaging intensity and cellularity in terms of slope and explained variance, respectively.

To specifically compare diagnosis-level differences in the relationship between MR imaging intensity and cellularity, we computed similar mixed-effects models for each image type, including a term for the interaction between image intensity and diagnosis, with diagnostic groups corresponding to GBM, non-GBM glioma (NGG), and Other. The Other category consisted of 1 patient with brain metastases originating from the colon and 1 patient with a classically hypercellular diffuse large B-cell lymphoma. Both patients did not receive treatment for their brain tumors and can thus provide a proxy for radiologic-pathologic relationships in the untreated state. Due to the large number of observations relative to the patient-level data set size, P values were considered a poor measure of meaningful significance (all $P < .00001$). Therefore, measures of effect size are reported for this subanalysis. Analogous models were also calculated for extracellular fluid and cytoplasm as the dependent variables to examine other cellular factors that may drive imaging values, which are presented in the Online Supplemental Data.

Radio-Pathomic Modeling. A random forest ensemble algorithm was used as the framework for developing a radio-pathomic model of cellularity in 30 subjects. Specifically, a bootstrap

Table 2: Clinical and demographic summary for training and test set groups^a

	Training	Test
Diagnosis (GBM/NGG/Other)	24/4/1	8/6/1
Age (yr)	62.5 (12.9)	55.8 (14.5)
Overall survival (mo)	39.9 (69.5)	41.3 (44.9)
Radiation treatment (y/n)	25/4	14/1
Chemotherapy (y/n)	26/3	14/1
Tumor-treating fields (y/n)	12/17	4/11
Other treatment (y/n)	3/26	4/11
Time between last MR imaging and death (days)	46.2 (39.2)	95.5 (83.9)

Note:—Y/n indicates yes/no.

^aQuantitative values are presented as mean (SD).

aggregating (bagging) model was used (100 learning cycles, learn rate = 1), which fits independent weak learners across several independent bootstrapped samples from the training data set to obtain a combined ensemble model that minimizes variance across learners.^{27,28} Inputs for this model were intensity values from 5×5 voxel tiles across each image to incorporate spatial and contextual information. The models were then applied to MRIs from 14 held out test set subjects to test generalizability (Table 2). Performance was quantified using root mean squared error (RMSE) values. Predictions were then plotted for test set subjects to assess successful identification of hypercellularity beyond traditional imaging signatures, defined for this study as a substantial relative increase in cell density compared with the surrounding tissue and corresponding area on the contralateral hemisphere. Due to the inter- and intratumoral heterogeneity of the tumors included in this study, an absolute threshold for tumor-related hypercellularity could not be defined, though relative hypercellularity estimations aligned well with pathologically identified regions of tumor on a subset of samples used for validation (Online Supplemental Data).

RESULTS

Single-Image Analyses

Mixed-effects model results for the single image analyses are presented in Fig 2. T1, T1C, and FLAIR images demonstrated positive associations with cellularity (T1 $\beta = 160.23$ [5.11], conditional $R^2 = 0.35$, marginal $R^2 = 0.012$; T1C $\beta = 480.60$ [4.00], conditional $R^2 = 0.44$, marginal $R^2 = -0.074$; FLAIR $\beta = 152.50$ [3.12], conditional $R^2 = 0.34$, marginal $R^2 = 0.010$). ADC values demonstrated a negative association with cellularity ($\beta = -153.72$ [5.45], conditional $R^2 = 0.34$, marginal $R^2 = 0.008$). When we split data by diagnostic group (GBM versus NGG versus Other), stronger relationships between image intensity and cellularity were observed for NGG and Other patients across each image except the precontrast T1, with the largest diagnostic discrepancy seen in the ADC-cellularity relationship (T1 $\beta = 135.56$ [4.10], conditional $R^2 = 0.15$, marginal $R^2 = 0.014$; T1C $\beta = 615.22$ [3.76], conditional $R^2 = 0.30$, marginal $R^2 = 0.126$; FLAIR $\beta = 277.51$ [2.83], conditional $R^2 = 0.18$, marginal $R^2 = 0.036$; ADC $\beta = 168.24$ [2.84], conditional $R^2 = 0.16$, marginal $R^2 = 0.016$). The GBM group showed an opposite-direction relationship compared with the Other group for the precontrast T1 intensity, with only a subtle relationship seen in the NGG group.

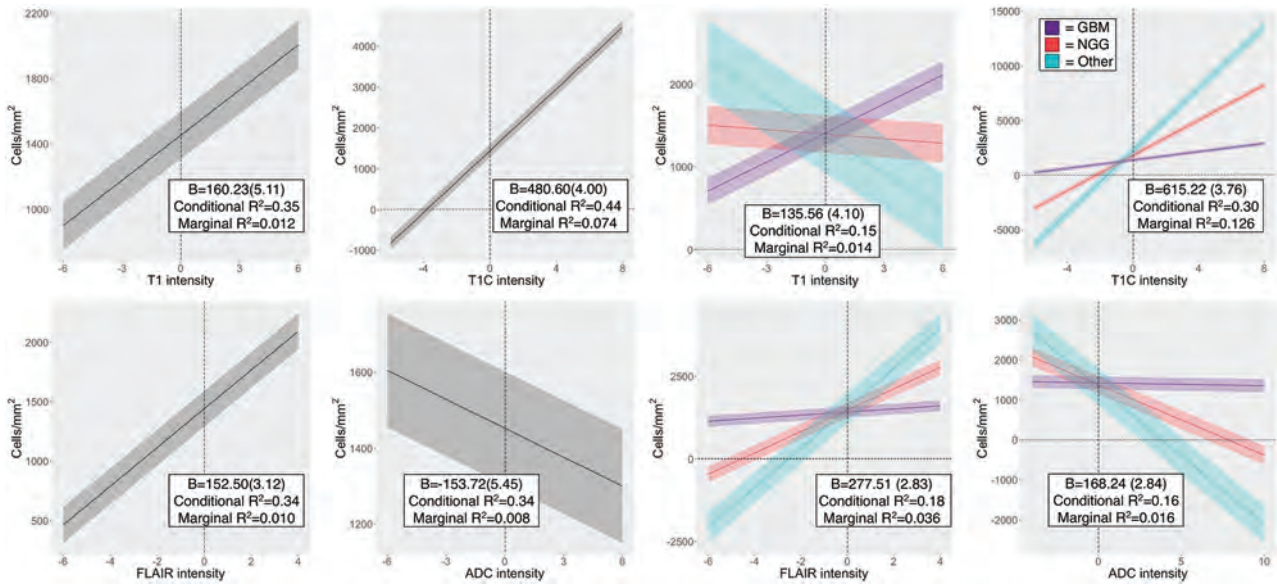


FIG 2. Single-image results depicting the relationship between image intensity and cellularity for each contrast. β values for the left-handed plots indicate the change in cellularity per SD increase in image intensity and indicate positive associations for T1, TIC, and FLAIR, with the expected negative association between ADC and cellularity present. β values for the right-handed plots indicate the difference in slope among patients with GBM and NGG and Other patients, indicating that patients with GBM show less pronounced cellularity associations than patients with NGG across all image types, with the exception of T1 intensity.

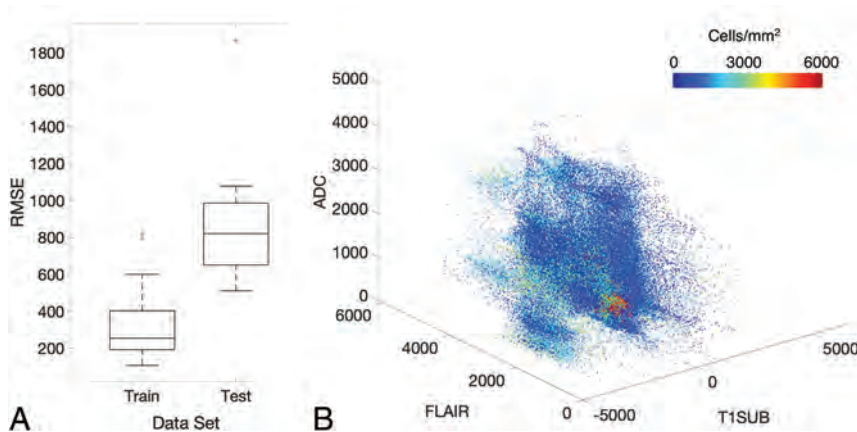


FIG 3. A, Subject-level RMSE values for the training and test data sets. Despite some degree of overfitting, the test set RMSE indicates that the radio-pathomic model is able to accurately predict cellularity across most subjects. B, Sample predictions for test set imaging values presented in terms of T1SUB, FLAIR, and ADC intensity values. Patterns suggest the presence of traditional imaging signatures but also indicate the lack of specificity for these signatures with regard to hypercellularity. T1SUB indicates TIC–T1.

Radio-Pathomic Mapping

A summary of model performance, including training and test set RMSE values and a scatterplot summarizing sample prediction values, is provided in Fig 3. Overall training and test set RMSE values (389 and 1015 cells/mm², respectively) show some degree of overfitting regarding the training data set, but they generally indicate accurate prediction of cellularity. A small subset of subjects also performed worse than the general test set, as indicated by the high RMSE outliers in Fig 3. The scatterplot, which demonstrates sample predictions in terms of T1SUB (T1C–T1), FLAIR, and ADC intensity values, shows indications of expected

relationships (ie, FLAIR-ADC mismatch associated with hypercellularity) but also shows that traditional hypercellularity signatures are often nonspecific. Sample predictions for test set subjects are included in Fig 4, in which cellularity predictive maps (CPM) for the whole brain are provided with the clinical images for each patient, as well as the pathologic ground truth from the aligned post-mortem slide. These sample predictions show that the CPMs calculated from the radio-pathomic model accurately predict several regions of increased cellularity beyond the traditional contrast-enhancing region and discriminate between hypercellular and nonhypercellular regions within contrast enhancement. Additionally, a tissue sample from a region of predicted hypercellularity beyond contrast enhancement on a 64-year-old

man's test set subject (diagnosed with a GBM) was sampled and immunohistochemically (IHC) stained to confirm the presence of active tumor (Fig 5). Specifically, Ki-67 staining, which is used to calculate the Mindbomb homolog-1 Index (MIB-1 index) as a measure of mitotic activity, and cluster of differentiation 31 (CD31), which stains positive in regions of angiogenesis, were collected in addition to standard H&E staining. Sample MR images and CPMs are presented for the test set subject designated for IHC analysis, along with tissue maps indicating the MIB-1 index, positive CD31 staining, and actual cellularity. The CPM identifies a region of hypercellularity toward the perimeter of the

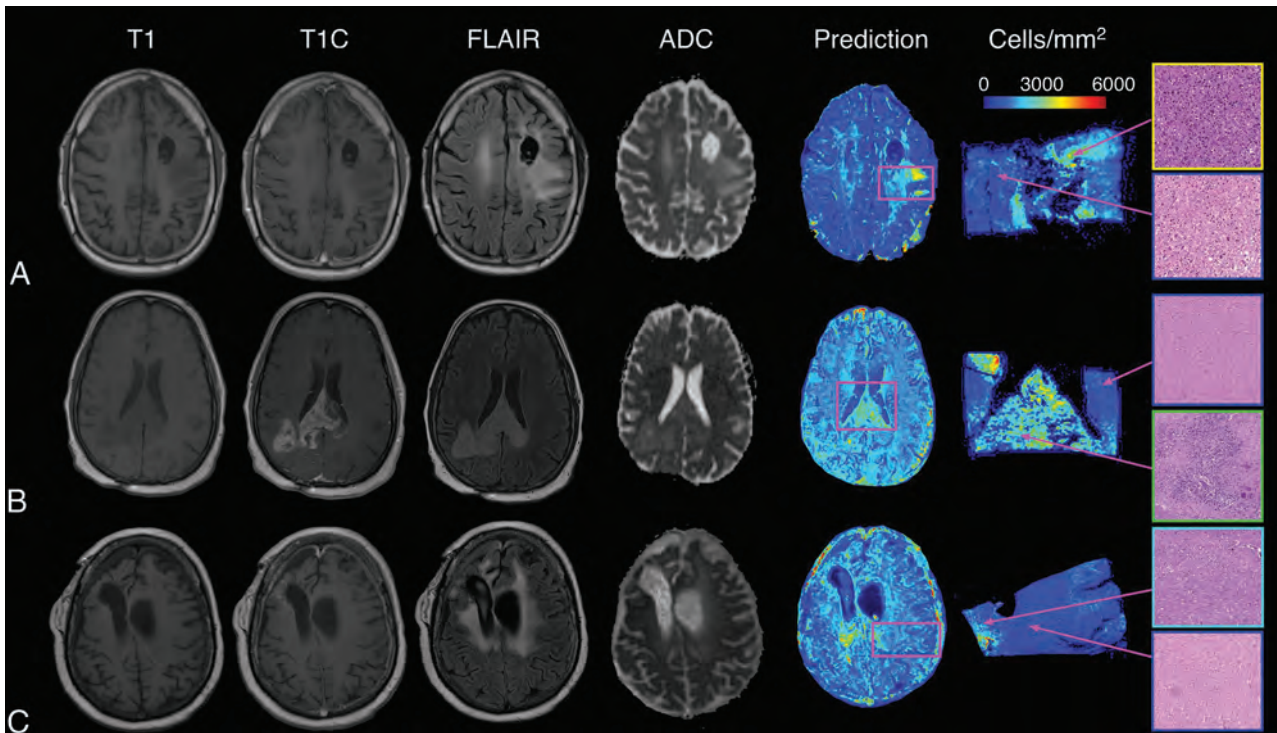


FIG 4. Sample predictions for 3 representative subjects, including a 43-year-old man diagnosed with a grade III anaplastic astrocytoma (A), a 48-year-old man diagnosed with a GBM (B), and a 31-year-old woman diagnosed with a grade III anaplastic astrocytoma (C). These predictions indicate that the radio-pathomic model is able to predict regions of hypercellularity beyond the contrast-enhancing region as well as in the absence of restricted diffusion on the ADC image.

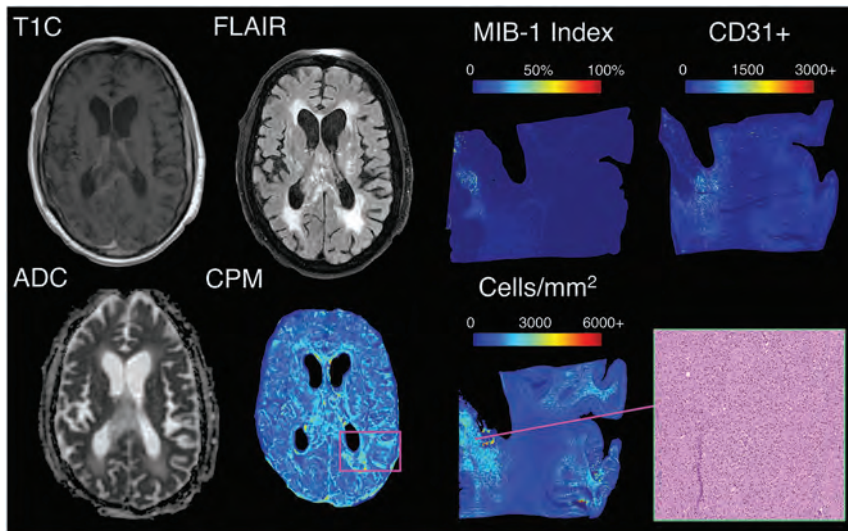


FIG 5. IHC staining for a nonenhancing region of predicted hypercellularity outside of contrast enhancement (a 64-year-old man diagnosed with GBM). The ROI corresponds to an actual region of hypercellularity seen on H&E staining as well as portions of high MIB-1 index and CD31 positivity. These molecular features indicate that this CPM-identified region contains active, proliferating tumor beyond the contrast-enhancing region. CPM indicates cellularity prediction map.

posterior FLAIR hyperintense region of the left hemisphere, outside the T1 contrast enhancement. The tissue-derived cellularity map confirms the presence of hypercellularity in this region, with MIB-1 staining indicating high mitotic activity in the left-handed portion of the hotspot and positive CD31 staining indicating

increased angiogenesis throughout the hotspot, confirming likely tumor presence.

DISCUSSION

By means of tissue samples taken at postmortem examination aligned to the patients' clinical imaging, this study assessed relationships between imaging and pathology in the posttreatment state, as well as beyond the contrast-enhancing region. Linear mixed-effects model-based analyses of image intensity values found that single-image signatures explain a relatively small proportion of cellularity variance. Additional analyses found an effect of tumor type on the cellularity-intensity relationship, with reduced cellularity associations seen in patients with GBM compared with those with NGG across all image types. We developed a radio-pathomic model using a bagging ensemble architecture, which predicted cellularity accurately on withheld sub-

jects, despite performing less reliably in a small subset of cases. The model accurately predicted regions of hypercellularity beyond contrast enhancement and other traditional imaging signatures, and IHC staining confirmed the presence of tumor within nonenhancing hypercellularity.

The general trends for increased cellularity associated with increased contrast enhancement and FLAIR intensity support the notion that these features relate to the pathologic effects of the tumor. However, these features failed to account for most cellularity variance and, in some cases, failed to identify regions of hypercellular tumor. Past studies have particularly highlighted ADC values as a correlate for cellularity. This study finds evidence of this negative association, though the strength of this relationship is more subtle in comparison with previous studies. Previous studies have suggested that radiation therapy and other treatments may influence these signatures because induced necrosis may confound traditional interpretations of these features.^{29,30} Diagnostic factors may play a role here as well because the results of this study show that GBM cases, which present with a wide range of pathologic characteristics, have less pronounced relationships between cellularity and imaging values than their lower-grade, more pathologically homogeneous counterparts.³¹⁻³³ Further studies probing the effects of different treatments and tumors on imaging characteristics may be able to further delineate these discrepancies between hypercellular and visually identifiable tumor. Particularly, studies comparing radio-pathomic signatures between patients who have and have not received treatment postsurgery could indicate how the relationship between MR imaging and pathology deviates in the treated state from that of the natural progression of glial tumors. Future studies modeling treatment duration and timing are warranted.

The performance statistics for our radio-pathomic model suggest that our model can accurately assess tumor cellularity in patients with brain cancer. Most subjects in the test set had a RMSE within an SD of each subject's cellularity, indicating that the model has the capacity to generalize to unseen data. These results thus demonstrate the feasibility of developing radio-pathomic models for pathologic features using postmortem tissue data, which have the added benefits of larger sampleable tissue areas and the presence of treatment-related effects. Sample whole-brain CPMs indicate that the radio-pathomic model can highlight regions of hypercellularity beyond contrast enhancement, suggesting that radio-pathomic modeling may provide improved localization of hypercellular tumor areas in the posttreatment setting. Posttreatment modeling is critical for tracking longitudinal tumor development in a clinical setting because models that can account for the effects of various treatments on imaging signature will provide more reliable estimates of tumor presence than those developed in the absence of treatment. Studies mapping genetic signatures associated with treatment resistance, immune response, and treatment receptivity using these techniques may even be able to noninvasively distinguish among areas of tissue that would benefit from different treatment types. Additionally, future studies with larger samples might use these maps to track differences in more specific brain cancer subtypes, such as monitoring nonenhancing behavior and the hypercellular growth rate between glioblastoma and other high-grade gliomas.

The CPMs generated from this radio-pathomic model provide early insight into clinical uses for noninvasive imaging models for pathologic information collected at postmortem examination. By using commonly acquired clinical scans (T1, T1C, FLAIR, ADC), this model can provide predictions on retrospective data as well as predict cellularity in future subjects without

adding additional scan time to a patient's clinical MR imaging acquisition. However, less common add-on acquisitions measuring perfusion, spectroscopy, and chemical exchange saturation transfer properties have shown great promise in identifying pathologic signatures of tumors, and it is likely that including these images in future studies may improve our models further.

Limitations

While the results of this study are promising, there are several limitations that warrant noting. This study developed voxelwise predictions across hundreds of thousands of observations, though the subject-level sample size is still small by machine learning standards. Additionally, cellularity was used as the ground truth measurement for this study due to its quantitative, calculatable nature. However, hypercellularity is a nonexclusive and indirect marker of tumor pathology, and future studies focused on predicting actual tumor presence may be better suited to distinguishing tumor hypercellularity from features like immune response. Likely, the largest contributing factor to the limits of this study is the time between MR imaging acquisition and tissue collection. While we statistically controlled for this factor, it is possible that confounding effects such as tumor growth within this period may influence the results beyond statistical covariance. While it is feasible to perform MR imaging on the postmortem brain to circumvent this time delay, changes in tissue perfusion and properties resulting from brain extraction and fixation would make the radio-pathomic model difficult to generalize to in vivo imaging. These specific weaknesses are avenues for future research, in which the delay between the time of death and final MR imaging are modeled extensively.

CONCLUSIONS

This study evaluated multiparametric MR imaging signatures of brain tumor pathology and developed a radio-pathomic model for brain cancer using machine learning. Our predictive maps of tumor cellularity highlighted tumor beyond conventional boundaries and plausibly tracked tumor growth using longitudinal imaging. We hope that these algorithms may be useful in the future for treatment planning and tumor monitoring.

ACKNOWLEDGMENTS

We would like to thank our patients for their participation in this study, the Medical College of Wisconsin Machine Learning Working Group for helpful feedback and discussions, and our funding sources.

Disclosure forms provided by the authors are available with the full text and PDF of this article at www.ajnr.org.

REFERENCES

1. Ostrom QT, Bauchet L, Davis FG, et al. **The epidemiology of glioma in adults: a "state of the science" review.** *Neuro Oncol* 2014;16:896–913 CrossRef Medline
2. Ellingson BM, Wen PY, Cloughesy TF. **Evidence and context of use for contrast enhancement as a surrogate of disease burden and treatment response in malignant glioma.** *Neuro Oncol* 2018;20:457–71 CrossRef Medline

3. Lasocki A, Gaillard F. **Non-contrast-enhancing tumor: a new frontier in glioblastoma research.** *AJNR Am J Neuroradiol.* 2019;40:758–65 CrossRef Medline
4. Hudak AM, Peng L, Marquez de la Plata C, et al. **Cytotoxic and vasogenic cerebral oedema in traumatic brain injury: assessment with FLAIR and DWI imaging.** *Brain Inj* 2014;28:1602–09 CrossRef Medline
5. Hawkins-Daarud A, Rockne RC, Anderson ARA, et al. **Modeling tumor-associated edema in gliomas during anti-angiogenic therapy and its impact on imageable tumor.** *Front Oncol* 2013;3:66 CrossRef Medline
6. Garrett MD, Yanagihara TK, Yeh R, et al. **Monitoring radiation treatment effects in glioblastoma: FLAIR volume as significant predictor of survival.** *Tomography* 2017;3:131–37 CrossRef Medline
7. Eidel O, Neumann JO, Burth S, et al. **Automatic analysis of cellularity in glioblastoma and correlation with ADC using trajectory analysis and automatic nuclei counting.** *PLoS One* 2016;11:e0160250 CrossRef Medline
8. Chenevert TL, Malyarenko DI, Galbán CJ, et al. **Comparison of voxel-wise and histogram analyses of glioma ADC maps for prediction of early therapeutic change.** *Tomography* 2019;5:7–14 CrossRef Medline
9. LaViolette PS, Mickevicius NJ, Cochran EJ, et al. **Precise ex vivo histological validation of heightened cellularity and diffusion-restricted necrosis in regions of dark apparent diffusion coefficient in 7 cases of high-grade glioma.** *Neuro Oncol* 2014;16:1599–606 CrossRef Medline
10. Surov A, Meyer HJ, Wienke A. **Correlation between apparent diffusion coefficient (ADC) and cellularity is different in several tumors: a meta-analysis.** *Oncotarget* 2017;8:59492–99 CrossRef Medline
11. Nguyen HS, Milbach N, Hurrell SL, et al. **Progressing bevacizumab-induced diffusion restriction is associated with coagulative necrosis surrounded by viable tumor and decreased overall survival in patients with recurrent glioblastoma.** *AJNR Am J Neuroradiol* 2016;37:2201–08 CrossRef Medline
12. Elder JB, Huntoon K, Otero J, et al. **Histologic findings associated with laser interstitial thermotherapy for glioblastoma multiforme.** *Diagn Pathol* 2019;14:19 CrossRef Medline
13. Hentschel SJ, Lang FF. **Current surgical management of glioblastoma.** *Cancer J* 2003;9:113–25 CrossRef Medline
14. Rong Y, Durden DL, Van Meir EG, et al. **“Pseudopalisading” necrosis in glioblastoma: a familiar morphologic feature that links vascular pathology, hypoxia, and angiogenesis.** *J Neuropathol Exp Neurol* 2006;65:529–39 CrossRef Medline
15. Louis DN, Perry A, Wesseling P, et al. **The 2021 WHO Classification of Tumors of the Central Nervous System: a summary.** *Neuro Oncol* 2021;23:1231–51 CrossRef Medline
16. Bobholz SA, Lowman AK, Barrington A, et al. **Radiomic features of multiparametric MRI present stable associations with analogous histological features in patients with brain cancer.** *Tomography* 2020;6:160–69 CrossRef Medline
17. McGarry SD, Hurrell SL, Kaczmarowski AL, et al. **Magnetic resonance imaging-based radiomic profiles predict patient prognosis in newly diagnosed glioblastoma before therapy.** *Tomography* 2016;2:223–28 CrossRef Medline
18. Jenkinson M, Bannister P, Brady M, et al. **Improved optimization for the robust and accurate linear registration and motion correction of brain images.** *Neuroimage* 2002;17:825–41 CrossRef Medline
19. Jenkinson M, Beckmann CF, Behrens TE, et al. **FSL.** *Neuroimage* 2012;62:782–90 CrossRef Medline
20. Jenkinson M, Smith S. **A global optimisation method for robust affine registration of brain images.** *Med Image Anal* 2001;5:143–56 CrossRef Medline
21. Ellingson BM, Aftab DT, Schwab GM, et al. **Volumetric response quantified using T1 subtraction predicts long-term survival benefit from cabozantinib monotherapy in recurrent glioblastoma.** *Neuro Oncol* 2018;20:1411–18 CrossRef Medline
22. Ellingson BM, Kim HJ, Woodworth DC, et al. **Recurrent glioblastoma treated with bevacizumab: contrast-enhanced T1-weighted subtraction maps improve tumor delineation and aid prediction of survival in a multicenter clinical trial.** *Radiology* 2014;271:200–10 CrossRef Medline
23. Ruifrok AC, Johnston DA. **Quantification of histochemical staining by color deconvolution.** *Anal Quant Cytol Histol* 2001;23:291–99 Medline
24. Bukowy JD, Foss H, McGarry SD, et al. **Accurate segmentation of prostate cancer histomorphometric features using a weakly supervised convolutional neural network.** *J Med Imaging (Bellingham)* 2020;7:057501 CrossRef Medline
25. McGarry SD, Hurrell SL, Iczkowski KA, et al. **Radio-pathomic maps of epithelium and lumen density predict the location of high-grade prostate cancer.** *Int J Radiat Oncol Biol Phys* 2018;101:1179–87 CrossRef Medline
26. McGarry SD, Bukowy JD, Iczkowski KA, et al. **Gleason probability maps: a radiomics tool for mapping prostate cancer likelihood in MRI space.** *Tomography* 2019;5:127–34 CrossRef Medline
27. Breiman L. **Random forests.** *Mach Learn* 2001;45:5–32 CrossRef
28. Breiman L. **Bagging predictors.** *Mach Learn* 1996;24:123–40 CrossRef
29. Ellingson BM, Chung C, Pope WB, et al. **Pseudoprogression, radionecrosis, inflammation or true tumor progression? Challenges associated with glioblastoma response assessment in an evolving therapeutic landscape.** *J Neurooncol* 2017;134:495–504 CrossRef Medline
30. Zikou A, Sioka C, Alexiou GA, et al. **Radiation necrosis, pseudo-progression, pseudoresponse, and tumor recurrence: imaging challenges for the evaluation of treated gliomas.** *Contrast Media Mol Imaging* 2018;2018:6828396 CrossRef Medline
31. Friedmann-Morvinski D. **Glioblastoma heterogeneity and cancer cell plasticity.** *Crit Rev Oncog* 2014;19:327–36 CrossRef Medline
32. Perrin SL, Samuel MS, Koszyca B, et al. **Glioblastoma heterogeneity and the tumour microenvironment: implications for preclinical research and development of new treatments.** *Biochem Soc Trans* 2019;47:625–38 CrossRef Medline
33. Qazi MA, Vora P, Venugopal C, et al. **Intratumoral heterogeneity: pathways to treatment resistance and relapse in human glioblastoma.** *Ann Oncol Off Oncol* 2017;28:1448–56 CrossRef Medline

DSC Perfusion MRI–Derived Fractional Tumor Burden and Relative CBV Differentiate Tumor Progression and Radiation Necrosis in Brain Metastases Treated with Stereotactic Radiosurgery

F. Kuo, N.N. Ng, S. Nagpal, E.L. Pollom, S. Soltys, M. Hayden-Gephart, G. Li, D.E. Born, and M. Iv



ABSTRACT

BACKGROUND AND PURPOSE: Differentiation between tumor and radiation necrosis in patients with brain metastases treated with stereotactic radiosurgery is challenging. We hypothesized that MR perfusion and metabolic metrics can differentiate radiation necrosis from progressive tumor in this setting.

MATERIALS AND METHODS: We retrospectively evaluated MRIs comprising DSC, dynamic contrast-enhanced, and arterial spin-labeling perfusion imaging in subjects with brain metastases previously treated with stereotactic radiosurgery. For each lesion, we obtained the mean normalized and standardized relative CBV and fractional tumor burden, volume transfer constant, and normalized maximum CBF, as well as the maximum standardized uptake value in a subset of subjects who underwent FDG-PET. Relative CBV thresholds of 1 and 1.75 were used to define low and high fractional tumor burden.

RESULTS: Thirty subjects with 37 lesions (20 radiation necrosis, 17 tumor) were included. Compared with radiation necrosis, tumor had increased mean normalized and standardized relative CBV ($P = .002$) and high fractional tumor burden (normalized, $P = .005$; standardized, $P = .003$) and decreased low fractional tumor burden (normalized, $P = .03$; standardized, $P = .01$). The area under the curve showed that relative CBV (normalized = 0.80; standardized = 0.79) and high fractional tumor burden (normalized = 0.77; standardized = 0.78) performed the best to discriminate tumor and radiation necrosis. For tumor prediction, the normalized relative CBV cutoff of ≥ 1.75 yielded a sensitivity of 76.5% and specificity of 70.0%, while the standardized cutoff of ≥ 1.75 yielded a sensitivity of 41.2% and specificity of 95.0%. No significance was found with the volume transfer constant, normalized CBF, and standardized uptake value.

CONCLUSIONS: Increased relative CBV and high fractional tumor burden (defined by a threshold relative CBV of ≥ 1.75) best differentiated tumor from radiation necrosis in subjects with brain metastases treated with stereotactic radiosurgery. Performance of normalized and standardized approaches was similar.

ABBREVIATIONS: ASL = arterial spin-labeling; AUC = area under the curve; DCE = dynamic contrast-enhanced; FTB = fractional tumor burden; K^{trans} = volume transfer constant; max = maximum; nCBF = normalized CBF; nRCBV = normalized relative CBV; RCBV = relative CBV; RN = radiation necrosis; sRCBV = standardized relative CBV; SRS = stereotactic radiosurgery; SUV = standardized uptake value

Perfusion and metabolic imaging markers such as relative CBV (RCBV) acquired with DSC, volume transfer constant (K^{trans})

acquired with dynamic contrast-enhanced (DCE) imaging, CBF acquired with arterial spin-labeling (ASL), and standardized uptake value (SUV) acquired with [18 F] FDG-PET have been investigated to overcome the diagnostic challenge of differentiating progressive tumor and radiation necrosis (RN) in the post-treatment brain tumor setting.¹⁻³ A relatively newly described DSC-derived metric, fractional tumor burden (FTB), which is defined as the volume fraction of contrast-enhancing voxels above or below a defined RCBV threshold, has also shown increasing potential for spatial discrimination of tumor and treatment effect.²

Single quantitative perfusion values (such as mean, median, or maximum RCBV) may not accurately reflect the spatial heterogeneity of tumor. FTB, however, can provide per-voxel assessment

Received December 2, 2021; accepted after revision March 14, 2022.

From the Department of Radiology, Division of Neuroimaging and Neurointervention (F.K., N.N.N., M.I.), and Departments of Neurology (Neuro-Oncology) (S.N.), Radiation Oncology (E.L.P., S.S.), Neurosurgery (M.H.-G., G.L.), and Pathology (D.E.B.), Stanford University, Stanford, California.

Frank Kuo and Nathan N. Ng are co-first authors and contributed equally to this work.

Please address correspondence to Michael Iv, MD, Stanford University, Center for Academic Medicine, Radiology + MC: 5659, Room 323A, 453 Quarry Rd, Palo Alto, CA 94304; e-mail: miv@stanford.edu; @Michael_Iv_MD

Indicates article with online supplemental data.

<http://dx.doi.org/10.3174/ajnr.A7501>

of the entire contrast-enhancing lesion volume. While a previous study used 1 RCBV threshold in the evaluation of tumor,³ we have recently shown, in a study of recurrent glioblastoma, that 2 normalized RCBV thresholds (1 and 1.75) can classify voxels into low- and high-FTB classes, which define fractions of the contrast-enhancing volume with low and high blood volume, respectively, and can help differentiate treatment necrosis from tumor as well as guide clinical decision-making.⁴ Therefore, FTB maps allow spatial representation of areas of suspected tumor and treatment effect, because both can coexist in various proportions within a given lesion.^{2,3} Standardization of RCBV, which uses a method to transform RCBV maps to a standardized intensity scale without the need for operator-defined reference ROIs (potentially minimizing variability in the acquisition of RCBV measurements),⁵ has also shown performance similar to that of normalized RCBV in distinguishing tumor from treatment effect.⁶

In this study, we evaluated the utility of DSC-derived FTB in patients with brain metastases after previous treatment with stereotactic radiosurgery (SRS). We hypothesized that the use of 2 RCBV thresholds (using normalized and standardized approaches) to define low and high FTB, as in our prior study of recurrent glioblastoma,⁴ could be effective in distinguishing progressive tumor from RN in previously treated brain metastases. In this study, RCBV refers to either normalized or standardized RCBV, while nRCBV and sRCBV refer specifically to normalized and standardized RCBV, respectively. A secondary goal was to evaluate the performance of metrics derived from other perfusion and metabolic techniques, including DCE, ASL, and FDG-PET.

MATERIALS AND METHODS

Subjects

This retrospective study was approved by Stanford University's institutional review board. Through a key word search of our PACS database, we identified subjects with brain metastases previously treated with SRS between May 2018 to October 2020. Inclusion criteria were the following: 18 years of age or older, history of brain metastases previously treated with SRS, and post-treatment perfusion MR imaging showing at least 1 suspicious contrast-enhancing lesion (defined by interval growth post-SRS), with the longest lesion diameter measuring ≥ 10 mm. Subjects were excluded if they had nonenhancing lesions, extensive susceptibility related to blood or surgical material (obscuring $>50\%$ of the target lesion) on raw precontrast DSC images, a histopathologic diagnosis of lymphoma or a primary brain tumor such as glioma, or if a clinical assessment of the lesion ground truth could not be established at the time of the study. In a subset of patients who had PET-MR imaging, evaluation of the presence of metabolic activity was performed. Clinical demographics, histopathologic information, and treatment history were obtained through the electronic medical record.

Imaging Acquisition

MRIs were performed on 3T scanners (Discovery MR750 or Signa Architect, GE Healthcare, $n = 28$; Magnetom Skyra, Siemens, $n = 2$). Most imaging was acquired as part of the RN protocol of our institution, which consisted of the following sequences (in order of acquisition): pregadolinium 3D T1-weighted inversion recovery fast-

spoiled gradient recalled, ASL, DCE, T2-weighted, DSC, and postgadolinium 3D T1 inversion recovery fast-spoiled gradient recalled.

ASL imaging (TR/TE = 4000/10 ms, in-plane spatial resolution = 3 mm, section thickness = 4 mm, skip = 0 mm, with the labeling plane at the level of the foramen magnum) was performed with a 3D background-suppressed fast spin-echo technique without vascular suppression using a pseudocontinuous labeling time of 1.5 seconds, followed by a 2-second postlabeling delay.

DCE imaging consisted of 5 axial 3D fast-spoiled gradient recalled flip angle series (2° , 5° , 10° , 15° , and 20°) used for T1 mapping, followed by acquisition of the dynamic images (TR/TE = 3–5/1–2 ms, flip angle = 30° , section thickness = 3 mm with 0-mm skip, FOV = 240 mm, matrix = 128×128 mm, 70 phases, 20 slices/phase, 4 seconds/phase) obtained after the intravenous injection of 0.05 mmol/kg of gadobenate dimeglumine (MultiHance; Bracco Diagnostics). This initial contrast load served as a preload dose to help correct for leakage effects in subsequent DSC imaging. Following DCE and T2-weighted acquisitions, a second 0.05-mmol/kg gadolinium dose was administered for DSC (TR/TE = 1800/35–40 ms, section thickness = 5 mm with 0 mm skip with 20 images covering the brain, flip angle = 60° , matrix = 128×128 mm, FOV = 240 mm). If DCE was not acquired, a dose of 0.05 mmol/kg of gadolinium was still administered as a preload dose before T2-weighted and DSC imaging.

A subset of subjects underwent FDG-PET imaging on a 3T PET-MRI scanner (Signa) using TOF capability, following an intravenous injection of 5–6 mCi of [18 F] FDG. The time from injection to imaging was 45–75 minutes. Attenuation correction was performed with zero TE MRI, using proton density differences to classify soft tissues, air, and bone in the head. While PET data were acquired, axial 3D T1 spoiled gradient-recalled images were acquired for PET attenuation correction, with generation of in-phase, out-of-phase, fat, and water images using the Dixon method. In addition, axial proton density-weighted zero TE images (TR/TE = 400/0.02 ms, FOV = 264 mm, matrix = 110×110 mm, section thickness = 2.4 mm with 0-mm skip) were acquired.

Image Processing and Analysis

A second-year neuroradiology fellow (F.K.) performed all image segmentation and ROI placement. All ROIs were reviewed, confirmed, and adjusted (if necessary) by a board-certified neuroradiologist with 10 years of brain tumor imaging interpretation and segmentation experience (M.I.). Each lesion was analyzed separately in subjects with >1 lesion.

DSC Processing and Analysis

We used a workstation equipped with OsiriX MD Imaging Software (Version 7.0; <http://www.osirix-viewer.com>) and a FDA-cleared plug-in (IB Neuro, Version 2.0; Imaging Biometrics), which uses established leakage-correction methods, to process perfusion data and calculate RCBV and FTB.^{2,3,7,8} For semiautomated image processing, we used IB Rad Tech (Version 2.0; Imaging Biometrics), a workflow engine that generates quantitative Δ T1 and FTB maps from the IB Delta Suite (Version 2.0; Imaging Biometrics) and IB Neuro plug-ins (Imaging Biometrics), according to a previously described workflow.^{4,8} Normalization was

Table 1: Demographics and clinical information

	RN (<i>n</i> = 20 Lesions)	Tumor (<i>n</i> = 17 Lesions)
Age (mean) (SD) (yr) ^a	65 (8.9)	54 (12.8)
Sex (male/female) ^a	9:8	3:10
Primary tumor ^b		
Lung	10 (50.0%)	3 (17.6%)
Breast	5 (25.0%)	9 (52.9%)
Melanoma	2 (10.0%)	0
Colorectal	2 (10.0%)	0
Tonsillar	1 (5.0%)	0
Sinonasal	0	3 (17.6%)
Ovarian	0	2 (11.8%)
Surgical resection for determination of histopathologic ground truth diagnosis ^b	7 (35.0%)	6 (35.2%)
Interval time between end of radiation and first MR imaging (median) (range) (mo)	24.9 (4–109)	16.3 (3–41)
Interval time between end of radiation and PET-MR imaging (median) (range) (mo) ^c	27.9 (14–117)	12.4 (6–37)
Total radiation dosage (mean) (SD) (Gy)	24.5 (4.2)	22.8 (3.1)

^aThirty subjects who had a total of 37 lesions (*n* = 20 RN; *n* = 17 tumor) were included in age and sex analyses.

^bPercentages for primary tumor type and surgical resection are relative to the total number of lesions within each column.

^cSubset of 17 subjects who had a total of 20 lesions (*n* = 8 RN, *n* = 12 tumor) who underwent PET-MRI.

performed relative to the contralateral normal-appearing white matter. Standardization was built into the software algorithm and did not require additional operator-defined input. For each approach, we used 2 previously tested RCBV thresholds (1 and 1.75) to define 3 FTB classes: FTB_{low}, percentage of contrast-enhancing voxels with RCBV of ≤ 1.0 ; FTB_{mid}, percentage of voxels with RCBV between 1.0 and 1.75; and FTB_{high}, percentage of voxels with RCBV of ≥ 1.75 . An sRCBV of 1.56 was also evaluated as a threshold for tumor, given a prior report of this value indicating >88% probability of tumor.^{3,9} Percentage values from the 3 FTB classes were summed to 100%. Mean nRCBV and sRCBV values of the contrast-enhanced volumes were generated for each subject. Contrast-enhanced T1-weighted images of the lesion superimposed on the FTB map containing assigned colored voxels for each class (FTB_{low} = blue; FTB_{mid} = yellow; FTB_{high} = red) and a histogram displaying voxels for the contrast-enhancing volume were also generated.

DCE Processing and Analysis

We used OsiriX MD (Version 7.0) and a commercially available plug-in for DCE analysis (IB DCE, Version 2.0; Imaging Biometrics). Using the semiautomated pipeline of the software, which includes automated generation of the vascular input function, operator-defined segmentation of the entire contrast-enhancing volume on contiguous dynamic contrast-enhanced T1-weighted images, and pharmacokinetic modeling using the 2-compartment Tofts model, we acquired mean K^{trans} values of the contrast-enhancing lesion volume.

ASL and PET Processing and Analysis

Postprocessed ASL imaging was performed by an automated reconstruction script that sent CBF images directly to the PACS.

PET images were reconstructed using TOF ordered subsets expectation maximization (32 subsets, 8 iterations, 256 × 256 mm matrix, standard z-axis filter, cutoff of 3) and zero TE MRI.

Analysis was performed by manually drawing an ROI around the margin of each enhancing lesion on a single image section that contained the area of maximum enhancement (excluding as

much cystic or necrotic areas as possible) on axial postgadolinium, T1-weighted imaging using OsiriX MD (Version 7.0). The ROI was then transferred to coregistered and postprocessed ASL images to obtain the maximum CBF value and coregistered MRI-based attenuation-corrected FDG-PET images calculated from the PET 45- to 75-minute summed raw data to obtain the maximum standardized uptake value (SUV_{max}). Studies have shown that SUV_{max} is a more reliable and accurate parameter for quantification.¹⁰ SUV_{max} ratios were then produced by normalizing the SUV maps to the pons, which was chosen as a reference area because its metabolism and volume are least affected by disease.¹¹ For consistency, the CBF_{max} of the lesion was also used for ASL, similar to use in prior studies of quantification,¹² and normalized to the pons to obtain the maximum normalized CBF value (nCBF).

Determination of Ground Truth Diagnoses

The diagnosis of tumor was based on fulfilling one of the following criteria: 1) final histopathologic diagnosis in the electronic medical record if the patient underwent resection (*n* = 6); 2) clinical determination by a radiation oncologist (S.S. and E.L.P.) of a tumor-progression diagnosis and need for further treatment (ie, repeat SRS or whole-brain radiation therapy or a CNS-penetrating systemic agent) (*n* = 3); and 3) a decreased contrast-enhancing size of the lesion after repeat SRS, performed after the study perfusion MR imaging (*n* = 8). The diagnosis of RN was based on fulfilling one of the following criteria: 1) final histopathologic diagnosis in the electronic medical record if the patient underwent resection (*n* = 7); and 2) clinical determination by a radiation oncologist (S.S. and E.L.P.) of an RN diagnosis without the need for further treatment (ie, the lesion became smaller on serial MR imaging without tumor-directed therapy, *n* = 13).

For FTB-histopathology correlation, a neuropathologist with >25 years of experience (D.E.B.) evaluated H&E stains of all submitted specimens (mean, 2; range, 1–5) in each subject who had undergone surgical resection. Percentages of tumor and necrosis/gliosis were visually estimated in each specimen. In subjects with

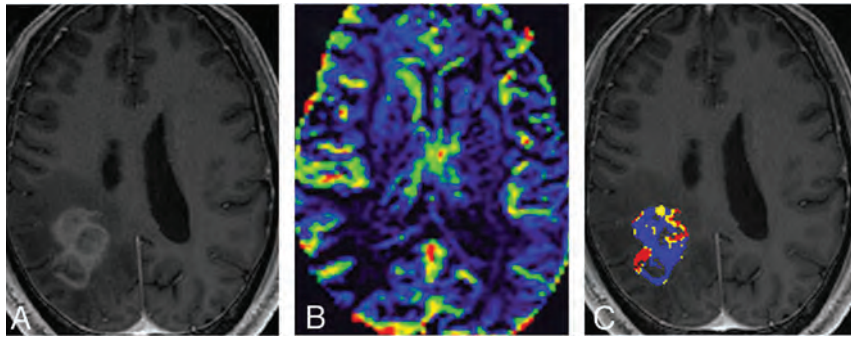


FIG 1. RN in a 58-year-old man with metastatic colon cancer presenting 17 months after surgical resection of a right parietal metastasis treated with SRS. A, Recurrent contrast-enhancing lesion at the site of the original tumor on axial T1-weighted postcontrast image. On DSC, the masslike lesion shows low RCBV (B) and predominantly FTB_{low} (blue) voxels (C). Low perfusion is consistent with pathology-proved RN (with <5% viable tumor cells).

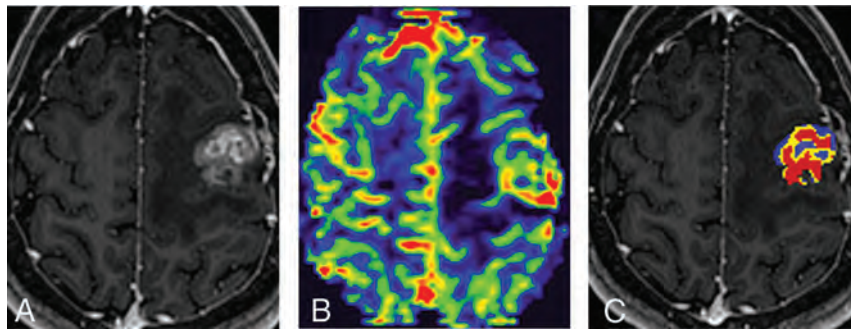


FIG 2. Progressive tumor in a 33-year-old woman with breast cancer presenting 8 months after surgical resection of a left frontal metastasis treated with stereotactic radiosurgery. A, A recurrent contrast-enhancing lesion at the site of the original tumor on an axial T1-weighted postcontrast image. On DSC, the masslike lesion shows high RCBV (B) and predominantly FTB_{high} (red) voxels (C). High perfusion is consistent with pathology-proved progressive tumor.

>1 specimen, percentages of tumor and necrosis/gliosis were obtained by taking the average across all submitted specimens.

Statistical Analyses

Descriptive statistics were used to report demographics, clinical information, and perfusion metrics. We used the non-parametric Mann-Whitney test to compare nRCBV and sRCBV, FTB (using nRCBV and sRCBV threshold values of 1 and 1.75), nCBF, K^{trans} , SUV, and $\Delta T1$ between the tumor and RN groups. The performance of each of these metrics to distinguish tumor from RN was evaluated with the area under the curve (AUC). Sensitivity, specificity, positive predictive value, and negative predictive value were determined for all tumor RCBV thresholds used in the study with MedCalc (Version 20.013; MedCalc Software). A Spearman ρ correlation was used to compare each FTB class with the percentages of tumor burden and necrosis/gliosis (RN) determined by histopathologic examination. $P < .05$ was considered statistically significant for all analyses. Statistical analyses and figures were conducted and created with GraphPad Prism software (Version 9.2.0; GraphPad Software).

RESULTS

Subjects

A total of 39 subjects were initially identified. Subjects were excluded if they had nonenhancing lesions ($n = 3$), extensive susceptibility on raw DSC images ($n = 2$), and a histopathologic diagnosis of lymphoma or other primary brain tumors ($n = 3$). One subject was excluded because a clinical assessment of the lesion ground truth could not be made at the time of the study ($n = 1$). After assessment of eligibility, 30 subjects with a total of 37 brain metastases ($n = 20$ RN, $n = 17$ tumor) were included in the analysis. All subjects underwent the study perfusion MR imaging, comprising DSC ($n = 30$), DCE ($n = 26$), and ASL ($n = 26$). A subset of 17 subjects with 20 total lesions ($n = 8$ RN, $n = 12$ tumor) underwent FDG-PET MR imaging. Table 1 summarizes the demographics and clinicopathologic information. Figures 1 and 2 demonstrate representative DSC imaging performed in subjects with RN and tumor, respectively.

Quantitative FTB and RCBV (DSC)

With the normalized approach, tumor had higher FTB_{high} ($P = .005$) and nRCBV ($P = .002$) and lower FTB_{low} ($P = .03$) than RN (Table 2). No significance was found with FTB_{mid} ($P = .17$). AUCs to differentiate tumor from RN were as follows: 0.71 for FTB_{low} (95% CI, 0.53–0.89; $P = .03$), 0.63 for FTB_{mid} (95% CI, 0.45–0.81; $P = .17$), 0.77 for FTB_{high} (95% CI, 0.60–0.93; $P = .005$), and 0.80 for nRCBV (95% CI, 0.64–0.96; $P = .002$) (Fig 3A and Table 2). For tumor prediction, the nRCBV threshold of ≥ 1.75 yielded a sensitivity of 76.5% and specificity of 70.0%, positive predictive value of 71.8%, and negative predictive value of 74.9% (Table 3).

With the standardized approach, tumor had higher FTB_{high} ($P = .003$) and sRCBV ($P = .002$) and lower FTB_{low} ($P = .01$) compared with RN (Table 2). No significance was found with FTB_{mid} ($P = .89$). AUCs to differentiate tumor from RN were as follows: 0.75 for FTB_{low} (95% CI, 0.57–0.92; $P = .01$), 0.51 for FTB_{mid} (95% CI, 0.32–0.71; $P = .89$), 0.78 for FTB_{high} (95% CI, 0.62–0.95; $P = .003$), and 0.79 for sRCBV (95% CI, 0.63–0.95; $P = .002$) (Fig 3B and Table 2). For tumor prediction, the sRCBV cutoff of ≥ 1.75 yielded a sensitivity of 41.2%, specificity of 95.0%, positive predictive value of 89.2%, and negative predictive value of 61.8% (Table 3). The sRCBV cutoff of ≥ 1.56 yielded similar results, with a sensitivity of 47.1%, specificity of 90.0%, positive predictive value of 82.5%, and negative predictive value of 63.0% (Table 3).

Table 2: Multiparametric perfusion, metabolic, and volumetric values in RN and tumor groups

	Radiation Necrosis ^b	Tumor ^b	P Value ^c	AUC ^d	AUC (95% CI)
DSC					
Normalized RCBV ^a					
FTB _{low} (%)	49.5 (30.1)	28.1 (23.8)	.03 ^e	0.71	0.53–0.89
FTB _{mid} (%)	17.7 (10.8)	13.4 (7.1)	.17	0.63	0.45–0.81
FTB _{high} (%)	32.8 (27.0)	58.6 (24.1)	.005 ^e	0.77	0.60–0.93
nRCBV	1.51 (0.9)	2.92 (1.5)	.002 ^e	0.80	0.64–0.96
Standardized RCBV ^a					
FTB _{low} (%)	62.6 (26.2)	33.8 (16.1)	.01 ^e	0.75	0.57–0.92
FTB _{mid} (%)	21.6 (15.7)	22.8 (7.2)	.89	0.51	0.32–0.71
FTB _{high} (%)	15.9 (14.0)	43.3 (20.9)	.003 ^e	0.78	0.62–0.95
sRCBV	0.94 (0.50)	1.63 (0.82)	.002 ^e	0.79	0.63–0.95
DCE					
K ^{trans} (min ⁻¹)	0.02 (0.02)	0.03 (0.04)	.23	0.64	0.43–0.85
ASL					
nCBF	1.25 (0.42)	1.67 (0.68)	.05	0.71	0.52–0.90
FDG-PET MR imaging					
SUV	1.33 (0.19)	1.62 (0.43)	.15	0.69	0.46–0.93
Volumetrics					
Δ T1 (cm ³)	3.24 (4.58)	3.76 (2.60)	.14	0.64	0.46–0.83

^a Thresholds of 1 and 1.75.

^b Values for RN and tumor groups are expressed in mean (SD).

^c P values obtained from nonparametric Mann-Whitney tests.

^d AUC obtained from receiver operating characteristic curves.

^e P values are statistically significant.

Quantitative K^{trans} (DCE), nCBF (ASL), SUV (FDG-PET), and Δ T1

Between RN and tumor, no significance was observed with mean K^{trans} ($P = .23$), nCBF ($P = .05$), SUV ($P = .15$), and Δ T1 ($P = .14$) (Table 2). AUCs for differentiating RN and tumor were as follows: 0.64 for K^{trans} (95% CI, 0.43–0.85; $P = .23$), 0.71 for nCBF (95% CI, 0.52–0.90; $P = .05$), 0.69 for SUV (95% CI, 0.46–0.93; $P = .15$), and 0.64 for Δ T1 (95% CI, 0.46–0.83, $P = .14$) (Fig 3C).

FTB-Histopathology Correlation

Thirteen subjects had surgical resection after the study perfusion MR imaging. However, only 11 subjects ($n = 5$ tumor and $n = 6$ RN) had specimens available for histopathologic analysis in this part of the study. With the normalized approach, no significant correlation was observed with FTB_{low} (versus percentage tumor: $\rho = -0.38$, $P = .25$; versus percentage necrosis/gliosis, $\rho = 0.38$, $P = .25$), FTB_{mid} (versus percentage tumor: $\rho = 0.26$, $P = .43$; versus percentage necrosis/gliosis, $\rho = -0.26$, $P = .43$), and FTB_{high} (versus percentage tumor: $\rho = 0.48$, $P = .13$; versus percentage necrosis/gliosis, $\rho = -0.48$, $P = .13$) (Online Supplemental Data).

With the standardized approach, no significant correlation was observed with FTB_{low} (versus percentage tumor: $\rho = -0.59$, $P = .06$; versus percentage necrosis/gliosis, $\rho = 0.59$, $P = .06$), FTB_{mid} (versus percentage tumor: $\rho = 0.42$, $P = .19$; versus percentage necrosis/gliosis, $\rho = -0.42$, $P = .19$), and FTB_{high} (versus percentage tumor: $\rho = 0.57$, $P = .07$; versus percentage necrosis/gliosis, $\rho = -0.57$, $P = .07$) (Online Supplemental Data).

With both approaches, however, FTB_{high} and FTB_{low} suggested a positive correlation, respectively, with the percentage of tumor and the percentage of necrosis/gliosis (Online Supplemental Data).

DISCUSSION

Our results show that the use of 2 RCBV thresholds (1 and 1.75) to define FTB classes, FTB_{low} and FTB_{high}, allowed differentiation

of tumor and RN in brain metastases following SRS. The performance of normalized and standardized approaches to achieve this task was similar. Additional perfusion and metabolic metrics of K^{trans} (DCE), nCBF (ASL), and SUV (FDG-PET), and Δ T1 did not reliably distinguish tumor from RN.

Results from the current study using 2 nRCBV thresholds (1 and 1.75) in treated brain metastases are similar to results from our previous study of treated recurrent glioblastomas, in which nRCBV and FTB_{high} best differentiated tumor from treatment effect.⁴ The use of 1 as a lower threshold for identifying RN and 1.75 as an upper threshold for identifying progressive tumor in posttreatment brain metastases is close to previously reported RCBV thresholds for differentiation of radiation-related changes (<1.35)¹³ and tumor (range, $>2-2.1$).^{14,15} As previously described, elevated blood volume and FTB_{high} are likely reflective of increased angiogenesis within tumors.⁴ FTB_{low} performed slightly less well because there is likely an overlap between hypovascular tumor and radiation-related coagulative necrosis/gliosis.¹⁶ FTB_{mid}, which includes all RCBV values between 1 and 1.75, did not reliably differentiate RN from tumor because there is likely an admixture of both in varying proportions within this range of values. Additionally, normalized and standardized RCBV and FTB approaches performed similarly, consistent with a recent study in high-grade gliomas.⁶ However, there was a trade-off in the sensitivity and specificity between the 2 approaches when using the ≥ 1.75 RCBV threshold for tumor prediction, possibly related to differences in postprocessing techniques (eg, the reference ROI in the contralateral normal-appearing white matter is required for normalization and not for standardization) and intrasubject variations with time.⁷ For tumor prediction, the sensitivity and specificity were similar for the sRCBV cutoff values of ≥ 1.75 and ≥ 1.56 . Nonetheless, standardization of DSC perfusion imaging, because sRCBV requires less operator-defined

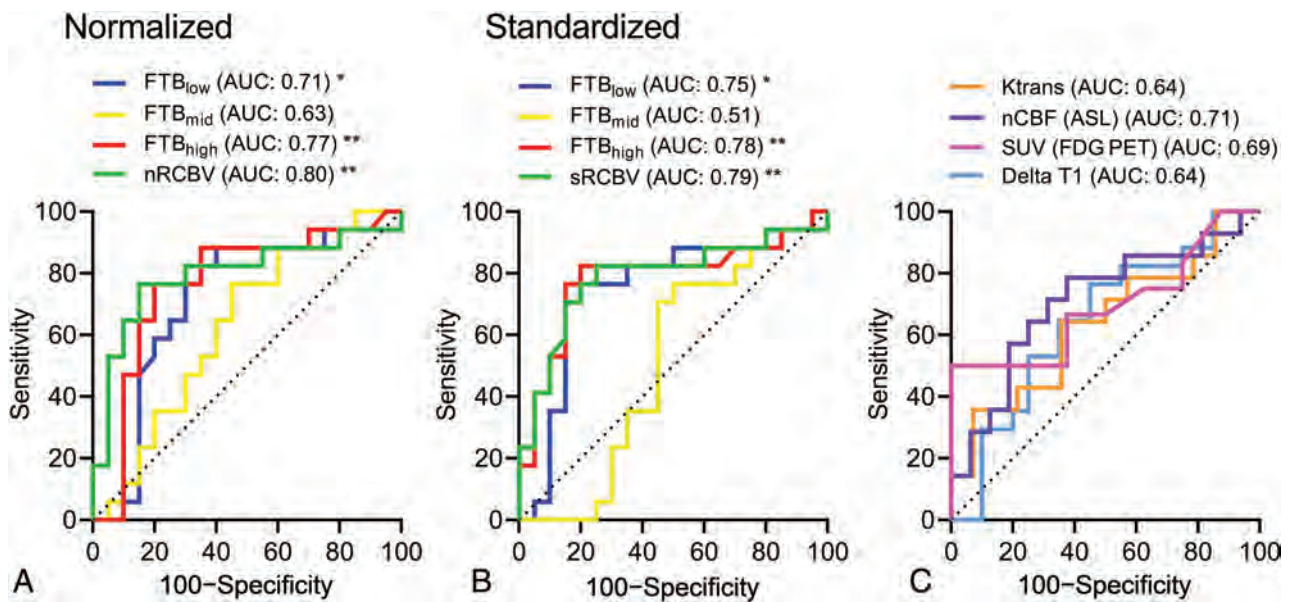


FIG 3. Receiver operating characteristic AUC analyses demonstrate that FTB and RCBV significantly differentiate RN from tumor. A, AUCs of FTB classes and nRCBV to differentiate RN from tumor were 0.71 for FTB_{low} (95% CI, 0.53–0.89; $P = .03$), 0.63 for FTB_{mid} (95% CI, 0.45–0.81; $P = .17$), 0.77 for FTB_{high} (95% CI, 0.60–0.93; $P = .005$), and 0.80 for nRCBV (95% CI, 0.64–0.96; $P = .002$). B, AUCs of FTB classes and sRCBV to distinguish RN and tumor were 0.75 for FTB_{low} (95% CI, 0.57–0.92; $P = .01$), 0.51 for FTB_{mid} (95% CI, 0.32–0.71; $P = .89$), 0.78 for FTB_{high} (95% CI, 0.62–0.95; $P = .003$), and 0.79 for sRCBV (95% CI, 0.63–0.95; $P = .002$). C, AUCs of K^{trans} , nCBF (ASL), SUV (FDG-PET), and $\Delta T1$ to differentiate RN from tumor were 0.64 for K^{trans} (95% CI, 0.43–0.85; $P = .23$), 0.71 for nCBF (ASL) (95% CI, 0.52–0.90; $P = .05$), 0.69 for SUV (FDG-PET) (95% CI, 0.46–0.93; $P = .15$), and 0.64 for $\Delta T1$ (95% CI, 0.46–0.83; $P = .14$). The asterisk and double asterisks denote $P < .05$ and $P < .01$, respectively.

Table 3: Sensitivity, specificity, PPV, and NPV of nRCBV and sRCBV thresholds for prediction of tumor

	Sens	Spec	PPV	NPV
nRCBV (1.75)	76.5	70.0	71.8	74.9
sRCBV (1.75)	41.2	95.0	89.2	61.8
sRCBV (1.56)	47.1	90.0	82.5	63.0

Note:—Sens indicates sensitivity; spec, specificity; PPV, positive predictive value; NPV, negative predictive value.

input than nRCBV, may represent an important step toward greater multicenter adoption and use.

One of the advantages of FTB maps is the potential for spatially mapping coexisting areas of tumor and treatment effect within a given lesion.² High-grade glioma studies using image-localized biopsies within contrast-enhancing lesions have shown that areas with low RCBV and FTB proved to be treatment effect and areas with high RCBV and FTB proved to be tumor on histopathology.^{2,3,6} In our study, though not significant (potentially related to the lower availability of surgical specimens for histopathologic examination), we similarly found a positive correlation between FTB_{high} and the percentage of tumor on histopathology and a positive correlation between FTB_{low} and the percentage of necrosis and gliosis on histopathology. However, additional investigations correlating tumor and necrosis fractions with defined FTB classes are needed for histologic confirmation.

Beyond DSC in our study, metrics of K^{trans} (DCE), nCBF (ASL), and SUV (FDG-PET) did not reliably differentiate tumor and RN, in contrast to other studies.^{1,17,18} Blood flow values derived from ASL and SUV from FDG-PET have shown utility in identifying tumor progression in treated brain metastases, with

an equivalent sensitivity of 83% and a specificity of 100% for ASL and 75% for FDG-PET in 1 study.¹⁹ Suh et al¹ found that the pooled sensitivity and specificity of 5 studies, including the aforementioned study, using FDG-PET to differentiate tumor from RN in post-SRS brain metastases, were 83% and 88%, respectively. Results from our study may differ from those of previously published studies because of differences in our cohorts (eg, types and numbers of included metastatic tumors). Due to the lack of validated thresholds for ASL, DCE, and FDG-PET, we did not perform a combined multimodal or multiparametric analysis, though it has been previously shown in treated glioblastomas that the combination of parameters such as RCBV and K^{trans} can improve the overall diagnostic accuracy in differentiating recurrent tumor and treatment effect (RCBV, 85.8%; K^{trans} , 75.5%; RCBV and K^{trans} , 92.8%).²⁰ In addition, as expected, the use of $\Delta T1$ as a volumetric measurement of gadolinium enhancement did not perform well in predicting tumor response, presumably related to the overlap of gadolinium leakage across a disrupted blood-brain barrier in both tumor and RN.²¹

Our study has important limitations. First, the small sample size consisting of retrospective data from a single institution limits the generalizability of our results. Second, we included various types of tumor histology in our analysis. Brain metastases have been shown to have different tumor perfusion values depending on the primary cancer type, with brain metastases derived from renal cell carcinoma and melanoma typically having higher RCBV values than those derived from lung, breast, and gastrointestinal tumors.²² Our subject cohort consisted primarily of lung- and breast-derived lesions, possibly accounting for less striking and prominent differences in tumor

RCBV.²² In addition, not all metastases are hypervascular; 1 study reported variation in tumor blood flow even between metastases derived from the same primary carcinoma, with approximately 40% of metastases overall showing blood flow less than or equivalent to blood flow from contralateral healthy cortex.¹⁸ In these cases, perfusion MR imaging alone may not be sufficiently sensitive to distinguish tumor growth and RN. In future studies, it may be helpful to establish baseline pretreatment values for comparison with posttreatment values or to combine perfusion imaging with other modalities, depending on the primary tumor histology.^{17,18}

Additionally, given the heterogeneity in tumor origin in studies of RN, it may be warranted in a future study to systematically stratify diagnostic accuracies of brain metastases according to tumor histology. Third, while we excluded lesions with blood products obscuring >50% of the lesion, metastases with minor blood products were still included in DSC analysis. This limitation is reflective of real-time clinical practice because blood products are common in post-SRS lesions. It may also underscore the use of other perfusion parameters and techniques to help with interpretation. Fourth, we did not have image-localized biopsy tissue from the 3 distinct FTB classes evaluated, limiting the direct per-voxel comparison of perfusion imaging metrics with fractions of tumor and necrosis present on histopathology.

CONCLUSIONS

DSC-derived FTB using nRCBV or sRCBV thresholds of 1 and 1.75 can provide per-voxel analysis of low and high blood volume and can differentiate progressive tumor from RN in brain metastases previously treated with SRS. Normalized and standardized approaches achieve similar performance for this task, though sRCBV may have the potential for better reproducibility across time and sites. Additional metrics of K^{trans} (DCE), nCBF (ASL), SUV (FDG-PET), and $\Delta T1$ did not reliably differentiate tumor from RN. Nonetheless, the evaluated RCBV thresholds and FTB classes in this study require further clinical and histologic validation in larger prospective studies.

Disclosure forms provided by the authors are available with the full text and PDF of this article at www.ajnr.org.

REFERENCES

1. Suh CH, Kim HS, Jung SC, et al. **Comparison of MRI and PET as potential surrogate endpoints for treatment response after stereotactic radiosurgery in patients with brain metastasis.** *AJR Am J Roentgenol* 2018;211:1332–41 CrossRef Medline
2. Hu LS, Eschbacher JM, Heiserman JE, et al. **Reevaluating the imaging definition of tumor progression: perfusion MRI quantifies recurrent glioblastoma tumor fraction, pseudoprogression, and radiation necrosis to predict survival.** *Neuro Oncol* 2012;14:919–30 CrossRef Medline
3. Prah MA, Al-Gizawiy MM, Mueller WM, et al. **Spatial discrimination of glioblastoma and treatment effect with histologically-validated perfusion and diffusion magnetic resonance imaging metrics.** *J Neurooncol* 2018;136:13–21 CrossRef Medline
4. Iv M, Liu X, Lavezo J, et al. **Perfusion MRI-based fractional tumor burden differentiates between tumor and treatment effect in recurrent glioblastomas and informs clinical decision-making.** *AJNR Am J Neuroradiol* 2019;40:1649–57 CrossRef Medline
5. Bedekar D, Jensen T, Schmainda KM. **Standardization of relative cerebral blood volume (rCBV) image maps for ease of both inter-**

- and intrapatient comparisons.** *Magn Reson Med* 2010;64:907–13 CrossRef Medline
6. Hoxworth JM, Eschbacher JM, Gonzales AC, et al. **Performance of standardized relative CBV for quantifying regional histologic tumor burden in recurrent high-grade glioma: comparison against normalized relative CBV using image-localized stereotactic biopsies.** *AJNR Am J Neuroradiol* 2020;41:408–15 CrossRef Medline
 7. Prah MA, Stufflebeam SM, Paulson ES, et al. **Repeatability of standardized and normalized relative CBV in patients with newly diagnosed glioblastoma.** *AJNR Am J Neuroradiol* 2015;36:1654–61 CrossRef Medline
 8. Schmainda KM, Prah MA, Hu LS, et al. **Moving toward a consensus DSC-MRI protocol: validation of a low-flip angle single-dose option as a reference standard for brain tumors.** *AJNR Am J Neuroradiol* 2019;40:626–63 CrossRef Medline
 9. Connelly JM, Prah MA, Santos-Pinheiro F, et al. **Magnetic resonance imaging mapping of brain tumor burden: clinical implications for neurosurgical management: case report.** *Neurosurgery Open* 2021;2:okab029 CrossRef Medline
 10. Ulaner GA. **Measuring treatment response on FDG PET/CT.** In: Ulaner GA. *Fundamentals of Oncologic PET/CT.* Elsevier; 2019:225–29
 11. Minoshima S, Frey KA, Foster NL, et al. **Preserved pontine glucose metabolism in Alzheimer disease: a reference region for functional brain image (PET) analysis.** *J Comput Assist Tomogr* 1995;19:541–47 CrossRef Medline
 12. Delgado AF, De Luca F, Hanagandi P, et al. **Arterial spin-labeling in children with brain tumor: a meta-analysis.** *AJNR Am J Neuroradiol* 2018;39:1536–42 CrossRef Medline
 13. Barajas RF, Chang JS, Sneed PK, et al. **Distinguishing recurrent intra-axial metastatic tumor from radiation necrosis following gamma knife radiosurgery using dynamic susceptibility-weighted contrast-enhanced perfusion MR imaging.** *AJNR Am J Neuroradiol* 2009;30:367–72 CrossRef Medline
 14. Sawlani V, Davies N, Patel M, et al. **Evaluation of response to stereotactic radiosurgery in brain metastases using multiparametric magnetic resonance imaging and a review of the literature.** *Clin Oncol (R Coll Radiol)* 2019;31:41–49 CrossRef Medline
 15. Hoefnagels FW, Lagerwaard FJ, Sanchez E, et al. **Radiological progression of cerebral metastases after radiosurgery: assessment of perfusion MRI for differentiating between necrosis and recurrence.** *J Neurol* 2009;256:878–87 CrossRef Medline
 16. Barajas R Jr, Chang JS, Segal MR, et al. **Differentiation of recurrent glioblastoma multiforme from radiation necrosis after external beam radiation therapy with dynamic susceptibility-weighted contrast-enhanced perfusion MR imaging.** *Radiology* 2009;253:486–96 CrossRef Medline
 17. Knitter JR, Erly WK, Stea BD, et al. **Interval change in diffusion and perfusion MRI parameters for the assessment of pseudoprogression in cerebral metastases treated with stereotactic radiation.** *AJR Am J Roentgenol* 2018;211:168175 CrossRef Medline
 18. Lambert EA, Holmes S. **Differentiating radiation-induced necrosis from tumor progression after stereotactic radiosurgery for brain metastases, using evaluation of blood flow with arterial spin labeling (ASL): the importance of setting a baseline.** *Acta Neurochir Suppl* 2021;128:113–19 CrossRef Medline
 19. Lai G, Mahadevan A, Hackney D, et al. **Diagnostic accuracy of PET, SPECT, and arterial spin-labeling in differentiating tumor recurrence from necrosis in cerebral metastasis after stereotactic radiosurgery.** *AJNR Am J Neuroradiol* 2015;36:2250–55 CrossRef Medline
 20. Nael K, Bauer AH, Hormigo A, et al. **Multiparametric MRI for differentiation of radiation necrosis from recurrent tumor in patients with treated glioblastoma.** *AJR Am J Roentgenol* 2018;210:18–23 CrossRef Medline
 21. Iv M, Bisdas S. **Neuroimaging in the era of the evolving WHO Classification of Brain Tumors, From the AJR Special Series on Cancer Staging.** *AJR Am J Roentgenol* 2021;217:3–15 CrossRef Medline
 22. Zhang H, Zhang G, Oudkerk M. **Brain metastases from different primary carcinomas: an evaluation of DSC MRI measurements.** *Neuroradiol J* 2012;25:67–75 CrossRef Medline

Interobserver Reliability on Intravoxel Incoherent Motion Imaging in Patients with Acute Ischemic Stroke

 K. Yamashita,  R. Kamei,  H. Sugimori,  T. Kuwashiro,  S. Tokunaga,  K. Kawamata,  K. Furuya,  S. Harada,  J. Maehara,  Y. Okada, and  T. Noguchi



ABSTRACT

BACKGROUND AND PURPOSE: Noninvasive perfusion-weighted imaging with short scanning time could be advantageous in order to determine presumed penumbral regions and subsequent treatment strategy for acute ischemic stroke (AIS). Our aim was to evaluate interobserver agreement and the clinical utility of intravoxel incoherent motion MR imaging in patients with acute ischemic stroke.

MATERIALS AND METHODS: We retrospectively studied 29 patients with AIS (17 men, 12 women; mean age, 75.2 [SD, 12.0] years; median, 77 years). Each patient underwent intravoxel incoherent motion MR imaging using a 1.5T MR imaging scanner. Diffusion-sensitizing gradients were applied sequentially in the x, y, and z directions with 6 different b-values (0, 50, 100, 150, 200, and 1000 seconds/mm²). From the intravoxel incoherent motion MR imaging data, diffusion coefficient, perfusion fraction, and pseudodiffusion coefficient maps were obtained using a 2-step fitting algorithm based on the Levenberg-Marquardt method. The presence of decreases in the intravoxel incoherent motion perfusion fraction and pseudodiffusion coefficient values compared with the contralateral normal-appearing brain was graded on a 2-point scale by 2 independent neuroradiologists. Interobserver agreement on the rating scale was evaluated using the κ statistic. Clinical characteristics of patients with a nondecreased intravoxel incoherent motion perfusion fraction and/or pseudodiffusion coefficient rated by the 2 observers were also assessed.

RESULTS: Interobserver agreement was shown for the intravoxel incoherent motion perfusion fraction ($\kappa = 0.854$) and pseudodiffusion coefficient ($\kappa = 0.789$) maps, which indicated almost perfect and substantial agreement, respectively. Patients with a nondecreased intravoxel incoherent motion perfusion fraction tended to show recanalization of the occluded intracranial arteries more frequently than patients with a decreased intravoxel incoherent motion perfusion fraction.

CONCLUSIONS: Intravoxel incoherent motion MR imaging could be performed in <1 minute in addition to routine DWI. Intravoxel incoherent motion parameters noninvasively provide feasible, qualitative perfusion-related information for assessing patients with acute ischemic stroke.

ABBREVIATIONS: AIS = acute ischemic stroke; D = diffusion coefficient; D* = pseudo-diffusion coefficient; EVT = endovascular thrombectomy; f = perfusion fraction; IVIM = intravoxel incoherent motion

MR imaging is one of the best modalities for diagnosing acute ischemic stroke (AIS) and plays a crucial role in treatment

Received November 10, 2021; accepted after revision February 11, 2022.

From the Departments of Radiology (K.Y., R.K., K.F., S.H., J.M., T.N.), Cerebrovascular Medicine and Neurology (H.S., T.K., Y.O.), Neuroendovascular Therapy (S.T.), Clinical Research Institute, and Medical Technology (K.K.), Division of Radiology, National Hospital Organization Kyushu Medical Center, Fukuoka, Japan.

This work was supported by Nishikawa Medical Foundation, and the Japan Society for the Promotion of Science (JSPS) KAKENHI Grant Number 22K07657.

Please address correspondence to Koji Yamashita, MD, PhD, Department of Radiology, Clinical Research Institute, National Hospital Organization Kyushu Medical Center, 1-8-1 Jigyohama, Chuo-ku, Fukuoka 810-0065 Japan; e-mail: yamakou@radiol.med.kyushu-u.ac.jp

 Indicates open access to non-subscribers at www.ajnr.org

<http://dx.doi.org/10.3174/ajnr.A7486>

decisions for procedures such as endovascular thrombectomy (EVT). A multicenter randomized clinical trial (Multicenter Randomized Clinical trial of Endovascular treatment for Acute ischemic stroke in the Netherlands; the MR CLEAN trial) revealed notable benefits from EVT in patients with AIS.¹ Positive results from the Endovascular Therapy Following Imaging Evaluation for Ischemic Stroke 3 (DEFUSE 3)² and Clinical Mismatch in the Triage of Wake Up and Late Presenting Strokes Undergoing Neurointervention with Trevo (DAWN) trials³ have extended the therapeutic windows for AIS.

Findings from DWI are important for determining ischemic cores and have been included for assessing infarct volume in randomized clinical trials such as DEFUSE 3 and DAWN.^{2,3} CT perfusion imaging provides useful information to identify presumed

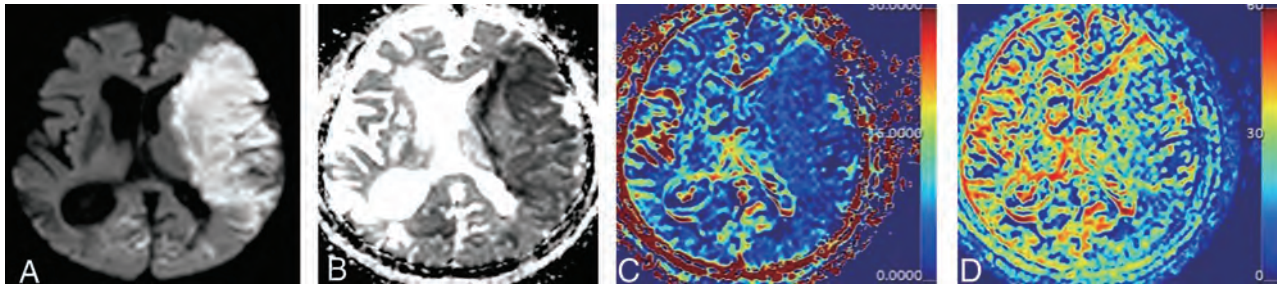


FIG 1. Representative DWI with a b-value of 1000 s/mm² (A), IVIM D (B), f (C), and D* (D) maps obtained using a 2-step algorithm. A 90-year-old woman with AIS. IVIM f and D* are expressed in units of percentage and $\times 10^{-3}$ mm²/s, respectively. Interobserver agreement is shown for IVIM f ($\kappa = 0.854$; $P < .001$) and D* ($\kappa = 0.789$; $P < .001$) using the 2-step algorithm, which indicated almost perfect and substantial agreement, respectively.

penumbral regions and has a large influence on decision-making for EVT. On the other hand, CT perfusion depends on factors such as motion, the time-density curve, determination of arterial input functions, and so forth.⁴ Technical pitfalls including core volume measurement error, misclassification of ischemic penumbra, and stroke mimics (seizure, migraines, and posterior reversible leukoencephalopathy) are also well-known.⁴ Theoretically, perfusion-weighted MR imaging provides less misregistration of lesions that appear hyperintense on DWI than other imaging modalities.

Dynamic susceptibility contrast, dynamic contrast enhancement, arterial spin-labeling, and intravoxel incoherent motion (IVIM) imaging offer perfusion-related parameters. Among these methods, IVIM imaging would provide advantages in terms of noninvasiveness as well as allowing registration with DWI. Le Bihan et al⁵ implemented the concept of IVIM MR imaging to separate the signal into diffusivity and microcapillary perfusion components with different exponential decays. IVIM MR imaging allows simultaneous extraction of perfusion and diffusion parameters and is reportedly useful for differentiating high- and low-grade gliomas,^{6,7} glioblastomas and lymphomas,^{8,9} and pediatric brain tumors.¹⁰ Ideally, a shorter scanning time using a small number of b-values would lead to advantages in reducing the time to subsequent reperfusion therapy. Federau et al¹¹ reported the feasibility of IVIM MR imaging using 6 b-values for AIS: 0, 50, 100, 150, 200, and 1000 s/mm². However, the interobserver reliability of IVIM MR imaging using these 6 b-values and the clinical characteristics of patients with decreased or nondecreased IVIM parameters have not been well-explored.

The goal of this study was, therefore, to evaluate interobserver agreement and the clinical utility of IVIM MR imaging in patients with AIS.

MATERIALS AND METHODS

Subjects

This retrospective study was approved by National Hospital Organization Kyushu Medical Center institutional review board for clinical research. The requirement of obtaining informed consent for study participation was waived due to the retrospective nature of this study. We studied 35 patients with nonlacunar AIS (21 men, 14 women; mean age, 75.6 [SD, 11.6] years; median age, 77 years) between August 2020 and June 2021. All subjects fulfilled the following criteria: MR imaging performed within 7 days

after either symptom onset or last seen well, and patients undergoing IVIM imaging. Six of the 35 patients were excluded from the study due to motion-related image degradation.

MR Imaging

All images were obtained using a 1.5T MR imaging scanner (Achieva; Philips Healthcare) and an 8-channel head array receiving coil for sensitivity encoding parallel imaging. IVIM imaging was performed using a single-shot spin-echo echo-planar sequence with the following parameters: TR, 3500 ms; TE, 75 ms; flip angle, 90°; NEX, 1; transverse sections, 23; sensitivity encoding factor, 2; section thickness, 5 mm; interslice gap, 1.5 mm; FOV, 220 \times 220 mm; matrix, 124 \times 105; and imaging time, 1 minute 24 seconds. Diffusion-sensitizing gradients were implemented in 3 orthogonal directions with 6 different b-values (0, 50, 100, 150, 200, and 1000 s/mm²). Directional averaging was performed before applying the IVIM model.

Postprocessing

From the IVIM imaging data, diffusion coefficient (D), perfusion fraction (f), and pseudodiffusion coefficient (D*) maps were obtained using a 2-step fitting algorithm based on the Levenberg-Marquardt method. The open-source platform ADCmap Plugin (Version 1.8, <http://web.stanford.edu/~bah/software/ADCmap/versions.html>), running OsiriX Lite, Version 8.0.1 (<https://www.osirix-viewer.com>) was applied for the fitting process for DWI data. In short, D values were calculated using a monoexponential signal equation for b-values ≥ 200 s/mm² in the first step. Subsequently, curve fitting was performed to obtain f and D* values using all 6 b-values, while the acquired D value was kept fixed.¹²

Image Evaluation

Representative DWI with $b=1000$ s/mm² and IVIM parameter (D, f, and D*) maps are shown in Fig 1. IVIM f and D* values were evaluated and graded on a 2-point scale by 2 independent neuroradiologists. Two observers determined the presence of decreases in f and D* values compared with the contralateral normal-appearing brain with reference to the hyperintense region on DWI with a b-value of 1000 s/mm².

Second, clinical characteristics of patients with nondecreased IVIM f and/or D* as rated by the 2 observers were assessed. Specifically, the cause of AIS was classified as cardioembolic,

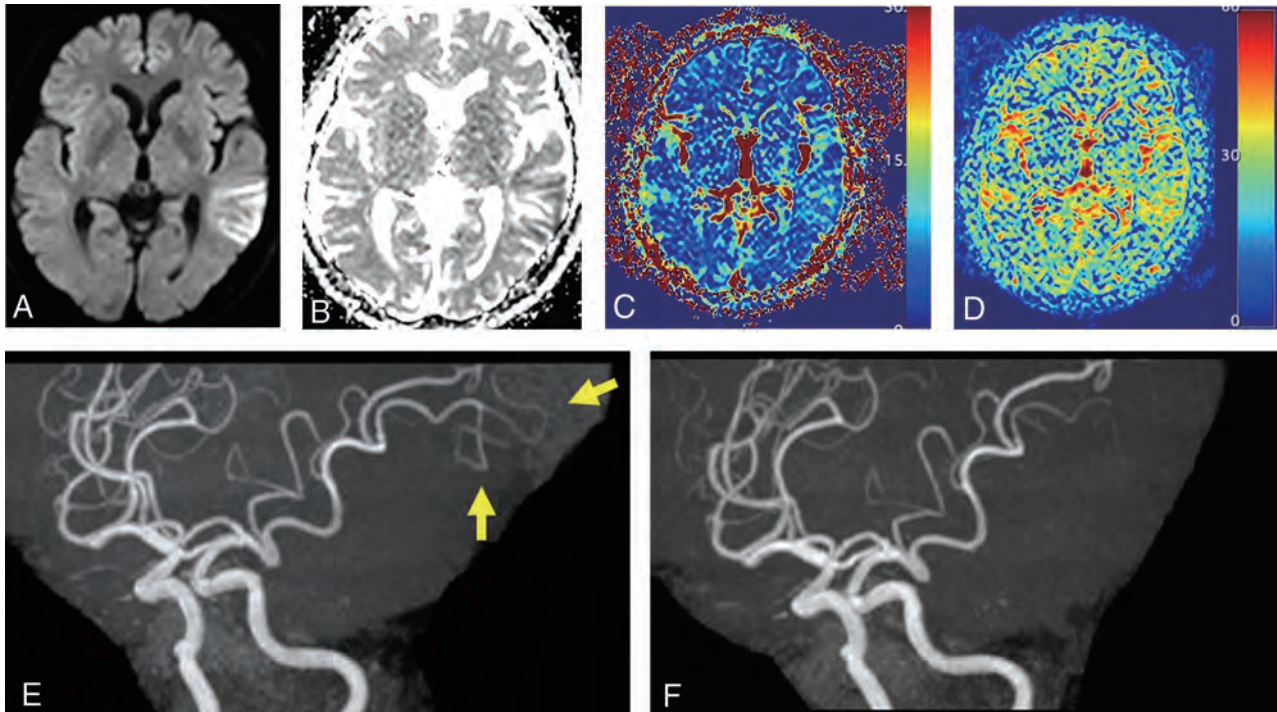


FIG 2. A DWI with a b-value of 1000 s/mm² (A), IVIM D (B), f (C), D* (D) maps, and MRA (E) of a 73-year-old man with AIS. MR imaging was performed 7 days after symptom onset. Nondecreased IVIM f and D* are identified on the f and D* maps. MR angiography represents spontaneous recanalization of the occluded left distal MCA (E; arrows). MRA performed 33 hours after symptom onset (F) is also shown as a reference.

atherothrombotic, or undetermined. The number of recanalized occluded intracranial arteries was also examined.

Next, a circular ROI (area, ≥ 10 mm²) was placed, as large as possible, within hyperintense lesions on DWI with a b-value of 1000 s/mm² by an experienced neuroradiologist. A mirrored ROI was also drawn in the corresponding contralateral region. ROIs on DWI were copied onto corresponding IVIM parameter (D, f, and D*) maps to calculate mean values for D, f, and D* (D_{mean} , f_{mean} , and D^*_{mean} , respectively).

Statistical Analyses

Interobserver agreement on the rating of IVIM f and D* maps was evaluated using κ statistics. κ values for interobserver agreement were evaluated as the following: 0, poor; 0.01–0.20, slight; 0.21–0.40, fair; 0.41–0.60, moderate; 0.61–0.80, substantial; and >0.80 , almost perfect. The difference in the frequency of recanalized occluded intracranial arteries between patients with decreased and nondecreased IVIM f was compared using the Pearson χ^2 test.

For the correlation between IVIM parameters (D_{mean} , f_{mean} , and D^*_{mean}) and time after stroke onset, a simple regression model was used to model trajectories with linear, quadratic, cubic, and logarithmic. The Akaike information criterion was used to determine the best fitting model.

IVIM D_{mean} , f_{mean} , and D^*_{mean} values were compared between the affected and contralateral unaffected sides using a 2-tailed paired Student *t* test. In all statistical analyses, the level of significance was set at $P < .05$. All statistical analyses were performed using R statistical and computing software, Version 3.5.1

(<http://www.r-project.org>), and graphs were plotted on GraphPad Prism, Version 7 (GraphPad Software).

RESULTS

As a result, a total of 29 patients with AIS (17 men, 12 women; mean age, 75.2 [SD 12.0] years; median age, 77 years) were included in this study. The median time from symptom onset or last seen well to MR imaging was 26 hours (range, 1 hour to 7 days), and the mean NIHSS score at presentation was 6.1 (SD, 7.4). We identified the cause of AIS as cardioembolic in 11 patients, atherothrombotic in 11, and undetermined in 7. A total of 7 cases showed recanalization of occluded intracranial arteries based on MR angiography.

Interobserver Agreement on the Rating of IVIM f and D* Maps

Interobserver agreement was shown for IVIM f ($\kappa = 0.854$, $P < .001$) and D* ($\kappa = 0.789$, $P < .001$), which indicated almost perfect and substantial agreement, respectively. Figure 1 shows representative IVIM f and D* maps obtained using the 2-step fitting algorithm.

Clinical Characteristics of Patients with Nondecreased IVIM f and/or D*

The 12 patients with nondecreased IVIM f as rated by observers showed recanalization of occluded intracranial arteries more frequently ($n = 6$; 6/12, 50%) than the 17 patients with decreased IVIM f (1/17, 5.9%; $P < .05$). Patients with nondecreased IVIM D* showed a trend similar to that in those with nondecreased

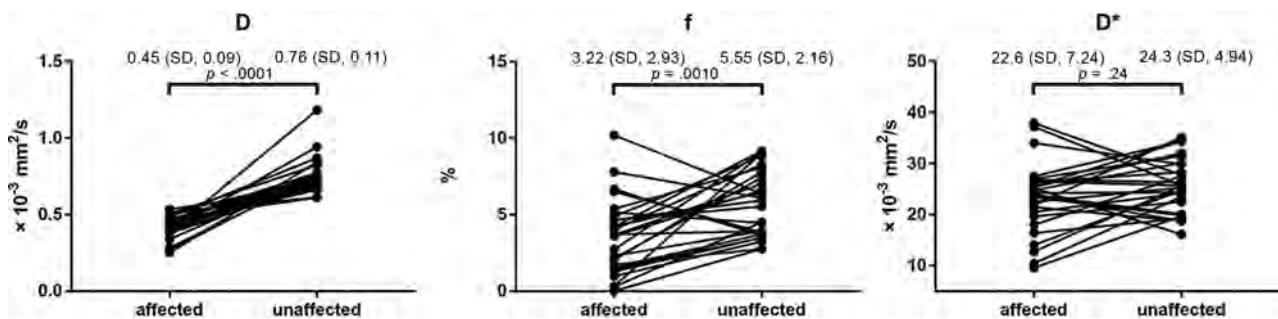


FIG 3. Plots of D_{mean} (A), f_{mean} (B), and D^*_{mean} (C) on both the affected and contralateral unaffected sides. The D_{mean} and f_{mean} values were lower on the affected side (mean $D_{\text{mean}} = 0.45$ [SD, 0.09] $\times 10^{-3}$ mm²/s; mean $f_{\text{mean}} = 3.22\%$ [SD, 2.93%]) than on the contralateral unaffected side (mean $D_{\text{mean}} = 0.76$ [SD, 0.11] $\times 10^{-3}$ mm²/s, $P < .0001$; mean $f_{\text{mean}} = 5.55\%$ [SD, 2.16%], $P = .0010$). No statistical difference in mean D^*_{mean} was evident between the affected side (22.6 [SD, 7.24] $\times 10^{-3}$ mm²/s) and the contralateral unaffected side (24.3 [SD, 4.94] $\times 10^{-3}$ mm²/s; $P = .24$).

IVIM f . Figure 2 shows the case of presumed spontaneous recanalization of an occluded MCA after AIS.

Correlation between IVIM Parameters and Time after Stroke Onset

The numbers in parentheses represent adjusted R^2 and P values using the best fitting model based on the Akaike information criterion. No statistical correlation was noted among IVIM D_{mean} (0.096, .10), f_{mean} (0.16, .06), and D^*_{mean} (−0.017, .47) in the presumed ischemic core and time after stroke onset.

D_{mean} , f_{mean} , and D^*_{mean} on Affected and Contralateral Unaffected Sides

Figure 3 shows plots of D_{mean} , f_{mean} , and D^*_{mean} for both affected and contralateral unaffected sides. Mean D_{mean} and f_{mean} values were lower on the affected side (mean $D_{\text{mean}} = 0.45$ [SD, 0.09] $\times 10^{-3}$ mm²/s; mean $f_{\text{mean}} = 3.22\%$ [SD, 2.93%]) than on the contralateral unaffected side (mean $D_{\text{mean}} = 0.76$ [SD, 0.11] $\times 10^{-3}$ mm²/s, $P < .0001$; mean $f_{\text{mean}} = 5.55 \pm 2.16\%$, $P = .001$). No statistical difference in mean D^*_{mean} was evident between the affected side (22.6 [SD, 7.24] $\times 10^{-3}$ mm²/s) and the contralateral unaffected side (24.3 [SD, 4.94] $\times 10^{-3}$ mm²/s; $P = .24$).

DISCUSSION

IVIM f and D^* using the 2-step fitting algorithm provided the χ values of 0.854 and 0.789, respectively, which demonstrated high interobserver agreement and feasible indicators for assessing patients with AIS. Patients with nondecreased IVIM f and D^* after AIS had a higher rate of the recanalization of occluded intracranial arteries in this study. IVIM MR imaging with its scanning time of <1 minute in addition to routine DWI with b -values of 0 and 1000 s/mm² offers a choice of noninvasive perfusion-weighted imaging for patients with suspected AIS.

In the present study, patients with nondecreased IVIM f and D^* as rated by the observers showed recanalization of occluded intracranial arteries more frequently than with decreased IVIM f and D^* . Padroni et al¹³ identified relative CBV as a strong indicator of recanalization status. MTT reportedly offers a valuable tool for assessing patients with AIS who may benefit from EVT.¹⁴ Our results are in line with the findings from previous studies. In addition, Eilaghi et al¹⁵ indicated that reperfusion indices for CBF, CBV, MTT, and time to maximum were more highly

associated with good clinical outcome than recanalization status. Validation using longitudinal data comprising values both before and after recanalization of occluded intracranial arteries would strengthen our results and represents the next step in our research.

Minimizing misinterpretation of IVIM parameter maps for clinical use is important. Almost perfect interobserver agreement was seen for IVIM f , and substantial agreement, for IVIM D^* as rated by the 2 observers in this study. A total of 6 b -values (0, 50, 100, 150, 200, and 1000 s/mm²) have been accepted as the reference standard for IVIM MR imaging when assessing AIS.^{11,16} More complex models would provide better results, while sophisticated models may cause the problem of overfitting due to data variations contaminated by noise and motion.¹⁷ IVIM parameter maps allow more accurate imaging evaluation with hyperintense lesions on DWI over other perfusion-weighted imaging such as dynamic susceptibility contrast, dynamic contrast enhancement, or arterial spin-labeling in terms of misregistration. MR perfusion-weighted imaging using IVIM is reportedly useful in patients with stroke with large-vessel occlusion.¹¹ IVIM parameter maps obtained from the 2-step fitting algorithm look less complicated with lower image noise than biexponential models, though which method is better for assessing AIS remains uncertain.

D_{mean} and f_{mean} values were lower on the affected side than on the contralateral unaffected side. IVIM f is related to blood volume.^{11,18} Our result is consistent with previous literature using MR imaging and PET.^{19,20} In contrast, we observed no statistical differences in D^*_{mean} values between the affected and contralateral unaffected sides. IVIM D^* is related to blood speed but fluctuates during the cardiac cycle, in contrast to the f and D values.²¹ IVIM D^* , thus, should be evaluated carefully along with other parameters.

In the present study, no correlation was observed between IVIM parameters in the presumed ischemic core and time after stroke onset. Fiebach et al²² reported the time course for the ADC in the ischemic core. Our results were not consistent with that research, possibly due to differences in the distribution of stroke subtypes and recanalization of occluded intracranial arteries.

Our study had several limitations. First, the present study comprised a small number of cases with various stroke subtypes and elapsed time from stroke onset. It is important to identify the

at-risk-but-viable penumbral tissue in the setting of AIS. Decreased IVIM f was presumed the infarct core with AIS²³ or a penumbral lesion in hyperacute brain stroke.¹¹ Further validation studies with larger sample sizes are needed. Second, this study was retrospective in nature, and selection bias due to nonrandom selection may have occurred. Third, a minimum of 6 directions should be acquired in the DTI framework, though it might take too long in the context of AIS.²⁴ Last, about half of the subjects had already undergone administration of intravenous recombinant tPA or endovascular treatment before MR imaging. Thus, further validation studies using longitudinal data are needed in the future. Nevertheless, we believe our results shed light on the availability of IVIM parameters in routine clinical practice.

CONCLUSIONS

IVIM MR imaging noninvasively provides feasible qualitative information in assessing patients with AIS.

Disclosure forms provided by the authors are available with the full text and PDF of this article at www.ajnr.org.

REFERENCES

- Berkhemer OA, Fransen PSS, Beumer D, et al; MR CLEAN Investigators. **A randomized trial of intraarterial treatment for acute ischemic stroke.** *N Engl J Med* 2015;372:11–20 CrossRef Medline
- Albers GW, Marks MP, Kemp S, et al. **Thrombectomy for stroke at 6 to 16 hours with selection by perfusion imaging.** *N Engl J Med* 2018;378:708–18 CrossRef Medline
- Nogueira RG, Jadhav AP, Haussen DC, et al. **Thrombectomy 6 to 24 hours after stroke with a mismatch between deficit and infarct.** *N Engl J Med* 2018;378:11–21 CrossRef Medline
- Vagal A, Wintermark M, Nael K, et al. **Automated CT perfusion imaging for acute ischemic stroke: pearls and pitfalls for real-world use.** *Neurology* 2019;93:888–98 CrossRef Medline
- Le Bihan D, Breton E, Lallemand D, et al. **MR imaging of intravoxel incoherent motions: application to diffusion and perfusion in neurologic disorders.** *Radiology* 1986;161:401–07 CrossRef Medline
- Federau C, Meuli R, O'Brien K, et al. **Perfusion measurement in brain gliomas with intravoxel incoherent motion MRI.** *AJNR Am J Neuroradiol* 2014;35:256–62 CrossRef Medline
- Togao O, Hiwatashi A, Yamashita K, et al. **Differentiation of high-grade and low-grade diffuse gliomas by intravoxel incoherent motion MR imaging.** *Neuro Oncol* 2016;18:132–41 CrossRef Medline
- Yamashita K, Hiwatashi A, Togao O, et al. **Diagnostic utility of intravoxel incoherent motion MR imaging in differentiating primary central nervous system lymphoma from glioblastoma multiforme.** *J Magn Reson Imaging* 2016;44:1256–61 CrossRef Medline
- Suh CH, Kim HS, Jung SC, et al. **MRI as a diagnostic biomarker for differentiating primary central nervous system lymphoma from glioblastoma: a systematic review and meta-analysis.** *J Magn Reson Imaging* 2019;50:560–72 CrossRef Medline
- Kikuchi K, Hiwatashi A, Togao O, et al. **Intravoxel incoherent motion MR imaging of pediatric intracranial tumors: correlation with histology and diagnostic utility.** *AJNR Am J Neuroradiol* 2019;40:878–84 CrossRef Medline
- Federau C, Wintermark M, Christensen S, et al. **Collateral blood flow measurement with intravoxel incoherent motion perfusion imaging in hyperacute brain stroke.** *Neurology* 2019;92:e2462–71 CrossRef Medline
- Federau C, Maeder P, O'Brien K, et al. **Quantitative measurement of brain perfusion with intravoxel incoherent motion MR imaging.** *Radiology* 2012;265:874–81 CrossRef Medline
- Padroni M, Bernardoni A, Tamborino C, et al. **Cerebral blood volume ASPECTS is the best predictor of clinical outcome in acute ischemic stroke: a retrospective, combined semi-quantitative and quantitative assessment.** *PLoS One* 2016;11:e0147910 CrossRef Medline
- Dababneh H, Bashir A, Guerrero WR, et al. **Mean transit time on Aquilion ONE and its utilization in patients undergoing acute stroke intervention.** *J Vasc Interv Neurol* 2014;7:73–81 Medline
- Eilaghi A, Brooks J, d'Esterre C, et al. **Reperfusion is a stronger predictor of good clinical outcome than recanalization in ischemic stroke.** *Radiology* 2013;269:240–48 CrossRef Medline
- Zhu G, Heit JJ, Martin BW, et al. **Optimized combination of b values for IVIM perfusion imaging in acute ischemic stroke patients.** *Clin Neuroradiol* 2020;30:535–44 CrossRef Medline
- Istratov AA, Vyvenko OF. **Exponential analysis in physical phenomena.** *Rev Sci Instrum* 1999;70:1233–57 CrossRef
- Le Bihan D, Turner R. **The capillary network: a link between IVIM and classical perfusion.** *Magn Reson Med* 1992;27:171–78 CrossRef Medline
- Sorensen AG, Copen WA, Ostergaard L, et al. **Hyperacute stroke: simultaneous measurement of relative cerebral blood volume, relative cerebral blood flow, and mean tissue transit time.** *Radiology* 1999;210:519–27 CrossRef Medline
- Sakoh M, Röhl L, Gyldensted C, et al. **Cerebral blood flow and blood volume measured by magnetic resonance imaging bolus tracking after acute stroke in pigs.** *Stroke* 2000;31:1958–64 CrossRef Medline
- Federau C, Hagmann P, Maeder P, et al. **Dependence of brain intravoxel incoherent motion perfusion parameters on the cardiac cycle.** *PLoS One* 2013;8:e72856 CrossRef Medline
- Fiebach JB, Jansen O, Schellinger PD, et al. **Serial analysis of the apparent diffusion coefficient time course in human stroke.** *Neuroradiology* 2002;44:294–98 CrossRef Medline
- Federau C, O'Brien K, Meuli R, et al. **Measuring brain perfusion with intravoxel incoherent motion (IVIM): initial clinical experience.** *J Magn Reson Imaging* 2014;39:624–32 CrossRef Medline
- Iima M, Partridge SC, Le Bihan D. **Six DWI questions you always wanted to know but were afraid to ask: clinical relevance for breast diffusion MRI.** *Eur Radiol* 2020;30:2561–70 CrossRef Medline

Brain Perfusion Alterations on 3D Pseudocontinuous Arterial Spin-Labeling MR Imaging in Patients with Autoimmune Encephalitis: A Case Series and Literature Review

R. Li, S. Jin, Y. Wang, J.-F. Li, H.-F. Xiao, Y.-L. Wang, and L. Ma



ABSTRACT

SUMMARY: Autoimmune encephalitis is a heterogeneous group of newly identified disorders that are being diagnosed with increasing frequency. Early recognition and treatment of autoimmune encephalitis are crucial for patients, but diagnosis remains challenging and time-consuming. In this retrospective case series, we describe the findings of conventional MR imaging and 3D pseudocontinuous arterial spin-labeling in patients with autoimmune encephalitis confirmed by antibody testing. All patients with autoimmune encephalitis showed increased CBF in the affected area, even when some of them presented with normal or slightly abnormal findings on conventional MR imaging. Additionally, serial 3D pseudocontinuous arterial spin-labeling showed perfusion reduction in 1 patient after therapy. For patients with highly suspected autoimmune encephalitis, 3D pseudocontinuous arterial spin-labeling may be added to the clinical work-up. Further studies and longitudinal data are needed to corroborate whether and to what extent 3D pseudocontinuous arterial spin-labeling improves the diagnostic work-up in patients with autoimmune encephalitis compared with conventional MR imaging.

ABBREVIATIONS: AE = autoimmune encephalitis; ASL = arterial spin-labeling; 3D pCASL = 3D pseudocontinuous arterial spin-labeling; MELAS = mitochondrial encephalopathy with lactic acidosis and strokelike episodes; rCBF = relative CBF

Autoimmune encephalitis (AE) is a blanket term for a group of diseases characterized by brain inflammation and circulating autoantibodies.¹ Its complicated and variable clinical manifestations present a diagnostic challenge for clinicians, probably leading to late diagnosis and interventions. It has been shown that early initiation of effective therapy for patients with AE may lead to improved clinical outcomes.^{2,3}

Currently, the diagnostic approach includes clinical manifestations, CSF analysis, electroencephalography, antibody testing, and MR imaging used together for AE (possible, probable, or definite).⁴ According to the 2016 diagnostic approach for AE from *Lancet Neurology*, brain MR imaging, as a standard imaging technique, plays a vital role in evaluating patients with AE, especially the T2 FLAIR sequence.⁴ However, in some cases, AE shows normal, mild, or transient abnormal findings on MR

imaging, despite the severe and persistent neurologic deficits of patients.⁵⁻⁷

Perfusion and metabolism abnormalities derived from CTP, SPECT, and PET/CT have been previously described in some patients with AE.⁸⁻¹¹ Arterial spin-labeling (ASL) perfusion imaging has broad clinical applications in routine neuroradiology practice in stroke, tumors, mitochondrial encephalopathy with lactic acidosis and strokelike episodes (MELAS), herpes simplex encephalitis, and so forth. However, the application of ASL for the assessment of AE in the clinic has seldom been described previously.^{6,12} Here, we conducted a retrospective study on a case series of 9 patients with AE to summarize the findings on conventional MR imaging and to investigate brain perfusion alterations.

CASE SERIES

Case Selection

From June 2015 to January 2020, a total of 21 consecutive patients with AE were enrolled. Twelve patients were excluded because 3D pseudocontinuous arterial spin-labeling (3D pCASL) was not performed. Nine patients with AE who underwent both conventional MR imaging and 3D pCASL were finally included. This retrospective study was approved by the institutional review board of the First Medical Center of PLA General Hospital, and informed consent was waived due to the retrospective nature of

Received July 27, 2021; accepted after revision February 8, 2022.

From the Department of Medical Imaging (R.L., S.J.), Tianjin Huanhu Hospital, Tianjin, China; Department of Radiology (R.L., Y.W., J.-F. L., H.-F. X., Y.-L. W., L.M.), The First Medical Center of PLA General Hospital, Beijing, China; and Department of Medical Imaging (R.L., S.J.), Affiliated Huanhu Hospital of Nankai University, Tianjin, China.

Please address correspondence to Lin Ma, MD, PhD, Department of Radiology, The First Medical Center of PLA General Hospital, 28 Fuxing Rd, Beijing 100853, China; e-mail: cjr.malin@vip.163.com

Indicates article with online supplemental data.

<http://dx.doi.org/10.3174/ajnr.A7478>

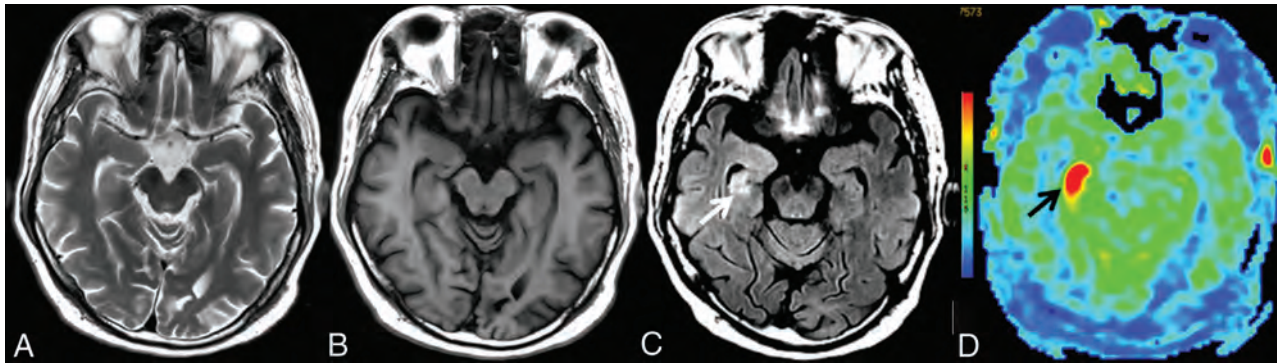


FIG 1. MR imaging of case 1. Findings on axial T2WI (A) and axial T1WI (B) are unremarkable. C, Axial T2 FLAIR reveals hyperintensity in the right hippocampus (white arrow). D, 3D pCASL demonstrates marked hyperperfusion in the corresponding region (black arrow).

the study. Patient information including clinical data, conventional MR imaging, and ASL findings was reviewed. There were 6 men and 3 women with ages ranging from 29 to 68 years (mean, 51.6 years). Meanwhile, 3D pCASL was acquired in 12 healthy individuals (6 men and 6 women; age range, 30–65 years; mean, 51.2 years) at the same time, considered as the control group.

The antibody panels were performed from serum and CSF in all patients by commercial laboratories. Autoantibodies were identified through a cell-based assay using an indirect immunofluorescence test (Euroimmun).

Imaging Acquisition

All MR imaging was performed on a 3T MR imaging system (Discovery 750; GE Healthcare). Conventional MR images included axial T2WI, axial T1WI, and axial and/or coronal T2 FLAIR with a section thickness/gap of 5.0/1.5 mm for the axial and coronal planes. Postcontrast T1WI was performed in 8 patients, including the axial, coronal, and sagittal planes (0.1 mmol/kg, Magnevist, Gd-DTPA; Bayer Schering Pharma).

The 3D pCASL sequence was a background-suppressed 3D spiral fast spin-echo technique with the following parameters: TR/TE = 4844/10.5 ms, postlabeling delay = 2025 ms, FOV = 24 × 24 cm, section thickness = 4.0 mm, number of sections = 36, and number of excitations = 3. In addition, a 3D T1-weighted fast-spoiled gradient recalled sequence, matched with 3D pCASL, was also performed after contrast injection. Follow-up 3D pCASL examinations were performed in 1 case.

Image Analysis

All MR images were visually assessed in a blinded manner. Two neuroradiologists with >5 years' experience reviewed the MR images. By empiric visual assessment, signal abnormalities in brain regions were reviewed on T2WI, T1WI, and T2 FLAIR, compared with the relatively normal brain. Similarly, by visual observations, the brain regions with hyperintense signal (compared with the relatively normal brain) were regarded as hyperperfusion regions, and the regions with hypointense signal (compared with the relatively normal brain) were regarded as hypoperfusion regions on 3D pCASL.

In addition to visual assessment, quantitative evaluation was also performed for each patient and healthy control. CBF values in healthy controls and lesions with AE were measured and compared. Three to 5 round ROIs (28–32 mm²) were manually

and carefully drawn in the lesion areas. The postcontrast 3D T1-fast-spoiled gradient recalled sequence, for accurate anatomic reference, was used for image matching with 3D pCASL. Then 3D T1 fast-spoiled gradient recalled and T2 FLAIR images were cross-referenced to determine the location of the lesion.¹³ For each patient, the mean CBF value was acquired and calculated from various brain areas. The mean, maximal CBF value within different lesions of the same brain regions was regarded as the final CBF value. To minimize interindividual differences in baseline CBF, we used relative CBF (rCBF), defined as the value of mean CBF for the ROI in the lesion or healthy controls divided by the mean CBF value for the ROI in the cerebellum.

Statistical Analysis

All CBF and rCBF values of lesions in patients with AE and 12 control subjects were presented as mean (SD). The Student *t* test was used for continuous variables with normal distribution; otherwise the Mann-Whitney *U* test was performed. A *P* value < .05 was considered statistically significant.

RESULTS

Clinical Data

Nine patients with AE were included in this study. Summary information is detailed in the Online Supplemental Data. The time from the onset of symptoms to admission in our hospital ranged from 18 to 90 days (mean, 49.33 days). All autoantibodies were detected in serum and CSF, including tests with positive findings for anti-N-methyl-D-aspartate receptor (NMDAR) (2 patients), anti-G-protein coupled receptors for gamma-aminobutyric acid (GABA_BR) (2 patients), and anti-leucine-rich, glioma inactivated 1 (LGI 1) (5 patients). Only 1 individual had a history of malignant tumor and pulmonary carcinoma-related anti-GABA_BR antibodies (case 6).

Empiric treatment was started when the diagnosis of possible AE was established, after excluding an infectious etiology while awaiting antibody test results. Treatment details are shown in the Online Supplemental Data.

Conventional MR Imaging and 3D pCASL Characteristics

The neuroimaging findings of the patients are summarized in the Online Supplemental Data. One patient had a lesion that was right-sided; 3, left-sided; and 5, bilateral, showing hypointensity or isointensity on T1WI (Figs 1B and 2B) and hyperintensity or isointensity

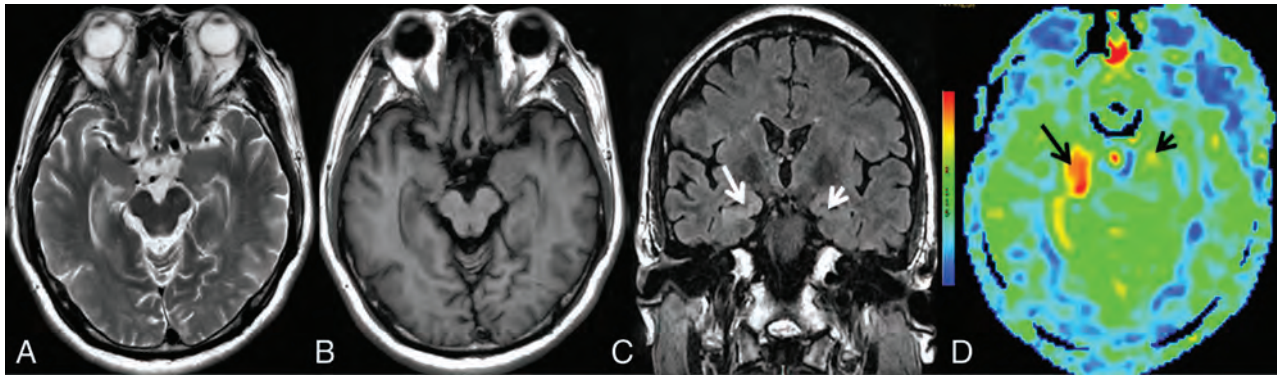


FIG 2. MR imaging of case 3. Findings on axial T2WI (A) and axial T1WI (B) are unremarkable. C, Coronal T2 FLAIR demonstrates hyperintensity in the right hippocampus (*white arrow*), whereas there are normal findings in the left hippocampus (*white arrowhead*). D, 3D pCASL depicts hyperperfusion in the corresponding regions on the FLAIR image, more obvious on the right side (*black arrows*).

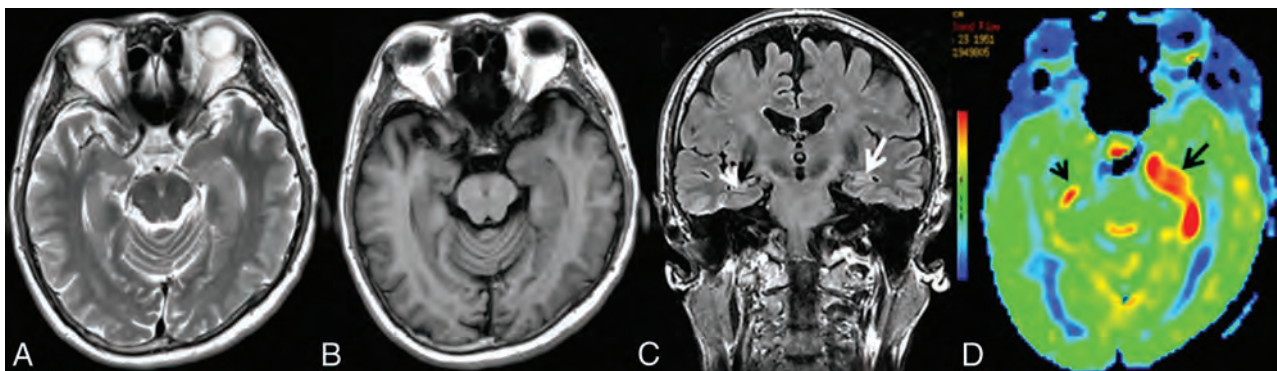


FIG 3. MR imaging of case 5. Findings on axial T2WI (A) and axial T1WI (B) are unremarkable. C, Coronal T2 FLAIR shows subtle hyperintensity with mild swelling in the left hippocampus (*white arrow*), whereas it shows normal findings in the right hippocampus (*white arrowhead*). D, Increased CBF in the bilateral hippocampi could be detected on 3D pCASL, the left (*black arrow*) greater than the right (*black arrowhead*).

on T2WI and T2 FLAIR (Figs 1C and 2C). Cases 3 and 5 were bilaterally involved, but abnormal signals were shown on only 1 side on T1WI, T2WI, and T2 FLAIR (Figs 2 and 3). All lesions showed no enhancement on postcontrast T1WI, except for mild patchy enhancement in case 6 (Online Supplemental Data).

On 3D pCASL, all patients were identified as having perfusion abnormalities, showing hyperperfusion patterns on visual inspection (Figs 1D and 2D). The CBF and rCBF values of the lesions with AE and control subjects are shown in the Online Supplemental Data. In 2 of these cases, hyperperfusion could be noted in the affected areas on 3D pCASL (Figs 2D and 3D), despite initial unremarkable or normal findings on T2 FLAIR (Figs 2C and 3C). Serial MR imaging and 3D pCASL scans were performed in a 47-year-old man, which revealed dynamic alterations in perfusion features in the involved area (Fig 4). The CBF and rCBF values in AE lesions were markedly higher than those in the control group (Fig 5).

DISCUSSION

This case series describes the signal changes on conventional MR imaging and perfusion alterations on 3D pCASL in a cohort of patients with AE. Our principal findings can be summarized as follows: 1) By visual assessment, patients with AE demonstrated elevated CBF in the affected area on 3D pCASL, though the affected area could be normal or present with slightly abnormal signals on

conventional MR imaging. 2) Quantitative analysis also indicated that the CBF and rCBF values of the lesions were significantly higher than those of control group. 3) 3D pCASL may potentially be applied in the evaluation of the therapeutic response in AE.

Encephalitis is a life-threatening disease associated with high morbidity and mortality throughout the world.^{2,14} In the past few years, increased awareness has been generated in relation to AE, and currently, the prevalence and incidence of AE are comparable with those of infectious encephalitis, and the detection of AE has been increasing with time.¹⁵ Early diagnosis is paramount for patients with encephalitis, thereby enabling clinicians to adopt earlier and more aggressive therapy and improve patients' outcomes. The diagnostic criteria vary depending on the types of encephalitis. For patients with AE, the initial diagnosis is based on the clinical presentation as well as antibody profiles and MR imaging. In addition, several clinical tools are now available and could be used by most clinicians. For example, a scoring system based on clinical features and the initial neurologic assessment of patients with epilepsy enables an earlier clinical diagnosis before the results of antibody tests are confirmed.¹⁶ Currently, the approach for a definite diagnosis of AE depends heavily on autoantibody detection.^{4,17} As a drawback, it is not readily available due to local conditions in many institutions, and it takes longer to obtain the results,^{4,18} thus leading to a delayed diagnosis and initiation of effective therapy.¹⁹

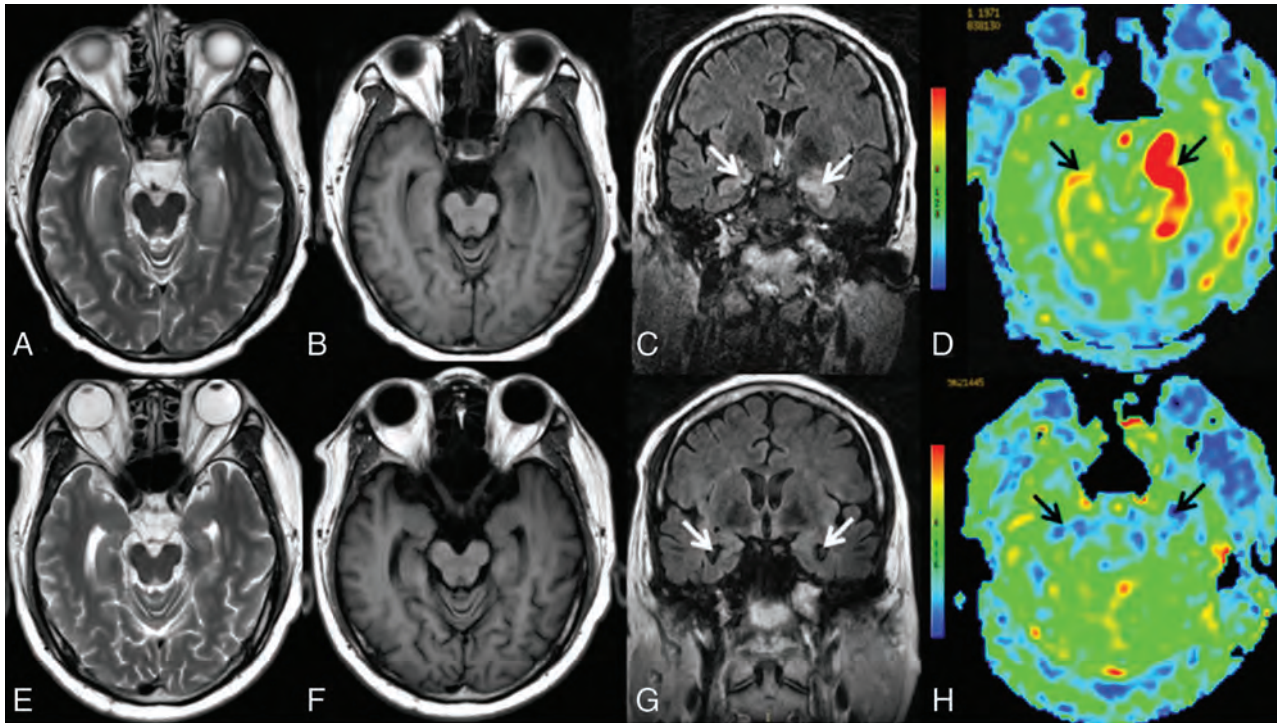


FIG 4. Serial MR imaging of case 7. On hospital day 3, the first conventional MR imaging examination findings were normal (not shown). On the second MR imaging check (26 days after admission), MR imaging shows swelling and hyperintensities on axial T2WI (A) and hypointensities on axial T1WI (B) in the bilateral hippocampi. C, Coronal T2 FLAIR shows hyperintensities in the bilateral hippocampi (white arrows). D, 3D pCASL reveals hyperperfusion in the bilateral medial temporal lobes (black arrows), the left greater than the right. On the third MR imaging check (96 days after admission), including axial T2WI (E), axial T1WI (F), and coronal T2 FLAIR (G), complete resolution of the inflammation in the bilateral medial temporal areas is seen, with enlargement of the bilateral temporal horns (white arrows), and 3D pCASL (H) shows decreased perfusion in the bilateral hippocampi (black arrows). The patient's condition markedly improved with the administration of high-dose glucocorticoids, intravenous immunoglobulin, and plasma exchange (3 times).

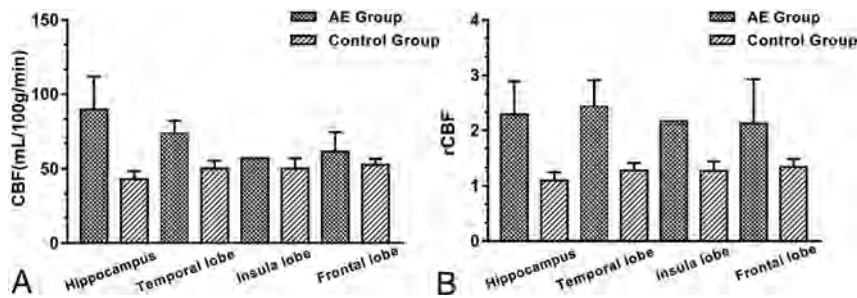


FIG 5. Bar chart with the SD for the CBF (A) and rCBF (B) values of the lesions in the AE and control groups. The unit of CBF was mL/100 g/min.

Conventional MR imaging plays a major role in the early diagnosis of AE and might be mandatorily performed when CT findings are negative in patients with serious neurologic disorders. However, the brain MR imaging has been reported to have normal findings in approximately 50%–60% of patients with anti-NMDAR encephalitis, 30%–40% with anti-LGI 1 encephalitis, and 30%–40% with anti-GABAb receptor encephalitis.^{20–22} In addition, different forms of AE could present with different patterns of MR imaging abnormalities. In our study, all patients had elevated CBF on 3D pCASL, even when some of them presented with mild abnormal findings on conventional MR imaging. Among them, unilateral abnormal signals were revealed on conventional MR imaging, but bilateral

involvement could be detected on 3D pCASL in 2 patients, suggesting that 3D pCASL is more sensitive than conventional MR imaging in the early detection of AE. Additionally, 3D pCASL in 1 case revealed dynamic alterations in perfusion features (CBF reduction with time), indicating its potential role in the assessment of therapeutic effects in AE.

Perfusion imaging studies in patients with AE in the literature are summarized in the Online Supplemental Data, with only a few cases using the ASL technique (2D imaging). 3D pCASL,

which potentially combines the advantages of both pulsed arterial spin-labeling and continuous arterial spin-labeling, was performed in this study, allowing 3D fast acquisitions and reduction of magnetic susceptibility artifacts, especially in those brain areas (eg, medial temporal lobes) near the skull base.^{23,24}

The exact pathophysiologic mechanism leading to perfusion alteration on 3D pCASL remains to be elucidated, and the candidate mechanisms will need to be evaluated in future studies. We speculated that 1 possible reason for increased regional CBF is an inflammatory process due to an antigen-antibody-mediated immune response, causing the blood vessels to expand.²⁵ Another reason could be the loss of vascular autoregulatory

mechanisms due to autonomic instability.⁶ In addition, some patients with AE may experience central hypoventilation that could lead to hypercarbia accounting for increased CBF, which usually presented with global cerebral hyperperfusion.²⁶ It is unclear whether the elevated CBF is related solely to the autoimmune processes or whether all the factors account for the increased CBF. Further study is needed to test this hypothesis.

Hyperperfusion on 3D pCASL can be seen in various conditions, including tumors, inflammation or infection, MELAS, seizure activity, and so forth.²⁶ MELAS, herpes simplex encephalitis, as well as high-grade glioma masquerading as AE²⁷ present with hyperperfusion on 3D pCASL, but differentiation can be made by combining the clinical manifestation, history, lesion location, and so forth. Seizure is a common clinical manifestation in AE, and seizure activity can also cause hyperperfusion, but its perfusion alterations were linked to the timing of ASL data acquisition, with patients usually presenting with hyperperfusion during the ictal and postictal periods and hypoperfusion in the interictal phase.^{24,28,29} Unfortunately, we were unable to verify this finding as previously reported³⁰ because the patients who had clinical seizures were imaged during the interictal phase in this study. Because no patients had epileptic seizures within 24 hours before the examination, we can, therefore, infer that increased ASL perfusion is caused by the underlying inflammatory process rather than being secondary to seizure activity. Furthermore, 3D pCASL can help exclude some AE-mimicking diagnoses with hypoperfusion, such as acute ischemic stroke and diffuse low-grade gliomas. In addition, AE-mimicking sporadic Creutzfeldt-Jakob disease has been reported,^{31,32} but Creutzfeldt-Jakob disease showed hypoperfusion on 3D pCASL.³³ As stated above, we think that 3D pCASL has clinical utility in differentiating AE from its mimics.

ASL and PET/CT, as 2 different imaging modalities (perfusion and metabolism), are closely linked in neurologic disorders due to the close coupling of perfusion and metabolism in the brain.³⁴ Dinoto et al¹² reported that ASL and PET/CT findings are strongly concordant in limbic encephalitis. This concordance is particularly intriguing because ASL, without contrast medium and radiation, may be used to evaluate perfusion status and subsequent therapeutic effects in patients with AE. Two main metabolic patterns of abnormalities (mixed hyper-/hypometabolic and neurodegenerative-like) on PET/CT have been reported,³⁵ and different “paradigms” of encephalitis (mainly limbic versus NMDAR) may have different PET/CT findings.¹² Additionally, studies have shown that metabolic patterns on PET/CT, to a certain extent, are associated with different autoantibody subtypes, implying that different pathophysiologic mechanisms may exist.²⁵ In this study, we found that all cases of AE showed patterns of hyperperfusion in the affected area. Further studies are needed to investigate the correlation between perfusion and metabolism in AE subtypes.

In clinical practice, the use of 3D pCASL seems to be feasible and reasonable in improving the sensitivity of lesion detection, especially in patients with suspected AE with normal conventional MR imaging findings. 3D pCASL could reveal abnormalities earlier than conventional MR imaging in some patients with AE and provide new insight into exploring the pathophysiologic mechanism of AE.^{6,36,37} Therefore, we suggest that 3D pCASL be

added to the clinical work-up for patients with suspected AE, and its efficacy should be further tested in clinical practice.

Several limitations are noteworthy. First, this was a retrospective, cross-sectional study, and the sample size was relatively small. Second, 3D pCASL was performed for imaging diagnosis and follow-up in only 1 patient. Larger cohort and longitudinal data are needed to validate the results. Third, many subtypes of AE are frequently accompanied by seizures that can affect CBF, and this effect cannot be completely excluded theoretically.

CONCLUSIONS

Conventional MR imaging remains the best option, while 3D pCASL may have added value in the early diagnosis of AE, and 3D pCASL may also be used in the assessment of therapeutic effects. Clinically, 3D pCASL may be recommended in patients with highly suspected AE, especially in those with normal or unremarkable findings on conventional MR imaging. Further studies and longitudinal data are needed to corroborate whether and to what extent 3D pCASL can improve the diagnostic work-up in AE compared with conventional MR imaging.

Disclosure forms provided by the authors are available with the full text and PDF of this article at www.ajnr.org.

REFERENCES

1. Bost C, Pascual O, Honnorat J. **Autoimmune encephalitis in psychiatric institutions: current perspectives.** *Neuropsychiatr Dis Treat* 2016;12:2775–87 CrossRef Medline
2. Vollmer TL, McCarthy M. **Autoimmune encephalitis: a more treatable tragedy if diagnosed early.** *Neurology* 2016;86:1655–56 CrossRef Medline
3. Abboud H, Probasco JC, Irani S, et al; Autoimmune Encephalitis Alliance Clinicians Network. **Autoimmune encephalitis: proposed best practice recommendations for diagnosis and acute management.** *J Neurol Neurosurg Psychiatry* 2021;92:757–68 CrossRef Medline
4. Graus F, Titulaer MJ, Balu R, et al. **A clinical approach to diagnosis of autoimmune encephalitis.** *Lancet Neurol* 2016;15:391–404 CrossRef Medline
5. Kalman B. **Autoimmune encephalitides: a broadening field of treatable conditions.** *Neurologist* 2017;22:1–13 CrossRef Medline
6. Sachs JR, Zapadka ME, Popli GS, et al. **Arterial spin labeling perfusion imaging demonstrates cerebral hyperperfusion in anti-NMDAR encephalitis.** *Radiol Case Rep* 2017;12:833–37 CrossRef Medline
7. Dalmau J, Lancaster E, Martinez-Hernandez E, et al. **Clinical experience and laboratory investigations in patients with anti-NMDAR encephalitis.** *Lancet Neurol* 2011;10:63–74 CrossRef Medline
8. Vallabhaneni D, Naveed MA, Mangla R, et al. **Perfusion imaging in autoimmune encephalitis.** *Case Rep Radiol* 2018;2018:3538645 CrossRef Medline
9. Llorens V, Gabilondo I, Gomez-Esteban JC, et al. **Abnormal multifocal cerebral blood flow on Tc-99m HMPAO SPECT in a patient with anti-NMDA-receptor encephalitis.** *J Neurol* 2010;257:1568–69 CrossRef Medline
10. Suárez JP, Domínguez ML, Gómez MA, et al. **Brain perfusion SPECT with ^{99m}Tc-HMPAO in the diagnosis and follow-up of patients with anti-NMDA receptor encephalitis** [in English, Spanish]. *Neurología (Engl Ed)* 2018;33:622–23 CrossRef Medline
11. Bordonne M, Chawki MB, Doyen M, et al. **Brain ¹⁸F-FDG PET for the diagnosis of autoimmune encephalitis: a systematic review and a meta-analysis.** *Eur J Nucl Med Mol Imaging* 2021;48:3847–58 CrossRef Medline

12. Dinoto A, Cheli M, Ajcöević M, et al. **ASL MRI and ¹⁸F-FDG-PET in autoimmune limbic encephalitis: clues from two paradigmatic cases.** *Neurol Sci* 2021;42:3423–25 CrossRef Medline
13. Li R, Shi PA, Liu TF, et al. **Role of 3D pseudocontinuous arterial spin-labeling perfusion in the diagnosis and follow-up in patients with herpes simplex encephalitis.** *AJNR Am J Neuroradiol* 2019;40:1901–07 CrossRef Medline
14. Solomon TH, Hart IJ, Beeching NJ. **Viral encephalitis: a clinician's guide.** *Pract Neurol* 2007;7:288–305
15. Dubey D, Pittock SJ, Kelly CR, et al. **Autoimmune encephalitis epidemiology and a comparison to infectious encephalitis.** *Ann Neurol* 2018;83:166–77 CrossRef Medline
16. Dubey D, Singh J, Britton JW, et al. **Predictive models in the diagnosis and treatment of autoimmune epilepsy.** *Epilepsia* 2017;58:1181–89 CrossRef Medline
17. Cyril AS, Nair SS, Mathai A, et al. **Autoimmune encephalitis: clinical diagnosis versus antibody confirmation.** *Ann Indian Acad Neurol* 2015;18:408–11 CrossRef Medline
18. Harutyunyan G, Hauer L, Dunser MW, et al. **Autoimmune encephalitis at the neurological intensive care unit: etiologies, reasons for admission and survival.** *Neurocrit Care* 2017;27:82–89 CrossRef Medline
19. Morbelli S, Arbizu J, Booij J, et al; European Association of Nuclear Medicine (EANM) and of the Society of Nuclear Medicine and Molecular Imaging (SNMMI). **The need of standardization and of large clinical studies in an emerging indication of [¹⁸F]FDG PET: the autoimmune encephalitis.** *Eur J Nucl Med Mol Imaging* 2017;44:353–57 CrossRef Medline
20. Armangue T, Leypoldt F, Dalmau J. **Autoimmune encephalitis as differential diagnosis of infectious encephalitis.** *Curr Opin Neurol* 2014;27:361–68 CrossRef Medline
21. Chow FC, Glaser CA, Sheriff H, et al. **Use of clinical and neuroimaging characteristics to distinguish temporal lobe herpes simplex encephalitis from its mimics.** *Clin Infect Dis* 2015;60:1377–83 CrossRef Medline
22. Celicanin M, Blaabjerg M, Maersk-Møller C, et al. **Autoimmune encephalitis associated with voltage-gated potassium channels-complex and leucine-rich glioma-inactivated 1 antibodies: a national cohort study.** *Eur J Neurol* 2017;24:999–1005 CrossRef Medline
23. Deibler AR, Pollock JM, Kraft RA, et al. **Arterial spin-labeling in routine clinical practice, Part 1: technique and artifacts.** *AJNR Am J Neuroradiol* 2008;29:1228–34 CrossRef Medline
24. Petcharunpaisan S, Ramalho J, Castillo M. **Arterial spin-labeling in neuroimaging.** *World J Radiol* 2010;2:384–98 CrossRef Medline
25. Baumgartner A, Rauer S, Mader I, et al. **Cerebral FDG-PET and MRI findings in autoimmune limbic encephalitis: correlation with autoantibody types.** *J Neurol* 2013;260:2744–53 CrossRef Medline
26. Deibler AR, Pollock JM, Kraft RA, et al. **Arterial spin-labeling in routine clinical practice, Part 3: hyperperfusion patterns.** *AJNR Am J Neuroradiol* 2008;29:1428–35 CrossRef Medline
27. Vogrig A, Joubert B, Ducray F, et al. **Glioblastoma as differential diagnosis of autoimmune encephalitis.** *J Neurol* 2018;265:669–77 CrossRef Medline
28. Gaxiola-Valdez I, Singh S, Perera T, et al. **Seizure onset zone localization using postictal hypoperfusion detected by arterial spin labelling MRI.** *Brain* 2017;140:2895–911 CrossRef Medline
29. Lee SM, Kwon S, Lee YJ. **Diagnostic usefulness of arterial spin labeling in MR negative children with new onset seizures.** *Seizure* 2019;65:151–58 CrossRef Medline
30. Espinosa-Jovel C, Toledano R, García-Morales I, et al. **Serial arterial spin labeling MRI in autonomic status epilepticus due to anti-LGI1 encephalitis.** *Neurology* 2016;87:443–44 CrossRef Medline
31. Chen Y, Xing XW, Zhang JT, et al. **Autoimmune encephalitis mimicking sporadic Creutzfeldt-Jakob disease: a retrospective study.** *J Neuroimmunol* 2016;295–296:1–8 CrossRef Medline
32. Maat P, de Beukelaar JW, Jansen C, et al. **Pathologically confirmed autoimmune encephalitis in suspected Creutzfeldt-Jakob disease.** *Neurol Neuroimmunol Neuroinflamm* 2015;2:e178 CrossRef Medline
33. Yuan J, Wang S, Hu W. **Combined findings of FDG-PET and arterial spin labeling in sporadic Creutzfeldt-Jakob disease.** *Prion* 2018;12:310–14 CrossRef Medline
34. Haller S, Zaharchuk G, Thomas DL, et al. **Arterial spin-labeling perfusion of the brain: emerging clinical applications.** *Radiology* 2016;281:337–56 CrossRef Medline
35. Fisher RE, Patel NR, Lai EC, et al. **Two different ¹⁸F-FDG brain PET metabolic patterns in autoimmune limbic encephalitis.** *Clin Nucl Med* 2012;37:e213–18 CrossRef Medline
36. Lapucci C, Boffa G, Massa F, et al. **Could arterial spin-labelling perfusion imaging uncover the invisible in N-methyl-D-aspartate receptor encephalitis?** *Eur J Neurol* 2019;26:e86–87 CrossRef Medline
37. Li X, Yuan J, Liu L, et al. **Antibody-LGI 1 autoimmune encephalitis manifesting as rapidly progressive dementia and hyponatremia: a case report and literature review.** *BMC Neurol* 2019;19:19 CrossRef Medline

Normative Data for Brainstem Structures, the Midbrain-to-Pons Ratio, and the Magnetic Resonance Parkinsonism Index

 S.T. Ruiz,  R.V. Bakklund,  A.K. Håberg, and  E.M. Berntsen



ABSTRACT

BACKGROUND AND PURPOSE: Imaging biomarkers derived from different brainstem structures are suggested to differentiate among parkinsonian disorders, but clinical implementation requires normative data. The main objective was to establish high-quality, sex-specific data for relevant brainstem structures derived from MR imaging in healthy subjects from the general population in their sixth and seventh decades of life.

MATERIALS AND METHODS: 3D TIWI acquired on the same 1.5T scanner of 996 individuals (527 women) between 50 and 66 years of age from a prospective population study was used. The area of the midbrain and pons and the widths of the middle cerebellar peduncles and superior cerebellar peduncles were measured, from which the midbrain-to-pons ratio and Magnetic Resonance Parkinsonism Index [MRPI = (Pons Area / Midbrain Area) × (Middle Cerebellar Peduncles / Superior Cerebellar Peduncles)] were calculated. Sex differences in brainstem measures and correlations to age, height, weight, and body mass index were investigated.

RESULTS: Inter- and intrareliability for measuring the different brainstem structures showed good-to-excellent reliability (intraclass correlation coefficient = 0.785–0.988). There were significant sex differences for the pons area, width of the middle cerebellar peduncles and superior cerebellar peduncles, midbrain-to-pons ratio, and MRPI (all, $P < .001$; Cohen D = 0.44–0.98), but not for the midbrain area ($P = .985$). There were significant very weak-to-weak correlations between several of the brainstem measures and age, height, weight, and body mass index in both sexes. However, no systematic difference in distribution caused by these variables was found, and because age had the highest and most consistent correlations, age-/sex-specific percentiles for the brainstem measures were created.

CONCLUSIONS: We present high-quality, sex-specific data and age-/sex-specific percentiles for the mentioned brainstem measures. These normative data can be implemented in the neuroradiologic work-up of patients with suspected brainstem atrophy to avoid the risk of misdiagnosis.

ABBREVIATIONS: BMI = body mass index; MCP = middle cerebellar peduncle; M/P = midbrain-to-pons; MRPI = Magnetic Resonance Parkinsonism Index; MSA = multiple system atrophy; PSP = progressive supranuclear palsy; PD = Parkinson disease; SCP = superior cerebellar peduncle

Distinguishing the different parkinsonian disorders, such as progressive supranuclear palsy (PSP), multiple system

atrophy (MSA) of the parkinsonian type, and Parkinson disease (PD) can be difficult due to their overlapping clinical presentations, especially in the early stages when the clinical presentations are ambiguous.¹⁻⁷ Differentiating these disorders is, however, highly relevant because PSP progresses more rapidly than PD,⁸ and neither PSP nor MSA responds well to levodopa therapy in contrast to PD.^{8,9} Reliable neuroradiologic biomarkers derived from standard MR imaging scans analyzed with conventional radiologic tools can be important for an early and correct diagnosis of these parkinsonian disorders.^{1-3,7,10-12} However, for such biomarkers to be reliable, they must be accurate and have high external validity, preferably based on normative data.

Neuroimaging used to identify specific patterns of atrophy is included in the diagnostic criteria for some parkinsonian disorders.^{9,13} In PSP, atrophy of the superior cerebellar peduncle

Received July 29, 2021; accepted after revision February 11, 2022.

From the Departments of Circulation and Medical Imaging (S.T.R., R.V.B., E.M.B.), Faculty of Medicine and Health Sciences, and Neuromedicine and Movement Sciences (A.K.H.), Norwegian University of Science and Technology, Trondheim, Norway; and Department of Radiology and Nuclear Medicine (A.K.H., E.M.B.), St. Olavs University Hospital, Trondheim, Norway.

S.T. Ruiz and R.V. Bakklund contributed equally to the work and share the first authorship.

Please address correspondence to Erik M. Berntsen, MD, PhD, EDiNR, EDiPNR, Department of Circulation and Medical Imaging, Faculty of Medicine and Health Sciences, Norwegian University of Science and Technology, Mailbox 8905, 7491 Trondheim, Norway; e-mail: erik.berntsen@ntnu.no; @BerntsenErikM

 Indicates open access to non-subscribers at www.ajnr.org

 Indicates article with online supplemental data.

<http://dx.doi.org/10.3174/ajnr.A7485>

(SCP) and midbrain is characteristic, the latter showing the well-known Hummingbird sign.^{1-3,5,12,14-17} In MSA, atrophy of the putamen is seen, and in the cerebellar variant of the disease, atrophy of the middle cerebellar peduncle (MCP) is typical.^{3,9,18} Both qualitative and quantitative analysis of the degree of midbrain atrophy, the midbrain-to-pons ratio (M/P ratio), and the Magnetic Resonance Parkinsonism Index [MRPI = (Pons Area / Midbrain Area) × (MCP / SCP)] have been used to investigate and distinguish patients with PSP, MSA, and PD from one another and from healthy controls.^{1-7,10,12,16-25} These studies demonstrate the potential of using easily accessible quantitative brainstem biomarkers to differentiate among parkinsonian disorders and between healthy controls and patients.

Nevertheless, what is missing for effective clinical translation of these quantitative brainstem biomarkers to neuroradiologic practice is sex-specific normative data from a large number of healthy subjects from the general population in the appropriate decades of life when parkinsonian disorders first present. The largest study to date consists of 92 healthy controls, mainly in their 60s, not separated by sex and not otherwise specified.²⁵ The largest study to date providing data separated by sex consists of 85 healthy individuals (42 women) between 50 and 80 years of age who were recruited as part of 3 different studies and who all had normal neurologic examination findings and no history of neurologic diseases.²⁶ The latter study found significant sex differences only for the area of the pons and not for the M/P ratio or the MRPI, concluding that there is no need to consider age or sex when using these biomarkers to differentiate parkinsonian disorders. There is, however, rising awareness of sex differences in the brain and brain disorders, justifying further investigation into potential sex differences in neuroimaging biomarkers.^{27,28}

The main goal of our study was to establish high-quality, sex-specific normative data for the midbrain and pons area, the width of the MCPs and SCPs, the M/P ratio, and the MRPI for use in clinical neuroradiology, facilitating a better diagnostic work-up of parkinsonian diseases. We also examined whether these brainstem measures were correlated to age, height, weight, and body mass index (BMI), which are reported to be correlated to brain size.^{29,30}

MATERIALS AND METHODS

Population

Participants in our study are from the HUNT MRI study,³¹ which is a part of the geographically defined prospective population study Nord-Trøndelag Health Study (HUNT),³² in which MR imaging was performed between July 2007 and December 2009. Inclusion criteria were age between 50 and 65 years at the time of inclusion; participation in HUNT1 (1984–86), HUNT2 (1995–1997), and HUNT3 (2006–2008); and residency within 45 minutes from Levanger Hospital where scanning was performed. The only exclusion criteria were standard MR imaging contraindications. Seventy-three percent of the invited participants accepted and have been shown to be representative of the whole population.^{31,33} Health information for each participant was obtained from questionnaires, blood samples, and a limited clinical examination. Participants with intracranial findings on MR imaging were contacted and underwent a clinical interview.³¹ The present study excluded all subjects with known neurodegenerative disease based

on their hospital records and MR imaging findings that could potentially confound our results. One subject with PSP, 3 with MS, 3 with pontine lacunar infarcts, 1 with a basilar dolichoectasia affecting the pons, 1 due to aberrant morphology, and 1 due to movement artifacts were excluded. In total, 996 subjects (99% of the original 1006 from HUNT MRI) were included in this study. The Regional Committee for Medical and Health Research Ethics in Central Norway has approved both the HUNT MRI study and this study (2011/456 and 2018/2231).

Measurements

Subjects' height and weight were measured in centimeters and kilograms to the first decimal using standardized methods in the HUNT3 study. Measurements of the different brainstem structures for this study were performed using the PACS software on aligned and saved images from a non-contrast-enhanced sagittal 3D T1WI IR-FSPGR volume (TR = 10.2 ms, TE = 4.1 ms, flip angle = 10°, section thickness = 1.2 mm, in-plane resolution = 0.975 × 0.975 mm²) acquired on the same 1.5T scanner (Signa HDx; GE Healthcare) with an 8-channel head coil. The first authors performed measurements on 496 and 500 subjects each, after receiving extensive training by a board-certified neuroradiologist (E.M.B.), who also was consulted and assisted in difficult cases. The resulting measurements were used to calculate the M/P ratio and the MRPI.

Measurements of the midbrain and pons area were performed on midsagittal images according to the method of Oba et al.¹ The midsagittal plane was obtained and saved to the PACS using the MPR module of the software in which the center of the interpeduncular cistern was aligned with the center of the aqueduct in the transverse plane and along the falx in the coronal plane. After magnifying the saved midsagittal image 4 times, we drew a straight line between the superior pontine notch and the inferior point of the quadrigeminal plate (line A, Figure). Due to the ambiguous caudal outline of the quadrigeminal plate, parasagittal views were inspected before defining the exact location of this inferior point. A parallel line to line A was placed at the inferior pontine notch, thus defining the lower border of the pons (line B, Figure). Once these borders were defined, the raters manually traced the midbrain area ventral to the aqueduct above line A, while the area of the pons was manually traced ventral to the fourth ventricle and between lines A and B (Figure). The software automatically calculated the areas traced.

The widths of the MCPs were measured according to the method of Quattrone et al.² The previously defined midsagittal plane was used as a starting point to identify the parasagittal images in which the left and right MCPs were clearly surrounded by peripeduncular CSF and visible between the pons and cerebellum (Figure). The widths of the MCPs were then measured by drawing a straight line between the superior and inferior borders of the MCPs. The mean width of the 2 MCPs was calculated and used for further analysis.

The widths of the SCPs were also measured according to the method of Quattrone et al.² In the previously defined midsagittal plane, the axis defining the coronal plane was placed parallel to the rhomboid fossa, creating an oblique-coronal plane. Moving posteriorly in this oblique-coronal plane, we defined the first section where the inferior colliculi and SCPs were clearly separated

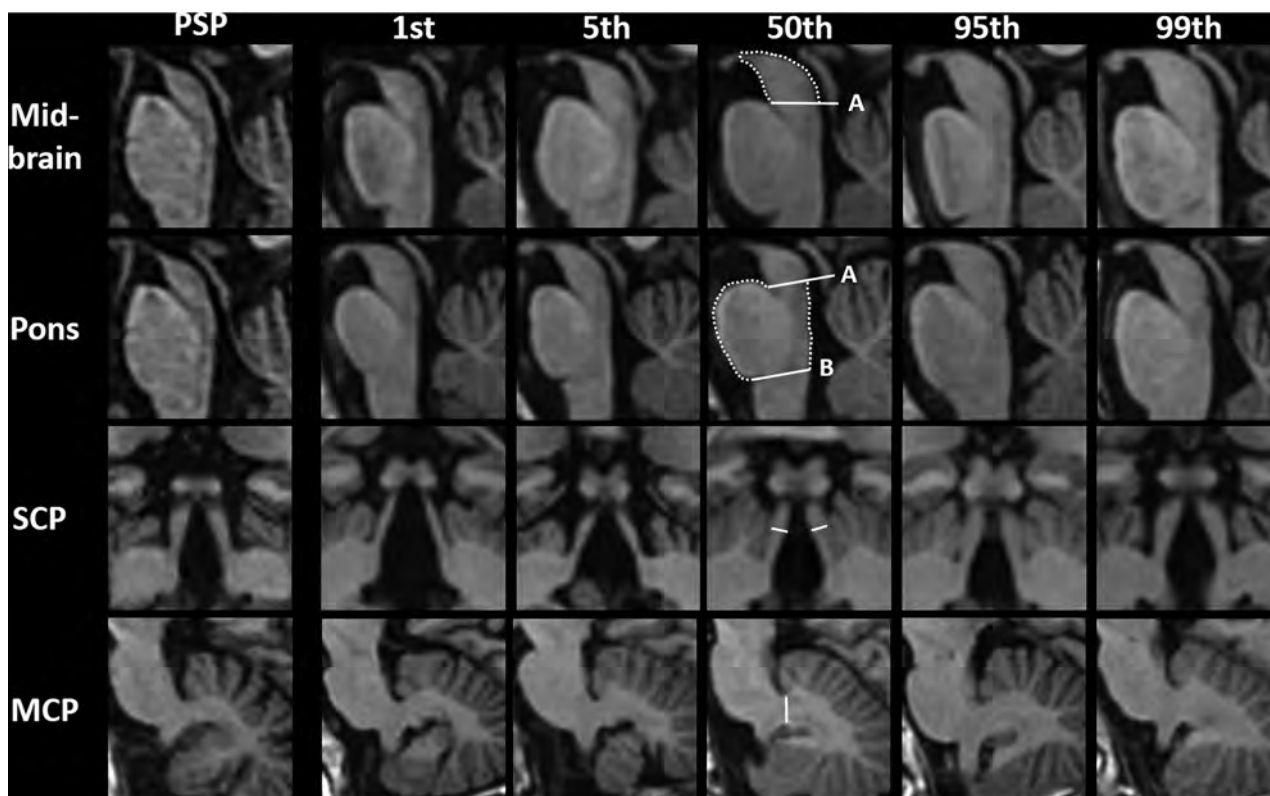


FIGURE. T1WI showing the 1st, 5th, 50th, 95th, and 99th percentiles for the midbrain and pons area, MCP and SCP widths for men as a whole group, as well as the same structures for the one male patient with verified PSP. Measurements of these structures are shown for the 50th percentile, which are also presented in high resolution in the Online Supplemental Data. The 50th percentile equals the mean. The line A is drawn between the superior pontine notch and the inferior point of the quadrigeminal plate, while line B is parallel to line A starting at the inferior pontine notch.

by CSF as the starting section and saved it. The SCPs were measured at their midpoint as the distance between the medial and lateral edges (Figure). Measurements were performed on both the left and right SCPs on the starting section and in the 2 following sections, resulting in a total of 3 saved images and 6 measurements. The mean value of these 6 measurements was calculated and used for further analysis.

Remeasurement

To investigate interrater reliability, each rater performed a second set of measurements on 50 random subjects from the other rater's pool of subjects. To investigate intrarater reliability, each rater performed a second set of measurements on 50 random subjects from their own pool of subjects. Remeasurement for inter-/intrarater reliability was performed twice. The first time, the 2 raters realigned and saved the new midsagittal, parasagittal, and oblique-coronal images on which remeasurement was performed. The second time, the remeasurement was performed on the original saved midsagittal, parasagittal, and oblique-coronal images where the original measurements had been performed. The remeasurement for inter-/intrarater reliability analysis was commenced and completed 4 weeks after the original measurements were finalized.

Statistical Analysis

SPSS statistical and computing software (IBM) was used for statistical analysis. The mean (SD) and range for the midbrain and pons areas, the width of the MCPs and SCPs, the M/P ratio, and the

MRPI were calculated for all 996 subjects and for each sex separately. A statistically significant difference of the mean of the brainstem measurements between the sexes was defined as $P < .05$ with a 2-tailed independent-samples t test. The effect size of significant sex differences was investigated using the Cohen D, in which values <0.50 were interpreted as small; values between 0.50 and 0.80, as medium; and values >0.80 , as large.³⁴ Correlations among age, sex, height, weight or BMI, and brainstem measurements were investigated using the Pearson correlation, and $P < .05$ was considered significant. A correlation coefficient of 0.19 was considered as very weak; 0.20–0.39, weak; 0.40–0.59, moderate; 0.60–0.79, strong; and 0.8–1.0, very strong.³⁵ Inter-/intrarater reliability was calculated using intraclass correlation coefficients using a 2-way mixed-effects model with absolute agreement and single measures. Values between 0.75 and 0.90 were interpreted as good, and values >0.90 were interpreted as excellent.³⁶

RESULTS

In total, 527 women (mean age, 58.7 [SD, 4.3] years; mean height, 165.2 [SD, 5.8] cm; mean weight, 72.6 [SD, 11.8] kg; mean BMI, 26.6 (SD, 4.1) kg/m²) and 469 men (mean age, 59.2 [SD, 4.2] years; mean height, 178.0 [SD, 6.1] cm; mean weight, 86.8 [SD, 11.1] kg; mean BMI, 27.4 [SD, 3.1] kg/m²) were included in the present study. The descriptives for the brainstem measures are presented in Table 1. There were statistically significant differences between the sexes for the pons area with a large effect size,

Table 1: Descriptives for all subjects and for each sex^a

	All Subjects (n = 996)	Women (n = 527)	Men (n = 469)	P Value ^b	Cohen D
Age (yr)	59.0 (SD, 4.2) (50.5–66.8)	58.7 (SD, 4.3) (50.5–66.3)	59.2 (SD, 4.2) (51.0–66.8)	<i>P</i> = .103	
Height ^c (cm)	171.2 (SD, 8.7) (148.4–196.7)	165.2 (SD, 5.8) (148.4–186.7)	178.0 (SD, 6.1) (161.9–196.7)	<i>P</i> < .001	2.17
Weight ^c (kg)	79.3 (SD, 13.5) (47.2–127.0)	72.6 (SD, 11.8) (47.2–119.6)	86.8 (SD, 11.1) (59.8–127.0)	<i>P</i> < .001	1.24
BMI ^c	27.0 (SD, 3.7) (18.3–41.7)	26.6 (SD, 4.1) (18.3–41.7)	27.4 (SD, 3.1) (19.6–40.1)	<i>P</i> < .001	0.21
Midbrain (mm ²)	136.7 (SD, 20.5) (76.0–222.4)	136.7 (SD, 19.7) (81.9–211.9)	136.7 (SD, 21.4) (76.0–211.9)	<i>P</i> = .985	
Pons (mm ²)	542.2 (SD, 57.8) (386.5–812.5)	518.2 (SD, 47.8) (386.5–695.7)	569.1 (SD, 56.2) (416.5–812.5)	<i>P</i> < .001	0.98
MCP (mm)	9.4 (SD, 0.8) (5.3–13.0)	9.1 (SD, 0.8) (5.3–11.5)	9.7 (SD, 0.8) (6.8–13.0)	<i>P</i> < .001	0.76
SCP (mm)	3.8 (SD, 0.5) (2.5–5.5)	3.7 (SD, 0.5) (2.6–5.2)	3.9 (SD, 0.5) (2.5–5.5)	<i>P</i> < .001	0.44
M/P ratio	0.25 (SD, 0.04) (0.14–0.41)	0.26 (SD, 0.04) (0.15–0.41)	0.24 (SD, 0.03) (0.14–0.36)	<i>P</i> < .001	0.67
MRPI	10.0 (SD, 1.9) (5.5–18.1)	9.5 (SD, 1.7) (5.5–15.6)	10.6 (SD, 2.0) (6.1–18.1)	<i>P</i> < .001	0.59

^a Data are mean (SD) and range.

^b Women versus men.

^c Missing data for 2 women and 1 man.

the width of the MCP with a medium effect size, the SCP with a small effect size, as well as the M/P ratio and MRPI both with moderate effects sizes (all, *P* < .001; Cohen *D* = 0.44–0.98), but none for the midbrain area. Scatterplots for each measured brainstem structure by age, height, weight, and BMI are presented for each sex in the Online Supplemental Data.

Correlations between the brainstem measurements and age, height, weight, and BMI were investigated in each sex separately. The significant correlations were as follows: For women, there were weak age-related correlations for the midbrain area and the M/P ratio [both *r*(525) = –0.28 (*P* < .001)] and very weak correlations for the width of the MCP [*r*(525) = –0.18 (*P* < .001)] and the MRPI [*r*(525) = 0.15 (*P* < .001)]. Height was weakly correlated to the pons area [*r*(523) = 0.20 (*P* < .001)] and very weakly to the width of the MCP [*r*(523) = 0.12 (*P* = .009)] and the midbrain area [*r*(523) = 0.11 (*P* = .014)]. Weight was very weakly correlated to the pons area [*r*(523) = 0.09 (*P* = .049)] and the M/P ratio [*r*(523) = –0.11 (*P* = .009)]. BMI was very weakly correlated to the midbrain area [*r*(523) = –0.10 (*P* = .027)] and the M/P ratio [*r*(523) = –0.11 (*P* = .013)]. For men, there were weak age-related correlations for the midbrain area [*r*(467) = –0.23 (*P* < .001)] and the M/P ratio [*r*(467) = –0.25 (*P* < .001)] and a very weak correlation for MRPI [*r*(467) = 0.16 (*P* < .001)]. Height was weakly correlated to the midbrain area [*r*(466) = 0.22 (*P* < .001)] and the pons area [*r*(466) = 0.21 (*P* < .001)] and very weakly correlated to the width of the SCP [*r*(466) = 0.11 (*P* = .018)], the M/P ratio [*r*(466) = 0.09 (*P* = .043)], and the MRPI [*r*(466) = –0.12 (*P* = .008)]. Weight was very weakly correlated to the pons area [*r*(466) = 0.10 (*P* = .041)]. BMI was very weakly correlated to the midbrain area and the M/P ratio [both *r*(466) = –0.14 (*P* = .002)] as well as the MRPI [*r*(466) = 0.13 (*P* = .006)].

The significant correlations were in the same direction and magnitude for both sexes, and no systematic difference between the sexes caused by these variables could be seen in the scatterplots.

Age was the variable with the highest and most consistent correlation with the brainstem measures. The normative percentile data are reported for 5-year age groups for men and women separately (Table 2).

Intraclass correlation coefficient values for both inter-/intra-rater reliability showed good-to-excellent reliability for all measurements based on the limits defined by Koo and Li.³⁶ When remeasurements were based on realigned and saved images, the intraclass correlation coefficient values ranged from 0.785 to 0.978. When remeasurements were based on the original saved images, intraclass correlation coefficient values ranged from 0.891 to 0.988 (Online Supplemental Data).

DISCUSSION

We present sex-specific normative data for the midbrain and pons areas, the widths of the MCPs and SCPs, the M/P ratio, and the MRPI based on representative general population data from individuals between 50 and 66 years of age.^{31,33} These are the decades of life when the parkinsonian disorders have their onset.^{8,13,37} Our measurements have mostly excellent reliability when measured both on the original and realigned, saved images, ensuring their usefulness in a clinical setting. There were highly significant sex differences for all brainstem measures except for the midbrain area. There were significant very weak-to-weak correlations of midbrain area, the M/P ratio, and the MRPI with age for both sexes. There were also some significant very weak-to-weak correlations for some of the brainstem measures and height, weight, and BMI, which are in line with findings in previous studies.^{29,30} However, because no systematic differences between the sexes caused by these variables were found, age-/sex-specific percentiles were created. These percentiles are easy to use in the clinic; nevertheless, height did have some very weak-to-weak correlations to some of the brainstem measures, which may be considered on an individual basis.

Table 2: Sex-specific percentiles in the different age groups

	Women (n = 527)					Men (n = 469)				
	1st	5th	50th	95th	99th	1st	5th	50th	95th	99th
Midbrain area										
50–54 yr (n = 121/91)	93	111	142	178	207	104	113	141	183	222
55–59 yr (n = 187/159)	101	110	137	174	196	95	107	140	176	195
60–66 yr (n = 219/219)	88	102	130	166	178	88	101	130	166	184
Pons area										
50–54 yr (n = 121/91)	405	431	517	591	616	417	478	565	670	703
55–59 yr (n = 187/159)	414	456	517	608	642	458	480	567	678	785
60–66 yr (n = 219/219)	413	436	516	610	664	443	476	565	659	689
MCP width										
50–54 yr (n = 121/91)	7.9	8.2	9.4	10.6	11.3	8.0	8.2	9.7	11.3	11.9
55–59 yr (n = 187/159)	7.7	8.1	9.2	10.4	10.8	7.5	8.6	9.8	11.2	12.2
60–66 yr (n = 219/219)	7.2	7.6	9.0	10.5	10.9	7.7	8.4	9.7	11.0	11.7
SCP width										
50–54 yr (n = 121/91)	2.6	3.1	3.7	4.5	5.1	2.5	3.2	3.9	4.7	5.5
55–59 yr (n = 187/159)	2.8	3.1	3.8	4.5	4.9	2.8	3.1	4.0	4.7	4.8
60–66 yr (n = 219/219)	2.7	2.9	3.7	4.5	4.9	2.9	3.2	4.0	4.8	5.2
M/P ratio										
50–54 yr (n = 121/91)	0.21	0.22	0.28	0.34	0.38	0.18	0.21	0.25	0.32	0.36
55–59 yr (n = 187/159)	0.20	0.21	0.27	0.32	0.37	0.16	0.18	0.25	0.30	0.32
60–66 yr (n = 219/219)	0.17	0.19	0.26	0.32	0.33	0.17	0.18	0.23	0.29	0.30
MRPI										
50–54 yr (n = 121/91)	6.2	6.7	9.0	12.5	13.6	6.1	7.6	9.4	13.6	16.5
55–59 yr (n = 187/159)	5.6	7.2	9.2	12.2	14.0	7.3	7.8	10.1	14.8	17.1
60–66 yr (n = 219/219)	6.7	7.1	9.5	13.2	15.3	6.8	8.0	10.6	14.5	17.1

Note:—n = X/Y; X women and Y men.

This is the first study to present sex-specific percentiles for these imaging biomarkers in different age groups. Previous studies have had smaller cohorts not suitable for estimating percentiles. Our study is 11 times larger than the second largest,²⁵ enabling us to precisely estimate and illustrate the normal variance in both men and women. In the following discussion, we compare our results with those in studies with cohorts of >20 healthy individuals from convenience or not-specified populations in which the midbrain and pons areas and the widths of the MCPs and SCPs have been measured according to Oba et al¹ and Quattrone et al.² The data from these studies are also presented in the Online Supplemental Data.^{1,2,4-7,15,16,19,20,25,26}

Brainstem Structures

We found a mean midbrain area of 137mm² for both sexes with no significant sex difference but with a significant weak age-correlated atrophy for both sexes. Previous studies have shown that the midbrain area is smaller in patients with PSP compared with healthy controls.^{1,2,5-7,15,19,20} Previous estimates of the midbrain area in healthy subjects ranged from 118 to 142 mm², with most of these studies reporting a smaller midbrain area than we do.^{1,2,5-7,15,16,19,20,25,26} The aforementioned studies have subjects with a mean age that is 7–12 years older than our cohort's mean age. This difference could explain their reported smaller midbrain area, considering that our study and others show significant weak age-related atrophy of midbrain area.^{13,31}

We found a mean pons area for all subjects of 542 mm², with a significantly different pons area of 518 mm² for women and 569 mm² for men with a large effect size (Cohen D = 0.98), but no significant age correlation for either sex. Our results are slightly higher than previous reported values for the pons area

for both sexes combined, which ranged from 469 to 541 mm².^{1,2,5-7,15,19,20,25,26} The 2 articles separating the sexes also found a significantly smaller pons area in women,^{1,26} while the 2 articles investigating age did not find any significant correlation.^{15,26}

We found a mean SCP width for all subjects of 3.8 mm, with significantly different SCP widths of 3.7 mm for women and 3.9 mm for men, with a low effect size (Cohen D = 0.44) and no significant age correlation for either sex. Earlier estimates of SCP width ranged from 3.5 to 3.9 mm for both sexes combined, which is very similar to our results.^{2,5-7,15,19,25,26} The only previous study separating the sexes found nonsignificant differences (P = .121) of 3.7 mm for women and 3.8 mm for men,²⁶ probably due to their lower sample size and lower statistical power, while we show a small but significant difference between the sexes with a small effect size. Neither of the 2 studies investigating age effects found any significant correlation between age and SCP width, corresponding to our findings.^{15,26}

We found a mean MCP width for all subjects of 9.4 mm, with significantly different MCP widths of 9.1 mm for women and 9.7 mm for men, with a medium effect size (Cohen D = 0.76) and a significant age correlation for women but not men. Previous studies have found MCP widths from 8.6 to 10.0 mm,^{2,5-7,15,19,25,26} with the only study separating the sexes finding a nonsignificant difference (P = .345) with 9.9 mm for women and 10.1 mm for men.²⁶ Again, the sex difference uncovered by our study is probably due to the larger sample size of our study. None of the 2 studies investigating age correlation found any significant correlation to age for MCP width,^{15,26} while we found a significant correlation for women but not men. As far as we know, this sex-specific, age-related MCP width atrophy in women has not been reported before, but sex-specific and age-related atrophy is described in different regions of the brain.³⁸

M/P Ratio

We found a mean M/P ratio for all subjects of 0.25, with significantly different M/P ratios of 0.26 for women and 0.24 for men, with a medium effect size (Cohen $D = 0.67$) and a significant age correlation for both sexes. These results are in line with previous estimates of the M/P ratio in healthy subjects, which ranges from 0.23 to 0.27 for both sexes combined (studies reporting the P/M ratio were converted as follows: $M/P \text{ ratio} = [P/M \text{ ratio}]^{-1}$).^{1,2,4-7,19,20,26} The only other study separating the sexes found an almost significant difference ($P = .052$) of 0.23 for women and 0.22 for men,²⁶ which resembles our results. This discrepancy is probably due to their lower sample size. The same study did not find a significant age correlation for the M/P ratio ($P = .109$); however, Morelli et al¹⁵ did report a significant correlation between age and the M/P ratio for the sexes combined ($P < .001$). Given our large cohort and previous literature indicating a sex difference in the pons area, we believe the presence of a significant sex difference in the pons area with a large effect size also indicates both age-/sex-specific differences in the M/P ratio, which need to be considered when used for clinical purposes.

MRPI

We found a mean MRPI of 10.0 for all subjects, with a significantly different MRPI of 9.5 for women and 10.6 for men, giving a medium effect size (Cohen $D = 0.59$). There was also a significant positive age correlation for both sexes. Most previous estimates of the MRPI ranged from 9.1 to 10.5, concurring with our findings.^{2,4-7,19,25} Mangesius et al²⁶ did, however, find an MRPI for all subjects of 12.2, with a nonsignificantly different MRPI of 12.0 for women and 12.3 for men ($P = .362$). They also reported lower values of the midbrain area and larger values of the MCP width than in our study and the literature in general, both resulting in an increase in the MRPI. The reason for this discrepancy in the midbrain area and MCP width measurements is unclear because they also used a 3D T1 MPRAGE sequence and performed their measurements the same way that we did. Considering that we have shown age-related atrophy of the midbrain, one explanation for their lower midbrain area could be that their population was on average 7 years older than ours. We also found a significant age correlation for MRPI in both sexes in our study, which was not shown in the 2 previous studies addressing this subject.^{15,26} Nevertheless, we do believe there are true age-/sex-specific differences, which should be addressed in the clinical and neuroradiologic settings through differentiated normal values for both age and sex, as we have presented in Table 2.

Which Biomarker to Use?

The Hummingbird sign has been shown to have high specificity (99.5%) but a rather low sensitivity (51.6%) when it comes to identifying patients with PSP.¹⁴ The general consensus in the literature is that the MRPI has a higher diagnostic accuracy when distinguishing patients with PSP from healthy controls than the midbrain area,^{1-3,12,17,22,23} SCP width,² and the M/P ratio.^{1,6,16} One reason for the superiority of the MRPI is that the values of the midbrain and pons area and the MCP and SCP widths overlap between patients with PSP and healthy subjects, giving a low

sensitivity and specificity.^{1-3,16,19,20,23} The usefulness of the M/P ratio is more uncertain. Some studies have found it useful to differentiate between patients with PSP and healthy controls,^{1,20} while others have not.^{2,6,15,16,19} Different studies have estimated cutoff values for MRPI that separate patients with PSP from healthy subjects with a sensitivity and specificity of 100%, ranging from 13.2 to 13.6 combined for both sexes.^{2,4,6,7,25} This cutoff corresponds well to our 95th percentile for MRPI for both sexes combined but becomes a bit more problematic when separated by sex, as discussed below.

Are Sex-Specific Norms Necessary?

Modern clinical medicine is slowly moving toward precision medicine, which includes sex-specific health care as there are important biologic sex differences requiring awareness in all aspects of medicine, including diagnostics.³⁹ Such sex differences have also been shown in patients with PSP.⁴⁰ We found significant sex-specific differences for all measurements except for midbrain area, and most notably in the MRPI, which is the most acknowledged biomarker for evaluating PSP. Currently, cutoff values are determined for entire cohorts and not for women and men separately. The given MRPI cutoff value of 13.2 to 13.6 in the literature corresponds well to the 95th percentile for our whole group, but when separated by sex, it corresponds to somewhere between the 95th and 99th percentile for women for all age groups and below the 95th percentile for men in all age groups. Thus, if the previous suggested cutoff values from the literature are applied, some women with PSP will risk not being diagnosed using the MRPI, while some men well within the normal variation will be misdiagnosed with PSP using the MRPI. This issue clearly shows the need for high-quality, sex-specific normative data when evaluating parkinsonian neurodegenerative diseases, which we provide in Table 2. Furthermore, considering that the sex difference could potentially increase the sensitivity and specificity for some of the other structures or ratios, it could perhaps make them as useful as the MRPI. Although the MRPI is considered the superior biomarker, it is still quite time-consuming in the clinical workflow, and measuring only the midbrain area or M/P ratio is far less time-consuming.

Strengths and Limitations

The predominant strength of our study is the large sample size, consisting of 996 subjects from the general population, imaged on the same scanner, with the same software, with a standardized MR imaging protocol and the same T1WI volume used in the Alzheimer Disease Neuroimaging Initiative, making our findings generalizable for everyone using this sequence.⁴¹ This feature is an advantage of our study because previous studies have large variations in acquisition parameters and section thickness, potentially causing variations in the measurements. To the best of our knowledge, this is the largest study on brainstem structures in healthy subjects, giving it a considerable statistical power and making it less prone to random variation. This size enables us to find significant differences and calculate percentiles for several age groups. Moreover, the 996 individuals included in our study were between 50 and 66 years of age, encompassing the age of

onset for several of the parkinsonian disorders better than previous studies.^{8,13,37}

An additional strength of our study is that we have manually measured the structures instead of using an automated approach. Currently, the manual approach is the preferred method and is considered the criterion standard. Given that our normative data are obtained manually and our inter-/intra-rater intraclass correlation coefficients showed good-to-excellent reliability, we believe our data and percentiles are of high quality and easy to use for clinicians and neuroradiologists. Furthermore, these measurements are easy to perform and not dependent on additional implementation or steps in the workflow such as automated atlas-based approaches, which are not accessible to all. The future is, however, computer-aided, with either atlas-based volumetric evaluation or artificial intelligence approaches, as shown in several studies.^{42,43} One multicenter study combining patients with PD ($n = 204$) and PSP ($n = 106$), MSA ($n = 81$), and healthy controls ($n = 73$) showed that fully automated atlas-based volumetry with subsequent support vector machine classification could differentiate the different syndromes on an individual level with sensitivities from 79% to 87% and specificities from 87% to 96%.⁴² In their study, the midbrain showed the most atrophy in PSP and the MCP in MSA of the cerebellar type.

A limitation of our study is that the participants included did not undergo a thorough neurologic examination at the time of the MR imaging study, which potentially could have identified subjects with prodromal disease. However, given our large sample size, we believe the possible inclusion of these subjects is less likely to substantially skew our results.

A second limitation is that our normative data do not reach beyond 66 years of age, which is in the lower range of when some of the parkinsonian diseases typically have their onset. However, on an individual level, many patients have earlier onset or prodromal phases in which the need for high-quality normative data is also important. Whether there is a need for even more specified or tailored percentiles based on additional demographic and/or health variables remains to be determined and may become standard as big data and artificial intelligence become more integrated in the clinic. For this data set, however, we limited the percentile to sex and age because height, weight, and BMI were only weakly and inconsistently related to the brainstem measures.

Another limitation is that the 2 raters who performed the measurements were not experienced neuroradiologists. In comparable studies, neuroradiologists or experienced raters have independently performed measurements. Nevertheless, the 2 raters in our study were given extensive training by an experienced neuroradiologist, and we consider this to be the best approach when performing manual measurements in such large studies. Despite these limitations, the 2 raters in our study achieved inter-/intra-rater reliability ranging from good to excellent. Comparable studies have not elaborated on the implementation of their reliability analysis. For example, they have not presented 95% CIs for their intraclass correlation coefficient values or mentioned whether the intraclass correlation coefficients were calculated on the basis of single or average measures or whether they had been measured on originally saved images or on realigned, saved images. Thus, comparing our intraclass correlation coefficient values with theirs

is difficult. As expected, the intraclass correlation coefficient values in our study decreased when performing measurements on realigned, saved images, as several additional steps of the procedure were added.

CONCLUSIONS

We present high-quality sex-/age-specific normative data as means and percentiles for the midbrain and pons area, the widths of the MCPs and SCPs, the M/P ratio, and the MRPI based on manual measurements in 996 healthy subjects between 50 and 66 years of age. Furthermore, we show that using sex-specific data is important to avoid misdiagnosing patients with suspected brainstem atrophy.

Disclosure forms provided by the authors are available with the full text and PDF of this article at www.ajnr.org.

REFERENCES

1. Oba H, Yagishita A, Terada H, et al. **New and reliable MRI diagnosis for progressive supranuclear palsy.** *Neurology* 2005;64:2050–55 CrossRef Medline
2. Quattrone A, Nicoletti G, Messina D, et al. **MR imaging index for differentiation of progressive supranuclear palsy from Parkinson disease and the Parkinson variant of multiple system atrophy.** *Radiology* 2008;246:214–21 CrossRef Medline
3. Chougar L, Pyatigorskaya N, Degos B, et al. **The role of magnetic resonance imaging for the diagnosis of atypical parkinsonism.** *Front Neurol* 2020;11:665 CrossRef Medline
4. Quattrone A, Morelli M, Nigro S, et al. **A new MR imaging index for differentiation of progressive supranuclear palsy-parkinsonism from Parkinson's disease.** *Parkinsonism Relat Disord* 2018;54:3–8 CrossRef Medline
5. Longoni G, Agosta F, Kostić VS, et al. **MRI measurements of brainstem structures in patients with Richardson's syndrome, progressive supranuclear palsy-parkinsonism, and Parkinson's disease.** *Mov Disord* 2011;26:247–55 CrossRef Medline
6. Morelli M, Arabia G, Salsone M, et al. **Accuracy of magnetic resonance parkinsonism index for differentiation of progressive supranuclear palsy from probable or possible Parkinson disease.** *Mov Disord* 2011;26:527–33 CrossRef Medline
7. Nigro S, Morelli M, Arabia G, et al. **Magnetic resonance parkinsonism index and midbrain to pons ratio: which index better distinguishes progressive supranuclear palsy patients with a low degree of diagnostic certainty from patients with Parkinson disease?** *Parkinsonism Relat Disord* 2017;41:31–36 CrossRef Medline
8. Testa D, Monza D, Ferrarini M, et al. **Comparison of natural histories of progressive supranuclear palsy and multiple system atrophy.** *Neurol Sci* 2001;22:247–51 CrossRef Medline
9. Gilman S, Wenning GK, Low PA, et al. **Second consensus statement on the diagnosis of multiple system atrophy.** *Neurology* 2008;71:670–76 CrossRef Medline
10. Whitwell JL, Höglinger GU, Antonini A, et al; Movement Disorder Society-endorsed PSP Study Group. **Radiological biomarkers for diagnosis in PSP: where are we and where do we need to be?** *Mov Disord* 2017;32:955–71 CrossRef Medline
11. Meissner WG, Fernagut PO, Dehay B, et al. **Multiple system atrophy: recent developments and future perspectives.** *Mov Disord* 2019;34:1629–42 CrossRef Medline
12. Cosottini M, Ceravolo R, Faggioni L, et al. **Assessment of midbrain atrophy in patients with progressive supranuclear palsy with routine magnetic resonance imaging.** *Acta Neurol Scand* 2007;116:37–42 CrossRef Medline
13. Höglinger GU, Respondek G, Stamelou M, et al; Movement Disorder Society-endorsed PSP Study Group. **Clinical diagnosis of progressive**

- supranuclear palsy: the Movement Disorder Society Criteria. *Mov Disord* 2017;32:853–64 CrossRef Medline
14. Mueller C, Hussl A, Krismer F, et al. **The diagnostic accuracy of the hummingbird and morning glory sign in patients with neurodegenerative parkinsonism.** *Parkinsonism Relat Disord* 2018;54:90–94 CrossRef Medline
 15. Morelli M, Arabia G, Messina D, et al. **Effect of aging on magnetic resonance measures differentiating progressive supranuclear palsy from Parkinson's disease.** *Mov Disord* 2014;29:488–95 CrossRef Medline
 16. Gröschel K, Kastrup A, Litvan I, et al. **Penguins and hummingbirds: midbrain atrophy in progressive supranuclear palsy.** *Neurology* 2006;66:949–50 CrossRef Medline
 17. Bacchi S, Chim I, Patel S. **Specificity and sensitivity of magnetic resonance imaging findings in the diagnosis of progressive supranuclear palsy.** *J Med Imaging Radiat Oncol* 2018;62:21–31 CrossRef Medline
 18. Brooks DJ, Seppi K; Neuroimaging Working Group on MSA. **Proposed neuroimaging criteria for the diagnosis of multiple system atrophy.** *Mov Disord* 2009;24:949–64 CrossRef Medline
 19. Sankhla CS, Patil KB, Sawant N, et al. **Diagnostic accuracy of Magnetic Resonance Parkinsonism Index in differentiating progressive supranuclear palsy from Parkinson's disease and controls in Indian patients.** *Neurol India* 2016;64:239–45 CrossRef Medline
 20. Ahn JH, Kim M, Kim JS, et al. **Midbrain atrophy in patients with presymptomatic progressive supranuclear palsy-Richardson's syndrome.** *Parkinsonism Relat Disord* 2019;66:80–86 CrossRef Medline
 21. Möller L, Kassubek J, Südmeyer M, et al. **Manual MRI morphometry in Parkinsonian syndromes.** *Mov Disord* 2017;32:778–82 CrossRef Medline
 22. Kato N, Arai K, Hattori T. **Study of the rostral midbrain atrophy in progressive supranuclear palsy.** *J Neurol Sci* 2003;210:57–60 CrossRef Medline
 23. Warmuth-Metz M, Naumann M, Csoti I, et al. **Measurement of the midbrain diameter on routine magnetic resonance imaging: a simple and accurate method of differentiating between Parkinson disease and progressive supranuclear palsy.** *Arch Neurol* 2001;58:1076–79 CrossRef Medline
 24. Armstrong MJ. **Progressive supranuclear palsy: an update.** *Curr Neurol Neurosci Rep* 2018;18:12 CrossRef Medline
 25. Nigro S, Arabia G, Antonini A, et al. **Magnetic Resonance Parkinsonism Index: diagnostic accuracy of a fully automated algorithm in comparison with the manual measurement in a large Italian multicentre study in patients with progressive supranuclear palsy.** *Eur Radiol* 2017;27:2665–75 CrossRef Medline
 26. Mangesius S, Hussl A, Tagwercher S, et al. **No effect of age, gender and total intracranial volume on brainstem MR planimetric measurements.** *Eur Radiol* 2020;30:2802–08 CrossRef Medline
 27. Cahill L. **Why sex matters for neuroscience.** *Nat Rev Neurosci* 2006;7:477–84 CrossRef Medline
 28. Tannenbaum C, Ellis RP, Eyssel F, et al. **Sex and gender analysis improves science and engineering.** *Nature* 2019;575:137–46 CrossRef Medline
 29. Jancke L, Liem F, Merillat S. **Weak correlations between body height and several brain metrics in healthy elderly subjects.** *Eur J Neurosci* 2019;50:3578–89 CrossRef Medline
 30. Willette AA, Kapogiannis D. **Does the brain shrink as the waist expands?** *Ageing Res Rev* 2015;20:86–97 CrossRef Medline
 31. Häberg AK, Hammer TA, Kvistad KA, et al. **Incidental intracranial findings and their clinical impact: the HUNT MRI study in a general population of 1006 participants between 50-66 years.** *PLoS One* 2016;11:e0151080 CrossRef Medline
 32. Krokstad S, Langhammer A, Hveem K, et al. **Cohort profile: the HUNT Study, Norway.** *Int J Epidemiol* 2013;42:968–77 CrossRef Medline
 33. Honningsvåg LM, Linde M, Häberg A, et al. **Does health differ between participants and non-participants in the MRI-HUNT study, a population-based neuroimaging study? The Nord-Trøndelag health studies 1984-2009.** *BMC Med Imaging* 2012;12:23 CrossRef Medline
 34. Cohen J. *Statistical Power Analysis for the Behavioral Sciences* (2nd ed). Hillsdale, NJ: Lawrence Earlbaum Associate; 1988
 35. Swinscow TDV. *Statistics at Square One*. 9th ed. Revised by MJ Campbell. BMJ Publishing Group; 1996
 36. Koo TK, Li MY. **A guideline of selecting and reporting intraclass correlation coefficients for reliability research.** *J Chiropr Med* 2016;15:155–63 CrossRef Medline
 37. Miki Y, Foti SC, Asi YT, et al. **Improving diagnostic accuracy of multiple system atrophy: a clinicopathological study.** *Brain* 2019;142:2813–27 CrossRef Medline
 38. Xu J, Kobayashi S, Yamaguchi S, et al. **Gender effects on age-related changes in brain structure.** *AJNR Am J Neuroradiol* 2000;21:112–18 Medline
 39. Regitz-Zagrosek V. **Sex and gender differences in health: Science & Society Series on Sex and Science.** *EMBO Rep* 2012;13:596–603 CrossRef Medline
 40. Mahale RR, Krishnan S, Divya KP, et al. **Gender differences in progressive supranuclear palsy.** *Acta Neurol Belg* 2021 Feb 17. [Epub ahead of print] CrossRef Medline
 41. Mueller SG, Weiner MW, Thal LJ, et al. **The Alzheimer's Disease Neuroimaging Initiative.** *Neuroimaging Clin N Am* 2005;15:869–77. xi-xii CrossRef Medline
 42. Huppertz HJ, Moller L, Sudmeyer M, et al. **Differentiation of neurodegenerative parkinsonian syndromes by volumetric magnetic resonance imaging analysis and support vector machine classification.** *Mov Disord* 2016;31:1506–17 CrossRef Medline
 43. Scherfler C, Gobel G, Muller C, et al. **Diagnostic potential of automated subcortical volume segmentation in atypical parkinsonism.** *Neurology* 2016;86:1242–49 CrossRef Medline

The Epidermal Growth Factor Domain of the Mutation Does Not Appear to Influence Disease Progression in CADASIL When Brain Volume and Sex Are Taken into Account

J. Lebenberg, J.-P. Guichard, A. Guillonnet, D. Hervé, N. Alili, A. Taleb, N. Dias-Gastellier, H. Chabriat, and E. Jouvent



ABSTRACT

BACKGROUND AND PURPOSE: By studying the evolution of brain volume across the life span in male and female patients, we aimed to understand how sex, brain volume, and the epidermal growth factor repeat domain of the mutation, the 3 major determinants of disability in CADASIL, interact in driving disease evolution.

MATERIALS AND METHODS: We used validated methods to model the evolution of normalized brain volume with age in male and female patients using nonparametric regression in a large, monocentric cohort with prospectively collected clinical and high-resolution MR imaging data. We used k-means clustering to test for the presence of different clinical course profiles.

RESULTS: We included 229 patients (mean age, 53 [SD, 12] years; 130 women). Brain volume was larger in women (mean size, 1024 [SD, 62] cm³ versus 979 [SD, 50] cm³; $P < .001$) and decreased regularly. In men, the relationship between brain volume and age unexpectedly suggested an increase in brain volume around midlife. Cluster analyses showed that this finding was related to the presence of a group of older male patients with milder symptoms and larger brain volumes, similar to findings of age-matched women. This group did not show specific epidermal growth factor repeat domain distribution.

CONCLUSIONS: Our results demonstrate a detrimental effect of male sex on brain volume throughout life in CADASIL. We identified a subgroup of male patients whose brain volume and clinical outcomes were similar to those of age-matched women. They did not have a specific distribution of the epidermal growth factor repeat domain, suggesting that yet-unidentified predictors may interact with sex and brain volume in driving disease evolution.

ABBREVIATIONS: EGFR = epidermal growth factor repeat; MDRS = Mattis Dementia Rating Scale; MMSE = Mini-Mental State Examination; SVD = small-vessel disease; TMTAT = Trail-Making Test A Time; TMTBT = Trail-Making Test B Time; WMH = white matter hyperintensities

CADASIL is the most frequent monogenic cerebral small-vessel disease (SVD). In this disorder, mutations lead to an odd number of cysteine residues within 1 of the 34 epidermal growth factor repeat (EGFR) domains of the *NOTCH3* gene.¹ Mutations in EGFR domains 7–34 were recently shown to be associated with less severe clinical outcomes.¹ Larger brain volumes were also associated with less severe clinical outcomes and predict

better clinical evolution.^{2,3} In addition, female patients show milder clinical phenotypes.^{2,4} However, this beneficial effect in female patients no longer appears significant in predictive models when brain volume is considered.² This finding suggests systematic innate (sex-related) and/or acquired differences in brain volume between male and female patients.³ While the identification of the EGFR domain as a predictor of disease evolution clearly improved our understanding of the disease, a considerable uncertainty remains regarding its evolution, and it is still unknown how sex, brain volume, the EGFR domain, and other MR imaging predictors, ie, lacunes, white matter hyperintensities (WMH), and cerebral microbleeds, interact in driving clinical outcomes. To better understand these interactions, we used a specifically designed approach to model life span brain volume in male and female patients from systematic high-resolution MR imaging scans obtained in a unique, large, prospective cohort of patients with CADASIL.

Received October 1, 2021; accepted after revision March 13, 2022.

From the Department of Neurology (E.J.), Neuroradiology (J.P.G., A.G.) and the Centre de Neurologie Vasculaire Translationnel (J.L., D.H., A.T., N.D.-G., H.C.), Assistance Publique–Hôpitaux de Paris, Hôpital Lariboisière, Paris, France; L'Institut National de la Santé et de la Recherche Médicale INSERM U1141, Université Paris Cité, Paris, France; and Federation Hospitalo-Universitaire NeuroVasc (J.L., N.D.-G., D.H., H.C., E.J.), Paris, France.

This work was funded by the RHU TRT_cSVD project (ANR-16-RHUS-004) and the Association de Recherche en Neurologie Vasculaire, Hôpital Lariboisière, France.

Please address correspondence to Eric Jouvent, MD, PhD; Hôpital Lariboisière, 2 rue Ambroise Paré, 75010 Paris, France; e-mail: eric.jouvent@aphp.fr



Indicates article with online supplemental data.

<http://dx.doi.org/10.3174/ajnr.A7499>

MATERIALS AND METHODS

Patients

Since 2003, patients with genetically confirmed *NOTCH3* mutations followed in the French referral center for rare vascular disease of the eye and the brain (CERVCO, <https://www.cervco.fr>) and willing to participate are included in a prospective cohort. They are systematically evaluated both clinically and with standardized MR imaging every 18–24 months. The EGFR domain is recorded in each patient at the time of genetic testing. The level of education is systematically recorded at inclusion.³ Beginning at inclusion and at each visit, patients undergo brain MR imaging, including 3D T1 high-resolution, FLAIR, and T2* sequences (scans were acquired on a 1.5T MR imaging scanner until 2014 and on a 3T thereafter) as well as comprehensive neurologic and neuropsychological assessments performed by experienced neurologists and neuropsychologists, respectively. In the present study, in line with previous reports,⁵ we used the Mini-Mental State Examination (MMSE: range, 0–30; with higher scores being better) and the Mattis Dementia Rating Scale (MDRS: range, 0–144; with higher scores being better) as proxies of global cognitive functions; the time to complete part B of the Trail-Making Test (TMTBT, recorded in seconds, shorter times are better) as a marker of executive functioning; and the time to complete part A (TMTAT, in seconds as well) as a marker of processing speed. Finally, we used the mRS (from 0, asymptomatic, to 5, bedridden) as a measure of disability.

Standard Protocol Approvals, Registrations, and Patient Consents

This study was approved by an independent ethics committee (updated agreement CEEI-IRB-17/388) and conducted in accordance with the Declaration of Helsinki and guidelines for Good Clinical Practice and General Data Protection Regulation (GDPR) in Europe.

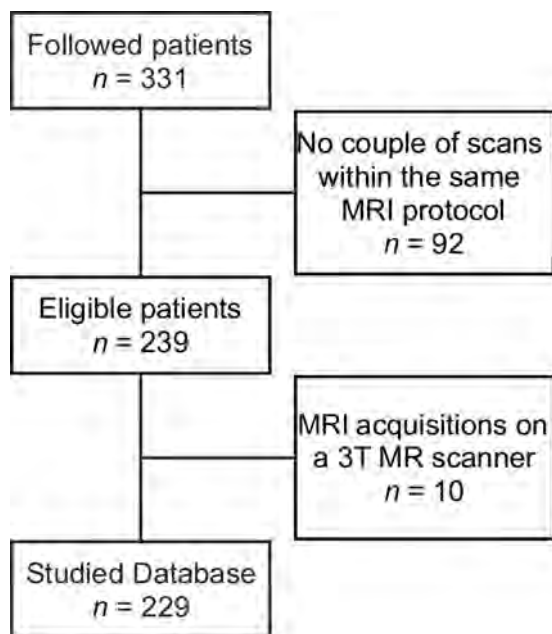


FIG 1. Flow diagram of patients included in the study.

MR Imaging Processing

We used BIANCA from the FSL suite (<https://fsl.fmrib.ox.ac.uk/fsl/fslwiki/BIANCA/Userguide>) to extract masks of WMH in all patients, as previously reported.^{6,7} The volume of WMH was obtained by multiplying the number of voxels in WMH masks by the corresponding voxel size. In agreement with recent guidelines,⁸ we registered these masks on 3D T1 images and replaced the intensity of the corresponding voxels in the native image with that of normal-appearing white matter. To obtain brain volume and brain volume changes, we used SIENAX (<http://support.qmenta.com/knowledge/sienax-2.6/-/fsl-6.0>) and SIENA (<https://fsl.fmrib.ox.ac.uk/fsl/fslwiki/SIENA/UserGuide>) from FSL, respectively.^{9,10} Their reliability in the context of SVD is considered good.¹¹ Given the long-term follow-up (17 years at the time of this writing), the MR imaging protocol underwent several alterations with concerns regarding the reliability of quantitative measures. Given the known influence of the sequence characteristics on segmentation results, we used SIENA only between time points obtained with the same 3D T1 sequence.¹² Because the number of longitudinal acquisitions largely differed among patients (from 1 to 10), we randomly selected for each patient 1 couple of MR imaging acquisitions to avoid overrepresentation of data from patients with the longest follow-ups, who are likely to be the least severe. We multiplied the baseline volume, obtained with SIENAX, by the associated percentage of brain volume change with SIENA, to obtain brain volume at follow-up. To control for interindividual variability, we systematically corrected brain volumes for head size, in line with current recommendations.⁸ Finally, lacunes and cerebral microbleeds, defined according to the STRIVE criteria (<https://harness-neuroimaging.org/strive-standards>),¹³ were manually identified by an experienced reader (E.J.), with previously validated methods.⁵

Statistical Analysis

All analyses were performed with Python 3.7¹⁴ and R 3.5 (<http://www.r-project.org/>).¹⁵ We used mean or median for continuous variables and SDs or interquartile range as measures of dispersion, depending on variable type and distribution. Group differences were evaluated with the Mann-Whitney test for continuous variables or the χ^2 test of independence for categorical variables. We built regression models to estimate the relationships between brain volume and age. Given the known effect of sex on disease severity, we built separate models for men and women. Considering possible nonlinearities with age, the evolution of brain volume with age across the whole life span was modeled using a nonparametric locally weighted regression approach (statmodels 0.12.1 in Python; <https://www.statmodels.org/v0.12.1/>).^{16,17} When considered necessary, cluster analysis with the k-means algorithm (scikit-learn library 0.22.1; <https://zenodo.org/record/3596890#.Ykcc9SjMJPY>)¹⁸ was performed to determine whether different subgroups could be identified on the basis of age at baseline, baseline brain volume, and annual percentage of brain volume change. We computed Silhouette scores (https://scikit-learn.org/stable/modules/generated/sklearn.metrics.silhouette_score.html), defined as the normalized difference between the minimal intercluster dissimilarity and the mean intracluster dissimilarity, to select the optimal number of clusters.¹⁹ The optimal number of clusters provides the best trade-off between the

Table 1: Baseline characteristics of the study sample^a

	Study Sample (n = 229)	Nonincluded Patients (n = 102)	P Value
Women ^b	130 (57%)	50 (49%)	.24
Age (mean) (range) (yr)	52.8 (SD 12.0) (24.1–79.4)	53.8 (SD, 12.1) (25.6–78.8)	.19
Genetic profile ^b			.19
Mutation in EGFR domains 1–6	164 (72%)	65 (64%)	
Mutation in EGFR domains 7–34	65 (28%)	37 (36%)	
Level of education (yr) ^{b,c,d}			.08
1–3	40 (17%)	16 (16%)	
4–6	122 (53%)	46 (45%)	
7	66 (29%)	32 (31%)	
mRS ^{b,e} (median) (IQR)	1 (0–2)	1 (0–2)	.22
MDRS ^f (mean)	133.9 (SD, 17.1)	133.0 (SD, 17.5)	.33
MMSE ^g (mean)	27.1 (SD, 4.3)	26.4 (SD, 4.9)	.43
TMTAT ^h (mean)	47.3 (SD, 33.9)	55.6 (SD, 50.2)	.48
TMTBT ⁱ (mean)	123.9 (SD, 99.7)	113.5 (SD, 90.4)	.45
Normalized brain volume (cm ³)	1004.4 (SD, 61.1)	1024.8 (SD, 80.9)	<.001

Note: —IQR indicates interquartile range.

^aCharacteristics of included and nonincluded patients were compared according to variable type and distribution (Mann-Whitney test by default or χ^2 test of independence for categorical variables).

^bComparisons performed using the χ^2 test of independence.

^cOn 228 studied patients and 94 excluded patients.

^dReference levels of education: 0 = illiterate, 3 = incomplete secondary school (<9 years), 6 = secondary school (13 years), 7 = university (\geq 16 years).

^eOn 216 and 100 patients, respectively.

^fOn 200 and 94 patients, respectively.

^gOn 209 and 90 patients, respectively.

^hOn 194 and 85 patients, respectively.

ⁱOn 182 and 76 patients, respectively.

average Silhouette score to maximize, and the number of negative scores representing mislabeling. To determine whether patients in different clusters actually show different disease course profiles, we built regression models to predict clinical outcomes (MMSE, MDRS, TMTAT, TMTBT, and mRS) based on the subgroup to which the patient pertained, age, level of education, the EGFR domain of the mutation (categorized as EGFR domains 1–6 versus EGFR domains 7–34, according to previous data¹), brain volume, volume of WMH, and number of lacunes and microbleeds, all measured at baseline. Missing values were imputed, considering the standard span of values in the data base (package Amelia in R; <https://www.rdocumentation.org/packages/Amelia/versions/1.8.0>).²⁰ The threshold for significance was set at .05.

RESULTS

As of this writing, the whole database comprises 331 patients with available follow-up data (2230 patient-years). The age at inclusion ranges from 24.1 to 79.4 years (mean age, 53.2 [SD, 12.2] years). Among the 331 patients, 239 had at least 2 acquisitions with the same protocol (229 at 1.5T, 10 at 3T). Given that <5% of scans were acquired at 3T, we herein provide results corresponding to the data obtained at 1.5T only (the flow chart is presented in Fig 1). However, including the few data obtained at 3T did not alter our results (data not shown). Characteristics of the 229 patients in the study sample are detailed Table 1. On average, the time elapsed between the 2 MR imaging evaluations for these 229 patients was 20.8 (SD, 6.5) months. While they were in general, similar to nonincluded patients, included patients showed significantly lower brain volumes ($P < .001$).

The mean brain volume was significantly larger in female patients throughout the life span (1024 [SD, 62] cm³ versus 979 [SD, 50] cm³ in male patients; $P < .001$), while mean age was not significantly different between sexes (52.8 [SD, 13.0] years in

women versus 52.8 [SD, 10.6] years in men, $P = .41$). The spread of brain volume was relatively constant across age for women but steadily increased for men (Fig 2A). By comparison with the regression line in female patients, which suggested a continuous decrease in brain volume across the life span, the regression line in male patients presented an unexpected 3-step curve (Fig 2A and Online Supplemental Data). Given that we considered unlikely that brain volume increases after middle age in male patients, we performed a cluster analysis to determine whether this aspect may be related to the presence of different subgroups of patients. As suggested by the homogeneous regression curve in female patients, cluster analysis among women did not identify any relevant subgroup.

According to the Silhouette algorithm, 4 subgroups of male patients could be identified (Fig 3 and Table 2 and Online Supplemental Data). One group corresponded to most male patients younger than 50 years of age (the “young” group, 24 patients). Two others, thereafter denoted “middle aged” (30 patients) and “older” patients (23 patients), roughly followed the global trend for brain volume reduction with age observed in women, with a downward shift (Fig 2B). A fourth group of 22 older male patients showed strikingly different characteristics, with brain volumes close to that of age-matched females (“older men with larger brains” group in Fig 2B). When excluding this subgroup, brain volume in male patients showed a shape similar to that of female patients with a downward shift (Fig 2B).

At the global level, analyses confirmed the previously reported relationships among age, lacunes, and brain volume and clinical outcomes as well as the inconsistent effect of the EGFR domain and sex on clinical outcomes when brain volume is considered (Online Supplemental Data). Among subgroups, male patients from the older with larger brain group showed significantly better clinical scores than the older male group (Table 2). Most noteworthy,

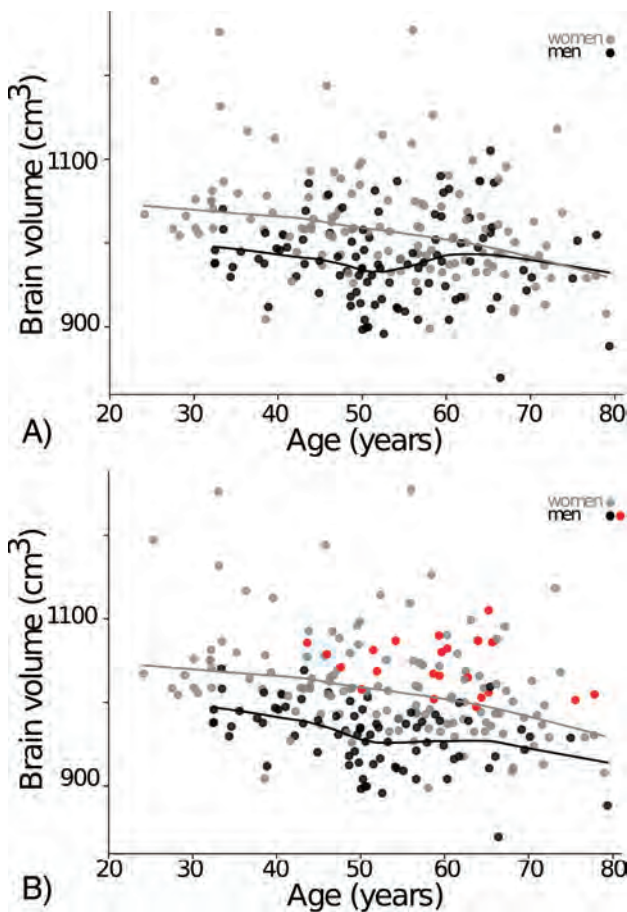


FIG 2. Evolution of brain volume with age. Scatterplot of brain volume measured at the first time point for each patient against age, with (A) and without (B) the “older with larger brains” group (red points in B). Weighted regressions were reconstructed separately for men and women, given the known detrimental effect of the disease in male patients (black and gray solid lines). When we built regression lines without considering the older with larger brains group (in red), they looked similar in male and female patients across the whole life span, though shifted downward in men, for yet-unknown reasons.

the difference between these groups was significant while considering the most well-known factors associated with clinical outcomes in CADASIL, namely age, level of education, and EGFR domain of the mutation. Further considering the burden of WMH, the number of lacunes or the number of microbleeds did not alter this finding. As expected however, the group effect was no longer significant when including brain volume as a covariate (Online Supplemental Data).

DISCUSSION

In the present study, we observed that in contrast to the general population,²¹ female patients have larger brain volumes than male patients across the life span in CADASIL, suggesting an innate or early-life difference in brain volume between male and female patients, long before the appearance on brain MR imaging of markers of SVD, which will be associated with the development of brain atrophy (Fig 2). We did not identify any obvious reason for such a detrimental effect of male sex on brain volume, in particular regarding the EGFR domain, which was not associated with sex. However, we identified a subgroup of

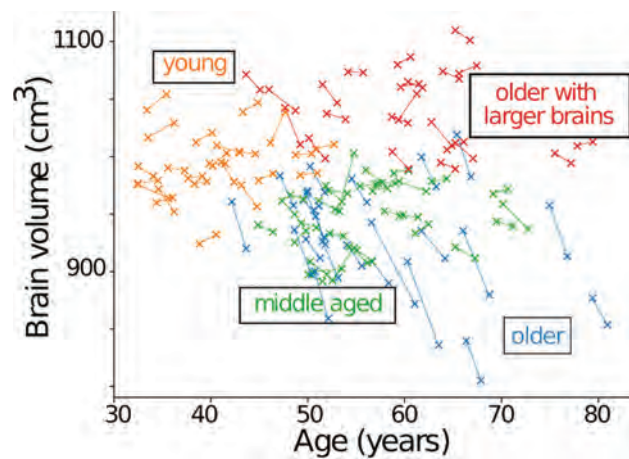


FIG 3. K-means clustering analysis in men. The clustering analysis used with the Silhouette criteria led to the definition of 4 distinct groups of patients. The group of young patients comprised nearly all individuals younger than 50 years of age. The middle-aged and older patient groups seemed to follow the age trend of female patients. In total contrast, the group of older with larger brains patients showed strikingly different characteristics, with larger brain volume and lower brain atrophy.

elderly male patients having larger brain volumes and milder clinical outcomes, similar to that of age-matched female patients, suggesting the existence of yet-undefined disease-modifying factors.

While the follow-up of our cohort was exceptionally long (17 years), we could not fully use these longitudinal data to model brain volume evolution, given the large impact of sequence and scanner alterations on quantitative metrics. This mostly cross-sectional nature of our analyses may yield unexpected findings, such as the crude regression line suggesting an increase of brain volume in male patients between 50 and 60 years of age. Because systematic brain volume enlargement in middle-aged male patients is unlikely, the shape of the regression curve could be explained, in part, by the gradual departure of the patients with the most severe disease as they age, which could lead to an overrepresentation of elderly patients with less severe disease, resulting in a tendency for group-wide brain volume to increase in cross-sectional analyses. However, this could not explain the presence of older male patients with brain volumes similar to those in male patients 20 years younger. Figure 2B shows that this subgroup appears more similar to age-matched female patients. For whatever reason, these patients may not be affected by the detrimental effect of male sex on brain volume. We expected to find a larger representation of EGFR domains 7–34, associated with better clinical outcomes in this subgroup, but this was not the case, suggesting that other factors may temper the detrimental effect of male sex in CADASIL. Further studies will be needed to understand the mechanisms underlying this phenomenon.

In line with results suggesting that the presence of extensive WMH in the anterior temporal poles is associated with a better prognosis,²² in the present study, older male patients with larger brain volumes also tended to have larger volumes of WMH in these areas, but the difference did not reach significance (data not shown). What is noteworthy, we recently reported the case of a patient whose large extent of WMH, particularly in the anterior temporal poles, was strongly reduced while taking valpromide for severe depression

Table 2: Baseline characteristics of “older with larger brains” men and older men in CADASIL^a

	Older with Larger Brains Men (n = 22)	Older Men (n = 23)	P Value
Age (mean) (range) (yr)	59.3 (SD, 8.5) (43.6–77.8)	56.4 (SD, 10.7) (42.1–79.4)	.12
Genetic profile ^b			.92
Mutation in EGFR domains 1–6	15 (68%)	17 (74%)	
Mutation in EGFR domains 7–34	7 (32%)	6 (26%)	
Level of education ^b (yr)			.30
1–3	2 (9%)	6 (26%)	
4–6	13 (59%)	10 (43%)	
7	7 (32%)	7 (30%)	
mRS ^{b,c} (median) (IQR)	1 (0–2)	3 (1–5)	.009
MDRS ^d (mean)	136.2 (SD, 8.7)	120.8 (SD, 28.5)	.04
MMSE ^e (mean)	28.2 (SD, 2.2)	22.9 (SD, 6.7)	.45
TMTAT ^f (mean)	52.6 (SD, 30.3)	42.9 (SD, 20.3)	.004
TMTBT ^g (mean)	125.4 (SD, 87.0)	142.0 (SD, 97.7)	.003
Normalized brain volume (mean) (cm ³)	1043.5 (SD, 30.8)	944.2 (SD, 40.1)	<.001
Annual PBVC (%)	–0.4 (0.7)	–2.0 (0.7)	<.001
Normalized WMH volume (%)	0.1 (0.1)	0.1 (0.0)	.03
No. of lacunes	6.8 (7.7)	10.6 (8.0)	.01
No. of microbleeds	11.0 (23.4)	8.6 (18.2)	.36

Note:—PBVC indicates percentage of brain volume change

^aCharacteristics of older men with larger brains and older men were compared with appropriate methods, depending on variable type and distribution (Mann-Whitney test by default or χ^2 test of independence for categorical variables).

^bComparisons performed using the χ^2 test of independence.

^cOn 22 older with men larger brains and 21 older men.

^dOn 20 and 12 patients, respectively.

^eOn 22 and 16 patients, respectively.

^fOn 19 and 9 patients, respectively.

^gOn 17 and 9 patients, respectively.

before re-inflating after the treatment was switched to lithium.²³ These results support the hypothesis that mechanisms underlying WMH in CADASIL may not be related only to chronic hypoperfusion but may involve large variations of water influx into the different brain compartments. Whether these changes might affect male and female patients differently and whether they might alter the natural history of the disease remain unknown. Future studies will help determine whether certain medications or conditions may lead male patients to switch from one group to another. The results might potentially lead to the identification of new therapeutic approaches.

Our study has several strengths. We evaluated a large cohort of patients in whom the diagnosis was, in all cases, confirmed genetically, while following the current standard for processing brain images in the context of severe SVD. We designed a specific approach to process brain images acquired during a very long period of time while avoiding biases due to overfitting the patients with the longest follow-ups. Finally, we based our subgroup analyses on unsupervised approaches, whose results were, thereafter, confirmed by testing associations with clinical outcomes.

We must also acknowledge some limitations. We could not use all the data gathered during the past 17 years due to methodologic constraints related to mandatory changes in MR imaging scanners or sequences. The differences in brain volume between included and nonincluded patients shown in Table 1 illustrate the importance of MR imaging scanner on brain volume metrics. Indeed, while the 229 included and the 102 nonincluded patients did not differ regarding clinical variables, the brain volume of nonincluded patients was significantly larger. However, after excluding the data obtained on the 3T scanner (55 of 102 patients), this difference was no longer significant, suggesting that sequences acquired on the 3T scanner

overestimate brain volume compared with those obtained on the 1.5T scanner. Finally, we could not formally exclude any bias due to data selection because we chose not to fully exploit longitudinal data in some patients. Indeed, some patients in our cohort have been followed for >15 years. This individual approach may well provide additional information, and we are currently working on specific postprocessing approaches allowing the exploitation of such valuable data, as illustrated by a recent case report of our group.²³

CONCLUSIONS

The present study results show that brain volume, a major determinant of clinical outcomes, is larger in female patients throughout life in CADASIL, in total contrast to the general population. For yet-undetermined reasons, some elderly male patients may exhibit larger brain volumes and milder clinical outcomes similar to those of age-matched female patients, suggesting the possibility of identifying new therapeutic targets in this disorder.

ACKNOWLEDGMENTS

The authors thank all patients for their collaboration on this study.

Disclosure forms provided by the authors are available with the full text and PDF of this article at www.ajnr.org.

REFERENCES

1. Rutten JW, Van Eijdsden BJ, Duering M, et al. **The effect of NOTCH3 pathogenic variant position on CADASIL disease severity: NOTCH3 EGFR 1-6 pathogenic variant are associated with a more severe phenotype and lower survival compared**

- with EGFR 7-34 pathogenic variant. *Genet Med* 2019;21:676–82 CrossRef Medline
2. Chabriet H, Hervé D, Duering M, et al. **Predictors of clinical worsening in cerebral autosomal dominant arteriopathy with subcortical infarcts and leukoencephalopathy: prospective cohort study.** *Stroke* 2016;47:4–11 CrossRef Medline
 3. Jouvent E, Duchesnay E, Hadj-Seleem F, et al. **Prediction of 3-year clinical course in CADASIL.** *Neurology* 2016;87:1787–95 CrossRef Medline
 4. Gunda B, Hervé D, Godin O, et al. **Effects of gender on the phenotype of CADASIL.** *Stroke* 2012;43:137–41 CrossRef Medline
 5. Viswanathan A, Guichard JP, Gschwendtner A, et al. **Blood pressure and haemoglobin A1c are associated with microhaemorrhage in CADASIL: a two-centre cohort study.** *Brain* 2006;129:2375–83 CrossRef Medline
 6. Griffanti L, Zamboni G, Khan A, et al. **BIANCA (Brain Intensity AbNormality Classification Algorithm): a new tool for automated segmentation of white matter hyperintensities.** *Neuroimage* 2016;141:191–205 CrossRef Medline
 7. Ling Y, Jouvent E, Cousyn L, et al. **Validation and optimization of BIANCA for the segmentation of extensive white matter hyperintensities.** *Neuroinformatics* 2018;16:269–81 CrossRef Medline
 8. De Guio F, Duering M, Fazekas F, et al. **Brain atrophy in cerebral small vessel diseases: Extent, consequences, technical limitations and perspectives: the HARNESS initiative.** *J Cereb Blood Flow Metab* 2020;40:231–45 CrossRef Medline
 9. Smith SM, Zhang Y, Jenkinson M, et al. **Accurate, robust, and automated longitudinal and cross-sectional brain change analysis.** *Neuroimage* 2002;17:479–89 CrossRef Medline
 10. Smith SM, Jenkinson M, Woolrich MW, et al. **Advances in functional and structural MR image analysis and implementation as FSL.** *Neuroimage* 2004;23(Suppl 1):S208–19 CrossRef Medline
 11. De Guio F, Jouvent E, Biessels GJ, et al. **Reproducibility and variability of quantitative magnetic resonance imaging markers in cerebral small vessel disease.** *J Cereb Blood Flow Metab* 2016;36:1319–37 CrossRef Medline
 12. Opfer R, Ostwaldt AC, Walker-Egger C, et al. **Within-patient fluctuation of brain volume estimates from short-term repeated MRI measurements using SIENA/FSL.** *J Neurol* 2018;265:1158–65 CrossRef Medline
 13. Wardlaw JM, Smith EE, Biessels GJ, et al; STandards for Reporting Vascular changes on nEuroimaging (STRIVE v1). **Neuroimaging standards for research into small vessel disease and its contribution to ageing and neurodegeneration.** *Lancet Neurol* 2013;12:822–38 CrossRef Medline
 14. van Rossum G, de Boer J. **Interactively testing remote servers using the Python programming language.** *CWI Quarterly* 1991;4:283–304
 15. R Core Team. *R: A Language Environment for Statistical Computing.* R Foundation for Statistical Computing; 2020. <https://www.R-project.org>.
 16. Cleveland WS. **Robust locally weighted regression and smoothing scatterplots.** *J Am Stat Assoc* 1979;74:829–36 CrossRef
 17. Seabold S, Perktold J. **Statsmodels: econometric and statistical modeling with Python.** In: *Proceedings of the Ninth Python in Science Conference*, Austin, Texas; November 15, 2010
 18. Pedregosa F, Varoquaux G, Gramfort A, et al. **Scikit-learn: machine learning in Python.** *J Mach Learn Res* 2011;12:2825–30
 19. Rousseeuw PJ. **Silhouettes: a graphical aid to the interpretation and validation of cluster analysis.** *J Comput Appl Math* 1987;20:53–65 CrossRef
 20. Honaker J, King G, Blackwell M. **Amelia II: a program for missing data.** *J Stat Software* 2011;45:1–47 CrossRef
 21. Ruigrok AN, Salimi-Khorshidi G, Lai MC, et al. **A meta-analysis of sex differences in human brain structure.** *Neurosci Biobehav Rev* 2014;39:34–50 CrossRef Medline
 22. Duchesnay E, Hadj Seleem F, De Guio F, et al. **Different types of white matter hyperintensities in CADASIL.** *Front Neurol* 2018;9:526 CrossRef Medline
 23. Jouvent E, Alili N, Herve D, et al. **Vanishing white matter hyperintensities in CADASIL: a case report with insight into disease mechanisms.** *J Alzheimers Dis* 2020;78:907–10 CrossRef Medline

Labeling Noncontrast Head CT Reports for Common Findings Using Natural Language Processing

 M. Iorga,  M. Drakopoulos,  A.M. Naidech,  A.K. Katsaggelos,  T.B. Parrish, and  V.B. Hill



ABSTRACT

BACKGROUND AND PURPOSE: Prioritizing reading of noncontrast head CT examinations through an automated triage system may improve time to care for patients with acute neuroradiologic findings. We present a natural language-processing approach for labeling findings in noncontrast head CT reports, which permits creation of a large, labeled dataset of head CT images for development of emergent-finding detection and reading-prioritization algorithms.

MATERIALS AND METHODS: In this retrospective study, 1002 clinical radiology reports from noncontrast head CTs collected between 2008 and 2013 were manually labeled across 12 common neuroradiologic finding categories. Each report was then encoded using an n-gram model of unigrams, bigrams, and trigrams. A logistic regression model was then trained to label each report for every common finding. Models were trained and assessed using a combination of L2 regularization and 5-fold cross-validation.

RESULTS: Model performance was strongest for the fracture, hemorrhage, herniation, mass effect, pneumocephalus, postoperative status, and volume loss models in which the area under the receiver operating characteristic curve exceeded 0.95. Performance was relatively weaker for the edema, hydrocephalus, infarct, tumor, and white-matter disease models (area under the receiver operating characteristic curve > 0.85). Analysis of coefficients revealed finding-specific words among the top coefficients in each model. Class output probabilities were found to be a useful indicator of predictive error on individual report examples in higher-performing models.

CONCLUSIONS: Combining logistic regression with n-gram encoding is a robust approach to labeling common findings in noncontrast head CT reports.

ABBREVIATIONS: AUPRC = area under the precision-recall curve; AUROC = area under the receiver operating characteristic curve; NLP = natural language processing

The noncontrast head CT examination is the technique of choice in assessing patients for most acute neurologic findings.¹⁻⁴ The presence of any critical findings is not known at the time of scanning, so patients without sufficient symptoms may inadvertently wait several hours before a result is available.⁵ In this time, the patient's condition may deteriorate or the opportunity for optimal treatment may close.^{6,7} This is an unmet clinical need that could be addressed by a prioritization system that

would expedite reading of examinations with a strong likelihood of emergent findings.

Deep learning models have demonstrated broad success on medical image-classification tasks.⁸⁻¹⁰ Specifically, several deep learning models have been trained to recognize acute hemorrhages in noncontrast head CTs.¹¹⁻¹⁵ A priority system for identifying intracranial hemorrhage has been implemented on the basis of an automated screening algorithm and has demonstrated that reading wait times for hemorrhage-positive scans can be reduced without significantly affecting overall turnaround time.¹⁶ These successes indicate the potential feasibility and clinical value of prioritization systems for reading head CT examinations.¹⁷ Developing algorithms that recognize a plurality of neurologic emergencies could realize similar benefits for a larger patient population.

Although deep learning methods can deliver the high performance needed for a robust head CT screening system, they require vast amounts of labeled data for training and evaluation.¹⁸ Manual dataset labeling places an excessive burden on clinical and research staff, raising the need for an alternative approach.¹⁹ Alternatively,

Received December 9, 2021; accepted after revision March 14, 2022.

From the Departments of Radiology (M.I., M.D., T.B.P., V.B.H.) and Neurology (A.M.N.), Northwestern University Feinberg School of Medicine, Chicago, Illinois; and Departments of Biomedical Engineering (M.I., A.K.K., T.B.P.), Electrical and Computer Engineering (A.K.K.), and Computer Science (A.K.K.), Northwestern University, Chicago, Illinois.

This work was funded by the fiscal year 2020 Dixon Translational Research Grants Initiative and the Northwestern Memorial Foundation.

Please address correspondence to Michael Iorga, Suite 1600, 737 N. Michigan Ave, Chicago, Illinois 60611; e-mail: michael.iorga@northwestern.edu

 Indicates article with online supplemental data.

<http://dx.doi.org/10.3174/ajnr.A7500>

the content of clinical radiology reports can be parsed and quantitatively summarized using natural language processing (NLP) algorithms.^{20,21} Rule-based approaches are a class of NLP algorithms in which a group of domain experts generate a set of classification rules. This approach has been applied successfully to identifying intracranial hemorrhage, fracture, midline shift, and mass effect in head CT reports.²² Although rule-based approaches can be effective, creating and modifying them may require substantial effort from domain experts, and these approaches may have difficulty generalizing beyond the training dataset. Instead, classifier-based approaches for labeling radiology reports can be developed using a training dataset. This approach has also demonstrated efficacy for detecting fracture, hemorrhage, or stroke in head CT reports.²³

In this article, we present a series of NLP models for labeling noncontrast head CT images using the corresponding clinical radiology reports. Our motivation is to develop a dataset labeling technique for a broad set of common findings. This technique may be used to generate larger datasets of labeled head CT examinations, which can be used to train more advanced head CT prioritization systems. The development of high-performing screening systems for head CT examinations may ultimately reduce the time to treatment for patients with acute neurologic findings.

MATERIALS AND METHODS

Dataset Acquisition and Labeling

Radiology reports for noncontrast head CTs performed in the Chicago metropolitan area were identified through an institutional data warehouse. The reports in this search originated from a combination of inpatient, outpatient, and emergency settings. All procedures for dataset acquisition, analysis, and storage were completed in compliance with the corresponding institutional review board. Criteria for inclusion or exclusion were the following: All subjects were between the ages of 18 and 89 when scanned. All scans occurred between 2008 and 2013. No subjects were known to be pregnant at the time of scanning, determined by filtering out any report that contained the word “pregnant.” If multiple reports were created for an examination, only the most updated report was kept. Finally, all scans without a corresponding accession number were discarded so that the examination could be referenced during labeling to clarify any ambiguities in reporting. There were no further inclusion or exclusion criteria at the report level.

This search yielded a total of 97,553 reports that met the above criteria. Of these, 1002 reports were randomly selected for manual labeling. The remaining reports could not be labeled and were discarded for the remaining analysis. This sample size was chosen so that common findings have a reasonable number of positive examples in the dataset for training logistic regression. All sampled reports were included in subsequent analyses. Labeling for all findings was performed by a medical student and confirmed by a practicing, board-certified neuroradiologist. Each report was labeled across 49 finding categories (see the Online Supplemental Data for in-depth labeling information). Findings were then further grouped by disease classes, to concatenate report categories with shared language for automated labeling. Findings classes with at least 5% data frequency were kept for

further analysis: edema, fracture, hemorrhage, herniation, hydrocephalus, infarct, mass effect, tumor, chronic white matter disease (abbreviated white matter), pneumocephalus, postsurgical status, and volume loss. This approach ensures that each subsequent finding model has at least 50 positive examples for training. Together, these 12 classes create a comprehensive set of common head CT findings that may summarize the examination reading priority for most patients.

Model Design and Training

The n-gram model is a technique for encoding text as a sequence of character or word symbols.²⁴ Our modeling approach was to encode head CT reports into a vector of word n-gram counts (bag of n-grams) and to independently train a logistic regression classifier for each finding type. We chose n-grams because neuro-radiologists often repeat concise phrases across reports with specific meaning regarding imaging findings (ie, no acute intracranial hemorrhage). N-grams are particularly sensitive to these phrases and are a simple-but-powerful encoding for summarizing document content. Simple models that combine n-grams and logistic regression classifiers have shown strong performance on radiology report labeling, comparable with the performance of deep learning or generative models.^{23,24} N-gram counts were not scaled by document length (to n-gram frequency) because the language used to describe abnormal findings is typically longer than the language used to describe normal findings and adjusting for document length may attenuate this signal. The entire report was used for training, including the impression, findings, and any described clinical history. No stop words were removed because common stop words (ie, “no,” “or,” “and”) are repeated in key phrases across reports and these phrases carry important diagnostic value. All reports were split into tokens of consecutive alphanumeric characters; then, the number of unigrams, bigrams, and trigrams was counted using the Natural Language Toolkit library.²⁵

One logistic regression classifier was trained for each of the 12 common findings. Logistic regression classifiers were chosen because of their robust performance, ease of interpretability, straightforward training, and tolerance to class imbalance. Models were trained using a combination of unigrams, bigrams, and trigrams. It was found during training that increasing the gram length improved model performance, but this effect saturated once quadgrams were added. This step indicates that the additional feature space provided by quadgrams does not clearly improve linear separability, so n-grams of a higher order than trigrams were excluded. Training was performed using L2 regularization, which limits coefficient magnitude and model overinterpretation of any single n-gram. Hyperparameter tuning was performed iteratively by setting the L2 coefficient to unity and then adjusting by a factor of 10 until locally maximal performance was realized.

Three other classifier types were tested to compare performance with logistic regression: a support vector machine classifier (radial basis function kernel, regularization term = 1), a random forest classifier (100 trees, Gini impurity criterion), and a multi-layer perceptron classifier (learning rate = 1e-4, L2 penalty = 1e-5, batch size = 100). It was found that smaller multilayer perceptron architectures performed better during iterative testing, and

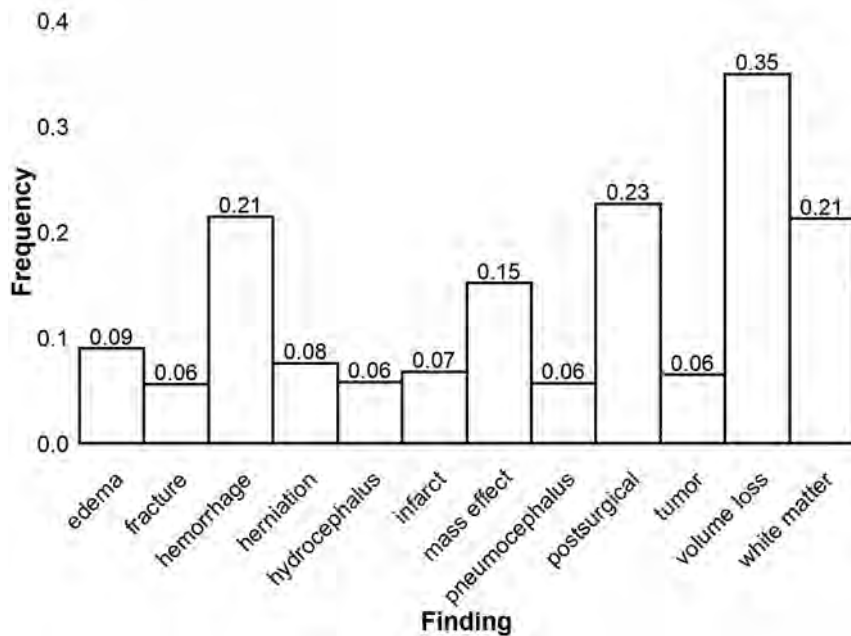


FIG 1. Frequencies of common findings. Bar lengths and numeric labels represent the frequency of each individual common finding across the labeled radiology reports. Each report may describe multiple findings or no findings at all.

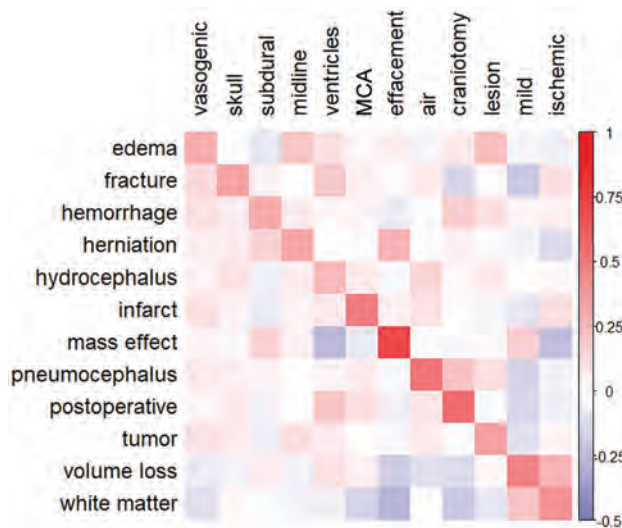


FIG 2. Model coefficient heatmap. Normalized model coefficients corresponding to selected unigrams (horizontal axis labels) are shown for each model (vertical axis labels). Red values indicate a positive association between unigram frequency and the probability of the corresponding finding. One unigram was chosen from a list of 5 n-grams with the largest coefficients in each model. Coefficient labels are ordered by model of origin (“vasogenic” is the selected unigram for the edema model, “skull” is the selected unigram for the fracture model, and so forth). Preference was given to n-grams that were closely related to the finding of interest. N-grams that contained the finding word or words were not chosen for display, though these were typically the n-grams with the highest coefficients in each model. Coefficients were normalized by row and column averages for better comparison across models because coefficients are strongly affected by the n-gram frequency and model regularization terms.

ultimately 3 layers of 32 neurons each were chosen. All models, including logistic regression, were trained using the package scikit-learn (<https://scikit-learn.org/stable/index.html>).²⁶

Statistical Analysis

Model performance was estimated by averaging the model accuracy, sensitivity, specificity, area under the receiver operating characteristic curve (AUROC), and the area under the precision-recall curve (AUPRC) across 5-fold cross-validation. Reported performance statistics correspond to the point on the receiver operating characteristic curve that maximizes the Sørensen-Dice coefficient (F1 measure), defined as the harmonic mean of the positive predictive value and specificity. This calibration step ensures that the reported results are not heavily skewed toward the majority class. Given the heavy class imbalance in our dataset, the AUROC and AUPRC are the primary outcomes for assessing model performance in this study. Each model was compared with chance using the Fisher exact

test for 2-way tables. Finally, we investigated the output probabilities of our models by iteratively removing points near the decision boundary and observing the change in error rate. Noisy labels are a barrier to training machine learning algorithms and could affect downstream models trained with a labeled dataset of head CT examinations. While training of machine learning algorithms is typically done with binary labels, training protocols that take into account class output probabilities are a possible solution to overcome the noisy labeling problem.²⁷

RESULTS

The frequencies of all 12 common findings are shown in Fig 1. Volume loss was the most frequent finding overall, described in just over one-third of all reports. The next most common findings were postsurgical status (23%), hemorrhage (21%), chronic white matter disease (21%), and mass effect (15%). The remaining findings were overall comparatively rare, occurring at a rate slightly above the inclusion threshold of 5% frequency for common findings. Expert labeling identified 223 reports with normal findings (22.3%) and 779 reports with at least 1 abnormality (77.7%). Reports with at least 1 abnormality described, on average, 2.44 of the 12 common findings. Furthermore, 97.8% of reports with abnormal findings described at least 1 of the 12 common findings.

Model Performance

The performance for each model is shown in the Online Supplemental Data. On the basis of the AUROC, the models for hemorrhage and herniation performed best (AUROC > 0.97), closely followed by those for volume loss, postsurgical status,

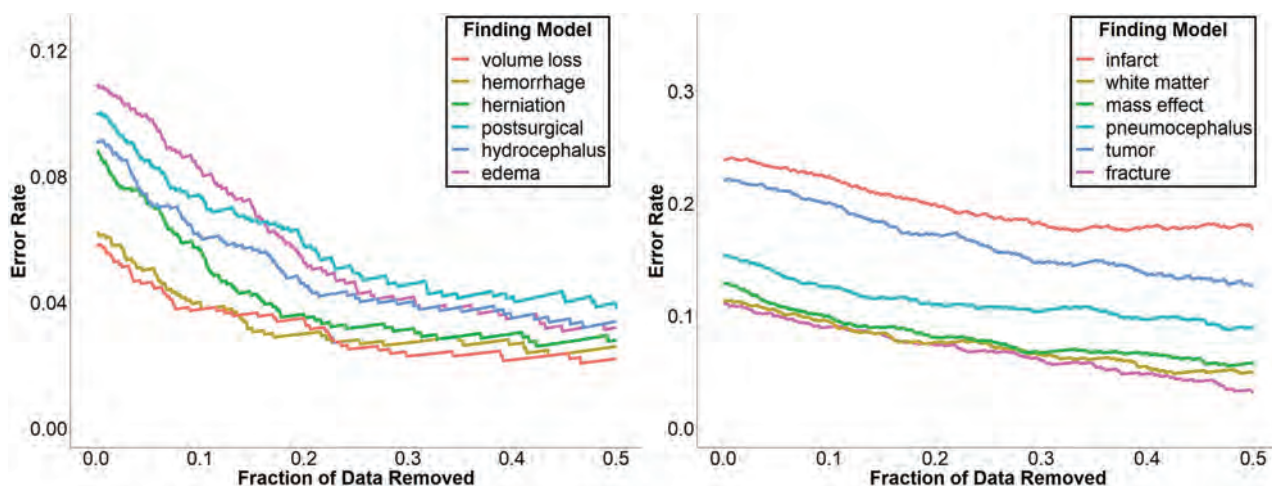


FIG 3. Visualizing model discrimination by filtering uncertain predictions. Changes in the error rate are shown for higher-performing models (*left*) and lower-performing models (*right*) when data near the decision boundary are removed. The error rate is calculated as 1 minus the model accuracy.

fracture, mass effect, and pneumocephalus (AUROC > 0.95). Receiver operating characteristic curves for each model are shown in the Online Supplemental Data. Models for detecting infarct and tumors were the weakest by all metrics. Sensitivity and specificity were relatively close for the hemorrhage and volume loss models. Otherwise, the model specificity was typically far higher than sensitivity. All models performed significantly better than chance.

Model Coefficients

A heatmap of selected model coefficients is shown in Fig 2. All models had unigrams that closely related to the finding pathology or description within the top 5 coefficients. The largest coefficients of most models were either unigrams or combinations of those same unigrams. For example, the terms “edema,” “vasogenic,” and “vasogenic edema” were among the highest for the edema model. N-grams with the most negative coefficients were generally lower in magnitude than n-grams with the most positive coefficients and were typically nonspecific or negatory (ie, “no acute intracranial” was a strongly negative trigram for the hemorrhage model). Selected coefficients had a higher magnitude for their corresponding model than for other models (visible through the red diagonal line), suggesting that each model identified important n-grams that were unique to the specific finding.

Model Output Probabilities

To better understand the validity of class output probabilities in our models, we iteratively removed data points closest to the decision boundary (ie, least certain predictions) and observed the change in the overall error rate (Fig 3). The error rate decreases for all models when uncertain predictions are removed, indicating that correct predictions are overall classified more confidently than incorrect ones. This effect is magnified for models with higher initial performance, in which the error rate tends to decrease approximately exponentially when data are removed, whereas the error rate of models with lower initial performance decreases linearly.

Classifier Comparison

The results shown above correspond to the performance of a logistic regression model. In addition, we tested the performance of support vector machines, random forests, and multilayer perceptrons for detecting findings in radiology reports. The average performance of each model across all findings is shown in the Table. See the Online Supplemental Data for the complete data. In aggregate, random forests models had the highest average AUROC and AUPRC, followed by logistic regression, support vector machines, and finally multilayer perceptrons. Logistic regression models were the most sensitive, with an average sensitivity of 0.748. However, the average performance for all models typically fell within 95% confidence bounds, except for the multilayer perceptron, which consistently underperformed the other models. On an individual finding level, logistic regression was best for hemorrhage, while random forests were best for edema, infarcts, and white matter disease.

DISCUSSION

We have presented a series of NLP models for labeling noncontrast head CT images using the corresponding radiology reports. The overall strong performance of our models suggests that the combination of n-grams and logistic regression is suitable for labeling common findings in head CT reports (Online Supplemental Data). Compared with other classifier types, logistic regression performed better than a support vector machine and a multilayer perceptron. Although random forests had higher average AUROC and AUPRC values, logistic regression significantly outperformed random forests on hemorrhage detection, which is a major application of this work. A combination of logistic regression and random forests may ultimately be a better approach.

When compared to models in a similar study by Zech et al,²³ we developed strong models for identifying fractures (AUROC: 0.951 versus 0.816–0.930) and hemorrhage (AUROC: 0.981 versus 0.918–0.945). This prior work also reported a strong model for stroke, infarction, or ischemia, which outperformed our model for infarction alone (AUROC: 0.846 versus 0.926–0.964);

Average model performance by classifier type^a

Model	LR	SVM	RF	MLP
AUROC	0.936 (0.910–0.959)	0.932 (0.907–0.954)	0.950 (0.931–0.967)	0.887 (0.848–0.922)
AUPRC	0.695 (0.610–0.779)	0.650 (0.565–0.740)	0.710 (0.626–0.792)	0.613 (0.525–0.704)
Sensitivity	0.748 (0.662–0.831)	0.679 (0.589–0.768)	0.728 (0.641–0.812)	0.660 (0.573–0.747)
Specificity	0.950 (0.935–0.964)	0.944 (0.929–0.959)	0.955 (0.940–0.968)	0.938 (0.921–0.952)
Accuracy	0.932 (0.916–0.947)	0.923 (0.906–0.938)	0.936 (0.921–0.951)	0.914 (0.896–0.930)

Note:—LR indicates logistic regression; SVM, support vector machine; RF, random forest; MLP, multilayer perceptron.

^a Average AUROC, AUPRC, sensitivity, specificity, and accuracy are shown for each model type across all findings. Numbers in parentheses are the range of values corresponding to the 95% confidence interval

however, the proportion of infarct cases within this larger combined group was not reported. This work differed in the technique for filtering stop words, as well as the choices of models and regularization penalty. Although some differences in model performance can be attributed to these methodologic differences, this attribution is difficult to infer without comparing on a shared test dataset.

While strong models were trained overall, the tumor and infarct models noticeably underperformed. Both findings have characteristics that would make them challenging to identify using our n-gram methodology. First, brain tumors are more variable in their location and underlying pathology than other findings. Reports in the tumor category were a mixture of parenchymal (20%), extra-axial (38%), osseous (22%), metastatic (16%), and orbital (4%) tumors. Because the language used to describe different types and locations of tumors is variable, it is even more challenging to collectively learn these subdivisions with a limited positive dataset (6% frequency of tumor findings).

Second, early brain infarcts can be challenging to detect on noncontrast head CT, even for experienced neuroradiologists.²⁸ While the hyperdense vessel sign is a specific infarct finding, this finding is not always present, so infarcts are often diagnosed through a combination of effacement and subtle ischemic changes such as transcortical hypoattenuation (ie, loss of gray-white matter differentiation). N-grams are limited to counting adjacent word combinations and can struggle with making inferences on combinations of findings across a report document. Higher-complexity NLP models, which can analyze subtler findings, may be necessary for identifying infarcts in radiology reports.

We demonstrated the interpretability of our models through comparison of pathologically relevant coefficient magnitudes across models (Fig 2). This comparison suggests that the model is engaging with neuroradiologic terminology and is promising for generalization to other datasets. In addition, we investigated using class output probabilities as a measure of prediction confidence and found that in stronger models, removing predictions near the decision boundary can lower the error rate substantially (Fig 3). First, this finding implies that class output probabilities contain information regarding the prediction confidence. Second, it allows creating higher-accuracy labels by discarding uncertain data. Because there is a surplus of unlabeled data in report labeling, this approach may be practical for generating higher-quality datasets.

There were several limitations encountered while performing this study. First, creating a criterion standard dataset of labeled reports is incredibly laborious, lead to a limited sample size. As a result, we lacked statistical power to assess model performance

on rarer but still important head CT findings. Concatenation of findings into 12 categories partially addressed this problem, but introducing finding heterogeneity into each category may have lowered the model performance. Second, all reports in this study originated from Northwestern Medicine medical centers. Report content and style may vary across radiologists, so additional work is needed to confirm model generalizability.

In addition to presenting models for labeling reports, we have developed a 12-dimensional framework for common head CT findings. Given the success of the already-tested head CT prioritization systems for acute intracranial hemorrhage, it may be possible to use a battery of labeling algorithms, such as those presented in this work, to develop head CT screening systems for a broader range of neuroradiologic findings.²⁹ Initial attempts at creating algorithms that detect critical findings have demonstrated that this is a challenging problem (model accuracy = 0.55) and progress may be limited by dataset labeling (NLP labeling accuracy = 0.71).³⁰ Increasing the number of labels may improve priority assessments by capturing interaction effects among findings. For example, a tumor that also presents with edema and mass effect is more severe than one that does not. Alternatively, the presence of pneumocephalus in a patient postsurgery is often expected, while an isolated pneumocephalus may have a more insidious cause and warrants higher priority.

CONCLUSIONS

Classifiers trained on n-grams demonstrated overall strong performance in detecting a broad range of neuroradiologic findings in head CT reports. Logistic regression demonstrated interpretability of model coefficients and class output probabilities. These algorithms can be used to generate large, labeled datasets of head CT examinations for training deep learning models to identify findings in images. Clinical implementation of these algorithms could support a prioritization system for reading head CT examinations and decrease the time to treatment for patients with emergent findings.

Disclosure forms provided by the authors are available with the full text and PDF of this article at www.ajnr.org.

REFERENCES

1. Buethe J, Nazarian J, Kalisz K, et al. **Neuroimaging wisely.** *AJNR Am J Neuroradiol* 2016;37:2182–88 CrossRef Medline
2. Hijaz TA, Cento EA, Walker MT. **Imaging of head trauma.** *Radiol Clin North Am* 2011;49:81–103 CrossRef Medline
3. Perry JJ, Stiell IG, Sivilotti ML, et al. **Sensitivity of computed tomography performed within six hours of onset of headache for**

- diagnosis of subarachnoid haemorrhage: prospective cohort study.** *BMJ* 2011;343:d4277 CrossRef Medline
4. Mullins ME. **Emergent neuroimaging of intracranial infection/inflammation.** *Radiol Clin North Am* 2011;49:47–62 CrossRef Medline
 5. Perotte R, Lewin GO, Tambe U, et al. **Improving emergency department flow: reducing turnaround time for emergent CT scans.** *AMIA Annu Symp Proc* 2018;2018:897–906 Medline
 6. Saver JL. **Time is brain—quantified.** *Stroke* 2006;37:263–66 CrossRef Medline
 7. McMullan JT, Knight WA, Clark JF, et al. **Time-critical neurological emergencies: the unfulfilled role for point-of-care testing.** *Int J Emerg Med* 2010;3:127–31 CrossRef Medline
 8. Topol EJ. **High-performance medicine: the convergence of human and artificial intelligence.** *Nat Med* 2019;25:44–56 CrossRef Medline
 9. Yasaka K, Abe O. **Deep learning and artificial intelligence in radiology: current applications and future directions.** *PLoS Med* 2018;15:e1002707 CrossRef Medline
 10. Yao AD, Cheng DL, Pan I, et al. **Deep learning in neuroradiology: a systematic review of current algorithms and approaches for the new wave of imaging technology.** *Radiol Artif Intell* 2020;2:e190026 CrossRef Medline
 11. Lee H, Yune S, Mansouri M, et al. **An explainable deep-learning algorithm for the detection of acute intracranial haemorrhage from small datasets.** *Nat Biomed Eng* 2019;3:173–82 CrossRef Medline
 12. Kuo W, Häne C, Mukherjee P, et al. **Expert-level detection of acute intracranial hemorrhage on head computed tomography using deep learning.** *Proc Natl Acad Sci U S A* 2019;116:22737–45 CrossRef Medline
 13. Chang PD, Kuoy E, Grinband J, et al. **Hybrid 3D/2D convolutional neural network for hemorrhage evaluation on head CT.** *AJNR Am J Neuroradiol* 2018;39:1609–16 CrossRef Medline
 14. Wang D, Wang C, Masters L, et al. **Masked multi-task network for case-level intracranial hemorrhage classification in brain CT.** *Med Image Comput Assist Interv* 2020;145–54 CrossRef
 15. Heit JJ, Coelho H, Lima FO, et al. **Automated cerebral hemorrhage detection using RAPID.** *AJNR Am J Neuroradiol* 2021;4:273–78 CrossRef Medline
 16. O'Connor SD, Bhalla M. **Should artificial intelligence tell radiologists which study to read next?** *Radiol Artif Intell* 2021;3:e210009 CrossRef Medline
 17. O'Neill TJ, Xi Y, Stehel E, et al. **Active reprioritization of the reading workload using artificial intelligence has a beneficial effect on the turnaround time for interpretation of head CT with intracranial hemorrhage.** *Radiol Artif Intell* 2021;3:e200024 CrossRef Medline
 18. Esteva A, Robicquet A, Ramsundar B, et al. **A guide to deep learning in healthcare.** *Nat Med* 2019;25:24–29 CrossRef Medline
 19. Willeminck MJ, Koszek WA, Hardell C, et al. **Preparing medical imaging data for machine learning.** *Radiology* 2020;295:4–15 CrossRef Medline
 20. Pons E, Braun LM, Hunink MG, et al. **Natural language processing in radiology: a systematic review.** *Radiology* 2016;279:329–43 CrossRef Medline
 21. Alex B, Grover C, Tobin R, et al. **Text mining brain imaging reports.** *J Biomed Semantics* 2019;10:23 CrossRef Medline
 22. Chilamkurthy S, Ghosh R, Tanamala S, et al. **Deep learning algorithms for detection of critical findings in head CT scans: a retrospective study.** *Lancet* 2018;392:2388–96 CrossRef Medline
 23. Zech J, Pain M, Titano J, et al. **Natural language-based machine learning models for the annotation of clinical radiology reports.** *Radiology* 2018;287:570–80 CrossRef Medline
 24. Barash Y, Guralnik G, Tau N, et al. **Comparison of deep learning models for natural language processing-based classification of non-English head CT reports.** *Neuroradiology* 2020;62:1247–56 CrossRef Medline
 25. Bird S, Klein E, Loper E. *Natural Language Processing with Python: Analyzing Text with the Natural Language Toolkit.* O'Reilly; 2009
 26. Garreta R, Moncecchi G. *Learning scikit-learn: Machine Learning in Python.* Packt Publishing; 2013
 27. Karimi D, Dou H, Warfield SK, et al. **Deep learning with noisy labels: exploring techniques and remedies in medical image analysis.** *Med Image Anal* 2020;65:101759 CrossRef Medline
 28. Mokli Y, Pfaff J, dos Santos DP, et al. **Computer-aided imaging analysis in acute ischemic stroke: background and clinical applications.** *Neurol Res Pract* 2019;1 CrossRef Medline
 29. Prevedello LM, Erdal BS, Ryu JL, et al. **Automated critical test findings identification and online notification system using artificial intelligence in imaging.** *Radiology* 2017;285:923–31 CrossRef Medline
 30. Titano JJ, Badgeley M, Schefflein J, et al. **Automated deep-neural-network surveillance of cranial images for acute neurologic events.** *Nat Med* 2018;24:1337–41 CrossRef Medline

Antithrombotic Treatment after Carotid Stenting in Patients with Concomitant Atrial Fibrillation

 B. Pardo-Galiana,  M. Medina-Rodriguez,  M. Millan-Vazquez,  J.A. Cabezas-Rodriguez,  L. Lebrato-Hernandez,  L. Ainz-Gomez,  E. Zapata-Arriaza,  J. Ortega,  A. de Albóniga-Chindurza,  J. Montaner,  A. Gonzalez, and  F. Moniche



ABSTRACT

BACKGROUND AND PURPOSE: Antithrombotic therapy following carotid artery stent placement with concomitant atrial fibrillation is not well-established. Our aim was to assess the safety and efficacy of the combination of direct oral anticoagulants and a P2Y12 inhibitor at 30 days after carotid artery stent placement in patients with atrial fibrillation.

MATERIALS AND METHODS: We designed an observational single-center study including patients who underwent carotid artery stent placement with concomitant atrial fibrillation. We studied 3 groups according to antithrombotic therapy: 1) the direct oral anticoagulants plus clopidogrel (DC) group: receiving direct oral anticoagulants plus a P2Y12 inhibitor; 2) the triple therapy group: anticoagulation and dual antiplatelet therapy; and 3) the dual antiplatelet therapy group: following dual antiplatelet therapy alone. The safety outcome was a major or clinically relevant non-major bleeding event at the first month. The efficacy outcomes were the thromboembolic events (myocardial infarction, stroke, systemic embolism, or stent thrombosis).

RESULTS: Of 959 patients with carotid artery stent placement, 91 met the inclusion criteria, including 24 patients in the DC group, 42 patients in the triple therapy group, and 25 in the dual antiplatelet therapy group. The mean age was 72.27 (SD, 8.1) years, with similar baseline characteristics. The median CHA₂DS₂-VAsc score for each group was 6 (interquartile range = 5–6), 5 (interquartile range = 4–6), and 5 (interquartile range = 4–6), respectively. The median HAS-BLED score was 4 in the 3 groups ($P = .17$). The primary safety end point was 23.8% in the triple therapy group compared with 4% in the dual antiplatelet therapy group ($P = .032$), with no bleeding events in the DC group ($P = .007$). There was 1 stent thrombosis in DC group and a cardioembolic stroke in the dual antiplatelet therapy group ($P = .41$).

CONCLUSIONS: Among patients with carotid artery stent placement with atrial fibrillation, triple therapy confers a high bleeding risk. A regimen of direct oral anticoagulants plus a P2Y12 inhibitor might confer a good safety profile with significantly lower rates of bleeding and optimal efficacy.

ABBREVIATIONS: AF = atrial fibrillation; CAS = carotid artery stent placement; CS = carotid stenosis; DAPT = dual antiplatelet therapy; DC = DOAC plus clopidogrel; DOAC = direct oral anticoagulants; ICH = intracerebral hemorrhage; PCI = percutaneous coronary intervention; TT = triple therapy

Carotid stenosis (CS) represents approximately 12%–19.3% of acute ischemic strokes.¹ During the past decade, carotid artery stent placement (CAS) has emerged as an alternative treatment option for CS when carotid endarterectomy is not feasible or as a first-line therapy.² After CAS, patients should follow a dual antiplatelet therapy (DAPT) regimen with aspirin and

clopidogrel from 1–3 months to minimize the risks of acute stent thrombosis secondary to platelet activation triggered by intimal injury and/or insertion of a foreign body (stent).³ However, when atrial fibrillation (AF) coexists, the best approach is yet to be elucidated. According to a recent meta-analysis, 12% of patients with AF have a moderate-severe CS, which doubles the risk of stroke in patients with AF after adjustment for classic clinical risk factors and antithrombotic therapy.^{4,5}

Received December 14, 2021; accepted after revision February 9, 2022.

From the Stroke Unit (B.P.-G., M.M.-R., J.A.C.-R., L.L.-H., L.A.-G., F.M.), Neurology Department (M.M.-V.), and Interventional Neuroradiology Unit (E.Z.-A., J.O., A.d.A.-C., A.G.), Radiology Department, University Hospital Virgen del Rocío, Seville, Spain; Neurovascular Lab (B.P.-G., M.M.-R., J.A.C.-R., L.L.-H., L.A.-G., E.Z.-A., J.O., A.d.A.-C., J.M., A.G., F.M.), Biomedicine Institute of Seville, Seville, Spain; and Stroke Unit (J.M.), Neurology Department, University Hospital Virgen Macarena, Seville, Spain.

This work was supported by the Instituto de Salud Carlos III (PI15/01197, PI18/01414, RD16/0019/0015 and CM21/00096), and cofunded by the European Regional Development Fund/European Social Fund, “A way to make Europe/Investing in your future”.

B. Pardo-Galiana and M. Medina-Rodriguez contributed equally to this work.

Please address correspondence to Francisco Moniche, MD, PhD, Stroke Unit, University Hospital Virgen del Rocío and Biomedicine Institute of Seville, Av/ Manuel Siurot S/N, 41013 Seville, Spain; e-mail: pmoniche@gmail.com; @pmoniche

 Indicates open access to non-subscribers at www.ajnr.org

 Indicates article with online supplemental data.

<http://dx.doi.org/10.3174/ajnr.A7482>

In this setting, DAPT plus oral anticoagulation is expected to be the most effective approach, but with an increment of bleeding rates. On the other hand, oral anticoagulation or DAPT alone may not be effective enough to prevent stent thrombosis or embolic events, respectively. Nevertheless, no clinical trials have addressed this question before. By contrast, 3 randomized clinical trials including patients with AF and a recent acute coronary syndrome or percutaneous coronary intervention (PCI) treated with a P2Y12 inhibitor and direct oral anticoagulants (DOACs) without aspirin resulted in less bleeding without an increment in the incidence of ischemic events compared with regimens that included a vitamin K antagonist, aspirin, or both.⁶⁻⁸

Our aim was to compare 3 different antithrombotic regimens: DOAC plus a P2Y12 inhibitor, anticoagulation plus DAPT, or DAPT alone in patients undergoing CAS with concomitant AF in a daily clinical practice.

MATERIALS AND METHODS

Study Strategy

The present study is a retrospective observational single-center study including patients undergoing CAS in a comprehensive stroke center from 2010 to March 2021. We included patients who met all the following criteria: previous, persistent, permanent, or paroxysmal nonvalvular AF; TIA or minor/mild stroke secondary to atherosclerotic CS who underwent CAS as secondary prevention or asymptomatic CS with revascularization criteria; and planned use of a P2Y12 inhibitor for at least 1 month. To stratify the risk of stroke among patients with AF, we assessed the CHA₂DS₂-VASc scores. The bleeding risk was measured by the HAS-BLED scores.

Data Collection

Baseline variables and ultrasound findings were prospectively recorded. Outcomes were retrospectively collected. The reporting of this study conforms to the STrengthening the Reporting of OBServational studies in Epidemiology (STROBE; <https://www.strobe-statement.org/>) statement (for the STROBE checklist of this study). The study was approved by the local ethics committee (University Hospital Virgen del Rocío Ethic Committee/1431-N-21) and followed the Declaration of Helsinki Ethical principles of medical research involving human subjects.

Regimen Strategy

We established 3 groups according to antithrombotic regimen: 1) DOAC plus clopidogrel (DC group), 2) DAPT with clopidogrel and aspirin plus anticoagulation (triple therapy [TT] group), and 3) DAPT with clopidogrel and aspirin alone (DAPT group). The direct oral anticoagulant doses administered to the DC group were rivaroxaban, 15 mg once daily, apixaban, 5 mg twice daily (2.5 mg daily if dose-reduction criteria were required), and dabigatran, 110 mg twice daily. The antithrombotic regimen was established by stroke physician criteria 24 hours after CAS. Clopidogrel was stopped at 1 month after CAS in patients included in the TT and DAPT groups and was switched to aspirin in patients in the DC group.

CAS

Patients were treated with double antithrombotic therapy for at least 5 days (aspirin, 100 mg/day, and clopidogrel, 75 mg/day)

before CAS or were treated with a loading dose of clopidogrel (300 mg) and aspirin (300 mg). Anticoagulation was stopped 24 hours before CAS and restored within 24 hours after CAS, except in those treated with DAPT alone. Predilation of the stenosis with a 2- to 4-mm balloon catheter was performed previous to a self-expanding stent being deployed. Postdilation with a 5- to 6-mm balloon was performed in cases with residual stenosis. Heparin was administered systematically during the procedure to maintain an activated clotting time between 250 and 300 seconds.

Follow-up Assessments

Neurologic and systemic evaluation was performed the day before the procedure, immediately after CAS, 24 hours after intervention, and at 1-month follow-up. On days 1 and 30 after CAS, a carotid ultrasound was performed to rule out stent thrombosis or restenosis.

Outcome Measures

The safety end point was major or clinically relevant nonmajor bleeding as defined by the International Society on Thrombosis and Haemostasis. Major bleeding was defined by the International Society on Thrombosis and Haemostasis as bleeding that resulted in death, occurred in a critical organ (intracranial, intraspinal, intraocular, retroperitoneal, intra-articular, intramuscular with compartment syndrome, or pericardial), or was associated with either a decrease in the hemoglobin level of at least 2 g/dL or a transfusion of at least 2 U of packed red cells. Clinically relevant nonmajor bleeding was defined as bleeding that resulted in hospitalization, medical or surgical intervention for bleeding, an unscheduled clinic visit, or a change in physician-directed antithrombotic therapy.⁹

The efficacy end point was stroke recurrence at 30 days from CAS or any ischemic event (myocardial infarction, stent thrombosis, stroke, and systemic embolism).

Statistical Analysis

Values for continuous variables with a normal distribution are presented as mean (SD), and 2-sample *t* tests were performed for comparisons. The Mann-Whitney test and medians and interquartile ranges were used for non-normal distributions. Categorical variables were analyzed with the χ^2 test or the Fisher exact test, as appropriate. We used SPSS 25.0 (IBM), with *P* < .05 considered statistically significant.

RESULTS

We analyzed 959 patients from 2010 to March 2021, of whom 91 met all the inclusion criteria (DC group = 24 patients, TT group = 42 patients, and DAPT group = 25 patients). Sixty-nine patients (75.82%) had symptomatic CS (DC group = 21, TT group = 31, and DAPT group = 17). The baseline characteristics are summarized in Table 1. The mean age was 72.27 (SD, 8.1) years, and 17.6% of the patients were women. The mean CHA₂DS₂-VASc score was 5.3 (SD, 1.3), and the mean HAS-BLED score was 3.9 (SD, 0.9). Among patients in the DC group, rivaroxaban was administered in 13 patients; apixaban, in 6 patients; and dabigatran, in 5. In TT group, 21 patients received vitamin K antagonists; 7 patients, low-molecular-weight heparin; and 14, DOAC (7 rivaroxaban, 4 dabigatran, and 3 apixaban). Clopidogrel was the P2Y12 inhibitor in the 3 groups (Fig 1).

Table 1: Baseline characteristics

	Total (n = 91)	DC Group (n = 24)	TT Group (n = 42)	DAPT Group (n = 25)	P
Age (mean) (SD) (yr)	72.27 (SD, 8.1)	72.4 (SD, 6.7)	72.6 (SD, 9)	71.6 (SD, 8.3)	.9
Female sex (No.) (%)	16 (17.6)	6 (25)	8 (19)	2 (8)	.119
CHA ₂ DS ₂ -VASc score (mean)	5.3 (SD, 1.3)	5.5 (SD, 1.1)	5.1 (SD, 1.4)	5.3 (SD, 1.4)	.548
HAS-BLED score (mean)	3.9 (SD, 0.9)	3.8 (SD, 0.6)	3.8 (SD, 0.9)	4.24 (SD, 0.9)	.168
Hypertension (No.) (%)	79 (86.8)	22 (91.7)	35 (83.3)	22 (88)	.616
Diabetes mellitus (No.) (%)	44 (48.4)	14 (58.3)	15 (35.7)	15 (60)	.082
Dyslipidemia (No.) (%)	68 (74.7)	20 (83.3)	31 (73.8)	17 (68)	.459
Heart failure (No.) (%)	41 (45.1)	14 (58.3)	17 (40.5)	10 (40)	.313
Smoker (No.) (%)	23 (25.27)	6 (25)	7 (16.7)	10 (40)	.1
Peripheral arteriopathy (No.) (%)	18 (18.5)	3 (12.5)	6 (25)	9 (36)	.57
Serum creatinine levels (No.) (%)					
<1.5 mg/dL	79 (86.8)	19 (79.2)	40 (95.2)	20 (80)	.956
≥1.5 mg/d	2 (13.2)	5 (20.8)	2 (4.8)	5 (20)	

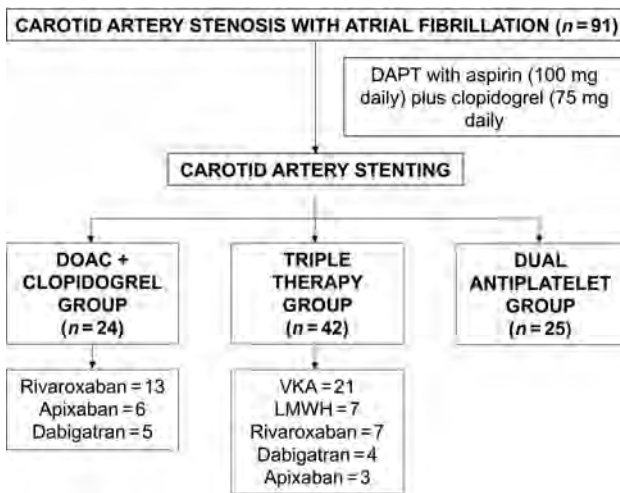


FIG 1. Antithrombotic strategy management. LMWH indicates low-molecular-weight heparin; VKA, vitamin K antagonist.

Safety Outcomes

At 1 month, 10 of 42 patients (23.8%) receiving triple therapy had a major or clinically relevant nonmajor bleeding event, compared with 1 of 24 (4%) receiving DAPT ($P = .032$) and no bleeding event in the DC group ($P = .007$) (Table 2). A major bleeding did not occur either in the DC or DAPT group, compared with 4 major bleeding events in the TT group (Online Supplemental Data). An intracranial hemorrhage was reported in the TT group.

Efficacy Outcomes

Neither systemic embolisms, myocardial infarction, nor stroke were reported in the TT group at 1 month after CAS. One patient in the DC group was hospitalized with minor stroke symptoms due to carotid stent thrombosis. In a patient included in DAPT group in whom a CAS in the right carotid artery was performed, a cardioembolic stroke involving the contralateral MCA was reported (Table 2).

DISCUSSION

To the best of our knowledge, our study evaluates, for the first time, the safety and efficacy of 3 different antithrombotic regimens in patients undergoing CAS with concomitant AF, including a combination of DOAC plus clopidogrel. Our study showed that

the regimen of DOAC plus clopidogrel during the first month resulted in a lower risk of a major or clinically relevant nonmajor bleeding event than the usual regimen with triple therapy, with no increment of thromboembolic events.

Regimens including DOAC therapy appear to offer the potential for less bleeding over the vitamin K antagonists in patients who underwent PCI.¹⁰ The Open-Label, Randomized, Controlled, Multicenter Study Exploring Two Treatment Strategies of Rivaroxaban and a Dose-Adjusted Oral Vitamin K Antagonist Treatment Strategy in Subjects with Atrial Fibrillation who Undergo Percutaneous Coronary Intervention (PIONEER AF-PCI) trial showed that a regimen involving low doses of rivaroxaban (15 mg once daily or 2.5 mg twice daily) plus a P2Y12 inhibitor had a lower incidence of bleeding rates compared with a regimen of vitamin K antagonist and DAPT.⁷ The Randomized Evaluation of Dual Anti-thrombotic Therapy with Dabigatran versus Triple Therapy with Warfarin in Patients with Nonvalvular Atrial Fibrillation Undergoing Percutaneous Coronary Intervention (REDUAL PCI) trial demonstrated that a regimen of dabigatran plus a P2Y12 inhibitor conferred lower rates of bleeding than triple therapy.⁸ Similar results were seen in the AUGUSTUS trial, in which the use of apixaban plus a P2Y12 inhibitor had a better safety profile than regimens that included a vitamin K antagonist, aspirin, or both.⁶ The decrement of bleeding risk was accompanied by similar thrombotic events as well. Because patients having undergone CAS usually have a higher risk of bleeding than patients having undergone PCI, the combination of DOAC plus clopidogrel might be also effective in our patients (Fig 2).

For the primary safety outcome of major or clinically relevant nonmajor bleeding at 30 days, a significant difference risk of 23.8% between a regimen of DOAC plus clopidogrel and a triple therapy was detected. Major bleeding was reported neither in the DC group nor the DAPT group. Patients included in our study had a specifically high risk of intracerebral hemorrhage (ICH) due to the following reasons: 1) recent previous stroke symptoms, 2) risk of developing hyperperfusion syndrome, and 3) a high HAS-BLED score. Nevertheless, ICH occurred in neither the DC group nor the DAPT group. Our findings support this regimen possibly providing a good safety profile in patients with AF in whom CAS is performed. There were no statistically significant differences in efficacy end points. However, a stent thrombosis that occurred in the DC group might have been related to

Table 2: Safety and efficacy outcomes

	DC Group	TT Group	DAPT Group	P
Major or clinically relevant nonmajor bleeding (No.) (%)	0	10 (23.8)	1 (4)	.006
Major bleeding (No.) (%)	0	4 (9.5)	0	.138
Efficacy outcome				
Stroke (No.) (%)	0	0	1 (4)	.41
Stent thrombosis (No.) (%)	1 (4.1)	0	0	

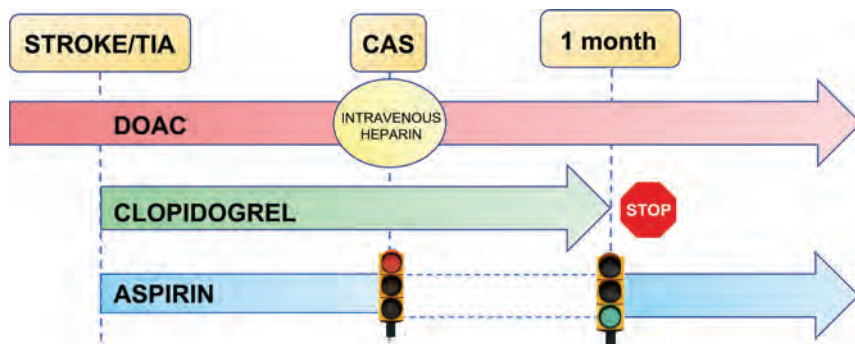


FIG 2. Management recommendations in patients undergoing CAS with concomitant AF. Once CS (if suitable for CAS) is diagnosed, we recommend dual antiplatelet therapy (aspirin and clopidogrel) plus anticoagulation with a DOAC at least 5 days before CAS. Anticoagulation should be stopped 24 hours before CAS and re-initiated 24 hours after. According to antiplatelet therapy after CAS, we recommend a regimen including DOAC plus clopidogrel during the first month after CAS and then switching clopidogrel to aspirin.

insufficient antiplatelet therapy or clopidogrel resistance. Also, a stroke was observed in the DAPT group, probably related to the absence of anticoagulation therapy. Our results suggest a balance of the risk of bleeding and the prevention of stent thrombosis or embolic events.

To our knowledge, there is only 1 report addressing this question to compare with our results.¹¹ The authors included 31 patients, of whom 14 received a DOAC plus a single antiplatelet therapy (aspirin or clopidogrel) with no bleeding event described. By contrast, in only 1 of 17 (5.9%) patients receiving vitamin K antagonists plus DAPT was a bleeding event reported. The low bleeding event rate might be related to either the INR target (1.5–2) compared with our higher INR target (2–3) or to the smaller sample size.

Our study has several limitations. This was a retrospective, nonrandomized study in which the choice of each antithrombotic regimen was uncontrolled. However, the treatment eligibility criteria were not related to bleeding or thrombotic risk because CHA₂DS₂-VASC and HAS-BLED scores were similar within groups, but they were due to publication of this new regimen in patients with AF undergoing PCI because 87.5% of patients in the DC group were included from 2017. In addition, we did not perform an evaluation of antiplatelet effects in our patients. Although the small sample size impedes obtaining robust evidence in terms of efficacy compared with triple therapy, it may allow setting up a hypothesis of a novel management in patients undergoing CAS with AF.

CONCLUSIONS

In patients who are eligible for CAS with concomitant AF, a regimen of triple therapy confers a high bleeding risk. Another regimen such as DOAC plus a P2Y₁₂ inhibitor, similar to that in patients undergoing PCI with concomitant AF, might confer a good safety profile with an optimal efficacy. A randomized clinical trial should be conducted to confirm the efficacy and safety of this therapy.

Disclosure forms provided by the authors are available with the full text and PDF of this article at www.ajnr.org.

REFERENCES

- Kolominsky-Rabas PL, Weber M, Gefeller O, et al. Epidemiology of ischemic stroke subtypes according to TOAST criteria: incidence, recurrence, and long-term survival in ischemic stroke subtypes: a population-based study. *Stroke* 2001;32:2735–40 CrossRef Medline
- Cole TS, Mezher AW, Catapano JS, et al. Nationwide trends in carotid endarterectomy and carotid artery stenting in the Post-CREST era. *Stroke* 2020;51:579–87 CrossRef Medline
- Sussman ES, Jin M, Pendharkar AV, et al. Dual antiplatelet therapy after carotid artery stenting: trends and outcomes in a large national database. *J Neurointerv Surg* 2021;13:8–13 CrossRef Medline
- Noubiap JJ, Agbaedeng TA, Ndoadoumgue AL, et al. Meta-analysis comparing the frequency of carotid artery stenosis in patients with atrial fibrillation and vice versa. *Am J Cardiol* 2021;138:72–79 CrossRef Medline
- Lehtola H, Airaksinen EJ, Hartikainen P, et al. Stroke recurrence in patients with atrial fibrillation: concomitant carotid artery stenosis doubles the risk. *Eur J Neurol* 2017;24:719–25 CrossRef Medline
- Lopes RD, Vora AN, Massaro T, et al. Antithrombotic therapy after acute coronary syndrome or PCI in atrial fibrillation. *N Engl J Med* 2019;380:1509–24 CrossRef Medline
- Gibson CM, Mehran R, Bode C, et al. Prevention of bleeding in patients with atrial fibrillation undergoing PCI. *N Engl J Med* 2016;375:2423–34 CrossRef Medline
- Cannon CP, Bhatt DL, Oldgren J, et al. Dual antithrombotic therapy with dabigatran after PCI in atrial fibrillation. *N Engl J Med* 2017;377:1513–24 CrossRef Medline
- Schulman S, Anger SU, Bergqvist D, et al. Subcommittee on Control of Anticoagulation of the Scientific and Standardization Committee of the International Society on Thrombosis and Haemostasis. Definition of major bleeding in clinical investigations of antihemostatic medicinal products in surgical patients. *J Thromb Haemost* 2010;8:202–04 CrossRef Medline
- Ruff CT, Giugliano RP, Braunwald E, et al. Comparison of the efficacy and safety of new oral anticoagulants with warfarin in patients with atrial fibrillation: a meta-analysis of randomised trials. *Lancet* 2014;383:955–62 CrossRef Medline
- Nii K, Takemura Y, Inoue R, et al. Safety of direct oral anticoagulant and antiplatelet therapy in patients with atrial fibrillation treated by carotid artery stenting. *J Stroke Cerebrovasc Dis* 2020;29:10–15 CrossRef Medline

Angiographically Occult Subarachnoid Hemorrhage: Yield of Repeat Angiography, Influence of Initial CT Bleed Pattern, and Sources of Diagnostic Error in 242 Consecutive Patients

I. Nguyen, M.T. Caton, D. Tonetti, A. Abla, A. Kim, W. Smith, and S.W. Hetts



ABSTRACT

BACKGROUND AND PURPOSE: Nearly 20% of patients with spontaneous SAH have no definitive source on initial DSA. The purpose of this study was to investigate the timing and yield of repeat DSA, to clarify the influence of initial CT bleed pattern, and to characterize sources of diagnostic error in this scenario.

MATERIALS AND METHODS: We evaluated the yield of repeat DSA and clinical outcomes stratified by hemorrhage pattern on CT in consecutive patients with nontraumatic SAH with negative initial DSA findings at a referral center. Cases in which the culprit lesion was subsequently diagnosed were classified as physiologically occult (ie, undetectable) on the initial DSA, despite adequate technique and interpretation or misdiagnosed due to operator-dependent error.

RESULTS: Two hundred forty-two of 1163 (20.8%) patients with spontaneous SAH had negative initial DSA findings between 2009 and 2018. The SAH CT pattern was nonperimesencephalic (41%), perimesencephalic (36%), sulcal (18%), and CT-negative (5%). Repeat DSA in 135/242 patients (55.8%) revealed a source in 10 patients (7.4%): 4 saccular aneurysms, 4 atypical aneurysms, and 2 arteriovenous shunts. The overall yield of repeat DSA was 11.3% with nonperimesencephalic and 2.2% for perimesencephalic patterns. The yield of the second and third DSAs with a nonperimesencephalic pattern was 7.7% and 12%, respectively. Physiologically occult lesions accounted for 6/242 (2.5%) and operator-dependent errors accounted for 7/242 (2.9%) of all angiographically occult lesions on the first DSA.

CONCLUSIONS: Atypical aneurysms and small arteriovenous shunts are important causes of SAH negative on angiography. Improving DSAs technique can modestly reduce the need for repeat DSA; however, a small fraction of SAH sources remain occult despite adequate technique. These findings support the practice of repeating DSA in patients with a nonperimesencephalic SAH pattern.

ABBREVIATIONS: NPM = nonperimesencephalic; PM = perimesencephalic

DSA is the criterion standard for detecting cerebral aneurysms and other sources of spontaneous SAH. However, approximately 15%–20% of patients with spontaneous (atraumatic) SAH have negative findings on the initial angiogram.^{1,2} In these cases, second and sometimes third catheter angiograms may be necessary to guide management. Previous studies estimated that source lesions are identified in 2%–17% of these cases when DSA is repeated.^{3–5} This yield may be influenced by the blood distribution

on CT, which can be categorized as perimesencephalic (PM), diffuse nonperimesencephalic (NPM), sulcal, or radiologically negative (eg, diagnosed by CSF examination).⁶ To date, the predictive value of the CT SAH pattern on the diagnostic yield of repeat DSA is uncertain, but this information could refine and simplify algorithms for repeating DSA in this population.

The initial DSA can yield false-negative results for a variety of reasons, which can be broadly categorized as physiologic (ie, obscuration due to vasospasm, thrombosis, or hematoma) or operator-dependent (eg, inadequate projections, magnification, or patient motion). Several schemata exist for framing and contextualizing operator-dependent error in diagnostic imaging.^{7–9} For example, Bruno et al¹⁰ proposed 2 principal error subtypes: perceptual and interpretive (cognitive). However, a systematic approach to error has not been applied to DSA in the context of occult, spontaneous SAH.

The purpose of this study was, therefore, 2-fold: First, we aimed to quantify the diagnostic yield of repeat DSA in patients with spontaneous SAH, accounting for differences in the CT

Received December 13, 2021; accepted after revision February 9, 2022.

From the Department of Neurology (I.N.), University of California, Davis, Sacramento, California; Departments of Neurology (I.N., A.K., W.S.), Radiology and Biomedical Imaging (M.T.C., S.W.H.), and Neurological Surgery (D.T., A.A.), University of California, San Francisco, San Francisco, California.

I. Nguyen and M.T. Caton contributed equally to the manuscript.

Please address correspondence M. Travis Caton, MD, University of California, 505 Parnassus Ave, Third Floor, Room L-349, San Francisco, CA 94143; e-mail: michael.caton2@ucsf.edu; @traviscaton; @DanTonettiMD; @UCSF_NIR; @NeurosurgUCSF; @neurores_ucsf

Indicates article with online supplemental data.

<http://dx.doi.org/10.3174/ajnr.A7483>

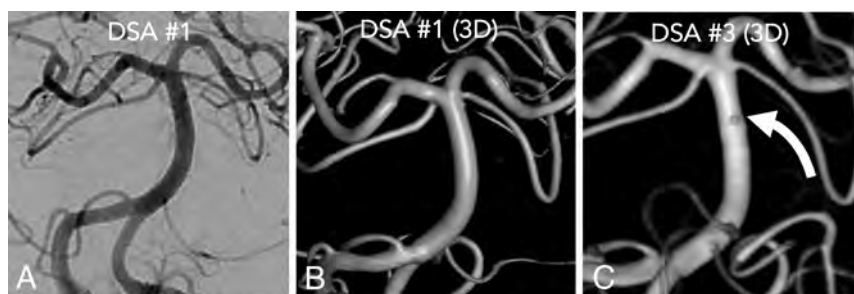


FIG 1. A 78-year-old woman with an example of a physiologically occult aneurysm on the initial DSA on the postbleed day 1. A frontal projection (A) with 3D reconstruction shows no source lesion (B). A second DSA on postbleed day 6 had normal findings. The patient was discharged and re-presented with worsening headache on postbleed day 12. A third DSA on postbleed day 12 (C) demonstrated a submillimeter basilar artery perforator blister aneurysm (curved white arrow) that was clipped.

blood distribution pattern. Second, we estimated the fraction of these cases that are attributable to physiologic versus operator-dependent factors and presented a framework for classifying diagnostic error in this setting.

MATERIALS AND METHODS

We performed a retrospective cohort study at a single, tertiary, academic medical center of consecutive adults (older than 18 years of age) admitted with SAH between January 1, 2009, and December 31, 2018. This study was approved by the local institutional review board with a waiver of informed consent. Patients were excluded if there was evidence of trauma or primarily intraparenchymal or intraventricular hemorrhage.

Clinical data were abstracted from the electronic health record, including demographics and risk factors for SAH (Online Supplemental Data). In addition to the CT hemorrhage pattern, the initial Hunt & Hess scores, modified Fisher grade, external ventricular drain placement, ventriculoperitoneal shunt placement, vasospasm, delayed cerebral ischemia, and rebleed events were documented.

DSA was performed in each case by an experienced neurointerventionalist in 1 of 3 biplane angiography suites (Artis Q or zee; Siemens). MRA of the brain and cervical spine was performed after initial negative findings on DSA. The decision to perform repeat DSA was determined by multidisciplinary consensus. The yield of identifying a vascular source was assessed for repeat DSA and MR imaging.

Neuroradiologic Review and Classification of Diagnostic Error on Initial DSA

Baseline head CT images were reviewed and categorized into 4 groups by a neuroradiologist on the basis of the SAH pattern: 1) diffuse NPM, 2) PM, 3) sulcal, or 4) CT-negative but confirmed by CSF examination. PM SAH was defined as hemorrhage limited to the prepontine, suprasellar, ambient, crural, and/or quadrigeminal cisterns without significant extension into the Sylvian or interhemispheric fissures according to the criteria of van Gijn et al.⁶

In each case in which a diagnosis was revealed only with repeat DSA or surgical exploration, the initial DSA (reported as having negative findings) was scrutinized independently by 2 neurointerventionalists. Lesions that were retrospectively evident were

classified as operator-dependent errors and subclassified as technical or cognitive errors. The cognitive error categories were further subdivided into specific error classes according to the framework of Bruno et al.¹⁰ When no diagnostic error was detected, the lesion was considered physiologically occult, meaning that the lesion could truly not be detected despite optimal technique and interpretation.

Statistical comparison of continuous variables between groups was assessed with the Student *t* test, the Mann-Whitney *U* test, or ANOVA.

Frequency data were compared using the Fisher exact test, and $P < .05$ was considered significant. Statistical analyses were performed using R statistical and computing software (Version 3.6.2; <http://www.r-project.org/>).

RESULTS

Patient Cohort Clinical Characteristics

During the 10-year study period, 242/1163 (20.8%) patients with spontaneous SAH had negative initial DSA findings. A visual summary of the characteristics and diagnostic results of these selected 242 patients is provided in the Online Supplemental Data. One hundred twenty-two were women (50.4%), and the mean age was 56 years (range, 18–91 years). The Hunt & Hess scores were grade 1 in 53 patients (22%), grade 2 in 143 patients (59%), grade 3 in 26 patients (11%), grade 4 in 8 patients (3%), and grade 5 in 8 patients (3%). The SAH pattern on the initial head CT was NPM in 41%, PM in 36%, sulcal in 18%, and CT-negative in 5% (Online Supplemental Data). Most patients were transferred from an outside hospital (214/242, 88%). Patients with high Hunt & Hess scores (3–5) included 3 patients (8.6%) with PM SAH and 32 patients (91.4%) with NPM SAH. Patients with NPM SAH had a higher incidence of moderate/severe vasospasm (19% versus 8%, $P = .03$), a need for an external ventricular drain (30% versus 6%, $P < .01$), persistent hydrocephalus requiring a ventriculoperitoneal shunt (11% versus 0%, $P < .01$), and a lower rate of discharge home (55% versus 92%, $P < .01$) than patients with PM SAH.

The rebleed rate was significantly higher in NPM SAH compared with PM SAH (8% versus 1%, $P = .04$), with 4 aneurysms identified after rebleed. In 8 patients who had a rebleed event and a high suspicion of an occult vascular source, the median time from the index SAH event and rebleed was 17 days (range, 1–49 days). The remaining rebleed events were attributed to vasculitis ($n = 1$), hypertension versus cerebral amyloid angiopathy ($n = 1$), and unknown etiology ($n = 3$).

Diagnostic Yield of Repeat DSA by CT Blood Distribution Pattern

Repeat DSA was performed in 135/242 patients (55.8%) and revealed a source of hemorrhage in 10 patients (7.4%; 8 aneurysms and 2 cervicomedullary AVFs). Of the 100 patients in the NPM group, 80 (80%) underwent repeat DSA, and a vascular source was identified in 9/80 (11.3%; Figs 1 and 2 and the Table).

Of the 87 patients in the PM group, 46 (52.9%) underwent repeat DSA and a cervicomedullary AVF was identified in 1/46 (2.2%). The difference in yield between NPM and PM was not statistically significant ($P = .09$). Repeat DSA was infrequently performed in patients with sulcal SAH (6/43, 13.9%) or CT-negative SAH (3/12, 25%) and did not identify a vascular source in any case for these SAH distribution patterns.

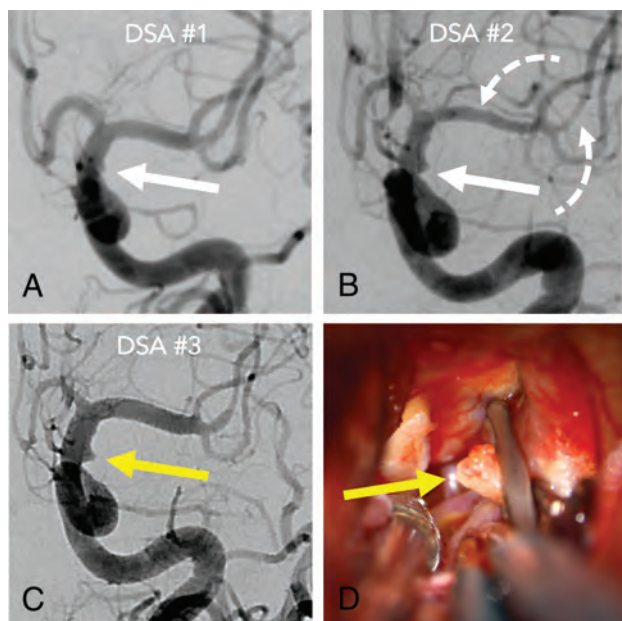


FIG 2. A 36-year-old woman admitted with an internal carotid artery blister aneurysm, misdiagnosed due to 2 forms of operator-dependent error. The initial DSA (A) shows a perceptual-type interpretive error in that a laterally projecting blister (white arrow) was not recognized. The blister was more evident on the second DSA (B) and perceived but misinterpreted as vasospasm due to developing vasospasm elsewhere (dashed arrows). Finally, the lesion (yellow arrow) was recognized on the third DSA (C) as vasospasm abated. Intraoperative photographs (D) confirm the rupture site (yellow arrow) secured with clipping.

Summary of data in patients with vascular source identified

Patient	Positive DSA Findings (No.)	Timing of Diagnosis (PBD)	SAH		Source
			Rebleed	Pattern	
1	2	5	No	NPM	A1 blister aneurysm
2	2	3	Day 2	NPM	PICA dissecting aneurysm
3	2	5	No	NPM	A1 blister aneurysm
4	2	7	No	NPM	Cervicomedullary AVF
5	2	8	No	NPM	Distal MCA mycotic aneurysm
6	2	39	Day 37	NPM	AcomA saccular aneurysm
7	3	5	No	NPM	A1 dissecting aneurysm
8	3	12	No	NPM	Basilar blister aneurysm
9	3	8	No	NPM	AcomA saccular aneurysm
10	3	7	No	PM	Cervicomedullary AVF
11 ^a	NA	17	Day 17	NPM	AcomA saccular aneurysm
12 ^a	NA	2	No	NPM	AcomA blister aneurysm
13 ^a	NA	16	Day 16	NPM	Thrombosed R MCA aneurysm

Note:—AcomA indicates anterior communicating artery; PBD, postbleed day; NA, not applicable; R, right.
^a Aneurysm identified at craniotomy.

In total, 6/135 patients (4.4%) had a vascular source identified on a second DSA, and 4 of 34 patients (11.8%) were diagnosed on a third DSA (Table). The diagnostic yield of the second and third DSAs in patients with NPM SAH was 7.7% and 12%, respectively. The median time from the index SAH event until identification of a vascular source on DSA was 7 days (range, 3–39 days). MRA of the brain and neck was performed in 182 of 242 patients (75.2%) and did not reveal an SAH source in any case.

Sources and Classification of Diagnostic Error in Initial DSA

In total, 13/242 patients (5.4%) with initially angiographically occult SAH were subsequently diagnosed with a vascular source: 2/13 (15.4%) at craniotomy, 10/13 (76.9%) by repeat DSA, and 1/13 (7.7%) by delayed CTA (Table). Of 9 patients in whom an aneurysm was identified on repeat DSA, most were <3-mm nonsaccular aneurysms, including blister aneurysms ($n = 4$), dissecting aneurysms ($n = 2$), and a mycotic aneurysm ($n = 1$). Two saccular aneurysms were thrombosed during the initial DSA. The anterior cerebral artery and anterior communicating artery were the most frequent locations ($n = 6$). A cervicomedullary AVF was the source of SAH in 2/13 (15.4%) patients.

Of this subset of 13 patients with initially angiographically occult SAH, 6/13 (46.1%) had lesions that were undetectable on detailed review by 2 neurointerventionalists despite a technically adequate DSA and were, therefore, classified as physiologically occult rather than missed due to operator-dependent error. Two (33.3%) of these were diagnosed only at exploratory craniotomy performed urgently for declining clinical status. All (4/4, 100%) of the remaining cases diagnosed by repeat DSA showed a change in the angiographic appearance (recanalization or growth), leading to the final diagnosis.

Seven of 13 (53.8%) cases were classified as operator-dependent errors. Four of 7 (57.1%) cases were subclassified as technical errors. These errors included the following: 1) lack of 3D rotational DSA of the relevant vessel ($n = 2$, 50%), 2) insufficient planar projections (lack of skull base and cervical vertebral artery views; $n = 1$, 25%), and 3) missed diagnosis of a cervicomedullary AVF due to failure to selectively inject the external carotid artery ($n = 1$, 25%). The remaining 3/7 (42.8%) operator-dependent errors were classified as cognitive errors. These were further subclassified as perceptual ($n = 1$, 14.3%) or interpretive ($n = 2$, 28.6%) errors. These included the following: 1) a subtle-but-present blister aneurysm of the A1 segment (error of perception), 2) a small fusiform PICA aneurysm in which an abnormal contour was recognized but misinterpreted, and 3) a small, dissecting aneurysm of the A1, which was recognized but not interpreted as a pathologic until it subsequently enlarged.

DISCUSSION

In this retrospective study of 242 consecutive patients with spontaneous SAH and negative initial DSA findings, a vascular source was ultimately identified in 13/242 (5.4%). The combined diagnostic yield of repeat DSA was 11.3% for the NPM pattern (9/80), 2.2% for the PM pattern (1/46), and 0% in the sulcal and CT-negative groups. Given the significantly higher rebleed rate, the risks of repeat DSA (including a third DSA) in the acute interval appear justified in the angiographically occult NPM SAH subgroup. This study also presents a new framework for diagnostic error analysis in angiographically occult SAH and found that technical and cognitive errors together occurred in 2.9% (7/242) of cases.

The rate of negative initial DSA findings in this 10-year cohort was 20.8% of all patients with SAH, consistent with previous studies.^{1,2,11} Also similar to prior studies, patients with negative SAH on angiography had lower complication rates and better functional outcomes than patients with aneurysmal SAH.¹² When stratified by CT pattern, patients with NPM SAH had more severe clinical presentations and complications and poorer outcomes (rebleeding, symptomatic vasospasm, external ventricular drain ventriculoperitoneal shunt placement, discharge home) compared with patients with PM SAH.^{4,13,14} These findings highlight an increased risk of NPM in patients with SAH compared with those with PM SAH.

Sources of Angiographically Occult SAH

Atypical lesions such as blisterlike and dissecting aneurysms were an important source of occult hemorrhage in patients with NPM SAH. Blister aneurysms are thought to account for 0.5%–2% of all aneurysmal SAHs but were estimated to comprise up to 25.2% of angiographically occult aneurysms.^{14,15} Blister aneurysms, which typically occur in the supraclinoid ICA, are exceedingly rare in other vessels.¹⁶ In this cohort, blister aneurysms were found in the anterior cerebral artery, anterior communicating artery, and a basilar perforator artery; blister aneurysms in such unusual locations, therefore, represent an important source of SAH that may be easily missed despite a good technique because they evade the standard neuroangiographic search pattern. Dissecting aneurysms are also difficult to detect because they often manifest subtle angiographic features that mimic intracranial atherosclerosis.¹⁷

Imaging Strategies in Angiographically Occult SAH

Rebleed events occurred in 3.7% of patients in this study and represent the leading rationale for repeat DSA in the acute setting. These findings are generally consistent with prior estimates of rebleed but are higher for patients with NPM SAH (8%) than previously reported.⁴ Most important, most rebleed events occurred >2 weeks after the index SAH and after hospital discharge. The median delay in detecting a vascular source was 7 days, while the median delay of rebleed events was 17 days. Together these findings support previous recommendations for routine DSA during this window.⁶ For patients with negative findings on 2 DSAs during hospitalization, the utility of a third DSA is less certain; in our study, 4 of 34 patients (11.8%) had a vascular source identified on the third angiogram, though patients with a high suspicion of an occult source were likely selected for repeat DSA. The incidence of positive findings on a third long-term follow-up DSA has been

reported to be between 7% and 10%,^{3,18} though these studies are also limited by small sample sizes, inconsistent imaging protocols, and selection bias. One study had a standardized protocol of obtaining a third angiogram at 6 weeks postictus and reported a yield of 4% for the third DSA (0% in PM SAH, 7.8% in NPM SAH).⁶ Therefore, it may be reasonable to obtain a delayed third angiogram, especially for patients with NPM-pattern SAH.

Notably, these data indicate that MR imaging of the brain and cervical spine has a relatively low diagnostic yield.^{3,19-21} However, there have been reports of an MR imaging diagnosis of an occult aneurysm, a cervical arteriovenous vascular malformation, or a cavernous malformation in patients with initial negative findings on DSA.^{19,22} Therefore, MR imaging may be useful in selected patients with atypical clinical presentations or patterns of hemorrhage.

The Role of Operator-Dependent Error in Angiographically Occult SAH

The present study found that operator-dependent error occurred in 7/242 (2.9%) cases of angiographically occult SAH and accounted for more than half (53.8%) of cases subsequently diagnosed by repeat DSA or craniotomy. Such operator-dependent errors (ie, sum of technical and cognitive errors) are underreported and underinvestigated in neuroangiography relative to noninvasive radiology. Technical error, believed to account for only 2% of errors in diagnostic radiology, represented 57.1% of errors in the current study.²³ A meticulous technique, including high-magnification planar projections, is essential to unmask common aneurysm “blind spots.”²⁴ 3D rotational DSA also increases the overall sensitivity of cerebral angiography, and our findings support prior recommendations that 3D DSA be performed routinely in each vascular territory for all patients with SAH of uncertain source. Finally, cervicomedullary/foramen magnum AVFs comprised 15.4% (2/13) of lesions in this series.²⁵ The frequency of these lesions emphasizes the importance of adequate projections of the skull base and the need for high-quality external carotid artery DSA.

The other major category of operator-dependent error in DSA is cognitive error. Cognitive-type errors accounted for 42.8% of missed diagnoses in the current study, whereas they are estimated to explain 60%–80% of errors in diagnostic radiology.^{7,10} Cognitive errors include errors of perception and interpretation.¹⁰ Perception errors including “scanning error” (incomplete review of acquired data), and “satisfaction of search” (a premature conclusion after an overt finding is noted) are influenced by human factors such as fatigue, inexperience, and distractors. Interpretation errors include the heuristic biases of framing (misleading contextual information), anchoring (failure to adjust the impression with new information), confirmation (commitment to pretest hypothesis), and availability (overweighted influence of recent experiences). One instructive case (Fig 2) highlights a perceptual error on initial DSA, an interpretive error on the second DSA, and the effect of anchoring bias because the interpreting physician was influenced by a concurrent vasospasm and failed to consider the possibility of an aneurysm.

Last, although DSA remains the criterion standard of diagnostic neurovascular imaging, our results clarify its physiologic limitations because 2.5% (6/242) of all angiographically occult SAH-source lesions were undetectable despite excellent technique and

critical retrospective review. These findings reiterate the concept that DSA is inherently a luminal technique; thus, thrombosed or nonopacifying lesions are undetectable. This finding suggests an upper bound on the sensitivity of DSA. Emerging extraluminal imaging techniques, including vessel wall imaging, endoluminal optical coherence tomography, high-field MR imaging, and cinematic 3D rendering may serve as complementary tools to DSA to improve the diagnostic yield and avoid delays in care.^{26,27}

This study has several important limitations. Although large and inclusive, the cohort is retrospective and therefore influenced by selection bias and referral patterns. In our cohort of 242 patients, only 135 (56%) had a second angiogram. Although there were no rebleed events or delayed complications in the remaining 107 patients, diagnostic follow-up for those patients was incomplete. The variation in the practice of repeat DSA and the lack of a standardized protocol also limit the generalizability of the findings. These limitations can be addressed with prospective, multi-institution registries.

CONCLUSIONS

The relatively high diagnostic yield of repeat DSA and the high rebleed rates in patients with the NPM SAH pattern and negative initial DSA support the practice of repeat DSA in this CT hemorrhage pattern subgroup. More than half (53.8%) of angiographically occult lesions were missed due to operator-dependent errors, and the remaining (46.2%) were undetectable by DSA, highlighting the limits of the sensitivity of DSA as a diagnostic technique.

Disclosure forms provided by the authors are available with the full text and PDF of this article at www.ajnr.org.

REFERENCES

- Maslehaty H, Barth H, Petridis AK, et al. **Special features of subarachnoid hemorrhage of unknown origin: a review of a series of 179 cases.** *Neurol Res* 2012;34:91–97 CrossRef Medline
- Rinkel GJ, van Gijn J, Wijdicks EF. **Subarachnoid hemorrhage without detectable aneurysm: a review of the causes.** *Stroke* 1993;24:1403–09 CrossRef Medline
- Topcuoglu MA, Ogilvy CS, Carter BS, et al. **Subarachnoid hemorrhage without evident cause on initial angiography studies: diagnostic yield of subsequent angiography and other neuroimaging tests.** *J Neurosurg* 2003;98:1235–40 CrossRef Medline
- Dalyai R, Chalouhi N, Theofanis T, et al. **Subarachnoid hemorrhage with negative initial catheter angiography: a review of 254 cases evaluating patient clinical outcome and efficacy of short- and long-term repeat angiography.** *Neurosurgery* 2013;72:646–52; discussion 651–52 CrossRef Medline
- Kang DH, Park J, Lee SH, et al. **Does non-perimesencephalic type non-aneurysmal subarachnoid hemorrhage have a benign prognosis?** *J Clin Neurosci* 2009;16:904–08 CrossRef Medline
- van Gijn J, van Dongen KJ, Vermeulen M, et al. **Perimesencephalic hemorrhage: a nonaneurysmal and benign form of subarachnoid hemorrhage.** *Neurology* 1985;35:493–97 CrossRef Medline
- Renfrew DL, Franken EA, Berbaum KS, et al. **Error in radiology: classification and lessons in 182 cases presented at a problem case conference.** *Radiology* 1992;183:145–50 CrossRef Medline
- Provenzale JM, Kranz PG. **Understanding errors in diagnostic radiology: proposal of a classification scheme and application to emergency radiology.** *Emerg Radiol* 2011;18:403–08 CrossRef Medline
- Kim YW, Mansfield LT. **Fool me twice: delayed diagnoses in radiology with emphasis on perpetuated errors.** *AJR Am J Roentgenol* 2014;202:465–70 CrossRef Medline
- Bruno MA, Walker EA, Abujudeh HH. **Understanding and confronting our mistakes: the epidemiology of error in radiology and strategies for error reduction.** *Radiographics* 2015;35:1668–76 CrossRef Medline
- Rinkel GJ, Wijdicks EF, Hasan D, et al. **Outcome in patients with subarachnoid haemorrhage and negative angiography according to pattern of haemorrhage on computed tomography.** *Lancet* 1991;338:964–68 CrossRef Medline
- Nesvick CL, Oushy S, Rinaldo L, et al. **Clinical complications and outcomes of angiographically negative subarachnoid hemorrhage.** *Neurology* 2019;92:e2385–94 CrossRef Medline
- Mohan M, Islim AI, Rasul FT, et al; British Neurosurgical Trainee Research Collaborative. **Subarachnoid haemorrhage with negative initial neurovascular imaging: a systematic review and meta-analysis.** *Acta Neurochir (Wien)* 2019;161:2013–26 CrossRef Medline
- Gonzalez AM, Narata AP, Yilmaz H, et al. **Blood blister-like aneurysms: single center experience and systematic literature review.** *Eur J Radiol* 2014;83:197–205 CrossRef Medline
- Abe M, Tabuchi K, Yokoyama H, et al. **Blood blisterlike aneurysms of the internal carotid artery.** *J Neurosurg* 1998;89:419–24 CrossRef Medline
- Peitz GW, Sy CA, Grandhi R. **Endovascular treatment of blister aneurysms.** *Neurosurg Focus* 2017;42:E12 CrossRef Medline
- Nakatomi H, Nagata K, Kawamoto S, et al. **Ruptured dissecting aneurysm as a cause of subarachnoid hemorrhage of unverified etiology.** *Stroke* 1997;28:1278–82 CrossRef Medline
- Andaluz N, Zuccarello M. **Yield of further diagnostic work-up of cryptogenic subarachnoid hemorrhage based on bleeding patterns on computed tomographic scans.** *Neurosurgery* 2008;62:1040–46; discussion 1047 CrossRef Medline
- Woodfield J, Rane N, Cudlip S, et al. **Value of delayed MRI in angiogram-negative subarachnoid haemorrhage.** *Clin Radiol* 2014;69:350–56 CrossRef Medline
- Maslehaty H, Petridis AK, Barth H, et al. **Diagnostic value of magnetic resonance imaging in perimesencephalic and nonperimesencephalic subarachnoid hemorrhage of unknown origin.** *J Neurosurg* 2011;114:1003–07 CrossRef Medline
- Rogg JM, Smeaton S, Doberstein C, et al. **Assessment of the value of MR imaging for examining patients with angiographically negative subarachnoid hemorrhage.** *AJR Am J Roentgenol* 1999;172:201–06 CrossRef Medline
- Wijdicks EF, Schievink WI, Miller GM. **MR imaging in pretruncal nonaneurysmal subarachnoid hemorrhage: is it worthwhile?** *Stroke* 1998;29:2514–16 CrossRef Medline
- Degnan AJ, Ghobadi EH, Hardy P, et al. **Perceptual and interpretive error in diagnostic radiology: causes and potential solutions.** *Acad Radiology* 2019;26:833–45 CrossRef Medline
- Dowd CF. **Cerebral angiography: techniques and practice.** *Handb Clin Neurol* 2021;176:107–19 CrossRef Medline
- Caton MT, Narsinh KH, Baker A, et al. **Dural arteriovenous fistulas of the foramen magnum region: clinical features and angioarchitectural phenotypes.** *AJNR Am J Neuroradiol* 2021;42:1486–91 CrossRef Medline
- Caton MT, Wiggins WF, Nunez D. **Three-dimensional cinematic rendering to optimize visualization of cerebrovascular anatomy and disease in CT angiography.** *J Neuroimaging* 2020;30:286–96 CrossRef Medline
- Jung HN, Suh SI, Ryoo I, et al. **Usefulness of 3D high-resolution vessel wall MRI in diffuse nonaneurysmal SAH patients.** *Clin Neuroradiol* 2021;31:1071–81 CrossRef Medline

Recovery from Cranial Nerve Symptoms after Flow Diversion without Coiling for Unruptured Very Large and Giant ICA Aneurysms

J.K. Lee, J.H. Choi, B.-S. Kim, and Y.S. Shin



ABSTRACT

BACKGROUND AND PURPOSE: Cranial nerve symptoms, including visual impairment and ophthalmoplegia, are one of the most common presentations of very large and giant (≥ 15 mm) ICA aneurysms. In this study, we evaluated the treatment outcomes of flow diversion and conventional coiling in terms of recovery from cranial nerve symptoms and postoperative complications.

MATERIALS AND METHODS: Seventy-nine patients with unruptured ICA aneurysms of >15 mm who were treated with flow diversion or conventional coiling between December 2009 and December 2020 were retrospectively evaluated. We compared the radiologic and clinical outcomes, including recovery from cranial nerve symptoms, between the 2 groups.

RESULTS: Twenty-eight of 49 patients (57.1%) treated with flow diversion and 10 of 30 patients (33.3%) treated with conventional coiling initially presented with cranial nerve symptoms ($P = .068$). In the clinical follow-up, the symptom recovery rate was significantly higher in those treated with flow diversion (15 [50%] versus 3 [25%] with conventional coiling, $P = .046$). Multivariate logistic regression analysis demonstrated that flow diversion was significantly associated with symptom recovery (OR, 7.425; 95% CI, 1.091–50.546; $P = .040$). The overall postoperative complication rate was similar (flow diversion, 10 [20.4%]; conventional coiling, 6 [20.0%], $P = .965$), though fatal hemorrhagic complications occurred only in patients with intradurally located aneurysms treated with flow diversion (4 [8.2%] versus 0 [0.0%] with coiling, $P = .108$).

CONCLUSIONS: Flow diversion without coiling for very large and giant ICA aneurysms yielded a higher rate of recovery from cranial nerve symptoms, but it may be related to an increased hemorrhagic complication rate, especially for intradurally located aneurysms.

ABBREVIATION: OKM = O'Kelly-Marotta

Flow diversion has shifted the paradigm of endovascular aneurysm treatment in recent years. The mechanism of flow diversion involves device endothelialization and endoluminal reconstruction of the parent artery with simultaneous intraneurysmal thrombosis.¹ The safety and efficacy of flow diversion have been extensively reviewed in the past decade.^{2–4} Consequently, flow diversion has emerged as a favorable treatment for large (10–25 mm) and giant (>25 mm) intracranial aneurysms, with several studies reporting a higher rate of aneurysm occlusion and a lower rate of recurrence compared with the

respective rates with conventional endovascular treatment.^{5–8} However, more recent studies found a lower long-term aneurysm complete occlusion rate after flow diversion, ranging from 72% to 78%.^{9,10} Moreover, a meta-analysis performed by Brinjikji et al¹¹ found that the morbidity and mortality in patients treated with flow diversion were 5% and 4%, respectively.

Giant intracranial aneurysms account for 2%–5% of all intracranial aneurysms, and they are associated with a higher risk of rupture compared with the smaller aneurysms.^{12,13} In addition to the risk of rupture, large and giant aneurysms in some locations can cause cranial nerve symptoms. For example, cranial nerves II, III, V, and VI may be compressed from large aneurysms of the ICA, leading to third nerve palsy, visual loss, diplopia, and facial numbness.^{14,15} Packing of coils in the aneurysm may create mass effect, whereas flow diversion may promote shrinkage of the aneurysm.^{14,16,17} In this study, we compared the clinical outcomes of patients treated with flow diversion without coiling and conventional coiling, specifically evaluating its efficacy on cranial nerve symptoms.

Received January 12, 2022; accepted after revision March 8.

From the Departments of Neurosurgery (J.K.L., J.H.C., Y.S.S.) and Radiology (B.-S.K.), Seoul St. Mary's Hospital, The Catholic University of Korea College of Medicine, Seoul, South Korea.

Please address correspondence to Jai Ho Choi, MD, PhD, Department of Neurosurgery, Seoul St. Mary's Hospital, The Catholic University of Korea, Seoul (06591), South Korea; e-mail: bivalvia98@gmail.com

 Indicates article with online supplemental data.

<http://dx.doi.org/10.3174/ajnr.A7498>

MATERIALS AND METHODS

Study Design and Population

A total of 3522 patients with unruptured intracranial aneurysms treated with the endovascular method at a single institution between December 2009 and December 2020 were retrospectively evaluated. Among them, 127 aneurysms of ≥ 15 mm were included. We excluded patients with previously ruptured or treated aneurysms, fusiform aneurysms, and aneurysms that did not arise from the ICA. Fifteen millimeters was selected because of the national insurance policy, which prohibits the use of flow diversion for aneurysms of < 15 mm. Additionally, the insurance policy prohibits interventionists from using coils in conjunction with flow diversion, limiting the treatment of these large and giant aneurysms. Consequently, we were able to specifically evaluate the effectiveness of flow diversion without coiling. We reached an ethical decision for each patient by selecting the treatment technique according to a multidisciplinary overview from our department. Patients treated with flow diversion without coiling were assigned to the flow-diversion group, while those treated with conventional coiling were assigned to the coiling group. This study was approved by the institutional review board at our institution.

Periprocedural Angiographic Evaluation and Endovascular Procedure

All patients underwent preprocedural diagnostic DSA of the intracranial vessels for a comprehensive evaluation of the aneurysm. Aneurysm features, including the size, shape, location, and thrombosis inside the aneurysm, were examined. Additionally, the size and morphology of the parent artery, as well as its relationship with the aneurysm, were assessed. Postoperative follow-up for each patient was performed 6–12 months after treatment with MRA and DSA for patients treated with conventional coiling and those treated with flow diversion, respectively. Clinical symptoms and complications were assessed at the time of follow-up imaging. The angiographic results of flow diversion were evaluated using the O'Kelly-Marotta (OKM) filling grade system. Radiologic and clinical evaluations were conducted with the consensus of 2 observers (J.K.L. and J.H.C.), who were blinded to the information on perioperative ischemic complications.

Statistical Analysis

Statistical analysis was performed using SPSS, Version 24 (IBM). We performed a χ^2 test or Fisher exact test for categorical variables and an independent t test for continuous variables, and $P < .05$ was considered statistically significant. Multivariate analysis was performed using a logistic regression model for variables that were significant in the univariate analysis ($P < .10$).

RESULTS

Patient Baseline Characteristics

Among the 79 patients with intracranial aneurysms, 49 patients (62.0%) were treated with flow diversion and 30 patients (38.0%) were treated with conventional coiling. Coiling procedures were performed using different endovascular techniques: 18 (60.0%) stent-assisted, 2 (6.7%) balloon-assisted, 6 (20.0%) single-catheter, and 4 (13.3%) multiple-catheter coiling. The baseline characteristics of the 2 groups are summarized in the Online

Supplemental Data. The mean patient age did not differ between the flow-diversion group (57.82 [SD, 11.96] years) and the coiling group (60.67 [SD, 13.05] years). The proportion of female patients was higher than that of males in both groups (flow diversion group, 47 of 49 patients [95.9%]; coiling group, 26 of 30 patients [86.7%]). Risk factors, including smoking, diabetes mellitus, hypertension, and hyperlipidemia, were similar between the 2 groups. Although the comparison was not statistically significant, flow diversion was used more frequently to treat patients with aneurysm-induced cranial nerve symptoms ($n = 28$, 57.1%) than coiling ($n = 10$, 33.3%). The most common cranial nerve symptoms were related to the eye and vision, except for 1 patient who initially presented with ipsilateral facial pain.

The mean maximal size of aneurysms among patients in the flow-diversion group was significantly larger than that among patients in the coiling group (22.04 [SD, 5.36] mm versus 18.27 [SD, 4.12] mm, $P = .001$). The proportion of aneurysms with diameters of > 25 mm was higher in the flow-diversion group (12 patients, 24.5%) than in the coiling group (1 patient, 3.3%). Most aneurysms treated with coiling ranged from 15 to 20 mm ($n = 23$, 76.7%). On inspection of the aneurysm location, there was no significant difference between the 2 groups; however, more extradural aneurysms were treated with flow diversion ($n = 23$, 46.9% versus $n = 8$, 26.7%). Among the aneurysms originating from the intradural segment of the ICA, 25 (51.0%) in the flow-diversion group and 12 (40%) in the coiling group were located within the ophthalmic segment.

Clinical and Radiologic Outcomes

The results of both treatment modalities are shown in Table 1. Because flow diversion promotes delayed occlusion of the aneurysm, initial aneurysm occlusion after treatment was evaluated only in patients who underwent coiling. Immediate complete occlusion was achieved in 13 of the 30 patients (43.5%) in the coiling group, and a remnant neck or sac was observed in 8 (26.7%) and 9 patients (30.0%), respectively.

A follow-up examination was not available for 4 patients in the flow-diversion group and 2 in the coiling group. Among the 45 patients who were followed up 1 year after undergoing treatment with flow diversion, 28 (62.2%) reached complete or near-complete occlusion assigned as grade D based on the OKM grading scale, 12 (26.7%) had a neck remnant (OKM C), and 5 (11.1%) had sac filling (OKM A and B).¹⁸ Aneurysm occlusion status did not change much for patients who underwent conventional coiling, with complete or near-complete occlusion seen in 13 patients (46.4%); a neck remnant, in 7 (25.0%); and sac filling, in 8 (28.6%). Furthermore, recurrence of once-occluded aneurysms during the subsequent follow-up was found in 12 patients (40.0%) in the coiling group but not in any in the flow-diversion group ($P < .001$). The retreatment rates for recurrent or remnant aneurysms were similar for both the flow-diversion and coiling groups (6 [12.2%] versus 7 [23.3%]).

Clinically, more patients showed improvement in initial cranial nerve symptoms after undergoing treatment with flow diversion than with coiling (15 [60.0%] versus 3 [25.0%], $P = .046$). Multivariate logistic regression analysis (Table 2) indicated that treatment with flow diversion without coiling was significantly

Table 1: Comparison of clinical and radiologic outcomes between patients treated with flow diversion and those treated with conventional coiling^a

Characteristics	Flow Diversion (n = 49)	Conventional Coiling (n = 30)	P Value
Radiologic outcomes			
Initial occlusion grade			
Not available	49 (100%)		<.001
Complete		13 (43.5%)	
Remnant neck		8 (26.7%)	
Sac filling		9 (30%)	
One-year follow-up occlusion grade (flow-diversion coiling)			.154
OKM D/complete or near-complete	28 (62.2%)	13 (46.4%)	
OKM C/remnant neck	12 (26.7%)	7 (25%)	
OKM A and B/sac filling	5 (11.1%)	8 (28.6%)	
Recurrence during follow-up	0 (0%)	12 (40%)	<.001
Retreatment	6 (12.2%)	7 (23.3%)	.197
Mean follow-up period (mo)	30.3 (SD, 18.7)	40.8 (SD, 25.6)	.111
Clinical outcomes			
Cranial nerve symptom change			.046
Improved	15 (60%)	3 (25%)	
Worsened or sustained	10 (40%)	9 (75%)	
mRS ≥2 at discharge	2 (4.1%)	0 (0%)	.262
mRS ≥2 at last follow-up	5 (10.2%)	0 (0%)	.071
Mean follow-up period (mo)	33.0 (SD, 21.1)	45.9 (SD, 35.8)	.073

^aData are mean or No. (%).

associated with recovery from cranial nerve symptoms (OR, 7.425; 95% CI, 1.091–50.546; $P = .040$). A representative case of improved visual field after treatment with flow diversion is shown in the Figure.

Treatment-Related Complications

Complications occurring after the procedure were compared between the groups, as summarized in Table 3. The total complication rate was similar for both groups; however, patients in the coiling group had a higher ischemic complication rate (4 [13.3%] versus 3 [6.1%], $P = .274$). Although not statistically significant, the hemorrhagic complication rate was higher in the flow-diversion group (4 [8.2%] versus 0 [0.0%], $P = .108$). Postoperative MR imaging within 24 hours after surgery for these 4 patients did not show evidence of intracranial hemorrhage, but they were re-admitted to the hospital with decreased consciousness from delayed aneurysmal rupture. Three of them had early delayed rupture between 1 and 4 weeks postoperatively, and 1 had late delayed rupture occurring after 5 months. All 4 of these patients were initially treated for aneurysms in the intradural location and died of intracranial hemorrhage.

DISCUSSION

In this retrospective analysis, we found higher recovery rate of cranial nerve symptoms due to very large-to-giant ICA aneurysms after flow diversion without coiling than after conventional coiling. Aneurysms originating from the ICA may cause compression symptoms of cranial nerves II, III, V, and VI, especially when they are large or giant. Although conventional coiling can achieve complete occlusion of these aneurysms, cranial nerve symptoms may be aggravated by the mass effect. There have been various studies showing better outcomes with flow diversion than with conventional coiling, with a higher occlusion rate but not a higher complication rate.^{4,19,20} In this study, we compared the outcomes of cranial nerve symptoms using flow diversion without coiling and conventional

coiling for very large and giant aneurysms, in addition to other clinical and radiologic parameters. Flow diversion has the advantage of redirecting blood flow and promoting thrombus formation in the aneurysm sac, subsequently reducing the mass effect. In this study, 15 of 28 patients (60.0%) treated with flow diversion showed a significantly higher symptom improvement rate compared with 3 of 10 patients (25.0%) treated with conventional coiling ($P = .046$). Moreover, the multivariate analysis identified flow diversion as the only predictor of recovery from cranial nerve symptoms (OR, 7.425; 95% CI, 1.091–50.546; $P = .040$). The benefit of decreased mass effect coincided with a higher occlusion rate (62.2% versus 46.4%, $P = .154$) and lower recurrence rate (0.0% versus 40%, $P < .001$). Similarly, Wang et al²¹ reported favorable outcomes of mass effect–related symptoms for aneurysms treated with flow diversion; however, flow diversion was combined with adjunctive loose coil embolization. Our study investigated the unequivocal effect of flow diversion without using coils inside the aneurysm, which can induce intra-aneurysmal thrombosis or protect the aneurysm wall from direct blood flow. Treating very large and giant aneurysms by flow diversion without adjunctive coiling may be undesirable, but the current national insurance policy prohibits such treatment options.

Our results suggest that flow diversion can notably reduce the mass effect of very large and giant aneurysms, especially in the absence of coils inside the sac. However, the complications associated with flow diversion should not be overlooked. The overall complication rate for both conventional coiling and flow diversion did not differ in comparative data by Chalouhi et al,²⁰ in agreement with our results (20.4% versus 20.0%, $P = .965$). In a previous meta-analysis, delayed aneurysm rupture from treatment with flow diversion was reported with an occurrence rate of 1.7%–3% among the complications.^{11,22} Furthermore, Cagnazzo et al⁵ found a 7% early rupture of aneurysms treated with flow diversion alone, and no cases of rupture in those treated with adjunctive coils. Although not statistically significant, we identified 4 (8.2%)

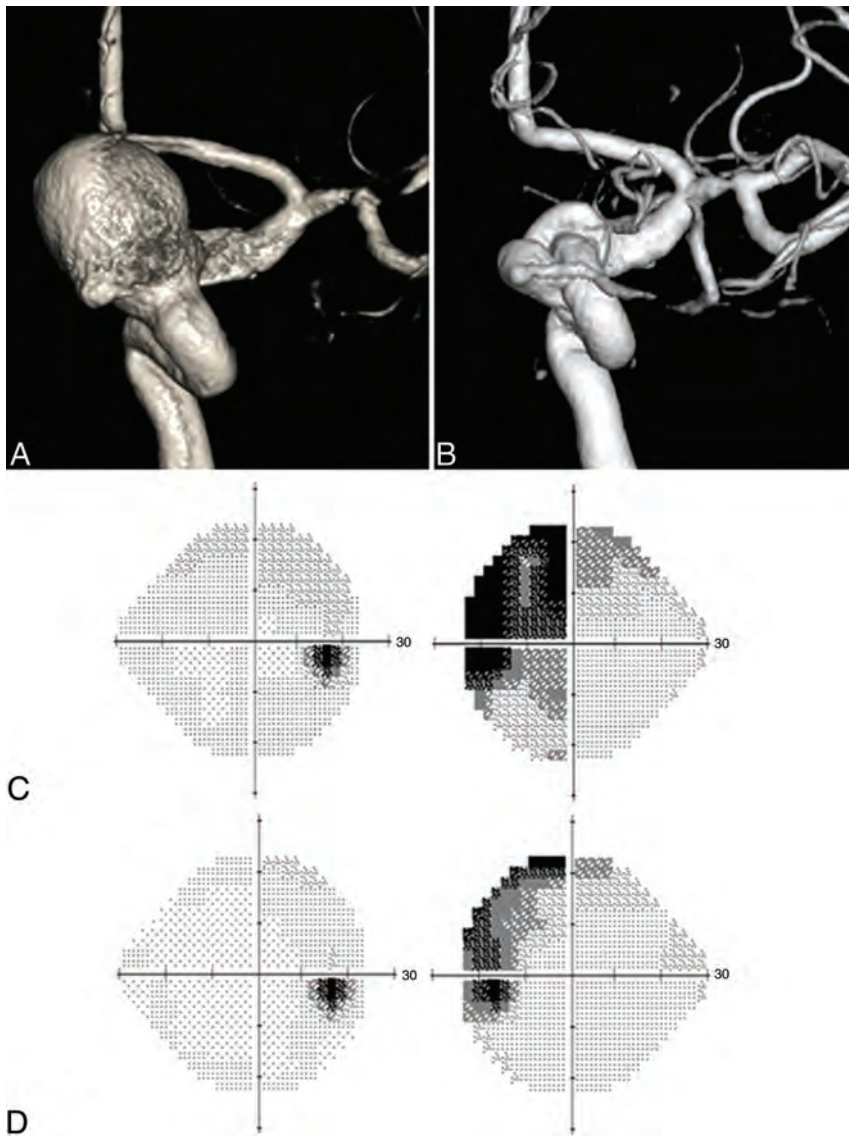


FIGURE. A, Left ICA angiogram showing a large aneurysm with a dome size of 19.0 mm located in the ophthalmic segment of the ICA. B, Follow-up angiogram at 1 year shows near-complete occlusion of the aneurysm. C, Visual field examination before treatment shows a visual field defect of the left eye. D, Follow-up examination at 1 year shows an improved visual field of the left eye. Additionally, the patient's visual acuity improved from 0.3 to 0.8.

fatal hemorrhagic complications from delayed aneurysm rupture after flow diversion and none after conventional coiling ($P=.108$), all of which were in aneurysms originating from the intradural location of the ICA. The hemorrhagic complication rate raises concerns about the safety of flow-diversion treatment in very large and giant intradural ICA aneurysms, especially when adjunctive coils are not used. Besides the 2 methods of treatment in our study, ICA occlusion after angiographic test occlusion may be an alternative treatment option with a low complication rate with favorable outcome because Bechan et al²³ reported 90% improvement rate of cranial nerve symptoms.²⁴

Our study has some limitations owing to its retrospective design and small sample size. Not all patients were evaluated by an ophthalmologist unless the patient experienced visual symptoms or the aneurysm was clearly in the direction of the cranial nerve. Thus, the occurrence of cranial nerve symptoms may be underestimated due to the lack of standard ophthalmic examinations. Furthermore, the symptom duration for each patient was not recorded appropriately. The recovery from symptoms may vary according to the duration of the nerve compression. Further prospective comparative studies are required to validate our findings.

CONCLUSIONS

Our findings suggest that cranial nerve symptoms caused by aneurysm compression may be adequately reduced

Table 2: Univariate and multivariate analyses of the predictors associated with improvement of cranial nerve symptoms^a

Variables	Univariate			Multivariate		
	Recovery from Cranial Nerve Symptoms		P Value	OR	95% CI	P Value
	Yes (n = 17)	No (n = 21)				
Age 60 years or older	6 (35.3%)	12 (57.1%)	.185			
Hypertension	8 (47.1%)	6 (28.6%)	.253			
Intradural location	8 (47.1%)	14 (66.7%)	.062	0.175	0.028–1.092	.092
Size ≥ 25 mm	5 (29.4%)	5 (23.8%)	.523			
Mean size (mm)	22.9 (SD, 4.5)	23.0 (SD, 6.6)				
Complete/near-complete occlusion Technique	10 (58.8%)	8 (38.1%)	.630			
Flow diversion	15 (88.2%)	13 (61.9%)	.093	7.425	1.091–50.546	.040
Conventional coiling	2 (11.8%)	8 (38.1%)				

^a Data are mean or No. (%).

Table 3: Treatment-related complications^a

Characteristics	Flow Diversion (n = 49)	Conventional Coiling (n = 30)	P Value
Total complications	10 (20.4%)	6 (20%)	.965
Ischemic complications	3 (6.1%)	4 (13.3%)	.274
Symptomatic infarction	3 (6.1%)	2 (6.66%)	
TIA or asymptomatic infarction	0 (0%)	2 (6.66%)	
Size ≥20 mm	2/27 (7.4%)	0/7 (0%)	.458
Intradural location	2/26 (7.7%)	3/22 (13.6%)	.502
Hemorrhagic complications	4 (8.2%)	0 (0%)	.108
Early delayed aneurysmal rupture	3 (6.1%)	0 (0%)	
Late delayed aneurysmal rupture	1 (2%)	0 (0%)	
Size ≥ 20 mm	2/27 (7.4%)	0/7 (0%)	.458
Intradural location	4/26 (15.4%)	0/22 (0%)	.055
Mortality	4 (8.2%)	0 (0%)	.108
Size ≥ 20 mm	2/27 (7.4%)	0/7 (0%)	.458
Intradural location	4/26 (15.4%)	0/22 (0%)	.055

^aData are No. (%).

by flow-diversion treatment. However, flow-diversion treatment without coiling may be associated with an increased rate of fatal hemorrhagic complications for the treatment of large and giant intradurally located ICA aneurysms. Flow diversion without coiling may be more suitable for aneurysms located extradurally that cause cranial nerve symptoms.

Disclosure forms provided by the authors are available with the full text and PDF of this article at www.ajnr.org.

REFERENCES

- Ravindran K, Salem MM, Alturki AY, et al. Endothelialization following flow diversion for intracranial aneurysms: a systematic review. *AJNR Am J Neuroradiol* 2019;40:295–301 CrossRef Medline
- Becke T, Kallmes DF, Saatci I, et al. Pipeline for uncoilable or failed aneurysms: results from a multicenter clinical trial. *Radiology* 2013;267:858–68 CrossRef Medline
- Chalouhi N, Starke RM, Yang S, et al. Extending the indications of flow diversion to small, unruptured, saccular aneurysms of the anterior circulation. *Stroke* 2014;45:54–58 CrossRef Medline
- Lanzino G, Crobbedu E, Cloft HJ, et al. Efficacy and safety of flow diversion for paraclinoid aneurysms: a matched-pair analysis compared with standard endovascular approaches. *AJNR Am J Neuroradiol* 2012;33:2158–61 CrossRef Medline
- Cagnazzo F, Mantilla D, Rouchaud A, et al. Endovascular treatment of very large and giant intracranial aneurysms: comparison between reconstructive and deconstructive techniques: a meta-analysis. *AJNR Am J Neuroradiol* 2018;39:852–58 CrossRef Medline
- Saatci I, Yavuz K, Ozer C, et al. Treatment of intracranial aneurysms using the Pipeline flow-diverter embolization device: a single-center experience with long-term follow-up results. *AJNR Am J Neuroradiol* 2012;33:1436–46 CrossRef Medline
- van Oel LI, van Rooij WJ, Sluzewski M, et al. Reconstructive endovascular treatment of fusiform and dissecting basilar trunk aneurysms with flow diverters, stents, and coils. *AJNR Am J Neuroradiol* 2013;34:589–95 CrossRef Medline
- Strauss I, Maimon S. Silk flow diverter in the treatment of complex intracranial aneurysms: a single-center experience with 60 patients. *Acta Neurochir (Wien)* 2016;158:247–54 CrossRef Medline
- Peschillo S, Caporlingua A, Resta MC, et al. Endovascular treatment of large and giant carotid aneurysms with flow-diverter stents alone or in combination with coils: a multicenter experience and long-term follow-up. *Oper Neurosurg (Hagerstown)* 2017;13:492–502 CrossRef Medline
- Fujii T, Teranishi K, Yatomi K, et al. Long-term follow-up results after flow diverter therapy using the Pipeline embolization device for large or giant unruptured internal carotid artery aneurysms: single-center retrospective analysis in the Japanese population. *Neurol Med Chir (Tokyo)* 2022;62:19–27 CrossRef Medline
- Brinjikji W, Murad MH, Lanzino G, et al. Endovascular treatment of intracranial aneurysms with flow diverters: a meta-analysis. *Stroke* 2013;44:442–47 CrossRef Medline
- Wiebers DO, Whisnant JP, Huston J 3rd, et al. Unruptured intracranial aneurysms: natural history, clinical outcome, and risks of surgical and endovascular treatment. *Lancet* 2003;362:103–10 CrossRef Medline
- Greving JP, Wermer MJ, Brown RD, Jr, et al. Development of the PHASES score for prediction of risk of rupture of intracranial aneurysms: a pooled analysis of six prospective cohort studies. *Lancet Neurol* 2014;13:59–66 CrossRef Medline
- Silva MA, See AP, Dasenbrock HH, et al. Vision outcomes in patients with paraclinoid aneurysms treated with clipping, coiling, or flow diversion: a systematic review and meta-analysis. *Neurosurg Focus* 2017;42:E15 CrossRef Medline
- Durner G, Piano M, Lenga P, et al. Giant Intracranial Aneurysm Study Group. Cranial nerve deficits in giant cavernous carotid aneurysms and their relation to aneurysm morphology and location. *Acta Neurochir (Wien)* 2018;160:1653–60 CrossRef Medline
- Carneiro A, Rane N, Küker W, et al. Volume changes of extremely large and giant intracranial aneurysms after treatment with flow diverter stents. *Neuroradiology* 2014;65:51–58 CrossRef Medline
- Miyachi S, Hiramatsu R, Ohnishi H, et al. Usefulness of the Pipeline embolic device for large and giant carotid cavernous aneurysms. *Neurointervention* 2017;12:83–90 CrossRef Medline
- O’Kelly CJ, Krings T, Fiorella D, et al. A novel grading scale for the angiographic assessment of intracranial aneurysms treated using flow diverting stents. *Interv Neuroradiol* 2010;16:133–37 CrossRef Medline
- Zanaty M, Chalouhi N, Starke RM, et al. Flow diversion versus conventional treatment for carotid cavernous aneurysms. *Stroke* 2014;45:2656–61 CrossRef Medline
- Chalouhi N, Tjoumakaris S, Starke RM, et al. Comparison of flow diversion and coiling in large unruptured intracranial saccular aneurysms. *Stroke* 2013;44:2150–54 CrossRef Medline
- Wang Z, Tian Z, Li W, et al. Variation of mass effect after using a flow diverter with adjunctive coil embolization for symptomatic unruptured large and giant intracranial aneurysms. *Front Neurol* 2019;10:1191 CrossRef Medline
- Arrese I, Sarabia R, Pintado R, et al. Flow-diverter devices for intracranial aneurysms: systematic review and meta-analysis. *Neurosurgery* 2013;73:193–99; discussion 99–200 CrossRef Medline
- Bechan RS, Majoie CB, Sprengers ME, et al. Therapeutic internal carotid artery occlusion for large and giant aneurysms: a single center cohort of 146 patients. *AJNR Am J Neuroradiol* 2016;37:125–29 CrossRef Medline
- Choi JH, Lee KS, Kim BS, et al. Treatment outcomes of large and giant intracranial aneurysms according to various treatment modalities. *Acta Neurochir (Wien)* 2020;162:2745–52 CrossRef Medline

Rabbit Elastase Aneurysm Model Mimics the Recurrence Rate of Human Intracranial Aneurysms following Platinum Coil Embolization

Y.-H. Ding, S. Ghozy, D. Dai, W. Brinjikji, D.F. Kallmes, and R. Kadirvel



ABSTRACT

BACKGROUND AND PURPOSE: Intracranial aneurysms treated with coils have been associated with incomplete occlusion, particularly in large or wide-neck aneurysms. This study aimed to validate the accuracy of the rabbit elastase model in predicting aneurysm recurrence in humans treated with platinum coils.

MATERIALS AND METHODS: Elastase-induced saccular aneurysms were induced in rabbits and embolized with conventional platinum coils. The recurrence rates of aneurysms were retrospectively analyzed. Morphologic characteristics of aneurysms, angiographic outcomes, and histologic healing were evaluated.

RESULTS: A total of 28 (15.3%) of 183 aneurysms recurred. The aneurysm recurrence rate observed in this study (15.3%) is similar to those reported in multiple analyses of aneurysm recurrence rates in humans (7%–27%). The rate of recurrence was higher in aneurysms treated without balloon assistance (19/66, 28.8%) compared with those treated with balloon assistance (9/117, 7.7%). Aneurysms treated with balloon-assisted coiling had a lower recurrence rate (OR = 0.17; 95% CI, 0.05–0.47; $P = .001$) and higher occlusion rate (OR = 6.88; 95% CI, 2.58–20.37; $P < .001$) compared with those treated without balloon-assisted coiling. In this rabbit elastase-induced aneurysm model, packing density and aneurysm volume were weak predictors of aneurysm recurrence; however, the packing density was a good predictor of the occlusion rate (OR = 1.05; 95% CI, 1.02–1.10; $P = .008$).

CONCLUSIONS: The rabbit elastase aneurysm model may mimic aneurysm recurrence rates observed in humans after platinum coil embolization. Moreover, balloon assistance and high packing densities were significant predictors of aneurysm recurrence and occlusion.

ABBREVIATIONS: CCA = common carotid artery; RCCA = right CCA

The prevalence of intracranial aneurysms in healthy adults is estimated to be 3%–5%.^{1,2} Endovascular embolization with platinum coils is the preferred treatment for unruptured and ruptured intracranial aneurysms because it is associated with lower morbidity and mortality rates compared with surgical clipping.^{3,4} However, coils have been associated with incomplete occlusion, leading to compaction and aneurysm recanalization, particularly in large aneurysms (diameter of ≥ 10 mm) or those with a wide

neck (>4 mm). The recurrence rate increases from 5% for aneurysms with a neck size between 4 and 10 mm to 20% for those with wider necks (>10 mm). Similarly, the recurrence rate of large aneurysms is 35%–50% compared with an overall recurrence rate of 20% in a heterogeneous population.^{5,6} To lower the recurrence rate of large and wide-neck aneurysms, a plethora of endovascular devices have been developed and tested in preclinical animal models.⁷

Preclinical trials of endovascular devices are necessary to evaluate their safety and efficiency. An ideal model requires aneurysm hemodynamic and histologic healing characteristics similar to those seen in humans. In models with surgical creation of aneurysms such as in both canine and rabbit venous pouch models, the presence of sutures at the aneurysm neck causes healing and fibrotic response, making it difficult to analyze healing after coil embolization. The canine venous pouch model, though widely used, cannot simulate the histologic and hemodynamic characteristics of humans.⁷ The swine model of intracranial aneurysms shows progressive occlusion and complete healing of aneurysms.⁸

Received October 7, 2021; accepted after revision March 9, 2022.

From the Department of Radiology, Mayo Clinic, Rochester, Minnesota.

Research reported in this publication was supported, in part, by the National Institutes of Health under Award Nos. R01NS076491, R43NS095455, U01NS089692, R01NS042646, and R21 HL072247.

Please address correspondence to Sherief Ghozy, MD, Mayo Clinic, Alfred Building 9-446, 200 First St. SW, Rochester, MN, 55905; e-mail: ghozy.sherief@mayo.edu; @SheriefGhozy; @WBrinjikji

Indicates open access to non-subscribers at www.ajnr.org

Indicates article with online supplemental data.

<http://dx.doi.org/10.3174/ajnr.A7497>

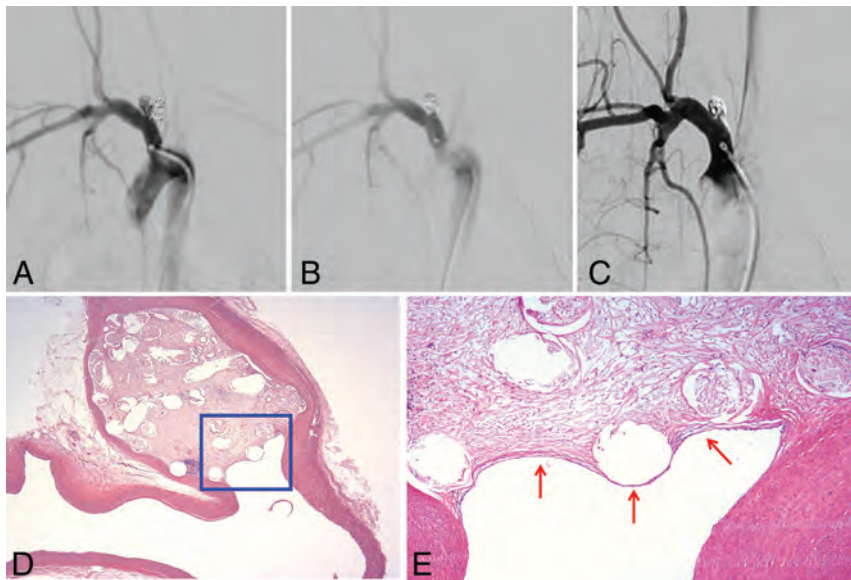


FIG 1. Angiographic and histopathologic evaluation of a completely occluded aneurysm on day 180. DSA images of the aneurysm before treatment (A), immediately after treatment showing complete occlusion (B), and before sacrifice demonstrating stable occlusion (C). Photomicrograph of an aneurysm section shows the aneurysm dome filled with organized connective tissue (D, H&E staining, original magnification $\times 12.5$) and the neck interface lined with a single layer of endothelium (arrows) (E, enlarged view of the box in D; H&E staining, original magnification $\times 40$).

This outcome makes the model irrelevant for testing aneurysm recurrence rates and the long-term efficiency of devices. In contrast, the rabbit aneurysm model has some advantages compared with clinical tissue. For instance, excising the aneurysm sac during the operation results in small segments of the aneurysm dome, while the rabbit model provides the opportunity to study the entire sac.⁹ Moreover, the rabbit model can be used to investigate the progressive wall degeneration of the aneurysm at multiple time points.⁹ Furthermore, the elastase-induced model has shown a similarity to the human intracranial aneurysm regarding geometric and hemodynamic aspects, including anatomy, size, long-term patency, and molecular characteristics.⁷ Nevertheless, as for all animal models, this model cannot account for the complex pathophysiology of human aneurysms, such as genetic predisposition, previous aneurysm history, comorbidities, wall inflammation, and individual lifestyle differences.

Typically, the elastase-induced aneurysm is created at the origin of right common carotid artery (RCCA) using a combination of open and endovascular techniques.¹⁰ Other modifications such as adjusting the position of the ligation, adjusting the position of the inflated balloon, injuring the aneurysm neck, and using the left common carotid artery (CCA) instead of the RCCA have been proposed as techniques to alter the volume, neck size, and configuration of the aneurysm, respectively.^{7,11-14} This model has been extensively used to study the healing response, occlusion rates, and recanalization rates after coil embolization. However, data are limited about the recurrence rate of aneurysms after platinum coil embolization in the rabbit elastase-induced aneurysm model. Therefore, the objective of this study was to evaluate the aneurysm recurrence rate in association with platinum coils in this aneurysm model.

MATERIALS AND METHODS

Rabbit Aneurysm Creation

Some of the rabbits used in this study were initially used as part of other investigations, in which we studied aneurysm healing mechanisms,¹⁵ developed a histologic healing scale,¹⁶ analyzed the relationship between aneurysm volume and healing,¹⁷ and compared the occlusion rates of platinum and modified coils.^{17,18} However, the original investigations were unrelated to this study. For this study, saccular aneurysms were created as described by Altes et al.¹⁰ By means of a sterile surgical technique, the RCCA was exposed to create a 1- to 2-mm beveled arteriotomy, and a 5F sheath was inserted retrograde in the midportion of the RCCA. Through this sheath, a 3F Fogarty balloon (Baxter Healthcare) was pushed to the origin of the RCCA and inflated to cause occlusion. Elastase (100 U/mL) mixed with equal amounts of iodinated contrast was intubated for 20 minutes, after which the balloon was deflated, the sheath was removed, and the RCCA was ligated. A 4-0 running

Vicryl suture (Ethicon) was used to close the skin before sending the rabbits to recovery.

Embolization Procedure

The embolization procedure was performed as described previously.¹⁸ Animals were anesthetized with the same procedure used during aneurysm creation. Under sterile conditions, the right common femoral artery was surgically exposed to place a 5F sheath and administer an injection of 500 U of heparin. Using the coaxial technique with continuous flushing with a heparin and normal saline solution, we advanced a 2 marker microcatheter into the aneurysm cavity. Radiopaque sizing devices were used to assess the size of the aneurysm during the 2D DSA. The aneurysm was embolized with ≥ 1 coil, depending on aneurysm diameter, and packing density was calculated as described in Herting et al.¹⁸ All the aneurysms were embolized as densely as possible using bare conventional platinum coils. A final control DSA was performed after coil placement and embolization, followed by removal of the catheters and sheath, ligation of femoral artery, and incision closure using a 4-0 Vicryl suture. Aneurysm occlusion was evaluated per the Raymond-Roy method: class 1, complete occlusion; class 2, near-complete occlusion; class 3, incomplete occlusion.¹⁹ We performed this evaluation on 2 occasions: postoperative and before sacrifice. We defined recanalization as any increased aneurysm filling in the follow-up angiography compared with the postoperative 2D DSA result. In contrast, recurrence was defined as a recurring or larger persistent filling defect on the follow-up angiography studies than the defect identified at the initial posttreatment and imaging (Figs 1 and 2).

Animal Sacrifice and Tissue Harvest

Angiographic follow-up was performed 15 days ($n=23$), 1 month ($n=100$), 1.5–2 months ($n=9$), 3 months ($n=8$), 4 months

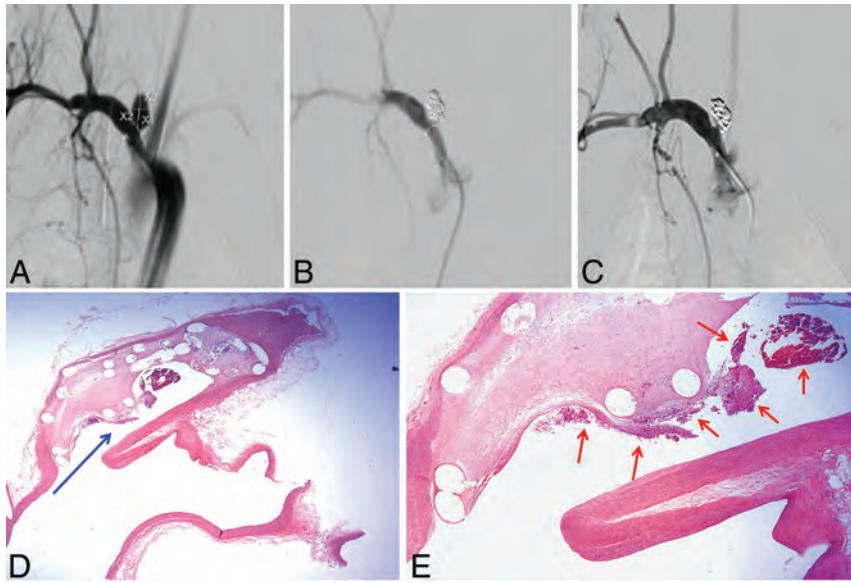


FIG 2. Angiographic and histopathologic evaluation of a recanalized aneurysm on day 180. DSA images of the aneurysm before treatment (A), immediately after treatment showing complete occlusion (B), and before sacrifice shows near-complete occlusion demonstrating recanalization (C). Photomicrograph of an aneurysm section shows a long, deep neck remnant that was wide open to parent artery connective tissue (D, H&E staining; original magnification $\times 12.5$). The tissue interface at the neck remnant appears to be macroconcaave in relation to the tissues filled in the dome (D) and contains poorly organized thrombus (E, enlarged view of arrow in D; H&E staining, original magnification $\times 40$).

($n = 10$), and 6–12 months ($n = 33$) after embolization. DSA was performed after deeply anesthetizing the animals, and aneurysm occlusion was evaluated as described before: class 1, complete occlusion; class 2, near-complete occlusion; and class 3, incomplete occlusion.¹⁹ As described earlier, to determine the durability of the embolization posttreatment and follow-up, we categorized the angiograms into 3 categories: stable, recurrent, and progressive aneurysm.^{17,18} A lethal injection of pentobarbital was used to euthanize animals and harvest the aneurysms and parent arteries. The tissue samples were immediately fixed in 10% neutral buffered formalin.

Histologic Evaluation

Harvested tissue samples were processed as described by Dai et al.¹⁵ Samples were dehydrated in increasing concentrations of alcohol, followed by clearing with xylene. Specimens were embedded in paraffin blocks and sectioned in a coronal orientation at 1000- μm intervals using an IsoMet Low Speed saw (NCI MICRO).

Metallic coil fragments were removed under a dissecting microscope before re-embedding sections in paraffin blocks. These blocks were then sectioned at 4- μm intervals using a microtome with disposable blades. The sections were floated in a 42°C water bath, mounted on Superfrost Plus slides (Cardinal Health), and dried overnight in an oven at 37°C. Slides were deparaffinized and hydrated in water before staining with H&E. An ordinal grading system was used to evaluate histologic healing as described earlier.¹⁸ The total score was calculated by adding together the neck average, microcompaction score, and healing score.

Statistical Analysis

Categorical variables were presented as frequencies and percentages, with χ^2 tests (or the Fisher exact test) used for testing the difference. Continuous variables were expressed as means (SD), with testing differences evaluated using a t test or Mann-Whitney U test based on the data distribution (normally distributed or not). Logistic regression was used to identify any possible predictors of aneurysm recurrence and occlusion. Regression results were expressed as ORs and 95% CIs. Receiver operating characteristic curves were also generated. The area under the curve was calculated; building the associated receiver operating characteristic curve to provide aggregate values of significant predictors correctly classified the occlusion status of each rabbit. All data were analyzed using R statistical and computing software (<http://www.r-project.org/software>), Version 4.1.1, using the “rcmdr” and “glm2” packages. $P < .05$ was considered significant for all statistical tests.

RESULTS

Aneurysm Characteristics

A total of 183 rabbits were included in this study (aneurysm characteristics are shown in Table 1), with a mean follow-up point of 2.3 (SD, 2.4) months, and balloon-assisted coiling was used in 63.9% (117/183) of aneurysms. Angiography before sacrifice showed complete occlusion in 79.8% of the subjects, while near-complete and incomplete occlusions were found in 11.5% and

Table 1: Characteristics of the included aneurysms

Variables	Balloon Used						P Value
	No		Yes		Total		
	Mean	SD	Mean	SD	Mean	SD	
Follow-up time point (mo)	3.1	2.2	1.8	2.4	2.3	2.4	<.001 ^a
Neck (mm)	3.8	5.0	2.8	1.2	3.2	3.1	.105
Width (mm)	3.7	1.0	3.6	1.0	3.6	1.0	.689
Height (mm)	8.2	2.2	7.9	2.4	8.0	2.3	.371
Volume (mm ³)	69.2	56.1	61.3	45.2	64.1	49.4	.676

Note:—SD, standard deviation.

^a Statistically significant.

Table 2: Summary of different outcomes following treatment

Variables	Balloon Used						P Value
	No		Yes		Total		
	Count	%	Count	%	Count	%	
Angio after treatment							
Complete	46	69.7	106	90.6	152	83.1	<.001 ^a
Incomplete	3	4.5	2	1.7	5	2.7	
Near-complete	17	25.8	9	7.7	26	14.2	
Angio before sacrifice							
Complete	41	62.1	105	89.7	146	79.8	<.001 ^a
Incomplete	13	19.7	3	2.6	16	8.7	
Near-complete	12	18.2	9	7.7	21	11.5	
Angio comparative score							
Progressive	3	4.5	6	5.1	9	4.9	<.001 ^a
Recurrence	19	28.8	9	7.7	28	15.3	
Stable	44	66.7	102	87.2	146	79.8	
Cross loop sign (coil bridging the neck)							
No	55	83.3	116	99.1	171	93.4	<.001 ^a
Yes	11	16.7	1	0.9	12	6.6	
Packing density (mean) (%)	24.8 (SD, 14.0)		30.5 (SD, 14.6)		28.5 (SD, 14.6)		.004 ^a
Total histologic healing score (mean)	5.6 (SD, 2.5)		5.4 (SD, 2.4)		5.5 (SD, 2.5)		.429

Note:—Angio indicates angiography; SD, standard deviation.
^a Statistically significant.

8.7% of the subjects, respectively. Comparing posttreatment angiographic occlusion with the presacrifice angiography showed a stable course in 79.8% of the subjects (146/183), recurrence in 15.3% (28/183), and a progressive course in 4.9%. The mean packing density was 28.5 (SD, 14.6), and the average histologic healing score was 5.5 (SD, 2.5). The recurrence rate was 7.7% (9/117) when a balloon was used compared with 28.8% (19/66) when a balloon was not used. The presence or absence of balloon-assisted coiling was a significant predictor of different outcomes (Table 2).

Predictors of Aneurysm Recurrence

Univariate and multivariate analyses of the potential predictors of the recurrence risk were performed. The predictors of recurrence risk identified by this method included follow-up time points, aneurysm characteristics (neck, width, height, volume), and balloon usage. The recurrence rate increased with lower packing density (OR = 0.95; 95% CI, 0.91–0.98; *P* = .006), wider neck diameters (OR = 1.75; 95% CI, 1.28–2.42; *P* = .001), higher aneurysm heights (OR = 1.36; 95% CI, 1.13–1.65; *P* = .001), larger aneurysm volumes (OR = 1.01; 95% CI, 1.00–1.02; *P* = .010), and the

absence of a balloon (OR = 0.21; 95% CI, 0.08–0.48; *P* < .001). In the multivariate model, only balloon usage (OR = 0.17; 95% CI, 0.05–0.47; *P* = .001) persisted as a significant predictor of recurrence (Table 3).

Predictors of Aneurysm Occlusion

Similarly, univariate and multivariate analyses of the potential predictors of the occlusion were performed. The occlusion rate was higher with narrower neck diameters (OR = 0.60; 95% CI, 0.44–0.80; *P* = .001), lower aneurysm heights (OR = 0.76; 95% CI, 0.64–0.90; *P* = .002), smaller aneurysm volumes (OR = 0.99; 95% CI, 0.99–1.00; *P* = .039), and the presence of a balloon (OR = 5.34; 95% CI, 2.50–11.95; *P* < .001). In the multivariate model, aneurysm width was significant (OR = 5.45; 95% CI, 1.54–19.76; *P* = .008), and only packing density (OR = 1.05; 95% CI, 1.02–1.10; *P* = .008) with balloon use (OR = 6.88; 95% CI, 2.58–20.37; *P* < .001) persisted as a significant predictor of recurrence (Table 4).

Packing Density Cutoff Values

Packing density cutoff values for predicting occlusion were obtained after analyzing the receiver operating characteristic

Table 3: Predictors of aneurysm recurrence^a

Predictors	Recurrence		OR (Univariable)	OR (Multivariable)
	No	Yes		
Packing density (mean) (%)	29.8 (14.6)	21.2 (12.2)	0.95 (0.91–0.98, <i>P</i> value = .006 ^b)	0.97 (0.93–1.01, <i>P</i> value = .129)
Follow-up time point (mean) (mo)	2.3 (2.5)	2.3 (2.0)	1.01 (0.84–1.18, <i>P</i> value = .887)	0.87 (0.67–1.11, <i>P</i> value = .297)
Neck (mean) (SD) (mm)	2.8 (1.2)	5.1 (7.4)	1.75 (1.28–2.42, <i>P</i> value = .001 ^b)	1.52 (0.99–2.37, <i>P</i> value = .054)
Width (mean) (SD) (mm)	3.6 (1.0)	3.8 (1.1)	1.30 (0.88–1.91, <i>P</i> value = .184)	0.27 (0.07–1.11, <i>P</i> value = .061)
Height (mean) (SD) (mm)	7.8 (2.2)	9.4 (2.6)	1.36 (1.13–1.65, <i>P</i> value = .001 ^b)	1.23 (0.91–1.71, <i>P</i> value = .191)
Volume (mean) (SD) (mm ³)	60.0 (44.1)	87.2 (68.8)	1.01 (1.00–1.02, <i>P</i> value = .010 ^b)	1.01 (0.98–1.05, <i>P</i> value = .354)
Balloon used (mean) (SD)				
No	47 (71.2)	19 (28.8)	Reference	
Yes	108 (92.3)	9 (7.7)	0.21 (0.08–0.48, <i>P</i> value <.001 ^b)	0.17 (0.05–0.47, <i>P</i> value = .001 ^b)

Note:—SD, standard deviation.

^a Model metrics: Akaike information criterion (AIC) = 135.5, C-statistic = 0.809, The Hosmer–Lemeshow test (H&L) = χ^2 (8) 4.62 (*P* = .798).

^b Statistically significant.

Table 4: Predictors of aneurysm occlusion^a

Predictors	Occlusion		OR (Univariable)	OR (Multivariable)
	No	Yes		
Packing density (mean) (SD) (%)	20.4 (11.9)	30.5 (14.5)	1.07 (1.03–1.11, <i>P</i> value < .001 ^b)	1.05 (1.02–1.10, <i>P</i> value = .008 ^b)
Follow-up time point (mean) (SD) (mo)	2.5 (2.1)	2.2 (2.5)	0.96 (0.84–1.12, <i>P</i> value = .576)	1.11 (0.89–1.42, <i>P</i> value = .398)
Neck (mean) (SD) (mm)	4.7 (6.5)	2.8 (1.1)	0.60 (0.44–0.80, <i>P</i> value = .001 ^b)	0.68 (0.45–1.02, <i>P</i> value = .065)
Width (mean) (SD) (mm)	3.7 (1.1)	3.6 (1.0)	0.89 (0.63–1.28, <i>P</i> value = .536)	5.45 (1.54–19.76, <i>P</i> value = .008 ^b)
Height (mean) (SD) (mm)	9.1 (2.5)	7.7 (2.2)	0.76 (0.64–0.90, <i>P</i> value = .002 ^b)	0.80 (0.60–1.05, <i>P</i> value = .123)
Volume (mean) (SD) (mm ³)	79.5 (65.1)	60.3 (44.1)	0.99 (0.99–1.00, <i>P</i> value = .039 ^b)	0.98 (0.96–1.01, <i>P</i> value = .229)
Balloon used (mean) (SD)				
No	25 (37.9)	41 (62.1)		Reference
Yes	12 (10.3)	105 (89.7)	5.34 (2.50–11.95, <i>P</i> value < .001 ^b)	6.88 (2.58–20.37, <i>P</i> value < .001 ^b)

Note:—SD, standard deviation.

^a Model metrics: Akaike information criterion (AIC) = 146.3, C-statistic = 0.849, The Hosmer–Lemeshow test (H&L) = χ^2 (8) 11.22 (*P* = .190).

^b Statistically significant.

curve of all study subjects, which showed an overall good performance (area under the curve = 0.72). The values tested ranged from 6.00% to 93.94% (Online Supplemental Data). It appeared that values of $\geq 18\%$ had good sensitivity and specificity for predicting aneurysm occlusion; however, a packing density of 26.9% had the best balance of sensitivity, specificity, and positive and negative predictive values. On the basis of these findings, we reconducted the regression analyses categorizing packing density to $\geq 26.9\%$ and values to $< 26.9\%$. The univariable results showed no changes in the identified predictors from the previously built model, but it was not the case in the multivariate results, in which a packing density of $\geq 26.9\%$ and aneurysm width (millimeters) were significant predictors of higher occlusion rates (OR = 3.48; 95% CI, 1.31–10.15; *P* = .016; and OR = 4.96; 95% CI, 1.42–17.74; *P* = .012, respectively). On the other hand, larger aneurysm necks (millimeters) were associated with reduced occlusion rates (OR = 0.65; 95% CI, 0.43–0.97; *P* = .035) (Online Supplemental Data).

DISCUSSION

The aneurysm recurrence rate observed in this study (15.3%) is similar to those reported in multiple analyses of aneurysm recurrence rates in humans (7%–27%).^{20–26} We also observed that the rate of aneurysm recurrence was significantly reduced in procedures with balloon-assisted coiling and in aneurysms showing complete occlusion immediately after coil embolization. In this rabbit elastase-induced aneurysm model, packing density and aneurysm volume were weak predictors of aneurysm recurrence; however, the packing density was a good predictor of the occlusion rate. Previous effort had been made to compare the histologic changes in human cerebral aneurysms with the findings in animal models. A retrospective histopathologic evaluation of 27 elastase-induced aneurysms in rabbits was conducted,⁹ matching the findings to the 4-point scale described by Frösen et al.²⁷ The authors found similarities between the 2 models in terms of underlying aneurysm wall degeneration mechanisms such as lack of an intact elastic lamina, loss of the endothelium, and hypocellular aneurysm walls.⁹ In the elastase-induced model, the progression and distribution of the histologic subtypes of the aneurysm wall were similar to those previously described in the Frösen et al model.

Aneurysm recurrence is a significant limitation of endovascular coiling procedures, with recurrence rates reported as high as 50%.^{20–22,28–30} Additionally, large aneurysms and wide-neck aneurysms have been

identified as significant risk factors for early recurrence and are also vulnerable to early recurrence.³¹ In a single-center retrospective study, complete aneurysm occlusion was obtained in 31.7% of patients who underwent endovascular coiling procedures, and at ≤ 24 months, aneurysm recurrence occurred in 35.9% of this patient population.³² The study-level recurrence rate of the present study is comparable with that found in the human study, thus indicating the utility of the rabbit elastase model to mimic what is found in humans.

Aneurysm recurrence rates after coil embolization have been associated with different factors in humans. Aneurysms with a small neck have a lower recurrence rate compared with those with wider necks.²¹ Similarly, smaller aneurysms have a lower recurrence rate compared with large or giant aneurysms.^{21,22,33} Furthermore, the degree of aneurysm occlusion after treatment has also been related to recurrence. Aneurysms with initial complete occlusion were less likely to recur at follow-up.²² Our observation of a zero recurrence rate in aneurysms with complete occlusion is in line with this finding.

Aneurysm recurrence may occur through multiple mechanisms. Lower packing density or aneurysm growth may lead to coil compaction,³⁴ affecting histologic healing and subsequently causing aneurysm recanalization. In clinical settings, a large aneurysm volume is associated with low packing density and higher compaction rates. It is reported that a packing density of 24% is required to prevent compaction in aneurysms with a volume of < 600 mm.^{3,35} Our analysis showed that aneurysm volume and packing density were weak predictors of aneurysm recurrence. This result may be due to specific differences found in this model and to our embolization procedure. While it is known that the range in values of hemodynamic factors such as pressure, oscillatory shear index, and wall shear stress found in the rabbit elastase-induced aneurysm model is similar to that seen in humans,³⁶ the model is also known for its aneurysm patency. One report observed no changes in aneurysm geometry during 24 months.³⁷ The mean volume of aneurysms created in this study was less than that found in humans,³⁵ while the mean packing density was higher than 24%. A higher packing density has been associated with better histologic healing in the rabbit elastase aneurysm model.³⁸ This model also showed a mild biologic response, with studies reporting poor healing with the formation of loose connective tissue, the absence of contractile cells, and a lack of collagen deposition.^{15,39,40} In this rabbit elastase aneurysm model, the curvature of the parent vessel causes substantial inertia-driven flow, similar to that in humans, which may also contribute to aneurysm growth and recurrence.⁴¹

The development of more efficient endovascular devices for the treatment of intracranial aneurysms relies on preclinical testing in animal models. The rabbit aneurysm model has been considered a criterion standard for preclinical testing of various neurointerventional devices.^{17,42-45} Our results show that the aneurysm occlusion rates in rabbit aneurysms are comparable with those of human aneurysms following the use of endoluminal and intrasaccular flow-diverting devices,^{45,46} making this an ideal model for testing endovascular devices.

Limitations

Our study has limitations. The follow-up times in this study were limited to 1 year, which should be extended in future studies. Additionally, this is an extracranial aneurysm model with thick aneurysm walls, making it difficult to assess potential complications that may arise in treating human intracranial aneurysms.⁷ Moreover, our model has the inherent limitation of animal models, with their inability to account for all factors involved in the human complex pathophysiology, including various cellular phenotypes in the aneurysm wall. Although the coils were all of the same type, they were not the same brand and the operator was not the same in all cases, possibly introducing some bias. Finally, Raymond et al²² demonstrated that almost half of all recurrences were present by 6 months after coiling. Unfortunately, typical follow-up imaging of patients would be done at 3–6 months after coiling, but there is not much literature available to compare humans versus rabbits. We believe that evaluating the aneurysm occlusion stability and recurrence at early (<1 month), sub-chronic (1–3 months), and chronic (>3 months) stages would provide valuable insight into the timing of the recurrence.

CONCLUSIONS

The rabbit elastase aneurysm model may be a mosaic piece in the evaluation process of aneurysm treatments and may mimic aneurysm recurrence rates in humans. However, a comparative study against a human sample is necessary to confirm this finding.

ACKNOWLEDGMENTS

We would like to thank Duncan J. Maitland, PhD (Texas A&M University, College Station, Texas) for his effort to make this work possible.

Disclosure forms provided by the authors are available with the full text and PDF of this article at www.ajnr.org.

REFERENCES

1. Vlak MHM, Algra A, Brandenburg R, et al. **Prevalence of unruptured intracranial aneurysms, with emphasis on sex, age, comorbidity, country, and time period: a systematic review and meta-analysis.** *Lancet Neurol* 2011;10:626–36 CrossRef Medline
2. Imaizumi Y, Mizutani T, Shimizu K, et al. **Detection rates and sites of unruptured intracranial aneurysms according to sex and age: an analysis of MR angiography-based brain examinations of 4070 healthy Japanese adults.** *J Neurosurg* 2018;130:1–578 CrossRef Medline
3. Brinjikji W, Rabinstein AA, Nasr DM, et al. **Better outcomes with treatment by coiling relative to clipping of unruptured intracranial aneurysms in the United States, 2001–2008.** *AJNR Am J Neuroradiol* 2011;32:1071–75 CrossRef Medline
4. Qureshi AI, Vazquez G, Tariq N, et al. **Impact of International Subarachnoid Aneurysm Trial results on treatment of ruptured intracranial aneurysms in the United States: clinical article.** *J Neurosurg* 2011;114:834–41 CrossRef Medline
5. Spiessberger A, Vogt DR, Fandino J, et al. **Formation of intracranial de novo aneurysms and recurrence after neck clipping: a systematic review and meta-analysis.** *J Neurosurg* 2019;132:456–64 CrossRef Medline
6. Darflinger R, Thompson LA, Zhang Z, et al. **Recurrence, retreatment, and rebleed rates of coiled aneurysms with respect to the Raymond-Roy scale: a meta-analysis.** *J Neurointerv Surg* 2016;8:507–11 CrossRef Medline
7. Brinjikji W, Ding YH, Kallmes DF, et al. **From bench to bedside: utility of the rabbit elastase aneurysm model in preclinical studies of intracranial aneurysm treatment.** *J Neurointerv Surg* 2016;8:521–25 CrossRef Medline
8. Byrne JV, Hope JK, Hubbard N, et al. **The nature of thrombosis induced by platinum and tungsten coils in saccular aneurysms.** *AJNR Am J Neuroradiol* 1997;18:29–33 Medline
9. Wang S, Dai D, Kolumam Parameswaran P, et al. **Rabbit aneurysm models mimic histologic wall types identified in human intracranial aneurysms.** *J Neurointerv Surg* 2018;10:411–15 CrossRef Medline
10. Altes TA, Cloft HJ, Short JG, et al. **1999 ARRS Executive Council Award: creation of saccular aneurysms in the rabbit—a model suitable for testing endovascular devices.** *American Roentgen Ray Society. AJR Am J Roentgenol* 2000;174:349–54 CrossRef Medline
11. Ding YH, Dai D, Lewis DA, et al. **Can neck size in elastase-induced aneurysms be controlled? A prospective study.** *AJNR Am J Neuroradiol* 2005;26:2364–67 Medline
12. Ding YH, Dai D, Danielson MA, et al. **Control of aneurysm volume by adjusting the position of ligation during creation of elastase-induced aneurysms: a prospective study.** *AJNR Am J Neuroradiol* 2007;28:857–59 Medline
13. Wang K, Huang Q, Hong B, et al. **Neck injury is critical to elastase-induced aneurysm model.** *AJNR Am J Neuroradiol* 2009;30:1685–87 CrossRef Medline
14. Ding YH, Kadirvel R, Dai D, et al. **Creation of bifurcation-type elastase-induced aneurysms in rabbits.** *AJNR Am J Neuroradiol* 2013;34:E19–21 CrossRef Medline
15. Dai D, Ding YH, Danielson MA, et al. **Histopathologic and immunohistochemical comparison of human, rabbit, and swine aneurysms embolized with platinum coils.** *AJNR Am J Neuroradiol* 2005;26:2560–68 Medline
16. Dai D, Ding YH, Lewis DA, et al. **A proposed ordinal scale for grading histology in elastase-induced, saccular aneurysms.** *AJNR Am J Neuroradiol* 2006;27:132–38 Medline
17. Ding YH, Dai D, Lewis DA, et al. **Angiographic and histologic analysis of experimental aneurysms embolized with platinum coils, Matrix, and HydroCoil.** *AJNR Am J Neuroradiol* 2005;26:1757–63 Medline
18. Herting SM, Ding Y, Boyle AJ, et al. **In vivo comparison of shape memory polymer foam-coated and bare metal coils for aneurysm occlusion in the rabbit elastase model.** *J Biomed Mater Res B Appl Biomater* 2019;107:2466–75 CrossRef Medline
19. Roy D, Milot G, Raymond J. **Endovascular treatment of unruptured aneurysms.** *Stroke* 2001;32:1998–2004 CrossRef Medline
20. Ferns SP, Sprengers ME, van Rooij WJ, et al. **Coiling of intracranial aneurysms: a systematic review on initial occlusion and reopening and retreatment rates.** *Stroke* 2009;40:e523–29 CrossRef Medline
21. Murayama Y, Nien YL, Duckwiler G, et al. **Guglielmi Detachable Coil embolization of cerebral aneurysms: 11 years' experience.** *J Neurosurg* 2003;98:959–66 CrossRef Medline
22. Raymond J, Guilbert F, Weill A, et al. **Long-term angiographic recurrences after selective endovascular treatment of aneurysms with detachable coils.** *Stroke* 2003;34:1398–1403 CrossRef Medline

23. Cognard C, Weill A, Spelle L, et al. **Long-term angiographic follow-up of 169 intracranial berry aneurysms occluded with detachable coils.** *Radiology* 1999;212:348–56 CrossRef Medline
24. Tan IY, Agid RF, Willinsky RA. **Recanalization rates after endovascular coil embolization in a cohort of matched ruptured and unruptured cerebral aneurysms.** *Interv Neuroradiol* 2011;17:27–35 CrossRef Medline
25. Nguyen TN, Hoh BL, Amin-Hanjani S, et al. **Comparison of ruptured vs unruptured aneurysms in recanalization after coil embolization.** *Surg Neurol* 2007;68:19–23 CrossRef Medline
26. Marbacher S, Niemelä M, Hernesniemi J, et al. **Recurrence of endovascularly and microsurgically treated intracranial aneurysms—review of the putative role of aneurysm wall biology.** *Neurosurg Rev* 2019;42:49–58 CrossRef Medline
27. Frösien J, Piippo A, Paetau A, et al. **Remodeling of saccular cerebral artery aneurysm wall is associated with rupture: histological analysis of 24 unruptured and 42 ruptured cases.** *Stroke* 2004;35:2287–93 CrossRef
28. Consoli A, Vignoli C, Renieri L, et al. **Assisted coiling of saccular wide-necked unruptured intracranial aneurysms: stent versus balloon.** *J Neurointerv Surg* 2016;8:52–57 CrossRef Medline
29. Chung EJ, Shin YS, Lee CH, et al. **Comparison of clinical and radiologic outcomes among stent-assisted, double-catheter, and balloon-assisted coil embolization of wide neck aneurysms.** *Acta Neurochir (Wien)* 2014;156:1289–95 CrossRef Medline
30. Pötin M, Biondi A, Sourour N, et al. **The LUNA aneurysm embolization system for intracranial aneurysm treatment: short-term, mid-term and long-term clinical and angiographic results.** *J Neurointerv Surg* 2018;10:e34 CrossRef Medline
31. Mortimer AM, Marsh H, Klimczak K, et al. **Is long-term follow-up of adequately coil-occluded ruptured cerebral aneurysms always necessary? A single-center study of recurrences after endovascular treatment.** *J Neurointerv Surg* 2015;7:373–79 CrossRef Medline
32. Colby GP, Paul AR, Radvany MG, et al. **A single center comparison of coiling versus stent assisted coiling in 90 consecutive paraophthalmic region aneurysms.** *J Neurointerv Surg* 2012;4:116–20 CrossRef Medline
33. Gruber A, Killer M, Bavinszki G, et al. **Clinical and angiographic results of endosaccular coiling treatment of giant and very large intracranial aneurysms: a 7-year, single-center experience.** *Neurosurgery* 1999;45:793–804 CrossRef Medline
34. Hope JK, Byrne JV, Molyneux AJ. **Factors influencing successful angiographic occlusion of aneurysms treated by coil embolization.** *AJNR Am J Neuroradiol* 1999;20:391–99 Medline
35. Sluzewski M, van Rooij WJ, Slob MJ, et al. **Relation between aneurysm volume, packing, and compaction in 145 cerebral aneurysms treated with coils.** *Radiology* 2004;231:653–58 CrossRef Medline
36. Zeng Z, Kallmes DF, Durka MJ, et al. **Hemodynamics and anatomy of elastase-induced rabbit aneurysm models: similarity to human cerebral aneurysms?** *AJNR Am J Neuroradiol* 2011;32:595–601 CrossRef Medline
37. Ding YH, Dai D, Lewis DA, et al. **Long-term patency of elastase-induced aneurysm model in rabbits.** *AJNR Am J Neuroradiol* 2006;27:139–41 Medline
38. Ding YH, Dai D, Kadirvel R, et al. **Relationship between aneurysm volume and histologic healing after coil embolization in elastase-induced aneurysms: a retrospective study.** *AJNR Am J Neuroradiol* 2008;29:98–101 CrossRef Medline
39. Kallmes DF, Fujiwara NH, Yuen D, et al. **A collagen-based coil for embolization of saccular aneurysms in a New Zealand white rabbit model.** *AJNR Am J Neuroradiol* 2003;24:591–96 Medline
40. Dai D, Ding YH, Kadirvel R, et al. **A longitudinal immunohistochemical study of the healing of experimental aneurysms after embolization with platinum coils.** *AJNR Am J Neuroradiol* 2006;27:736–41 Medline
41. Meng H, Wang Z, Kim M, et al. **Saccular aneurysms on straight and curved vessels are subject to different hemodynamics: implications of intravascular stenting.** *AJNR Am J Neuroradiol* 2006;27:1861–65 Medline
42. Ding YH, Lewis DA, Kadirvel R, et al. **The Woven EndoBridge: a new aneurysm occlusion device.** *AJNR Am J Neuroradiol* 2011;32:607–11 CrossRef Medline
43. Kwon SC, Ding YH, Dai D, et al. **Preliminary results of the LUNA aneurysm embolization system in a rabbit model: a new intrasaccular aneurysm occlusion device.** *AJNR Am J Neuroradiol* 2011;32:602–06 CrossRef Medline
44. Kallmes DF, Ding YH, Dai D, et al. **A second-generation, endoluminal, flow-disrupting device for treatment of saccular aneurysms.** *AJNR Am J Neuroradiol* 2009;30:1153–58 CrossRef Medline
45. Kallmes DF, Ding YH, Dai D, et al. **A new endoluminal, flow-disrupting device for treatment of saccular aneurysms.** *Stroke* 2007;38:2346–52 CrossRef Medline
46. Rouchaud A, Brinjikji W, Ding YH, et al. **Evaluation of the angiographic grading scale in aneurysms treated with the WEB device in 80 rabbits: correlation with histologic evaluation.** *AJNR Am J Neuroradiol* 2016;37:324–29 CrossRef Medline

Iodine Maps from Dual-Energy CT to Predict Extrathyroidal Extension and Recurrence in Papillary Thyroid Cancer Based on a Radiomics Approach

X.-Q. Xu, Y. Zhou, G.-Y. Su, X.-W. Tao, Y.-Q. Ge, Y. Si, M.-P. Shen, and F.-Y. Wu



ABSTRACT

BACKGROUND AND PURPOSE: Accurate prediction of extrathyroidal extension and subsequent recurrence is crucial in papillary thyroid cancer clinical management. Our aim was to conduct iodine map–based radiomics to predict extrathyroidal extension and to explore its prognostic value for recurrence-free survival in papillary thyroid cancer.

MATERIALS AND METHODS: A total of 452 patients with papillary thyroid cancer were retrospectively recruited between June 2017 and June 2020. Radiomics features were extracted from noncontrast images, dual-phase mixed images, and iodine maps, respectively. Random forest and least absolute shrinkage and selection operator (LASSO) were applied to build 6 radiomics scores (noncontrast radiomics score_random forest; noncontrast rad-score_LASSO; mixed rad-score_random forest; mixed rad-score_LASSO; iodine radiomics score_random forest; iodine radiomics score_LASSO) respectively. Logistic regression was used to construct 6 radiomics models incorporating 6 radiomics scores with clinical risk factors and to compare them with the clinical model. A radiomics model that achieved the highest performance was presented as a nomogram and assessed by discrimination, calibration, clinical usefulness, and prognosis evaluation.

RESULTS: Iodine radiomics scores performed significantly better than mixed radiomics scores. Both of them outperformed noncontrast radiomics scores. Iodine map–based radiomics models significantly surpassed the clinical model. A radiomics nomogram incorporating size, capsule contact, and iodine radiomics score_random forest was built with the highest performance (training set, area under the curve = 0.78; validation set, area under the curve = 0.84). Stratified analysis confirmed the nomogram stability, especially in group negative for CT-reported extrathyroidal extension (area under the curve = 0.69). Nomogram-predicted extrathyroidal extension risk was an independent predictor of recurrence-free survival. A high risk for extrathyroidal extension portended significantly lower recurrence-free survival than low risk ($P < .001$).

CONCLUSIONS: Iodine map–based radiomics might be a supporting tool for predicting extrathyroidal extension and subsequent recurrence risk in patients with papillary thyroid cancer, thus facilitating clinical decision-making.

ABBREVIATIONS: AUC = area under the curve; BMI = body mass index; ETE = extrathyroidal extension; DECT = dual-energy CT; LASSO = least absolute shrinkage and selection operator; PTC = papillary thyroid cancer; rad-score = radiomics score; RF = random forest; RFS = recurrence-free survival

Although papillary thyroid cancer (PTC) has a favorable prognosis, it is prone to local-regional recurrence.¹ A dynamic risk-stratification system can predict postoperative recurrence and

determine the clinical treatment plan in patients with PTC.¹ Extrathyroidal extension (ETE) is considered an adverse prognostic factor of PTC and plays an important role in the risk-stratification system.¹⁻³ Patients with PTC with ETE are recommended for a more aggressive initial therapy, likely total thyroidectomy and intensive follow-up.¹⁻³ Therefore, a preoperative diagnosis of ETE is essential in the clinical management of PTC.

Some aggressive signs in conventional ultrasound and CT are used to assess ETE in clinical practice; however, these signs are subjective, and the sensitivity is relatively low due to that micro ETE can only be determined by tumor histopathological examination.⁴⁻⁶ Because of the difficulty in ETE clinical diagnosis, some previous studies have attempted to use clinical risk factors and tumor morphologic features to predict ETE. However, the results of these studies were inconsistent, and morphologic features are subjective.^{7,8}

Received July 24, 2021; accepted after revision February 12, 2022.

From the Departments of Radiology (X.-Q.X., Y.Z., G.-Y.S., F.-Y.W.), and Thyroid Surgery (Y.S., M.-P.S.), The First Affiliated Hospital of Nanjing Medical University, Nanjing, China; and Siemens Healthineers (X.-W.T., Y.-Q.G.), Shanghai, China.

Xiao-Quan Xu and Yan Zhou contributed equally to this study.

This work received funding by the Natural Science Foundation of China (82171928) and the Natural Science Foundation of Jiangsu Province (BK20201494).

Please address correspondence to Fei-Yun Wu, MD, PhD, Department of Radiology, The First Affiliated Hospital of Nanjing Medical University, No. 300, Guangzhou Rd, Gulou District, Nanjing, China; e-mail: wfy_njmu@163.com

Indicates open access to non-subscribers at www.ajnr.org

Indicates article with online supplemental data.

<http://dx.doi.org/10.3174/ajnr.A7484>

Radiomics is a rapidly evolving field that quantifies high-throughput features from medical images and is useful in cancer scanning, diagnosis, and prognosis evaluation.^{9,10} Concerning radiomics applications in PTC, some studies have verified their value in evaluating tumor aggressiveness, predicting *BRAF* gene status, and diagnosing or predicting cervical lymph node metastasis.¹¹⁻¹⁴ For preoperative prediction of ETE, Chen et al¹⁵ established a CT-based radiomics nomogram and confirmed its predictive efficiency.

Compared with conventional CT, dual-energy CT (DECT) allows material decomposition and offers iodine maps that directly quantify the content and portray the distribution of iodine.^{16,17} As is well known, the thyroid gland is the primary source of iodine storage in the human body, and PTC destructs thyroid follicles leading to a decrease in iodine concentration to various degrees.¹ Therefore, iodine uptake of PTC in dual-phase iodine maps is affected by both the thyroidal parenchyma and external iodine (contrast media), which correlate with tumor perfusion. In addition, some previous studies have confirmed that quantitative iodine concentration is effective in differentiating thyroid malignancy and diagnosing metastatic lymph nodes from PTC.¹⁸⁻²⁰

Radiomics of iodine maps can be used to further assess the heterogeneity of iodine uptake.^{21,22} In previous studies, iodine map-based radiomics has proved useful in diagnosing and predicting lymph node metastasis from PTC,^{22,23} indicating that iodine map-based radiomics is promising in PTC investigation. However, no previous study has used iodine map-based radiomics to predict ETE and further correlate with prognosis in PTC, leaving a gap in the current knowledge.

Therefore, in the current study, we evaluated the value of dual-phase iodine map-based radiomics for predicting ETE and recurrence-free survival (RFS) in patients with PTC.

MATERIALS AND METHODS

Study Population

Ethics approval was obtained for this retrospective study from The First Affiliated Hospital of Nanjing Medical University institutional review board, and the requirement of written informed consent was waived. A total of 858 consecutive patients suspicious for PTC who underwent DECT for preoperative assessment from June 2017 to June 2020 were retrospectively recruited. The inclusion and exclusion criteria are listed in the Online Supplemental Data. The final study cohort included 452 patients, divided into a training set (317 patients) and a validation set (135 patients) according to the time of the operation. Detailed demographic characteristics are summarized in the Online Supplemental Data. A total of 84 and 272 patients with PTC were included in our previous studies, which conducted radiomics analysis for diagnosing and predicting lymph metastasis from PTC, respectively.^{22,23} Taking the final histopathologic reports of tumor specimens as a criterion standard, we divided the patients into groups without ETE (training cohort, $n = 195$; validation cohort, $n = 73$) and with ETE (training cohort, $n = 122$; validation cohort, $n = 62$).

Postoperative Follow-up and Recurrence

A total of 245 patients who underwent an operation from June 2017 to June 2019 were routinely followed up every 3–6 months

in the first year and annually thereafter. The follow-up protocol is summarized in the Online Supplemental Data.

Recurrence was defined as clinical evidence (biochemical, structural, and functional) of new disease after the initial operation. Indicators of biochemical recurrence were suppressed thyroglobulin, ≥ 1 ng/mL, stimulated thyroglobulin, ≥ 2 ng/mL, and a detectable thyroglobulin antibody. Pathology-proved disease or morphologic evidence of disease on cross-sectional imaging was considered a structural recurrence. Suspicious findings on whole-body scintigraphy or PET/CT were considered to indicate functional recurrence. The end point of our study was RFS, which was defined as the period from the date of the initial operation to the date of the first recurrence (biochemical, structural, and functional) or the last follow-up visit.^{1,24}

DECT Imaging Technique and Postprocessing

The DECT examination was performed with a third-generation DECT scanner (Somatom Force; Siemens) equipped with 2 x-ray tubes at different voltages (tube A, 80 kV[peak]; tube B, Sn150 kVp).²⁵ Postprocessing was performed using a commercially available software (Syngo Dual Energy, Version VB10B; Siemens). The DECT image-acquisition parameters and postprocessing are detailed in the Online Supplemental Data.

Clinicopathologic Information

Clinical information including age, sex, body mass index (BMI), nodular goiter, Hashimoto thyroiditis, and serology examination results, was acquired from medical records. Age was categorized by 45 and 55 years separately in accordance with the seventh and eighth American Joint Committee on Cancer staging systems.¹ BMI (kilograms/square meter) was calculated as weight (kilograms)/(height \times height) (square meter). *BRAF* V600E gene status was obtained from genetic reports of preoperative fine-needle aspiration biopsy and confirmed in the final tumor surgical specimens.

Tumor Morphologic CT Features and CT-Reported ETE Status

Qualitative CT image analysis was performed by readers 1 and 2 (with 6 and 5 years' experience in head and neck oncologic imaging, respectively) on mixed images. If discrepant interpretations occurred, reader 3 (with 8 years' experience in head and neck oncologic imaging) performed a further assessment and made the final decision. All the observers were blinded to clinical data and permanent pathologic results.

The morphologic CT features of the tumors evaluated in the study are described in the Online Supplemental Data. The degree of tumor capsule contact assessed on the CT image is presented in the Online Supplemental Data. CT-reported ETE-positive criteria are summarized in the Online Supplemental Data. Examples of CT-reported ETE-positive PTC patients using corresponding criteria are shown in the Online Supplemental Data.

Tumor Segmentation and Radiomics Feature Extraction

The workflow of our study is shown in Fig 1. Tumor segmentation was performed semiautomatically by reader 2 using syngo.via Frontier radiomics (Siemens) on noncontrast images, dual-phase mixed images, and iodine maps.^{26,27} The process of semiautomatic tumor segmentation is summarized in the Online Supplemental Data. All tumor segmentation was confirmed again by reader 3.

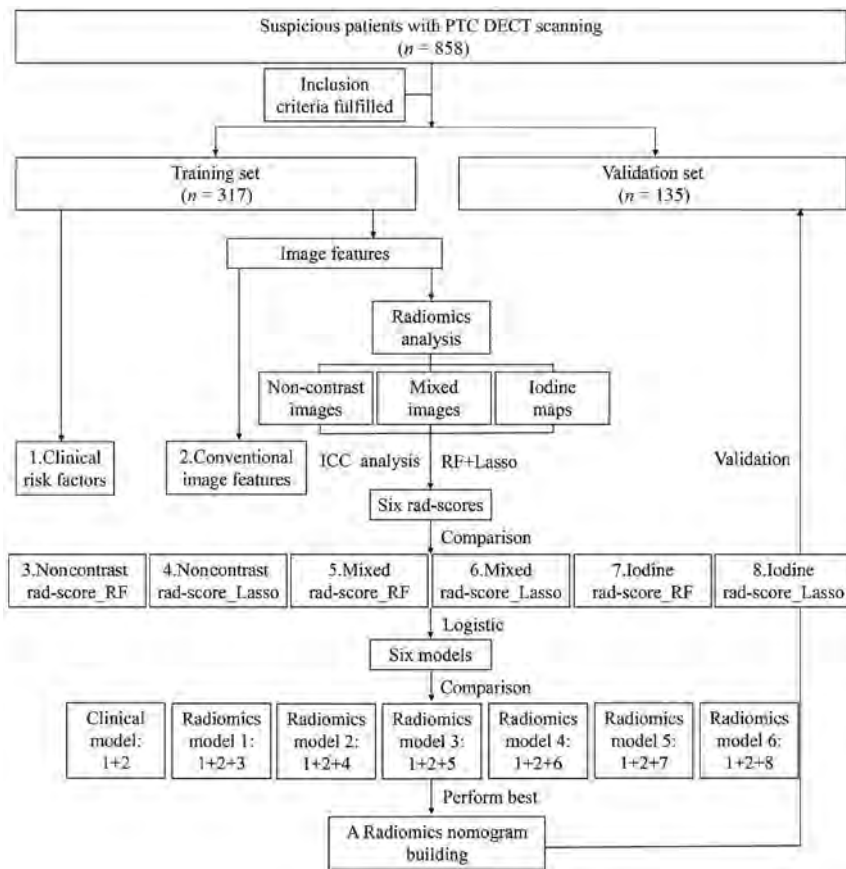


FIG 1. Our study flow chart and radiomics workflow.

After tumor segmentation, radiomics features from VOIs were automatically computed using syngo.via Frontier radiomics interfaces with the PyRadiomics library (<https://github.com/AIM-Harvard/pyradiomics>).²⁸ Detailed information on radiomics feature extraction is described in the Online Supplemental Data.

Radiomics Features: Mining and Signature Building

A 2-step procedure was devised for the high-dimensional radiomics feature mining. First, 183 patients were randomly selected for test and retest, and the intraclass correlation coefficient was calculated to assess the reproducibility of the features. Features with an intraclass correlation coefficient of <0.8 were excluded from the subsequent analysis. Second, random forest (RF) and the least absolute shrinkage and selection operator (LASSO) logistic regression were respectively implemented for radiomics-feature selection and signatures building (Online Supplemental Data).

Through the above dimensionality-reduction procedure, 6 radiomics scores (rad-scores) were built on the basis of noncontrast images or mixed images or iodine maps using RF or LASSO, respectively (noncontrast rad-score_RF; noncontrast rad-score_LASSO; mixed rad-score_RF; mixed rad-score_LASSO; iodine rad-score_RF; iodine rad-score_LASSO). The predictive performance of the 6 rad-scores was compared through receiver operating characteristic analysis calculated from the area under the curve (AUC) using the DeLong test.

Establishment, Performance, and Validation of Radiomics Models

Six radiomics models logistic regression analysis and were incorporated into the 6 constructed rad-scores with other independent risk factors (Fig 1). Backward stepwise variable selection was implemented with the Bayesian information criterion. The variance inflation factor was checked for each factor contained in the final radiomics models. A clinical model was also built containing other pertinent risk factors (except rad-scores) for comparison.

Receiver operating characteristic analysis with the AUC calculated as a performance indicator was used for predictive efficacy assessment. Internal validation was tested in an independent validation cohort. Comparisons of predictive efficacy among the 6 radiomics models and the clinical model were applied through the AUC using the DeLong test.

Radiomics Nomogram Construction

To provide the clinicians with easy-to-use tools, we developed a radiomics nomogram based on the radiomics

model that achieved the highest predictive performance. Consistency between the nomogram-predicted probability of ETE and the actual results accompanied by the Hosmer-Lemeshow goodness of fit test was tested, using calibration curves by bootstrapping with 1000 resamples.²⁹

Stratified and Subgroup Analysis

To confirm the robustness of the established nomogram, we performed stratified analysis for ETE prediction according to age, sex, BMI, and *BRAF* V600E gene status. CT-reported ETE-negative subgroup analysis was also used.

Clinical Utility

The clinical usefulness of the constructed nomogram was assessed by decision curve analysis by quantifying the net benefits at different threshold probabilities for the entire set.³⁰

RFS Analysis

Univariable and multivariable analyses with Cox proportional hazards regression were used to determine risk factors for RFS. Variables with $P < .050$ in the univariable analysis were incorporated into the multivariable Cox regression. The RFS curve was generated using the Kaplan-Meier method, and the nomogram-predicted ETE low- and high-risk groups were compared using log-rank tests.

Table 1: Results of multivariate logistic analysis for constructed clinical and radiomics models

Models	β	Odds Ratio (95% CI)	P Value	VIF
Clinical model				
Size	0.04	1.03 (0.98–1.09)	.009	1.61
Capsule contact	1.53	3.55 (2.32–5.44)	<.001	1.68
Radiomics model 1				
Size	0.04	1.04 (0.98–1.10)	.041	1.57
Capsule contact	1.29	3.61 (2.34–5.59)	<.001	1.56
Noncontrast rad-score_RF	–0.51	0.60 (0.44–0.83)	.002	1.00
Radiomics model 2				
Size	0.04	1.04 (0.98–1.09)	.045	1.57
Capsule contact	1.28	3.58 (2.33–5.50)	.001	1.56
Noncontrast rad-score_LASSO	–0.43	0.65 (0.41–1.04)	.007	1.01
Radiomics model 3				
Capsule contact	1.26	3.51 (2.41–5.13)	<.001	1.62
Mixed rad-score_RF	2.86	17.44 (1.71–177.60)	<.001	1.30
Radiomics model 4				
Size	0.02	1.02 (0.97–1.08)	.036	1.83
Capsule contact	1.24	3.45 (2.24–5.33)	<.001	1.47
Mixed rad-score_LASSO	1.49	14.44 (1.05–120.93)	<.001	1.51
Radiomics model 5				
Size	0.01	1.00 (0.95–1.06)	.034	1.78
Capsule contact	1.11	3.03 (1.95–4.71)	<.001	1.69
Iodine rad-score_RF	3.63	37.64 (6.76–209.59)	<.001	1.34
Radiomics model 6				
Size	0.01	0.99 (0.94–1.05)	.048	1.74
Capsule contact	1.09	2.98 (1.92–4.64)	<.001	1.62
Iodine rad-score_LASSO	2.86	35.32 (2.29–289.19)	<.001	1.37

Note.—VIF indicates variance inflation factor.

Statistical Analysis

Statistical analyses were performed using SPSS (Version 23.0; IBM), MedCalc (Version 15.0; MedCalc Software), and the statistical package R (Version 3.4.3; <http://www.r-project.org>). A 2-sided $P < .050$ indicated a statistically significant difference.

RESULTS

Clinical Characteristics

No significant differences were found between the training and validation sets in any of the clinicopathologic and radiographic characteristics (Online Supplemental Data) (P all $> .050$). The ETE-positive rates were 38.5% (122 of 317) in the training cohort and 45.9% (62 of 135) in the validation cohort. CT-reported ETE had a high specificity (97.4%) but a poor sensitivity (40.2%) in the entire cohort. Univariate analyses indicated BMI, size, capsule contact, and CT-reported ETE with $P < .050$ in estimating ETE (Online Supplemental Data). A clinical model was built containing size and capsule contact, which were identified as independent risks for ETE through multivariable logistic regression analysis (Table 1).

Features Selection and Radiomics Scores Calculation

In total, 573 stable features extracted from noncontrast images, 1565 stable features (707 arterial and 858 venous phase) extracted from mixed images, and 1461 stable features (738 arterial and 723 venous phase) extracted from iodine maps with the intraclass correlation coefficient of > 0.8 were retained. The reproducibility of the extracted features is shown in the Online Supplemental Data. The RF classifier selected 6 features of noncontrast images, 14 features (8 arterial phase and 6 venous phase) of mixed images, and 15 features (7 arterial phase and 8 venous phase) of

iodine maps, respectively. RF feature-importance ranking is presented in the Online Supplemental Data. LASSO logistic regression shrank these stable features, resulting in 9 features of noncontrast images, 22 features (8 arterial phase and 14 venous phase) of mixed images, and 11 features (5 arterial phase and 6 venous phase) of iodine maps with nonzero coefficients, respectively. The results of LASSO logistic shrinking are depicted in the Online Supplemental Data. Ultimately, 6 rad-scores of noncontrast images, mixed images, and iodine maps using RF or LASSO logistic were established (noncontrast rad-score_RF; noncontrast rad-score_LASSO; mixed rad-score_RF; mixed rad-score_LASSO; iodine rad-score_RF; iodine rad-score_LASSO).

Mixed or Iodine Rad-Scores versus Noncontrast Rad-Scores

Significant differences were found between patients with and without ETE in all 6 established rad-scores (P all < 0.050). There were no significant differences between different rad-scores using the RF or LASSO method (P all > 0.050). Mixed and iodine rad-scores both performed better than noncontrast rad-scores, irrespective of whether RF (training set, $P = .171$ and $P < .001$; validation set, $P = .198$ and $P = .001$) or LASSO (training set, $P = .172$ and $P < .001$; validation set, $P = .318$ and $P = .004$) was used, with significant differences between iodine and noncontrast rad-scores ($P < .005$). Detailed predictive ability comparisons of 6 rad-scores are summarized in the Online Supplemental Data. Receiver operating characteristic analyses are also shown in the Online Supplemental Data.

Iodine versus Mixed Rad-Scores

Iodine rad-scores significantly outperformed mixed rad-scores in both the training and validation cohorts, irrespective of whether

Table 2: Prediction efficiency comparisons of 6 radiomics models and the clinical model

Radiomics vs Clinical Models (AUC)	Training Set (317)	P Value	Validation Set (135)	P Value
Radiomics model 1 vs clinical model	0.73 vs 0.72	.920	0.73 vs 0.72	.838
Radiomics model 2 vs clinical model	0.73 vs 0.72	.877	0.73 vs 0.72	.777
Radiomics model 3 vs clinical model	0.76 vs 0.72	.022	0.76 vs 0.72	.132
Radiomics model 4 vs clinical model	0.75 vs 0.72	.064	0.74 vs 0.72	.179
Radiomics model 5 vs clinical model	0.78 vs 0.72	<.001	0.84 vs 0.72	<.001
Radiomics model 6 vs clinical model	0.77 vs 0.72	<.001	0.80 vs 0.72	.032

RF or LASSO was used ($P < .050$). Iodine rad-score_RF obtained the optimal performance, with an AUC of 0.74 in the training cohort and 0.74 in the validation cohort. Radiomics feature composition of the iodine rad-score_RF is summarized in the Online Supplemental Data, and distribution is shown as a violin plot in the Online Supplemental Data.

Development, Performance, and Validation of Radiomics Models

Six radiomics models were constructed using the 6 rad-scores incorporating other clinical risk factors through multivariable logistic regression analysis. The results of logistic regression are presented in Table 1. The variance inflation factor of all variables included in the 6 radiomics models ranged from 1.00 to 1.83, indicating that there is no multicollinearity. The AUCs of all 6 radiomics models were all >0.73 in both the training and validation cohorts. The predictive performance of the 6 radiomics models is detailed in the Online Supplemental Data. The predictive performances of radiomics models improved when adding the clinical risk factors (tumor size and capsule contact) in addition to different rad-scores. Among the 6 radiomics models, radiomics model 5, which incorporated size, capsule contact, and iodine rad-score_RF, achieved the highest performance with an AUC of 0.78 in the training cohort and 0.84 in the validation cohort.

Radiomics versus Clinical Models

All 6 radiomics models yielded higher discrimination than the clinical model both in the training and validation cohorts. In addition, the performance improvement of radiomics models 5 and 6 (radiomics of iodine maps using RF and LASSO) added to the clinical model reached a significant difference ($P < .050$). Predictive performance comparisons of radiomics models and the clinical model are summarized in Table 2.

Radiomics Nomogram Building

A radiomics nomogram was built on the basis of radiomics model 5 (radiomics of iodine maps using RF), which had the highest predictive ability with AUCs of 0.78 and 0.84, sensitivities of 0.73 and 0.74, specificities of 0.69 and 0.78, positive predictive values of 0.62 and 0.67, negative predictive values of 0.77 and 0.81, and accuracies of 0.70 and 0.77 in the training and validation sets, respectively. Moreover, the radiomics nomogram added a significant incremental performance to the clinical model (Table 2 and Online Supplemental Data). Favorable calibration of the nomogram was confirmed in both the training and validation sets (Online Supplemental Data). The Hosmer–Lemeshow test demonstrated that the nomogram yielded P values of .66 and .45 in the training and validation cohorts, respectively.

Stratified and Subgroups Analyses within the CT-Reported ETE-Negative Group

Stratified analysis demonstrated that performance of the radiomics nomogram was good and stable in different subgroups. In the CT-reported ETE-negative group, the nomogram still achieved an AUC of 0.69, a sensitivity of 0.68, a specificity of 0.66, and an accuracy of 0.64. The results of the receiver operating characteristic curve analysis are summarized and presented in the Online Supplemental Data. In our study, 110 of 184 (59.8%) patients with PTC with ETE were misdiagnosed using conventional CT signs. Of these misdiagnosed patients, 77 were correctly reclassified using the radiomics nomogram. The rate of misdiagnosis was dramatically decreased from 59.8% (110 of 184) to 17.9% (33 of 184).

Clinical Practice

Decision curve analysis revealed that if the threshold probability was $>.09$, the radiomics nomogram added more benefit than the clinical model (Online Supplemental Data), thus indicating the potential value of the nomogram in clinical practice.

RFS Analysis

The median follow-up was 26 months (interquartile range = 23–30) for 245 patients with PTC, and 46 of 245 (18.8%) patients had recurrence (local-regional in 43 patients and distant metastasis in 3 patients).

Size, capsule contact, and nomogram-predicted ETE showed a significant association with ETE in univariate Cox regression analysis. Only nomogram-predicted ETE was identified as an independent preoperative factor for PTC recurrence in multivariable Cox analysis ($P = .011$) (Table 3). The median RFS was 23 months (95% CI, 20–26) in the nomogram-predicted ETE high-risk group and 31 months (95% CI, 29–34) in the low-risk group. The Kaplan-Meier cumulative event curve for recurrence stratified by the nomogram-predicted ETE risk classification is shown in Fig 2.

DISCUSSION

ETE is a significant prognostic risk factor for patients with PTC. Patients with ETE are recommend for a more aggressive initial therapy, likely total thyroidectomy and intensive follow-up.¹⁻³ However, ETE varies to some degree: Some ETE involves only the perithyroid soft tissues identified under a microscope, which could only be detected through postoperative pathologic evaluation.^{1,5,15} On the basis of conventional imaging techniques (ultrasound and CT) and their morphologic features, it is difficult to detect the ETE that could only be determined by tumor histopathologic examination.⁴⁻⁶ In our study, 110 of 184 (59.8%) patients with PTC with

Table 3: Univariable and multivariable Cox regression analysis for risk factors associated with recurrence

Variable	Univariable Analysis		Multivariable Analysis	
	Hazard Ratio (95% CI)	P Value	Hazard Ratio (95% CI)	P Value
Size	1.07 (1.03–1.12)	.011	NA	NA
Capsule contact	1.56 (1.09–2.24)	.015	NA	NA
Nomogram-predicted ETE	1.75 (1.14–2.69)	.001	1.07 (1.02–1.12)	.011

Note:—NA indicates not applicable.

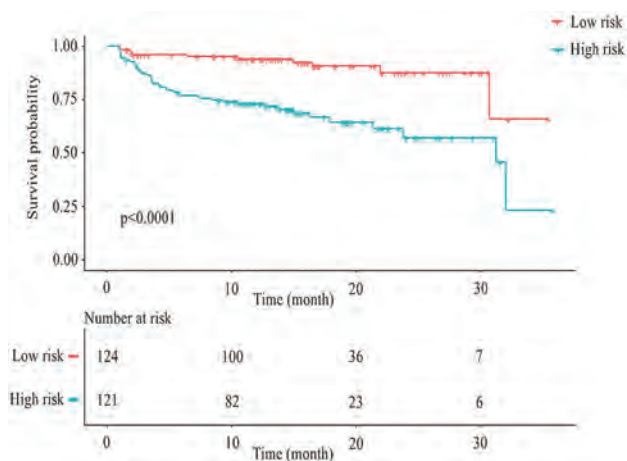


FIG 2. Kaplan-Meier cumulative event curve for PTC recurrence stratified by the nomogram-predicted ETE risk classification (log-rank statistic, $P < .001$).

ETE were misdiagnosed using conventional CT signs. Therefore, a more effective and reliable approach was needed.

Radiomics analysis can extract massive quantitative image features, which enable mineable high-dimensional data to be applied to support clinical decision-making.^{9,10} Chen et al¹⁵ conducted radiomics analysis of conventional structural CT to predict ETE and verify its potential value. We found that 6 radiomics models all had favorable performance, with AUCs all > 0.73 , and they surpassed the clinical model, similar to findings in a previous study. These findings indicate that radiomics approaches might be promising in predicting ETE. Notably, the incremental performance of radiomics models 5 and 6 (radiomics of iodine maps using RF and LASSO) added to the clinical model indicated a significant difference. To make the results of radiomics analysis more stable, we applied 2 machine learning algorithms, RF and LASSO, and no significant differences were found between the 2 methods.

The thyroid gland is the primary storage organ for iodine, so radiomics analysis of PTC in contrast-enhanced images is affected by both the thyroidal parenchyma and external iodine. To eliminate iodine effects on the thyroidal parenchyma and truly reflect contrast media uptake in PTC, we compared radiomics analysis of unenhanced CT images with enhanced images (mixed images and iodine maps). We found that the mixed and iodine rad-scores performed better than noncontrast rad-scores, irrespective of whether RF or LASSO was used. Compared with noncontrast images, dual-phase mixed images and iodine maps may provide additional information on tumor perfusion that correlates with tumor vascularity.^{16,17} Our results are consistent with

those in previous studies, which indicated that intratumor vascular heterogeneity was highly associated with migration, invasion, and metastasis of PTC.^{1,31}

Iodine rad-scores significantly outperformed mixed rad-scores, irrespective of whether RF or LASSO was used. In addition, iodine rad-score_RF obtained optimal performance in both the training and validation cohorts. Previous studies have confirmed an advantage of DECT-derived quantitative iodine concentration over conventional Hounsfield unit values in assessing enhancement, suggesting that iodine maps represent a more reliable detection method for lesion-enhancement differences than conventional CT images.³² In addition, iodine maps can effectively suppress the background CT value and neck root artifacts, further affecting subsequent radiomics analysis.^{16,32} Previously, Zhou et al^{22,23} reported that radiomics analysis of iodine maps can realize effective diagnosis and prediction for lymph node metastasis in patients with PTC. Radiomics of iodine maps can truly reflect tissue iodine heterogeneity, which aids in predicting ETE for PTC, similar to findings in previous studies.

On the basis of above the results, we finally established a radiomics nomogram incorporating the iodine rad-score_RF with clinical risk factors (size and capsule contact) to predict ETE. Size, capsule contact, and the iodine rad-score_RF complement each other. The efficiency of the nomogram improved when combining clinical risk factors and radiomics features. It is understandable that tumors with larger size and greater exposure to the capsule are more likely to disseminate into the glandular lobes and interrupt the thyroid edge.^{5,8} Fifteen radiomics features, including 7 arterial phase and 8 venous phase, were used to construct the iodine rad-score_RF, most of which (13 of 15) described the distribution of voxel intensities that were relevant to tumor heterogeneity. In addition, more than half of the selected features (10 of 15) were wavelet filters. The wavelet transformation decomposes the original image into 3 different frequency directions, which can further explore the spatial heterogeneity of target tumors at multiple scales.²⁸

To confirm the stability and robustness of the radiomics nomogram, we performed stratified analysis in different subgroups. In addition, the radiomics nomogram performed well, with AUCs of > 0.80 in all subgroups with different age, sex, BMI, and *BRAF* gene statuses. Encouragingly, the nomogram still achieved an AUC of 0.69 in the CT-reported ETE-negative group. Moreover, the rate of misdiagnosis is dramatically decreased from 59.8% to 17.9% when using the radiomics nomogram.

The prognostic value of the nomogram-predicted ETE risk was also analyzed in our study. Most promising, nomogram-predicted ETE was regarded as an independent preoperative predictor of RFS in patients with PTC through multivariable Cox analysis. High-risk patients had a significantly increased risk of

recurrence compared with low-risk patients. Given that the incidence of a recurrence is not low in patients with PTC,¹ nomogram-predicted ETE as a potential operative recurrence predictor may help to decide the extent of the initial operation, postoperative adjuvant therapy, and the intensity of postoperative follow-up.

The current study has several limitations. First, this retrospective study conducted radiomics analysis in a single center, and prospective multicenter studies with larger data sets are needed to validate our results. Second, the use of iodinated contrast agents may delay radioactive iodine therapy in patients with PTC, though radioactive iodine therapy was routinely performed at least 2 months after the operation in our institution. A previous study reported that the uptake of iodine 131 can return to normal at this interval.^{1,20} Third, increased radiation exposure using contrast-enhanced DECT should not be ignored. A further effective technique is required to reduce the radiation dose.

CONCLUSIONS

Radiomics of iodine maps performed significantly better than that of conventional CT images for predicting ETE in PTC. An iodine map-based radiomics nomogram demonstrated higher performance than the clinical model in predicting ETE and subsequent recurrence risk, thus serving as a supporting tool in PTC clinical decision-making.

Disclosure forms provided by the authors are available with the full text and PDF of this article at www.ajnr.org.

REFERENCES

- Haugen BR, Alexander EK, Bible KC, et al. **2015 American Thyroid Association management guidelines for adult patients with thyroid nodules and differentiated thyroid cancer: the American Thyroid Association Guidelines Task Force on Thyroid Nodules and Differentiated Thyroid Cancer.** *Thyroid* 2016;26:1–133 CrossRef Medline
- Liu G, Liu Q, Sun SR. **Nomograms for estimating survival in patients with papillary thyroid cancer after surgery.** *Cancer Manag Res* 2019;11:3535–44 CrossRef Medline
- Youngwirth LM, Adam MA, Scheri RP, et al. **Extrathyroidal extension is associated with compromised survival in patients with thyroid cancer.** *Thyroid* 2017;27:626–31 CrossRef Medline
- Kuo EJ, Thi WJ, Zheng F, et al. **Individualizing surgery in papillary thyroid carcinoma based on a detailed sonographic assessment of extrathyroidal extension.** *Thyroid* 2017;27:1544–49 CrossRef Medline
- Lee DY, Kwon TK, Sung MW, et al. **Prediction of extrathyroidal extension using ultrasonography and computed tomography.** *Int J Endocrinol* 2014;2014:351058 CrossRef Medline
- Seo YL, Yoon DY, Lim KJ, et al. **Locally advanced thyroid cancer: can CT help in prediction of extrathyroidal invasion to adjacent structures?** *AJR Am J Roentgenol* 2010;195:W240–44 CrossRef Medline
- Kim WY, Kim HY, Son GS, et al. **Clinicopathological, immunohistochemical factors and recurrence associated with extrathyroidal extension in papillary thyroid microcarcinoma.** *J Can Res Ther* 2014;10:50–55 CrossRef Medline
- Kim SS, Lee BJ, Lee JC, et al. **Preoperative ultrasonographic tumor characteristics as a predictive factor of tumor stage in papillary thyroid carcinoma.** *Head Neck* 2011;33:1719–26 CrossRef Medline
- Zhou M, Scott J, Chaudhury B, et al. **Radiomics in brain tumor: image assessment, quantitative feature descriptors, and machine-learning approaches.** *AJNR Am J Neuroradiol* 2018;39:208–16 CrossRef Medline
- O'Connor JP, Rose CJ, Waterton JC, et al. **Imaging intratumor heterogeneity: role in therapy response, resistance, and clinical outcome.** *Clin Cancer Res* 2015;21:249–57 CrossRef Medline
- Wang H, Song B, Ye N, et al. **Machine learning-based multiparametric MRI radiomics for predicting the aggressiveness of papillary thyroid carcinoma.** *Eur J Radiol* 2020;122:108755 CrossRef Medline
- Kwon MR, Shin JH, Park H, et al. **Radiomics study of thyroid ultrasound for predicting BRAF mutation in papillary thyroid carcinoma: preliminary results.** *AJNR Am J Neuroradiol* 2020;41:700–05 CrossRef Medline
- Patel NU, Lind KE, McKinney K, et al. **Clinical validation of a predictive model for the presence of cervical lymph node metastasis in papillary thyroid cancer.** *AJNR Am J Neuroradiol* 2018;39:756–61 CrossRef Medline
- Yu J, Deng Y, Liu T, et al. **Lymph node metastasis prediction of papillary thyroid carcinoma based on transfer learning radiomics.** *Nat Commun* 2020;11:4807 CrossRef Medline
- Chen B, Zhong L, Dong D, et al. **Computed tomography radiomic nomogram for preoperative prediction of extrathyroidal extension in papillary thyroid carcinoma.** *Front Oncol* 2019;9:829 CrossRef Medline
- McCollough CH, Leng S, Yu L, et al. **Dual- and multi-energy CT: principles, technical approaches, and clinical applications.** *Radiology* 2015;276:637–53 CrossRef Medline
- Agrawal MD, Pinho DF, Kulkarni NM, et al. **Oncologic applications of dual-energy CT in the abdomen.** *Radiographics* 2014;34:589–612 CrossRef Medline
- Li M, Zheng X, Li J, et al. **Dual-energy computed tomography imaging of thyroid nodule specimens: comparison with pathologic findings.** *Invest Radiol* 2012;47:58–64 CrossRef Medline
- Gao SY, Zhang XY, Wei W, et al. **Identification of benign and malignant thyroid nodules by in vivo iodine concentration measurement using single-source dual energy CT: a retrospective diagnostic accuracy study.** *Medicine (Baltimore)* 2016;95:e4816 CrossRef Medline
- Liu X, Ouyang D, Li H, et al. **Papillary thyroid cancer: dual-energy spectral CT quantitative parameters for preoperative diagnosis of metastasis to the cervical lymph nodes.** *Radiology* 2015;275:167–76 CrossRef Medline
- Choe J, Lee SM, Do KH, et al. **Prognostic value of radiomic analysis of iodine overlay maps from dual-energy computed tomography in patients with resectable lung cancer.** *Eur Radiol* 2019;29:915–23 CrossRef Medline
- Zhou Y, Su GY, Hu H, et al. **Radiomics analysis of dual-energy CT-derived iodine maps for diagnosing metastatic cervical lymph nodes in patients with papillary thyroid cancer.** *Eur Radiol* 2020;30:6251–62 CrossRef Medline
- Zhou Y, Su GY, Hu H, et al. **Radiomics from primary tumor on dual-energy CT derived iodine maps can predict cervical lymph node metastasis in papillary thyroid cancer.** *Acad Radiol* 2022;29 (Suppl 3):S222–31 CrossRef Medline
- Kim SY, Kwak JY, Kim EK, et al. **Association of preoperative US features and recurrence in patients with classic papillary thyroid carcinoma.** *Radiology* 2015;277:574–83 CrossRef Medline
- Park JE, Lee JH, Ryu KH, et al. **Improved diagnostic accuracy using arterial phase CT for lateral cervical lymph node metastasis from papillary thyroid cancer.** *AJNR Am J Neuroradiol* 2017;38:782–88 CrossRef Medline
- Wels MG, Lades F, Muehlberg A, et al. **General purpose radiomics for multi-modal clinical research.** In: Proceedings of SPIE Medical Imaging, San Diego, California. March 13, 2019 CrossRef
- Moltz JH, Bornemann L, Kuhnigk JM, et al. **Advanced segmentation techniques for lung nodules, liver metastases, and enlarged lymph nodes in CT scans.** *IEEE J Sel Top Signal Process* 2009;3:122–34 CrossRef

28. van Griethuysen JJM, Fedorov A, Parmar C, et al. **Computational radiomics system to decode the radiographic phenotype.** *Cancer Res* 2017;77:e104–07 CrossRef Medline
29. Kramer AA, Zimmerman JE. **Assessing the calibration of mortality benchmarks in critical care: the Hosmer-Lemeshow test revisited.** *Crit Care Med* 2007;35:2052–56 CrossRef Medline
30. Fitzgerald M, Saville BR, Lewis RJ. **Decision curve analysis.** *JAMA* 2015;313:409–10 CrossRef Medline
31. Rajabi S, Dehghan MH, Dastmalchi R, et al. **The roles and role-players in thyroid cancer angiogenesis.** *Endocr J* 2019;66:277–93 CrossRef Medline
32. Deniffel D, Sauter A, Dangelmaier J, et al. **Differentiating intrapulmonary metastases from different primary tumors via quantitative dual-energy CT based iodine concentration and conventional CT attenuation.** *Eur J Radiol* 2019;111:6–13 CrossRef Medline

Microstructural Visual Pathway White Matter Alterations in Primary Open-Angle Glaucoma: A Neurite Orientation Dispersion and Density Imaging Study

S. Haykal, A. Invernizzi, J. Carvalho, N.M. Jansonius, and F.W. Cornelissen



ABSTRACT

BACKGROUND AND PURPOSE: DTI studies of patients with primary open-angle glaucoma have demonstrated that glaucomatous degeneration is not confined to the retina but involves the entire visual pathway. Due to the lack of direct biologic interpretation of DTI parameters, the structural nature of this degeneration is still poorly understood. We used neurite orientation dispersion and density imaging (NODDI) to characterize the microstructural changes in the pregeniculate optic tracts and the postgeniculate optic radiations of patients with primary open-angle glaucoma, to better understand the mechanisms underlying these changes.

MATERIALS AND METHODS: TI- and multishell diffusion-weighted scans were obtained from 23 patients with primary open-angle glaucoma and 29 controls. NODDI parametric maps were produced from the diffusion-weighted scans, and probabilistic tractography was used to track the optic tracts and optic radiations. NODDI parameters were computed for the tracked pathways, and the measures were compared between both groups. The retinal nerve fiber layer thickness and visual field loss were assessed for the patients with glaucoma.

RESULTS: The optic tracts of the patients with glaucoma showed a higher orientation dispersion index and a lower neurite density index compared with the controls ($P < .001$ and $P = .001$, respectively), while their optic radiations showed a higher orientation dispersion index only ($P = .003$).

CONCLUSIONS: The pregeniculate visual pathways of the patients with primary open-angle glaucoma exhibited a loss of both axonal coherence and density, while the postgeniculate pathways exhibited a loss of axonal coherence only. Further longitudinal studies are needed to assess the progression of NODDI alterations in the visual pathways of patients with primary open-angle glaucoma across time.

ABBREVIATIONS: AUC = area under the curve; FA = fractional anisotropy; FISO = fraction of isotropic diffusion; LGN = lateral geniculate nucleus; MD = mean diffusivity; NDI = neurite density index; NODDI = neurite orientation dispersion and density imaging; ODI = orientation dispersion index; OR = optic radiation; OT = optic tract; POAG = primary open-angle glaucoma; RNFL = retinal nerve fiber layer; ROC = receiver operating characteristic; V1 = primary visual cortex; VFMD = visual field mean deviation

Primary open-angle glaucoma (POAG) is a leading cause of irreversible blindness worldwide.¹ It is characterized by the death of retinal ganglion cells, which leads to progressive visual field loss and structural degeneration of the retina.² While clinical assessment of POAG remains focused on examining the eye, MR imaging studies of patients with POAG have demonstrated that

glaucomatous degeneration spreads downstream from the pregeniculate retinal ganglion cells to the postgeniculate visual pathways through anterograde transsynaptic degeneration, eventually reaching the visual cortex.³ Specifically, DWI studies have shown evidence of WM degeneration throughout the visual pathways, including the optic tracts (OTs) and optic radiations (ORs).⁴⁻¹⁸ However, the underlying pathophysiology of this degeneration is yet to be determined.

Received April 26, 2021; accepted after revision February 26, 2022.

From the Laboratory for Experimental Ophthalmology (S.H., A.I., J.C., F.W.C.) and Department of Ophthalmology (N.M.J.), University of Groningen, University Medical Center Groningen, Groningen, the Netherlands.

S. Haykal, A. Invernizzi, and J. Carvalho received funding from the European Union's Horizon 2020 research and innovation program under the Marie Skłodowska-Curie grant agreements No. 675033 (EGRET-plus), No. 661883 (EGRET-cofund), and No. 641805 (NextGenVis), respectively. S. Haykal, A. Invernizzi, and J. Carvalho were additionally supported by the Graduate School of Medical Sciences, University of Groningen, the Netherlands.

The funding organizations had no role in the design, conduct, analysis, or publication of this research.

Please address correspondence to Shereif Haykal, MD, Laboratory for Experimental Ophthalmology, University Medical Center Groningen, PO Box 30.001, 9700 RB, Groningen, the Netherlands; e-mail: s.a.m.m.haykal@umcg.nl

Indicates open access to non-subscribers at www.ajnr.org

Indicates article with online supplemental data.

<http://dx.doi.org/10.3174/ajnr.A7495>

Most DWI studies of visual pathway WM degeneration in POAG have relied on the DTI approach to data analysis. DTI uses a tensor to model water diffusion within every voxel, producing parameters such as fractional anisotropy (FA) and mean diffusivity (MD). A decrease of FA and an increase of MD are generally interpreted as an indication of WM structural integrity loss. However, these DTI parameters are nonspecific because they reflect a wide range of WM structural changes, including changes in axonal density, myelination, axonal orientation, and membrane permeability.¹⁹ Higher order biophysical models of DWI have been recently developed to provide more specific and biologically interpretable measures of WM degeneration to address this issue. Neurite orientation dispersion and density imaging (NODDI) is such a higher order biophysical model.²⁰

NODDI models water diffusion in the different biologic tissue compartments. It models restricted diffusion in the intraneurite space, hindered diffusion in the extraneurite space, and isotropic diffusion in the CSF.²⁰ By doing so, NODDI produces 3 parameters: the neurite density index (NDI), the orientation dispersion index (ODI), and the fraction of isotropic diffusion (FISO). NDI indicates the volume fraction occupied by the intraneurite space and thus represents the density of neurites (axons and dendrites) within a voxel. A low NDI is generally associated with a loss of neurites and hence neurodegeneration. ODI indicates the variation of axonal orientation in the extraneurite space and, hence, represents how well-aligned and coherent axons are in a voxel. A high ODI indicates axonal dispersion, while a low ODI indicates axonal coherence. Last, FISO is the volume fraction occupied by CSF in a voxel. A multicompartment model such as NODDI can provide new insights into WM changes occurring in degenerative disorders previously studied exclusively using DTI.

In this study, we present the first application of NODDI to investigate WM changes in POAG, specifically in the pregeniculate OTs and the postgeniculate ORs. By doing so, we aim to characterize the structural nature of these glaucomatous WM changes in terms of axonal density and coherence, to better understand their underlying pathophysiology. Additionally, we assess the diagnostic performance of the NODDI measures of glaucomatous WM degeneration. Finally, for comparison, we use the conventional DTI approach for DWI data analysis.

MATERIALS AND METHODS

Ethics Approval

This study was approved by the Medical Ethical Committee of the University Medical Center Groningen. The study adhered to the tenets of the Declaration of Helsinki. All participants granted written informed consent before participation.

Participants

This study included 2 groups: patients with POAG and healthy controls. Patients with POAG were diagnosed on the basis of having reproducible visual field loss and optic neuropathy consistent with glaucoma in at least 1 eye, accompanied by open angles on gonioscopy. All included patients with POAG were under medical treatment to keep their intraocular pressure within the normal range (≤ 21 mm Hg). Inclusion criteria for the controls were having intact visual fields, a decimal visual acuity score of 0.8 or

higher, and an intraocular pressure of ≤ 21 mm Hg bilaterally. Exclusion criteria for both groups included having an ophthalmic disorder (other than glaucoma in the POAG group), a history of neurologic or psychiatric disorders, a history of brain surgery, and having an MR imaging contraindication. In total, 23 patients with POAG and 29 controls were included in this study.

Ophthalmic Tests

Visual acuity was tested using a Snellen chart with optimal correction for the viewing distance. Intraocular pressure was measured using a Tonoref Noncontact Tonometer (Nidek). Optical coherence tomography was used to measure the average peripapillary retinal nerve fiber layer (RNFL) thickness using an OCT-HS100 device (Canon Medical Systems). For patients with POAG, visual fields were assessed using a Humphrey Field Analyzer (Carl Zeiss Meditec). A 24-2 test grid was used for 11 patients and a 30-2 grid was used for 12 patients, and the results were expressed as visual field mean deviation (VFMD). For the controls, visual fields were screened for defects using a Humphrey FDT perimeter (Carl Zeiss Meditec) with a C20-1 screening mode (no reproducibly abnormal test locations allowed at $P < .01$).

MR Imaging Data Acquisition

MR imaging data were acquired on a Magnetom Prisma 3T MR imaging scanner (Siemens) with a 64-channel head coil. High-resolution 3D T1-weighted MPRAGE scans were performed using the following parameters: TR = 2300 ms, TE = 2.98 ms, TI = 900 ms, flip angle = 9°, bandwidth = 240 Hz, FOV = 240 × 256 mm², voxel size = 1 × 1 × 1 mm, slices per slab = 176. DWI scans were performed using the following parameters: TR = 5500 ms, TE = 85 ms, bandwidth = 2404 Hz, FOV = 210 × 210 mm², voxel size = 2.0 × 2.0 × 2.0 mm, number of slices = 66, acceleration factor = 2. DWI data were acquired using a bipolar diffusion scheme at $b=1000$ s/mm² and $b=2500$ s/mm² in 64 noncollinear directions for each shell in an anterior-posterior phase-encoding direction, and 3 images were acquired at $b=0$ s/mm² in both anterior-posterior and posterior-anterior directions to allow correction of susceptibility-induced image artifacts. The acquisition time was around 10 minutes for the T1-weighted scan and 14 minutes for the DWI scan.

MR Imaging Data Preprocessing and Coregistration

DWI data were first denoised using MRtrix3 (www.mrtrix.org).^{21,22} Then, the $b=0$ s/mm² images acquired in the anterior-posterior and posterior-anterior phase-encoding directions were used to estimate the susceptibility-induced distortions using the “topup” function of the FMRIB Software Library (FSL v5.0 11, <https://fsl.fmrib.ox.ac.uk/fsl>). Subsequently, the “eddy” function of FSL (<https://fsl.fmrib.ox.ac.uk/fsl/fslwiki/eddy>) was used to correct for motion, susceptibility,²³ and eddy current-induced²⁴ distortions. Finally, rigid body transformation was used to coregister the T1-weighted scan of each participant to the preprocessed DWI scan using the FMRIB Linear Image Registration Tool (FLIRT; <http://www.fmrib.ox.ac.uk/fslwiki/FLIRT>).²⁵

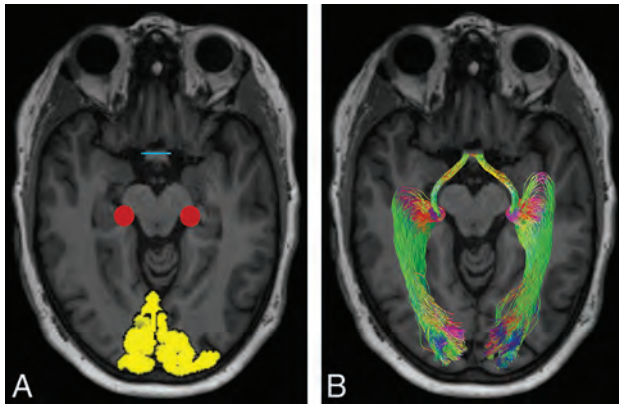


FIG 1. A representative example of visual pathway tractography. *A*, ROI placement overlaid on an axial section of a T1-weighted image. Yellow indicates V1 masks; red, representation of the LGN spherical ROI; blue, the optic chiasm. *B*, Probabilistic OT and OR fiber tracts. Red indicates transverse fibers; green, anterior-posterior fibers; blue, craniocaudal fibers.

Visual Pathway Tractography

Unless stated otherwise, all tractography steps were performed using MRtrix3. First, a 5TT image was produced from the coregistered T1-weighted images using FSL commands invoked through MRtrix3.^{26,27} 5TT images comprise 5 volumes corresponding to different brain tissues, namely WM, cortical gray matter, subcortical gray matter, CSF, and pathologic tissue. Fiber orientation distributions were then computed from the DWI data for each tissue type using multishell multitissue constrained spherical deconvolution.²⁸ The produced WM fiber orientation distribution maps were subsequently used for tracking the OTs and the ORs.

The OR fibers were tracked between the lateral geniculate nucleus (LGN) and the primary visual cortex (V1; Fig 1). The LGN was identified manually, and a spherical ROI with a 4-mm radius was used to circumscribe it. The T1-weighted images were automatically segmented and parcellated using Freesurfer (<https://surfer.nmr.mgh.harvard.edu>)²⁹ to produce V1 masks. Probabilistic anatomically constrained tractography²⁷ was then used to produce a total of 5000 streamlines between the LGN ROI and the V1 mask to delineate the ORs using the following parameters for all subjects: maximum length = 120 mm, minimum length = 70 mm, maximum angle between successive steps = 22.5°, fiber orientation distribution amplitude cutoff value = 0.05.

The OTs were tracked between the LGN and the optic chiasm (Fig 1). The optic chiasm was identified manually, and a rectangular ROI covering its coronal cross-section was created. Due to the small size of the OTs, it was not possible to use anatomically constrained tractography. Instead, we adapted a method originally described for OR tracking to remove anatomically improbable streamlines.³⁰ First, probabilistic tractography was used to track a total of 50,000 streamlines between the LGN and optic chiasm ROIs using the following parameters for all subjects: maximum length = 50 mm, minimum length = none set, maximum angle between successive steps = 45°, fiber orientation distribution amplitude cutoff value = 0.05. A track density image based on the number

Table 1: Demographics and clinical characteristics of participants^a

	POAG (n = 23)	Controls (n = 29)	P Value
Age (yr)	69.0 (8.5)	66.7 (6.7)	.277
Males	12 (52.2%)	18 (62.1%)	.473
IOP (mm Hg)			
Right eye	13.1 (2.6)	13.0 (2.9)	.947
Left eye	13.1 (3.7)	13.5 (3.3)	.444
Mean	13.1 (2.8)	13.2 (3.0)	.825
RNFL thickness (μm)			
Right eye	69.4 (11.3)	96.9 (8.6)	<.001
Left eye	67.2 (11.5)	97.3 (8.7)	<.001
Mean	68.3 (9.3)	97.1 (7.9)	<.001
VFMD (dB)			
Better eye	-4.0 (5.2)		
Worse eye	-13.0 (9.3)		
Mean	-8.5 (6.0)		

Note:—IOP indicates intraocular pressure.

^a Values are presented as mean (SD) or number (%).

of streamlines passing through each voxel was then produced from the streamlines. Subsequently, a threshold was set at the 99th percentile of the intensity distribution of the track density image to exclude voxels containing anatomically improbable streamlines, and a binarized mask was then created from the resulting image. Finally, 500 streamlines were tracked between the LGN and the optic chiasm ROIs using the same parameters described for initially tracking the OTs, while using the thresholded track density image mask to constrain the fiber tracking. All tracked OTs were visually inspected to ensure their anatomic plausibility.

Estimation of NODDI and DTI Parameters

The NODDI model was fitted to the DWI data on a voxel-by-voxel basis using the NODDI Matlab Toolbox (<http://mig.cs.ucl.ac.uk/index.php?n=Tutorial.NODDI matlab>), producing NDI, ODI, and FISO parameter maps. For comparison, standard DTI parameter maps for FA and MD were computed from the $b = 1000$ s/mm² shell in MRtrix3. Finally, average measures of the NODDI and DTI parameters were computed for the tracked OTs and ORs of each subject.

Statistical Analysis

Demographics and clinical characteristics of patients with POAG and controls were compared using an independent samples *t* test for parametric continuous variables, a Mann-Whitney *U* test for nonparametric continuous variables, and a χ^2 test for categorical variables. NODDI and DTI measures of the visual pathways were averaged over both hemispheres and then compared using ANCOVA, including sex and age as nuisance covariates. The results of the clinical eye examinations were averaged over both eyes, and their correlation with NODDI and DTI measures was tested using the Pearson correlation coefficient. Receiver operating characteristic (ROC) curve analysis was used to assess the diagnostic performance of NODDI and DTI measures in discriminating between healthy and glaucomatous visual pathway WM. All statistical analyses were performed using SPSS (Version 25; IBM), and statistical significance was reported at $P < .05$.

Table 2: Comparison of NODDI and DTI measures between patients with POAG and controls^a

Visual Tract/Parameter	POAG	Controls	Partial η^2	P Value
OT				
NDI	0.64 (0.07)	0.70 (0.07)	0.12	.001
ODI	0.21 (0.03)	0.18 (0.02)	0.26	<.001
FISO	0.51 (0.06)	0.49 (0.07)	0.02	.375
FA	0.32 (0.04)	0.39 (0.03)	0.50	<.001
MD	1.55 (0.10)	1.45 (0.11)	0.18	.002
OR				
NDI	0.55 (0.04)	0.57 (0.03)	0.02	.301
ODI	0.17 (0.01)	0.16 (0.01)	0.17	.003
FISO	0.13 (0.02)	0.13 (0.02)	0.00	.800
FA	0.51 (0.02)	0.53 (0.02)	0.20	.001
MD	0.87 (0.04)	0.85 (0.04)	0.01	.447

^a Values are presented as mean (SD).

RESULTS

Demographics and Clinical Characteristics

Patients with POAG and the controls did not differ significantly in age, sex, or intraocular pressure. The average RNFL thickness was significantly lower in patients with POAG compared with controls. Details are provided in Table 1.

Differences in NODDI and DTI Parameters between Groups

The OTs of the patients with POAG exhibited lower NDI and FA values and higher ODI and MD values compared with the controls, while the FISO did not differ between the groups. The ORs of the patients with POAG had a higher ODI and FA, while the NDI, FISO, and MD did not differ between the groups. Statistical details and boxplots of the comparisons can be found in Table 2 and Fig 2, respectively.

Correlations with Ophthalmic Measures of Glaucoma Severity

The NDI and FA of the OTs showed a significant positive correlation with VFMD ($r = 0.60, P < .005$ and $r = 0.42, P < .05$, respectively), while only the FA showed a significant correlation with RNFL thickness ($r = 0.42, P < .05$). The ODI, MD, and FISO of the OTs and all tested parameters of the ORs showed no significant correlation with VFMD or RNFL thickness (Online Supplemental Data).

ROC Curve Analysis

For the OTs, all tested parameters except FISO were able to discriminate between healthy and glaucomatous WM ($P < .05$), with FA having the largest area under the curve (AUC = 0.90). For the ORs, only the ODI and FA were able to discriminate between healthy and glaucomatous WM. ROC curves are shown in Fig 3, and AUC results are listed in Table 3.

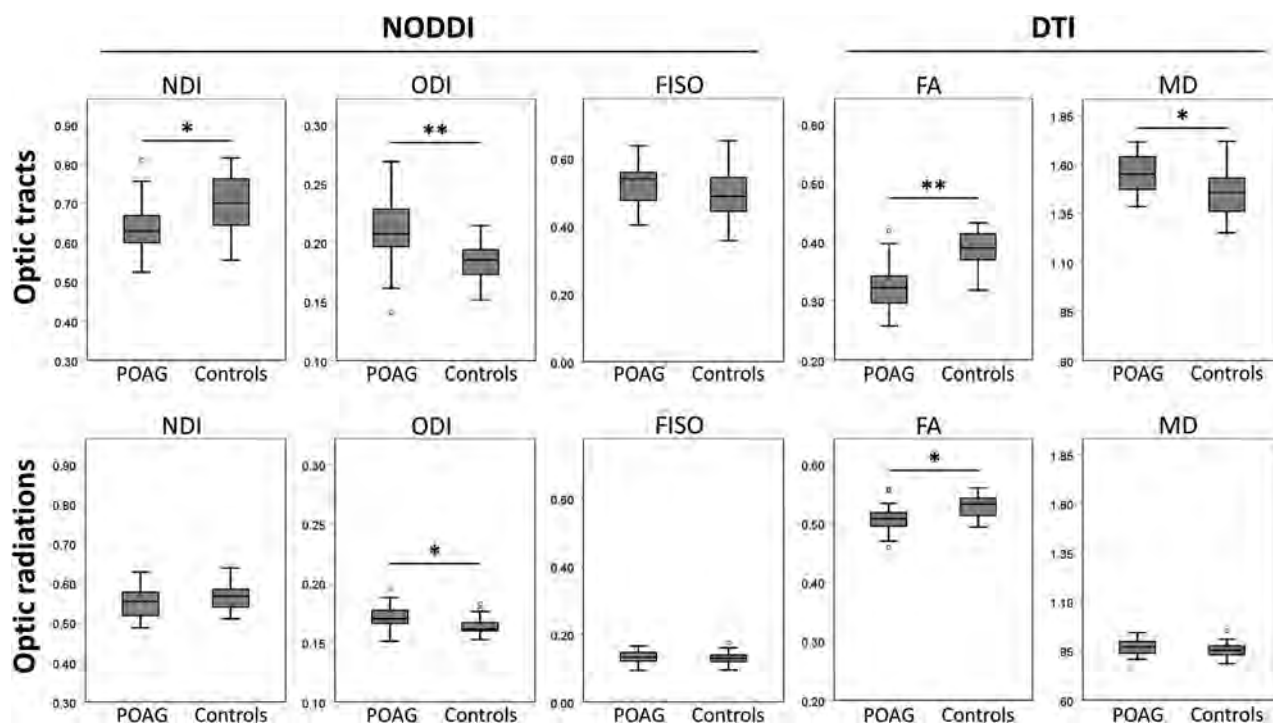


FIG 2. Boxplots showing the distribution of NODDI and DTI measures of the OTs and ORs of patients with POAG and the control group. Asterisks indicate a statistically significant difference between groups. The asterisk indicates $P < .01$; double asterisks, $P < .001$.

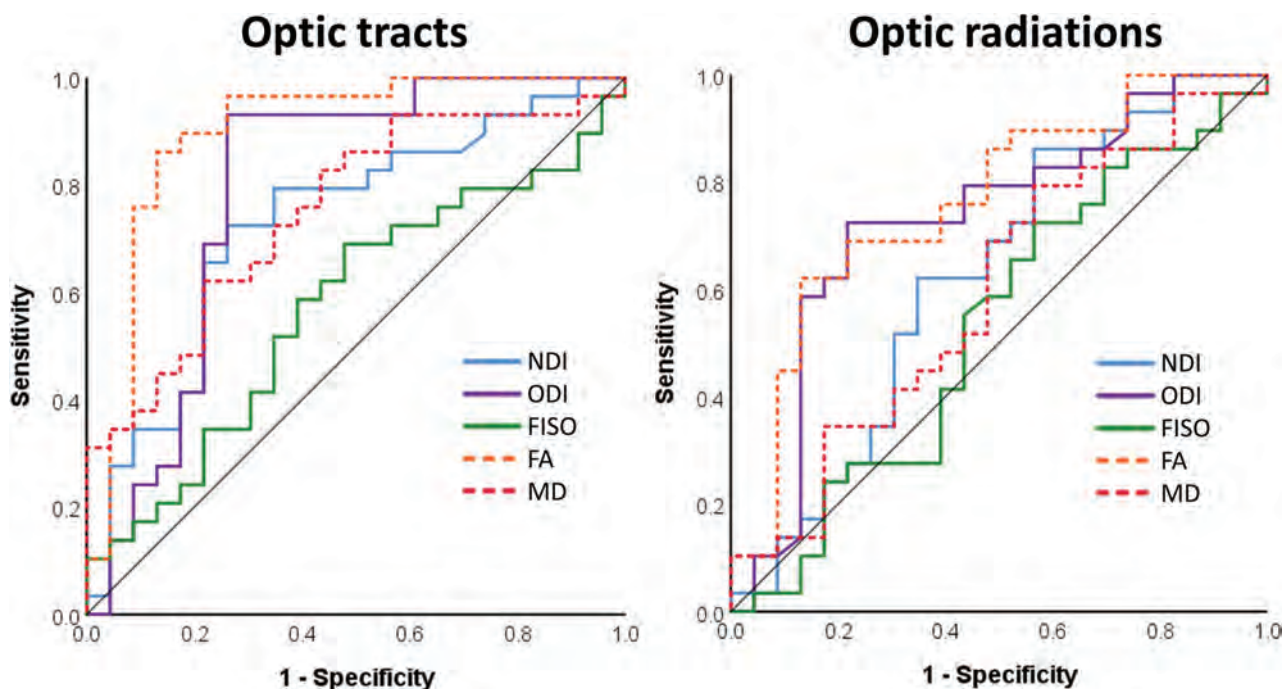


FIG 3. ROC curves assessing the ability of NODDI and DTI measures to discriminate between healthy and glaucomatous visual pathway WM.

Table 3: AUC for NODDI and DTI measures

Visual Tract/Parameter	AUC	95% CI	P Value
OT			
NDI	0.73	0.59–0.90	.005
ODI	0.79	0.65–0.93	<.001
FISO	0.57	0.42–0.73	.372
FA	0.90	0.80–1.00	<.001
MD	0.75	0.62–0.88	.002
OR			
NDI	0.63	0.47–0.78	.124
ODI	0.73	0.58–0.87	.005
FISO	0.53	0.37–0.69	.713
FA	0.76	0.62–0.90	.001
MD	0.59	0.44–0.75	.250

DISCUSSION

In this cross-sectional study, we present the first application of NODDI to investigate visual pathway WM degeneration in POAG. We found a disruption of axonal coherence in both the pre- and postgeniculate visual pathways and a loss of axonal density in the pregeniculate pathways only. These findings and their possible interpretations are discussed within the context of current NODDI and transsynaptic degeneration literature.

Pattern of Axonal Density and Coherence Changes in the Visual Pathways of Patients with POAG

The OTs of patients with POAG had a lower NDI and a higher ODI compared with those of controls, implying a loss of both axonal density and coherence. The ORs, on the other hand, showed a higher ODI only, implying a loss of axonal coherence with a preserved axonal density.

The axonal loss found in the OTs is expected because glaucoma causes the death of retinal ganglion cells, the axons of which form the OTs. Evidence of OT axonal loss has also been

previously reported in both animal models of glaucoma and patients with POAG.^{17,31} However, the lack of OR axonal loss is surprising because previous evidence of LGN^{32–35} and visual cortex^{36–38} volume loss implies the death of the neurons of the ORs. Because glaucomatous degeneration starts in the pregeniculate pathways and then spreads to the postgeniculate ones, there is a time lag between the degeneration occurring in the OTs and ORs of patients with POAG.³⁹ This time lag could possibly explain the discrepancy in axonal density changes of the OTs and ORs in our group of patients with POAG.

The loss of OR axonal coherence (as indicated by an increased ODI) in the presence of preserved OR axonal density suggests that disruption of axonal coherence precedes axonal loss in postgeniculate glaucomatous WM degeneration. Indeed, a longitudinal study of anterograde degeneration in an animal model of optic nerve injury found a loss of the “highly coherent appearance” of OR WM preceding axonal loss.⁴⁰ Furthermore, a longitudinal NODDI study of patients with stroke found an increase of ODI and no alteration in the NDI in the WM tracts downstream of the stroke lesions at the subacute stage, followed by a decrease in the NDI and a persistently high ODI later at the chronic stage.⁴¹ These findings support the notion that the loss of axonal coherence in the ORs of our patients with POAG is an early sign of postgeniculate WM degeneration.

ODI as a Potential Proxy Marker of Postgeniculate Visual Pathway Demyelination

A study of anterograde transsynaptic degeneration in the visual pathways of both patients with POAG and a glaucoma animal model demonstrated that demyelination of the postgeniculate visual pathways precedes axonal loss.⁴⁰ The increase of the ODI and the absence of NDI changes in the ORs of our patients with POAG could potentially be a reflection of the described

postgeniculate demyelination preceding axonal loss. This interpretation is based on the findings of recent NODDI studies of MS. First, a NODDI study of patients with MS found a marked increase of the ODI in active MS lesions in comparison with inactive lesions and normal-appearing WM, suggesting that an increased ODI is a sign of active demyelination.⁴² Furthermore, a longitudinal NODDI study of a de- and remyelinating MS animal model reported an increase in ODI during the peak of the demyelination phase, followed by a drop in the ODI during the remyelination phase.⁴³ Whether the reported increase of the ODI is a direct result of demyelination or a result of other histopathologic changes associated with demyelination is unclear. Nonetheless, the association between active demyelination and increased ODI together with the evidence of demyelination preceding axonal loss in transsynaptic degeneration of the visual pathways suggests that ODI could potentially be a proxy marker of early postgeniculate demyelination.

Comparison to DTI Studies of POAG

We found a loss of FA in both the OTs and ORs of patients with POAG, which is congruent with previous DTI studies of visual pathway WM changes in POAG.⁴⁻¹⁶ These findings give the impression that both pre- and postgeniculate visual pathways exhibit the same form of WM degenerative changes, whereas our NODDI findings show that the OTs experience a loss in axonal density and coherence, while the ORs experience a loss in axonal coherence only. Our findings challenge the interpretations of previous DTI studies of POAG and highlight the importance of using biophysical models such as NODDI for studying WM microstructural changes.

Correlations with Ophthalmic Tests of Glaucoma Severity and Diagnostic Performance of NODDI Parameters

Glaucoma severity is commonly assessed over 2 domains: structural and functional. To assess retinal structural glaucomatous degeneration, we measured RNFL thickness using optical coherence tomography, and to assess functional glaucomatous changes, we measured VFMD using a Humphrey Field Analyzer. No correlation was found between the RNFL thickness and any of the tested NODDI parameters. This is surprising because the RNFL is formed of the same retinal ganglion cell axons as the OTs, so a correlation between the NDI of the OTs and the RNFL thickness was expected. Yet, a positive correlation was found between VFMD and the NDI of the OTs. The FA of the OTs showed a significant correlation with both the RNFL thickness and the VFMD, which is in line with findings in previous DTI studies.^{11,16}

For the OTs, ROC curve analysis revealed that FA is the best discriminator (AUC = 0.90) of glaucomatous and healthy WM, followed by ODI, MD, and NDI. FA likely surpasses the ODI and NDI in diagnostic ability because the aspects of WM degeneration assessed separately by the ODI and NDI contribute to FA values collectively, producing a larger FA effect size in comparison. This idea is also supported by the results of the ROC curve analysis of the ORs, in which the NDI could not discriminate between glaucomatous and healthy WM, resulting in the FA and ODI AUC values being more comparable (0.76 and 0.73,

respectively). While this result makes FA a better binary classifier of glaucomatous WM degeneration, it lacks the biologic interpretability of NODDI parameters. If our suggestion of increased ODI as an early sign of transsynaptic degeneration is accurate, NODDI measures would be more useful in discriminating between healthy WM and different stages of glaucomatous WM degeneration in comparison with DTI measures.

Clinical Implications

Our current findings contribute to the fundamental understanding of the underlying mechanisms of POAG visual pathway degeneration and may also have implications for future glaucoma diagnostics and therapeutics. More specifically, our suggestion of ODI as a marker of early postgeniculate WM degeneration could prove to be useful for early detection of transsynaptic spread of glaucomatous degeneration. Such a marker could play an important role in the development of new glaucoma therapies such as retinal ganglion cell transplantation and neuroprotection, for which assessing the state of the postgeniculate visual pathway would be crucial.

Limitations and Future Directions

A main limitation of this study is the relatively moderate group sizes, which may have contributed to the lack of detectable axonal loss that we found in the ORs of patients with POAG. Furthermore, the inherent limitations of the NODDI approach, specifically its inability to individually assess different crossing fibers within the same voxel, may have influenced our findings. The presence of crossing fibers in the ORs and their absence in the OTs may be partially responsible for the discrepancy in NDI changes that we found between the ORs and the OTs. Future longitudinal NODDI studies of patients with early-stage POAG or a glaucoma animal model are needed to confirm our findings.

CONCLUSIONS

We found that the pregeniculate visual pathways of patients with POAG exhibit a loss of axonal density and coherence, while the postgeniculate pathways exhibit a loss of axonal coherence and a preserved axonal density. Further longitudinal studies are needed to assess the progression of NODDI alterations in the visual pathways of patients with POAG across time.

Disclosures: Shereif Haykal—RELATED: Grant: European Union's Horizon 2020, Comments: European Union's Horizon 2020 research and innovation program under the Marie Skłodowska-Curie grant agreements No. 675033 (EGRET-plus)*; Fees for Participation in Review Activities such as Data Monitoring Boards, Statistical Analysis, Endpoint Committees, and the Like: European Union's Horizon 2020, Comments: European Union's Horizon 2020 research and innovation program under the Marie Skłodowska-Curie grant agreements No. 675033 (EGRET-plus)*; Payment for Writing or Reviewing the Manuscript: European Union's Horizon 2020, Comments: European Union's Horizon 2020 research and innovation program under the Marie Skłodowska-Curie grant agreements No. 675033 (EGRET-plus)*; Provision of Writing Assistance, Medicines, Equipment, or Administrative Support: European Union's Horizon 2020, Comments: European Union's Horizon 2020 research and innovation program under the Marie Skłodowska-Curie grant agreements No. 675033 (EGRET-plus)*; Other: Graduate School of Medical Sciences, University of Groningen, the Netherlands, Comments: I conducted my work on this study as a PhD student, so I received some financial support from the Graduate School of Medical Sciences at the University of Groningen. Azzurra Invernizzi—RELATED: Grant: European Union's Horizon 2020, Comments: European Union's Horizon 2020 research and innovation program under the Marie Skłodowska-Curie grant agreements No. 661883

(EGRET)*; Fees for Participation in Review Activities such as Data Monitoring Boards, Statistical Analysis, Endpoint Committees, and the Like: European Union's Horizon 2020, Comments: European Union's Horizon 2020 research and innovation program under the Marie Skłodowska-Curie grant agreements No. 661883 (EGRET)*; Payment for Writing or Reviewing the Manuscript: European Union's Horizon 2020, Comments: European Union's Horizon 2020 research and innovation program under the Marie Skłodowska-Curie grant agreements No. 661883 (EGRET)*; Provision of Writing Assistance, Medicines, Equipment, or Administrative Support: European Union's Horizon 2020, Comments: European Union's Horizon 2020 research and innovation program under the Marie Skłodowska-Curie grant agreements No. 661883 (EGRET)*; Other: Graduate School of Medical Sciences, University of Groningen, the Netherlands, Comments: I collaborated on this study as a PhD student, so I received some financial support from the Graduate School of Medical Sciences at the University of Groningen.* Joana Carvalho—RELATED: Grant: European Union's Horizon 2020 research and innovation program under the Marie Skłodowska-Curie grant agreement No. 641805 (NextGenVis)*; UNRELATED: Employment: Champalimaud Center for the Unknown. Nomdo Jansonius—RELATED: Grant: European Union, Funding: S. Haykal, A. Invernizzi, and J. Carvalho received funding from the European Union's Horizon 2020 research and innovation program under the Marie Skłodowska-Curie grant agreements No. 675033 (EGRET-plus), No. 661883 (EGRET-cofund), and No. 641805 (NextGenVis), respectively. S. Haykal, A. Invernizzi, and J. Carvalho were additionally supported by the Graduate School of Medical Sciences, University of Groningen, the Netherlands. The funding organizations had no role in the design, conduct, analysis, or publication of this research.* Frans Cornelissen—RELATED: Grant: European Commission, Comments: European training grant Egret-plus*; UNRELATED: Grants/Grants Pending: European Commission/Uitzicht, Comments: European Training Grant NexGenVis and Uitzicht-related foundations on visual impairment research financed the costs of some studies. *Money paid to the institution.

REFERENCES

- Tham YC, Li X, Wong TY, et al. **Global prevalence of glaucoma and projections of glaucoma burden through 2040: a systematic review and meta-analysis.** *Ophthalmology* 2014;121:2081–90 CrossRef Medline
- Weinreb RN, Khaw PT. **Primary open-angle glaucoma.** *Lancet* 2004;363:1711–20 CrossRef Medline
- Nuzzi R, Dallorto L, Rolle T. **Changes of visual pathway and brain connectivity in glaucoma: a systematic review.** *Front Neurosci* 2018;12:363 CrossRef Medline
- Frezzotti P, Giorgio A, Toto F, et al. **Early changes of brain connectivity in primary open angle glaucoma.** *Hum Brain Mapp* 2016;37:4581–96 CrossRef Medline
- Kaushik M, Graham SL, Wang C, et al. **A topographical relationship between visual field defects and optic radiation changes in glaucoma.** *Investig Ophthalmol Vis Sci* 2014;55:5770–75 CrossRef Medline
- Sidek S, Ramli N, Rahmat K, et al. **Glaucoma severity affects diffusion tensor imaging (DTI) parameters of the optic nerve and optic radiation.** *Eur J Radiol* 2014;83:1437–41 CrossRef Medline
- Zikou AK, Kitsos G, Tzarouchi LC, et al. **Voxel-based morphometry and diffusion tensor imaging of the optic pathway in primary open-angle glaucoma: a preliminary study.** *AJNR Am J Neuroradiol* 2012;33:128–34 CrossRef Medline
- Tellouck L, Durieux M, Coupé P, et al. **Optic radiations microstructural changes in glaucoma and association with severity: a study using 3Tesla-magnetic resonance diffusion tensor imaging.** *Invest Ophthalmol Vis Sci* 2016;57:6539–47 CrossRef Medline
- Zhou W, Muir ER, Chalfin S, et al. **MRI study of the posterior visual pathways in primary open angle glaucoma.** *J Glaucoma* 2017;26:173–81 CrossRef Medline
- Nucci C, Mancino R, Martucci A, et al. **3-T diffusion tensor imaging of the optic nerve in subjects with glaucoma: correlation with GDx-VCC, HRT-III and Stratus optical coherence tomography findings.** *Br J Ophthalmol* 2012;96:976–80 CrossRef Medline
- Chen Z, Lin F, Wang J, et al. **Diffusion tensor magnetic resonance imaging reveals visual pathway damage that correlates with clinical severity in glaucoma.** *Clin Experiment Ophthalmol* 2013;41:43–49 CrossRef Medline
- Michelson G, Engelhorn T, Wärtges S, et al. **DTI parameters of axonal integrity and demyelination of the optic radiation correlate with glaucoma indices.** *Graefes Arch Clin Exp Ophthalmol* 2013;251:243–53 CrossRef Medline
- Murai H, Suzuki Y, Kiyosawa M, et al. **Positive correlation between the degree of visual field defect and optic radiation damage in glaucoma patients.** *Jpn J Ophthalmol* 2013;57:257–62 CrossRef Medline
- Garaci FG, Bolacchi F, Cerulli A, et al. **Optic nerve and optic radiation neurodegeneration in patients with glaucoma: in vivo analysis with 3-T diffusion-tensor MR imaging.** *Radiology* 2009;252:496–501 CrossRef Medline
- Lu P, Shi L, Du H, et al. **Reduced white matter integrity in primary open-angle glaucoma: A DTI study using tract-based spatial statistics.** *J Neuroradiol* 2013;40:89–93 CrossRef Medline
- Song X, Puyang Z, Chen A-H, et al. **Diffusion tensor imaging detects microstructural differences of visual pathway in patients with primary open-angle glaucoma and ocular hypertension.** *Front Hum Neurosci* 2018;12:426 CrossRef Medline
- Haykal S, Curcic-Blake B, Jansonius NM, et al. **Fixel-based analysis of visual pathway white matter in primary open-angle glaucoma.** *Invest Ophthalmol Vis Sci* 2019;60:3803–12 CrossRef Medline
- Haykal S, Jansonius NM, Cornelissen FW. **Investigating changes in axonal density and morphology of glaucomatous optic nerves using fixel-based analysis.** *Eur J Radiol* 2020;133:109356 CrossRef Medline
- Jones DK, Knösche TR, Turner R. **White matter integrity, fiber count, and other fallacies: the do's and don'ts of diffusion MRI.** *Neuroimage* 2013;73:239–54 CrossRef Medline
- Zhang H, Schneider T, Wheeler-Kingshott CA, et al. **NODDI: practical in vivo neurite orientation dispersion and density imaging of the human brain.** *Neuroimage* 2012;61:1000–16 CrossRef Medline
- Veraart J, Fieremans E, Novikov DS. **Diffusion MRI noise mapping using random matrix theory.** *Magn Reson Med* 2016;76:1582–93 CrossRef Medline
- Tournier JD, Smith R, Raffelt D, et al. **MRtrix3: a fast, flexible and open software framework for medical image processing and visualisation.** *Neuroimage* 2019;202:116137 CrossRef Medline
- Andersson JL, Skare S, Ashburner J. **How to correct susceptibility distortions in spin-echo echo-planar images: application to diffusion tensor imaging.** *Neuroimage* 2003;20:870–88 CrossRef Medline
- Andersson JL, Sotiropoulos SN. **An integrated approach to correction for off-resonance effects and subject movement in diffusion MR imaging.** *Neuroimage* 2016;125:1063–78 CrossRef Medline
- Jenkinson M, Bannister P, Brady M, et al. **Improved optimization for the robust and accurate linear registration and motion correction of brain images.** *Neuroimage* 2002;17:825–41 CrossRef Medline
- Zhang Y, Brady M, Smith S. **Segmentation of brain MR images through a hidden Markov random field model and the expectation-maximization algorithm.** *IEEE Trans Med Imaging* 2001;20:45–57 CrossRef Medline
- Smith RE, Tournier JD, Calamante F, et al. **Anatomically-constrained tractography: improved diffusion MRI streamlines tractography through effective use of anatomical information.** *Neuroimage* 2012;62:1924–38 CrossRef Medline
- Jeurissen B, Tournier JD, Dhollander T, et al. **Multi-tissue constrained spherical deconvolution for improved analysis of multi-shell diffusion MRI data.** *Neuroimage* 2014;103:411–26 CrossRef Medline
- Dale AM, Fischl B, Sereno MI. **Cortical surface-based analysis, I: segmentation and surface reconstruction.** *Neuroimage* 1999;9:179–94 CrossRef Medline
- Martínez-Heras E, Varriano F, Prcökovska V, et al. **Improved framework for tractography reconstruction of the optic radiation.** *PLoS One* 2015;10:e0137064 CrossRef Medline
- Ebneter A, Casson RJ, Wood JPM, et al. **Microglial activation in the visual pathway in experimental glaucoma: spatiotemporal characterization and correlation with axonal injury.** *Invest Ophthalmol Vis Sci* 2010;51:6448–60 CrossRef Medline
- Lee JY, Jeong HJ, Lee JH, et al. **An investigation of lateral geniculate nucleus volume in patients with primary open-angle glaucoma using 7 Tesla magnetic resonance imaging.** *Invest Ophthalmol Vis Sci* 2014;55:3468–76 CrossRef Medline

33. Zhang YQ, Li J, Xu L, et al. **Anterior visual pathway assessment by magnetic resonance imaging in normal-pressure glaucoma.** *Acta Ophthalmol* 2012;90:e295–302 CrossRef Medline
34. Chen Z, Wang J, Lin F, et al. **Correlation between lateral geniculate nucleus atrophy and damage to the optic disc in glaucoma.** *J Neuroradiol* 2013;40:281–87 CrossRef Medline
35. Gupta N, Greenberg G, de Tilly LN, et al. **Atrophy of the lateral geniculate nucleus in human glaucoma detected by magnetic resonance imaging.** *Br J Ophthalmol* 2009;93:56–60 CrossRef Medline
36. Boucard CC, Hernowo AT, Maguire RP, et al. **Changes in cortical grey matter density associated with long-standing retinal visual field defects.** *Brain* 2009;132:1898–1906 CrossRef Medline
37. Zhang S, Wang B, Xie Y, et al. **Retinotopic changes in the gray matter volume and cerebral blood flow in the primary visual cortex of patients with primary open-angle glaucoma.** *Invest Ophthalmol Vis Sci* 2015;56:6171–78 CrossRef Medline
38. Fukuda M, Omodaka K, Tatewaki Y, et al. **Quantitative MRI evaluation of glaucomatous changes in the visual pathway.** *PLoS One* 2018;13:e0197027 CrossRef Medline
39. Haykal S, Jansonius NM, Cornelissen FW. **Progression of visual pathway degeneration in primary open-angle glaucoma: a longitudinal study.** *Front Hum Neurosci* 2021;15:630898–11 CrossRef Medline
40. You Y, Joseph C, Wang C, et al. **Demyelination precedes axonal loss in the transneuronal spread of human neurodegenerative disease.** *Brain* 2019;142:426–42 CrossRef Medline
41. Mastropietro A, Rizzo G, Fontana L, et al. **Microstructural characterization of corticospinal tract in subacute and chronic stroke patients with distal lesions by means of advanced diffusion MRI.** *Neuroradiology* 2019;61:1033–45 CrossRef Medline
42. Sacco S, Caverzasi E, Papinutto N, et al. **Neurite orientation dispersion and density imaging for assessing acute inflammation and lesion evolution in MS.** *AJNR Am J Neuroradiol* 2020;41:2219–26 CrossRef Medline
43. Luo T, Oladosu O, Rawji KS, et al. **Characterizing structural changes with devolving remyelination following experimental demyelination using high angular resolution diffusion MRI and texture analysis.** *J Magn Reson Imaging* 2019;49:1750–59 CrossRef Medline

An In-Depth Analysis of Brain and Spine Neuroimaging in Children with Abusive Head Trauma: Beyond the Classic Imaging Findings

G. Orman, S.F. Kralik, N.K. Desai, T.G. Singer, S. Kwabena, S. Risen, and T.A.G.M. Huisman



ABSTRACT

BACKGROUND AND PURPOSE: Abusive head trauma is the leading cause of morbidity and mortality in young children. Radiology provides valuable information for this challenging diagnosis, but no single neuroimaging finding is independently diagnostic of abusive head trauma. Our purposes were to describe the prevalence of brain and spine neuroimaging findings and to analyze the association of neuroimaging findings with clinical factors to determine which neuroimaging findings may be used as prognostic indicators.

MATERIALS AND METHODS: Children with a confirmed abusive head trauma diagnosis between January 2018 to February 2021 were included in this single-center retrospective study. Patient demographics, survival, Glasgow Coma Scale score on admission, length of hospital stay, and intensive care unit stay were examined. Brain neuroimaging findings were categorized as classic and nonclassic findings. Spine MRIs were also assessed for spinal ligamentous injury, compression fracture, and hemorrhage. The χ^2 test or the Wilcoxon rank-sum test was used for the analysis.

RESULTS: One hundred two children (male/female ratio: 75:27; average age, 9.49; range, 0.27–53.8 months) were included. Subdural hematoma was the most common (83.3%) classic neuroimaging finding. Bridging vein thrombosis was the most common (30.4%) nonclassic neuroimaging finding. Spinal ligamentous injury was seen in 23/49 patients. Hypoxic-ischemic injury was significantly higher in deceased children ($P = .0001$). The Glasgow Coma Scale score was lower if hypoxic-ischemic injury ($P < .0001$) or spinal ligamentous injury were present ($P = .017$). The length of hospital stay was longer if intraventricular hemorrhage ($P = .04$), diffuse axonal injury ($P = .017$), hypoxic-ischemic injury ($P = .001$), or arterial stroke ($P = .0003$) was present. The intensive care unit stay was longer if intraventricular hemorrhage ($P = .02$), diffuse axonal injury ($P = .01$), hypoxic-ischemic injury ($P < .0001$), or spinal ligamentous injury ($P = .03$) was present.

CONCLUSIONS: Our results may suggest that a combination of intraventricular hemorrhage, diffuse axonal injury, hypoxic-ischemic injury, arterial stroke, and/or spinal ligamentous injury on neuroimaging at presentation may be used as potential poor prognostic indicators in children with abusive head trauma.

ABBREVIATIONS: AHT = abusive head trauma; AS = arterial stroke; BVT = bridging vein thrombosis; DAI = diffuse axonal injury; EDH = epidural hematoma; GCS = Glasgow Coma Scale; HII = hypoxic-ischemic injury; ICU = intensive care unit; IVH = intraventricular hemorrhage; LOS = length of hospital stay; PL = parenchymal laceration; SDH = subdural hematoma; SPH = subpial hemorrhage; VS = venous stroke

Quality neuroimaging and careful imaging interpretation are essential for the diagnosis and treatment of abusive head trauma (AHT), a leading cause of preventable morbidity and mortality.¹ A diagnosis of AHT is often challenging. The main diagnostic challenges are that abused children are usually too young to provide an adequate history, perpetrators are unlikely to provide a truthful account of the trauma, and/or clinicians

may be biased that AHT is more or less likely in specific settings, for example, depending on the socioeconomic situation of the parents.^{2,3} Both false-positive or false-negative AHT diagnoses may have critical implications for social and familial dynamics as well as the child's health. A false-positive diagnosis may result in infants being removed from their homes and parents losing child custody permanently or going to jail by mistake.³ In addition, children who are abused are more likely to sustain repeat abuse;

Received January 28, 2022; accepted after revision February 23.

From the Edward B. Singleton Department of Radiology (G.O., S.F.K., N.K.D., T.A.G.M.H.), Global Child Health Residency (T.G.S.), Department of Pediatrics (S.K.), Division of Public Health Pediatrics, and Department of Pediatrics (S.R.), Division of Child Neurology and Developmental Neuroscience, Texas Children's Hospital, Baylor College of Medicine, Houston, Texas; and Division of General Surgery (T.G.S.), Department of Surgery, David Geffen School of Medicine, University of California, Los Angeles, Los Angeles, California.

Please address correspondence to Gunes Orman, MD, Texas Children's Hospital, Edward B. Singleton Department of Radiology, 6701 Fannin St, Suite 470.12, Houston, TX 77030; e-mail: gorman@texaschildrens.org

Indicates article with online supplemental data.

<http://dx.doi.org/10.3174/ajnr.A7492>

therefore, a false-negative diagnosis or missed diagnosis puts the child at risk of possible future injury, including a fatal brain injury.^{4,5}

Radiology often provides critical diagnostic information for patients with suspected AHT, especially when the clinical history and physical examination may not reveal an abusive injury etiology at the time of presentation.⁶ The optimal recommended imaging studies are not standardized, and no single neuroimaging finding is independently specific or diagnostic of AHT.² Rather, the diagnosis of AHT depends on the multiplicity and severity of imaging findings as well as consideration of the veracity of the provided clinical history and reported mechanism of trauma.⁷ Therefore, familiarity with the classic as well as the nonclassic neuroimaging findings of AHT will assist radiologists and clinicians in a specific, sensitive, and timely diagnosis. The most common classic finding in AHT includes subdural hematoma (SDH) of varying CT densities and varying MR imaging signal intensities suggesting repeated injuries. Recently, nonclassic neuroimaging findings such as the “lollipop sign” or “tadpole sign,” parenchymal or cortical lacerations, and subpial hemorrhage (SPH) have been described in the scientific literature.^{2,8-11} However, there is limited evidence describing and evaluating the multiplicity of neuroimaging findings in a well-defined large group of children with confirmed AHT.

AHT is associated with a variable outcome scale, including mild developmental delay to severe disability and even mortality. Neuroimaging may be helpful in identifying the prognosis of patients with AHT by defining the extent of brain injury. However, prognostic markers in neuroimaging in children with AHT were rarely reported previously.

The goals of this study were the following: 1) to describe the prevalence of classic and nonclassic brain and spine neuroimaging findings in a well-defined large group of children with a confirmed AHT diagnosis at a quaternary Children’s Hospital; and 2) to analyze the association of neuroimaging findings with survival, Glasgow Coma Scale (GCS) score on admission, length of hospital stay (LOS), and length of intensive care unit (ICU) stay, to determine which of the neuroimaging findings or combination of findings may be used as prognostic indicators.

MATERIALS AND METHODS

Following institutional review board approval (H-45947), all children with a confirmed diagnosis of AHT through a multidisciplinary approach with radiology, neurology, and child abuse specialists and ultimate determination by the board-certified Child Abuse Pediatricians at Texas Children’s Hospital, seen between January 2018 and February 2021, were included in this single-center retrospective study. Informed consent was waived due to the retrospective nature of the study.

Patient demographic, clinical, and neuroimaging (CT and/or MR imaging) data were gathered through electronic medical record review. Patient age, sex, race, survival after AHT, GCS on admission, LOS, and ICU stay were noted.

CT studies of the brain were performed using standard departmental protocols without IV contrast. The scanning volume covered the region from up to 10 mm below the skull base to 10 mm superior to the skull vertex with the FOV ranging from 20

to 50 cm with 1- to 3-mm section thickness. All examinations were subject to volume-rendered 3D reconstruction algorithms with 360° feet-to-brain spin and 360° left-to-right spin for standardization processes and then were stored on the PACS system.

MR imaging studies of the brain were performed using standard departmental protocols on a 1.5T or 3T MR imaging scanner. Basal available sequences included noncontrast axial and sagittal T1-weighted, axial and/or coronal T1 and/or T2-FLAIR, axial and coronal T2-weighted, axial T2*-weighted gradient-echo or susceptibility weighted imaging, axial diffusion-weighted imaging, or diffusion tensor imaging. Section thickness varied between 3 and 4 mm, depending on the sequence used and age of the child.

MR imaging of the spine was performed using standard departmental protocols on a 1.5T or 3T MR imaging scanner. Routine conventional sequences of the spine were performed, including axial and sagittal T1- and T2-weighted turbo spin-echo imaging and sagittal short inversion recovery sequences.

Two experienced board-certified pediatric neuroradiologists (N.K.D. with 10 years’ and S.F.K. with 9 years’ experience) who knew that all children had a confirmed diagnosis of AHT but were blinded to data regarding GCS, LOS, ICU stay, and survival after AHT reviewed all patient neuroimaging studies independently. Any discrepancies in interpretation were resolved in a second consensus reading session. Consensus reading results were used for the final analysis.

Neuroimaging study findings of the brain were then categorized as classic and nonclassic findings based on previous literature.² Classic findings included skull fractures, epidural hematoma (EDH), SDH, SAH, intraventricular hemorrhage (IVH), contusions, diffuse axonal injury (DAI), and hypoxic-ischemic injury (HII). To define DAI, we included the presence of multiple microhemorrhages on MR imaging at the interface of gray matter and white matter, in addition to the commissures, corpus callosum, internal capsule, and brainstem. HII associated with AHT included changes in CT density and/or MR imaging signal intensity in the cortex, subcortical white matter, and/or deep gray matter. Nonclassic findings included bridging vein thrombosis (BVT), SPH, parenchymal laceration (PL), arterial stroke (AS), and venous stroke (VS). Spinal MRIs were also assessed for ligamentous injury (cruciform, apical, tectorial, anterior atlanto-occipital, posterior atlanto-occipital, posterior atlanto-axial, posterior longitudinal, anterior longitudinal, interspinous, and nuchal), compression fracture, and spinal hematoma (SDH and EDH). Each of the neuroimaging-based parameters was recorded as a yes/no response. The time period between admission and initial neuroimaging was also noted.

All statistical analyses were performed using SAS/STAT Software, Version 9.3 (SAS Institute). All variables were assessed for normality. Comparisons between the 2 groups were then evaluated by the χ^2 test or Wilcoxon rank-sum test. A *P* value < .05 was considered statistically significant.

RESULTS

One hundred two children were diagnosed with AHT during the study period and included in this study. There were 73.5% males (*n* = 75) and 26.5% females (*n* = 27) with an average age of 9.49

(range, 0.27–53.8) months. All patients had initial head CT imaging the same day or next day at admission. Race distribution of the patients was Asian ($n=4$), Black ($n=30$), Hispanic ($n=37$), White ($n=29$), and unknown ($n=2$).

Thirty-six children had only brain CT, and 66 children had both brain CT and MR imaging for neuroimaging evaluation. Classic neuroimaging findings were the following: 1) skull fractures, 32.4% of the children ($n=33$). These fractures were either single ($n=25$) or multiple ($n=8$) and linear ($n=26$) or comminuted ($n=7$). 2) EDH was found in 6.8% of the children ($n=7$), ranging from 2- to 42-mm thickness. 3) SDH was seen in 83.3% of the children ($n=85$), ranging from 2- to 35-mm thickness. Thirteen patients had SDH in a single location, and 72 patients had SDH in multiple locations. These locations were frontal 89.4% ($n=76$), parietal 87% ($n=74$), temporal 68.2% ($n=58$), occipital 77.6% ($n=66$), tentorial 75.3% ($n=64$), and posterior fossa 43.5% ($n=37$). 4) SAH was seen in 30.4% of the children ($n=31$). Nine patients had SAH in a single location, and 22 had SAH in multiple locations. These locations were frontal 93.5% ($n=29$), parietal 71% ($n=22$), temporal 48.4% ($n=15$), occipital 25.8% ($n=8$), posterior fossa 6.5% ($n=2$), and basal cisterns 14.3% ($n=5$). 5) IVH was seen in 15.7% of children ($n=16$). 6) Contusions were found in 20.6% of children ($n=21$). 7) DAI was seen in 6.9% of the patients ($n=7$), and 8) HII was found in 47.1% of the children ($n=48$) in the cortex 100% ($n=48$), subcortical white matter 62.5% ($n=30$), and/or deep gray matter 60.4% ($n=29$) (Online Supplemental Data).

Nonclassic neuroimaging findings were the following: 1) BVT was found in 30.4% of the children ($n=31$); 2) SPH, in 5% of the children ($n=5$) in the frontal ($n=2$) and parietal ($n=3$) regions; 3) PL, in 10% of the children ($n=10$); 4) AS, in 5% of the children ($n=5$); and 5) VS, in 1% of the patients ($n=1$) in the frontoparietal region (Online Supplemental Data).

Neuroimaging findings when only brain CT was available ($n=36$) were the following: 1) Classic neuroimaging findings were 33.3% skull fracture ($n=12$), 11.1% EDH ($n=4$), 72.2% SDH ($n=26$), 27.8% SAH ($n=10$), 5.6% IVH ($n=2$), 13.9% contusions ($n=5$), 0% DAI ($n=0$), and 47.2% HII ($n=17$); and 2) nonclassic neuroimaging findings were the following: 5.6% BVT ($n=2$), 0% SPH ($n=0$), 2.8% PL ($n=1$), 2.8% AS ($n=1$), and 0% VS ($n=0$).

Forty-nine spine MRIs were available for the study. Spine MR imaging findings included the following: 1) ligamentous injury in 46.9% of the children ($n=23$), of whom 3 had nuchal ligament injury and 21 had interspinous and nuchal ligament injury; 2) 2% of the children had compression fracture ($n=1$) at the T1 vertebra; and finally 3) spinal hemorrhage was seen in 22.4% of the children ($n=11$): SDH ($n=7$), EDH ($n=2$), and SDH+EDH ($n=2$) (Online Supplemental Data).

We noted the survival rates during hospital admission due to AHT and found that 82.4% of the children ($n=84$) survived and 17.6% of the children ($n=18$) died within an average of 6.7 (range, 1–33) days. We compared the neuroimaging findings between surviving and deceased children (Online Supplemental Data). HII was significantly higher in deceased children (88.9%) compared with surviving children (38.1%) ($P=.0001$), and BVT was significantly lower in deceased children (5.9%) compared with surviving children (36.1%) ($P=.01$) (Online Supplemental

Data). No significant difference was found for the rest of the neuroimaging findings between the 2 groups.

The GCS score at admission ranged between 3 and 15 for 99 patients; 3 patients had no GCS records available. We compared the median (interquartile range) GCS scores between negative and positive neuroimaging findings (Online Supplemental Data). We found that the median (interquartile range) GCS was significantly lower if the patient had HII (3.0 [3–15]) on brain neuroimaging compared with negative findings on neuroimaging (15.0 [3–15]) ($P<.0001$) and if the patient had ligamentous injury (4.5 [3–9]) on spine MR imaging compared with negative results (12.5 [3–15]) ($P=.017$) (Online Supplemental Data). No significant difference was found for the rest of the neuroimaging findings for median (interquartile range) GCS scores.

The average LOS was 15.62 (range, 1–97) days. We found a significantly longer LOS if IVH (23.6 days versus 14.1 days, $P=.04$), DAI (30.4 versus 14.5 days, $P=.017$), HII (21.3 versus 10.5 days, $P=.001$), and AS (42.2 versus 14.3 days, $P=.0003$) or a combination was present on initial neuroimaging (Online Supplemental Data).

A total 68.6% of the patients ($n=70$) were admitted to the ICU for an average of 10.38 (range, 1–53) days. We found significantly longer ICU stays if IVH (12.2 versus 6.2 days, $P=.02$), DAI (15.6 versus 6.5 days, $P=.01$), HII (11.8 versus 2.9 days, $P<.0001$), or ligamentous injury (14.6 versus 8.2 days, $P=.03$) or a combination was present on initial neuroimaging (Online Supplemental Data).

Representative patients are shown in the Online Supplemental Data.

DISCUSSION

In this detailed neuroimaging analysis in a well-defined large group of children with a confirmed AHT diagnosis, our findings of the prevalence of the classic neuroimaging findings including SDH, skull fracture, EDH, SAH, IVH, contusions, and DAI were consistent with prior reports. The incidence of HII was reported between 31% and 39% previously,^{12–14} but HII was found in nearly half of our patient group, emphasizing the need to keep AHT in the differential diagnosis of infants and children presenting with HII and lack of a specific etiology. BVT was the most common nonclassic neuroimaging finding, observed in 30.4% of the children with AHT in our study. In previous literature, BVT was reported between 29% and 44%.^{8,9,15} Although less frequent, the additional nonclassic imaging findings are critical to recognize clinically to suggest a diagnosis of AHT. SPH in neonates following vaginal delivery was reported previously.¹⁶ PL has been described in subjects with AHT younger than 5 months of age.¹⁷ Khan et al¹⁸ reported 28% cerebrovascular accidents in patients, of whom 23% had AS, in their retrospective study of 282 children with AHT. The incidence of AS in their study was 6.4%, which was similar to our results. However, in the same study, Khan et al reported that 8% of their study population had VS. Spinal ligamentous injury was the most common (46.9%) spinal MR imaging finding in our study, and interspinous and nuchal ligaments were the most commonly affected ligaments. Ligamentous injury in child abuse was reported between 36% and 78% in the previous literature.^{19–21} Spinal ligamentous injury is a clinically critical

finding highly suggestive of AHT, resulting from violent shaking. Therefore, our results may suggest that the utility of spinal MR imaging is extremely helpful in patients with suspected AHT. A recent study reported that whole-spine MR imaging is helpful in AHT diagnosis and may be superior to cervical spine MR imaging to avoid missing, isolated thoracolumbar injuries.²²

We also analyzed the association of neuroimaging findings with critical acute clinical data, including survival, GCS on admission, LOS, and length of ICU stay. We found that HII is the most important neuroimaging finding associated with critical clinical variables. We found that HII was significantly higher (89% versus 38%) in deceased children, and the median GCS on admission was significantly lower if HII was present on brain MRIs. HII represents severe and possibly irreversible injury to the brain.²³ Previously, Gencturk et al²³ reported a significant association between outcome severity and the presence of HII in their study, in which they evaluated clinical outcome based on abuse specialists' clinical assessment for the 6-month follow-up scoring. Therefore, in surviving children with AHT, the presence of HII has critical clinical prognostic value and emphasizes the need for neuroimaging in the evaluation of infants and children with suspected abuse. Most interesting, spinal ligamentous injury was associated with a lower GCS score and thus more severe injury. In AHT, spinal ligament injury is believed to be secondary to rigorous shaking of the child, which has been the most commonly reported (50%–63%) injury mechanism in AHT, resulting in hyperextension/flexion of the craniocervical junction.^{24–26} Neuropathology literature suggested that damage to the lower brainstem (likely direct injury to the medulla) and upper cervical cord could be responsible for apnea events and may lead to HII and brain swelling.^{27,28} Our results match the suggested hypothesis.

Kadom et al¹⁹ reported that bilateral HII occurred more frequently in AHT, and almost half of bilateral HIIs in their cohort were among children who also had cervical soft-tissue injury on MR imaging. Our results show a higher incidence of HII in deceased children and also a lower GCS score when HII is present on neuroimaging. The similarity of the correlation between HII and mortality and markers of clinical severity emphasizes the critical importance of brain MR imaging evaluation for HII in the evaluation of AHT. Most interesting, although less sensitive than brain MR imaging, CT showed a similar incidence with a combination of CT and MR imaging. We also found a significantly higher LOS and/or ICU stay for IVH, DAI, HII, AS, and/or ligamentous injury in the initial neuroimaging studies in our patient cohort. This may suggest that a combination of these neuroimaging findings may be used as prognostic indicators and should be explored further in future studies of AHT and long-term developmental outcomes.

The strengths of this study include the large number of patients in a quaternary children's center. Additionally, this is the first study focused solely on classic and nonclassic neuroimaging findings in AHT with systematic completion of detailed imaging analysis of all patient studies. Limitations of this study are the following: 1) Clinical information was obtained through retrospective chart review; however, as the main focus of the study, the neuroimaging was re-read by 2 expert readers; 2) the children included had a confirmed diagnosis of AHT, which may have introduced bias in the reading of images, though 2 expert readers

re-read images to mitigate this limitation; 3) although expected considering the high mortality of AHT, there was a discrepancy in number of children between the deceased and surviving patient groups, which has the potential to affect analyses; 4) CT is less sensitive than MR imaging for certain diagnoses, and not all patients had brain MR imaging available for the analysis; therefore, this limitation may have affected the statistical analysis and results; 5) a limited number of spinal MR imaging studies might have affected the statistical analysis and results; 6) this was a single-center evaluation of patients; and 7) heterogeneity of the imaging protocols performed may have an impact on the detection of subtle pathologies.

CONCLUSIONS

AHT is a leading cause of preventable mortality and significant morbidity for children. Given the difficulty in making this diagnosis often with incomplete history, head CT, brain MR imaging, and spine MR imaging are each critical tools in the evaluation of a child with suspected abuse. In this notably large cohort study for AHT, we found that SDH is the most common classic neuroimaging finding, and BVT is the most common nonclassic neuroimaging finding. Most important, ligamentous injury is seen in almost half of the spinal MRIs. HII is the most severe neuroimaging finding associated with higher mortality and other markers of clinical severity. Finally, we propose that the simultaneous presence of IVH, DAI, HII, AS, and/or ligamentous injury on the initial neuroimaging studies may be used as potential poor prognostic indicators, but prospective studies assessing the association between these neuroimaging findings and long-term developmental outcomes are needed to further support this conclusion.

ACKNOWLEDGMENTS

We would like to thank Haleh Sangi-Haghpeykar, PhD, from the Edward B. Singleton Department of Radiology and Department of Obstetrics and Gynecology, Texas Children's Hospital and Baylor College of Medicine, Houston, Texas, for the excellent and professional statistical support.

Disclosure forms provided by the authors are available with the full text and PDF of this article at www.ajnr.org.

REFERENCES

1. Spies EL, Klevens J. **Fatal abusive head trauma among children aged <5 years: United States, 1999–2014.** *MMWR Morbid Mortal Wkly Rep* 2016;65:505–09 CrossRef Medline
2. Orman G, Kralik SF, Meoded A, et al. **MRI findings in pediatric abusive head trauma: a review.** *J Neuroimaging* 2020;30:15–27 CrossRef Medline
3. Leventhal JM, Asnes AG, Pavlovic L, et al. **Diagnosing abusive head trauma: the challenges faced by clinicians.** *Pediatr Radiol* 2014;44 (Suppl 4):S537–42 CrossRef
4. Jenny C, Hymel KP, Ritzen A, et al. **Analysis of missed cases of abusive head trauma.** *JAMA* 1999;281:621–26 CrossRef Medline
5. Pollanen MS, Smith CR, Chiasson DA, et al. **Fatal child abuse-maltreatment syndrome: a retrospective study in Ontario, Canada, 1990–1995.** *Forensic Sci Int* 2002;126:101–04 CrossRef Medline
6. Pfeifer CM, Hammer MR, Mangona KL, et al. **Non-accidental trauma: the role of radiology.** *Emerg Radiol* 2017;24:207–13 CrossRef Medline

7. Choudhary AK, Servaes S, Slovis TL, et al. **Consensus statement on abusive head trauma in infants and young children.** *Pediatr Radiol* 2018;48:1048–65 CrossRef Medline
8. Choudhary AK, Bradford R, Dias MS, et al. **Venous injury in abusive head trauma.** *Pediatr Radiol* 2015;45:1803–13 CrossRef Medline
9. Hahnemann ML, Kinner S, Schweiger B, et al. **Imaging of bridging vein thrombosis in infants with abusive head trauma: the “tadpole sign.”** *Eur Radiol* 2015;25:299–305 CrossRef Medline
10. Palifka LA, Frasier LD, Metzger RR, et al. **Parenchymal brain laceration as a predictor of abusive head trauma.** *AJNR Am J Neuroradiol* 2016;37:163–68 CrossRef Medline
11. Gunda D, Cornwell BO, Dahmouh HM, et al. **Pediatric central nervous system imaging of nonaccidental trauma: beyond subdural hematomas.** *Radiographics* 2019;39:213–28 CrossRef Medline
12. Zimmerman RA, Bilaniuk LT, Farina L. **Non-accidental brain trauma in infants: diffusion imaging, contributions to understanding the injury process.** *J Neuroradiol* 2007;34:109–14 CrossRef Medline
13. Ichord RN, Naim M, Pollock AN, et al. **Hypoxic-ischemic injury complicates inflicted and accidental traumatic brain injury in young children: the role of diffusion-weighted imaging.** *J Neurotrauma* 2007;24:106–18 CrossRef Medline
14. Orru E, Huisman T, Izbudak I. **Prevalence, patterns, and clinical relevance of hypoxic-ischemic injuries in children exposed to abusive head trauma.** *J Neuroimaging* 2018;28:608–14 CrossRef Medline
15. Zuccoli G, Khan AS, Panigrahy A, et al. **In vivo demonstration of traumatic rupture of the bridging veins in abusive head trauma.** *Pediatr Neurol* 2017;72:31–35 CrossRef Medline
16. Huang AH, Robertson RL. **Spontaneous superficial parenchymal and leptomeningeal hemorrhage in term neonates.** *AJNR Am J Neuroradiol* 2004;25:469–75
17. Jaspan T, Narborough G, Punt JA, et al. **Cerebral contusional tears as a marker of child abuse—detection by cranial sonography.** *Pediatr Radiol* 1992;22:237–45 CrossRef Medline
18. Khan NR, Fraser BD, Nguyen V, et al. **Pediatric abusive head trauma and stroke.** *J Neurosurg Pediatr* 2017;20:183–90 CrossRef Medline
19. Kadom N, Khademian Z, Vezina G, et al. **Usefulness of MRI detection of cervical spine and brain injuries in the evaluation of abusive head trauma.** *Pediatr Radiol* 2014;44:839–48 CrossRef Medline
20. Jacob R, Cox M, Koral K, et al. **MR imaging of the cervical spine in nonaccidental trauma: a tertiary institution experience.** *AJNR Am J Neuroradiol* 2016;37:1944–50 CrossRef Medline
21. Choudhary AK, Ishak R, Zacharia TT, et al. **Imaging of spinal injury in abusive head trauma: a retrospective study.** *Pediatr Radiol* 2014;44:1130–40 CrossRef Medline
22. Karmazyn B, Reher TA, Supakul N, et al. **Whole spine MRI in children with suspected child abuse.** *AJR Am J Roentgenol* 2022 Jan 12. [Epub ahead of print] CrossRef Medline
23. Gencturk M, Tore HG, Nascene DR, et al. **Various cranial and orbital imaging findings in pediatric abusive and non-abusive head trauma, and relation to outcomes.** *Clin Neuroradiol* 2019;29:253–61 CrossRef Medline
24. Christian CW, Block R; Committee on Child Abuse and Neglect; American Academy of Pediatrics. **Abusive head trauma in infants and children.** *Pediatrics* 2009;123:1409–11 CrossRef Medline
25. Starling SP, Patel S, Burke BL, et al. **Analysis of perpetrator admissions to inflicted traumatic brain injury in children.** *Arch Pediatr Adolesc Med* 2004;158:454–58 CrossRef Medline
26. Adamsbaum C, Grabar S, Mejean N, et al. **Abusive head trauma: judicial admissions highlight violent and repetitive shaking.** *Pediatrics* 2010;126:546–55 CrossRef Medline
27. Geddes JF, Hackshaw AK, Vowles GH, et al. **Neuropathology of inflicted head injury in children, I: patterns of brain damage.** *Brain* 2001;124:1290–98 CrossRef Medline
28. Geddes JF, Vowles GH, Hackshaw AK, et al. **Neuropathology of inflicted head injury in children, II: microscopic brain injury in infants.** *Brain* 2001;124:1299–1306 CrossRef Medline

Dorsal Root Ganglion Volumetry by MR Gangliography

S. Weiner, M. Strinitz, J. Herfurth, F. Hessenauer, C. Nauroth-Krefß, T. Kampf, G.A. Homola, N. Üçeyler, C. Sommer, M. Pham, and M. Schindehütte



ABSTRACT

BACKGROUND AND PURPOSE: Dorsal root ganglion MR imaging (MR gangliography) is increasingly gaining clinical-scientific relevance. However, dorsal root ganglion morphometry by MR imaging is typically performed under the assumption of ellipsoid geometry, which remains to be validated.

MATERIALS AND METHODS: Sixty-four healthy volunteers (37 [57.8%] men; mean age, 31.5 [SD, 8.3] years) underwent MR gangliography of the bilateral L4–S2 levels (3D-T2WI TSE spectral attenuated inversion recovery–sampling perfection with application-optimized contrasts by using different flip angle evolution, isotropic voxels = 1.1 mm³, TE = 301 ms). Ground truth dorsal root ganglion volumes were bilaterally determined for 96 dorsal root ganglia (derivation cohort) by expert manual 3D segmentation by 3 independent raters. These ground truth dorsal root ganglion volumes were then compared with geometric ellipsoid dorsal root ganglion approximations as commonly practiced for dorsal root ganglion morphometry. On the basis of the deviations from ellipsoid geometry, improved volume estimation could be derived and was finally applied to a large human validation cohort (510 dorsal root ganglia).

RESULTS: Commonly used equations of ellipsoid geometry underestimate true dorsal root ganglion volume by large degrees (factor = 0.42–0.63). Ground truth segmentation enabled substantially optimizing dorsal root ganglion geometric approximation using its principal axes lengths by deriving the dorsal root ganglion volume term of $\frac{2}{3} \times A \times B \times C + 75 \text{ mm}^3$. Using this optimization, the mean volumes of 510 lumbosacral healthy dorsal root ganglia were as follows: L4: 211.3 (SD, 52.5) mm³, L5: 290.7 (SD, 90.9) mm³, S1: 384.2 (SD, 145.0) mm³, and S2: 192.4 (SD, 52.6) mm³. Dorsal root ganglion volume increased from L4 to S1 and decreased from S1 to S2 ($P < .001$). Dorsal root ganglion volume correlated with subject height ($r = .22$, $P < .001$) and was higher in men ($P < .001$).

CONCLUSIONS: Dorsal root ganglion volumetry by measuring its principal geometric axes on MR gangliography can be substantially optimized. By means of this optimization, dorsal root ganglion volume distribution was estimated in a large healthy cohort for the clinically most relevant lumbosacral levels, L4–S2.

ABBREVIATIONS: DRG = dorsal root ganglion; DRG_{vol} = dorsal root ganglion volume; DRG_{vol}(*r*) = real dorsal root ganglion volume

The dorsal root ganglia (DRGs) are embedded in the posterior spinal nerve root and contain the cell somata of all primary afferent sensory neurons.¹ DRGs are located within or laterally

adjacent to the intervertebral neural foramina and represent an interface between the peripheral nervous system and CNS, participating in somatosensory and pain-signal processing. The DRG is increasingly coming into focus as a therapeutic target for interventional pain therapy by local electrical neuromodulation.^{2,3} These procedures would benefit from direct imaging determination of local DRG anatomy and morphometry.

MR neurography allows the improved imaging resolution of peripheral nerves down to their fascicular level and has the capability of deriving novel quantitative estimates of microstructural integrity.^{4,5} MR gangliography is an extension of MR neurography and detects the DRG contour, which is challenging because the DRG shape is highly variable. The first observations of DRG volume by MR gangliography were promising by revealing surprisingly strong clinical-radiologic associations between disease

Received October 28, 2021; accepted after revision February 12, 2022.

From the Departments of Neuroradiology (S.W., M.S., J.H., F.H., C.N.-K., T.K., G.A.H., M.P., M.S.) and Neurology (N.U., C.S.), University Hospital Würzburg, Würzburg, Germany.

This work was funded by the German Research Foundation (255156212-SFB 1158) and the University of Würzburg, IZKF Project F-405.

Please address correspondence to Mirko Pham, MD, Department of Neuroradiology, University Hospital Würzburg, Josef-Schneider-Str 11, D-97080 Würzburg, Germany; e-mail: pham_m@ukw.de

Indicates open access to non-subscribers at www.ajnr.org

Indicates article with online supplemental data.

<http://dx.doi.org/10.3174/ajnr.A7487>

phenotypes and pathologically altered DRG volume.⁶⁻¹⁰ As a result, DRG volume (DRG_{vol}) as estimated in vivo by MR gangliography has emerged as a promising novel disease marker in pain research and for studying pain already at the peripheral nervous system level where most pain syndromes originate.¹¹ Already, DRG_{vol} is serving as a novel biomarker in schwannomatosis,⁷ oxaliplatin-induced painful sensory polyneuropathy,⁸ Fabry disease,⁹ and diabetic polyneuropathy.¹⁰ To reliably measure, reproduce, and compare DRG_{vol} in larger cohorts and to be able to also reliably detect smaller degrees of volume change, validation of DRG morphometry by MR imaging is required, which so far is lacking.

Specifically, it is a prerequisite for future research to validate whether true DRG_{vol} can be estimated with sufficient accuracy by approximation using measurements of the principal geometric axes of the DRG. Finally, the variation of DRG_{vol} between individuals and over spinal segments in a larger representative healthy human cohort would be of interest. Because automated quantitative volumetric 3D analysis of DRG_{vol} is not yet feasible, DRG_{vol} so far has usually been estimated by calculations using the manually determined maximal diameters in coronal (A), axial (B), and sagittal (C) reformations. These parameters were then heuristically used to fill the typical equation of a perfect geometric ellipsoid body ($\frac{4}{3} \times \pi \times \frac{A}{2} \times \frac{B}{2} \times \frac{C}{2}$). Even stronger simplifications of this equation were adopted to further enhance the ease of use for scientific or clinical purpose.¹²⁻¹⁴

We hypothesized that the assumption of the DRG as a perfect ellipsoid represents an oversimplification, which would render volumetric estimates substantially inaccurate. This hypothesis is supported by known anatomic observations describing a vast variety in DRG morphologic shapes and also peculiar variations such as biganglia or even tri- or multipartite ganglia.¹⁵ These challenging variations of basic DRG anatomy have only now, with the application of 3D isotropic MR gangliography such as proposed here, become observable and measurable in a reliable manner.

MATERIALS AND METHODS

Study Design

This investigation was designed as a prospective study consisting of 3 consecutive parts.

Part 1: Ground truth segmentation and volumetry (derivation/training cohort)

Part 2: Observation of ground truth deviation from ellipsoid body geometry (derivation/training cohort)

Part 3: Optimization with determination of DRG_{vol} and variations in an independent, large cohort of healthy subjects (validation cohort).

Ethics approval was obtained from the ethics committee of the University of Würzburg (89/19-me). All healthy participants provided written informed consent.

Participants

Sixty-four healthy volunteers without any previously known neurologic diseases were recruited, regardless of any other restriction or requirement (37 [57.8%] men; mean age, 31.5 [SD, 8.3] years). For our derivation cohort, 12 healthy volunteers (7 [58.3%]

women; mean age, 25.9 [SD, 3.5] years) of the overall cohort underwent MR gangliography of the bilateral L4-S2 levels.

Imaging Protocol

All MR gangliography examinations were conducted on the same MR imaging 3T scanner (Magnetom Prisma Fit; Siemens) between April 2019 and October 2020 at our facility. All participants underwent MR imaging, including using a high-resolution 3D T2WI FSE sequence (sampling perfection with application optimized contrasts by using different flip angle evolution [SPACE]) with spectral fat saturation of the lumbosacral plexus and spine (scanning parameters: FOV = 300 × 295 × 106 mm³, voxel size = 1.1 × 1.1 × 1.1 mm³, ΔTE = 4.4 ms, TE = 301 ms, TR = 2000 ms). The imaging slab was aligned perpendicular to the L4 vertebral body.

Image Analysis

DRGs were analyzed using the MERLIN Diagnostic Workcenter (Phoenix-PACS) and FSLeves (McCarthy, Paul; <http://doi.org/10.5281/zenodo.3937147>).

Part 1. The derivation cohort was chosen as a representative sample group with a balanced sex and age ratio from the total cohort. Ground truth estimation was performed by voxel-based volumetric analysis for 96 DRGs (L4: 24, L5: 24, S1: 24, S2: 24) by 3 expert raters. Real DRG_{vol} (DRG_{vol} [r]) was defined as the mean average value over the ground truth results from the 3 independent expert raters with at least 4 years of neuroradiology and image analysis experience. Furthermore, the principal geometric axes (axial, coronal, sagittal) were also measured in the same fashion using 3D reformations in these standard anatomic orientations (Online Supplemental Data). Axial, coronal, and sagittal section orientations were aligned with the principal axes of each DRG in anatomic space.

Part 2. DRG_{vol} (r) was then compared with the most frequently used approximations of DRG_{vol} under the basic assumption of ellipsoid geometry (Equations 1–4, [e1–e4]).¹²⁻¹⁴ We tested the following 6 equations:

Existing equations.

$$1) \quad \text{DRG}_{\text{vol}}(\text{e1}) = \frac{4}{3} \times \pi \times \frac{A}{2} \times \frac{B}{2} \times \frac{C}{2}$$

$$2) \quad \text{DRG}_{\text{vol}}(\text{e2}) = \frac{A \times B \times C}{2}$$

$$3) \quad \text{DRG}_{\text{vol}}(\text{e3}) = \frac{A \times B \times C}{3}$$

$$4) \quad \text{DRG}_{\text{vol}}(\text{e4}) = 2.5 \times \frac{A \times B \times C}{6}$$

Novel equations.

5) Because Equations 1–4 represent the same model:

$$\text{DRG}_{\text{vol}} = \text{coefficient} \times A \times B \times C,$$

we adapted this model for the new Equation 5 (e5) on the basis of this design by linear least squares approximation. DRG_{vol} (e5) was calculated for the 96 DRGs.

6) Furthermore, we extended the existing linear model by adding an intercept to reflect the true volume more accurately. The geometric reason for this intercept is that an ellipse tapers substantially at its proximal and distal ends, in contrast to the real DRG, which does not merge in a pointlike fashion into the adjacent nerve but connects to it over a broader area (Online Supplemental Data). As the simplest approximation, this missing offset volume can be set as a constant, which is represented by this intercept added to the equation. The design of Equation 6 was $DRG_{vol} = coefficient \times A \times B \times C + intercept$. DRG_{vol} (e6) was calculated for the 96 DRGs.

Part 3. The principal axes of 510 DRGs (L4: 128, L5: 128, S1: 128, S2: 126) of 64 healthy participants were measured according to Part 1, and DRG_{vol} (e6) = $\frac{2}{3} \times A \times B \times C + 75 \text{ mm}^3$ was obtained by linear least squares regression. Additionally, the length of the nerve roots (defined as the takeoff from the thecal sac to the proximal pole of DRG) and the takeoff the angle of the nerve roots in the coronal plane were measured to incorporate information from local anatomy.

For 1 participant, measurements for both DRGs of level S2 were not possible because of numerous cystic variations along the DRG. These 2 DRGs of level S2 were treated as missing values.

Statistical Analysis

Statistical analyses were performed using SPSS Statistics, Version 26 (IBM). All results were documented as mean (SD) and 95% confidence intervals. The Wilcoxon signed-rank test and Mann-Whitney *U* test were performed to compare the differences between 2 dependent/independent samples, respectively. Statistical dependence between the rankings of the 2 variables was tested using the Spearman rank correlation coefficient. Interrater reliability was examined using the intraclass correlation coefficient. Bland-Altman plots and intraclass correlation coefficients (2-way mixed, single measures, consistency) were used to compare 2 different methods of volumetric calculation. Correction coefficients and intercepts for improved DRG_{vol} calculation were obtained by linear regression analysis. Probability values of $< .05$ were considered significant. Adjustment of *P* values for multiple testing was made using the Bonferroni-Holm method. Data visualization was performed using Amira 2020.2 (Thermo Fisher Scientific).

RESULTS

Anthropometric Data

Sixty-four healthy subjects (women: 27 [42.2%]; men: 37 [57.8%]) participated in the study. The mean age was 31.5 (SD, 8.3) years; range, 19–63 years; mean height, 177.0 (SD, 9.4) cm; mean weight, 76.3 (SD, 14.7) kg; and mean body mass index, 24.2 (SD, 3.7) kg/m^2 . The mean height of the 27 female subjects was 169.4 (SD, 7.2) cm; the mean weight of the female subjects was 66.8 (SD, 12.1) kg; and the mean body mass index of the female subjects was 23.3 (SD, 4.3) kg/m^2 . The mean height of the 37 male subjects was 182.6 (SD, 6.5) cm; the mean weight of the male subjects was 83.2 (SD, 12.5) kg; and the mean body mass index of the male subjects was 24.9 (SD, 3.1) kg/m^2 . Parts 1 and 2 of the study were limited to 12 randomly chosen healthy participants (women: 7/58.3%; men: 5/41.7%). The mean age of these 12

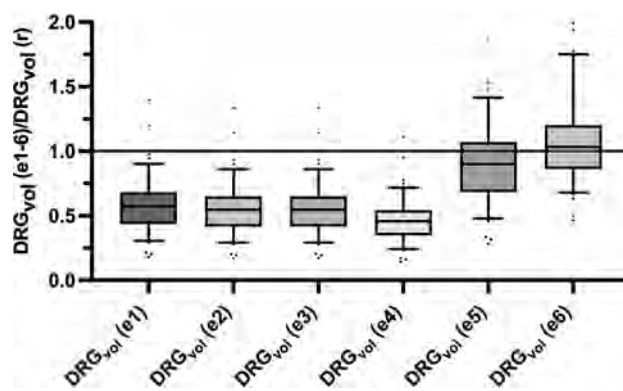


FIG 1. Evaluation of 6 equations (e1–e6) for estimating DRG volume: Boxplots show deviation of estimated DRG_{vol} (e1–e6) from ground truth volume (DRG_{vol} (r)) by calculating the quotient of estimated volume and ground truth volume. The closest approximation to ground truth was attained for Equation 6 (DRG_{vol} [e6], far right): = $\frac{2}{3} \times A \times B \times C + 75 \text{ mm}^3$. The top of the box represents the 75th percentile, the bottom of the box represents the 25th percentile. The line in the middle represents the 50th percentile (median). The whiskers represent the 5th and 95th percentiles, and values beyond the lower and upper bounds represent outliers and extreme values.

participants was 25.9 (SD, 3.5) years; range, 20–34 years. The mean height was 170.8 (SD, 6.7) cm; the mean weight was 66.08 (SD, 6.9) kg; and the mean body mass index was 22.8 (SD, 3.3) kg/m^2 .

Part 1. The intraclass correlation coefficient for volumetric determination based on voxelwise segmentation among the 3 raters was .84. The mean of 3 raters' voxelwise segmentation of 96 DRGs was defined as DRG_{vol} (r) and showed mean DRG volumes of 202.3 (SD, 64.1) mm^3 for L4, 299.7 (SD, 91.9) mm^3 for L5, 421.0 (SD, 243.5) mm^3 for S1, and 197.2 (SD, 80.7) mm^3 for S2. The DRG_{vol} (r) was significantly higher for S1 compared with L5 and for L5 compared with L4 ($P < .001$, respectively). The analysis showed a significant correlation between height and DRG_{vol} (r) (Spearman correlation coefficient = 0.38, $P < .001$). The DRG_{vol} (r) of male subjects was significantly higher than the DRG_{vol} (r) of female subjects ($P < .001$). The Online Supplemental Data show a more detailed overview of DRG_{vol} (r) values.

Part 2. The principal geometric axes of the 96 DRGs were measured in sagittal, coronal, and axial image reformations (Online Supplemental Data) and were used to calculate the estimated DRG_{vol} from the existing equations DRG_{vol} (e1) to DRG_{vol} (e4), respectively. Data are summarized in the Online Supplemental Data. Compared with DRG_{vol} (r), all tested approximating equations showed an underestimation of DRG_{vol} (Fig 1 and Online Supplemental Data). Equation 1 turned out to be the best-fitting approximation, showing a mean underestimation of 42.3%. The other equations showed a mean underestimation among 44.9% (e2), 54.1% (e4), and 63.3% (e3). The different results of DRG_{vol} are visualized in Fig 2.

To correct the calculations to the best fitting coefficient for DRG_{vol} (r), we performed linear regression analysis of DRG_{vol} (r) without an intercept. The resulting Equation 5, DRG_{vol} (e5) = $.82 \times A \times B \times C$, was used to calculate DRG_{vol} (Equation 5),

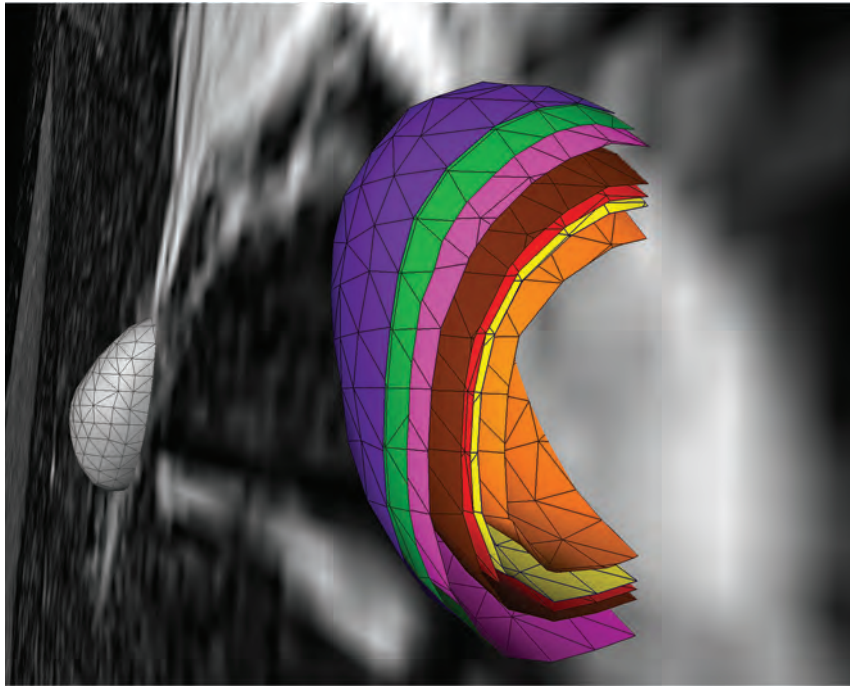


FIG 2. Colored 3D and surface volume-rendered and volume cut visualization of the volumetric results of the 6 different equations for estimation of ipsilateral DRG volume. The green shell represents the ground truth voxelwise segmentation result, $DRG_{vol}(t)$. The purple shell just at and very close to the outside of the ground truth shell (green) corresponds to the best optimization result, which was obtained from the new Equation 6, including an intercept, only slightly overestimating voxelwise ground truth segmentation. The pink shell just at the inside of the green shell corresponds to the new and second-best-performing Equation 5, without an intercept, slightly underestimating $DRG_{vol}(t)$. These 2 equations have provided the best results for estimating DRG_{vol} . For the purpose of visualization, the shells of these 2 optimized equations are slightly offset to allow macroscopic differentiation of the small differences. Significant underestimation of volume was observed for commonly used equations e1–e4; (brown = e1, red = e2, orange = e3, and yellow = e4). The contralateral DRG is surface volume-rendered in gray).

which is shown in the Online Supplemental Data. The intraclass correlation coefficient between $DRG_{vol}(t)$ and $DRG_{vol}(e5)$ was 0.95.

An extended model for a linear regression analysis with an intercept of $DRG_{vol}(t)$ was performed and resulted in equation Equation 6: $DRG_{vol}(e6) = \frac{2}{3} \times A \times B \times C + 75 \text{ mm}^3$. $DRG_{vol}(e6)$ was calculated for the 96 DRGs, which is shown in the Online Supplemental Data. The intraclass correlation coefficient between $DRG_{vol}(t)$ and $DRG_{vol}(e6)$ was .95. The comparison between the results of the 2 fitted equations, once with and once without an intercept, is shown in Fig 1 and in the Online Supplemental Data. Figure 3 shows the comparison between the manually segmented ground truth $DRG_{vol}(t)$ and the best ellipsoidal approximation of DRG_{vol} derived from Equation 6. Even though DRGs are not geometrically perfect ellipsoidal objects, both an accurate volumetric approximation and a purely visual, geometric approximation of DRG shape are possible.

Part 3. The volume of 510 DRGs from level L4 to S2 of 64 healthy volunteers was calculated using Equation 6. Values for mean diameters A, B, and C of the DRG were determined, and estimated volumes $DRG_{vol}(e6)$ are summarized in the Online Supplemental Data. DRG_{vol} increased significantly from L4 to S1 and decreased

significantly from level S1 to S2 ($P < .001$, respectively) as shown in Fig 4. There is a significant correlation between the subject's height and $DRG_{vol}(e6)$ (Spearman correlation coefficient = 0.22, $P < .001$). $DRG_{vol}(e6)$ of male subjects was significantly higher than $DRG_{vol}(e6)$ of female subjects ($P < .001$).

The mean values for the nerve root takeoff angle from the dural sac in coronal reformations decreased from level L4 (37.9° [SD, 9.0°]) over levels L5 (35.5° [SD, 8.0°]) and S1 (22.8° [SD, 6.4°]) to level S2 (17.4° [SD, 5.0°]). The mean values for nerve root lengths increased from level L4 (9.2 [SD, 2.1] mm) over levels L5 (13.0 [SD, 2.9] mm) and S1 (14.6 [SD, 4.0] mm) to level S2 (16.5 [SD, 4.4] mm). Data of nerve root takeoff angles and lengths are summarized in the Online Supplemental Data.

DISCUSSION

We demonstrate that common methods for MR imaging-based DRG volumetry, which, until now, have been grounded on the assumption of simple ellipsoid geometry, substantially underestimate true DRG volume (observed factor of underestimation: 0.42–0.63). Moreover, we demonstrated how to optimize geometric equations for substantially more accurate DRG volume estimation.

Increasing attention to the DRG within the fields of pain research and pain medicine has been paralleled by methodologic progress in human DRG imaging. In particular, recent progress by structural and functional advances in MR gangliography stand out.^{6–8,16} The DRG microstructure consists of a cell body-rich area, which is oriented toward the DRG rim and is embedded in a uniquely dense microvascular network.¹⁷ With more central topography, a nerve fiber-rich area is located within the DRG.¹⁷ Pathophysiologic changes in 1 or both compartments are associated with DRG_{vol} change. DRG_{vol} is, therefore, an innovative and novel biomarker promising to become clinically and scientifically useful for a variety of diagnostic and research questions, particularly in the field of pain research, because most pain syndromes originate at the peripheral level of the nervous system.¹¹ In pain and somatosensory afferent signal processing, the DRG organ represents the interface between the peripheral and central nervous systems. Also in the context of degenerative or traumatic processes, the imaging observation of DRG_{vol} seems valuable because it correlates strongly with the number of DRG sensory neurons, allowing conclusions about local neurodegeneration and loss of neurons.¹⁸ For example, changes in the quantity of neurons could be observed in experimental diabetes models with a loss of large DRG neurons that, on a functional level, was associated with slowed sensory

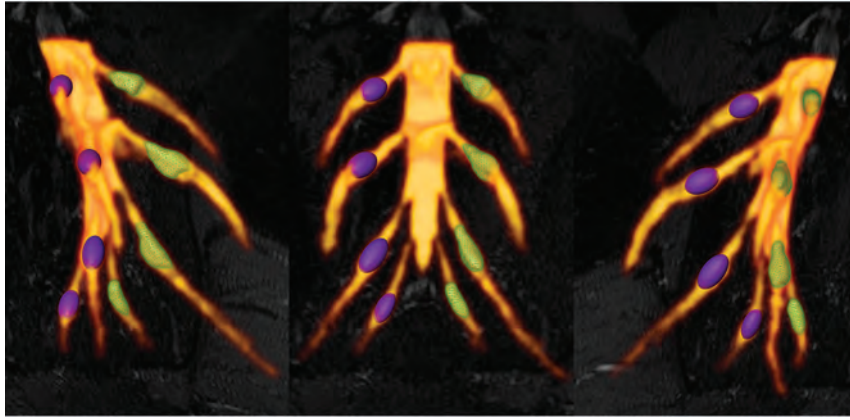


FIG 3. Comparative DRG volume-rendered visualization of ground truth volume $DRG_{vol}(r)$ versus best estimated volume by $DRG_{vol}(e6)$. Left: right-anterior-oblique plane. Middle: frontal plane. Right: left-anterior-oblique. Purple DRGs on the right side with smooth surfaces correspond to estimated volumes using Equation 6 for the most accurate approximation. Green DRGs on the left side with mesh surface correspond to ground truth volumes from expert manual segmentation and contour locations.

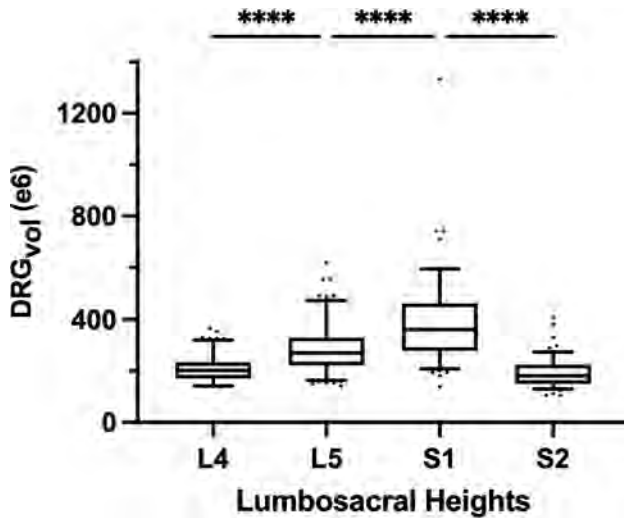


FIG 4. Boxplot of $DRG_{vol}(e6)$ showing the DRG_{vol} (cubic millimeters) for the different lumbosacral heights L4–S2. Equation 6 ($DRG_{vol}(e6)$) provided the best approximation to ground truth. By means of this equation, these boxplots display human MR imaging DRG morphometry over the clinically most relevant segments, L4–S2, in a large validation cohort ($n=510$). The top of the box represents the 75th percentile; the bottom of the box represents the 25th percentile. The line in the middle represents the 50th percentile (median). The whiskers represent the 5th and 95th percentiles, and values beyond the lower and upper bounds represent outliers and extreme values. Significances are marked with *asterisks* (indicating $P < .0001$).

nerve conduction velocity.¹⁹ Another example in which the DRG_{vol} decrease reflects DRG neurodegeneration is Friedreich ataxia. In this disease, severe neurologic deficits are tightly associated with hypoplasia of the DRG neurons, which translates into decreased DRG_{vol} on the macrostructural level.²⁰

The imaging methodical key to substantially improve the accuracy of DRG morphometry by MR gangliography is to increase the resolution and contrast of the DRG and of its local vicinity using high-resolution isotropic voxels. The MR imaging signal is

heavily T2-weighted with efficient fat suppression as an established contrast for MR gangliography and MR neurography.²¹ In this study, the principal protocol component of MR gangliography was an optimized 3D isotropic fast spin-echo sequence (SPACE). It improved the sharp-edged contrast between the DRG contour and surrounding tissue. It visualized more accurately the distinctive shape and contour of the DRG itself and, most important, differentiated it more accurately than possible before, in particular from the proximally and distally adjacent segments of the posterior nerve root.

In this study, the ground truth of $DRG_{vol}(r)$ was obtained as a volume average from extensive voxelwise manual segmentation of 96 single

DRGs across a total of 1152 slices by 3 independent expert raters. Interrater reliability among the 3 blinded raters was good²² to very good.²³ These ground truth DRG volumes confirm, in vivo and in humans, the previously reported ex vivo studies showing a continuous increase of DRG_{vol} toward the caudal region (L4–S1) with continuous decrease towards the sacral level.²⁴ The DRGs of levels L5 and S1 were significantly more voluminous compared with other vertebral heights. This finding represents the main reason why these 2 functionally important DRG levels can be proposed as index levels to investigate disease-related DRG_{vol} alterations. Finally, these findings were further validated in the largest human cohort so far observed for DRG volume estimation (510 DRGs).

To substantially optimize DRG_{vol} estimation, we tested several equations of ellipsoid body volume against ground truth. In the selection of equations, we applied the following rationale: Model-based approximation of disease target lesions or organ volumes is widely used to facilitate radiologic measurements, eg, for tumor volume estimation. The equation that is typically used for such purposes delivers volume estimation from standard diameter lengths and is typically represented by the term $(\frac{A \times B \times C}{2})$. This term was first described by Kwak et al,¹³ and it has been verified by Lisk et al²⁵ and found wider establishment through the work of Kothari et al¹² as well as Kazui et al.²⁶ It represents a simplification of the complete term of ellipsoid volume, which is $\frac{4}{3} \times \pi \times \frac{A}{2} \times \frac{B}{2} \times \frac{C}{2}$ because π can be simply approximated to 3. In this pragmatic form, it is widely and easily used as a very simple tool for fast linear measurements that are practically available in virtually every PACS. In contrast, more accurate volume estimation requires fundamental understanding of the target structure shape, is not easily incorporated into PACS, and is considerably more time-consuming. However, more accurate volume estimation can also be relevant clinically as it has been shown by using the example of vestibular schwannoma volume estimation to detect changes earlier.^{27–29} Also for intracerebral hemorrhage, it was shown that simple volume approximations

may substantially overestimate true hemorrhage volume by as much as 45%.³⁰

In the case of the DRG, so far, volumetry has been mainly derived from measurements of its maximum diameter in only 1 or 2 planes.^{24,31} Only a few studies performed more detailed measurements in which maximum diameters^{6,7} were determined in 3 orthogonal planes to estimate DRG_{vol} by the typical simplified ellipsoid equation: $DRG_{vol} = \frac{A \times B \times C}{2}$, which corresponded to Equation 2 in this study. Equation 1 of this study represented the mathematically precise equation for a perfect ellipsoidal body ($\frac{4}{3} \times \pi \times \frac{A}{2} \times \frac{B}{2} \times \frac{C}{2}$). Equations 2, 3, and 4 corresponded to different simplifications of this formula, which have been used in prior research.¹⁴ All of these 4 existing equations to estimate DRG_{vol} (e1–e4) led to considerable underestimation of DRG_{vol} in this study compared with ground truth DRG_{vol} (r) (observed factor of underestimation: 0.42–0.63).

According to a prior study on volumetry of the kidneys,³² we performed linear regression of DRG_{vol} (r) without and with the intercept and used the resulting regression equations to derive equations DRG_{vol} (e5) and DRG_{vol} (e6), which were substantially more accurate. The best approximation was achieved for DRG_{vol} (e6) = $\frac{2}{3} \times A \times B \times C + 75 \text{ mm}^3$. It unifies both the rapidity of measurement and very high accuracy compared with the ground truth. Equation 6, with its additional intercept, also better accounts for nonellipsoid variation in DRG shape, such as the more tubular shape that regularly applies especially to smaller DRGs that are more closely aligned with the posterior nerve root. The performance of all tested equations relative to ground truth is visualized by Fig 2 using cut volume shells.

In the final part of our study, Equation 6, which provided the best approximation (cut purple versus green volume shell in Fig 3), was applied to the largest human DRG cohort so far investigated volumetrically, to the best of our knowledge. In addition, our study also analyzed nerve root length, measured from the origin of the dural sac to the onset of the ellipsoidal structure of the DRG, as well as their angulation relative to the DRG, showing a significant decrease in the root angles from lumbar to sacral. The length of the nerve root, on the contrary, increased continuously from lumbar to sacral (L4–S2). These results, for the most part, correspond closely to a cadaver study of DRG length and root angulation.³³

To be able to also observe more subtle therapy or disease-specific changes of DRG_{vol} in larger cohorts in the future, a more accurate assessment and normative reference values of DRG_{vol} are needed and are both provided by this study. Already in the recent past, MR gangliography could show promising results in the observation of disease-related volume change, for example in chemotoxic polyneuropathy, painful diabetic polyneuropathy, and Fabry disease.^{7,9,10}

Our study comes with the following limitations: Imaging coverage had to be limited to the lower spine. Our findings may not be transferrable to the cervical or thoracic spine where significant heart motion or lung- and breathing-related artifacts would have to be considered. At these other levels, other intercepts might have to be used to obtain accurate estimates given the slightly different geometric shape of these DRGs. Our observations were made in a

large cohort of healthy subjects. Accuracy might be compromised if DRG shape is grossly altered by disease, which, however, seems unlikely, especially during the early disease course, which represents the typical stage of clinical-scientific focus.

Although rare, there remain anatomic variations such as arachnoid or dural cysts that may involve the proximal nerve roots and, in extreme cases, the DRG. These extreme-but-rare variations will continue to complicate the delineation of DRG boundaries in a few cases.

Finally, and obviously, full automation of DRG morphometry and volumetry need to be long-term goals. This seems achievable through the use of machine learning and/or artificial neural networks. Still, the application of equation-based 3D DRG volume estimation methods to larger cohorts as investigated here will certainly be needed as training datasets for this future purpose of automated image processing and analysis.

CONCLUSIONS

DRG_{vol} is a promising novel imaging biomarker in the fields of pain research and peripheral nervous system-related diseases. Existing ellipsoid-based equations for estimation of DRG_{vol} substantially underestimate true DRG_{vol} to a large degree. The following fitted equation could be derived and validated to avoid underrating DRG_{vol}: $\frac{2}{3} \times A \times B \times C + 75 \text{ mm}^3$.

Disclosure forms provided by the authors are available with the full text and PDF of this article at www.ajnr.org.

REFERENCES

1. Devor M. **Unexplained peculiarities of the dorsal root ganglion.** *Pain* 1999;82:S27–35 CrossRef Medline
2. Deer TR, Levy RM, Kramer J, et al. **Dorsal root ganglion stimulation yielded higher treatment success rate for complex regional pain syndrome and causalgia at 3 and 12 months: a randomized comparative trial.** *Pain* 2017;158:669–81 CrossRef Medline
3. Deer TR, Grider JS, Lamer TJ, et al. **A systematic literature review of spine neurostimulation therapies for the treatment of pain.** *Pain Med* 2020;21:1421–32 CrossRef Medline
4. Pham M, Oikonomou D, Hornung B, et al. **Magnetic resonance neurography detects diabetic neuropathy early and with proximal predominance.** *Ann Neurol* 2015;78:939–48 CrossRef Medline
5. Jende JME, Hauck GH, Diem R, et al. **Peripheral nerve involvement in multiple sclerosis: Demonstration by magnetic resonance neurography.** *Ann Neurol* 2017;82:676–85 CrossRef Medline
6. Godel T, Bäumer P, Pham M, et al. **Human dorsal root ganglion in vivo morphometry and perfusion in Fabry painful neuropathy.** *Neurology* 2017;89:1274–78 CrossRef Medline
7. Godel T, Mautner VF, Farschtschi S, et al. **Dorsal root ganglia volume differentiates schwannomatosis and neurofibromatosis 2.** *Ann Neurol* 2018;83:854–57 CrossRef Medline
8. Apostolidis L, Schwarz D, Xia A, et al. **Dorsal root ganglia hypertrophy as in vivo correlate of oxaliplatin-induced polyneuropathy.** *PLoS One* 2017;12:e0183845 CrossRef Medline
9. Godel T, von Cossel K, Friedrich RE, et al. **Assessment of peripheral nervous system alterations in patients with the Fabry related GLA-variant p.A143T.** *Diagnostics* 2020;10:1027 CrossRef Medline
10. Jende JM, Kender Z, Rother C, et al. **Diabetic polyneuropathy is associated with pathomorphological changes in human dorsal root ganglia: a study using 3T MR neurography.** *Front Neurosci* 2020;14:570744 CrossRef Medline

11. Devor M. Neuropathic pain: pathophysiological response of nerves to injury. In: McMahon SL, Koltzenburg M, Tracey I, eds. *Wall and Melzack's Textbook of Pain*. 6th ed. Elsevier; 2013:861–88
12. Kothari RU, Brott T, Broderick JP, et al. **The ABCs of measuring intracerebral hemorrhage volumes.** *Stroke* 1996;27:1304–05 CrossRef Medline
13. Kwak R, Kadoya S, Suzuki T. **Factors affecting the prognosis in thalamic hemorrhage.** *Stroke* 1983;14:493–500 CrossRef Medline
14. Zhao B, Jia WB, Zhang LY, et al. **1/2SH: a simple, accurate, and reliable method of calculating the hematoma volume of spontaneous intracerebral hemorrhage.** *Stroke* 2020;51:193–201 CrossRef Medline
15. Sperry ZJ, Graham RD, Peck-Dimit N, et al. **Spatial models of cell distribution in human lumbar dorsal root ganglia.** *J Comp Neurol* 2020;528:1644–59 CrossRef Medline
16. Birnbaum J, Duncan T, Owoyemi K, et al. **Use of a novel high-resolution magnetic resonance neurography protocol to detect abnormal dorsal root ganglia in Sjögren patients with neuropathic pain: case series of 10 patients and review of the literature.** *Medicine (Baltimore)* 2014;93:121–34 CrossRef Medline
17. Jimenez-Andrade JM, Herrera MB, Ghilardi JR, et al. **Vascularization of the dorsal root ganglia and peripheral nerve of the mouse: implications for chemical-induced peripheral sensory neuropathies.** *Mol Pain* 2008;4:10 CrossRef Medline
18. West CA, Ljungberg C, Wiberg M, et al. **Sensory neuron death after upper limb nerve injury and protective effect of repair.** *Neurosurgery* 2013;73:632–40 CrossRef Medline
19. Kishi M, Tanabe J, Schmelzer JD, et al. **Morphometry of dorsal root ganglion in chronic experimental diabetic neuropathy.** *Diabetes* 2002;51:819–24 CrossRef Medline
20. Koeppen AH, Becker AB, Qian J, et al. **Friedreich ataxia: hypoplasia of spinal cord and dorsal root ganglia.** *J Neuropathol Exp Neurol* 2017;76:nlw111 CrossRef Medline
21. Kollmer J, Bendszus M, Pham M. **MR neurography: diagnostic imaging in the PNS.** *Clin Neuroradiol* 2015;25:283–9. 252 2015 CrossRef Medline
22. Koo TK, Li MY. **A guideline of selecting and reporting intraclass correlation coefficients for reliability research.** *J Chiropr Med* 2016;15:155–63 CrossRef Medline
23. Cicchetti DV. **Guidelines, criteria, and rules of thumb for evaluating normed and standardized assessment instruments in psychology.** *Psychol Assess* 1994;6:284–90 CrossRef
24. Haberberger RV, Barry C, Dominguez N, et al. **Human dorsal root ganglia.** *Front Cell Neurosci* 2019;13:271 CrossRef Medline
25. Lisk D, Pasteur W, Rhoades H, et al. **Early presentation of hemispheric intracerebral hemorrhage: prediction of outcome and guidelines for treatment allocation.** *Neurology* 1994;44:133–39 CrossRef Medline
26. Kazui S, Naritomi H, Yamamoto H, et al. **Enlargement of spontaneous intracerebral hemorrhage: incidence and time course.** *Stroke* 1996;27:1783–87 CrossRef Medline
27. Bathla G, Policeni B, Hansen MR, et al. **Calculating the tumor volumes in vestibular schwannomas: are the ABC/2 and volumetric methods comparable?** *Otol Neurotol* 2017;38:889–94 CrossRef Medline
28. Walz PC, Bush ML, Robinett Z, et al. **Three-dimensional segmented volumetric analysis of sporadic vestibular schwannomas: comparison of segmented and linear measurements.** *Otolaryngol Head Neck Surg* 2012;147:737–43 CrossRef Medline
29. Van De Langenberg R, De Bondt BJ, Nelemans PJ, et al. **Follow-up assessment of vestibular schwannomas: volume quantification versus two-dimensional measurements.** *Neuroradiology* 2009;51:517–24 CrossRef Medline
30. Xue W, Vegunta S, Zwart CM, et al. **Retrospective validation of a computer-assisted quantification model of intracerebral hemorrhage volume on accuracy, precision, and acquisition time, compared with standard ABC/2 manual volume calculation.** *AJNR Am J Neuroradiol* 2017;38:1536–42 CrossRef Medline
31. Tortora F, Negro A, Russo C, et al. **Chronic intractable lumbosacral radicular pain, is there a remedy? Pulsed radiofrequency treatment and volumetric modifications of the lumbar dorsal root ganglia.** *Radiology Med* 2021;126:124–32 CrossRef Medline
32. Higashihara E, Nutahara K, Okegawa T, et al. **Kidney volume estimations with ellipsoid equations by magnetic resonance imaging in autosomal dominant polycystic kidney disease.** *Nephron* 2015;129:253–62 CrossRef Medline
33. Garfin SR, Wall EJ, Cohen MS, et al. **Cauda equina anatomy II: Extrathecal nerve roots and dorsal root ganglia.** *Spine (Phila Pa 1976)* 1990;15:1248–51 CrossRef Medline

Minimally Invasive Stent Screw–Assisted Internal Fixation Technique Corrects Kyphosis in Osteoporotic Vertebral Fractures with Severe Collapse: A Pilot “Vertebra Plana” Series

A. Cianfoni, R.L. Delfanti, M. Isalberti, P. Scarone, E. Koetsier, G. Bonaldi, J.A. Hirsch, and M. Pileggi



ABSTRACT

BACKGROUND AND PURPOSE: Fractures with “vertebra plana” morphology are characterized by severe vertebral body collapse and segmental kyphosis; there is no established treatment standard for these fractures. Vertebroplasty and balloon kyphoplasty might represent an undertreatment, but surgical stabilization is challenging in an often elderly osteoporotic population. This study assessed the feasibility, clinical outcome, and radiologic outcome of the stent screw–assisted internal fixation technique using a percutaneous implant of vertebral body stents and cement-augmented pedicle screws in patients with non-neoplastic vertebra plana fractures.

MATERIALS AND METHODS: Thirty-seven consecutive patients with vertebra plana fractures were treated with the stent screw–assisted internal fixation technique. Vertebral body height, local and vertebral kyphotic angles, outcome scales (numeric rating scale and the Patient’s Global Impression of Change), and complications were assessed. Imaging and clinical follow-up were obtained at 1 and 6 months postprocedure.

RESULTS: Median vertebral body height restoration was 7 mm (+74%), 9 mm (+150%), and 3 mm (+17%) at the anterior wall, middle body, and posterior wall, respectively. Median local and vertebral kyphotic angles correction was 8° and 10° and was maintained through the 6-month follow-up. The median numeric rating scale score improved from 8/10 preprocedure to 3/10 at 1 and 6 months ($P < .001$). No procedural complications occurred.

CONCLUSIONS: The stent screw–assisted internal fixation technique was effective in obtaining height restoration, kyphosis correction, and pain relief in patients with severe vertebral collapse.

ABBREVIATIONS: ant = anterior; BKP = balloon kyphoplasty; IQR = interquartile range; LKA = local kyphotic angle; mid = middle; NRS = numeric rating scale; PGIC = Patient’s Global Impression of Change; post = posterior; SAIF = stent screw–assisted internal fixation; VB = vertebral body; VBH = vertebral body height; VKA = vertebral kyphotic angle; VP = vertebra plana; VBS = Vertebral Body Stenting System; VCF = vertebral compression fracture

Painful osteoporotic vertebral compression fractures (VCFs) are commonly treated with traditional vertebral augmentation techniques, particularly vertebroplasty and balloon kyphoplasty

(BKP), which reinforce the anterior column, arrest wedge deformity, and palliate pain. The VCFs characterized by severe vertebral body (VB) collapse (>70% VB height loss) are generally termed “vertebra plana” (VP)¹ and demonstrate extreme osseous structural loss and resorption with anterior and middle column injury. Furthermore, they may present with intravertebral pseudoarthrosis (also termed cleft or Kümmel disease), posterior wall retropulsion, and pediculo-somatic junction fractures. The accompanying kyphosis can limit breathing² and activities of daily living and is likely associated with an increased mortality risk.³

Ideally, treatment of these fractures should stabilize, restore height, correct sagittal spinal alignment, correct kyphotic deformity, and achieve pain relief. Although standard augmentation techniques are effective in achieving pain palliation,^{1,4-6} they do not address middle column and pediculo-somatic junction fractures.⁷ Furthermore, secondary loss of stability has been reported at follow-up in VP cases treated with augmentation.^{8,9} At the

Received October 17, 2021; accepted after revision February 9, 2022.

From the Departments of Neuroradiology (A.C., R.L.D., M.I., M.P.), Neurosurgery (P.S.), and Pain Management Center (E.K.), Neurocenter of Southern Switzerland, Lugano, Switzerland; Department of Interventional and Diagnostic Neuroradiology (A.C.), Inselspital University Hospital of Bern, Bern, Switzerland; Faculty of Biomedical Sciences (E.K.), Università della Svizzera Italiana, Lugano, Switzerland; Neurosurgical Department (G.B.), Casa di Cura Igea, Milan, Italy; and Department of Radiology (J.A.H.), Massachusetts General Hospital, Harvard Medical School, Boston, Massachusetts.

A. Cianfoni and R.L. Delfanti share first co-authorship.

M. Pileggi and J.A. Hirsch share last co-authorship.

Please address correspondence to Rachel Delfanti, MD, Rolling Oaks Radiology, 415 Rolling Oaks D, Suite 125, Thousand Oaks, CA 91361; e-mail: Racheldelfanti@gmail.com; @JoshuaAHirsch; @Marco_Pileggi

Indicates open access to non-subscribers at www.ajnr.org

<http://dx.doi.org/10.3174/ajnr.A7493>

same time, these fractures often affect elderly and fragile patients, making surgical stabilization problematic^{10,11} because stand-alone posterior fixation techniques carry high risk of failure in conditions of poor bone quality,^{12,13} while anterior or circumferential approaches are associated with higher intraoperative blood loss and perioperative complications.¹⁴ Thus, there is no standard treatment for these challenging VCFs.^{1,15}

The stent screw–assisted internal fixation (SAIF) technique includes percutaneous insertion and balloon-expansion of 2 vertebral body stents (Vertebral Body Stenting System [VBS]; DePuy Synthes–Johnson & Johnson), followed by placement of cannulated and fenestrated pedicular screws (Injection pin, 2B1, Milan, Italy) in the lumen of the stents and cement augmentation through the screws. SAIF is currently being used for the treatment of severe osteoporotic and neoplastic fractures in 5 international centers.^{16–18}

The purpose of this study was to assess the feasibility and safety of performing SAIF in this cohort of patients with non-neoplastic VP. In addition, height restoration and kyphosis correction of the target vertebrae and the clinical outcome in terms of pain relief were studied.

MATERIALS AND METHODS

Patient Selection

This retrospective analysis included all thoracic and lumbar non-neoplastic VP treated with the stand-alone SAIF technique at a single institution between August 2017 and June 2020. Cases without comparable pre- and postoperative imaging (pre- and postoperative standing plain films, and/or pre- and postoperative CT/MR imaging) were excluded. The decision to treat with SAIF was made by a multidisciplinary group (composed of interventional neuroradiologists, spine surgeons, and pain specialists) for recent (<1 month) or nonhealed fractures causing persistent pain despite conservative treatment (≥ 5 on the numeric rating scale [NRS]; range, 0–10) or progressive collapse with kyphotic deformity. Nonhealed fractures were defined as osteoporotic fractures occurring >1 month earlier or at an unknown time with persistent pain and evidence of pseudoarthrosis (characterized by an intrasomatic cavity filled with gas or fluid and fracture mobility) and/or bone edema on MR imaging (STIR pulse sequence). Fractures were graded according to the AO Spine Spinal Section of the German Orthopedic and Trauma Society osteoporotic fracture classification system.¹⁹ Patients with neurologic deficits that required decompressive laminectomy and patients treated with SAIF combined with posterior instrumentation were excluded. All patients gave informed consent. The local ethics committee of Canton Ticino and EOC institutional review board approved the study.

SAIF Procedure

11 procedures were performed percutaneously with the patient under general anesthesia, with biplane fluoroscopic guidance using a previously described technique.¹⁶ Two VBSs were balloon-expanded in the VB with the intent to reduce local kyphosis. Transpedicular cannulated-fenestrated screws (Injection Pin 2B1; HealthManagement.org) were inserted over a Kirschner wire inside the VBS lumen and augmented with high-viscosity polymethylmethacrylate (Vertaplex HV; Stryker) under fluoroscopic

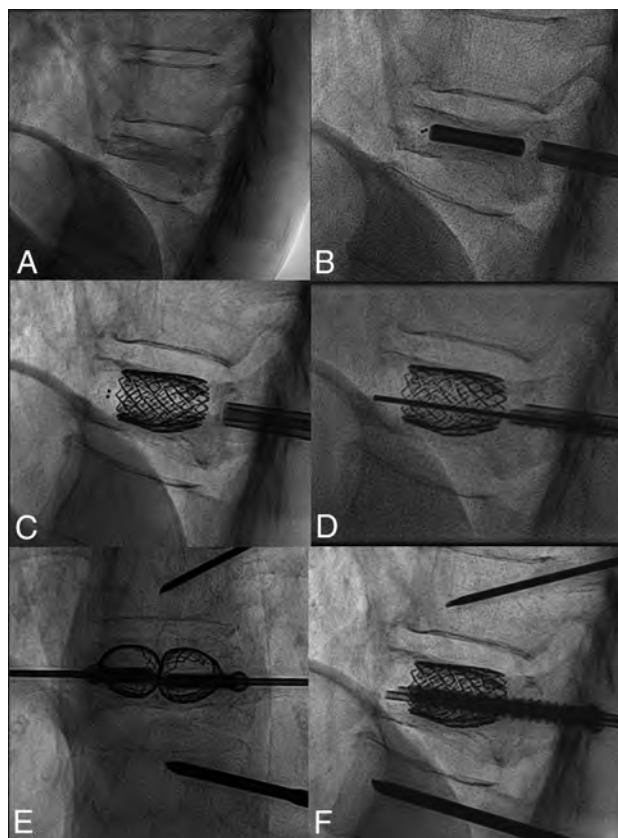


FIG 1. A, Procedural steps of the SAIF technique. Preprocedural lateral view of a T11 VP fracture. B, Balloon-mounted vertebral body stent insertion in the vertebral body. C, Balloon expansion of the stents. D, Access trocars are exchanged with transpedicular, cannulated-fenestrated screws over a Kirschner wire. Anterior-posterior and lateral views (E and F) obtained before cement injection through the screws.

control. Concomitant adjacent vertebroplasty was performed to treat milder VCFs (non-VP fracture: ie, with a minor degree of collapse) or with prophylactic intent when deemed appropriate per institutional protocol.²⁰ The main procedural steps are summarized in Fig 1.

Clinical and Imaging Assessment and Follow-up

Intraprocedural and postprocedural complications were recorded according to the Clavien-Dindo classification.²¹ In patients with pre- and postoperative cross-sectional imaging (CT and/or MR imaging), the VB height (VBH) was measured on midsagittal images at the anterior wall (ant-VBH), middle body (mid-VBH), and posterior wall (post-VBH) (Fig 2). The percentage of VBH gain was calculated as the ratio of gained height/preprocedural height. In patients with standing x-rays, the local kyphotic angle (LKA, kyphotic angle of the 2 adjacent vertebral bodies) and the vertebral kyphotic angle (VKA, kyphotic angle of the fractured vertebral body)²² were measured pre- and postprocedure (Fig 2) and at follow-up. The percentage of kyphotic correction was calculated as the ratio of gained height/preprocedural height. All radiologic measurements were performed by 2 fellowship-trained neuroradiologists with 4 and 3 years of experience, respectively, not involved in the procedures.

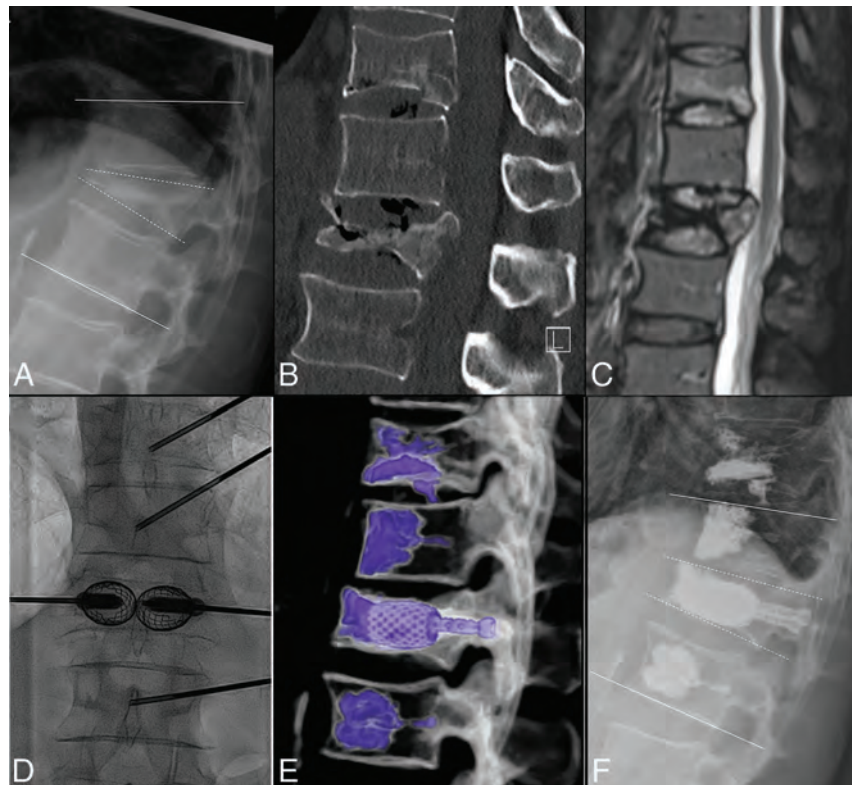


FIG 2. A, Standing plain film shows a L1 VP with kyphotic angulation. *White lines* along the endplates of T12 and L2 indicate the LKA, while the *dashed white lines* along the L1 endplates indicate the VKA. B, Sagittal CT shows a pseudoarthrosis with a gas cleft in L1 and increased vertebral body height in supine decubitus positioning, in keeping with a mobile fracture. An additional fracture of T11 was treated with vertebroplasty. Sagittal fat-suppressed T2WI (C) shows posterior wall retropulsion and central canal stenosis without cord compression and an additional milder fracture at T11. Anterior-posterior intraoperative fluoroscopic image (D) demonstrates SAIF implants, with pedicular screws inserted in the expanded stents before cement injection. Volume-rendering postprocedure CT (E) shows the SAIF treatment of L1 and vertebral augmentation at T11, T12, and L2. Postprocedural standing plain film (F) shows reduction of the LKA from 28° to 16° and of the VKA from 30° to 11°.

Preprocedural imaging was assessed to detect a cleft with pseudoarthrosis on CT/MR imaging and/or fracture mobility; fractures were categorized as mobile when VBH on standing views was reduced compared with supine views (Fig 2).

Clinical follow-up was performed at 1 and 6 months postoperatively and included the NRS (range, 0–10) and the Patient’s Global Impression of Change scale (PGIC; range, 1 = extremely worse, 4 = unchanged, to 7 extremely better).²³ Kyphotic angles, mobilization of the implants, and refractures of the treated segment were assessed with standing x-rays.

Statistical Analysis

Analyses used SPSS, Version 20.0.0 (IBM). Descriptive statistics for demographic and clinical data were expressed as median with interquartile range (IQR). Differences in VBH, LKA, VKA, and NRS scores before and after treatment were tested by the Wilcoxon matched-pairs test; comparison between mobile and nonmobile fracture groups was tested by the Wilcoxon unpaired test. A *P* value < .05 was considered statistically significant.

RESULTS

Patients, Procedures, and Safety

The consecutive series of patients with vertebra plana treated with SAIF consisted of 42 cases; 5 were excluded due to lack of

comparable pre- and postprocedure imaging. We, thus, included 37 SAIF procedures performed in 37 patients (11:26 male/female ratio; mean age, 81.6 years; range, 65–98 years). Between T3 and L4, 19/37 (51.3%) thoracic and 18/37 (48.6%) lumbar (overall, 27/37) (73%) fractures were located at the thoracolumbar junction (T10–L2). Thirty-four of 37 fractures were classified as osteoporotic fracture 4; three/37 fractures were classified as osteoporotic fracture 5 because of spinous process fracture (1/37) or mild posterior ligamentous complex lesions/edema (2/37) for which surgical instrumentation was withheld on the basis of the multidisciplinary spine care group recommendations. In 35/37 patients (94.6%), prophylactic vertebroplasty of adjacent levels was also performed (2/35 at the vertebra above, 33/35 above and below) at the operator’s choice per institutional protocol. All procedures were successfully completed without symptomatic cement leakage at the index level or clinical or technical complications.

Follow-up

Follow-up data with imaging and the patients’ outcome scales were available for 32/37 (86.5%; among them, 30 patients had comparable pre- and postprocedure CT/MR imaging and 29 patients had pre- and postprocedure standing x-rays) patients at 1 month and for 28/37 (75.7%) at 6 months. The remaining patients were contacted by a nurse on the phone to ascertain that no specific

Radiologic outcome: median measurements of anterior, middle, and posterior VBH, LKA, and VKA pre- and postoperatively (with IQR), for all fractures, mobile and nonmobile fracture groups

	Preoperative (IQR)	Postoperative (IQR)	Median Gain	Correction Loss at 6 Months (IQR)
Ant VBH				
All	9.5 mm (8.0–13.0)	17 mm (15.0–19.25)	7 mm, +74% ($P < .001$)	
Mobile	11.5 mm (9.0–15.25)	18 mm (16.5–19.5)	7 mm, +64% ($P < .001$)	
Nonmobile	11 mm (5.5–12.5)	19 mm (16.5–17.5)	8 mm, +73% ($P = .03$)	
Mid VBH				
All	6 mm (5.0–7.75)	15.5 mm (13.0–17.25)	9 mm, +150% ($P < .001$)	
Mobile	6.5 mm (5.75–9.5)	16 mm (15.0–18.0)	9 mm, +138% ($P < .001$)	
Nonmobile	5 mm (4.5–5.5)	15.5 mm (13.5–16.75)	11 mm, +220% ($P = .03$)	
Post VBH				
All	17.5 mm (16.0–19.0)	20 mm (18.0–22.0)	3 mm, +17% ($P < .001$)	
Mobile	18 mm (16.0–19.25)	20 mm (18.5–23.5)	3 mm, +17% ($P < .001$)	
Nonmobile	17 mm (15.0–18.0)	21 mm (20.0–22.0)	4.5 mm, +26% ($P = .04$)	
LKA				
All	25° (12.0–29.0)	14° (6.0–22.0)	8° ($P < .001$)	1° (0.0–1.0)
Mobile	25° (15.5–31.5)	14° (6.0–22.0)	8° ($P < .001$)	1° (0.0–1.7)
Nonmobile	21.5° (11.25–27.75)	13° (4.5–15.0)	4.5° ($P = .009$)	1° (0.5–1.0)
VKA				
All	21° (12.0–27.0)	9° (5.5–12.0)	10° ($P < .001$)	0° (0.0–1.0)
Mobile	23° (12.0–27.0)	9° (5.5–12.0)	11° ($P < .001$)	0° (0.0–1.0)
Nonmobile	19.5° (13.25–22.5)	7° (3.75–12.0)	9.5° ($P = .006$)	0° (0.0–1.0)

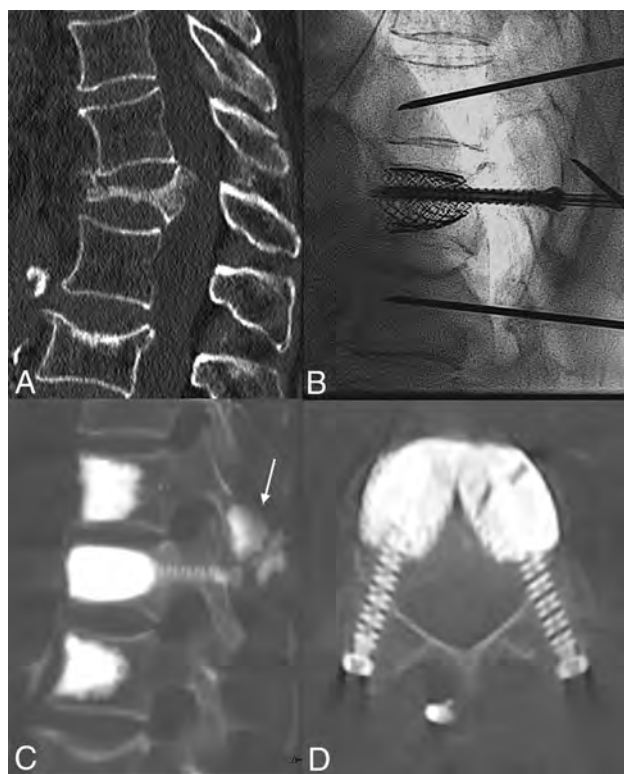


FIG 3. Sagittal CT (A) shows a T12 VP, with segmental kyphosis and a T11 spinous process fracture. Intraoperative fluoroscopic lateral view (B) shows fracture reduction by the SAIF technique before cement augmentation. Postprocedural sagittal (C) and axial (D) CT images show the final results obtained with the SAIF construct. There is cement augmentation of the T11 spinous process fracture (arrow), which was particularly tender at palpation, and the prophylactic augmentation of the adjacent levels.

spinal problems had occurred, but in the absence of imaging and formal clinical data, those patients were not included in this analysis.

Radiologic Outcome

The Table summarizes the results.

VBH. Pre- and postoperative cross-sectional studies (CT or MR imaging) were available in 30/37 (81.1%) patients. In this group, the median ant-VBH, mid-VBH, and post-VBH were 9.5 mm (IQR = 8.0–13.0 mm), 6 mm (IQR = 5.0–7.75 mm), and 17.5 mm (IQR = 16.0–19.0 mm), respectively, preprocedure, and 17 mm (IQR = 15.0–19.25 mm), 15.5 mm (IQR = 13.0–17.25 mm), and 20 mm (IQR = 18.0–22.0 mm) postprocedure; the median height gain was 7 mm at the ant-VBH (+74%; range, 2–15 mm), 9 mm at the mid-VBH (+150%; range, 4–13 mm), and 3 mm at the post-VBH (+17%; range, 0–7 mm). All differences were statistically significant ($P < .001$).

LKA and VKA. Pre- and postoperative standing x-rays were available for 29/37 (78.4%) patients.

In this group, the median LKA was 25° preoperatively (IQR = 12.0°–29.0°), and 14° postoperatively (IQR = 6.0°–22.0°). The median gain was 8° (range, 0°–19°) and was statistically significant ($P < .001$).

The median VKA was 21° preoperatively (IQR = 12.0°–27.0°) and 9.0° postoperatively (IQR = 5.5°–12.0°). The median gain was 10° (range, 1°–23°) and was statistically significant ($P < .001$).

In the patients with 6 months' follow-up (28/37), the median LKA and VKA gains were substantially maintained, respectively, at 7° and 9°.

Mobile and Nonmobile Fractures. Among 29 patients with preoperative standing x-rays available, a mobile fracture was present in 19 (65.5%) patients.

In this group, the median VBH gain was 7.0 mm (IQR = 5.5–8.5 mm) at the ant-VBH, 9 mm (IQR = 6.5–11.0 mm) at the mid-

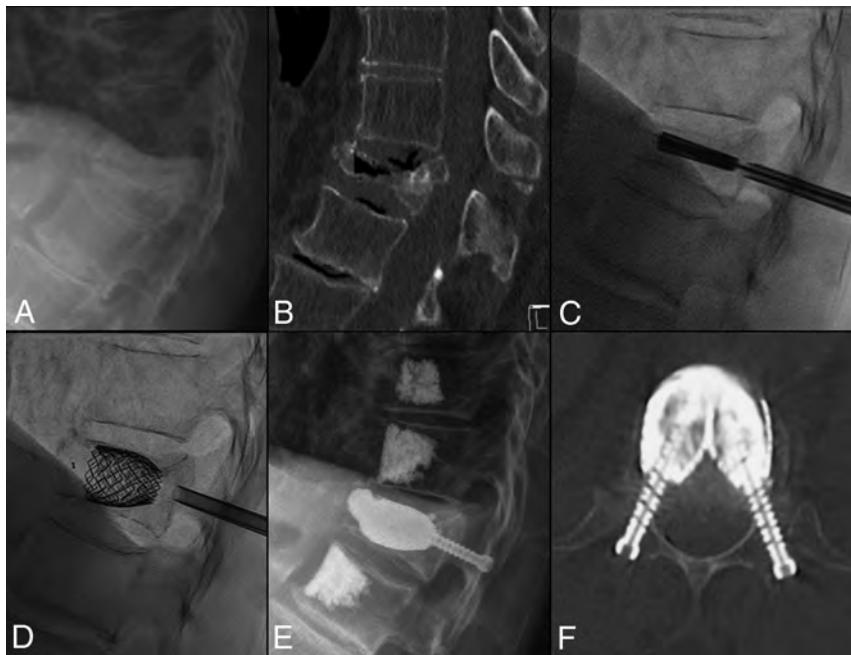


FIG 4. Standing plain film (A) and sagittal CT (B) show a T12 VP with pseudoarthrosis, gas cleft, and fracture mobility. Lateral intraprocedural fluoroscopic images before (C) and after (D) stent expansion with consequent fracture reduction. Postoperative standing plain film (E) demonstrates T12 height restoration and kyphosis correction, stable at 6 months' follow-up (F). Axial CT (F) at the T12 level shows the stent-cement complex reconstructing the vertebral body and the transpedicular screws cemented inside the stents acting as "anchors" to the posterior elements.

VBH, and 3 mm (IQR = 2.0–3.5 mm) at the post-VBH; the median correction of VKA and LKA was 11° (IQR = 5.0°–17.0°) and 8° (IQR = 7.0°–12.5°), respectively.

In patients with a nonmobile fracture (10/29), the median VBH gain was 8 mm (IQR = 7.0–9.75 mm) at the ant-VBH, 11 mm (IQR = 9.5–11.75 mm) at the mid-VBH, and 4.5 mm (IQR = 2.5–5.75 mm) at post-VBH; the median correction of VKA and LKA was 9.5° (IQR = 5.5°–15.5°) and 4.5° (IQR = 3.25°–7.75°), respectively.

The VBH and VKA corrections did not show significant differences between mobile and nonmobile fractures, while the LKA gain appeared greater in the mobile group, compared with nonmobile group, without reaching statistical significance ($P = .07$).

Refractures during Follow-up

No refracture occurred. No salvage surgery or new procedure was necessary at the index level during the available follow-up.

Pain Assessment

The median preoperative NRS pain score was 8 (range, 5–10; IQR = 7.0–9.0), while it was 3 (range, 0–8; IQR = 2.0–5.0) after 1 month and 3 (range, 0–7; IQR = 2.0–4.0) after 6 months. The differences were significant ($P < .001$). The median PGIC score was 6 (corresponding to "much better") after 1 month (range, 4–7; IQR = 5.0–7.0) and remained 6 after 6 months (range, 3–7; IQR = 6.0–7.0). No significant difference was observed between mobile and nonmobile fractures in patients' outcome scales ($P = .35$).

DISCUSSION

In this osteoporotic plana series, the SAIF technique was both feasible and safe. SAIF resulted in vertebral height restoration, kyphosis correction, and pain palliation. These results were sustained at 6 months' follow-up.

Vertebral compression fractures with VP morphology are considered severe fractures,^{24,25} and surgical stabilization is generally recommended to restore segmental stability, allow early mobilization, and avoid pseudoarthrosis.^{10,26–28} Kyphosis correction is important because kyphotic deformity is an independent risk factor for breathing difficulties and pulmonary complications, increasing morbidity and mortality.^{29,30}

Open surgical treatment is typically recommended, including anterior instrumentation to reconstruct the anterior spinal column.¹⁴ However, these approaches may result in implant failure due to high strain^{31,32} and anterior or anterolateral approaches carrying higher risks of blood loss and respiratory complications in elderly and fragile patients.³³

Vertebroplasty or BKP is less invasive and might provide pain relief but may represent an undertreatment for these severe fractures.^{4,6,8,34,35}

Most published reports on the treatment of vertebral compression by BKP alone measured the postprocedure improvement of the VKA,³⁶ but this measure might not translate into an effective segmental kyphosis correction.^{1,37} BKP might also be limited in effective kyphosis correction by the deflation effect before cement placement.^{38,39} The use of third-generation, rigid, intrasomatic distraction devices, such as SpineJack (Stryker) has been reported as a potential minimally invasive transpedicular replacement of expandable cages and, combined with posterior instrumentation, has been reported as a possible solution to treat VP fractures.²⁷

The SAIF technique applies a treatment rationale that is well-suited to patients with severe vertebral collapse. The rigid stents obtain and maintain predictable fracture reduction, avoid deflation effect, and create room for cement, thus reducing the risk of leakage. The metallic mesh of the VBS scaffolds the vertebral body from within, offering ample cross-sectional support for the disc endplates. Cement injection then solidifies the structure and support. Percutaneous pedicle screws anchor the VBS-cement complex to the posterior elements. In addition, the screws offer osteosynthesis for pedicular fractures and act to transfer the spinal load to the neural arch, unloading the middle column.¹⁶ The "reinforced concrete" construct rebuilds the VB, offering a 360° nonfusion internal stabilization of the vertebra (Figs 3 and 4). Two biomechanical studies provide support for this approach in both neoplastic and osteoporotic models.^{7,40}

In this series, SAIF obtained high degrees of VB height restoration, and VBH gain was much higher than previously reported with BKP.¹ Yokoyama et al,⁴¹ using BKP, obtained 3.6-, 2.0-, and 0.5-mm VBH gain at the anterior, middle, and posterior VB, respectively. By means of the same measurements, SAIF obtained a median gain of 7.0, 9.0, and 3.0 mm.

LKA on standing plain radiographs was used to assess kyphosis correction. LKA has been demonstrated to be a valid and reliable measure of thoracic kyphosis in patients with osteoporosis, in addition to VKA.³⁷ The LKA correction is usually less than the VKA correction because it is also influenced by the adjacent disc height loss but more reliably assesses the real effect of the treatment on segmental kyphosis (Fig 2).

In the present series, the LKA and VKA median correction was 8° and 10°, respectively, outperforming the previously reported results achieved with BKP, in which the LKA correction ranged between 1.94° and 6.5° and the VKA correction ranged between 4.2° and 7.3°.^{37,42-44} Diel et al⁴⁵ reported an average correction of LKA of 4.2° using VBS. Even when surgical posterior fixation was combined with vertebral augmentation, the LKA correction ranged between 5° and 9° in 3 studies.¹¹ A recent prospective study reported an LKA correction of 9° at 1-year follow-up, obtained with augmentation, posterior instrumentation, and arthrodesis, followed by a plastic thoracolumbar orthosis to be worn for 6 months postsurgery.²⁶ SAIF results on VBH and kyphosis correction were comparable with those obtained with 360° surgical approaches, but with a reduced complication rate.³¹

At 6-month follow-up, the achieved kyphosis correction was substantially stable, with an average loss of correction of only 1° at 6 months. In keeping with the previously reported results of Becker et al¹ and Yokoyama et al,⁴¹ the LKA gain tended to be greater in the mobile fracture group, though the difference did not reach statistical significance, likely due to small numbers in the nonmobile group. Nevertheless, significant VBH and VKA correction was also obtained in nonmobile fractures. These results might be explained by the efficient distraction forces exerted by the stents and the avoidance of the deflation effect, with polymethylmethacrylate anchoring the entire complex to the vertebral body.

The axis of insertion of the vertebral body stent into the VB is of paramount importance to optimize craniocaudal distraction, fracture reduction, and height restoration. Pedicular access should, therefore, be adapted to optimize device placement inside the VB along an axis parallel to the anticipated alignment of the original prefracture endplates. The distraction performed perpendicular to this axis approximates the original prefracture shape of the VB and allows the device to achieve maximum expansion and fracture reduction.⁴⁶ With the plana morphology, trocar access is usually through the lower half of the pedicle (Figs 3 and 4).

Prophylactic vertebroplasty of adjacent levels, the role of which remains controversial, was performed in 35/37 patients. High-quality evidence supporting improved patient outcome has not been confirmed.⁴⁷ Of note, this study was performed in Switzerland where prophylactic augmentation is more commonly performed than in the United States.

Patients treated with SAIF had satisfactory pain relief and an overall subjective impression of improvement as measured by the

NRS and the PGIC score, respectively. While pain relief has been similarly reported by standard augmentation techniques,⁴⁸ the SAIF approach achieves greater improvement in kyphosis, potentially improving biomechanics, ambulation, and breathing function.

Patients requiring laminectomy were excluded from this series, but SAIF can be combined with decompression and posterior instrumentation when needed.

The main limitations of this study are the retrospective design and lack of a control group. Follow-up was generally limited to 6 months because our clinical practice does not require further medical visits for this fragile elderly population in the absence of persistent or new back pain. The single-center design limits its generalizability, and larger, multicenter prospective studies are warranted. Finally, the augmentation of the adjacent vertebral bodies (either to treat milder VCFs or for prophylactic intent) is an additional potential confounder with respect to pain relief. Of note, these specific vertebral body stents and percutaneous fenestrated screws lack US Food and Drug Administration approval, and these procedures have, thus far, all been performed in Europe.

CONCLUSIONS

This study suggests that SAIF can be performed safely in patients with severe vertebral collapse. SAIF was effective in obtaining vertebral body height restoration, kyphosis correction, and pain relief in this cohort with stability of these results at the 6-month follow-up assessment. Based on these preliminary results, SAIF could overcome some of the limitations of standard vertebral augmentation and present a minimally invasive option in patients with osteoporotic vertebra plana.

Disclosure forms provided by the authors are available with the full text and PDF of this article at www.ajnr.org.

REFERENCES

1. Becker S, Tuschel A, Chavanne A, et al. **Balloon kyphoplasty for vertebra plana with or without osteonecrosis.** *J Orthop Surg (Hong Kong)* 2008;16:14-19 CrossRef Medline
2. Schlaich C, Minne HW, Bruckner T, et al. **Reduced pulmonary function in patients with spinal osteoporotic fractures.** *Osteoporos Int* 1998;8:261-67 CrossRef Medline
3. Kado DM, Huang MH, Karlamangla AS, et al. **Hyperkyphotic posture predicts mortality in older community-dwelling men and women: a prospective study.** *J Am Geriatr Soc* 2004;52:1662-67 CrossRef Medline
4. Pedicelli A, Lozupone E, Gatto A, et al. **Vertebra plana: reappraisal of a contraindication to percutaneous vertebroplasty.** *Eur J Radiol* 2013;82:2303-08 CrossRef Medline
5. Sigaux J, Guignard S, Tuilier T, et al. **Efficacy and feasibility of vertebroplasty for severe vertebral fracture: a retrospective study of 12 vertebroplasties.** *Joint Bone Spine* 2013;80:328-31 CrossRef Medline
6. Young C, Munk PL, Heran MK, et al. **Treatment of severe vertebral body compression fractures with percutaneous vertebroplasty.** *Skeletal Radiol* 2011;40:1531-36 CrossRef Medline
7. La Barbera L, Cianfoni A, Ferrari A, et al. **Stent-screw assisted internal fixation of osteoporotic vertebrae: a comparative finite element analysis on SAIF technique.** *Front Bioeng Biotechnol* 2019;7:291 CrossRef Medline
8. Laredo JD. **Expert's comment concerning Grand Rounds case entitled "Kümmell's disease: delayed post-traumatic osteonecrosis of the vertebral body" (by R. Ma, R. Chow, F. H. Shen).** *Eur Spine J* 2010;19:1071-72 CrossRef Medline

9. Wagner AL, Baskurt E. **Refracture with cement extrusion following percutaneous vertebroplasty of a large interbody cleft.** *AJNR Am J Neuroradiol* 2006;27:230–31 Medline
10. Dickman CA, Fessler RG, MacMillan M, et al. **Transpedicular screw-rod fixation of the lumbar spine: operative technique and outcome in 104 cases.** *J Neurosurg* 1992;77:860–70 CrossRef Medline
11. Lu W, Wang L, Xie C, et al. **Analysis of percutaneous kyphoplasty or short-segmental fixation combined with vertebroplasty in the treatment of Kümmell disease.** *J Orthop Surg Res* 2019;14:311 CrossRef Medline
12. El Saman A, Meier S, Sander A, et al. **Reduced loosening rate and loss of correction following posterior stabilization with or without PMMA augmentation of pedicle screws in vertebral fractures in the elderly.** *Eur J Trauma Emerg Surg* 2013;39:455–60 CrossRef Medline
13. Sawakami K, Yamazaki A, Ishikawa S, et al. **Polymethylmethacrylate augmentation of pedicle screws increases the initial fixation in osteoporotic spine patients.** *J Spinal Disord Tech* 2012;25:E28–35 CrossRef Medline
14. Sudo H, Ito M, Kaneda K, et al. **Anterior decompression and strut graft versus posterior decompression and pedicle screw fixation with vertebroplasty for osteoporotic thoracolumbar vertebral collapse with neurologic deficits.** *Spine J* 2013;13:1726–32 CrossRef Medline
15. Yang H, Pan J, Wang G. **A review of osteoporotic vertebral fracture nonunion management.** *Spine (Phila Pa 1976)* 2014;39:26 Spec No.):B4–6 CrossRef Medline
16. Cianfoni A, Distefano D, Isalberti M, et al. **Stent-screw-assisted internal fixation: The SAIF technique to augment severe osteoporotic and neoplastic vertebral body fractures.** *J Neurointerv Surg* 2019;11:603–09 CrossRef Medline
17. Cianfoni A, Distefano D, Scarone P, et al. **Stent screw-assisted internal fixation (SAIF): clinical report of a novel approach to stabilizing and internally fixating vertebrae destroyed by malignancy.** *J Neurosurg Spine* 2020;32:507–18 CrossRef Medline
18. Distefano D, Scarone P, Isalberti M, et al. **The “armed concrete” approach: stent-screw-assisted internal fixation (SAIF) reconstructs and internally fixates the most severe osteoporotic vertebral fractures.** *J Neurointerv Surg* 2021;13:63–68 CrossRef Medline
19. Schnake KJ, Blattner TR, Hahn P, et al; Spine Section of the German Society for Orthopaedics and Trauma. **Classification of osteoporotic thoracolumbar spine fractures: recommendations of the spine section of the German Society for Orthopaedics and Trauma (DGOU).** *Global Spine J* 2018;8:46S–49S CrossRef Medline
20. Kobayashi N, Numaguchi Y, Fuwa S, et al. **Prophylactic vertebroplasty: cement injection into non-fractured vertebral bodies during percutaneous vertebroplasty.** *Acad Radiol* 2009;16:136–43 CrossRef Medline
21. Dindo D, Demartines N, Clavien PA. **Classification of surgical complications: a new proposal with evaluation in a cohort of 6336 patients and results of a survey.** *Ann Surg* 2004;240:205–13 CrossRef Medline
22. Ulmar B, Brunner A, Gühring M, et al. **Inter- and intraobserver reliability of the vertebral, local and segmental kyphosis in 120 traumatic lumbar and thoracic burst fractures: evaluation in lateral x-rays and sagittal computed tomographies.** *Eur Spine J* 2010;19:558–66 CrossRef Medline
23. Maughan EF, Lewis JS. **Outcome measures in chronic low back pain.** *Eur Spine J* 2010;19:1484–94 CrossRef Medline
24. Ito M, Kaneda K, et al. **Osteopenia: vertebrectomy and fusion.** In: Herkowitz H, Dvorak J, Bell GR, et al. *The Lumbar Spine*. 3rd ed. Lippincott Williams and Wilkins; 2004:683–89
25. Sudo H, Ito M, Abumi K, et al. **One-stage posterior instrumentation surgery for the treatment of osteoporotic vertebral collapse with neurological deficits.** *Eur Spine J* 2010;19:907–15 CrossRef Medline
26. Katsumi K, Hirano T, Watanabe K, et al. **Surgical treatment for osteoporotic thoracolumbar vertebral collapse using vertebroplasty with posterior spinal fusion: a prospective multicenter study.** *Int Orthop* 2016;40:2309–15 CrossRef Medline
27. Vanni D, Pantalone A, Magliani V, et al. **Corpectomy and expandable cage replacement versus third generation percutaneous augmentation system in case of vertebra plana: rationale and recommendations.** *J Spine Surg* 2017;3:379–86 CrossRef Medline
28. Rajasekaran S, Kanna RM, Schnake KJ, et al. **Osteoporotic thoracolumbar fractures-how are they different?-classification and treatment algorithm.** *J Orthop Trauma* 2017;31(Suppl 4):S49–56 CrossRef Medline
29. Hirsch JA, Chandra RV, Carter NS, et al. **Number needed to treat with vertebral augmentation to save a life.** *AJNR Am J Neuroradiol* 2020;41:178–82 CrossRef Medline
30. Hinde K, Maingard J, Hirsch JA, et al. **Mortality outcomes of vertebral augmentation (vertebroplasty and/or balloon kyphoplasty) for osteoporotic vertebral compression fractures: a systematic review and meta-analysis.** *Radiology* 2020;295:96–103 CrossRef Medline
31. Oda I, Abumi K, Yu BS, et al. **Types of spinal instability that require interbody support in posterior lumbar reconstruction: an in vitro biomechanical investigation.** *Spine (Phila Pa 1976)* 2003;28:1573–80 Medline
32. Singh V, Mahajan R, Das K, et al. **Surgical trend analysis for use of cement augmented pedicle screws in osteoporosis of spine: a systematic review (2000–2017).** *Global Spine J* 2019;9:783–95 CrossRef Medline
33. Kanayama M, Ishida T, Hashimoto T, et al. **Role of major spine surgery using Kaneda anterior instrumentation for osteoporotic vertebral collapse.** *J Spinal Disord Tech* 2010;23:53–56 CrossRef Medline
34. Jacobson RE, Granville M, Hatgis J, et al. **Low volume vertebral augmentation with Cortoss® cement for treatment of high degree vertebral compression fractures and vertebra plana.** *Cureus* 2017;9:e1058 CrossRef Medline
35. Gangi A, Sabharwal T, Irani FG, Standards of Practice Committee of the Society of Interventional Radiology, et al. **Quality assurance guidelines for percutaneous vertebroplasty.** *Cardiovasc Intervent Radiol* 2006;29:173–78 CrossRef Medline
36. Wang B, Zhao CP, Song LX, et al. **Balloon kyphoplasty versus percutaneous vertebroplasty for osteoporotic vertebral compression fracture: a meta-analysis and systematic review.** *J Orthop Surg Res* 2018;13:264 CrossRef Medline
37. Pradhan BB, Bae HW, Kropf MA, et al. **Kyphoplasty reduction of osteoporotic vertebral compression fractures: correction of local kyphosis versus overall sagittal alignment.** *Spine (Phila Pa 1976)* 2006;31:435–41 CrossRef Medline
38. Wang D, Zheng S, Liu A, et al. **The role of minimally invasive vertebral body stent on reduction of the deflation effect after kyphoplasty: a biomechanical study.** *Spine (Phila Pa 1976)* 2018;43:E341–47 CrossRef Medline
39. Feltes C, Fountas KN, Machinis T, et al. **Immediate and early post-operative pain relief after kyphoplasty without significant restoration of vertebral body height in acute osteoporotic vertebral fractures.** *Neurosurg Focus* 2005;18:E5 CrossRef Medline
40. La Barbera L, Cianfoni A, Ferrari A, et al. **Stent screw-assisted internal fixation (SAIF) of severe lytic spinal metastases: a comparative finite element analysis of the SAIF technique.** *World Neurosurg* 2019;128:E370–77 CrossRef Medline
41. Yokoyama K, Kawanishi M, Yamada M, et al. **In not only vertebroplasty but also kyphoplasty, the resolution of vertebral deformities depends on vertebral mobility.** *AJNR Am J Neuroradiol* 2013;34:1474–78 CrossRef Medline
42. Voggenteiter G. **Balloon kyphoplasty is effective in deformity correction of osteoporotic vertebral compression fractures.** *Spine (Phila Pa 1976)* 2005;30:2806–12 CrossRef Medline
43. Xu C, Liu HX, Xu HZ. **Analysis of related factors on the deformity correction of balloon kyphoplasty.** *AJNR Am J Neuroradiol* 2014;35:202–06 CrossRef Medline

44. Lee JH, Kwon JT, Kim YB, et al. **Segmental deformity correction after balloon kyphoplasty in the osteoporotic vertebral compression fracture.** *J Korean Neurosurg Soc* 2007;42:371–76 CrossRef Medline
45. Diel P, Röder C, Perler G, et al. **Radiographic and safety details of vertebral body stenting: results from a multicenter chart review.** *BMC Musculoskelet Disord* 2013;14:233 CrossRef Medline
46. Cianfoni A. **If you aim at height restoration, mind the access!** In: Beall D, Brook AI, Chambers MR, et al. *Vertebral Augmentation: The Comprehensive Guide to Vertebroplasty, Kyphoplasty, and Implant Augmentation.* Thieme; 2020:237–40
47. Yen CH, Teng MM, Yuan WH, et al. **Preventive vertebroplasty for adjacent vertebral bodies: a good solution to reduce adjacent vertebral fracture after percutaneous vertebroplasty.** *AJNR Am J Neuroradiol* 2012;33:826–32 CrossRef Medline
48. Halvachizadeh S, Stalder AL, Bellut D, et al. **Systematic review and meta-analysis of 3 treatment arms for vertebral compression fractures: a comparison of improvement in pain, adjacent-level fractures, and quality of life between vertebroplasty, kyphoplasty, and nonoperative management.** *JBJS Rev* 2021;9 CrossRef Medline

MRI Findings after Recent Image-Guided Lumbar Puncture: The Rate of Dural Enhancement and Subdural Collections

I.T. Mark, W.P. Dillon, M.B. Richie, and J.E. Villanueva-Meyer



ABSTRACT

BACKGROUND AND PURPOSE: The rate of abnormal intracranial MR imaging findings including subdural collections and dural enhancement after recent lumbar puncture is not known. The purpose of our study was to examine the intracranial MR imaging findings after recent image-guided lumbar puncture.

MATERIALS AND METHODS: Patients who underwent contrast-enhanced MR imaging of the brain within 7 days of a CT-guided lumbar puncture between January 2014 and April 2021 were included. Contrast-enhanced MR images were reviewed for diffuse dural enhancement, morphologic findings of brain sag, dural venous sinus distension, and subdural collections.

RESULTS: Of the 160 patients who met the inclusion criteria, only 6 patients (3.9%) had new diffuse dural enhancement, though none had dural enhancement when the MR imaging was within 2 days of lumbar puncture. All 6 patients with dural enhancement had small, concurrent subdural collections. Two additional patients had subdural collections, for a total of 5.2% of our population.

CONCLUSIONS: Our study is the first to examine intracranial MR imaging after recent lumbar puncture and has 2 key findings: First, 5.2% of patients had small, bilateral subdural collections after recent lumbar puncture, suggesting that asymptomatic subdural collections after recent lumbar puncture are not atypical and do not require further work-up. Additionally, when MR imaging was performed within 2 days of lumbar puncture, none of our patients had diffuse dural enhancement. This argues against the commonly held practice of performing MR imaging before lumbar puncture to avoid findings of dural enhancement, and should not delay diagnostic work-up.

ABBREVIATIONS: LP = lumbar puncture; SIH = spontaneous intracranial hypotension; WBC = white blood cell

MR imaging findings after lumbar puncture (LP) have not been thoroughly studied. The incidence of diffuse dural enhancement within 30 days after lumbar puncture has been described,^{1,2} but no prior studies have focused on the incidence of abnormal MR imaging findings immediately after LP. The concern for possible dural enhancement after LP often directs providers to perform MR imaging before LP—a paradigm that can lead to diagnostic and management delays.²

The commonly accepted mechanism causing post-LP dural enhancement is a CSF leak from the puncture site, which leads to low CSF volume and subsequent venous engorgement within the dura per the Monro-Kellie hypothesis.³ Additional intracranial

findings associated with spontaneous intracranial hypotension (SIH) in the setting of LP, including subdural collections, are rare and have not been studied except for several case reports.⁴⁻¹⁰

The purpose of our study was to identify immediate post-LP imaging findings including the frequency of dural enhancement as well as other findings associated with SIH.

MATERIALS AND METHODS

We retrospectively reviewed 2319 patients who underwent an image-guided LP between January 2013 and April 2021. One hundred sixty patients had contrast-enhanced MR imaging of the brain within 7 days of the procedure and were included in our study. All LPs were CT-guided. The indications for the MR imaging and LP were reviewed, as well as infectious, inflammatory, and neoplastic comorbidities that could explain the dural enhancement. Routine CSF evaluation was also reviewed.

All MR imaging studies were reviewed by a neuroradiology fellow (I.T.M.), with equivocal findings additionally reviewed by a neuroradiologist with 4 years' experience (J.E.V.-M.). This

Received January 16, 2022; accepted after revision March 4.

From the Departments of Radiology and Biomedical Imaging (I.T.M., W.P.D., J.E.V.-M.) and Neurology (M.B.R.), University of California, San Francisco, San Francisco, California.

Please address correspondence Ian Mark, MD, University of California, San Francisco, 505 Parnassus Ave, Room L352, San Francisco, CA 94143; e-mail: ian.mark@ucsf.edu; @iantmark

<http://dx.doi.org/10.3174/ajnr.A7496>

Table 1: Contrast-enhanced MR imaging findings of patients who underwent imaging within 7 days of an image-guided LP^a

	Subdural Collections	Dural Enhancement	Brain Sag	Venous Distension
All patients	5.2% (8/153)	3.9% (6/153)	0.6% (1/159)	1.3% (2/158)
MR imaging <2 days of LP	2.5% (2/80)	0% (0/85)	0% (0/85)	2.4% (2/83)
Large-volume LP (>30 mL)	0% (0/6)	0% (0/6)	0% (0/6)	0% (0/6)

^aImaging findings present on pre-LP imaging were not included in this analysis.

Table 2: Eight patients who had subdural collections on MR imaging within 7 days after LP^a

	Presenting Diagnosis/ Reason for Procedure	Age (yr)	Days between LP and MR Imaging	CSF Removed (mL)	CSF Opening Pressure (cm H ₂ O)	Brain Sag	Venous Distension	Diffuse Dural Enhancement
Patient 1	Mycosis fungoides	35	4	9	NA	Yes	Yes	Yes
Patient 2	Leukemia	42	4	8	NA	No	Yes	Yes
Patient 3	AMS	54	3	16	NA	No	No	Yes
Patient 4	AMS	61	0	14	NA	No	No	No
Patient 5	Multiple myeloma	69	3	16	NA	No	No	Yes
Patient 6	Leukemia	69	1	6	NA	No	No	No
Patient 7	Pulmonary adenocarcinoma	69	6	15	13	No	No	Yes
Patient 8	AMS	71	4	14	14	No	No	Yes

Note:—NA indicates not available; AMS, altered mental status.

^aNone of the patients had a definite etiology on CSF analysis to explain dural enhancement. Each patient underwent an LP with a 22-ga Quincke tip spinal needle.

review included any pre-LP MRIs to assess pre-existing findings. In addition to dural enhancement, we evaluated imaging findings associated with CSF hypotension: morphologic findings of brain sag, dominant transverse sinus venous distension,¹¹ and subdural fluid collections.¹² A mamillopontine distance of <5.5 mm was used as a quantitative marker of brain sag.¹³ Basic statistical analysis (mean [SD]) was performed with Excel (Microsoft).

RESULTS

All Patients

The mean age of the 160 patients included in this study was 54.8 (SD, 17.6) years (range, 21–93 years). Sixty-nine patients (43.1%) were women. The mean time from LP to MR imaging was 2.1 days. We used the following needle sizes: 22-ga Quincke tip (BD Medical) (144 patients), 20-ga Quincke tip (10 patients), 17-ga Tuohy (B. Braun Medical Inc.) (5 patients), and 25-ga Quincke tip (1 patient). One hundred fifty-six patients had CSF removed, with a mean volume of 15.6 (SD, 6.8) mL. Opening pressure was recorded in 54 patients, with a mean of 20.3 (SD, 8.9) cm H₂O (range, 7–43 cm H₂O). Seven patients had pre-existing dural enhancement before LP. Of the remaining 153 patients, 6 patients (3.9%) had diffuse dural enhancement (Table 1).

Patients with Subdural Collections

Seven patients had subdural collections before LP. Of the remaining 153 patients, 8 patients (5.2%) had small bilateral subdural collections with a mean of 3.1 days between LP and MR imaging (range, 0–6 days) (Table 2). The mean age was 58.8 years (range, 35–71 years). All procedures used a 22-ga Quincke tip needle for the LP with a mean of 12.3 mL of CSF removed (range, 6–16 mL). The opening pressure was obtained in 2 patients (13 and 14 cm H₂O). Of the 8 patients, 6 had diffuse dural enhancement (Figs 1 and 2). Of the 7 excluded for prior subdural collections, 2 collections were at the site of prior craniotomies, 1 patient had diffuse dural metastases, 2 had thrombocytopenia, 1 had coccidioidal meningitis, and 1

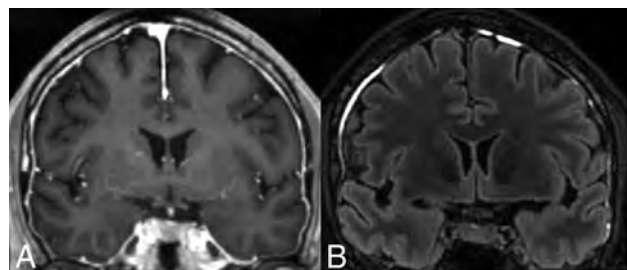


FIG 1. A 42-year-old woman (patient 2) with B-cell acute lymphoblastic leukemia who had an LP for intrathecal chemotherapy followed by MR imaging 4 days later. CSF did not show signs of infection, inflammation, or malignancy. A, T1-weighted postcontrast coronal MR imaging shows smooth, diffuse dural enhancement. B, FLAIR coronal MR imaging shows small bilateral subdural fluid collections without mass effect.

collection was idiopathic. None of these patients had a known connective tissue disorder.

Patient 1. A 35-year-old man who was hospitalized for a neutropenic fever in the setting of mycosis fungoides that involved the superficial soft tissues of the face with diffuse lymphadenopathy. MR imaging performed 4 days after LP demonstrated brain sag, venous distension, small subdural fluid collections, and diffuse dural enhancement, which were not present on an MR imaging 24 days before LP. However, since the comparison MR imaging, the patient had 4 additional LPs. The patient reported a long-standing headache on admission that predated the comparison MR imaging with normal findings. One week after the last LP, the patient was evaluated for a blood patch on the basis of the persistent headache and abnormal MR imaging findings; however, this was not performed secondary to a large skin ulcer over the lumbar spine. The headache improved without a blood patch by day 11 after LP. CSF analysis showed elevated glucose (93 mg/dL) and total protein levels (185 mg/dL) with a normal white

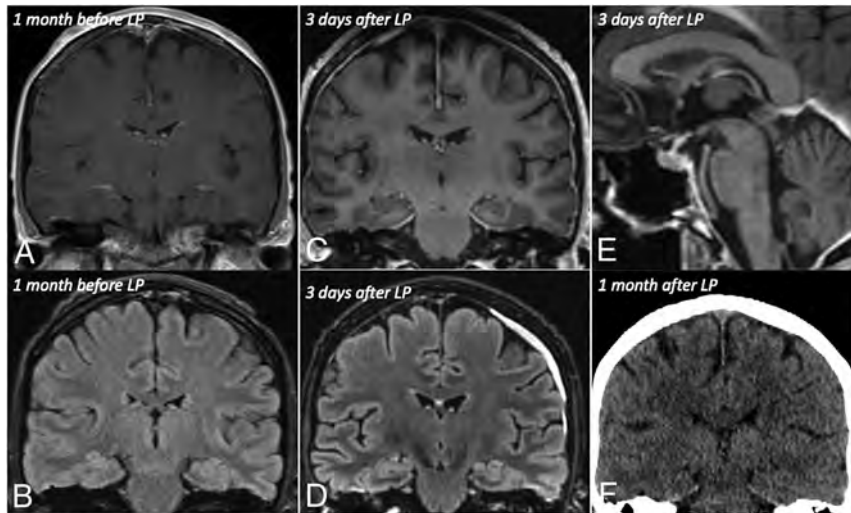


FIG 2. A 69-year-old man (patient 5) with a history of multiple myeloma underwent an LP followed by MR imaging 3 days later. Coronal T1-weighted postcontrast (A) and FLAIR (B) images 1 month before LP do not show subdural collections or dural enhancement. However, 3 days after the LP, MR images show smooth diffuse dural enhancement on coronal T1-weighted postcontrast imaging (C) and a left frontal convexity subdural fluid collection on coronal FLAIR imaging (D) but no morphologic findings of brain sag on T1-weighted sagittal imaging (E). F, Coronal reformatted CT 1 month after LP shows resolution of the subdural fluid collection.

blood cell (WBC) count and benign CSF findings on cytopathology analysis.

Patient 2. A 42-year-old woman presented for treatment of B-cell acute lymphoblastic leukemia (Fig 1). She had an LP 15 days before the LP included in our study. MR imaging performed 4 days after the LP demonstrated venous distension, small subdural fluid collections, and diffuse dural enhancement without brain sag. She did not have comparison MR imaging. The patient reported a headache the day after the LP; however, this resolved by day 5 without a blood patch. CSF had a normal total protein level, WBC count, and cytology findings.

Patient 3. A 54-year-old man with a history of a renal transplant who presented with fever of unknown origin. He did not have a prior LP. MR imaging performed 3 days after LP demonstrated diffuse dural enhancement and small subdural fluid collections without venous distension or brain sag. Comparison MR imaging was not available. He remained in the hospital for 21 days after his LP and did not report a headache or require a blood patch. CSF had a normal total protein level and WBC count.

Patient 4. A 61-year-old woman admitted for a prolonged spinal infection who underwent an LP and MR imaging for new-onset encephalopathy. Given the extensive spinal infection, the CT-guided LP was performed via a C1–C2 puncture. There was no history of a prior cervical or lumbar puncture. MR imaging performed on the same day as the C1–C2 puncture demonstrated small subdural fluid collections in addition to separate extra-axial blood at the puncture site without brain sag, venous distension, or diffuse dural enhancement. MR imaging 35 days before the C1–C2 puncture did not show subdural fluid collections. The patient did not have a headache or require a blood patch throughout the

remainder of the hospitalization, which lasted 23 days after the C1–C2 puncture. CSF had normal total protein level and WBC count.

Patient 5. A 69-year-old man was admitted for treatment of multiple myeloma (Fig 2). There was no history of LP. MR imaging performed 3 days after the LP demonstrated diffuse dural enhancement and small subdural fluid collections without brain sag or venous distension. These findings were new on the basis of comparison MR imaging 40 days prior. CSF had normal total protein levels, WBC count, and cytology findings. He did not have a headache or require a blood patch during the remaining 38 days of his hospitalization.

Patient 6. A 69-year-old woman underwent an LP for intrathecal chemotherapy in the setting of mixed phenotype acute leukemia. Within the 30 days before her LP, she had 5 additional LPs. The MR imaging performed 1 day after the LP demonstrated small subdural fluid collections without brain sag, venous distension, or diffuse dural enhancement. These findings were new compared with the most recent comparison MR imaging 44 days prior. CSF had a normal total protein level, WBC count, and cytology findings. She did not have a headache or require a blood patch during the remaining 48 days of her hospitalization.

Patient 7. A 69-year-old man presented with new left abducens nerve palsy with an acute right MCA territory infarct and was found to have newly diagnosed metastatic lung cancer. A bedside LP was attempted before the image-guided LP. MR imaging performed 6 days after the LP demonstrated diffuse dural enhancement and small subdural fluid collections without brain sag or venous distension. These findings were new compared with the most recent comparison MR imaging 16 days prior. CSF demonstrated elevated total protein level (118 mg/dL) without an elevated WBC count. CSF cytology was not performed. He did not have a headache during the 17 days before being transitioned to comfort care in the setting of metastatic carcinoma.

Patient 8. A 71-year-old man presented with altered mental status in the setting of atypical chronic myeloid leukemia. A bedside LP was attempted before the image-guided LP. The MR imaging performed 4 days after the LP demonstrated diffuse dural enhancement and small subdural fluid collections without brain sag or venous distension. These findings were new compared with the most recent comparison noncontrast MR imaging 24 days prior, though comparison for dural enhancement was limited because there was no overt dural thickening. CSF had a normal total protein level and WBC count. He did not have a

headache or require a blood patch during the remaining 13 days of his hospitalization.

MR Imaging Immediately after LP

Of the patients who had MR imaging performed on the same day (40 patients), 1 day after (35 patients), and 2 days after LP (10 patients), none had new diffuse dural enhancement or morphologic findings of brain sag. Two patients had venous distension not seen on prior imaging. Seven patients had subdural collections; however, 5 were unchanged from pre-LP MR imaging.

High-Volume Lumbar Puncture

Six patients (3.9%) had at least 30 mL of CSF removed. Of these patients, the mean CSF removed was 33 mL (range, 30–40 mL). None of these patients had dural enhancement, subdural collection, venous distension, or brain sag.

Intrathecal Chemotherapy

Thirteen patients underwent LP for the administration of intrathecal chemotherapy, one of whom had diffuse dural enhancement (Table 2).

DISCUSSION

Our study found that of patients undergoing brain MR imaging within 7 days of LP, 5.2% of patients had small subdural collections. Subdural collections after LP have been previously reported in case reports in symptomatic patients,^{4–8} without prior studies to describe the incidence. Additionally, while 3.9% of our total population had dural enhancement, none of the patients who underwent MR imaging within 2 days of LP or who had large-volume CSF removal had dural enhancement.

These 2 findings are important but for different reasons. Previous studies have examined the incidence of dural enhancement after LP; however, they focused on MR imaging examinations that occurred within 1 month after LP. Mittl et al¹ found that 11 patients of 97 had diffuse dural enhancement within 1 month after LP; however, 10 of the 11 patients had a comorbidity to explain the findings. Wesley et al² studied 77 patients who underwent an MR imaging within 30 days after LP and found only a single case of unexplained dural enhancement in a patient who underwent a large-volume tap. Our study is the first to focus on patients who underwent MR imaging within 2 days of LP, none of whom had dural enhancement. This finding suggests that the commonly held practice of performing an MR imaging before LP to avoid findings of dural enhancement should not delay the diagnostic work-up.

Furthermore, we are the first study to examine the rate of subdural collections after LP. Prior authors have demonstrated subdural collections in 20%–45% of patients with SIH.¹⁴ In the setting of SIH, the tearing of the bridging veins or rupture of the dilated thin-walled blood vessels in the subdural zone has been proposed as the causative mechanism.¹⁵ While this is the most likely mechanism in our patients, 2 of our patients had isolated subdural collections without additional SIH findings. Tosaka et al¹² examined serial images of 8 patients with SIH and found that dural enhancement resolved before the subdural collections and could be a possible explanation in our study. De Noronha et al¹⁶ described a case

series of patients with SIH, of whom 2 patients had subdural collections without dural enhancement. The mechanism that leads to subdural collections without dural enhancement is not well-understood, but it could be related to pre-existing susceptibility of the cortical vessels that places them at greater risk of damage in the setting of SIH. Additionally, the timing of dural enhancement in SIH has been shown to be variable, and some patients can take a longer time to develop dural enhancement than the duration of our study.¹⁷ Most interesting, of the 8 patients with subdural collections, 3 had a prior image-guided LP within the past month (ranging from 1 to 5 prior LPs) and 2 had failed bedside LP attempts. This scenario further supports CSF leakage and SIH as the etiology for the abnormal MR imaging findings.

Our study has several limitations, starting with its retrospective nature. Second, our patients underwent an LP with image guidance; however, this in line with recent Medicare trends.¹⁸ Additionally, none of our patients received an epidural blood patch, compared with a previously reported 4.2% rate with image-guided LP.¹⁹ Given this discordance, it raises the question of whether our technique and sample size are reflective of the greater population. All our patients underwent CT guidance for their LP, reflecting our group practice. In theory, the improved needle localization of CT over fluoroscopy would allow a less traumatic procedure with possibly fewer dural punctures. In this case, our study could underrepresent the incidence of abnormal MR imaging findings. However, the benefits of CT guidance help with navigation around degenerative osteophytes rather than changing the number of dural punctures. Final limitations that may affect the generalizability of our study include the selection of the needle size (most of our cases involved a 22-ga spinal needle) and age (pediatric patients were excluded).

CONCLUSIONS

Our study is the first to examine the intracranial MR imaging findings after recent CT-guided LP and has 2 key findings: First, 5.2% of patients had small, bilateral subdural collections after recent LP, suggesting that subdural collections are not atypical and, if asymptomatic, do not require further work-up. Additionally, when MR imaging was performed within 2 days of LP, none of our patients had diffuse dural enhancement. This finding argues against the commonly held practice of performing MR imaging before LP to avoid findings of dural enhancement, and it should not delay diagnostic work-up.

Disclosure forms provided by the authors are available with the full text and PDF of this article at www.ajnr.org.

REFERENCES

1. Mittl RL Jr, Yousem DM. Frequency of unexplained meningeal enhancement in the brain after lumbar puncture. *AJNR Am J Neuroradiol* 1994;15:633–38 Medline
2. Wesley SF, Garcia-Santibanez R, Liang J, et al. Incidence of meningeal enhancement on brain MRI secondary to lumbar puncture. *Neurol Clin Pract* 2016;6:315–20 CrossRef Medline
3. Smirniotopoulos JG, Murphy FM, Rushing EJ, et al. Patterns of contrast enhancement in the brain and meninges. *Radiographics* 2007;27:525–51 CrossRef Medline

4. Abdullah M, Elkady A, Bushnag A, et al. **Acute subdural haemorrhage as a complication of diagnostic lumbar puncture.** *Cureus* 2020;12:e7515 CrossRef Medline
5. Kim HJ, Cho YJ, Cho JY, et al. **Acute subdural hematoma following spinal cerebrospinal fluid drainage in a patient with freezing of gait.** *J Clin Neurol* 2009;5:95–96 CrossRef Medline
6. Vos PE, de Boer WA, Wurzer JA, et al. **Subdural hematoma after lumbar puncture: two case reports and review of the literature.** *Clin Neurol Neurosurg* 1991;93:127–32 CrossRef Medline
7. Samuelson S, Long DM, Chou SN. **Subdural hematoma as a complication of shunting procedures for normal pressure hydrocephalus.** *J Neurosurg* 1972;37:548–51 CrossRef Medline
8. Samdani A, Garonzik IM, Zahos P. **Subdural hematoma after diagnostic lumbar puncture.** *Am J Emerg Med* 2004;22:316–17 CrossRef Medline
9. Zekaj E, Saleh C, Minichiello M, et al. **How to treat repeated subdural hematomas after lumbar puncture?** *Asian J Neurosurg* 2019;14:249–52 CrossRef Medline
10. Gaucher DJ Jr, Perez JA Jr. **Subdural hematoma following lumbar puncture.** *Arch Intern Med* 2002;162:1904–05 CrossRef Medline
11. Farb RI, Forghani R, Lee SK, et al. **The venous distension sign: a diagnostic sign of intracranial hypotension at MR imaging of the brain.** *AJNR Am J Neuroradiol* 2007;28:1489–93 CrossRef Medline
12. Tosaka M, Sato N, Fujimaki H, et al. **Diffuse pachymeningeal hyperintensity and subdural effusion/hematoma detected by fluid-attenuated inversion recovery MR imaging in patients with spontaneous intracranial hypotension.** *AJNR Am J Neuroradiol* 2008;29:1164–70 CrossRef Medline
13. Kranz PG, Tanpitukpongse TP, Choudhury KR, et al. **Imaging signs in spontaneous intracranial hypotension: prevalence and relationship to CSF pressure.** *AJNR Am J Neuroradiol* 2016;37:1374–78 CrossRef Medline
14. Xia P, Hu XY, Wang J, et al. **Risk factors for subdural haematoma in patients with spontaneous intracranial hypotension.** *PLoS One* 2015;10:e0123616 CrossRef Medline
15. Schievink WI. **Spontaneous spinal cerebrospinal fluid leaks and intracranial hypotension.** *JAMA* 2006;295:2286–96 CrossRef Medline
16. de Noronha RJ, Sharrack B, Hadjivassiliou M, et al. **Subdural haematoma: a potentially serious consequence of spontaneous intracranial hypotension.** *J Neurol Neurosurg Psychiatry* 2003;74:752–55 CrossRef Medline
17. Fuh JL, Wang SJ, Lai TH, et al. **The timing of MRI determines the presence or absence of diffuse pachymeningeal enhancement in patients with spontaneous intracranial hypotension.** *Cephalalgia* 2008;28:318–22 CrossRef Medline
18. Johnson DR, Waid MD, Rula EY, et al. **Comparison of radiologists and other specialists in the performance of lumbar puncture procedures over time.** *AJNR Am J Neuroradiol* 2021;42:1174–81 CrossRef Medline
19. Hatfield MK, Handrich SJ, Willis JA, et al. **Blood patch rates after lumbar puncture with Whitacre versus Quincke 22- and 20-gauge spinal needles.** *AJR Am J Roentgenol* 2008;190:1686–89 CrossRef Medline

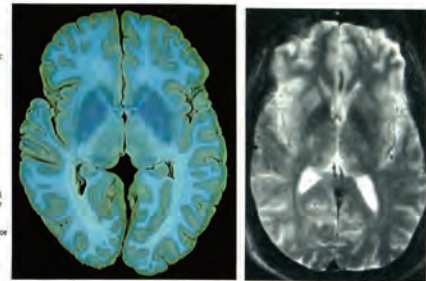
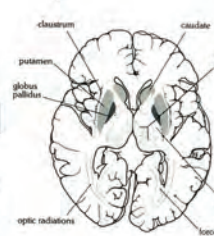
Celebrating 35 Years of the AJNR

May 1987 edition

Study of Movement Disorders and Brain Iron by MR

J. Neal Rutledge^{1,2}
Sadek K. Hikal¹
A. John Silver¹
Richard Defendorf³
Stanley Fahn⁴

Heavily T2-weighted high-field MR images provide a unique opportunity for the evaluation of the extrapyramidal motor system. The images are affected by the presence of small amounts of naturally occurring paramagnetic substances—principally iron—that delineate the neostriatum (caudate and putamen), globus pallidus, red nucleus, substantia nigra, and dentate nucleus, primarily by a decrease in signal secondary to the T2* effect. Movement disorders are associated with either increased or decreased signal or both in these structures, depending on the pathologic process. In the initial evaluation of 113 patients with a variety of movement disorders, good correlation of imaging abnormalities can be made with a simplified scheme of the extrapyramidal pathways and a system of classification of abnormal movements, parkinsonism (tremor, dystonia, chorea, myoclonus, and hemiballismus), Parkinsonisms are characterized by abnormalities of the cortico-ponto-cerebello-identical-subthalamic-corticospinal tract or the nigrostriatal tract. Dystonias are characterized by abnormalities of the neostriatum predominantly affecting the putamen. Chorea are also characterized by abnormalities of the neostriatum but predominantly affecting the caudate nucleus. Hemiballismus is characterized by lesions affecting the subthalamic nucleus or associated pathway.



Iron

Interest in movement disorders is heightened by the recent ability to map the distribution of macromolecular complexes of Fe(II) in the brain with heavily T2-weighted images. This is accomplished through contrast created by the T2* effect, a local inhomogeneity in the magnetic field that dephases spin and results in loss of signal [1]. This effect is different from the paramagnetic effect of smaller soluble contrast agents, such as gadolinium, and corresponds roughly with the ferric iron

This article appears in the May/June 1987 issue of AJNR and the August 1987 issue of AJR. Received July 10, 1986; accepted after revision November 20, 1986.

Presented at the annual meeting of the American Society of Neuroradiology, San Diego, January 1986.

This work was supported in part by National Institutes of Health grant CA 26681 and by Philips Medical Systems, Inc.

¹Department of Radiology, Division of Neuro-radiology, Columbia Presbyterian Medical Center, New York, NY 10032.

²Present address: 10 Medical Arts Square, Suite 1E, 70705; Address reprint requests to J. N. Rutledge.

³Department of Pathology, Division of Neuro-radiology, Columbia Presbyterian Medical Center, New York, NY 10032.

⁴Department of Neurology, Division of Movement Disorders, Columbia Presbyterian Medical Center, New York, NY 10032.

AJNR 8:397-411, May/June 1987
0195-4108/87/0803-0397
© American Society of Neuroradiology

Radiation Effects on Cerebral White Matter: MR Evaluation

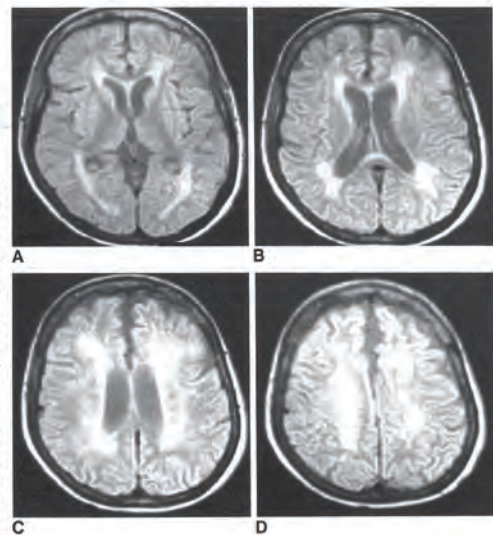
Jay S. Tsuruda^{1,2}
Keith E. Kortman^{1,3}
William G. Bradley^{1,3}
Donald C. Wheeler¹
William Van Dalsen¹
Thomas P. Bradley¹

The purpose of this study was to evaluate the white-matter changes associated with external beam radiation for a wide variety of central nervous system tumors reviewed. Moderately T2-weighted spin-echo images with a 2000-msec repeat and 56-msec-echo time were analyzed for white-matter abnormalities without in the patient's history. These were correlated with radiation dose, port, and time since completion of therapy, and then compared with an age-matched control 180 patients with nonirradiated, space-occupying, intracranial lesions. Radiatic lesions were characterized as symmetric, high-signal foci in the periventricular matter. Relative sparing of the posterior horns, basal ganglia, and internal capsule noted. In patients older than 20 years, these changes paralleled those seen in but were more prevalent ($p < .005$). In 25 patients with sequential MR scan findings remained stable. In those patients with limited treatment fields, for pituitary adenomas, no statistical differences were seen between radiation-treated and nonradiated groups. Cerebral white-matter changes that mimic deep white-matter are frequently seen in response to therapeutic radiation. There is an incidence of radiation effects, becoming more marked in older patients. MR must consider the neuropathologic consequences of therapeutic radiation, white demyelination, microvascular occlusion, and blood-brain barrier breakdown.

The goal of therapeutic radiology is to provide a sufficient dose to the nervous system (CNS) tumors without affecting adjacent healthy tissue. therapeutic regimens have been implemented, long-term effects of neurotoxicity of the surviving patients have been recognized [1-3]. A spectrum of CNS changes has been noted on CT including atrophy, decreased attenuation of the deep white matter, and rarely focal, enhancing radionecrosis [4-7]. The fibro-neurotoxicity have been correlated with clinical findings in both patients and experiments [1]. More recently, similar findings of radiotherapy-related changes to the brain have been described with MR [8-10]. Of interest, is the formation white-matter periventricular foci characterized by prolonged T1 and T2 ρ times compared with normal white matter [10] in a pattern suggestive demyelination or ischaemia. Both can be identified readily by MR [11]; natural prevalence and severity of focal periventricular abnormalities (e.g., deep white-matter infarction) increase with age [11, 12]. These abnormalities must be considered before ascribing changes to radiotherapy. For this reason, a retrospective review of a large patient population was undertaken; MR was used to further characterize the effects of radiation on cerebral white matter with respect to age, prevalence, time of onset, and both the temporal and spatial stability of these lesions.

Materials and Methods

MR imaging was performed using a Diagnostica MT/S system operating at 0.35 T. Multiple-



This article appears in the May/June 1987 issue of AJNR and the July 1987 issue of AJR. Received August 20, 1986; accepted after revision December 18, 1986.

Presented at the annual meeting of the American Roentgen Ray Society, Washington, DC, April 1986.

¹MR Imaging Laboratory, Huntington Medical Research Institutes, 19 Park St., Pasadena, CA 91105. Address reprint requests to W. G. Bradley.

²Present address: Department of Radiology, University of California, San Francisco, CA 94143.

³Department of Radiology, Huntington Memorial Hospital, Pasadena, CA 91105.

AJNR 8:421-427, May/June 1987
0195-4108/87/0803-0421
© American Society of Neuroradiology